WILEY

Lightwave Technology

Telecommunication Systems

Govind P. Agrawal

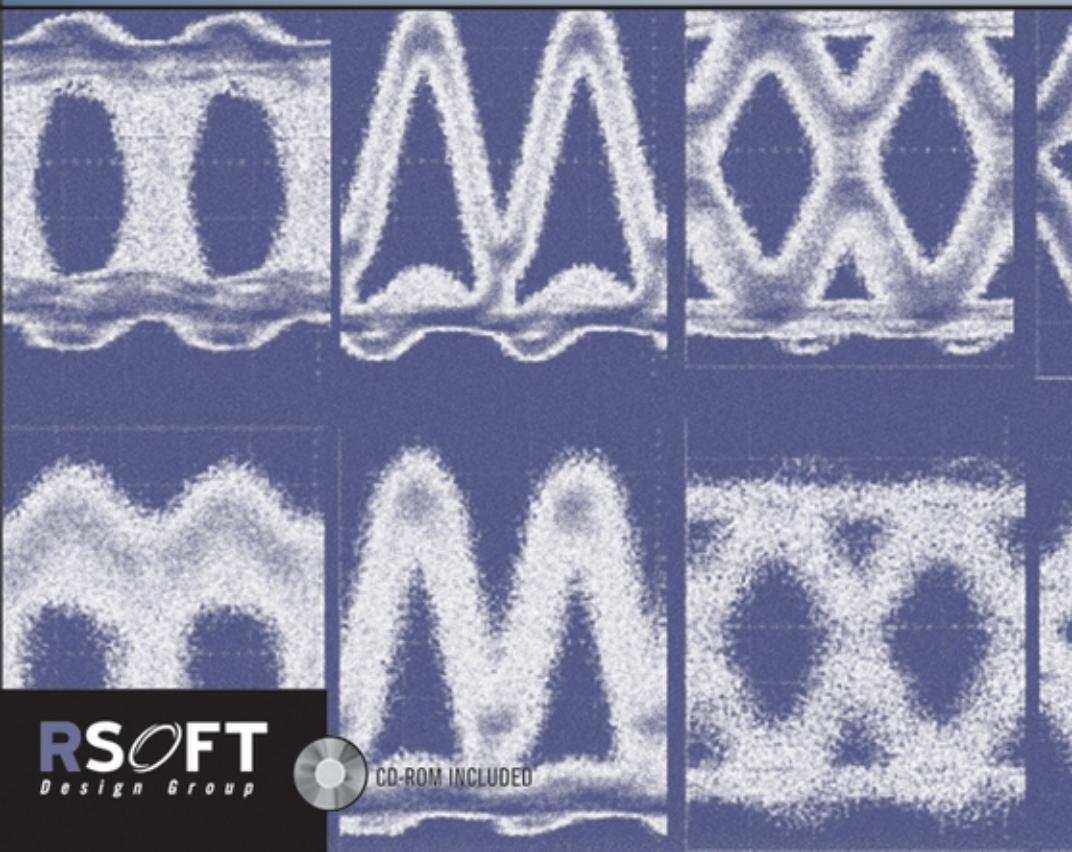

RSOFT Design Group

CD-ROM INCLUDED

LIGHTWAVE TECHNOLOGY

Telecommunication Systems

This Page Intentionally Left Blank

LIGHTWAVE TECHNOLOGY

This Page Intentionally Left Blank

LIGHTWAVE TECHNOLOGY

Telecommunication Systems

Govind P. Agrawal

The Institute of Optics
University of Rochester
Rochester, NY

A JOHN WILEY & SONS, INC., PUBLICATION

Published by John Wiley & Sons, Inc., Hoboken, New Jersey.
Published simultaneously in Canada.

Library of Congress Cataloging-in-Publication Data:

Agrawal, G. P. (Govind P.), 1951–
Lightwave technology : telecommunication systems / Govind P. Agrawal.
p. cm.
Includes bibliographical references and index.
ISBN-13 978-0-471-21572-1
ISBN-10 0-471-21572-4
1. Optical communications. 2. Electrooptics. I. Title.

TK5103.59.A39 2005
621.382'7—dc22

Printed in the United States of America

10 9 8 7 6 5 4 3 2 1

For Anne, Sipra, Caroline, and Claire

This Page Intentionally Left Blank

Contents

Preface

The term *lightwave technology* was coined as a natural extension of microwave technology and refers to the developments based on the use of light in place of microwaves. The beginnings of lightwave technology can be traced to the decade of 1960s during which significant advances were made in the fields of lasers, optical fibers, and nonlinear optics. The two important milestones were realized in 1970, the year that saw the advent of low-loss optical fibers as well as the room-temperature operation of semiconductor lasers. By 1980, the era of commercial lightwave transmission systems has arrived.

The first generation of fiber-optic communication systems debuting in 1980 operated at a meager bit rate of 45 Mb/s and required signal regeneration every 10 km or so. However, by 1990 further advances in lightwave technology not only increased the bit rate to 10 Gb/s (by a factor of 200) but also allowed signal regeneration after 80 km or more. The pace of innovation in all fields of lightwave technology only quickened during the 1990s, as evident from the development and commercialization of erbium-doped fiber amplifiers, fiber Bragg gratings, and wavelength-division-multiplexed lightwave systems. By 2001, the capacity of commercial terrestrial systems exceeded 1.6 Tb/s. At the same time, the capacity of transoceanic lightwave systems installed worldwide exploded. A single transpacific system could transmit information at a bit rate of more than 1 Tb/s over a distance of 10,000 km without any signal regeneration. Such a tremendous improvement was possible only because of multiple advances in all areas of lightwave technology. Although commercial development slowed down during the economic downturn that began in 2001, it was showing some signs of recovery by the end of 2004, and lightwave technology itself has continued to grow.

The primary objective of this two-volume book is to provide a comprehensive and up-to-date account of all major aspects of lightwave technology. The first volume, subtitled *Components and Devices*, is devoted to a multitude of silica- and semiconductor-based optical devices. The second volume, subtitled *Telecommunication Systems*, deals with the design of modern lightwave systems; the acronym LT1 is used to refer to the material in the first volume. The first two introductory chapters cover topics such as modulation formats and multiplexing techniques employed to form an optical bit stream. Chapters 3 through 5 consider the degradation of such an optical signal through loss, dispersion, and nonlinear effects during its transmission through optical fibers and how they affect the system performance. Chapters 6 through 8 focus on the management of the degradation caused by noise, dispersion, and fiber nonlinearity. Chapters 9

and 10 cover the engineering issues related to the design of WDM systems and optical networks.

This text is intended to serve both as a textbook and a reference monograph. For this reason, the emphasis is on physical understanding, but engineering aspects are also discussed throughout the text. Each chapter also includes selected problems that can be assigned to students. The book's primary readership is likely to be graduate students, research scientists, and professional engineers working in fields related to lightwave technology. An attempt is made to include as much recent material as possible so that students are exposed to the recent advances in this exciting field. The reference section at the end of each chapter is more extensive than what is common for a typical textbook. The listing of recent research papers should be helpful to researchers using this book as a reference. At the same time, students can benefit from this feature if they are assigned problems requiring reading of the original research papers. This book may be useful in an upper-level graduate course devoted to optical communications. It can also be used in a two-semester course on optoelectronics or lightwave technology.

A large number of persons have contributed to this book either directly or indirectly. It is impossible to mention all of them by name. I thank my graduate students and the students who took my course on optical communication systems and helped improve my class notes through their questions and comments. I am grateful to my colleagues at the Institute of Optics for numerous discussions and for providing a cordial and productive atmosphere. I thank, in particular, René Essiambre and Qiang Lin for reading several chapters and providing constructive feedback. Last, but not least, I thank my wife Anne and my daughters, Sipra, Caroline, and Claire, for their patience and encouragement.

Govind P. Agrawal

Rochester, NY
December 2004

This Page Intentionally Left Blank

Chapter 1

Introduction

Lightwave systems represent a natural extension of microwave communication systems inasmuch as information is transmitted over an electromagnetic carrier in both types of systems. The major difference from a conceptual standpoint is that, whereas carrier frequency is typically ~1 GHz for microwave systems, it increases by five orders of magnitude and is typically ~100 THz in the case of lightwave systems. This increase in carrier frequency translates into a corresponding increase in the system capacity. Indeed, whereas microwave systems rarely operate above 0.2 Gb/s, commercial lightwave systems can operate at bit rates exceeding 1 Tb/s. Although the optical carrier is transmitted in free space for some applications related to satellites and space research, terrestrial lightwave systems often employ optical fibers for information transmission. Such fiber-optic communication systems have been deployed worldwide since 1980 and constitute the backbone behind the Internet. One can even claim that the lightwave technology together with advances in microelectronics was responsible for the advent of the "information age" by the end of the twentieth century. The objective of this book is to describe the physics and engineering behind various kinds of lightwave systems. The purpose of this introductory chapter is to present the basic concepts together with the background material. Section 1.1 provides a historical perspective on the development of lightwave communication systems. Section 1.2 focuses on the building blocks of such a system and describes briefly the three components known as optical transmitters, fibers, and receivers. Section 1.3 covers the concepts such as analog and digital signals and the technique used to convert between the two. Channel multiplexing in the time and frequency domains is described in Section 1.4 where we also discuss the technique of code-division multiplexing.

1.1 Evolution of Lightwave Systems

Microwave communication systems were commercialized during the decade of 1940s, and carrier frequencies of up to 4 GHz were used by 1947 for a commercial system operating between New York and Boston [1]. During the next 25 years or so, microwave as well as coaxial systems evolved considerably. Although such systems were able to

operate at bit rates of up to 200 Mb/s or so, they were approaching the fundamental limits of the technology behind them. It was realized in the 1950s that an increase of several orders of magnitude in the system capacity should be possible if optical waves were used in place of microwaves as the carrier of information. However, neither a coherent optical source, nor a suitable transmission medium, was available during the 1950s. The invention of the laser solved the first problem [2]. Attention was then focused on finding ways of transmitting laser light over long distances. In contrast with the microwaves, optical beams suffer from many problems when they are transmitted through the atmosphere. Many ideas were advanced during the 1960s to solve these problems [3], the most noteworthy being the idea of light confinement using a sequence of gas lenses [4].

In a parallel but unrelated development, optical glass fibers were developed during the 1950s, mainly from the standpoint of medical applications [5]–[9]. It was suggested in 1966 that optical fibers might be the best choice for transporting optical signals in lightwave systems [10] as they are capable of guiding the light in a manner similar to the guiding of electrons in copper wires. The main problem was their high losses since fibers available during the 1960s had losses in excess of 1,000 dB/km.

A breakthrough occurred in 1970 when fiber losses were reduced to below 20 dB/km in the wavelength region near 1 μm using a novel fabrication technique [11]. At about the same time, GaAs semiconductor lasers, operating continuously at room temperature, were demonstrated [12]. The simultaneous availability of *compact* optical sources and *low-loss* optical fibers led to a worldwide effort for developing fiber-optic communication systems during the 1970s [13]. After a successful Chicago field trial in 1977, terrestrial lightwave systems became available commercially beginning in 1980 [14]–[16]. Figure 1.1 shows the increase in the capacity of lightwave systems realized after 1980 through several generations of development. As seen there, the commer-

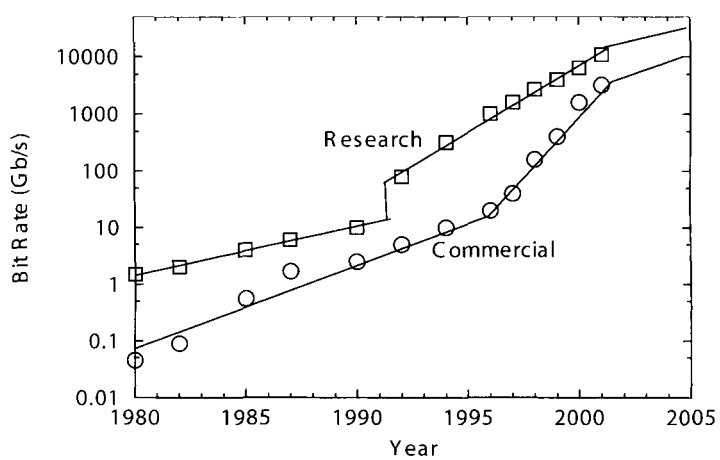

Figure 1.1: Increase in the capacity of lightwave systems realized after 1980. Commercial systems (circles) follow research demonstrations (squares) with a few-year lag. The change in the slope after 1992 is due to the advent of WDM technology.

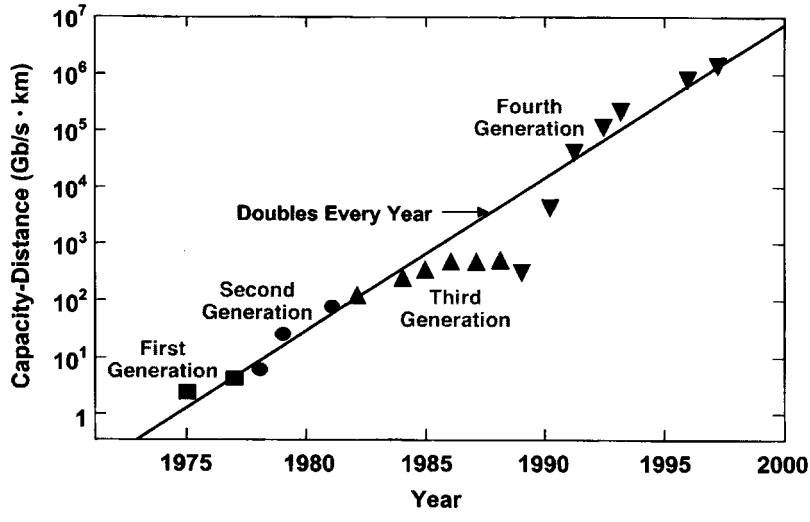

Figure 1.2: Increase in the *BL* product from 1975 to 2000 through four generations of lightwave systems. Different symbols are used for successive generations. (After Ref. [17]; ©2000 IEEE.)

cial deployment of lightwave systems followed the research and development phase closely. The progress has indeed been rapid as evident from an increase in the system capacity by a factor of 100,000 over a period of less than 25 years. The saturation of the capacity after 2000 is partly due to the economic slowdown experienced by the lightwave industry (known popularly as the bursting of the telecom bubble).

The distance over which a lightwave system can transmit data without introducing errors is also important while judging the system performance. Since signal is degraded during transmission, most lightwave systems require periodic regeneration of the optical signal through devices known as "repeaters." A commonly used figure of merit for any communication system is the *bit rate–distance product*, *BL*, where *B* is the bit rate and *L* is the repeater spacing. The research phase of lightwave systems started around 1975. The first-generation systems operated in the near infrared at a wavelength close to 800 nm and used GaAs semiconductor lasers as an optical source. They were able to work at a bit rate of 45 Mb/s and allowed repeater spacings of up to 10 km. The 10-km value may seem too small from a modern perspective, but it was 10 times larger than the 1-km spacing prevalent at that time in coaxial systems.

The enormous progress realized over the 25-year period extending from 1975 to 2000 can be grouped into four distinct generations. Figure 1.2 shows the increase in the *BL* product over this time period as quantified through various laboratory experiments [17]. The straight line corresponds to a doubling of the *BL* product every year. In every generation, *BL* increases initially but then saturates as the technology matures. Each new generation brings a fundamental change that helps to improve the system performance further.

It was clear during the 1970s that the repeater spacing could be increased considerably by operating the lightwave system in the wavelength region near 1.3 μm, where

fiber losses were below 0.5 dB/km. Furthermore, optical fibers exhibit minimum dispersion in this wavelength region. This realization led to a worldwide effort for the development of semiconductor lasers and detectors operating near 1.3 μm. The second generation of fiber-optic communication systems became available in the early 1980s, but the bit rate of early systems was limited to below 100 Mb/s because of dispersion in multimode fibers [18]. This limitation was overcome by the use of *single-mode* fibers. A laboratory experiment in 1981 demonstrated transmission at 2 Gb/s over 44 km of single-mode fiber [19]. The introduction of commercial systems soon followed. By 1987, second-generation lightwave systems, operating at bit rates of up to 1.7 Gb/s with a repeater spacing of about 50 km, were commercially available.

The repeater spacing of the second-generation lightwave systems was limited by fiber losses at the operating wavelength of 1.3 μm (typically 0.5 dB/km). Losses of silica fibers become minimum near 1.55 μm. Indeed, a 0.2-dB/km loss was realized in 1979 in this spectral region [20]. However, the introduction of third-generation lightwave systems operating at 1.55 μm was considerably delayed by a relatively large dispersion of standard optical fibers in the wavelength region near 1.55 μm. The dispersion problem can be overcome either by using *dispersion-shifted* fibers designed to have minimum dispersion near 1.55 μm or by limiting the laser spectrum to a single longitudinal mode. Both approaches were followed during the 1980s. By 1985, laboratory experiments indicated the possibility of transmitting information at bit rates of up to 4 Gb/s over distances in excess of 100 km [21]. Third-generation lightwave systems operating at 2.5 Gb/s became available commercially in 1990. Such systems are capable of operating at a bit rate of up to 10 Gb/s [22]. The best performance is achieved using dispersion-shifted fibers in combination with distributed-feedback (DFB) semiconductor lasers.

A drawback of third-generation 1.55-μm systems was that the optical signal had to be regenerated periodically using electronic repeaters after 60 to 70 km of transmission because of fiber losses. Repeater spacing could be increased by 10 to 20 km using homodyne or heterodyne detection schemes because their use requires less power at the receiver. Such *coherent* lightwave systems were studied during the 1980s and their potential benefits were demonstrated in many system experiments [23]. However, commercial introduction of such systems was postponed with the advent of fiber amplifiers in 1989.

The fourth generation of lightwave systems makes use of *optical amplification* for increasing the repeater spacing and of *wavelength-division multiplexing* (WDM) for increasing the bit rate. As evident from different slopes in Figure 1.1 before and after 1992, the advent of the WDM technique started a revolution that resulted in doubling of the system capacity every 6 months or so and led to lightwave systems operating at a bit rate of 10 Tb/s by 2001. In most WDM systems, fiber losses are compensated periodically using erbium-doped fiber amplifiers spaced 60 to 80 km apart. Such amplifiers were developed after 1985 and became available commercially by 1990. A 1991 experiment showed the possibility of data transmission over 21,000 km at 2.5 Gb/s, and over 14,300 km at 5 Gb/s, using a recirculating-loop configuration [24]. This performance indicated that an amplifier-based, all-optical, submarine transmission system was feasible for intercontinental communication. By 1996, not only transmission over 11,300 km at a bit rate of 5 Gb/s had been demonstrated by using actual submarine

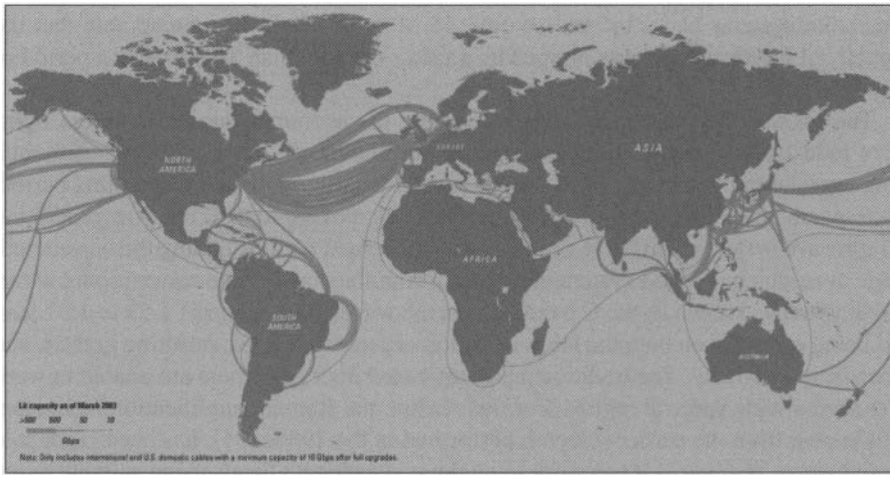

Figure 1.3: International network of submarine fiber-optic cables in 2004. (*Source:* TeleGeography Research Group, PriMetrica, Inc. ©2004.)

cables [25], but commercial transatlantic and transpacific cable systems also became available. Since then, a large number of submarine lightwave systems have been deployed worldwide.

Figure 1.3 shows the international network of submarine fiber-optic cables as it existed in 2004. The 27,000-km fiber-optic link around the globe (known as FLAG) became operational in 1998, linking many Asian and European countries [26]. Another major lightwave system, known as *Africa One*, was operational by 2000; it circles the African continent and covers a total transmission distance of about 35,000 km [27]. Several WDM systems were deployed across the Atlantic and Pacific oceans from 1998 to 2001 in response to the Internet-induced increase in the data traffic; they have increased the total capacity by orders of magnitudes [28]. One can indeed say that the fourth generation of lightwave systems led to an information revolution that was fuelled by the advent of the Internet.

At the dawn of the twenty-first century, the emphasis of lightwave systems was on increasing the system capacity by transmitting more and more channels through the WDM technique. With increasing WDM signal bandwidth, it was often not possible to amplify all channels using a single amplifier. As a result, new kinds of amplification schemes were explored for covering the spectral region extending from 1.45 to 1.62 μm. This approach led in 2000 to a 3.28-Tb/s experiment in which 82 channels, each operating at 40 Gb/s, were transmitted over 3,000 km, resulting in a *BL* product of almost 10,000 (Tb/s)-km. Within a year, the system capacity could be increased to nearly 11 Tb/s (273 WDM channels, each operating at 40 Gb/s) but the transmission distance was limited to 117 km [29]. By 2003, in a record experiment 373 channels, each operating at 10 Gb/s, were transmitted over 11,000 km, resulting in a *BL* product of more than 41,000 (Tb/s)-km [30]. On the commercial side, terrestrial systems with the capacity of 1.6 Tb/s were available by the end of 2000. Given that the first-

generation systems had a bit rate of only 45 Mb/s in 1980, it is remarkable that the capacity of lightwave systems jumped by a factor of more than 30,000 over a period of only 20 years.

The pace slowed down considerably during the economic turndown in the lightwave industry that began in 2000 and was not completely over in 2004. Although commercial deployment of new lightwave systems virtually halted during this period, the research phase has continued worldwide and is moving toward the fifth generation of lightwave systems. This new generation is concerned with extending the wavelength range over which a WDM system can operate simultaneously. The conventional wavelength window, known as the C band, covers the wavelength range of 1.53 to 1.57 μm. It is being extended on both the long- and short-wavelength sides, resulting in the L and S bands, respectively. The traditional erbium-based fiber amplifiers are unable to work over such a wide spectral region. For this reason, the Raman amplification technique, well known from the earlier research performed in the 1980s [31], has been readopted for lightwave systems as it can work in all three wavelength bands using suitable pump lasers [32]–[35]. A new kind of fiber, known as the *dry fiber*, has been developed with the property that fiber losses are small over the entire wavelength region extending from 1.30 to 1.65 μm [36]. Research is also continuing in several other directions to realize optical fibers with suitable loss and dispersion characteristics. Most noteworthy are photonic-crystal fibers whose dispersion can be changed drastically using an array of holes within the cladding layer [37]–[41]. Moreover, if the central core itself is in the form of a hole, light can be transmitted through air while guided by the photonic-crystal structure of the cladding [42]–[46]. Such fibers have the potential of transmitting optical signal with virtually no losses and little nonlinear distortion!

The fifth-generation systems also attempt to enhance the spectral efficiency by adopting new modulation formats, while increasing the bit rate of each WDM channel. Starting in 1996, many experiments used channels operating at 40 Gb/s [47]–[54], and by 2003 such 40-Gb/s lightwave systems had reached the commercial stage. At the same time, the research phase has moved toward WDM systems with 160 Gb/s per channel [55]–[58]. Such systems require an extremely careful management of fiber dispersion. Novel techniques capable of compensating chromatic and polarization-mode dispersions in a dynamic fashion are being developed to meet such challenges. An interesting approach is based on the concept of *optical solitons*—pulses that preserve their shape during propagation in a lossless fiber by counteracting the effect of dispersion through the fiber nonlinearity. Although the basic idea was proposed [59] as early as 1973, it was only in 1988 that a laboratory experiment demonstrated the feasibility of data transmission over 4,000 km by compensating fiber losses through Raman amplification [31]. Since then, many system experiments have demonstrated the eventual potential of soliton communication systems [60]. Starting in 1996, the WDM technique was also used for solitons in combination with dispersion-management and Raman amplification schemes [61]–[64]. Many new modulation formats are being proposed for advancing the state of the art. Even though the lightwave communication technology is barely 25 years old, it has progressed rapidly and has reached a certain stage of maturity. Many books were published during the 1990s on topics related to optical communications and WDM networks, and this trend is continuing in the twenty-first century [65]–[80].

Figure 1.4: A generic optical communication system.

1.2 Components of a Lightwave System

As mentioned earlier, lightwave systems differ from microwave systems only in the frequency range of the carrier wave used to carry the information. Both types of systems can be divided into three major parts. Figure 1.4 shows a generic optical communication system consisting of an optical transmitter, a communication channel, and an optical receiver. Lightwave systems can be classified into two broad categories depending on the nature of the communication channel. The optical signal propagates unguided in air or vacuum for some applications [81]. However, in the case of guided lightwave systems, the optical beam emitted by the transmitter remains spatially confined inside an optical fiber. This text focuses exclusively on such fiber-optic communication systems.

1.2.1 Optical Transmitters

The role of optical transmitters is to convert an electrical signal into an optical form and to launch the resulting optical signal into the optical fiber acting as a communication channel. Figure 1.5 shows the block diagram of an optical transmitter. It consists of an optical source, a modulator, and electronic circuits used to power and operate the two devices. Semiconductor lasers or light-emitting diodes are used as optical sources because of their compact nature and compatibility with optical fibers. The source emits light in the form of a continuous wave at a fixed wavelength, say, λ_0. The carrier frequency ν_0 is related to this wavelength as $\nu_0 = c/\lambda_0$, where c is the speed of light in vacuum.

In modern lightwave systems, ν_0 is chosen from a set of frequencies standardized by the International Telecommunication Union (ITU). It is common to divide the spectral region near 1.55 μm into two bands known as the conventional or C band

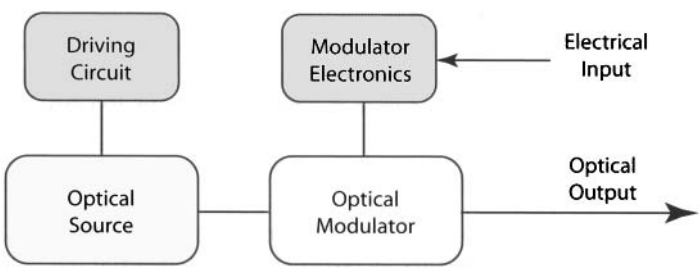

Figure 1.5: Block diagram of an optical transmitter.

and the long-wavelength or L band. The C band covers carrier frequencies from 191 to 196 THz (in steps of 50 GHz) and spans roughly the wavelength range of 1.53 to 1.57 μm. In contrast, L band occupies the range 1.57 to 1.61 μm and covers carrier frequencies from 186 to 191 THz, again in steps of 50 GHz. The short-wavelength or S band covering the wavelength region from 1.48 to 1.53 μm may be used for future lightwave systems as the demand for capacity grows. It is important to realize that the source wavelength needs to be set precisely for a given choice of the carrier frequency. For example, a channel operating at 193 THz requires an optical source emitting light at a wavelength of 1.5533288 μm if we use the precise value c = 299,792,458 km/s for the speed of light in vacuum.

Before the source light can be launched into the communication channel, the information that needs to be transmitted should be imposed on it. This step is accomplished by an optical modulator in Figure 1.5. The modulator uses the data in the form of an electrical signal to modulate the optical carrier. Although an external modulator is often needed at high bit rates, it can be dispensed with at low bit rates using a technique known as direct modulation. In this technique, the electrical signal representing information is applied directly to the driving circuit of the semiconductor optical source, resulting in the modulated source output. Such a scheme simplifies the transmitter design and is generally more cost-effective. In both cases, the modulated light is coupled into a short piece of fiber (called a pigtail) with a connector attached to its other end. Chapter 2 provides more details on how the optical signal is generated within an optical transmitter.

An important design parameter is the average optical power launched into the communication channel. Clearly, it should be as large as possible to enhance the signal-to-noise ratio (SNR) at the receiver end. However, the onset of various *nonlinear effects* limits how much power can be launched at the transmitter end. The launched power is often expressed in "dBm" units with 1 mW acting as the reference level. The general definition is (see Appendix A)

$$\text{power (dBm)} = 10\log_{10}\left(\frac{\text{power}}{1\text{ mW}}\right). \tag{1.2.1}$$

Thus, 1 mW is 0 dBm, but 1 μW corresponds to -30 dBm. The launched power is rather low (less than -10 dBm) for light-emitting diodes but semiconductor lasers can launch power levels exceeding 5 dBm.

Although light-emitting diodes are useful for some low-end applications related to local-area networking and computer-data transfer, most lightwave systems employ semiconductor lasers as optical sources. The bit rate of optical transmitters is often limited by electronics rather than by the semiconductor laser itself. With proper design, optical transmitters can be made to operate at a bit rate of up to 40 Gb/s.

1.2.2 Communication Channel

The role of a communication channel is to transport the optical signal from transmitter to receiver with as little loss in quality as possible. Most terrestrial lightwave systems employ optical fibers as the communication channel because they can transmit light with losses as small as 0.2 dB/km when the carrier frequency lies in the spectral region

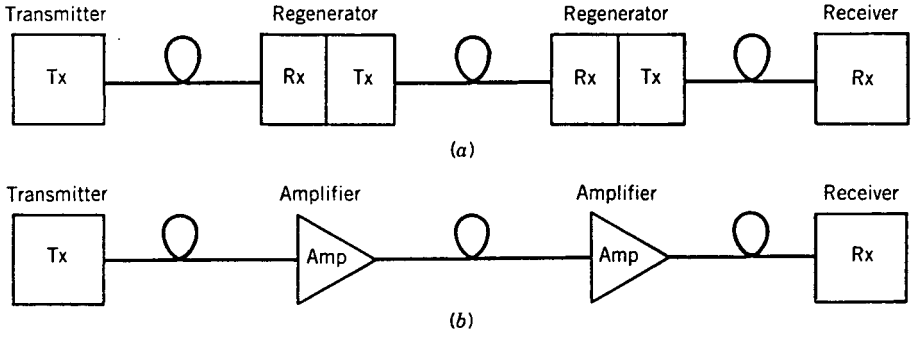

Figure 1.6: (a) Regenerators or (b) optical amplifiers used periodically for compensating fiber losses in a lightwave system; Tx and Rx stand for transmitter and receiver, respectively.

near 1.5 μm. Even then, optical power reduces to only 1% after 100 km. For long-haul lightwave systems, it is common to employ optical amplifiers or regenerators to compensate for fiber losses and boost the signal power back to its original level. Figure 1.6 shows how amplifiers or regenerators can be cascaded to transmit optical signal over distances exceeding hundreds and even thousands of kilometers. Fiber losses play an important role in such systems because they determine the repeater or amplifier spacing. The issue of loss management is discussed in Section 3.2.

Ideally, a communication channel should not degrade the quality of the optical signal launched into it. In practice, optical fibers broaden light pulses transmitted through them through modal or chromatic dispersion. As discussed later, if optical pulses spread significantly outside their allocated bit slot, the transmitted signal is degraded so severely that it becomes impossible to recover the original signal with high accuracy. The dispersion problem is most severe for multimode fibers. It is for this reason that most modern lightwave systems employ single-mode fibers. Chromatic dispersion still leads to pulse broadening but its impact can be reduced by controlling the spectral width of the optical source or by employing a dispersion-management technique. We discuss in Section 3.3 how an optical signal is affected by fiber dispersion.

A third source of signal distortion results from the nonlinear effects related to the intensity dependence of the refractive index of silica. Although most nonlinear effects are relatively weak for silica fibers, they can accumulate to significant levels when many optical amplifiers are cascaded in series to form a long-haul system. Nonlinear effects are especially important for undersea lightwave systems for which the total fiber length can approach thousands of kilometers. Chapter 4 focuses on the impact of several nonlinear effects that affect the performance of modern lightwave systems.

1.2.3 Optical Receivers

An *optical receiver* converts the optical signal received at the output end of the fiber link back into the original electrical signal. Figure 1.7 shows the main components of an optical receiver. Optical signal arriving at the receiver is first directed toward a photodetector that converts it into an electrical form. Semiconductor photodiodes

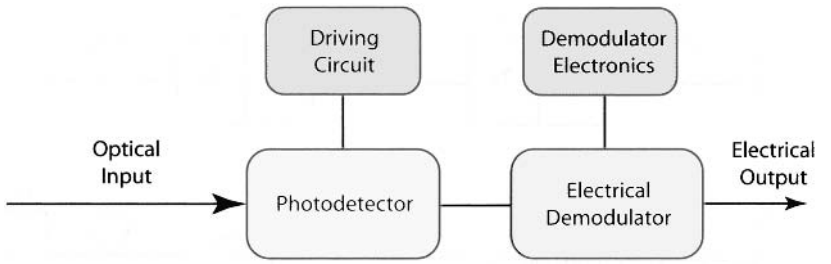

Figure 1.7: Block diagram of an optical receiver.

are used as photodetectors because of their compact size and relatively high quantum efficiency. In practice, a *p–i–n* or an avalanche photodiode produces electric current that varies with time in response to the incident optical signal. It also adds invariably some noise to the signal, thereby reducing the SNR of the electrical signal.

The role of the demodulator is to reconstruct the original electrical signal from the time-varying current in spite of the channel-induced degradation and the noise added at the receiver. The design of a demodulator depends on the nature of the signal (analog versus digital) and the modulation format used by the lightwave system. Most modern systems employ a digital binary scheme referred to as *intensity modulation with direct detection*. As discussed in Chapter 5, demodulation in the digital case is done by a decision circuit that identifies bits as 1 or 0, depending on the amplitude of the electrical signal. The accuracy of the decision circuit depends on the SNR of the electrical signal generated at the photodetector. It is important to design the receiver such that its noise level is not too high.

The performance of a digital lightwave system is characterized through the *bit-error rate* (BER). Although BER can be defined as the number of errors made per second, such a definition makes the BER bit-rate dependent. It is customary to define the BER as the average probability of identifying a bit incorrectly. For example, a BER of 10^{-9} corresponds to on average one error per billion bits. We discuss in Section 5.3 how BER can be calculated for digital signals. Most lightwave systems specify a BER of less than 10^{-9} as the operating requirement; some even require a BER as small as 10^{-15}. Depending on the system design, it is sometimes not possible to realize such low error rates at the receiver. Error-correcting codes are then used to improve the raw BER of a lightwave system.

An important parameter for any receiver is its sensitivity, defined as the minimum average optical power required to realize a BER of 10^{-9}. Receiver sensitivity depends on the SNR, which in turn depends on various noise sources that corrupt the electrical signal produced at the receiver. Even for a perfect receiver, some noise is introduced by the process of photodetection itself. This quantum noise is referred to as the *shot noise* as it has its origin in the particle nature of electrons. No practical receiver operates at the quantum-noise limit because of the presence of several other noise sources. Some of the noise sources, such as *thermal noise*, are internal to the receiver. Others originate at the transmitter or during propagation along the fiber link. For instance, any amplification of the optical signal along the transmission line with the help of optical

amplifiers introduces the so-called *amplifier noise* that has its origin in the fundamental process of spontaneous emission. Several nonlinear effects occurring within optical fibers can manifest as an additional noise that is added to the optical signal during its transmission through the fiber link. The receiver sensitivity is determined by a cumulative effect of all possible noise mechanisms that degrade the SNR at the decision circuit. In general, it also depends on the bit rate as the contribution of some noise sources (e.g., shot noise) increases in proportion to the signal bandwidth.

1.3 Electrical Signals

In any communication system, information to be transmitted is generally available as an electrical signal that may take *analog* or *digital* form [82]–[84]. Most lightwave systems employ digital signals because of their relative insensitivity to noise. This section describes the two types of signals together with the scheme used to convert an analog signal into a digital one.

1.3.1 Analog and Digital Signals

As shown schematically in Figure 1.8(a), an analog signal (e. g., electric current or voltage) varies continuously with time. Familiar examples include audio and video signals formed when a microphone converts voice or a video camera converts an image into an electrical signal. By contrast, a digital signal takes only a few discrete values. For example, printed text in this book can be thought of as a digital signal because it is composed of about 50 or so symbols (letters, numbers, punctuation marks, etc.).

The most important example of a digital signal is a *binary signal* for which only two values are possible. The modern "information age" is based entirely on binary digital signals because such signals can be manipulated electronically using electrical gates and transistors. In a binary signal, the electric current is either on or off as shown in Figure 1.8(b). These two possibilities are called bit 1 and bit 0, respectively. The word *bit* itself is a contracted form of *b*inary dig*it*. A binary signal thus takes the form of an apparently random sequence of 1 and 0 bits. Each bit lasts for a certain duration T_B, known as the bit period or *bit slot*. Since one bit of information is conveyed in a time interval T_B, the bit rate B, defined as the number of bits per second, is simply $B = T_B^{-1}$. A well-known example of digital signals is provided by the text stored on a computer's hard drive. Each letter of the alphabet together with other common symbols (decimal numerals, punctuation marks, etc.) is assigned a code number (ASCII code) in the range 0 to 127 whose binary representation corresponds to a 7-bit digital signal. The original ASCII code has been extended to represent 256 characters in the form of 8-bit bytes. Each key pressed on the keyboard of a computer generates a sequence of 8 bits that is stored as data in its memory or hard drive.

Both analog and digital signals are characterized by their bandwidth, which is a measure of the spectral contents of the signal. The *signal bandwidth* represents the range of frequencies contained within the signal. It is determined mathematically

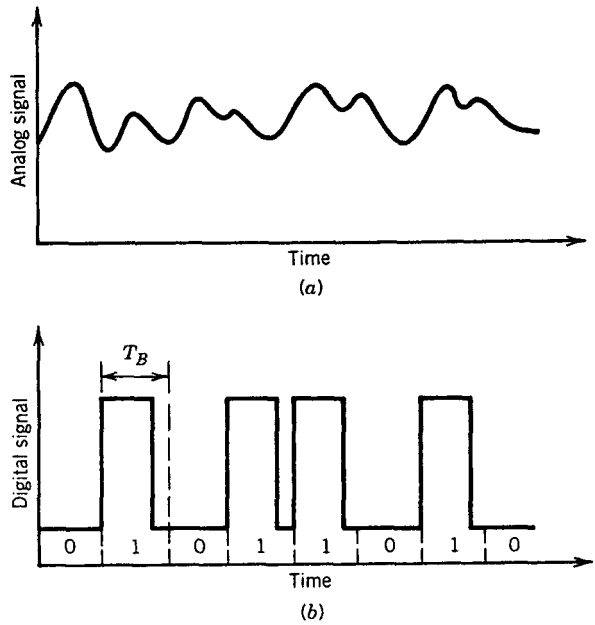

Figure 1.8: Representation of (a) an analog signal and (b) a digital signal.

through the Fourier transform $\tilde{s}(\omega)$ of a time-dependent signal $s(t)$ defined as

$$s(t) = \frac{1}{2\pi}\int_{-\infty}^{\infty} \tilde{s}(\omega)\exp(-i\omega t)\,d\omega, \tag{1.3.1}$$

where $\omega = 2\pi\nu$ is the angular frequency corresponding to the actual frequency ν (measured in hertz). The choice of sign within the exponential function is arbitrary; this text adopts the notation shown in Eq. (1.3.1). Even though the integral in this equation extends from $-\infty$ to ∞, all practical signals have a finite bandwidth, indicating that $\tilde{s}(\omega)$ vanishes outside some frequency range known as the signal bandwidth.

1.3.2 Advantages of Digital Format

A lightwave system can transmit information over optical fibers in both the analog and digital formats. However, except for a few special cases related to the transmission of cable television over fibers, all lightwave systems employ a digital format. The reason behind this choice is related to the relative ease with which a digital signal can be recovered at the receiver even after it has been distorted and corrupted with noise while being transmitted.

Figure 1.9 shows schematically why digital signals are relatively immune to noise and distortion in comparison to analog signals. As seen in part (a), the digital signal oscillates between two values, say, 0 and S, for 0 and 1 bits, respectively. Each 1 bit is in the form of a rectangular pulse at the transmitter end. During transmission, the signal is distorted by the dispersive and nonlinear effects occurring within the fiber.

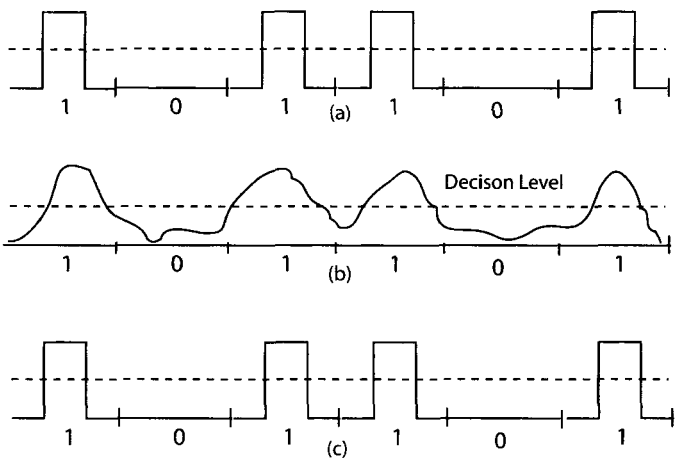

Figure 1.9: (a) Transmitted digital signal, (b) distorted and noisy electrical signal at the receiver, and (c) reconstructed digital signal. The thin solid line in the middle shows the decision level.

The addition of noise at the receiver transforms this electrical signal into that shown in part (b). In spite of the signal appearance, the decision circuit at the receiver can still decide between 1 and 0 bits correctly, and reconstruct the original bit sequence as seen in part (c). The reason is related to the fact that the bit identification does not depend on the signal shape but only on whether the signal level exceeds a threshold value at the moment of decision. One can set this threshold value in the middle at $S/2$ to provide the maximum leverage. An error will be made in identifying each 1 bit only if the original value S has dropped to below $S/2$. Similarly, a 0 bit has to acquire an amplitude $> S/2$ before an error is made. In contrast, when an analog signal is transmitted through the fiber link, the signal value $s(t)$ at any time t should not change even by 0.1% if one were to ensure fidelity of the transmitted signal because the information is contained in the actual shape of the signal. Mathematically, the SNR of the electrical signal at the receiver should exceed 30 dB for analog signals but, as we shall see in later chapters, it can be lower than 10 dB for digital signals.

The important question one should ask is whether this advantage of digital signals has a price tag attached to it. In other words, what are the consequences of transmitting the same information in a digital format? The answer is related to the signal bandwidth. A digital signal has a much wider bandwidth compared to the analog signal even when the two have the same information content. This feature can be understood from Figure 1.8 if we note that the digital signal has much more rapid temporal variations compared with an analog signal. We discuss next how much bandwidth is increased when an analog signal is converted into a digital format.

1.3.3 Analog to Digital Conversion

An analog signal can be converted into digital form by sampling it at regular intervals of time and digitizing the sampled values appropriately [82]–[84]. Figure 1.10 shows

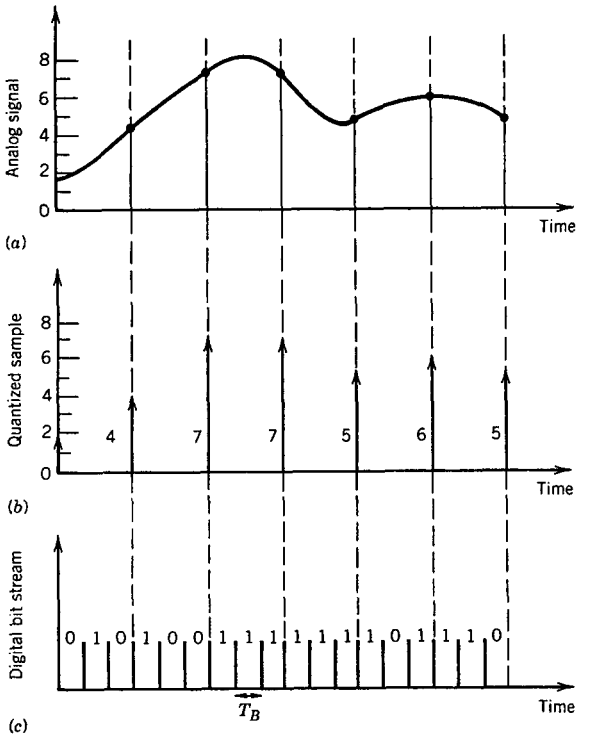

Figure 1.10: Three steps of (a) sampling, (b) quantization, and (c) coding required for converting an analog signal into a binary digital signal.

schematically the three main steps involved in the conversion process.

The first step requires sampling of the analog signal at a rate fast enough that no information is lost. The sampling rate depends on the bandwidth Δf of the analog signal. According to the *sampling theorem* [85], a bandwidth-limited signal can be fully represented by discrete samples, without any loss of information, provided sampling frequency f_s satisfies the *Nyquist criterion* [86] $f_s \geq 2\Delta f$. The sampled values can be anywhere in the range $0 \leq A \leq A_{\max}$, where $A_{\max}$ is the maximum amplitude of the given analog signal. We have assumed for simplicity that the minimum value of the signal is zero; this can always be realized by a simple scaling of the signal.

The second step involves quantization of the sampled values. For this purpose, $A_{\max}$ is divided into M discrete intervals (not necessarily equally spaced). Each sampled value is quantized to correspond to one of these discrete values. Clearly, this procedure adds noise, known as the *quantization noise*, that adds to the noise already present in the analog signal. The effect of quantization noise can be minimized by choosing the number of discrete levels such that $M > A_{\max}/A_N$, where A_N is the root-mean-square (RMS) noise level of the analog signal. The ratio $A_{\max}/A_N$ is called the *dynamic range* and is related to the SNR of the analog signal by the relation

$$\text{SNR} = 20 \log_{10}(A_{\max}/A_N), \tag{1.3.2}$$

where SNR is expressed in decibel (dB) units. Any ratio R can be converted into decibels with the general definition $R(\text{indB}) = 10 \log_{10} R$ (see Appendix A). Equation (1.3.2) contains a factor of 20 in place of 10 because the SNR for electrical signals is defined with respect to the electrical power, whereas A represents either electric current or voltage.

The last step involves conversion of the quantized sampled values into a digital bit stream consisting of 0 and 1 bits using a suitable coding technique. In one scheme, known as *pulse-position modulation*, pulse position within the bit slot is a measure of the sampled value. In another, known as *pulse-duration modulation*, the pulse width is varied from bit to bit in accordance with the sampled value. These two techniques are rarely used in practical lightwave systems as it is difficult to maintain the pulse position or pulse width to high accuracy during propagation inside an optical fiber. The coding technique used almost universally is known as *pulse-code modulation* (PCM). A binary code is used to convert each sampled value into a string of 1 and 0 bits. The number of bits m needed to code each sample is related to the number of quantized signal levels M by the relation

$$M = 2^m \quad \text{or} \quad m = \log_2 M. \tag{1.3.3}$$

The bit rate associated with the PCM digital signal is thus given by

$$B = m f_s \geq (2\Delta f) \log_2 M, \tag{1.3.4}$$

where the Nyquist criterion, $f_s \geq 2\Delta f$, was used. By noting that $M > A_{\max}/A_N$ and using Eq. (1.3.2) together with $\log_2 10 \approx 3.33$, we obtain

$$B > (\Delta f/3)\,\text{SNR}, \tag{1.3.5}$$

where the SNR is expressed in decibel units.

Equation (1.3.5) provides the minimum bit rate required for digital representation of an analog signal of bandwidth Δf with a specific SNR. Typically, the SNR exceeds 30 dB for analog signals, and the required bit rate is more than $10\,\Delta f$. Clearly, there is a considerable increase in the bandwidth when an analog signal is converted into a digital format. Despite this increase, the digital format is almost always used for lightwave systems. This choice is made because, as discussed earlier in this section, a digital bit stream is relatively immune to noise and distortion occurring during its transmission through the communication channel, resulting in superior system performance. Lightwave systems offer such an enormous increase in the system capacity compared with microwave systems that some bandwidth can be traded for an improved performance.

As an illustration of Eq. (1.3.5), consider digital conversion of an audio signal generated during a telephone conversation. Such analog audio signals contain frequencies in the range of 0.3 to 3.4 kHz (bandwidth $\Delta f = 3.1$ kHz) and have a SNR of about 30 dB. Equation (1.3.5) indicates that the bit rate B would exceed 31 kb/s if such an audio signal is converted into a digital format. In practice, each digital audio channel operates at 64 kb/s. The analog signal is sampled at intervals of 125 μs (sampling rate $f_s = 8$ kHz), and each sample is represented by 8 bits. The required bit rate for a digital video signal is higher by more than a factor of 1,000. The analog television signal has a bandwidth $\sim$4 MHz with a SNR of about 50 dB. The minimum bit rate from Eq. (1.3.5) is 66 Mb/s. In practice, a digital video signal requires a bit rate of 100 Mb/s or more unless it is compressed by using a standard format (such as the MPEG format).

1.4 Channel Multiplexing

As seen in the preceding section, a digital voice channel operates at a bit rate of 64 kb/s. Most lightwave systems are capable of transmitting information at a bit rate of more than 1 Gb/s, and the capacity of the fiber channel itself exceeds 10 Tb/s. To utilize the system capacity fully, it is necessary to transmit many channels simultaneously over the same fiber link. This can be accomplished through several multiplexing techniques; the two most common ones are known as *time-division* multiplexing (TDM) and *frequency-division* multiplexing (FDM). A third scheme, used often for cellular phones and called *code-division* multiplexing (CDM), can also be used for lightwave systems. We discuss all three schemes in this section.

1.4.1 Time-Division Multiplexing

In the case of TDM, bits associated with different channels are interleaved in the time domain to form a composite bit stream. For example, the bit slot is about 15 μs for a single voice channel operating at 64 kb/s. Five such channels can be multiplexed through TDM if bit streams of successive channels are interleaved by delaying them 3 μs. Figure 1.11(a) shows the resulting bit stream schematically at a composite bit rate of 320 kb/s. TDM is readily implemented for digital signals and is commonly used worldwide for telecommunication networks.

The concept of TDM has been used to form *digital hierarchies*. In North America and Japan, the first level corresponds to multiplexing of 24 voice channels with a composite bit rate of 1.544 Mb/s (hierarchy DS-1), whereas in Europe 30 voice channels are multiplexed, resulting in a composite bit rate of 2.048 Mb/s. The bit rate of the multiplexed signal is slightly larger than the simple product of 64 kb/s with the number of channels because of extra control bits that are added for separating (demultiplexing) the channels at the receiver end. The second-level hierarchy is obtained by multiplexing four DS-1 channels in the time domain. This resulted in a bit rate of 6.312 Mb/s (hierarchy DS-2) for systems commercialized in North America and Japan. At the next level (hierarchy DS-3), seven DS-2 channels were multiplexed through TDM, resulting in a bit rate of close to 45 Mb/s. The first generation of commercial lightwave systems (known as FT–3, short for fiber transmission at DS-3) operated at this bit rate. The same procedure was continued to obtain higher-level hierarchies. For example, at the fifth level of hierarchy, the bit rate was 417 Mb/s for lightwave systems commercialized in North America but 565 Mb/s for systems sold in Europe.

The lack of an international standard in the telecommunication industry during the 1980s led to the advent of a new standard, first called the *synchronous optical network* (SONET) and later termed the *synchronous digital hierarchy* or SDH [87]–[89]. This international standard defines a synchronous frame structure for transmitting TDM digital signals. The basic building block of the SONET has a bit rate of 51.84 Mb/s. The corresponding optical signal is referred to as OC-1, where OC stands for optical carrier. The basic building block of the SDH has a bit rate of 155.52 Mb/s and is referred to as STM-1, where STM stands for a *synchronous transport module*. A useful feature of the SONET and SDH is that higher levels have a bit rate that is an exact multiple of the basic bit rate. Table 1.1 lists the correspondence between SONET and SDH bit

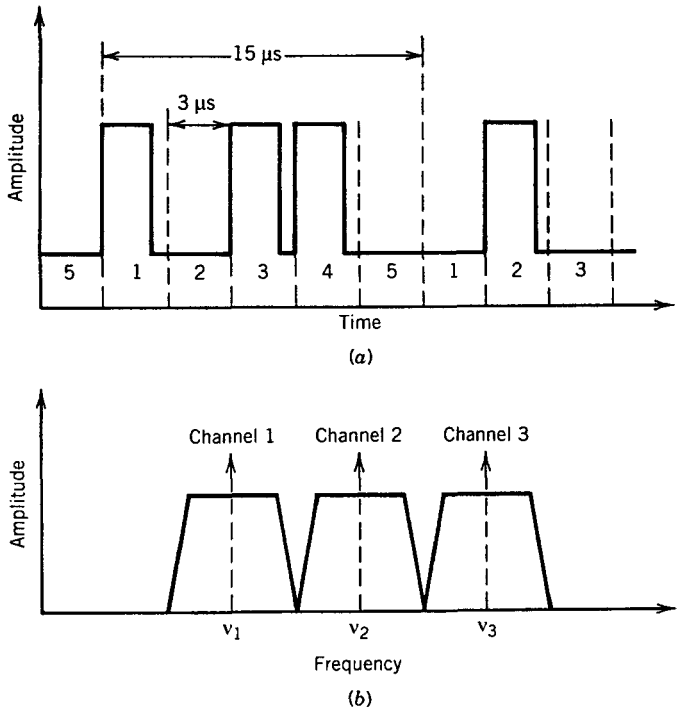

Figure 1.11: (a) Time-division multiplexing of five digital voice channels operating at 64 kb/s; (b) frequency-division multiplexing of three analog signals.

rates for several levels. The SDH provides an international standard that has been well adopted. Indeed, lightwave systems operating at the STM-64 level ($B \approx 10$ Gb/s) have been available since 1995 [22]. Commercial STM-256 (OC-768) systems operating near 40 Gb/s became available around 2002. Table 1.2 lists the operating characteristics of terrestrial systems developed since 1980. The last column shows the number of voice channels that can be transmitted simultaneously over the same fiber using the TDM technique. A single optical carrier carried 672 TDM channels in the first lightwave system deployed in 1980. By 2002, the same carrier could carry more than half a

Table 1.1: SONET/SDH bit rates

SONET	SDH	B (Mb/s)	Channels
OC-1		51.84	672
OC-3	STM-1	155.52	2,016
OC-12	STM-4	622.08	8,064
OC-48	STM-16	2,488.32	32,256
OC-192	STM-64	9,953.28	129,024
OC-768	STM-256	39,813.12	516,096

Table 1.2: Characteristics of commercial lightwave systems

System	Year	λ (μm)	B (Mb/s)	L (km)	Voice Channels
FT–3	1980	0.85	45	<10	672
FT–3C	1983	0.85	90	<15	1,344
FT–3X	1984	1.30	180	<25	2,688
FT–G	1985	1.30	417	<40	6,048
FT–G-1.7	1987	1.30	1,668	<46	24,192
STM–16	1991	1.55	2,488	<85	32,256
STM–64	1996	1.55	9,953	<90	129,024
STM–256	2002	1.55	39,813	<90	516,096

million telephone conversations simultaneously over a single fiber.

It is important to realize that TDM can be implemented in both the electrical and optical domains. In the optical domain, it is used to combine multiple 10- or 40-Gb/s channels to form an optical bit stream at bit rates exceeding 100 Gb/s. For example, sixteen 10-Gb/s channels, or four 40-Gb/s channels, can be combined through optical TDM for producing bit streams at 160 Gb/s. Optical signal at such high bit rates cannot be generated using an external modulator because of limitations imposed by electronics. We discuss optical TDM in Section 8.6.

1.4.2 Frequency-Division Multiplexing

In the case of FDM, the channels are spaced apart in the frequency domain but can overlap in the time domain. Each channel is assigned a unique carrier frequency. Moreover, carrier frequencies are spaced more than the channel bandwidth so that channel spectra do not overlap, as seen Figure 1.11(b). FDM is suitable for both analog and digital signals. It was first developed for radio waves in the beginning of the 20th century and was later adopted by the television industry for broadcasting multiple video channels over microwaves.

FDM can be easily implemented in the optical domain and is commonly referred to as *wavelength-division multiplexing* (WDM). Each channel is assigned a unique carrier frequency, and an optical source at the precise wavelength corresponding to that frequency is employed within the optical transmitter. The transmitters and receivers used for WDM systems become increasingly complex as the number of WDM channels increases. Figure 1.12 shows the basic design of a WDM system schematically. Multiple channels at distinct wavelengths are combined together using a *multiplexer* and then launched within the same fiber link. At the receiver end, channels are separated using a *demultiplexer*, typically an optical filter with transmission peaks exactly at the channel wavelengths. Chapter 9 is devoted to WDM systems.

It is common to make all channels equally spaced so that channel spacing remains constant. A guard band is left around each channel to minimize interchannel crosstalk. Typically, channel spacing is close to 50 GHz for channels operating at 10 Gb/s. How-

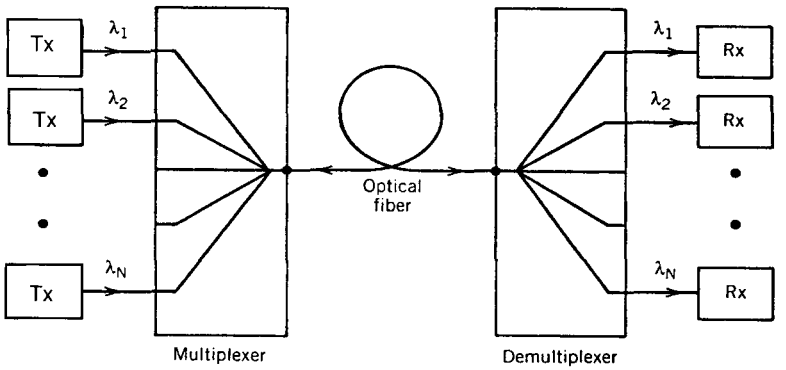

Figure 1.12: Schematic of a WDM lightwave system. Multiple channels, each operating at a fixed assigned wavelength, are first combined using a multiplexer and then separated at the receiver end using a demultiplexer.

ever, the exact value of channel spacing depends on a number of factors. In fact, WDM systems are often classified as being *coarse* or *dense* depending on the channel spacing used. For some applications, only a few channels need to be multiplexed, and channel spacing can be made as large as 1 Tb/s to reduce the system cost. In contrast, dense WDM systems are designed to serve as the backbone of an optical network and often multiplex more than a hundred channels to increase the system capacity. The channel spacing in this case can be as small as 25 GHz for 10-Gb/s channels. The ultimate capacity of a WDM fiber link depends on how closely channels can be packed in the wavelength domain. The minimum channel spacing is limited by interchannel crosstalk. Typically, channel spacing $\Delta\nu_{ch}$ should exceed $2B$ at the bit rate B. It is common to introduce a measure of the spectral efficiency of a WDM system as $\eta_s = B/\Delta\nu_{ch}$. Attempts are made to make η_s as large as possible.

As mentioned earlier, channel frequencies (or wavelengths) of WDM systems were first standardized by the ITU on a 100-GHz grid in the frequency range of 186 to 196 THz (covering the C and L bands in the wavelength range 1,530–1,612 nm). For this reason, channel spacing for most commercial WDM systems was set at 100 GHz. This value leads to a spectral efficiency of only 0.1 (b/s)/Hz at a bit rate of 10 Gb/s. More recently, ITU has specified WDM channels with a frequency spacing of 50 GHz. The use of this channel spacing in combination with the bit rate of 40 Gb/s has the potential of increasing the spectral efficiency to 0.8 (b/s)/Hz.

An example of how the WDM technique has impacted society is provided by the transatlantic lightwave systems connecting North America to the European continent. Table 1.3 lists the total capacity and other important characteristics of several transatlantic submarine cable systems. The first undersea fiber-optic cable (TAT–8) was a second-generation system. It was installed in 1988 in the Atlantic Ocean for operation at a bit rate of 280 Mb/s with a repeater spacing of up to 70 km. By 2001, several WDM systems have been laid across the Atlantic Ocean with a combined capacity of more than 10 Tb/s. The resulting increase in the number of voice channels lowered the prices so much by 2003 that a North American could talk to anyone in Europe at a cost

Table 1.3: Characteristics of transatlantic submarine systems

System	Year	Capacity (Gb/s)	L (km)	Comments
TAT–8	1988	0.28	70	1.3 μm, multimode lasers
TAT–9	1991	0.56	80	1.55 μm, DFB lasers
TAT–10/11	1993	0.56	80	1.55 μm, DFB lasers
TAT–12/13	1996	5.00	50	1.55 μm, optical amplifiers
AC–1	1998	80.0	50	1.55 μm, WDM with amplifiers
TAT–14	2001	1,280	50	1.55 μm, dense WDM
AC–2	2001	1,280	50	1.55 μm, dense WDM
360Atlantic-1	2001	1,920	50	1.55 μm, dense WDM
Tycom	2001	2,560	50	1.55 μm, dense WDM
FLAG Atlantic-1	2001	4,800	50	1.55 μm, dense WDM

of 5 cents per minute or less! The same call would have cost in 1988 more than 50 times in inflation-adjusted dollars.

1.4.3 Code-Division Multiplexing

Although the TDM and WDM techniques are often employed in practice, both suffer from some drawbacks. The use of TDM to form a single high-speed channel in the optical domain shortens the bit slot to below 10 ps and forces one to use shorter and shorter optical pulses that suffer from dispersive and nonlinear effects. This problem can be solved using the WDM technique but only at the expense of an inefficient utilization of the channel bandwidth. Some of these drawbacks can be overcome by using a multiplexing scheme based on the *spread-spectrum technique* [90] and is well known in the domain of wireless communications. This scheme is referred to as *code-division multiplexing* (CDM) because each channel is coded in such a way that its spectrum spreads over a much wider region than occupied by the original signal.

Although spectrum spreading may appear counterintuitive from a spectral point of view, this is not the case because all users share the same spectrum, In fact, CDM is used extensively in the microwave domain for cell phones as it provides the most flexibility in a multiuser environment. The term code-division multiple access is often employed to emphasize the asynchronous and random nature of multiuser connections. Conceptually, the difference between the WDM, TDM, and CDM can be understood as follows. The WDM and TDM techniques partition, respectively, the channel bandwidth or the time slots among users. In contrast, all users share the entire bandwidth and all time slots in a random fashion in the case of CDM.

The new components needed for CDM systems are the encoders and decoders located at the transmitter and receiver ends, respectively [91]–[94]. The encoder spreads the signal spectrum over a much wider region than the minimum bandwidth necessary for transmission. Spectral spreading is accomplished by means of a unique code that is independent of the signal itself. The decoder uses the same code for compressing

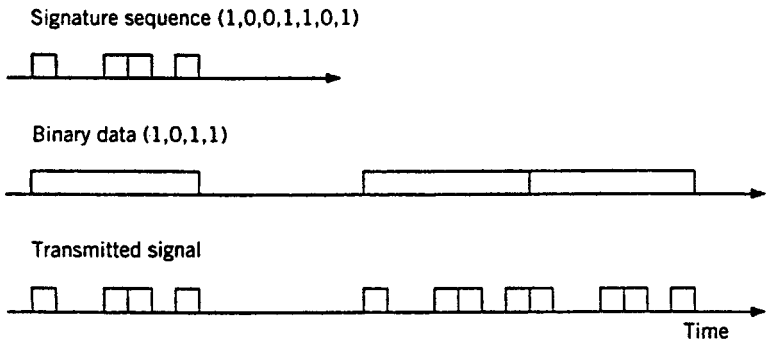

Figure 1.13: Schematic illustration of a coding scheme for CDM systems. In this example, a signature sequence in the form of a 7-chip code is employed.

the signal spectrum and recovering the data. The spectrum-spreading code is called a *signature sequence*. An advantage of the spread-spectrum method is that it is difficult to jam or intercept the signal because of its coded nature. The CDM technique is thus especially useful when security of the data is of concern.

Figure 1.13 shows an example of how a bit stream is constructed for optical CDM systems. Each bit of data is coded using a signature sequence consisting of a large number, say, M, of shorter bits, called time "chips" borrowing the terminology used for wireless ($M = 7$ in the example shown). The effective bit rate (or the chip rate) increases by the factor of M because of coding. The signal spectrum is spread over a much wider region related to the bandwidth of individual chips. For example, the signal spectrum becomes broader by a factor of 64 if $M = 64$. Of course, the same spectral bandwidth is used by many users distinguished on the basis of different signature sequences assigned to them. The recovery of individual signals sharing the same bandwidth requires that the signature sequences come from a family of the orthogonal codes. The orthogonal nature of such codes ensures that each signal can be decoded accurately at the receiver end. The receiver recovers messages by decoding the received signal using the same signature sequence that was employed at the transmitter.

Problems

1.1 Calculate the carrier frequency for optical communication systems operating at 0.88, 1.3, and 1.55 μm. What is the photon energy (in eV) in each case?

1.2 Calculate the transmission distance over which the optical power will attenuate by a factor of 10 for three fibers with losses of 0.2, 20, and 2,000 dB/km. Assuming that the optical power decreases as $\exp(-\alpha L)$, calculate α (in cm^{-1}) for the three fibers.

1.3 Assume that a digital communication system can be operated at a bit rate of up to 1% of the carrier frequency. How many audio channels at 64 kb/s can be transmitted over a microwave carrier at 5 GHz and an optical carrier at 1.55 μm?

1.4 A 1-hour lecture script is stored on the computer hard disk in the ASCII format. Estimate the total number of bits, assuming a delivery rate of 200 words per minute and on average 5 letters per word. How long will it take to transmit the script at a bit rate of 1 Gb/s?

1.5 A 1.55-μm digital communication system operating at 1 Gb/s receives an average power of -40 dBm at the detector. Assuming that 1 and 0 bits are equally likely to occur, calculate the number of photons received within each 1 bit.

1.6 An analog voice signal that can vary over the range 0 to 50 mA is digitized by sampling it at 8 kHz. The first four sample values are 10, 21, 36, and 16 mA. Write the corresponding digital signal (a string of 1 and 0 bits) by using a 4-bit representation for each sample.

1.7 Describe the technique of time-division multiplexing. If 16 channels, each operating at 2.5 Gb/s, need to be multiplexed using this technique, how short should each optical pulse be?

1.8 What is meant by wavelength-division multiplexing? If 20 channels, each operating at 10 Gb/s, are multiplexed using this technique with a spectral efficiency of 0.4 (b/s)/Hz, what is the total bandwidth of the signal?

References

[1] A. A. Huurdeman, *The Worldwide History of Telecommunications*, Wiley, New York, 2003, Chap. 21.

[2] T. H. Maiman, *Nature* **187**, 493 (1960).

[3] W. K. Pratt, *Laser Communication Systems*, Wiley, New York, 1969.

[4] S. E. Miller, *Sci. Am.* **214** (1), 19 (1966).

[5] A. C. S. van Heel, *Nature* **173**, 39 (1954).

[6] H. H. Hopkins and N. S. Kapany, *Nature* **173**, 39 (1954).

[7] B. O'Brian, U.S. Patent 2,825,260 (1958).

[8] B. I. Hirschowitz, U.S. Patent 3,010,357 (1961).

[9] N. S. Kapany, *Fiber Optics: Principles and Applications*, Academic Press, New York, 1967.

[10] K. C. Kao and G. A. Hockham, *Proc. IEE* **113**, 1151 (1966); A. Werts, *Onde Electr.* **45**, 967 (1966).

[11] F. P. Kapron, D. B. Keck, and R. D. Maurer, *Appl. Phys. Lett.* **17**, 423 (1970).

[12] I. Hayashi, M. B. Panish, P. W. Foy, and S. Sumski, *Appl. Phys. Lett.* **17**, 109 (1970).

[13] A. E. Willner, Ed., *IEEE J. Sel. Topics Quantum Electron.* **6**, 827 (2000). Several historical articles in this millennium issue cover the development of lasers and optical fibers. See, for example, the articles by Z. Alferov, W. A. Gambling, T. Izawa, D. Keck, H. Kogelnik, and R. H. Rediker.

[14] R. J. Sanferrare, *AT&T Tech. J* **66**, 95 (1987).

[15] C. Fan and L. Clark, *Opt. Photon. News* **6** (2), 26 (1995).

[16] I. Jacobs, *Opt. Photon. News* **6** (2), 19 (1995).

[17] H. Kogelnik, *IEEE J. Sel. Topics Quantum Electron.* **6**, 1279 (2000).

[18] D. Gloge, A. Albanese, C. A. Burrus, E. L. Chinnock, J. A. Copeland, A. G. Dentai, T. P. Lee, T. Li, and K. Ogawa, *Bell Syst. Tech. J.* **59**, 1365 (1980).

[19] J. I. Yamada, S. Machida, and T. Kimura, *Electron. Lett.* **17**, 479 (1981).

[20] T. Miya, Y. Terunuma, T. Hosaka, and T. Miyoshita, *Electron. Lett.* **15**, 106 (1979).

[21] A. H. Gnauck, B. L. Kasper, R. A. Linke, R. W. Dawson, T. L. Koch, T. J. Bridges, E. G. Burkhardt, R. T. Yen, D. P. Wilt, J. C. Campbell, K. C. Nelson, and L. G. Cohen, *J. Lightwave Technol.* **3**, 1032 (1985).

[22] K. Nakagawa, *Trans. IECE Jpn. Pt. J* **78B**, 713 (1995).

[23] R. A. Linke and A. H. Gnauck, *J. Lightwave Technol.* **6**, 1750 (1988); P. S. Henry, *Coherent Lightwave Communications*, IEEE Press, New York, 1990.

[24] N. S. Bergano, J. Aspell, C. R. Davidson, P. R. Trischitta, B. M. Nyman, and F. W. Kerfoot, *Electron. Lett.* **27**, 1889 (1991).

[25] T. Otani, K. Goto, H. Abe, M. Tanaka, H. Yamamoto, and H. Wakabayashi, *Electron. Lett.* **31**, 380 (1995).

[26] T. Welsh, R. Smith, H. Azami, and R. Chrisner, *IEEE Commun. Mag.* **34** (2), 30 (1996).

[27] W. C. Marra and J. Schesser, *IEEE Commun. Mag.* **34** (2), 50 (1996).

[28] N. S. Bergano and H. Kidorf, *Opt. Photon. News* **12** (3), 32 (2001).

[29] K. Fukuchi, T. Kasamatsu, M. Morie, R. Ohhira, T. Ito, K. Sekiya, D. Ogasahara, and T. Ono, Paper PD24, *Proc. Optical Fiber Commun. Conf.*, Optical Society of America, Washington, DC, 2001.

[30] J.-X. Cai, D. G. Foursa, C. R. Davidson, Y. Cai, G. Domagala, H. Li, L. Liu, W. W. Patterson, A. N. Pilipetskii, M. Nissov, N. Bergano, Paper PD22, *Proc. Optical Fiber Commun. Conf.*, Optical Society of America, Washington, DC, 2003.

[31] L. F. Mollenauer and K. Smith, *Opt. Lett.* **13**, 675 (1988).

[32] S. Namiki and Y. Emori, *IEEE J. Sel. Topics Quantum Electron.* **7**, 3 (2001).

[33] K. Rottwitt and A. J. Stentz, in *Optical Fiber Telecommunications*, Vol. 4A, I. Kaminow and T. Li, Eds., Academic Press, San Diego, 2002, Chap. 5.

[34] M. N. Islam, Ed., *Raman Amplifiers for Telecommunications*, Springer, New York, 2003.

[35] C. Headly III and G. P. Agrawal, Eds., *Raman Amplification in Optical Fiber Communication System*, Academic Press, San Diego, 2005.

[36] G. A. Thomas, B. L. Shraiman, P. F. Glodis, and M. J. Stephan, *Nature* **404**, 262 (2000).

[37] J. C. Knight, J. Broeng, T. A. Birks, P. S. J. Russell, *Science* **282**, 1476 (1998).

[38] J. Broeng, D. Mogilevstev, S. E. Barkou, and A. Bjarklev, *Opt. Fiber Technol.* **5**, 305 (1999).

[39] T. M. Monro, P. J. Bennett, N. G. R. Broderick, and D. J. Richardson, *Opt. Lett.* **25**, 206 (2000).

[40] M. Ibanescu, Y. Fink, S. Fan, E. L. Thomas, J. D. Joannopoulos, *Science* **289**, 415 (2000).

[41] P. S. J. Russell, *Science* **299**, 358 (2003).

[42] R. F. Cregan, B. J. Mangan, J. C. Knight, T. A. Birks, P. S. J. Russell, P. J. Roberts, and D. C. Allan, *Science* **285**, 1537 (1999).

[43] K. Suzuki, H. Kubota, S. Kawanishi, M. Tanaka, and M. Fujita, *Electron. Lett.* **37**, 1399 (2001).

[44] C. M. Smith, N. Venkataraman, M. T. Gallagher, D. Muller, J. A. West, N. F. Borrelli, D. C. Allan, and K. W. Koch, *Nature* **424**, 657 (2003).

[45] B. Zsigri, C. Peucheret, M. D., Nielsen, and P. Jeppesen, *Electron. Lett.* **39**, 796 (2003).

[46] K. Saitoh and M. Koshiba, *IEEE Photon. Technol. Lett.* **15**, 1384 (2003).

[47] K. I. Suzuki, S. Kawai, and S. Iwatsuki, *Electron. Lett.* **32**, 2173 (1996).

[48] A. H. Gnauck, G. Raybon, S. Chandrasekhar, J. Leuthold, C. Doerr, L. Stulz, and E. Burrows, *IEEE Photon. Technol. Lett.* **15**, 467 (2003).

[49] A. Agarwal, S. Banerjee, D. F. Grosz, A. P. Kung, D. N. Maywar, A. Gurevich, and T. H. Wood, *IEEE Photon. Technol. Lett.* **15**, 470 (2003).

[50] T. Otani, M. Hayashi, M. Daikoku, K. Ogaki, Y. Nagao, K. Nishijima, and M. Suzuki, *J. Lightwave Technol.* **21**, 947 (2003).

[51] G. C. Gupta, L. L. Wang, O. Mizuhara, R. E. Tench, N. N. Dang, P. Tabaddor, and A. Judy, *IEEE Photon. Technol. Lett.* **15**, 996 (2003).

[52] C. Wree, N. Hecker-Denschlag, E. Gottwald, P. Krummrich, J. Leibrich, E. D. Schmidt, B. Lankl, and W. Rosenkran, *IEEE Photon. Technol. Lett.* **15**, 1303 (2003).

[53] B. Zhu, C. R. Doerr, P. Gaarde, L. E. Nelson, S. Stulz, L. Stulz, L. Gruner-Nielsen, *Electron. Lett.* **39**, 1528 (2003).

[54] A. Agarwal, S. Banerjee, D. F. Grosz, A. P. Kung, D. N. Maywar, and T. H. Wood, *IEEE Photon. Technol. Lett.* **15**, 1779 (2003).

[55] S. Kawanishi, H. Takara, K. Uchiyama, I. Shake, and K. Mori, *Electron. Lett.* **35**, 826 (1999).

[56] R. Ludwig, U. Feiste, S. Diez, C. Schubert, C. Schmidt, H. J. Ehrke, and H. G. Weber, *Electron. Lett.* **36**, 1405 (2000).

[57] M. Daikoku, T. Otani, and M. Suzuki, *IEEE Photon. Technol. Lett.* **15**, 1165 (2003).

[58] A. H. Gnauck, G. Raybon, P. G. Bernasconi, J. Leuthold, C. R. Doerr, and L. G. Stulz, *IEEE Photon. Technol. Lett.* **15**, 1618 (2003).

[59] A. Hasegawa and F. Tappert, *Appl. Phys. Lett.* **23**, 142 (1973).

[60] L. F. Mollenauer, *Opt. Photon. News* **11** (4), 15 (1994).

[61] L. F. Mollenauer, P. V. Mamyshev, J. Gripp, M. J. Neubelt, N. Mamysheva, L. Grüner-Nielsen, and T. Veng, *Opt. Lett.* **25**, 704 (2000).

[62] M. Nakazawa, H. Kubota, K. Suzuki, E. Yamada, and A. Sahara, *IEEE J. Sel. Topics Quantum Electron.* **6**, 363 (2000).

[63] M. Nakazawa, *IEEE J. Sel. Topics Quantum Electron.* **6**, 1332 (2000).

[64] L. F. Mollenauer, A. Grant, X. Liu, X. Wei, C. J. Xie, and I. Kang, *Opt. Lett.* **28**, 2043 (2003).

[65] G. E. Keiser, *Optical Fiber Communications*, 3rd ed., McGraw-Hill, New York, 2000.

[66] B. Ramamurthy, *Design of Optical WDM Networks*, Kluwer Academic, Norwell, MA, 2000.

[67] G. P. Agrawal, *Applications of Nonlinear Fiber Optics*, Academic Press, San Diego, CA, 2001.

[68] J. P. Laude, *DWDM Fundamentals, Components and Applications* Artech House, Norwood, MA, 2002.

[69] R. Ramaswami and K. Sivarajan, *Optical Networks: A Practical Perspective*, 2nd ed., Morgan Kaufmann Publishers, San Francisco, 2002.

[70] G. P. Agrwal, *Fiber-Optic Communication Systems*, 3rd ed., Wiley, New York, 2002.

[71] I. P. Kaminow and T. Li, Eds., *Optical Fiber Telecommunications IV*, Academic Press, San Diego, CA, 2002.

[72] J. Chesnoy, *Undersea Fiber Communication Systems*, Academic Press, San Diego, CA, 2002.

[73] R. L. Freeman, *Fiber-Optic Systems for Telecommunications*, Wiley, New York, 2002.

[74] M. Kolimbiris, *Fiber Optics Communications*, Prentice Hall PTR, Upper Saddle River, NJ, 2002.

[75] S. C. Gupta, *Optical Fiber Communication and Its Applications*, Prentice Hall India, New Delhi, 2004.

[76] A. K. Dutta and N. K. Dutta, Eds., *WDM TEchnologies: Optical Networks*, Academic Press, San Diego, CA, 2004.

[77] G. P. Agrwal, *Lightwave Technology: Components and Devices*, Wiley, New York, 2004.

[78] J. Zheng and H. T. Mouftah, *Optical WDM Networks: Concepts and Design Principles*, Wiley, New York, 2004.

[79] A. Stavdas, *Ultra-Wideabnd WDM Networks*, Wiley, New York, 2004.

[80] M. Cvijetic, *Optical Transmission Systems Engineering*, Artech House, Norwood, MA, 2004.

[81] S. G. Lambert and W. L. Casey, *Laser Communications in Space*, Artec House, Norwood, MA, 1995.

[82] M. Schwartz, *Information Transmission, Modulation, and Noise*, 4th ed., McGraw-Hill, New York, 1990.

[83] L. W. Couch II, *Modern Communication Systems: Principles and Applications*, 4th ed., Prentice Hall, Upper Saddle River, NJ, 1995.

[84] B. P. Lathi, *Modern Digital and Analog Communication Systems*, 3rd ed., Oxford University Press, New York, 1998.

[85] C. E. Shannon, *Proc. IRE* **37**, 10 (1949); A. J. Jerri, *Proc. IEEE* **65**, 1565 (1977).

[86] H. Nyquist, *Trans. AIEE* **47**, 617 (1928).

[87] R. Ballart and Y.-C. Ching, *IEEE Commun. Mag.* **27** (3), 8 (1989).

[88] T. Miki, Jr. and C. A. Siller, Eds., *IEEE Commun. Mag.* **28** (8), 1 (1990).

[89] S. V. Kartalopoulos, *Understanding SONET/SDH and ATM*, IEEE Press, Piscataway, NJ, 1999.

[90] A. J. Viterbi, *CDMA: Principles of Spread Spectrum Communication*, Reading, MA: Addison-Wesley, Reading, MA, 1995.

[91] P. C. Teh, P. Petropoulos, M. Ibsen, and D. J. Richardson, *J. Lightwave Technol.* **19**, 1352 (2001).

[92] X. Wang and K. T. Chan, *IEEE J. Quantum Electron.* **39**, 83 (2003).

[93] R. P. Scott, W. Cong, K. Li, V. J. Hernandez, B. H. Kolner, J. P. Heritage, S. J. B. Yoo, *IEEE Photon. Technol. Lett.* **16**, 2186 (2004).

[94] K. Matsushima, X. Wang, S. Kutsuzawa, A. Nishiki, S. Oshiba, N. Wada, and K.-I. Kitayama, *IEEE Photon. Technol. Lett.* **16**, 2192 (2004).

Chapter 2

Optical Signal Generation

As discussed in the preceding chapter, the first step in any lightwave system is to generate a digital bit stream at the optical transmitter in the form of a coded train of optical pulses such that it contains all the information available in the corresponding electrical signal. It turns out that the conversion of a bit stream from electrical to optical domain can be carried out in several different formats. The choice of an appropriate modulation format depends on a large number of factors and can be critical for designing and operating the system successfully. The objective of this chapter is to introduce various modulation formats and discuss how they can be used in practice. Section 2.1 describes the three major formats employed to modulate the optical carrier; they are based on whether the information is coded using the amplitude, phase, or frequency of the optical carrier. Section 2.2 deals with the two principal digital data formats known as return-to-zero and nonreturn-to-zero formats, depending on whether the optical pulse representing 1 bit occupies a fraction of or the entire bit slot. Section 2.3 then focuses on the techniques used to generate an optical bit stream within the transmitter. The discussion includes several new modulation formats, borrowed from the field of microwaves, whose use helps to improve the performance of modern lightwave systems. Section 2.4 is devoted to several design issues important for optical transmitters such as coupling losses, optical feedback, stability and tuning of the carrier wavelength, and long-term reliability.

2.1 Modulation Formats

Electrical-to-optical conversion of a bit stream requires modulation of an optical carrier. An important issue is related to the choice of the physical quantity that is modulated to encode the data on the optical carrier. The optical carrier before modulation is in the form of a continuous wave (CW) and its electric field can be written as

$$\mathbf{E}(t) = \hat{\mathbf{e}} A_0 \cos(\omega_0 t - \phi_0) = \mathrm{Re}[\hat{\mathbf{e}} A_0 e^{i\phi_0} \exp(-i\omega_0 t)], \tag{2.1.1}$$

where Re denotes the real part, $\mathbf{E}$ is the electric field vector, $\hat{\mathbf{e}}$ is a unit vector representing the state of the polarization of the optical field, A_0 is its amplitude, ω_0 is its carrier

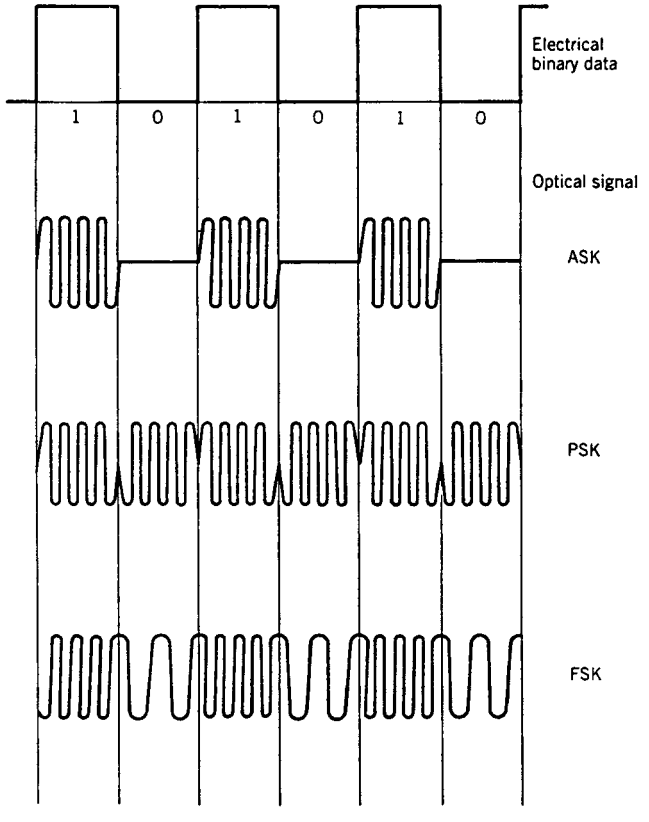

Figure 2.1: Modulated optical carrier in the case of the ASK, PSK, and FSK formats for a specific bit pattern shown on the top.

frequency, and ϕ_0 is its phase. The spatial dependence of $\mathbf{E}$ is suppressed for simplicity of notation; it follows the shape of the fundamental mode of the fiber when single-mode fibers are used as a communication channel. In the "phasor" notation adopted in this text, an optical carrier is described by its frequency ω_0 and its complex amplitude $A = A_0 e^{i\phi_0}$. The choice of $\exp(-i\omega_0 t)$ in place of $\exp(i\omega_0 t)$ is arbitrary. In many engineering textbooks, the factor $\exp(j\omega_0 t)$ is employed; the substitution $i \rightarrow -j$ can be used for conversion.

Similar to an electrical communication system, one may choose to modulate the amplitude A_0, the frequency ω_0, or the phase ϕ_0 of the optical carrier [1]–[4]. In the case of an analog signal, the three modulation choices are known as amplitude modulation (AM), frequency modulation (FM), and phase modulation (PM). In the digital case, they are called amplitude-shift keying (ASK), frequency-shift keying (FSK), and phase-shift keying (PSK), depending on whether the amplitude, frequency, or phase of the carrier wave is shifted between the two levels of a binary digital signal. Figure 2.1 shows schematically the time dependence of the modulated optical carrier for the three modulation formats using a specific bit pattern.

In principle, binary electrical data can also be encoded by changing the state of polarization of the optical carrier governed by the unit vector $\hat{\mathbf{e}}$ in Eq. (2.1.1). In such a polarization-shift keying (PoSK) technique, 0 and 1 bits are represented by two orthogonally polarized unit vectors, $\hat{\mathbf{e}}_0$ and $\hat{\mathbf{e}}_1$, such that $\hat{\mathbf{e}}_0 \cdot \hat{\mathbf{e}}_1 = 0$. Although this modulation format can be easily adopted for space and satellite communications, it is not yet practical for fiber-optic lightwave systems because the state of polarization of an optical field is not maintained in optical fibers, unless especially designed polarization-maintaining fibers are employed. We ignore the vector nature of the optical field in this chapter and employ a scalar notation in the following discussion.

2.1.1 ASK Format

Since only the amplitude A_0 is modulated in Eq. (2.1.1) in the case of ASK, the electric field associated with the modulated carrier can be written as

$$E(t) = \mathrm{Re}[A_0(t)e^{i\phi_0}\exp(-i\omega_0 t)], \tag{2.1.2}$$

where $A_0(t)$ changes with time in the same fashion as the electrical bit stream. In the digital case,

$$A_0(t) = \sqrt{P_0}\sum_n b_n f_p(t - nT_b), \tag{2.1.3}$$

where P_0 is the peak power, $f_p(t)$ represents the optical pulse shape, $T_b = 1/B$ is the bit slot at the bit rate B, and the random variable b_n takes values 0 and 1, depending on whether the nth bit in the optical signal corresponds to a 0 or 1. In most practical situations, A_0 is set to zero during transmission of 0 bits. The ASK format is also known as the *on–off keying*. Most digital lightwave systems employ ASK because its use simplifies the design of optical transmitters and receivers considerably.

The implementation of on–off keying in an optical transmitter requires that the intensity (or the power) of the optical carrier is turned on and off in response to an electrical bit stream. The simplest approach makes use of a direct-modulation technique in which the electrical signal is applied directly to the driving circuit of a semiconductor laser or a light-emitting diode. Typically, the laser is biased slightly below threshold so that it emits no light (except for some spontaneous emission). During each 1 bit, the laser goes beyond its threshold and emits a pulse whose duration is nearly equal to that of the electrical pulse. Such an approach works as long as the laser can be turned on and off as fast as the bit rate of the signal to be transmitted.

In practice, direct modulation suffers from a "chirping" problem (see Section 5.3.3 of LT1). The reason is related to phase changes that invariably occur when laser power is changed by modulating the current applied to a semiconductor laser. Physically, one must inject additional electrons and holes into the active region of the laser. This increase in the charge-carrier density changes the refractive index of the active region slightly and modifies the carrier phase ϕ_0 in Eq. (2.1.2) in a time-dependent fashion. Although such unintentional phase changes are not seen by a photodetector (as it responds only to optical power), they chirp the optical pulse and broaden its spectrum by adding new frequency components. Such spectral broadening is undesirable because it can lead to temporal broadening of optical pulses as they propagate through an optical

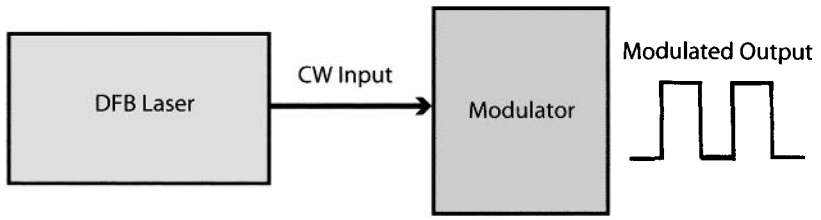

Figure 2.2: Schematic illustration of the external-modulation scheme. A DFB laser is biased at a constant current while the time-dependent electrical signal is applied to the modulator.

fiber. For this reason, direct modulation of the laser output becomes impractical as the bit rate of a lightwave system is increased beyond 2.5 Gb/s. The effects of frequency chirp on pulse broadening are considered in Section 3.2 where we discuss the impact of fiber dispersion.

The chirping problem can be solved to a large extent by operating a distributed-feedback (DFB) semiconductor laser continuously at a constant current and modulating its CW output through an external modulator. Figure 2.2 shows the basic idea schematically. As discussed in Chapter 6 of LT1, two types of external modulators are employed for lightwave systems. Figure 2.3 shows an example of each kind. The modulator shown in part (a) makes use of the electro-optic effect through which the refractive index of a suitable material ($LiNbO_3$ in practice) can be changed by applying a voltage across it. Changes in the refractive index modify the phase of an optical field propagating inside that material. Phase changes are converted into amplitude modulation using a Mach–Zehnder (MZ) interferometer made of two $LiNbO_3$ waveguides as shown in Figure 2.3(a).

$LiNbO_3$ modulators are often used for generating optical bit streams. They can easily provide an on–off contrast of more than 20 between 1 and 0 bits and can be modulated at speeds of up to 75 GHz [5]. The driving voltage is typically 5 V but can be reduced to near 3 V with a suitable design. Materials other than $LiNbO_3$ can also be employed. For example, polymeric electro-optic modulators can be designed such that they require less than 2 V for shifting the phase of a 1.55-μm signal by π in one of the arms of the MZ interferometer [6]. Since all external modulators have some insertion loss, the transmitted power is invariably affected when an external modulator is employed.

Insertion losses can be reduced significantly (to below 1 dB) by using an electroabsorption modulator shown schematically in Figure 2.3(b). The reason behind this reduction is that an electroabsorption modulator is made with the same material used for semiconductor lasers, and thus it can be integrated monolithically with the optical source. An added advantage is that electroabsorption modulators do not require an optical interferometer because they can change optical power directly in response to an applied voltage (see Section 6.4 of LT1). Optical transmitters with an integrated electroabsorption modulator, capable of modulating at a bit rate of 10 Gb/s, were available commercially by 1999 and are used routinely for lightwave systems. By 2001, such integrated modulators were able to operate at bit rates of 40 Gb/s.

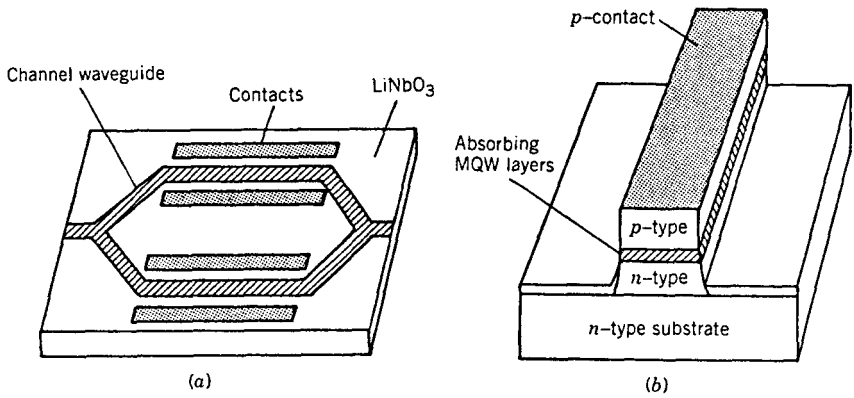

Figure 2.3: Two kinds of external modulators: (a) a $LiNbO_3$ modulator in the Mach–Zehnder configuration; (b) an electroabsorption modulator with multiquantum-well (MQW) absorbing layers.

2.1.2 PSK Format

In the case of PSK format, the optical bit stream is generated by modulating the phase ϕ_0 in Eq. (2.1.1), while the amplitude A_0 and the frequency ω_0 of the optical carrier are kept constant. The electric field of the optical bit stream can now be written as

$$E(t) = \mathrm{Re}\{A_0 \exp[i\phi_0(t) - i\omega_0 t]\}, \tag{2.1.4}$$

where the phase $\phi_0(t)$ changes with time in the same fashion as the electrical bit stream. For binary PSK, the phase ϕ_m takes two values, commonly chosen to be 0 and π, and it can be written in the form

$$\phi_0(t) = \sum_n b_n \pi f_p(t - nT_b), \tag{2.1.5}$$

where $f_p(t)$ represents the temporal profile and the random variable b_n takes values 0 and 1, depending on whether the nth bit in the optical signal corresponds to a 0 or 1. Figure 2.1 shows the binary PSK format schematically for a specific bit pattern. An interesting aspect of the PSK format is that the optical power remains constant during all bits, and the signal appears to have a CW form.

Direct detection cannot be used for lightwave systems employing the PSK format as all phase information is lost when such a bit stream is converted into electrical current using a photodetector. The only solution is to employ a *homodyne* or a *heterodyne* detection technique in which the optical bit stream is combined coherently with the CW output of a local oscillator (a DFB laser) before the signal is detected. The interference between the two optical fields creates a time-dependent electric current that contains all the information transmitted through PSK. This can be seen mathematically by writing the total field incident on the photodetector as (in the complex notation)

$$E_d(t) = A_0 \exp[i\phi_0(t) - i\omega_0 t] + A_L \exp(i\phi_L - i\omega_L t), \tag{2.1.6}$$

where the subscript L denotes the corresponding quantity for the local oscillator. The current generated at the photodetector is given by $I_d = R_d|E_d(t)|^2$, where R_d is the responsivity of the photodetector. It is easy to see that I_d varies with time as

$$I_d(t) = R_d(A_0^2 + A_L^2) + 2R_d A_0 A_L \cos[(\omega_0 - \omega_L)t + \phi_0(t) - \phi_L]. \tag{2.1.7}$$

Since $I_d(t)$ changes from bit to bit as $\phi_0(t)$ changes, one can reconstruct the original bit stream from this electrical signal.

The implementation of PSK requires an external modulator capable of changing the optical phase in response to an applied voltage. A $LiNbO_3$ modulator can be used for this purpose. In fact, the design of such a phase modulator is much simpler than that of an amplitude modulator as a MZ interferometer is no longer needed. Semiconductors can also be used to make phase modulators if they exhibit the electro-optic effect. However, the PSK format is rarely used in practice for lightwave systems because it requires the phase of the optical carrier to remain stable so that phase information can be extracted at the receiver without ambiguity. This requirement puts a stringent condition on the tolerable line widths of the DFB lasers used as an optical source at the transmitter and as a local oscillator at the receiver.

A variant of the PSK format, known as *differential* PSK or DPSK, is much more practical for lightwave systems. In the case of DPSK, information is coded by using the phase difference between two neighboring bits. For instance, if ϕ_k represents the phase of the kth bit, the phase difference $\Delta\phi = \phi_k - \phi_{k-1}$ is changed by 0 or π, depending on whether the kth bit is a 0 or 1. The DPSK format does not suffer from the phase-stability problem because information coded in the phase difference between two neighboring bits can be recovered successfully as long as the carrier phase remains stable over a duration of two bits. This condition is easily satisfied in practice at bit rates above 1 Gb/s because the line width of a DFB laser is typically below 10 MHz, indicating that the carrier phase does not change significantly over a duration of 1 ns or so.

A modulation format that can be useful for enhancing the spectral efficiency of lightwave systems is known as quaternary PSK (QPSK). In this format, the phase modulator takes two bits at a time and produces one of the four possible phases of the carrier, typically chosen to be 0, $\pi/2$, π, and $3\pi/2$ for bit combinations 00, 01, 11, and 10, respectively. Such a signal has half the bandwidth compared with that of the binary PSK as its bit rate is lower by a factor of 2. Of course, the QPSK format suffers from the same phase-stability issue as the binary PSK. This problem can be avoided by adopting a differential QPSK (DQPSK) format, as has been done in some recent WDM experiments [7].

2.1.3 FSK Format

In the case of FSK modulation, information is coded on the optical carrier by shifting the carrier frequency ω_0 itself [see Eq. (2.1.1)]. For a binary digital signal, ω_0 takes two values, say, $\omega_0 - \Delta\omega$ and $\omega_0 + \Delta\omega$, depending on whether a 0 or 1 bit is being transmitted. The shift $\Delta f = \Delta\omega/2\pi$ is called the *frequency deviation*. The quantity $2\Delta f$ is sometimes called tone spacing, as it represents frequency separation between 0 and 1 bits. Figure 2.1 shows schematically how the electric field varies in the case of

FSK format. Mathematically, it can be written as

$$E(t) = \mathrm{Re}\{A_0 \exp[i\phi_0 - i(\omega_0 \pm \Delta\omega)t]\}, \tag{2.1.8}$$

where + and − signs correspond to 1 and 0 bits, respectively. Noting that the argument of the exponential function can be written as $\omega_0 t + (\phi_0 \pm \Delta\omega t)$, the FSK format can also be viewed as a special kind of PSK modulation for which the carrier phase increases or decreases linearly over the bit duration. Similar to the PSK case, the modulated carrier has constant power, and the information encoded within the bit stream cannot be recovered through direct detection: One must employ heterodyne detection for decoding an FSK-coded optical bit stream.

Implementation of the FSK format requires modulators capable of shifting the frequency of the incident optical signal. Electro-optic materials such as $LiNbO_3$ normally produce a phase shift proportional to the applied voltage. They can be used for FSK by applying a triangular voltage pulse (sawtooth-like) since a linear phase change corresponds to a frequency shift. An alternative technique makes use of Bragg scattering from acoustic waves inside an acousto-optic modulator. Such modulators can be fabricated in a compact form by exciting surface acoustic waves within a $LiNbO_3$ waveguide. The device structure is similar to that used for acousto-optic filters (see Section 8.1.4 in LT1). The maximum frequency shift is typically limited to below 1 GHz for such modulators.

The simplest method for producing an FSK signal makes use of the direct modulation capability of semiconductor lasers (see Section 5.4.2 of LT1). As discussed earlier, a change in the operating current of a semiconductor laser leads to changes in both the amplitude and frequency of emitted light. In the case of ASK, the frequency shift, or chirping of the emitted optical pulse, is undesirable. But the same frequency shift can be used to advantage for the purpose of FSK. Typical values of frequency shifts are ∼1 GHz/mA. Therefore, only a small change in the operating current (∼1 mA) is required for producing the FSK signal. Such current changes are small enough that the amplitude does not change much from bit to bit. In spite of this simple method, the FSK format is rarely used for lightwave systems because of the complexities involved in recovering the frequency-coded information.

2.2 Digital Data Formats

In the case of the ASK format, a digital bit stream uses one optical pulse in each bit slot representing 1 (also called a mark). There still remains open the following question: how wide this pulse should be relative to the bit duration. The pulse can occupy the entire bit slot or only a part of it, leading to two main choices for the format of optical bit streams [1]–[3]. These two choices are shown in Figure 2.4 and are known as the return-to-zero (RZ) and nonreturn-to-zero (NRZ) formats. We discuss the relative merits of the RZ and NRZ formats in this section. Variants of RZ as well as several other formats such as DPSK are considered in Section 2.3.

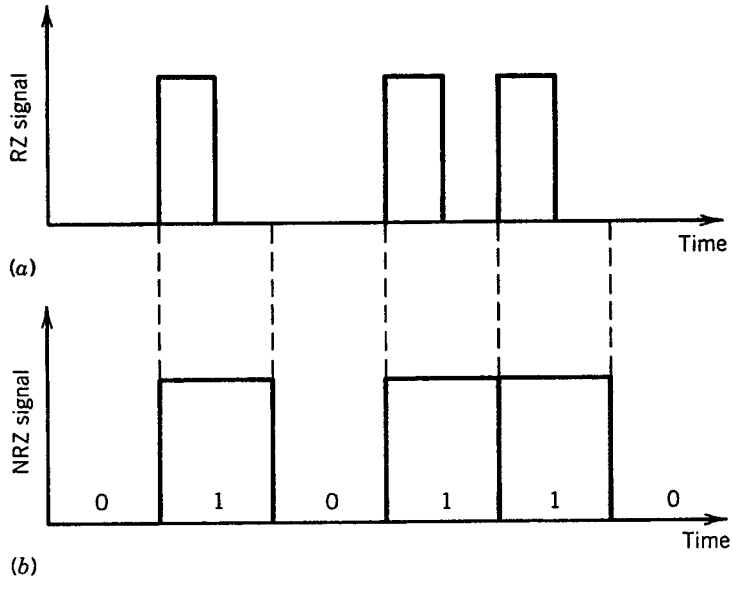

Figure 2.4: Optical bit stream 010110... coded using (a) return-to-zero (RZ) and (b) nonreturn-to-zero (NRZ) formats.

2.2.1 Nonreturn-to-Zero Format

In the NRZ format, the optical pulse representing each 1 bit occupies the entire bit slot. The natural question is what happens at the bit boundary when two (or more) 1 bits are next to each other. As seen in Figure 2.4(b), the optical field does not drop to zero between two or more successive 1 bits. The main consequence of this choice is that pulses in an NRZ bit stream do not have the same width. Rather, pulse width varies depending on the bit pattern. Each isolated 1 is represented by a rectangular pulse of width T_b, where $T_b = 1/B$ is the bit duration at the bit rate B, but the pulse width doubles for a pair of 1 bits surrounded by 0 bits. If ten 1 bits occur in succession, a single optical pulse of width $10T_b$ is used to represent all 10 bits. An optical receiver can still function if it first extracts an electrical clock (a sinusoidal signal at the bit rate B) from the bit stream and then uses it to sample the signal during each bit.

The main advantage of the NRZ format is that the bandwidth associated with this format is smaller than that of the RZ format by about a factor of 2. The reduced bandwidth of an NRZ signal can be understood qualitatively from Figure 2.4(b) by noting that on–off transitions occur much less often for an NRZ signal. This is the reason why the NRZ format is used extensively in the case of microwave and coaxial-cable systems for which the bandwidth should be economized as much as possible. However, the use of NRZ format for lightwave systems is not always the right choice because of the dispersive and nonlinear effects that can distort optical pulses during transmission and spread them outside their assigned bit slot. Since the pulse occupies the entire bit slot, the NRZ format cannot tolerate even a relatively small amount of pulse broadening and is quite vulnerable to intersymbol crosstalk. Moreover, a long sequence of 1 or 0 bits

contains no information about the bit duration and makes it difficult to extract the clock electronically with a high accuracy. In spite of these difficulties, the NRZ format is still often used for lightwave systems, especially at low bit rates. The use of NRZ format becomes questionable at bit rates higher than 10 Gb/s.

2.2.2 Return-to-Zero Format

In the RZ format, each optical pulse representing 1 bit is chosen to be shorter than the bit slot, and its amplitude returns to zero before the bit duration is over, as seen in Figure 2.4(a). Thus, all pulses are identical in an RZ bit stream at the transmitter end, before they are launched into the fiber, but the spacing among them depends on the bit pattern. For example, pulses are spaced apart by the bit duration T_b when two or more 1 bits occur in succession, but they become separated further and further apart as the number of 0 bits between two 1 bits increases.

Although the RZ format is essential for optical TDM and soliton-related applications, its use for lightwave systems was not pursued seriously until after it was found that the RZ format may help in improving the performance of high-capacity lightwave systems [9]–[11]. An important issue from the design standpoint is how wide the optical pulse should be compared to the bit slot. The ratio T_p/T_b, where T_p is the pulse width, is referred to as the *duty cycle* of an RZ bit stream. It is common to use a 50% duty cycle so that the pulse occupies one half of the bit slot. However, more often than not, duty cycle is just another design parameter for RZ systems that can be tailored to help meet the design goals. For example, a duty cycle of 30% or smaller is often used for dispersion-managed soliton systems (see Section 8.3) in which pulses should not be too close to each other to avoid any nonlinear interaction.

In an interesting variant of the RZ format, known as the chirped RZ (CRZ) format, optical pulses in each bit slot are chirped suitably before they are launched into the fiber link. As discussed in Chapter 3, pulses can be chirped by simply passing them through an optical fiber of appropriate length. Another RZ-related data format that is well known in the field of microwave communications and is attracting attention for lightwave systems is known as the carrier-suppressed RZ (CSRZ) format [12]–[16]. Its main advantage is that it has a smaller signal bandwidth than the conventional RZ format. Several other variations of the RZ format exist. We discuss such formats in Section 2.3 after introducing the concept of power spectral density whose knowledge provides an estimate of the signal bandwidth associated with an optical bit stream.

2.2.3 Power Spectral Density

To find the power spectrum of an optical bit stream, we begin with the electric field, $E(t) = \mathrm{Re}[A(t)\exp(-i\omega_0 t)]$, where $A(t)$ is the complex amplitude of the modulated carrier. In the case of the ASK format, $A(t)$ can be written as

$$A(t) = \sum_n b_n A_p(t - nT_b) \equiv \int_{-\infty}^{\infty} b(t')A_p(t - t')\,dt', \tag{2.2.1}$$

where b_n is a random number taking values 0 or 1, $A_p(t)$ represents the pulse shape, and we have introduced $b(t)$ as

$$b(t) = \sum_n b_n \delta(t - nT_b), \tag{2.2.2}$$

where $\delta(t)$ represents the delta function defined to be zero for all values of $t \neq 0$ and normalized such that $\int_{-\infty}^{\infty} \delta(t)\,dt = 1$. Physically, one can interpret $b(t)$ as the impulse response of a filter.

If we assume that $A(t)$ represents a stationary stochastic process, its power spectral density $S_A(\omega)$ can be found from the Wiener–Khintchine theorem using [8]

$$S_A(\omega) = \int_{-\infty}^{\infty} \Gamma_A(\tau) \exp(i\omega\tau)\,d\tau, \tag{2.2.3}$$

where $\Gamma_A(\tau) = \langle A^*(t)A(t+\tau)\rangle$ is the autocorrelation function of $A(t)$ and the angle brackets denote ensemble averaging. It follows from Eqs. (2.2.1) through (2.2.3) that

$$S_A(\omega) = |\tilde{A}_p(\omega)|^2 S_b(\omega), \tag{2.2.4}$$

where the power spectral density $S_b(\omega)$ is defined similar to Eq. (2.2.3) and $\tilde{A}_p(\omega)$ is the Fourier transform of the pulse amplitude $A_p(t)$ defined as

$$\tilde{A}_p(\omega) = \int_{-\infty}^{\infty} A_p(t) \exp(i\omega t)\,dt. \tag{2.2.5}$$

To find $S_b(\omega)$, we first calculate the autocorrelation function of $b(t)$ using $\Gamma_b(\tau) = \langle b(t)b(t+\tau)\rangle$. If we use $b(t)$ from Eq. (2.2.2), we obtain

$$\Gamma_b(\tau) = \sum_n \sum_k \langle b_n b_k \rangle \delta(t - kT_b)\delta(t + \tau - nT_b). \tag{2.2.6}$$

If we replace the ensemble average with a time average over the entire bit stream and make the substitution $n - k = m$, Eq. (2.2.6) can be written as [3]

$$\Gamma_b(\tau) = \frac{1}{T_b} \sum_m r_m \delta(\tau - mT_b), \tag{2.2.7}$$

where the correlation coefficient r_m is defined as

$$r_m = \lim_{N\to\infty} \frac{1}{N} \sum_n b_n b_{n+m}. \tag{2.2.8}$$

Taking the Fourier transform of Eq. (2.2.7) and substituting that in Eq. (2.2.4), we obtain the following expression for the power spectral density of an optical bit stream:

$$S_A(\omega) = |\tilde{A}_p(\omega)|^2 \frac{1}{T_b} \sum_{m=-\infty}^{\infty} r_m \exp(im\omega T_b). \tag{2.2.9}$$

The correlation coefficients can be easily calculated by noting that 1 and 0 bits are equally likely to occur in any realistic bit stream. It is easy to show that when b_n takes values 1 or 0 with equal probabilities,

$$r_0 = 1/2, \qquad r_m = 1/4 \ (m \neq 0). \tag{2.2.10}$$

Using these values in Eq. (2.2.11), we obtain

$$S_A(\omega) = \frac{|\tilde{A}_p(\omega)|^2}{4T_b}\left(1 + \sum_{m=-\infty}^{\infty} \exp(im\omega T_b)\right). \tag{2.2.11}$$

If we use the well-known identity [3]

$$\sum_{n=-\infty}^{\infty} \exp(in\omega T_b) = \frac{2\pi}{T_b}\sum_{n=-\infty}^{\infty} \delta\left(\omega - \frac{2\pi n}{T_b}\right), \tag{2.2.12}$$

the power spectral density can be written as

$$S_A(\omega) = \frac{|\tilde{A}_p(\omega)|^2}{4T_b}\left[1 + \frac{2\pi}{T_b}\sum_{m=-\infty}^{\infty} \delta\left(\omega - \frac{2\pi m}{T_b}\right)\right]. \tag{2.2.13}$$

The spectrum consists of a continuous part and a discrete part resulting from the sum over delta functions in Eq. (2.2.13).

We now apply Eq. (2.2.13) to the RZ and NRZ formats. In the case of the NRZ format, each pulse occupies the entire bit slot. Assuming a rectangular shape, $A_p(t)$ equals $\sqrt{P_0}$ within the bit slot of duration T_b but becomes zero outside of it. Taking the Fourier transform of $A_p(t)$, we obtain

$$|\tilde{A}_p(\omega)|^2 = P_0 T_b^2 \mathrm{sinc}^2(\omega T_b/2), \tag{2.2.14}$$

where $\mathrm{sinc}(x) \equiv \sin(x)/x$ is the so-called sinc function. Substituting the preceding expression in Eq. (2.2.13), we obtain

$$S_A(\omega) = \frac{P_0 T_b}{4}\mathrm{sinc}^2(\omega T_b/2) + \frac{\pi}{2}P_0. \tag{2.2.15}$$

Only the $m = 0$ term survives in the sum in Eq. (2.2.13) as the sinc function vanishes at all frequencies such that $\omega = 2\pi m/T_b$ except when $m = 0$. This spectrum is shown in Figure 2.5(a). The spectrum contains a discrete component at the zero frequency. However, recall that the zero-frequency component of $S_A(\omega)$ is actually located at ω_0 when one considers the spectrum of the electric field. The continuous part of the spectrum is spread around the carrier in a symmetric fashion. Most of the spectrum is confined within the bandwidth $2B$ for an NRZ bit stream at the bit rate B, and the 3-dB bandwidth (full width at half maximum or FWHM) is about B.

In the case of an RZ bit stream, spectral density depends on the duty cycle of the RZ pulse. Assuming that each 1 bit occupies a fraction d_c of the bit slot and assuming a rectangular shape for the optical pulse, the pulse spectrum is found to be

$$|\tilde{A}_p(\omega)|^2 = P_0 T_b^2 d_c \mathrm{sinc}^2(\omega T_b d_c/2). \tag{2.2.16}$$

As expected, this spectrum is wider than that given in Eq. (2.2.14) by a factor of $1/d_c$. However, when we substitute Eq. (2.2.16) in Eq. (2.2.13), we notice another important difference. The discrete spectral components no longer vanish for $m \neq 0$ because of the presence of d_c in the argument of the sinc function. Which ones survive depends on the duty factor. For example, for a duty cycle of 50% every even component (except $m = 0$) vanishes but all odd components survive. This case is shown in Figure 2.5(b). In general, all discrete components can be present in an RZ bit stream depending on the pulse shape and the duty factor used.

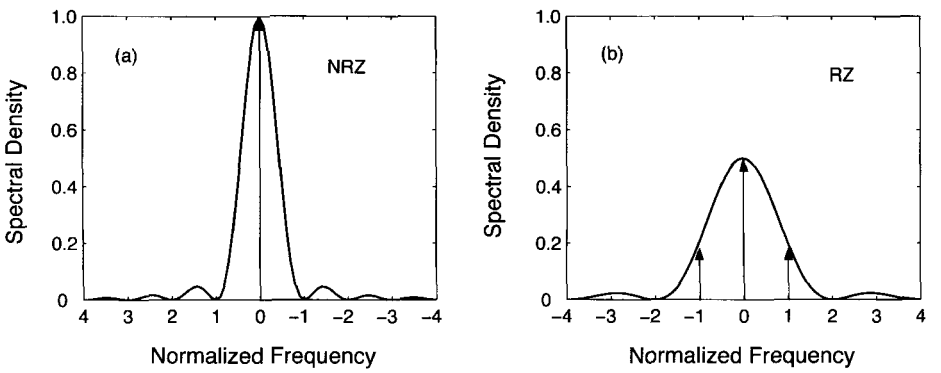

Figure 2.5: Power spectral density of (a) NRZ bit stream and (b) RZ bit stream with 50% duty cycle. Frequencies are normalized to the bit rate and the discrete part of the spectrum is shown by vertical arrows.

2.3 Bit-Stream Generation

As mentioned earlier, the format of choice for most lightwave systems is the ASK format. It can be implemented using both the RZ and NRZ coding schemes. In an attempt to improve the spectral efficiency of dense WDM systems, several new formats mix the basic RZ scheme with phase modulation [12]–[16]. Another format that has attracted attention since 2000 is a variant of the basic DPSK format, known as the intensity-modulated DPSK or the RZ-DPSK format [17]–[22]. In this format, an optical pulse is present in all bit slots, but the information is coded in the phase of the optical bit stream. This section focuses on the design of transmitters used for implementing various modulation formats.

2.3.1 NRZ Transmitters

The design of an NRZ transmitter is relatively simple since the electrical signal that needs to be transmitted is itself usually in the NRZ format. It is thus sufficient to use the scheme shown in Figure 2.2, where a single modulator, known as the data modulator, converts the CW light from a DFB semiconductor laser into an optical bit stream in the NRZ format. The data modulator can be integrated with the DFB laser if it is based on the electroabsorption effect (see Section 6.4 of LT1). Alternatively, an external $LiNbO_3$ modulator provides the same functionality. It employs a MZ interferometer for converting a voltage-induced relative phase shift into amplitude modulation of the input CW beam (see Section 6.2 of LT1).

Figure 2.6 shows schematically the design of a $LiNbO_3$ modulator. The input CW beam is split into two parts by a 3-dB coupler that are recombined back by another 3-dB coupler after different phase shifts have been imposed on them by applying voltages across two waveguides that form the two arms of the MZ interferometer. To understand this conversion process, we consider the transmission characteristics of such a modulator. Using the transfer matrix of a 3-dB coupler (see Section 2.3.4 of LT1), the outputs

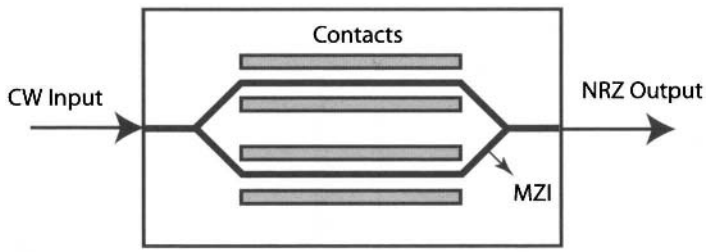

Figure 2.6: Schematic of a $LiNbO_3$ modulator. The Mach–Zehnder configuration converts the input CW beam into an optical bit stream by applying appropriate voltages across the two arms of the interferometer.

A_b and A_c exiting from the bar and cross ports of an MZ interferometer, respectively, can be obtained from the matrix equation

$$\begin{pmatrix} A_b \\ A_c \end{pmatrix} = \frac{1}{2}\begin{pmatrix} 1 & i \\ i & 1 \end{pmatrix}\begin{pmatrix} e^{i\phi_1} & 0 \\ 0 & e^{i\phi_2} \end{pmatrix}\begin{pmatrix} 1 & i \\ i & 1 \end{pmatrix}\begin{pmatrix} A_i \\ 0 \end{pmatrix}, \tag{2.3.1}$$

where A_i is the incident field and $\phi_j(t) = \pi V_j(t)/V_\pi$ is the phase shift in the jth arm when a voltage V_j is applied across it ($j = 1,2$). Here, V_π is the voltage required to produce a π phase shift; this parameter is generally known for any $LiNbO_3$ modulator and is typically in the range of 3 to 5 V.

The transfer function for the bar or cross port is easily obtained from Eq. (2.3.1). For the cross port, the modulator response is governed by

$$t_m = A_b/A_i = \cos[(\phi_1 - \phi_2)/2]\exp[i(\phi_1 + \phi_2 + \pi)/2]. \tag{2.3.2}$$

The phase shift $\phi_1 + \phi_2$ can be reduced to a constant if we choose voltages in the two arms such that $V_2(t) = -V_1(t) + V_b$, where V_b is a constant bias voltage. Then, the power transfer function, or the time-dependent transmissivity of the modulator, takes the form

$$T_m(t) = |t_m|^2 = \cos^2\left(\frac{\pi}{2V_\pi}[2V_1(t) - V_b]\right). \tag{2.3.3}$$

It is important to note that the transfer function of a MZ modulator is nonlinear in applied voltage V_1. To generate the NRZ bit stream, the modulator is typically biased at the half-power point by choosing $V_b = -V_\pi/2$. The applied voltage $V_1(t)$ is then changed using a bipolar electrical NRZ signal that changes from $-V_\pi/4$ to $+V_\pi/4$ between 0 and 1 bits.

2.3.2 RZ Transmitters

The situation is somewhat different when an optical bit stream needs to be generated in the RZ format from an electrical signal available in the NRZ format. One possibility is to use an actively mode-locked semiconductor laser (or fiber laser) in place of the continuously operating DFB laser. Such a laser should produce a periodic train of

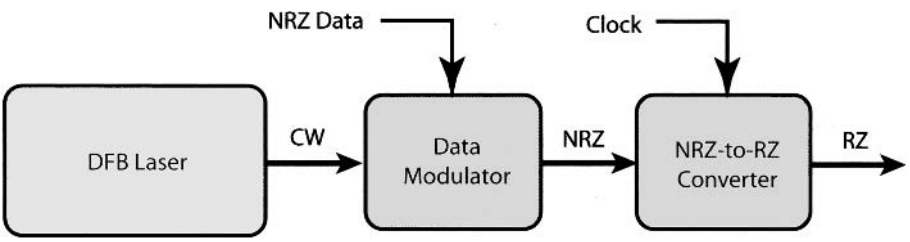

Figure 2.7: Schematic of an RZ transmitter. The data modulator creates an NRZ signal that is transformed into an RZ bit stream by the second modulator acting as a pulse carver.

pulses of appropriate width at a repetition rate equal to the bit rate B at which the channel is designed to operate. In essence, the laser produces an "11111$\cdots$" bit stream as an optical pulse is present in each bit slot. The modulator is then operated such that it blocks the pulse in all slots representing 0 bits. Although such an approach is indeed used in laboratory experiments designed to make use of optical solitons [23]–[25], it is rarely used for commercial lightwave systems because mode-locked lasers may not prove as reliable as a CW semiconductor laser.

An alternative approach makes use of the scheme shown in Figure 2.7. It first generates an NRZ signal using a data modulator and then converts it into an RZ bit stream using a second modulator that is driven by a sinusoidal signal (an electrical clock) at the bit rate. The second modulator is sometimes called the "pulse carver" because it splits a long optical pulse representing several 1 bits into multiple pulses, each being shorter than the bit slot [26]. Three different biasing configurations can be used to create RZ bit streams with duty cycles ranging from 33 to 67% [27]. In one configuration, the bias voltage is set to be $V_b = V_\pi/2$ in Eq. (2.3.3), and $V_1(t) = (V_\pi/4)\cos(2\pi Bt)$ is varied in a periodic fashion at a frequency equal to the bit rate B. Since the phase shift equals $\pi/2$ once during each cycle, each long pulse representing a string of 1's is split into multiple pulses while 0's are unaffected. Such a device acts as an NRZ-to-RZ converter for the optical bit stream by forcing the output to reduce to zero at the boundaries of each bit. For a sinusoidal clock, the transfer function or the transmissivity of the second modulator becomes

$$T_m(t) = \cos^2[\tfrac{1}{2}\pi \sin^2(\pi Bt)]. \tag{2.3.4}$$

Figure 2.8 shows the clock signal at 40 Gb/s together with the RZ pulses obtained with such a clock by plotting T_m as a function of time. The duty cycle of RZ pulses is about 50%. In practice, duty cycle can be adjusted by reducing the voltage swing and adjusting the bias voltage applied to the modulator, or using a third modulator.

In the second configuration, the bias voltage is set to be $V_b = 2V_\pi$ (point of maximum transmission), and $V_1(t)$ is modulated at a frequency equal to $B/2$ with the peak value $V_\pi/2$. The resulting RZ pulses are considerably shorter and have a duty cycle of 33%. In the third configuration, the bias voltage is set at $V_b = V_\pi$ (point of minimum transmission), and $V_1(t)$ is again modulated in periodic fashion at a frequency equal to $B/2$. This configuration provides a duty cycle of 67%. We discuss it in the next subsection as it also introduces a phase difference between neighboring pulses.

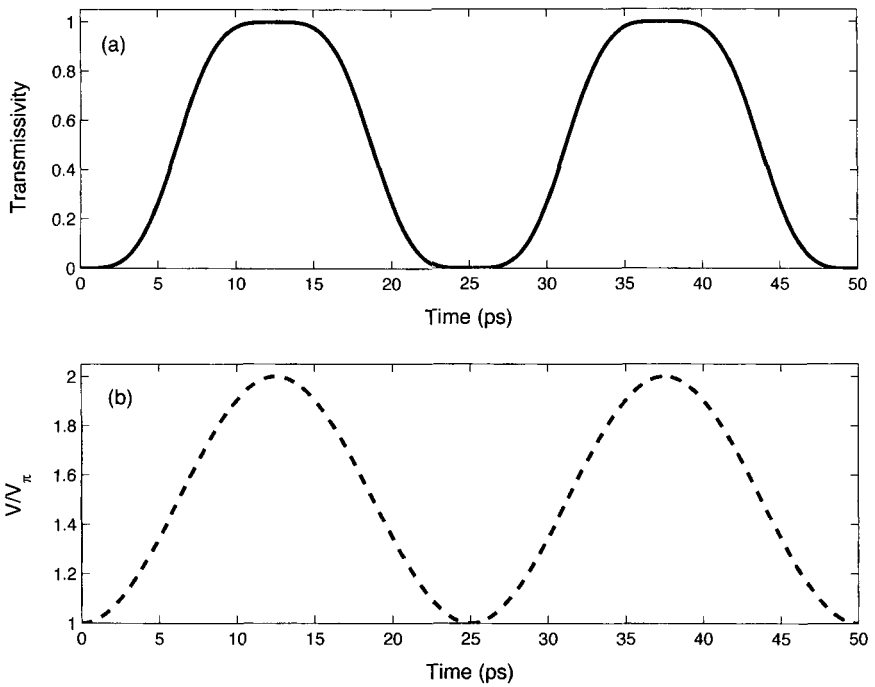

Figure 2.8: RZ pulses (a) created by a pulse carver driven by a sinusoidal clock (b) at the bit rate.

The main drawback of the RZ transmitter shown in Figure 2.7 is that it requires synchronization between the two radio-frequency (RF) signals applied to two modulators. A chirp-based technique has been used with success for realizing such synchronization when an electroabsorption modulator is used as a data modulator [26]. Another technique detects the microwave power spectrum of the transmitted signal and uses it to align the two modulators in a dynamic fashion [28].

2.3.3 Modified RZ Transmitters

The use of RZ format suffers from a drawback in that the bandwidth of an RZ bit stream is enhanced considerably compared with that of an NRZ bit stream (see Figure 2.5). The enhancement factor depends on the duty cycle, and the bandwidth is nearly doubled for a 50% duty cycle. This increase in the channel bandwidth forces one to increase the wavelength separation between two neighboring WDM signals, which in turn reduces the spectral efficiency of dense WDM systems.

The performance of RZ-format lightwave systems can be improved with suitable design modifications. In the case of the CRZ format, optical pulses representing 1 bits are chirped before they are launched into the fiber. Chirping can be realized using either phase modulation or by passing the RZ bit stream through a fixed length of optical fiber (see Section 3.3). As seen from Eq. (2.3.1), the former can be implemented by adjusting

the voltages applied to one of the $LiNbO_3$ modulators in Figure 2.7 so that the optical phase of the signal becomes time-dependent. The later is also easy to implement as it requires only the addition of a fiber of controlled length before the signal is launched into the fiber link used for transmission. Even though chirping of optical pulses does not reduce the signal bandwidth directly (and, in fact, increases it), the CRZ format offers several benefits discussed in Chapters 8 and 9 and is used often in practical long-haul systems.

The idea of phase modulation can be used with success for reducing the signal bandwidth using a format known as the CSRZ format. More specifically, phase modulation is used to introduce a π phase shift between any two neighboring bits. This phase alternation modifies the signal spectrum such that the central peak located at the carrier frequency is suppressed (hence the name CSRZ) and produces a narrower spectrum compared with that of the RZ signal. Figure 2.9 shows the experimentally recorded optical spectra at 42.7 Gb/s for several different formats [22]. The top row compares the CSRZ-format spectrum with the spectra obtained when the RZ and NRZ formats are employed. While both the RZ and NRZ formats contain a dominant peak at the carrier frequency, this peak is absent in the CSRZ spectrum. In all cases, spectral peaks are separated by 42.7 GHz, but the signal bandwidth is generally smaller for the CSRZ bit stream. Notice that the bandwidth depends on the duty cycle of the RZ pulse train and increases when duty cycle is reduced from 67% to 33% (shorter pulses in each bit slot). A duobinary format, in which phase is changed only when an odd number of 0 bits occur between two successive 1 bits, is sometimes employed because its use reduces intersymbol interference. However, the use of this format requires considerable electronic processing of the NRZ data at the transmitter. Optical spectrum of the RZ-duobinary format is shown in the middle row of Figure 2.9.

To understand how the CSRZ format helps in reducing signal bandwidth, it is important to realize that a π phase shift for alternate bits is equivalent to changing the sign of the pulse amplitude. Thus, the modulated signal can be written as

$$A(t) = \sum_n (-1)^n b_n A_p(t - nT_b) \equiv \sum_n \bar{b}_n A_p(t - nT_b). \tag{2.3.5}$$

As seen above, one can absorb the factor $(-1)^n$ in the definition of a new random number $\bar{b}$ that is allowed to take three values (-1, 0, and 1) for each bit. In this sense, the CSRZ format falls in the category of bipolar or ternary schemes commonly used for electrical communication systems [3].

It is easy to see from Eq. (2.2.9) that the phase modulation would change the spectrum of the bit stream because the correlation coefficients r_m appearing in this equation become different when b_n is allowed to take three values. We can calculate these coefficients by remembering that in a bit stream containing N bits, where N is an infinitely large number, $b_n = 0$ for $N/2$ bits but the remaining $N/2$ bits should be divided into two categories such that $b_n = 1$ for $N/4$ bits and -1 for the other $N/4$ bits. Using these three categories, we obtain

$$r_0 = 1/2, \qquad r_m = (-1)^m/4 \ (m \neq 0). \tag{2.3.6}$$

It is this sign reversal of r_m that suppresses the carrier in CSRZ bit streams and, at the same time, reduces the signal bandwidth.

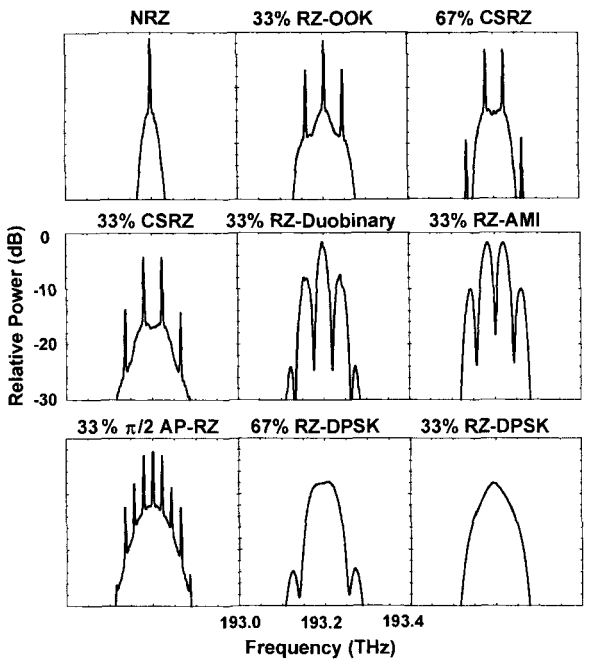

Figure 2.9: Experimentally recorded optical spectra for nine different modulation formats for a 42.7-Gb/s optical bit stream. (After Ref. [22]; ©2004 IEEE.)

The CSRZ scheme can be implemented in practice using the same two-modulator configuration shown in Figure 2.7 for the conventional RZ format [12]. The only difference is that the second modulator (the pulse carver) is operated at half the bit rate ($B/2$) with twice the peak voltage ($V_1 = V_\pi/2$). Moreover, the modulator is biased at the point of minimum transmission ($V_b = V_\pi$) and produces pulses with a 67% duty cycle [27]. From Eq. (2.3.2), the amplitude transmission of the modulator under such driving conditions is given by

$$t_m(t) = \cos[\pi \sin^2(\pi Bt/2)]. \tag{2.3.7}$$

Figure 2.10 shows the electrical clock together with $t_m(t)$ using $B = 40$ Gb/s. During a single clock cycle, two optical pulses with a relative phase shift of π are created by such a modulator. The CSRZ format can be thought of as a phase-modulated carrier on which information is imposed through the ASK format.

A variant of the CSRZ format, known as the alternate-mark-inversion RZ (RZ-AMI) format (also called pseudo-ternary), is used with success in electrical communication systems [3]. This format can also be adopted for lightwave systems [29]. As seen in Figure 2.9, the spectrum for the RZ-AMI format is quite different than that of the CSRZ format. The main difference between the two formats is that a π phase shift is introduced in the case of the RZ-AMI format only for 1's so that alternate 1 bits have their amplitudes inverted. This simple change affects the signal spectrum because the correlation coefficients in Eq. (2.2.9) are different for the RZ-AMI format than those

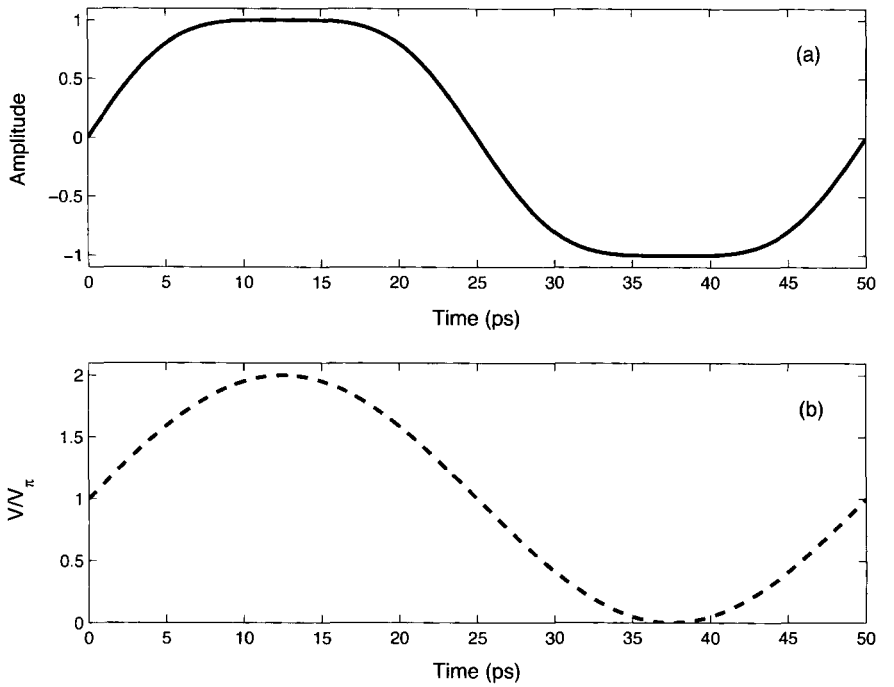

Figure 2.10: (a) Amplitude of CSRZ pulses for a 40-Gb/s bit stream and the (b) sinusoidal clock at half the bit rate used to generate it. Two pulses created during a single clock cycle are shifted in phase by π.

obtained for the CSRZ format. It is easy to see that $r_0 = 1/2$ while $r_1 = r_{-1} = -1/4$ because the product $b_n b_{n+1}$ is negative when both bits are 1 (and zero in all other cases). On the other hand, r_m vanishes for all $|m| > 1$ because both 1 and -1 values are likely for any two 1 bits. As a result, only three terms survive in the sum appearing in Eq. (2.2.9), and the power spectral density becomes

$$S_A(\omega) = \frac{1}{2T_b}|\tilde{A}_p(\omega)|^2[(1 - \cos(\omega T_b)]. \tag{2.3.8}$$

Using $|\tilde{A}_p(\omega)|^2$ from Eq. (2.2.16) with $d_c = \frac{1}{2}$ (50% duty cycle), we obtain

$$S_A(\omega) = \frac{P_0 T_b}{4}\text{sinc}^2(\omega T_b/4)\sin^2(\omega T_b/2). \tag{2.3.9}$$

It is important to note that the power spectral density completely vanishes at $\omega = 0$ in contrast with the case of CSRZ for which only the discrete component vanishes at $\omega = 0$. This suppression of the spectral density in the vicinity of the carrier frequency represents a major benefit of the RZ-AMI format.

Another variant of the RZ format is known as alternate-phase RZ (AP-RZ). In this format, the phase of two neighboring bits is alternated between two values that differ by a value other than π. Phase alternation by $\pi/2$ is often used in practice. As seen in

Figure 2.9, the spectrum for the AP-RZ format is quite different from that of the CSRZ format. It contains more spectral peaks because peaks are separated by only $B/2$, rather than B, at a bit rate B. A peak appears even at the carrier frequency. Although this spectrum appears undesirable at first sight, experimental results show that the AP-RZ format can provide a better system performance under certain conditions compared with the NRZ, RZ, and CSRZ formats [22].

The signal bandwidth of any modulation format can be reduced by 50% by adopting a single-sideband scheme in which only one sideband located on either side of the carrier frequency is transmitted [1]–[4]. This is possible because the signal spectrum is symmetric around the carrier frequency, and both the upper and lower sidebands contain the entire information content of the signal. However, the generation of an optical bit stream with a single sideband is not a simple task [16]. Moreover, the nonlinear effects occurring inside the fiber link tend to regenerate the suppressed sideband.

The double-modulator configuration of Figure 2.7, as mentioned earlier, suffers from a synchronization problem. It would be much more preferable if an RZ bit stream can be generated with a single modulator. It turns out that an RZ pulse train can be generated using a single modulator provided it is driven by a differentially encoded NRZ signal, and one exploits the nonlinear switching characteristics of MZ modulators [30]. As mentioned earlier, NRZ transmitter operates by biasing the modulator at the half-power point. To create the RZ pulse train from the same transmitter, the modulator is biased at the peak of its transmission while the amplitude of the differentially encoded NRZ signal is doubled. Setting $V_b = V_\pi$ in Eq. (2.3.3), the transmissivity of the modulator is given by

$$T_m(V_1) = \sin^2\left(\frac{\pi}{2V_\pi}[2V_1(t) - V_\pi]\right) = \cos^2[\pi V_1(t)/V_\pi]. \tag{2.3.10}$$

Since an optical pulse is produced whenever the electrical signal changes from low to high or high to low, the transmitter produces an RZ-coded bit stream from a differentially encoded NRZ signal in which information is coded such that the voltage level changes between its two values whenever the next bit is a "1" bit.

Figure 2.11 shows another scheme in which a single phase modulator produces an RZ signal from a differentially encoded NRZ bit stream [31]. It makes use of a

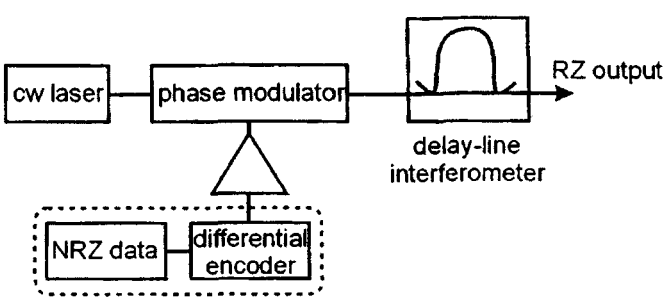

Figure 2.11: Block diagram of an RZ transmitter constructed using a single phase modulator in combination with a delay-line interferometer. (After Ref. [31]; ©2001 IEEE.)

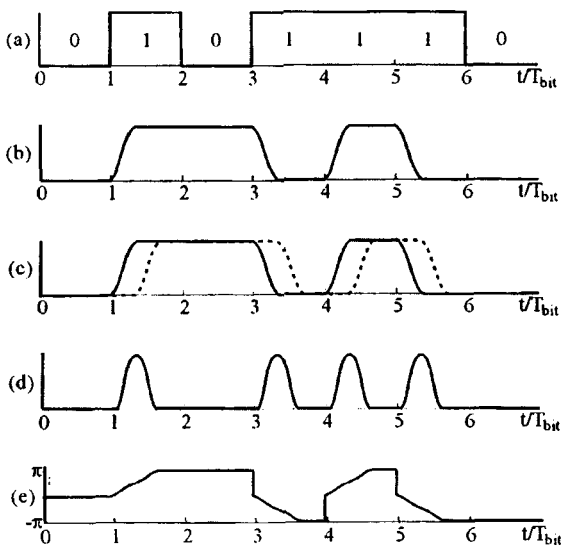

Figure 2.12: (a) The NRZ data; (b) its differentially encoded version; (c) original (solid) and delayed (dashed) phase profiles at the output coupler; (d) final RZ bit stream; and (e) phase variations across it. (After Ref. [31]; ©2001 IEEE.)

passive optical delay-line (MZ) interferometer to produce the RZ output from a phase-modulated optical signal. Figure 2.12 shows how such a device functions. The differential encoder takes the NRZ data in part (a) and converts it into another electrical bit stream shown in part (b). This new bit stream drives the phase modulator and modifies the phase of an optical carrier such that a π phase shift is produced whenever the voltage is nonzero. The phase-encoded optical signal is split into two equal parts inside a MZ interferometer and is delayed in one branch by a fixed amount (a fraction of the bit slot). Figure 2.12(c) shows the phase profiles for the two fields. When these two optical fields are combined using a 3-dB coupler, constructive or destructive interference occurs depending on whether the relative phase shift is 0 or π. The resulting output shown in part (d) consists of an RZ bit stream corresponding to the original NRZ signal. The width of the RZ pulse can be controlled by adjusting the optical delay in the longer branch of the interferometer.

As expected from Eq. (2.3.2) and seen in Figure 2.12(e), the phase of the RZ signal is not uniform across all bits when a delay-line interferometer is used and appears to change in an erratic manner from bit to bit. Although not immediately apparent, this phase nonuniformity is, in fact, beneficial because it corresponds to a phase change of π across every 1 bit. Moreover, the direction of phase change is opposite for any two neighboring 1 bits. This is exactly what is required for producing the AMI format. Thus, the transmitter shown in Figure 2.11 produces an RZ-AMI signal. As discussed earlier, this format produces a smaller channel bandwidth compared with that of the traditional RZ format. It is also beneficial for lightwave systems whose performance is limited by the nonlinear effects occurring within the fiber link [29].

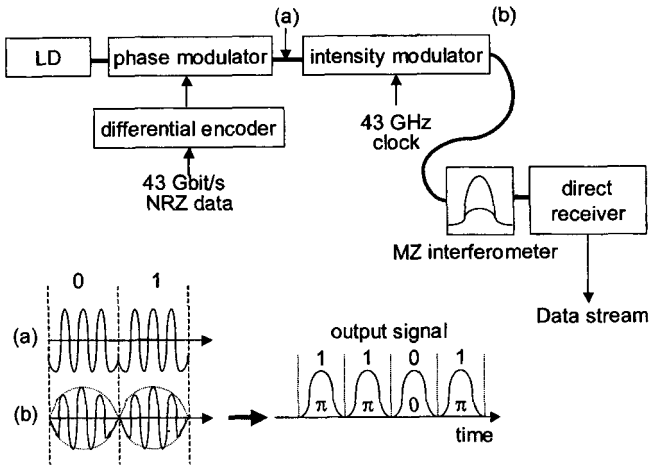

Figure 2.13: Schematic of an RZ-DPSK transmitter together with the receiver design. The insets (a) and (b) show how the electric field varies across two bits after first and second modulators, respectively. (After Ref. [14]; ©2002 IEEE.)

2.3.4 DPSK Transmitters and Receivers

In this subsection we focus on the RZ-DPSK format that has been found quite useful for reducing the impact of cross-phase modulation (see Section 4.2) in WDM lightwave systems [17]–[22]. Similar to the formats such as CSRZ and RZ-AMI, both the intensity and the phase of an optical carrier are modulated in the RZ-DPSK case but with one important difference: Whereas information is coded using ASK in all previous formats, it is coded in the phase of the optical carrier in the RZ-DPSK case.

To create an RZ-DPSK signal, the carrier's amplitude is first modulated to produce a regular pulse train in which an optical pulse is present in every bit slot. The information is coded by changing the phase of these pulses using the DPSK scheme such that a phase difference of π between any two neighboring pulses corresponds to 1 bits. Figure 2.9 compares the spectra of a 42.7-Gb/s bit stream in the RZ-DPSK format with several other RZ-based formats. The DPSK format has been used in the past in the context of coherent lightwave systems but only the phase of the carrier was modulated. The use of intensity modulation makes this format more robust to the dispersive and nonlinear effects for WDM systems transmitting multiple channels simultaneously. One can also employ the CSRZ-DPSK format by shifting the phase of alternating pulses by π, in addition to the phase and amplitude changes associated with the transmitted data.

Figure 2.13 shows how two modulators in series can be used to create an optical bit stream in the RZ-DPSK format [14]. The CW output from a DFB laser is first modulated using a phase modulator driven by the differentially encoded NRZ signal. The output after this modulator still has constant intensity since information is hidden in the phase of the optical carrier as shown in the inset (a). The second modulator driven at the bit rate creates pulses in each bit slot without affecting the phase, resulting in the form of electric field shown in the inset (b). The phase information is converted into

current variations at the receiver by first passing the optical signal through a delay-line interferometer similar to that shown in Figure 2.11. The only difference is that the length difference between the two arms of the MZ interferometer is chosen such that it delays the signal by exactly one bit slot. It is this one-bit delay that allows one to reconstruct the original bit stream using a conventional direct-detection scheme.

One can understand the operation of such a receiver by noting that the output of the interferometer is formed through a superposition of the transmitted signal with its one-bit-delay version. We can use the transfer-matrix approach of Eq. (2.3.1) but we have to remember that the input field is now time-dependent. An MZ interferometer acts as an optical filter that shifts the phase of each frequency component of the pulse by a different amount. We should thus work in the spectral domain and write Eq. (2.3.1) as follows:

$$\begin{pmatrix} \tilde{A}_b \\ \tilde{A}_c \end{pmatrix} = \frac{1}{2}\begin{pmatrix} 1 & i \\ i & 1 \end{pmatrix}\begin{pmatrix} e^{i\omega T_b} & 0 \\ 0 & 1 \end{pmatrix}\begin{pmatrix} 1 & i \\ i & 1 \end{pmatrix}\begin{pmatrix} \tilde{A}(\omega) \\ 0 \end{pmatrix}, \tag{2.3.11}$$

where a tilde represents the Fourier transform. We have written the additional phase shift in one of the arms as $e^{i\omega T_b}$ to stress its frequency dependence. Noting that this extra phase shift amounts to a temporal delay of the field by T_b when one takes the inverse Fourier transform of the output field, the power of optical signal falling at the photodetector can be written as

$$P(t) = \tfrac{1}{4}|A(t) \pm A(t - T_b)|^2, \tag{2.3.12}$$

where the choice of sign depends on whether the bar or cross port of the MZ interferometer is used for photodetection. Using $A(t) = \sqrt{P(t)}\exp[i\phi(t)]$ and assuming that pulse shape is the same for all bits, the current at the receiver can be written as

$$I_d(t) = R_d P(t)\tfrac{1}{2}[1 \pm \cos(\Delta\phi)], \tag{2.3.13}$$

where $\Delta\phi(t) = \phi(t) - \phi(t - T_b)$ is the phase difference between the two neighboring bits. Since $\Delta\phi = 0$ for 0 bits but changes to π for 1 bits, one can reconstruct the original bit stream from temporal variations in the received electrical signal.

2.4 Transmitter Design

Design of optical transmitters requires attention to many details that differ from application to application [32]–[36]. For example, applications related to computer-data and access networks have low cost as a major design objective and need relatively low-power optical transmitters, based on LEDs or vertical-cavity surface-emitting lasers (VCSELs), that can operate over a wide temperature range without internal cooling. For metropolitan networks, low cost remains important but bit rates are also higher (typically 2.5 Gb/s). Such networks require semiconductor lasers that can be directly modulated at such bit rates. In contrast, submarine and terrestrial long-haul lightwave systems operate at high speeds and employ multiple WDM channels, each operating at 10 Gb/s or more. The design requirements are most stringent for such systems. A DFB laser is invariably used for stabilizing the channel wavelength. CW light from the DFB laser is coupled to a modulator as efficiently as possible. The modulator is

often integrated with the laser. If that is not possible, an external $LiNbO_3$ modulator is employed. In both cases, the optical bit stream generated needs to be launched into the fiber link without experiencing significant coupling losses and without undesirable feedback into the transmitter. This section focuses on the major design issues relevant to optical transmitters.

2.4.1 Coupling Losses and Output Stability

A design objective for any transmitter is to couple as much light as possible into the optical fiber. In practice, coupling efficiency depends on the type of optical source (LED versus laser) as well as on the type of fiber (multimode versus single mode). The coupling can be very inefficient when light from an LED is coupled into a single-mode fiber. In contrast, coupling efficiency for semiconductor lasers is typically 40 to 50% and can exceed 80% for VCSELs because of their circular spot size. A small piece of fiber (known as the pigtail) is included with every transmitter so that the coupling efficiency can be maximized during packaging; a splice or connector is used to join the pigtail with the fiber cable.

Two approaches have been used for coupling the optical bit stream into an optical fiber efficiently; both are shown schematically in Figure 2.14. In one approach, known as butt coupling, one end of the fiber pigtail is brought almost in contact with the laser (if direct modulation is used) or with the last modulator, and the two are held in place by epoxy. In the other scheme, known as lens coupling, a lens is used to maximize the coupling efficiency. Each approach has its own merits, and the choice generally depends on other factors such as packaging and cost. An important criterion is that the coupling efficiency should not change with time; long-term mechanical stability of the coupling scheme is therefore a necessary requirement.

The butt coupling of a semiconductor laser to a fiber provides only 10 to 20% efficiency if no attempt is made to match the mode sizes of the laser and the fiber. Typically, index-guided InGaAsP lasers have an elliptical spot size with dimensions in the range of 1 to 2 μm, whereas the mode diameter of a single-mode fiber exceeds 6 μm. The coupling efficiency can be improved considerably by tapering the fiber end and forming a lens at the fiber tip. Figure 2.14(a) shows such a butt-coupling scheme for a commercial transmitter. The fiber is attached to a jewel, and the jewel is attached to the laser submount through an epoxy [34]. The fiber tip is aligned with the emitting region of the laser to maximize the coupling efficiency (typically 40%). The use of a lensed fiber improves the coupling efficiency, and values close to 80% have been realized with an optimum design [37]–[39].

Figure 2.14(b) shows the lens-coupling scheme for transmitters. The coupling efficiency can exceed 70% for a confocal design in which a sphere is used to collimate the laser light and focus it onto the fiber core. The alignment of the fiber core is less critical for the confocal design because the spot size is magnified to match the fiber's mode size. The mechanical stability of the package is ensured by soldering the fiber into a ferrule that is secured to the body by two sets of laser alignment welds. One set of welds establishes proper axial alignment, while the other set provides transverse alignment.

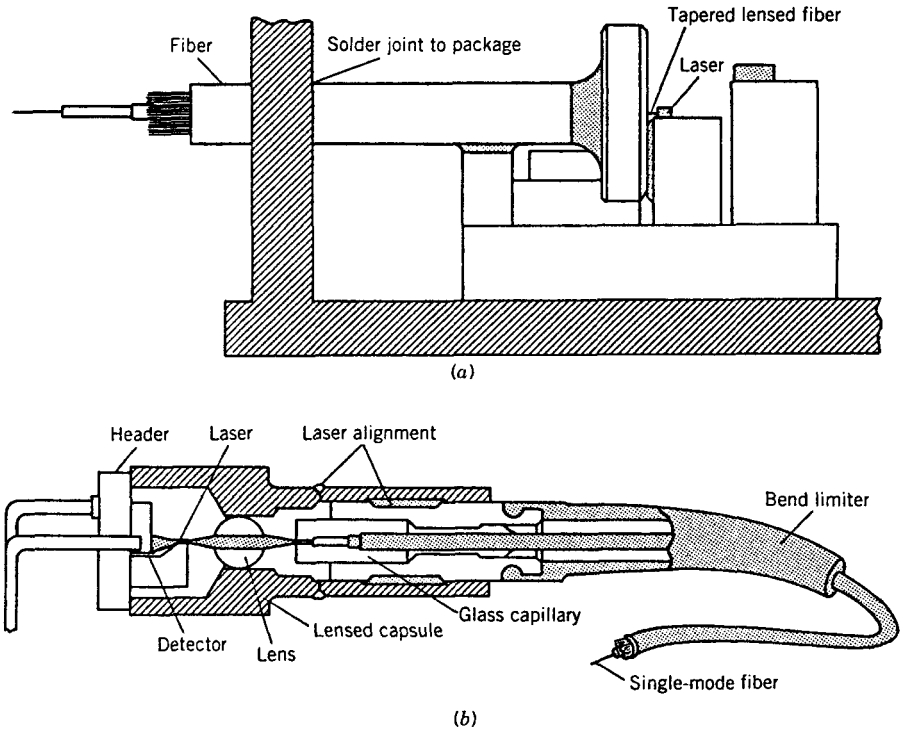

Figure 2.14: Transmitters employing (a) butt-coupling and (b) lens-coupling designs. (After Ref. [34]; ©1989 AT&T).

The coupling issue for transmitters is important enough that several new schemes were developed during the 1990s [40]–[44]. In one approach, a silicon optical bench is used to align the laser and the fiber [40]. In another, a silicon micromirror fabricated using a micro-machining technique is used for optical alignment [41]. In a different approach, a directional coupler is used as the *spot-size converter* for maximizing the coupling efficiency [42]. Coupling efficiencies of >80% have been realized by integrating a spot-size converter with semiconductor lasers [44].

An important problem that needs to be addressed in designing an optical transmitter is related to the extreme sensitivity of semiconductor lasers to optical feedback [45]. Even a relatively small amount of feedback (<0.1%) can destabilize the laser and affect the system performance through phenomena such as linewidth broadening, mode hopping, and the enhancement of relative intensity noise [45]–[48]. While designing an optical transmitter, attempts are made to reduce the feedback into the laser cavity using antireflection coatings. Feedback can also be reduced by cutting the fiber tip at a slight angle so that the reflected light does not hit the active region of the laser. Such precautions are generally enough to reduce the feedback to a tolerable level. However, it may be necessary to use an optical isolator between the laser and the fiber in transmitters designed for more demanding applications. A very compact isolator can be

designed if the lens in Figure 2.14(b) is replaced by a YIG sphere so that it serves a dual purpose [49]. As light from a semiconductor laser is already polarized, a signal polarizer placed between the YIG sphere and the fiber can reduce the feedback by more than 30 dB.

Another issue that must be addressed is the stability of the transmitter output. Each lightwave system is designed to operate with a certain amount of average power launched into the fiber link, and it is important that this power level is maintained throughout the system lifetime. In practice, power level can change if coupling losses change because of mechanical motion of the transmitter components. It can also change if the threshold current of the semiconductor laser itself increases because of aging-related degradations when the laser is biased at a constant current. To keep the output power level constant, most transmitters incorporate a built-in mechanism that adjusts the driving current in a dynamic fashion. This is realized by incorporating a photodiode that monitors the laser output and generates an electrical control signal that can be used to adjust the laser bias level. The rear facet of the laser is generally used for the monitoring purpose (see Figure 2.14). In some transmitters a front-end tap is used to divert a small fraction of the output power to the detector.

2.4.2 Wavelength Stability and Tunability

Dense WDM lightwave systems operate with a channel spacing as small as 25 GHz (or 0.2 nm). It is thus essential that the wavelength of each optical carrier remains stable to within 1 GHz or so, or to within 10 pm, throughout the operating lifetime of the transmitter. The use of DFB lasers helps because the carrier wavelength is set by a built-in grating internal to the laser structure. However, the Bragg wavelength λ_B of this grating is set by the grating period Λ through the relation $\lambda_B = 2\bar{n}\Lambda$, where $\bar{n}$ is the effective index of the laser mode. The stability of λ_B requires $\bar{n}$ to remain constant. In fact, since λ_B is near 1,550 nm, it can remain stable to within 10 pm only if changes in $\bar{n}$ are below 10^{-5}. Since a temperature variation of even 1°C within the active region of the laser can change $\bar{n}$ by an amount larger than that, one must control the laser temperature to a fraction of 1°C. This is realized in practice by including a thermoelectric cooler within the transmitter.

Since wavelength stability of the optical carrier is paramount for WDM systems, high-performance transmitters employ a wavelength-monitoring scheme and control the laser wavelength using a servo-loop mechanism. Several different schemes have been employed for this purpose [50]–[54]. Figure 2.15 shows a DFB laser module in which both the optical power and the wavelength of the laser are monitored and maintained to constant values using the feedback loop shown in Figure 2.16. Light from the back facet of the DFB laser is split into two branches using a prism. A Fabry–Perot étalon in one branch serves as a wavelength reference; it is designed such that one of its transmission peaks occurs precisely at the wavelength at which the laser is designed to operate.

The use of a Fabry–Perot étalon as a wavelength reference suffers from one problem. Variations in the étalon temperature can affect both its cavity length and the refractive index and shift the transmission peaks in an uncontrolled manner. One could employ another thermoelectric cooler to keep the temperature of the étalon constant.

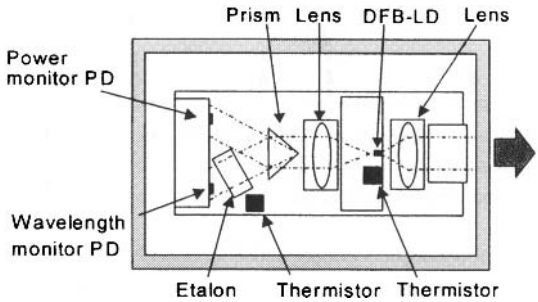

Figure 2.15: Schematic of a DFB laser-diode (LD) module with a built-in étalon for monitoring and stabilizing the laser wavelength; PD stands for photodiode. (After Ref. [54]; ©2003 IEEE.)

The feedback loop shown in Figure 2.16 solves this problem by monitoring the temperature of the étalon in addition to monitoring the laser wavelength and power and adjusting the feedback signal accordingly [54]. The laser wavelength is kept constant by adjusting the current applied to the thermoelectric cooler and changing the laser temperature. With this approach, the wavelength of the laser module drifted by less than 1 pm even when the module temperature varied from 5 to 70°C. Reliability tests indicated that wavelength drift for such lasers should be less than 5 pm during a 25-year operating period.

A large number of DFB lasers, each designed to operate at a fixed wavelength chosen from the ITU grid, is required for dense WDM systems. The maintenance of such a WDM transmitter with 100 or more channels is impractical because one must maintain a large inventory of individual DFB lasers. A solution is provided by the so-called tunable semiconductor laser whose wavelength can be tuned over a wide range electronically while maintaining its stability. Indeed, multisection DFB and distributed

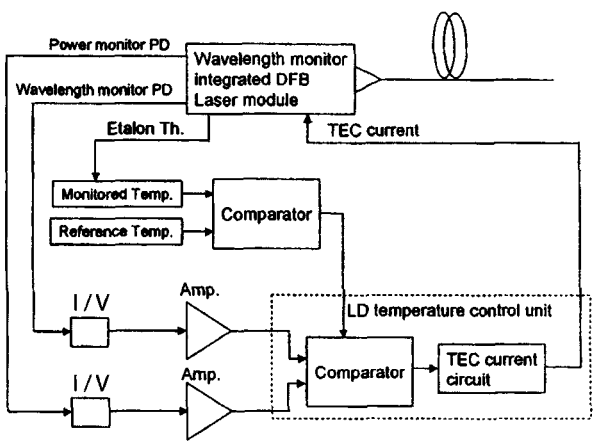

Figure 2.16: Block diagram of the feedback loop used to monitor and maintain the laser wavelength and optical power simultaneously. (After Ref. [54]; ©2003 IEEE.)

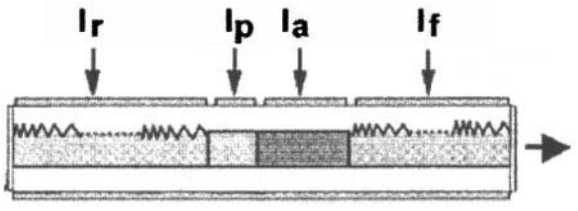

Figure 2.17: Schematic of a sampled-grating DBR laser with four sections, each of which can be biased independently to realize tuning over a wide range. (After Ref. [59]; ©2000 IEEE.)

Bragg reflector (DBR) lasers have been developed to meet the somewhat conflicting requirements of stability and tunability [55]–[60].

In its simple form, a tunable DBR laser consists of three sections, referred to as the active section, the phase-control section, and the Bragg section (see Section 5.2.3 of LT1). Each section can be biased independently by injecting different amounts of currents. The current injected into the Bragg section is used to change the Bragg wavelength through carrier-induced changes in the refractive index $\bar{n}$. The current injected into the phase-control section is used to change the phase of the feedback from the DBR through carrier-induced index changes in that section. The laser wavelength can be tuned almost continuously over the range of 10 to 15 nm by controlling the currents in the phase and Bragg sections. By 1998, such lasers exhibited a tuning range of 17 nm and output powers of up to 100 mW with high reliability [55].

More recently, several new designs have been developed for tunable semiconductor lasers. Figure 2.17 shows one such structure known as the sampled-grating DBR (SG-DBR) laser [59]. It consists of four sections, each of which can be controlled electronically by injecting four different electrical currents. The current I_a applied to the active section controls the output power. The current I_p is applied to the phase-control section for changing the feedback phase. The two outer sections act as DBRs, each designed with a superstructure or sampled grating, so that they can provide feedback at multiple wavelengths, or carrier frequencies, that are spaced apart exactly by the required channel spacing (typically 50 GHz). The currents I_f and I_r applied to the front and rear sections can be tuned in combination with I_a and I_p such that the laser can operate at any of these discrete wavelengths while maintaining almost the same optical power. Such multisection DBR lasers can be tuned over a wavelength range exceeding 100 nm using the Vernier effect. Each SG-DBR section supports its own comb of wavelengths but the spacing in each comb is not the same. The wavelength coinciding in the two combs becomes the output wavelength that can be tuned over a wide range.

Figure 2.18 shows another tunable laser structure in which a grating-assisted directional coupler is inserted between the active and phase-control sections, and a single DBR section with a sampled grating is employed. The coupler section has two vertically separated waveguides having different thickness and material composition so that they form an asymmetric directional coupler. The grating can selectively transfer a single wavelength from the wavelength comb supported by the DBR section. Such lasers can also provide a tuning range of more than 110 nm with a suitable design.

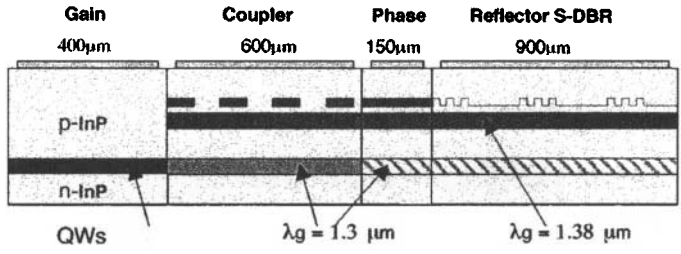

Figure 2.18: Schematic of a tunable DBR laser with an integrated grating-assisted directional coupler. (After Ref. [59]; ©2000 IEEE.)

2.4.3 Monolithic Integration

The electrical components used in the driving circuit determine the speed at which transmitter output can be modulated. For lightwave transmitters operating at bit rates above 1 Gb/s, electrical parasitics associated with various transistors and other components often limit the transmitter performance. The performance of high-speed transmitters can be improved considerably by integrating monolithically the laser with driver electronics. Such monolithic transmitters are referred to as optoelectronic integrated circuits (OEICs) as optical and electrical devices are fabricated on the same chip.

The OEIC approach was first applied to integration of GaAs lasers simply because the technology for fabrication of GaAs electrical devices was relatively well established [61]–[63]. However, since most lightwave systems employ InGaAsP lasers, attention soon turned toward the fabrication of InP-based OEICs [64]–[69]. By 1995, 10-Gb/s laser transmitters were fabricated by integrating 1.55-μm DFB lasers with field-effect transistors made with the InGaAs/InAlAs material system [66].

The concept of monolithic integration can be extended to build single-chip transmitters by adding as much functionality as possible on the same chip. Considerable effort has been directed toward developing such devices, often called *photonic* integrated circuits; they integrate on the same chip multiple optical components such as lasers, detectors, modulators, and amplifiers [70]–[80]. Such an approach also provides an opportunity to fabricate WDM devices in which multiple DFB or DBR lasers are integrated within a single transmitter. The use of such WDM transmitters reduces the complexity of lightwave systems as a single component can generate multiple bit streams at different carrier frequencies.

The integration of an electroabsorption modulator with a DFB or DBR laser was pursued during the decade of 1990s because such a device generates an optical bit stream directly [81]–[93]. By 1999, 10-Gb/s optical transmitters with an integrated modulator were available commercially, and they are used routinely for WDM lightwave systems [85]. By 2001, modulator-integrated transmitters were able to operate at a bit rate of 40 Gb/s [87]. In a 2003 experiment, such a device was used for transmitting a 40-Gb/s signal over 1,200 km [92].

Integration of a tunable DBR laser with an electroabsorption modulator results in transmitters whose output is tunable over a wide wavelength range. In a 2002 demonstration, a four-section SG-DBR laser (see Figure 2.17) was integrated with a mod-

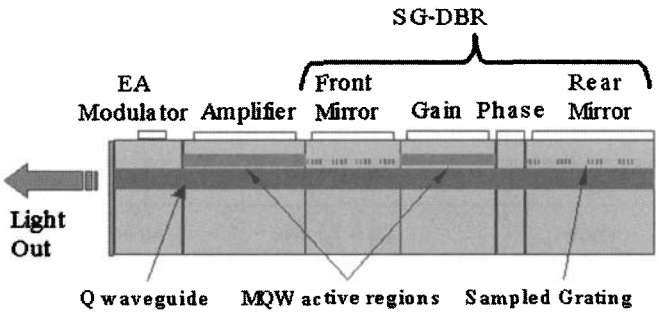

Figure 2.19: Schematic of an SG-DBR laser integrated with an electroabsorption (EA) modulator and a semiconductor optical amplifier. (After Ref. [90]; ©2002 IEEE.)

ulator and a semiconductor optical amplifier (SOA), resulting in a six-section device shown schematically in Figure 2.19. Such devices were tunable over 40 nm while maintaining an extinction ratio better than 10 dB [90]. The use of a built-in optical amplifier permitted power levels high enough that more than 10 mW of optical power could be coupled to a single-mode fiber over the entire tuning range. At the same time, the use of two sampled gratings allowed operation in a single longitudinal mode with a sidemode suppression ratio of better than 40 dB.

The technique of monolithic integration is being pursued to combine as many discrete elements as possible on the same chip. Even an MZ modulator can be integrated with a semiconductor laser because the InP material used to make the laser also exhibits the electrorefraction effect that can be used to change the refractive index by applying a voltage across a passive waveguide. Indeed, a MZ modulator has been integrated with a four-section tunable SG-DBR laser [79]. Figure 2.20 shows the layout of such a chip schematically. It also incorporates a back-facet power detector and an SOA between the laser and the modulator. The 1-mm-long modulator section incorporates two multimode-interference (MMI) couplers (see Section 4.5.2 of LT1 for a discussion of such couplers) to couple the light into and out of two passive waveguides serving as two arms of the MZ interferometer. The whole device is only 3.4 mm long. Clearly, such photonic integrated circuits are likely to be quite useful for further advances in lightwave technology.

Monolithic integration of multiple DFB lasers on the same chip provides an alternative solution to tunability and results in transmitters whose wavelength can be changed over a wide range by simply selecting different lasers. Such a device is sometimes referred to as the wavelength-selectable laser (WSL). Figure 2.21 shows the design of such a transmitter schematically [78]. It combines a WSL unit with a wavelength-locking unit that locks the laser wavelength using a Fabry–Perot étalon. The WSL unit incorporates an array of eight DFB lasers whose output is sent to a single SOA through an MMI coupler. Each DFB laser can be tuned over a few nanometers by changing its temperature; this fine tuning permits setting of the transmitter wavelength precisely on a carrier frequency on the ITU grid. The wavelength can be changed by a much larger value by turning on individual DFB lasers selectively within the array. The combination

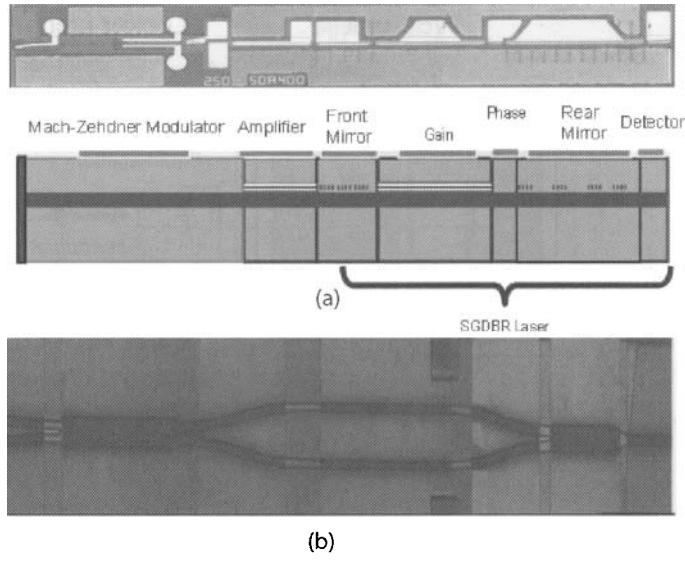

Figure 2.20: (a) Schematic of a tunable SG-DBR laser integrated with a detector, an SOA, and a Mach–Zender modulator; top view of the chip is also shown. (b) Details of the modulator section showing two waveguides and two MMI couplers at the two end. (After Ref. [79]; ©2003 IEEE.)

of temperature tuning and multi-wavelength arrays can produce, in principle, transmitters that can be operated anywhere within the S, C, and L bands covering a wavelength range from 1,460 to 1,620 nm. As shown in Figure 2.21, the entire transmitter can be fitted inside a standard butterfly package with dimensions of 12.7 mm $\times$ 20.8 mm.

2.4.4 Reliability and Packaging

An optical transmitter should operate reliably over a relatively long period of time (10 years or more) in order to be useful as a major component of lightwave systems. The reliability requirements are even more stringent for submarine lightwave systems for which repairs and replacement are prohibitively expensive, and all components are designed to last at least 25 years. By far the major reason for failure of optical transmitters is the optical source itself. Considerable testing is performed during assembly and manufacture of transmitters to ensure a reasonable lifetime for the optical source. It is common [32] to quantify the lifetime by a parameter t_F known as *mean time to failure* (MTTF). Its use is based on the assumption of an exponential failure probability [$P_F = \exp(-t/t_F)$]. Typically, t_F should exceed 10^5 hours (about 11 years) for the optical source. Reliability of semiconductor lasers has been studied extensively to ensure their survival under realistic operating conditions [94]–[99].

Both LEDs and semiconductor lasers can stop operating suddenly (catastrophic degradation) or may exhibit a gradual mode of degradation in which the device efficiency degrades with aging [95]. Attempts are made to identify devices that are likely to degrade catastrophically. A common method is to operate the device at high temper-

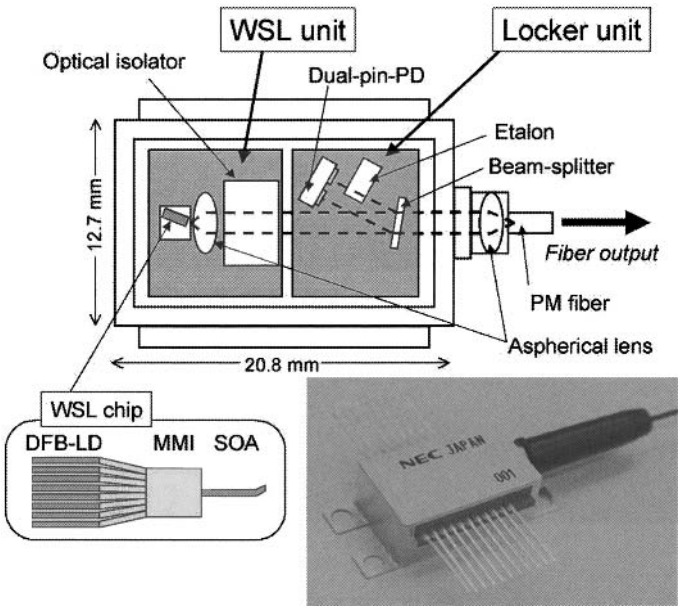

Figure 2.21: Schematic view of a wavelength-selective transmitter designed with a WSL chip (left inset) in which the output of multiple DFB lasers is coupled into a single SOA through a MMI coupler. The right inset shows photograph of the butterfly package housing the transmitter. (After Ref. [78]; ©2002 IEEE.)

atures and high current levels. This technique is referred to as burn-in or accelerated aging [94] and is based on the assumption that under high-stress conditions weak devices will fail, while others will stabilize after an initial period of rapid degradation. The change in the operating current at a constant power is used as a measure of device degradation. The degradation rate can be used to estimate the laser lifetime and the MTTF at the elevated temperature. The MTTF at the normal operating temperature is then extrapolated by using an Arrhenius-type relation $t_F = t_0 \exp(-E_a/k_B T)$, where t_0 is a constant and E_a is the activation energy with typical values of around 1 eV [95]. Physically, gradual degradation is due to the onset of dark-line or dark-spot defects within the active region of the laser [45].

Extensive tests have shown that LEDs are normally more reliable than semiconductor lasers under the same operating conditions. The MTTF for GaAs LEDs easily exceeds 10^6 hours and can be $>10^7$ hours at 25°C [95]. The MTTF for InGaAsP LEDs is even larger, approaching a value $\sim 10^9$ hours. By contrast, the MTTF for InGaAsP lasers is generally limited to 10^6 hours at 25°C [96]–[98]. Nonetheless, this value is large enough that semiconductor lasers can be used in undersea optical transmitters designed to operate reliably for a period of 25 years. Because of the adverse effect of high temperatures on device reliability, most transmitters use a thermoelectric cooler to maintain the source temperature near 20°C even when the outside temperature may be as high as 80°C.

Even with a reliable optical source, a transmitter may fail in an actual system if the coupling between the source and the fiber degrades with aging. Coupling stability is an important issue in the design of reliable optical transmitters. It depends ultimately on the packaging of transmitters. Although LEDs are often packaged nonhermetically, a hermetic environment is essential for semiconductor lasers. It is common to package the laser separately so that it is isolated from other transmitter components. Figure 2.14 shows two examples of laser packages. In the butt-coupling scheme, an epoxy is used to hold the laser and fiber in place. Coupling stability in this case depends on how epoxy changes with aging of the transmitter. In the lens-coupling scheme, laser welding is used to hold various parts of the assembly together. The laser package becomes a part of the transmitter package, which includes other electrical components associated with the driving circuit. The choice of transmitter package depends on the type of application. A dual-in-line package or a butterfly housing with multiple pins is typically used. Figure 2.21 shows an example of the butterfly package.

Problems

2.1 Sketch how the electric field of a carrier would change with time for the PSK format during 5 bits with the pattern 01010. Assume that the phase of the carrier is shifted by 180° during each 1 bit.

2.2 Explain what is meant by the DPSK format. Sketch how the electric field varies for this format using the same 5-bit pattern 01010 used in the preceding problem.

2.3 A 1.55-μm lightwave system is transmitting digital signals over 100 km at 2 Gb/s. The transmitter launches 2 mW of average power into the fiber cable, having a net loss of 0.3 dB/km. How many photons are incident on the receiver during a single 1 bit? Assume that 0 bits carry no power, while 1 bits are in the form of a rectangular pulse occupying the entire bit slot (NRZ format).

2.4 Sketch the variation of optical power with time for a digital NRZ bit stream 010111101110, assuming a bit rate of 10 Gb/s. What is the duration of the shortest and widest optical pulse? What is the peak power when an average power of 2 mW is launched into the fiber?

2.5 A 0.8-μm optical receiver needs at least 1,000 photons to detect the 1 bits accurately. What is the maximum possible length of the fiber link for a 100-Mb/s lightwave system designed to transmit -10 dBm of average power? The fiber loss is 2 dB/km at 0.8 μm. Assume the NRZ format and a rectangular pulse shape.

2.6 A 1.3-μm optical transmitter is used to generate a digital bit stream at a bit rate of 2 Gb/s. Calculate the number of photons contained in a single 1 bit when the average power emitted by the transmitter is 4 mW. Assume that the 0 bits carry no energy.

2.7 Discuss the conditions under which the Wiener–Khintchine theorem can be used for a fluctuating optical field. You may consult any book on stochastic processes.

2.8 Prove that the relation $S_A(\omega) = S_b(\omega)|\tilde{A}_p(\omega)|^2$ indeed follows from Eqs. (2.2.1) through (2.2.3).

2.9 Prove the identity given in Eq. (2.2.12). What is the physical meaning of this relation?

2.10 Starting from Eq. (2.2.13), find the power spectral density of an RZ bit stream with 50% duty cycle.

2.11 Derive an expression for the bar-port transmissivity of a Mach–Zehnder modulator as a function of applied voltage V when the voltage drop across its two arms is equal in magnitude but opposite in sign. Assume that both couplers are ideal 3-dB couplers.

2.12 Describe how two modulators can be used to create an RZ bit stream from an electrical bit stream in the NRZ format.

2.13 Explain why a phase shift of π between any two neighboring bits of an RZ bit stream results in no power at the carrier frequency. How would you obtain such a phase shift from a modulator acting as a pulse carver?

2.14 Describe what is meant by the RZ-AMI format. Sketch the design of an optical transmitter that can produce an optical bit stream in this format.

2.15 Sketch the design of optical receivers used to recover an optical bit streams transmitted in the RZ-DPSK format. Explain how such a receiver can detect phase information with direct detection.

2.16 Describe a wavelength-monitoring scheme for WDM transmitters. Use diagrams as necessary to make your point clear.

References

[1] M. Schwartz, *Information Transmission, Modulation, and Noise*, 4th ed., McGraw-Hill, New York, 1990.

[2] L. W. Couch II, *Modern Communication Systems: Principles and Applications*, 4th ed., Prentice Hall, Upper Saddle River, NJ, 1995.

[3] B. P. Lathi, *Modern Digital and Analog Communication Systems*, 3rd ed., Oxford University Press, New York, 1998.

[4] D. R. Smith, *Digital transmission systems*, 3rd ed., Kluwer Academic, Boston, 2004.

[5] K. Noguchi, O. Mitomi, and H. Miyazawa, *J. Lightwave Technol.* **16**, 615 (1998).

[6] H. Zhang, M. C. Oh, A. Szep, W. H. Steier, L. R. Dalton, H. Erlig, Y. Chang, D. H. Chang, and H. R. Fetterman, *Appl. Phys. Lett.* **78**, 3136 (2001).

[7] H. Kim and R. J. Essiambre, *IEEE Photon. Technol. Lett.* **15**, 769 (2003).

[8] M. Born and E. Wolf, *Principles of Optics*, 7th ed., Cambridge University Press, New York, 1999, Chap. 10.

[9] M. I. Hayee and A. E. Willner, *IEEE Photon. Technol. Lett.* **11**, 991 (1999).

[10] R. Ludwig, U. Feiste, E. Dietrich, H. G. Weber, D. Breuer, M. Martin, and F. Kuppers, *Electron. Lett.* **35**, 2216 (1999).

[11] M. Nakazawa, H. Kubota, K. Suzuki, E. Yamada, and A. Sahara, *IEEE J. Sel. Topics Quantum Electron.* **6**, 363 (2000).

[12] A. Sano and Y. Miyamoto, *J. Lightwave Technol.* **19**, 1864 (2001).

[13] G. Bosco, A. Carena, V. Curri, R. Gaudino, and P. Poggiolini, *J. Lightwave Technol.* **20**, 1694 (2002).

[14] T. Hoshida, O. Vassilieva, K. Yamada, S. Choudhary, R. Pecqueur, and H. Kuwahara, *J. Lightwave Technol.* **20**, 1989 (2002).

[15] Y. Miyamoto, A. Hirano, S. Kuwahara, M. Tomizawa, and Y. Tada, *J. Lightwave Technol.* **20**, 2067 (2002).

[16] J. Conradi, in *Optical Fiber Telecommunications*, Vol. 4B, I. P. Kaminow and T. L. Koch, Eds., Academic Press, San Diego, CA, 2002, Chap. 16.

[17] M. Rohde, C. Caspar, N. Heimes, M. Konitzer, E.-J. Bachus, and N. Hanik, *Electron. Lett.* **36**, 1483 (2000).

[18] J. Leibrich, C. Wree, and W. Rosenkranz, *IEEE Photon. Technol. Lett.* **14**, 155 (2002).

[19] Y. Awaji, T. Kuri, and W. Chujo, *IEEE Photon. Technol. Lett.* **14**, 1007 (2002).

[20] A. H. Gnauck, G. Raybon, S. Chandrasekhar, J. Leuthold, C. Doerr, L. Stulz, and E. Burrows, *IEEE Photon. Technol. Lett.* **15**, 467 (2003).

[21] B. Zhu, C. R. Doerr, P. Gaarde, L. E. Nelson, S. Stulz, L. Stulz, and L. Gruner-Nielsen, *Electron. Lett.* **39**, 1528 (2003).

[22] A. H. Gnauck, X. Liu, X. Wei, D. M. Gill, and E. C. Burrows, *IEEE Photon. Technol. Lett.* **16**, 909 (2004).

[23] P. A. Morton, V. Mizrahi, G. T. Harvey, L. F. Mollenauer, T. Tanbun-Ek, R. A. Logan, H. M. Presby, T. Erdogan, A. M. Sergent, and K. W. Wecht, *IEEE Photon. Technol. Lett.* **7**, 111 (1995).

[24] K. Sato, I. Kotaka, Y. Kondo, and M. Yamamoto, *Appl. Phys. Lett.* **69**, 2626 (1996).

[25] V. Mikhailov, P. Bayvel, R. Wyatt, and I. Lealman, *Electron. Lett.* **37**, 909 (2001).

[26] I. Kang, L. Mollenauer, B. Greene, and A. Grant, *IEEE Photon. Technol. Lett.* **14**, 1357 (2002).

[27] P. J. Winzer, C. Doerr. R.-J. Essiambre, and I. Kang, *IEEE Photon. Technol. Lett.* **16**, 1379 (2004).

[28] J. H. Sinsky, *J. Lightwave Technol.* **21**, 412 (2003).

[29] P. J. Winzer, A. H. Gnauck, G. Raybon, S. Chandrasekhar, Y. Su, and J. Leuthold, *IEEE Photon. Technol. Lett.* **15**, 766 (2003).

[30] J. J. Veselka and S. K. Korotky, *IEEE J. Sel. Topics Quantum Electron.* **2**, 300 (1996).

[31] P. J. Winzer and J. Leuthold, *IEEE Photon. Technol. Lett.* **13**, 1298 (2001).

[32] P. W. Shumate, in *Optical Fiber Telecommunications II*, S. E. Miller and I. P. Kaminow, Eds., Academic Press, San Diego, CA, 1988, Chap. 19.

[33] T. P. Lee, C. A. Burrus, and R. H. Saul, in *Optical Fiber Telecommunications II*, S. E. Miller and I. P. Kaminow, Eds., Academic Press, San Diego, CA, 1988, Chap. 12.

[34] D. S. Alles and K. J. Brady, *AT&T Tech. J.* **68**, 183 (1989).

[35] D. A. Fishman and B. S. Jackson, in *Optical Fiber Telecommunications* Vol. 3B, I. P. Kaminow and T. L. Koch, Eds., Academic Press, San Diego, CA, 1997, Chap. 3.

[36] B. L. Kasper, O. Mizuhara, and Y.-K. Chen, in *Optical Fiber Telecommunications* Vol. 4A, I. P. Kaminow and T. Lee, Eds., Academic Press, San Diego, CA, 2002, Chap. 16.

[37] H. M. Presby and C. A. Edwards, *Electron. Lett.* **28**, 582 (1992).

[38] R. A. Modavis and T. W. Webb, *IEEE Photon. Technol. Lett.* **7**, 798 (1995).

[39] K. Shiraishi, N. Oyama, K. Matsumura, I. Ohisi, and S. Suga, *J. Lightwave Technol.* **13**, 1736 (1995).

[40] P. C. Chen and T. D. Milster, *Laser Diode Chip and Packaging Technology*, Vol. 2610, SPIE Press, Bellingham, WA, 1996.

[41] M. J. Daneman, O. Sologaard, N. C. Tien, K. Y. Lau, and R. S. Muller, *IEEE Photon. Technol. Lett.* **8**, 396 (1996).

[42] B. M. A. Rahman, M. Rajarajan, T. Wongcharoen, and K. T. V. Grattan, *IEEE Photon. Technol. Lett.* **8**, 557 (1996).

[43] I. Moerman, P. P. van Daele, and P. M. Demeester, *IEEE J. Sel. Topics Quantum Electron.* **3**, 1306 (1997).

[44] B. Hubner, G. Vollrath, R. Ries, C. Gréus, H. Janning, E. Ronneberg, E. Kuphal, B. Kempf, R. Gobel, F. Fiedler, R. Zengerle, and H. Burkhard, *IEEE J. Sel. Topics Quantum Electron.* **3**, 1372 (1997).

[45] G. P. Agrawal, *Semiconductor Lasers*, 2nd ed., Van Nostrand Reinhold, New York, 1993, Chap. 6.

[46] A. T. Ryan, G. P. Agrawal, G. R. Gray, and E. C. Gage, *IEEE J. Quantum Electron.* **30**, 668 (1994).

[47] G. H. M. van Tartwijk and D. Lenstra, *Quantum Semiclass. Opt.* **7**, 87 (1995).

[48] K. Petermann, *IEEE J. Sel. Topics Quantum Electron.* **1**, 480 (1995).

[49] T. Sugie and M. Saruwatari, *Electron. Lett.* **18**, 1026 (1982).

[50] M. Teshima, M. Koga, and K. Sato, *J. Lightwave Technol.* **14**, 2277 (1996).

[51] Y. Park, S. Lee, Chang, and C. Chae, *IEEE Photon. Technol. Lett.* **10**, 1446 (1998).

[52] Y. Katagiri, K. Aida, Y. Tachikawa, S. Nagaoka, H. Abe, and F. Ohira, *IEEE Photon. Technol. Lett.* **11**, 102 (1999).

[53] S. Lee, Y. Hsu, and C. Pien, *IEEE Photon. Technol. Lett.* **13**, 872 (2001).

[54] H. Nasu, T. Takagi, M. Oike, T. Nomura, and A. Kasukawa, *IEEE Photon. Technol. Lett.* **15**, 380 (2003).

[55] F. Delorme, *IEEE J. Quantum Electron.* **34**, 1706 (1998).

[56] M. C. Aman and J. Buus, *Tunable Semiconductor Lasers*, Artech House, Norwood, MA, 1998.

[57] E. Kapon, Ed., *Semiconductor Lasers*, Part II, Academic Press, San Diego, CA, 1999, Chap. 3.

[58] F. Delorme, G. Terol, H. de Bailliencourt, S. Grosmaire, and P. Devoldere, *IEEE J. Sel. Topics Quantum Electron.* **5**, 480 (1999).

[59] L. A. Coldren, *IEEE J. Sel. Topics Quantum Electron.* **6**, 988 (2000).

[60] D. A. Ackerman, J. E. Johnson, L. J. P. Ketelsen, L. E. Eng, P. A. Kiely, and T. G. B. Mason, *Optical Fiber Telecommunications*, Vol. 4A, I. P. Kaminow and T. P. Lee, Eds., Academic Press, San Diego, CA, 2002, Chap. 12.

[61] O. Wada, T. Sakurai, and T. Nakagami, *IEEE J. Quantum Electron.* **22**, 805 (1986).

[62] T. Horimatsu and M. Sasaki, *J. Lightwave Technol.* **7**, 1613 (1989).

[63] M. Dagenais, R. F. Leheny, H. Temkin, and P. Battacharya, *J. Lightwave Technol.* **8**, 846 (1990).

[64] N. Suzuki, H. Furuyama, Y. Hirayama, M. Morinaga, K. Eguchi, M. Kushibe, M. Funamizu, and M. Nakamura, *Electron. Lett.* **24**, 467 (1988).

[65] K. Pedrotti, *Proc. SPIE* **2149**, 178 (1994).

[66] O. Calliger, A. Clei, D. Robein, R. Azoulay, B. Pierre, S. Biblemont, and C. Kazmierski, *IEE Proc.* **142**, Pt. J, 13 (1995).

[67] R. Pu, C. Duan, and C. W. Wilmsen, *IEEE J. Sel. Topics Quantum Electron.* **5**, 201 (1999).

[68] K. Shuke, T. Yoshida, M. Nakano, A. Kawatani, and Y. Uda, *IEEE J. Sel. Topics Quantum Electron.* **5**, 217 (1999).

[69] H.-G. Bach, A. Beling, G. G. Mekonnen, and W. Schlaak, *IEEE J. Sel. Topics Quantum Electron.* **8**, 1445 (2002).

[70] T. L. Koch and U. Koren, *IEE Proc.* **138**, Pt. J, 139 (1991); *IEEE J. Quantum Electron.* **27**, 641 (1991).

[71] R. Matz, J. G. Bauer, P. C. Clemens, G. Heise, H. F. Mahlein, W. Metzger, H. Michel, and G. Schulte-Roth, *IEEE Photon. Technol. Lett.* **6**, 1327 (1994).

[72] M. N. Armenise and K.-K. Wong, Eds., *Functional Photonic Integrated Circuits*, SPIE Proc. Series, Vol. 2401, SPIE Press, Bellingham, WA, 1995.

[73] W. Metzger, J. G. Bauer, P. C. Clemens, G. Heise, M. Klein, H. F. Mahlein, R. Matz, H. Michel, and J. Rieger, *Opt. Quantum Electron.* **28**, 51 (1996).

[74] M. Ishizaka, Y. Yamaguchi, Y. Sakata, Y. Inomoto, J. Shimizu, and K. Komatsu, *IEEE Photon. Technol. Lett.* **9**, 1406 (1997).

[75] T. L. Koch, in *Optical Fiber Telecommunications* Vol. 3B, I. P. Kaminow and T. L. Koch, Eds., Academic Press, San Diego, CA, 1997, Chap. 4.

[76] S. Menezo, A. Rigny, A. Talneau, F. Delorme, S. Grosmaire, H. Nakajima, E. Vergnol, F. Alexandre, and F. Gaborit, *IEEE J. Sel. Topics Quantum Electron.* **6**, 185 (2000).

[77] H. Debregeas-Sillard, A. Vuong, F. Delorme, J. David, V. Allard, A. Bodere, O. LeGouezigou, F. Gaborit, J. Rotte, M. Goix, V. Voiriot, and J. Jacquet, *IEEE Photon. Technol. Lett.* **13**, 4 (2001).

[78] H. Hatakeyama, K. Kudo, Y. Yokoyama, K. Naniwae, and T. Sasaki, *IEEE J. Sel. Topics Quantum Electron.* **8**, 1341 (2002).

[79] J. S. Barton, E. J. Skogen, M. L. Masanovic, S. P. Denbaars, and L. A. Coldren, *IEEE J. Sel. Topics Quantum Electron.* **9**, 1113 (2003).

[80] S. Kim, Y. Chung, S. H. Oh, and M.-H. Park, *IEEE Photon. Technol. Lett.* **16**, 15 (2004).

[81] H. Takeuchi, K. Tsuzuki, K. Sato, H. Yamamoto, M. Itaya, A. Sano, M. Yoneyama, and T. Otsuji, *IEEE J. Sel. Topics Quantum Electron.* **3**, 336 (1997).

[82] T. Tanbun-Ek, L. E. Adams, G. Nykolak, C. Bethea, R. People, A. M. Sergent, P. W. Wisk, P. F. Sciortino, S. N. G. Chu, T. Fullowan, R. Pawelek, and W. T. Tsang, *IEEE J. Sel. Topics Quantum Electron.* **3**, 960 (1997).

[83] K. Sato, A. Hirano, and H. Ishii, *IEEE J. Sel. Topics Quantum Electron.* **5**, 590 (1999).

[84] Y. Miyazaki, E. Ishimura, T. Aoyagi, H. Tada, K. Matsumoto, T. Takiguchi, K. Shimizu, M. Noda, T. Mizuochi, T. Nishimura, and E. Omura, *IEEE J. Quantum Electron.* **36**, 909 (2000).

[85] Y. Kim, S. K. Kim, J. Lee, Y. Kim, J. Kang, W. Choi, and J. Jeong, *Opt. Fiber Technol.* **7**, 84 (2001).

[86] Y. Akage, K. Kawano, S. Oku, R. Iga, H. Okamoto, Y. Miyamoto, and H. Takeuchi, *Electron. Lett.* **37**, 299 (2001).

[87] H. Kawanishi, Y. Yamauchi, N. Mineo, Y. Shibuya, H. Mural, K. Yamada, and H. Wada, *IEEE Photon. Technol. Lett.* **13**, 954 (2001).

[88] R. A. Salvatore, R. T. Sahara, M. A. Bock, and I. Libenzon, *IEEE J. Quantum Electron.* **38**, 464 (2002).

[89] Y. Miyazaki, H. Tada, T. Aoyagi, T. Nashimuraand, and Y. Mitsui, *IEEE J. Quantum Electron.* **38**, 1075 (2002).

[90] Y. A. Akulova, G. A. Fish, P. C. Koh, C. L. Schow, P. Kozodoy, A. P. Dahl, S. Nakagawa, M. C. Larson, M. P. Mack, T. A. Strand, C. W Coldren, E. Hegblom, S. K. Penniman, T. Wipiejewski, and L. A. Coldren, *IEEE J. Sel. Topics Quantum Electron.* **8**, 1349 (2002).

[91] K. Sato, *J. Lightwave Technol.* **20**, 2035 (2002).

[92] Y. Su, G. Raybon, H. Feng, X. Wei, and T. Makino, *IEEE Photon. Technol. Lett.* **15**, 1156 (2003).

[93] N. C. Frateschi, J. Zhang, W. J. Choi, H. Gebretsadik, R. Jambunathan, and A. E. Bond, *Electron. Lett.* **40**, 141 (2004).

[94] F. R. Nash, W. B. Joyce, R. L. Hartman, E. I. Gordon, and R. W. Dixon, *AT&T Tech. J.* **4**, 671 (1985).

[95] N. K. Dutta and C. L. Zipfel, in *Optical Fiber Telecommunications II*, S. E. Miller and I. P. Kaminow, Eds., Academic Press, San Diego, CA, 1988, Chap. 17.

[96] B. W. Hakki, P. E. Fraley, and T. F. Eltringham, *AT&T Tech. J.* **64**, 771 (1985).

[97] M. Fallahi and S. C. Wang, Eds., *Fabrication, Testing, and Reliability of Semiconductor Lasers*, Vol. 2863, SPIE Press, Bellingham, WA, 1995.

[98] O. Ueda, *Reliability and Degradation of III–V Optical Devices*, Artec House, Boston, 1996.

[99] N. W. Carlson, *IEEE J. Sel. Topics Quantum Electron.* **6**, 615 (2000).

Chapter 3

Signal Propagation in Fibers

In any fiber-optic lightwave system, optical bit stream generated at the transmitter propagates through a fiber link that may contain several different types of optical fibers. The link length may vary from a few kilometers to thousands of kilometers. During its propagation, the optical signal is invariably degraded in quality. An objective of any lightwave system is to control transmission-related degradations as much as possible so that the original information can be retrieved at the receiver without errors. This chapter focuses on several linear degradation mechanisms that occur in silica fibers and affect the optical bit stream; the nonlinear degradations mechanisms are discussed in Chapter 4. In Section 3.1 we derive a basic propagation equation that should be solved to study how single-mode fibers affect an optical bit stream. Section 3.2 shows that losses in optical fibers reduce the average signal power that must be restored periodically through lumped or distributed amplification, even though signal quality is invariably degraded because of the added noise. Section 3.3 focuses on the role of fiber dispersion and shows through a simple example of Gaussian pulses that dispersion can broaden optical pulses beyond their allocated bit slot. The limitations on the bit rate and the transmission distance imposed by fiber dispersion are also discussed in this section. Sections 3.4 and 3.5 are devoted to the polarization effects occurring inside optical fibers. The phenomenon of polarization-mode dispersion is discussed in Section 3.4, whereas polarization-dependent loss is the subject of Section 3.5.

3.1 Basic Propagation Equation

Modern lightwave systems employ step-index fibers, designed to support a single optical mode (see Chapter 1 of LT1). When an optical signal from the transmitter is launched into a single-mode fiber, it excites the fundamental HE_{11} mode of the fiber, and its transverse spatial distribution does not change during propagation. Thus, the electric field associated with the optical bit stream can be written as

$$\mathbf{E}(\mathbf{r},t) = \mathrm{Re}[\hat{\mathbf{e}}F(x,y)A(z,t)\exp(i\beta_0 z - i\omega_0 t)], \tag{3.1.1}$$

where $\hat{\mathbf{e}}$ is the polarization unit vector, $F(x,y)$ is the spatial distribution of the fundamental fiber mode, $A(z,t)$ is the complex amplitude of the field envelope at a distance z inside the fiber, and β_0 is the mode-propagation constant at the carrier frequency ω_0. Although the polarization unit vector $\hat{\mathbf{e}}$ changes in a random fashion along the fiber because of a small but fluctuating birefringence, we assume until Section 3.4 that such birefringence effects can be ignored and treat $\hat{\mathbf{e}}$ as a constant. Since $F(x,y)$ does not depend on z, the only quantity that changes with propagation is the complex amplitude $A(z,t)$ associated with the optical signal. In this section we derive an equation governing the evolution of $A(z,t)$ within the fiber.

The analysis of fiber modes (see Section 1.3 of LT1) shows that each frequency component of the optical field propagates in a single-mode fiber with a slightly different propagation constant. For this reason, it is useful to work in the spectral domain. We introduce the Fourier transform of $A(z,t)$ as

$$A(z,t) = \frac{1}{2\pi}\int_{-\infty}^{\infty} \tilde{A}(z,\omega)\exp(-i\Delta\omega t)\,d(\Delta\omega), \tag{3.1.2}$$

where $\Delta\omega = \omega - \omega_0$ and $\tilde{A}(z,\omega)$ represents the Fourier spectrum of the optical bit stream. As discussed in Section 2.2.3, the signal bandwidth depends on the bit rate B and the modulation format used for the bit stream.

Consider a specific spectral component $\tilde{A}(z,\omega)$. It propagates inside the optical fiber with the propagation constant $\beta_p(\omega)$ that is different than β_0 appearing in Eq. (3.1.1) and thus acquires an extra phase shift given by

$$\tilde{A}(z,\omega) = \tilde{A}(0,\omega)\exp[i\beta_p(\omega)z - i\beta_0 z], \tag{3.1.3}$$

where $\tilde{A}(0,\omega)$ is the Fourier transform of the input signal $A(0,t)$ at $z=0$. The propagation constant β_p is, in general, complex and can be written in the form [1]

$$\beta_p(\omega) = [\bar{n}(\omega) + \delta n_{NL}(\omega)](\omega/c) + i\alpha(\omega)/2, \tag{3.1.4}$$

where $\bar{n}$ is the effective mode index and α is the attenuation constant responsible for fiber losses. The nonlinear effects are included through δn_{NL} that represents a small power-dependent change in the effective mode index. Even though $\delta n_{NL} < 10^{-10}$ at typical power levels used in lightwave systems, its impact becomes quite important for long-haul lightwave systems designed with optical amplifiers [1]–[3].

Pulse broadening results from the frequency dependence of the mode index $\bar{n}$. Since the exact functional form of this dependence is not known in general, it is useful to write the propagation constant β_p as

$$\beta_p(\omega) = \beta_L(\omega) + \beta_{NL}(\omega_0) + i\alpha(\omega_0)/2, \tag{3.1.5}$$

where $\beta_L(\omega) = \bar{n}(\omega)\omega/c$ is its linear part, β_{NL} is the nonlinear part, and α is the fiber-loss parameter. In general, all three parts of β_p depend on frequency. However, optical pulses used as bits in lightwave systems are relatively wide (>1 ps) compared with the duration of a single optical cycle ($\approx$5 fs), and their spectrum is much narrower compared with the carrier frequency ω_0. This feature allows us to treat α and β_{NL} as

Table 3.1: Dispersion characteristics of several commercial fibers

Fiber Type and Trade Name	A_{eff} (μm^2)	λ_{ZD} (nm)	D (C band) [ps/(km-nm)]	Slope S [ps/(km-nm^2)]
Corning SMF-28	80	1,302–1,322	16 to 19	0.090
Lucent AllWave	80	1,300–1,322	17 to 20	0.088
Alcatel ColorLock	80	1,300–1,320	16 to 19	0.090
Corning Vascade	101	1,300–1,310	18 to 20	0.060
Lucent TrueWave-RS	50	1,470–1,490	2.6 to 6	0.050
Corning LEAF	72	1,490–1,500	2 to 6	0.060
Lucent TrueWave-XL	72	1,570–1,580	−1.4 to −4.6	0.112
Alcatel TeraLight	65	1,440–1,450	5.5 to 10	0.058

frequency-independent over the signal bandwidth and expand $\beta_L(\omega)$ in a Taylor series around ω_0. If we retain terms up to third order, we obtain

$$\beta_L(\omega) \approx \beta_0 + \beta_1(\Delta\omega) + \frac{\beta_2}{2}(\Delta\omega)^2 + \frac{\beta_3}{6}(\Delta\omega)^3, \tag{3.1.6}$$

where $\beta_m = (d^m\beta/d\omega^m)_{\omega=\omega_0}$. The three dispersion parameters appearing in this equation are known in practice for any fiber used for signal transmission.

Physically, the parameter β_1 is related inversely to the group velocity v_g of the pulse as $\beta_1 = 1/v_g$. The parameters β_2 and β_3 are known as the second- and third-order dispersion parameters and are responsible for pulse broadening in optical fibers. More specifically, β_2 is related to the dispersion parameter D as (see Section 1.5 of LT1)

$$D = \frac{d}{d\lambda}\left(\frac{1}{v_g}\right) = -\frac{2\pi c}{\lambda^2}\beta_2. \tag{3.1.7}$$

This parameter is expressed in units of ps/(km-nm). It varies with wavelength for any fiber and vanishes at a wavelength known as the *zero-dispersion wavelength* and denoted as λ_{ZD}. Near this wavelength, D varies linearly as $D = S(\lambda - \lambda_{\text{ZD}})$, where S represents the dispersion slope at λ_{ZD}. The parameter β_3 is related to the dispersion slope S as $S = (2\pi c/\lambda^2)^2\beta_3$. The parameters λ_{ZD}, D, and S vary from fiber to fiber. Table 3.1 lists their values for several commonly used fibers. Fibers with relatively small values of D in the spectral region near 1.55 μm [$|D| < 8$ ps/(km-nm)] are called *dispersion-shifted* fibers and are often used in designing modern lightwave systems [4]–[7].

We substitute Eqs. (3.1.5) and (3.1.6) in Eq. (3.1.3), calculate the derivative $\partial\tilde{A}/\partial z$, and convert the resulting equation into the time domain by replacing $\Delta\omega$ with the differential operator $i(\partial/\partial t)$. The resulting time-domain equation can be written as [1]

$$\frac{\partial A}{\partial z} + \beta_1\frac{\partial A}{\partial t} + \frac{i\beta_2}{2}\frac{\partial^2 A}{\partial t^2} - \frac{\beta_3}{6}\frac{\partial^3 A}{\partial t^3} = i\beta_{NL}A - \frac{\alpha}{2}A. \tag{3.1.8}$$

This is the basic propagation equation governing pulse evolution inside a single-mode fiber. Before using it, we need to write the nonlinear term in its explicit form. From Eq.

(3.1.4), the nonlinear part of the propagation constant is given by $\beta_{NL} = \delta n_{NL}(\omega_0/c)$. For optical fibers, the nonlinear change in the refractive index has the form $\delta n_{NL} = n_2 I$ (similar to a Kerr medium), where n_2 is a constant parameter with values around 2.6×10^{-20} m^2/W and I represents the optical intensity [1]. The intensity is related to optical power at any distance z as $I(z,t) = P(z,t)/A_{\text{eff}}$, where A_{eff} is the effective core area of the fiber and is generally different than the physical core area because a part of the optical mode propagates outside the core.

It is common to normalize the amplitude A in Eq. (3.1.8) such that $|A|^2$ represents optical power. With this identification and using $\omega_0 = 2\pi c/\lambda_0$, where λ_0 is the carrier wavelength, we obtain

$$\beta_{NL} = \gamma |A|^2, \qquad \gamma = \frac{2\pi n_2}{\lambda_0 A_{\text{eff}}}, \tag{3.1.9}$$

where the parameter γ takes into account various nonlinear effects occurring within the fiber. The value of this parameter can be tailored to some extent by controlling the effective core area of an optical fiber. Table 3.1 lists the values of A_{eff} for several commonly used fibers. As an example, $\gamma \approx 2.1$ W^{-1}/km for a fiber with $A_{\text{eff}} = 50\ \mu$m^2. Fibers with a relatively large value of A_{eff} are called large-effective-area fibers (LEAFs) and are useful for designing lightwave systems because they reduce the impact of fiber nonlinearities [8]–[10].

We can simplify Eq. (3.1.8) somewhat by noting that the β_1 term simply corresponds to a constant delay experienced by the optical signal as it propagates through the fiber. Since this delay does not affect the signal quality in any way, it is useful to work in a reference frame moving with the signal. This can be accomplished by introducing the new variables t' and z' as

$$t' = t - \beta_1 z, \qquad z' = z, \tag{3.1.10}$$

and rewriting Eq. (3.1.8) in terms of them as

$$\frac{\partial A}{\partial z'} + \frac{i\beta_2}{2}\frac{\partial^2 A}{\partial t'^2} - \frac{\beta_3}{6}\frac{\partial^3 A}{\partial t'^3} = i\gamma |A|^2 A - \frac{\alpha}{2}A, \tag{3.1.11}$$

where we also used Eq. (3.1.9). For simplicity of notation, we drop the primes over z' and t' whenever no confusion is likely to arise. Also, the third-order dispersive effects are negligible in practice as long as β_2 is not too close to zero, or pulses are not shorter than 5 ps. Setting $\beta_3 = 0$, Eq. (3.1.11) reduces to

$$\frac{\partial A}{\partial z} + \frac{i\beta_2}{2}\frac{\partial^2 A}{\partial t^2} = i\gamma |A|^2 A - \frac{\alpha}{2}A. \tag{3.1.12}$$

For historical reasons, this equation is known as the nonlinear Schrödinger (NLS) equation. It is used extensively for modeling lightwave systems and leads to predictions that can be verified experimentally. The three parameters, α, β_2, and γ, take into account three distinct kinds of degradations that can occur when an optical signal propagates through optical fibers. In the following two sections, we focus on the linear degradation mechanisms related to the nonzero values of α and β_2.

3.2 Impact of Fiber Losses

The loss parameter α appearing in Eq. (3.1.12) reduces not only the signal power but it also impacts the strength of the nonlinear effects. This can be seen mathematically by introducing

$$A(z,t) = B(z,t)\exp(-\alpha z/2) \tag{3.2.1}$$

in Eq. (3.1.12) and writing it in terms of $B(z,t)$ as

$$\frac{\partial B}{\partial z} + \frac{i\beta_2}{2}\frac{\partial^2 B}{\partial t^2} = i\gamma e^{-\alpha z}|B|^2 B. \tag{3.2.2}$$

The physical interpretation of the preceding two equations is clear. Equation (3.2.1) shows that the optical power $|A(z,t)|^2$ decreases exponentially as $e^{-\alpha z}$ at a distance z because of fiber losses. As seen from Eq. (3.2.2), this decrease in the signal power also makes the nonlinear effects weaker, as expected intuitively.

The loss in signal power is quantified in terms of the average power defined as

$$P_{\text{av}}(z) = \lim_{T\to\infty}\frac{1}{T}\int_{T/2}^{T/2}|A(z,t)|^2\,dt = P_{\text{av}}(0)e^{-\alpha z}, \tag{3.2.3}$$

where we used Eq. (3.2.1) and assumed that no other source of energy losses exists so that the integral $\int |B(z,t)|^2\,dt$ over the entire bit stream remains constant in spite of changes in the shape of individual pulses. The average power decreases by a factor of $e^{\alpha L}$ for a fiber of length L. This factor exceeds 20 dB for a 100-km-long fiber cable even in the spectral region near 1.55 μm where α has the smallest value of around 0.2 dB/km. Numerical values of α depend on the operating wavelength and exceed 0.4 dB/km in the spectral region near 1.3 μm.

3.2.1 Loss Compensation

Fiber losses must be compensated for lightwave systems designed to operate over more than 100 km because their cumulative effects eventually make the signal so weak that information cannot be recovered at the receiver. Since long-haul and submarine lightwave systems typically extend over thousands of kilometers, it is evident that fiber losses must be compensated in such systems to boost the signal power periodically back to its original value.

As discussed in Section 1.1, the only loss-management technique available to the system designer until 1990 consisted of inserting an optoelectronic regenerator, often called a *repeater*, within the fiber link after every 80 km or so. A repeater is nothing but a receiver–transmitter pair in which the receiver output is directly fed into an optical transmitter. In such a device, the optical bit stream is first converted into the electric domain and then regenerated with the help of an optical transmitter. This technique becomes quite cumbersome and expensive for WDM systems as it requires demultiplexing of individual channels at each repeater.

Several kinds of optical amplifiers were developed during the 1980s to solve the loss-management problem (see Chapter 3 of LT1). These amplifiers can amplify multiple WDM channels simultaneously in the optical domain itself and are much more

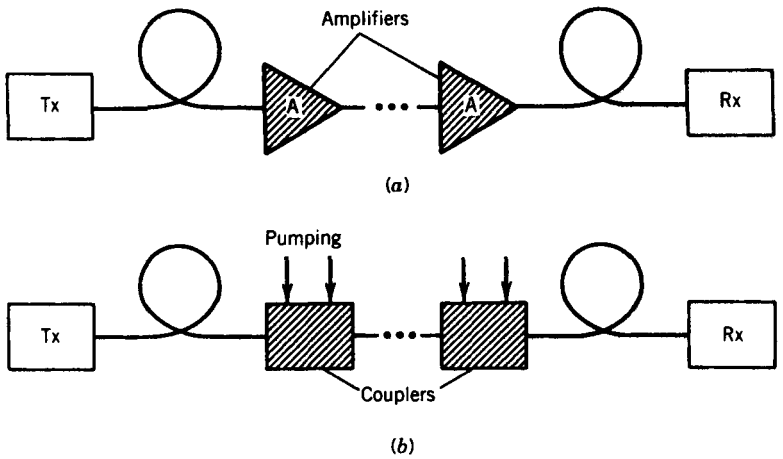

Figure 3.1: Schematic of fiber-loss management using (a) lumped or (b) distributed amplification schemes. Tx and Rx stand for optical transmitters and receivers, respectively.

cost-effective. For this reason, almost all WDM lightwave systems employ optical amplifiers for compensating fiber losses. Figure 3.1(a) shows how amplifiers can be cascaded in a periodic manner to form a chain and thus enable one to transmit an optical bit stream over distances as long as 10,000 km, while retaining the signal in its original optical form.

Depending on the amplification scheme used, one can divide amplifiers into two categories known as lumped and distributed amplifiers. Most systems employ lumped erbium-doped fiber amplifiers (EDFAs) in which losses accumulated over 60 to 80 km of fiber lengths are compensated using short lengths ($\sim$10 m) of erbium-doped fibers [11]–[13]. In contrast, the distributed amplification scheme shown in Figure 3.1(b) uses the transmission fiber itself for signal amplification by exploiting the nonlinear phenomenon of stimulated Raman scattering (SRS). Such amplifiers are known as Raman amplifiers and have been developed for lightwave systems in recent years [14]–[16]. Their use for loss compensation requires that optical power from one or more pump lasers is injected periodically using fiber couplers, as shown in Figure 3.1(b).

Any loss-management technique based on optical amplification degrades the signal-to-noise ratio (SNR) of the optical bit stream since all amplifiers add noise to the signal through spontaneous emission. As discussed in Chapter 6, this noise can be included by adding a noise term to the NLS equation together with the gain term. With the addition of such terms, Eq. (3.1.12) takes the form

$$\frac{\partial A}{\partial z} + \frac{i\beta_2}{2}\frac{\partial^2 A}{\partial t^2} = i\gamma|A|^2 A + \frac{1}{2}[g_0(z) - \alpha]A + f_n(z,t), \tag{3.2.4}$$

where $g_0(z)$ is the gain coefficient whose functional form depends on the amplification scheme used. The last term $f_n(z,t)$ accounts for the amplifier-induced noise. We discuss the implications of this term in Chapter 6 and ignore it in this section.

3.2.2 Lumped and Distributed Amplification

When EDFAs are used periodically along a fiber link, the length l_a of each amplifier (typically $l_a < 0.1$ km) is much shorter than the spacing L_A between two amplifiers. Since $g_0 = 0$ everywhere except within each amplifier, one can solve the standard NLS equation (3.1.12) in each fiber section of length L_A. As seen from Eq. (3.2.3), losses in each section reduce the average power by a factor of $\exp(\alpha L_A)$ and they can be fully compensated by operating each lumped amplifier such that its gain $G_A = \exp(g_0 l_a) = \exp(\alpha L_A)$. Thus, in a loss-managed long-haul system, EDFAs are inserted periodically after a distance L_A and their gain is adjusted such that $G_A = \exp(\alpha L_A)$. It is not necessary that amplifier spacing be uniform throughout the link. In the case of nonuniform spacing, if the nth amplifier is placed at a distance L_n from the transmitter, its gain G_n is chosen to be $G_n = \exp[\alpha(L_n - L_{n-1})]$ so that each amplifier fully compensates the losses of each fiber spam preceding it.

In the case of distributed amplification, Eq. (3.2.4) should be solved along the entire fiber link, after $g_0(z)$ has been determined for a given pumping scheme. Similar to Eq. (3.2.1), it is useful to write the general solution of Eq. (3.2.4) in the form

$$A(z,t) = \sqrt{p(z)}\,B(z,t), \tag{3.2.5}$$

where $p(z)$ governs variations in the time-averaged power of the optical bit stream along the link length because of fiber losses and signal amplification. Substituting Eq. (3.2.5) in Eq. (3.2.4), $p(z)$ is found to satisfy a simple ordinary differential equation

$$\frac{dp}{dz} = [g_0(z) - \alpha]p, \tag{3.2.6}$$

whereas $B(z,t)$ satisfies Eq. (3.2.2) with $p(z)$ replacing the factor $e^{-\alpha z}$.

If $g_0(z)$ were constant and equal to α for all z, the average power of the optical signal would remain constant along the fiber link. This is the ideal situation in which the fiber is effectively lossless. In practice, distributed gain is realized by injecting pump power periodically into the fiber link (see Figure 3.1). Since pump power does not remain constant because of considerable fiber losses at the pump wavelength, $g(z)$ cannot be kept constant along the fiber. However, even though fiber losses cannot be compensated everywhere locally, they can be compensated fully over a distance L_A provided the following condition is satisfied:

$$\int_0^{L_A} g_0(z)\,dz = \alpha L_A. \tag{3.2.7}$$

Every distributed amplification scheme is designed to satisfy Eq. (3.2.7). The distance L_A is referred to as the *pump-station spacing*.

As mentioned earlier, stimulated Raman scattering is often used to provide distributed amplification. The scheme works by launching CW power at several wavelengths from a set of high-power semiconductor lasers located at the pump stations [16]. The wavelengths of pump lasers should be in the vicinity of 1.45 μm for amplifying optical signals in the 1.55-μm spectral region. These wavelengths and pump-power levels are chosen to provide a uniform gain over the entire C band (or C and L bands in the case of

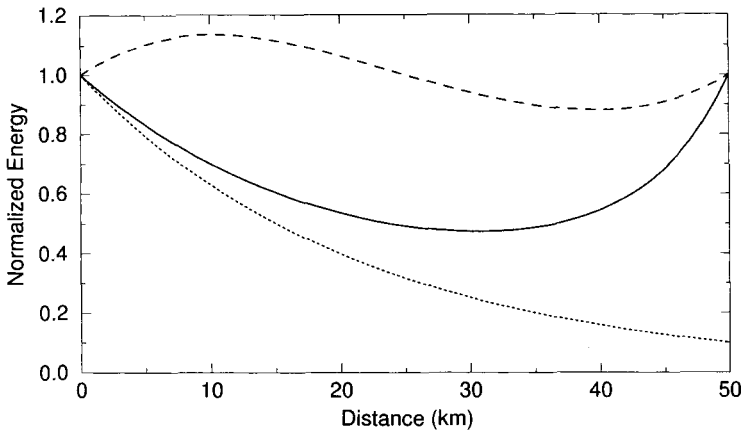

Figure 3.2: Variations in average signal power between two neighboring pump stations for backward (solid line) and bidirectional (dashed line) pumping schemes with $L_A = 50$ km. The lumped-amplifier case is shown by the dotted line.

dense WDM systems). Backward pumping is commonly used for distributed Raman amplification because such a configuration minimizes the transfer of pump-intensity noise to the amplified signal.

The use of a bidirectional pumping scheme is beneficial in some cases. To provide physical insight, we consider the case in which one pump laser is used at both ends of a fiber section for compensating losses induced by that section. In this case, the gain coefficient $g(z)$ can be approximated as

$$g(z) = g_1 \exp(-\alpha_p z) + g_2 \exp[-\alpha_p (L_A - z)], \tag{3.2.8}$$

where α_p is the fiber loss at the pump wavelength and the constants g_1 and g_2 are related to the pump powers injected at the two ends. Assuming equal pump powers and integrating Eq. (3.2.6), the average power of the optical signal, normalized to its fixed value at the pump stations, is found to vary as [3]

$$p(z) = \exp\left[\alpha L_A \left(\frac{\sinh[\alpha_p(z - L_A/2)] + \sinh(\alpha_p L_A/2)}{2\sinh(\alpha_p L_A/2)}\right) - \alpha z\right]. \tag{3.2.9}$$

In the case of backward pumping, $g_1 = 0$ in Eq. (3.2.8), and the solution of Eq. (3.2.6) is found to be

$$p(z) = \exp\left\{\alpha L_A \left[\frac{\exp(\alpha_p z) - 1}{\exp(\alpha_p L_A) - 1}\right] - \alpha z\right\}, \tag{3.2.10}$$

where g_2 was again chosen to ensure that $p(L_A) = 1$.

The solid line in Figure 3.2 shows how $p(z)$ varies along the fiber in the case of backward pumping for $L_A = 50$ km using $\alpha = 0.2$ dB/km and $\alpha_p = 0.25$ dB/km. The case of bidirectional pumping is shown with a dashed line. The case of lumped amplification is also shown for comparison by a dotted line. Whereas average signal power

varies by a factor of 10 in the lumped case, it varies by less than a factor of 2 in the case of backward-pumped distributed amplification. Moreover, it varies by less than 15% in the case of a bidirectional pumping scheme, showing that this scheme is close to the ideal situation in which fiber losses are compensated fully all along the fiber. The range over which $p(z)$ varies depends on the pump-station spacing L_A. For example, $p(z)$ varies by a factor of 100 or more when $L_A = 100$ km if lumped amplification is used but by less than a factor of 2 when a bidirectional pumping scheme is employed.

3.3 Impact of Fiber Dispersion

As seen in Eq. (3.1.4), the effective refractive index of the fiber mode depends on the frequency of light launched into it. As a result, different spectral components of the signal travel at slightly different group velocities within the fiber, a phenomenon referred to as *group-velocity dispersion* (GVD). The GVD parameter β_2 appearing in Eq. (3.1.12) governs the strength of such dispersive effects. We discuss in this section how GVD limits the performance of lightwave systems. To simplify the following discussion, we neglect the nonlinear effects in this section and set $\gamma = 0$ in Eq. (3.1.12). Assuming that fiber losses are compensated periodically, we also set $\alpha = 0$ in this equation. Dispersive effects are then governed by a simple *linear* equation:

$$\frac{\partial A}{\partial z} + \frac{i\beta_2}{2}\frac{\partial^2 A}{\partial t^2} = 0. \tag{3.3.1}$$

This equation is similar to the paraxial wave equation governing diffraction of optical beams in free space in one transverse dimension [17]. The only difference is that the GVD parameter β_2 can be positive or negative depending on whether the optical signal experiences normal or anomalous dispersion. In the diffraction case, the second term in Eq. (3.3.1) is always positive. Nevertheless, the analogy between dispersion in time and diffraction in space can often be exploited to advantage.

3.3.1 Chirped Gaussian Pulses

The propagation equation (3.3.1) can easily be solved with the Fourier-transform method and has the general solution

$$A(z,t) = \frac{1}{2\pi}\int_{-\infty}^{\infty} \tilde{A}(0,\omega)\exp\left(\frac{i}{2}\beta_2 z\omega^2 - i\omega t\right) d\omega, \tag{3.3.2}$$

where $\tilde{A}(0,\omega)$ is the Fourier transform of $A(0,t)$ and is obtained using

$$\tilde{A}(0,\omega) = \int_{-\infty}^{\infty} A(0,t)\exp(i\omega t)\, dt. \tag{3.3.3}$$

In general, $A(0,t)$ represents an entire optical bit stream and has the form of Eq. (2.2.1). However, it follows from the linear nature of Eq. (3.3.1) that we can study the dispersive effects for individual pulses without any loss of generality. We thus focus on a single

pulse and use its amplitude at $z = 0$ as the initial condition in Eq. (3.3.3). For simplicity of notation, we assume that the peak of the pulse is initially located at $t = 0$.

Even though the shape of optical pulses representing 1 bits in a bit stream is not necessarily Gaussian, one can gain considerable insight into the effects of fiber dispersion by focusing on the case of a chirped Gaussian pulse with the input field

$$A(0,t) = A_0 \exp[-\tfrac{1}{2}(1+iC)(t/T_0)^2], \tag{3.3.4}$$

where A_0 is the peak amplitude and T_0 represents the half-width of the pulse at $1/e$ power point. This width is related to the full width at half-maximum (FWHM) of the input pulse by the relation

$$T_{\text{FWHM}} = 2(\ln 2)^{1/2} T_0 \approx 1.665 T_0. \tag{3.3.5}$$

The parameter C in Eq. (3.3.4) governs the frequency chirp imposed on the pulse. Quadratic changes in the phase in Eq. (3.3.4) correspond to linear frequency variations. For this reason, such pulses are said to be linearly chirped.

The spectrum of a chirped pulse is always broader than that of an unchirped pulse of the same width. This can be seen for Gaussian pulses by substituting Eq. (3.3.4) in Eq. (3.3.3). The integration over t can be performed analytically using the well-known identity [18]

$$\int_{-\infty}^{\infty} \exp(-ax^2 + bx)\, dx = \sqrt{\frac{\pi}{a}} \exp\left(-\frac{b^2}{4a}\right). \tag{3.3.6}$$

The result is found to be

$$\tilde{A}(0,\omega) = A_0 \left(\frac{2\pi T_0^2}{1+iC}\right)^{1/2} \exp\left[-\frac{\omega^2 T_0^2}{2(1+iC)}\right]. \tag{3.3.7}$$

The spectral half-width (at $1/e$ power point) is given by

$$\Delta\omega_0 = \sqrt{1+C^2}/T_0. \tag{3.3.8}$$

In the absence of frequency chirp ($C = 0$), the spectral width satisfies the relation $\Delta\omega_0 T_0 = 1$. Such a pulse has the narrowest spectrum and is called *transform-limited*. The spectral width is enhanced by a factor of $(1+C^2)^{1/2}$ for a linearly chirped Gaussian pulse.

To find the pulse shape at a distance z inside the fiber, we substitute Eq. (3.3.7) in Eq. (3.3.2). The integration over ω can also be performed analytically using Eq. (3.3.6) and leads to the expression

$$A(\xi,t) = \frac{A_0}{\sqrt{b_f}} \exp\left[-\frac{(1+iC_1)t^2}{2T_0^2 b_f^2} + \frac{i}{2}\tan^{-1}\left(\frac{\xi}{1+C\xi}\right)\right], \tag{3.3.9}$$

where the normalized distance $\xi = z/L_D$ is introduced using the *dispersion length* L_D defined as $L_D = T_0^2/|\beta_2|$. The parameters b_f and C_1 vary with ξ as

$$b_f(\xi) = [(1+sC\xi)^2 + \xi^2]^{1/2}, \qquad C_1(\xi) = C + s(1+C^2)\xi, \tag{3.3.10}$$

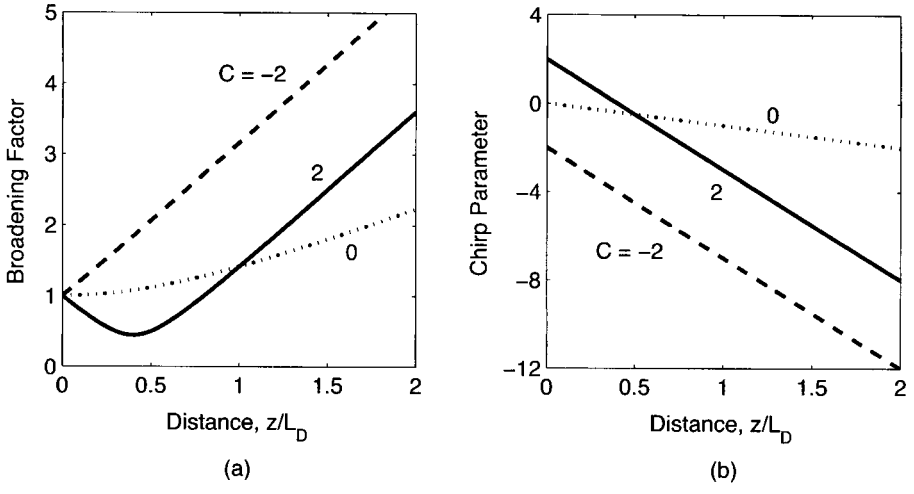

Figure 3.3: Broadening factor (a) and the chirp parameter (b) as a function of distance for a chirped Gaussian pulse propagating in the anomalous-dispersion region of a fiber. Dashed curves correspond to the case of an unchirped Gaussian pulse. The same curves are obtained for normal dispersion ($\beta_2 > 0$) if the sign of C is reversed.

where $s = \text{sgn}(\beta_2)$ takes values $+1$ or -1, depending on whether the pulse propagates in the normal- or the anomalous-dispersion region of the fiber.

It is evident from Eq. (3.3.9) that a Gaussian pulse remains Gaussian on propagation but its width and chirp change as dictated by Eq. (3.3.10). At a distance ξ, the width of the pulse changes from its initial value T_0 to $T_1(\xi) \equiv T_0 b_f(\xi)$. Clearly, the quantity b_f represents the broadening factor. In terms of the pulse and fiber parameters, it can be expressed as

$$b_f(z) = \left[\left(1 + \frac{C\beta_2 z}{T_0^2}\right)^2 + \left(\frac{\beta_2 z}{T_0^2}\right)^2\right]^{1/2}. \tag{3.3.11}$$

The chirp parameter of the pulse also changes from C to C_1 as it is transmitted through the fiber. It is important to note that the evolution of the pulse is affected by the signs of both β_2 and C.

Figure 3.3 shows (a) the broadening factor b_f and (b) the chirp parameter C_1 as a function of the normalized distance $\xi = z/L_D$ in the case of anomalous dispersion ($\beta_2 < 0$). An unchirped pulse ($C = 0$) broadens monotonically by a factor of $(1+\xi^2)^{1/2}$ and develops a negative chirp such that $C_1 = -\xi$ (the dotted curves). Chirped pulses, on the other hand, may broaden or compress depending on whether β_2 and C have the same or opposite signs. When $\beta_2 C > 0$, a chirped Gaussian pulse broadens monotonically at a rate faster than that of the unchirped pulse (the dashed curves). The reason is related to the fact that the dispersion-induced chirp adds to the input chirp because the two contributions have the same sign.

The situation changes dramatically for $\beta_2 C < 0$. In this case, the contribution of the dispersion-induced chirp is of a kind opposite to that of the input chirp. As seen from

Figure 3.3(b) and Eq. (3.3.10), C_1 becomes zero at a distance $\xi = |C|/(1+C^2)$, and the pulse becomes unchirped. This is the reason why the pulse width initially decreases in Figure 3.3(a) and becomes minimum at that distance. The minimum value of the pulse width depends on the input chirp parameter as

$$T_1^{\min} = T_0/\sqrt{1+C^2}. \tag{3.3.12}$$

By comparing this equation with Eq. (3.3.8), one can conclude that the pulse becomes transform-limited at that distance. The pulse rebroadens beyond this point and its width eventually becomes larger than the input value. One can understand this behavior using the analogy noted earlier between temporal dispersion and spatial diffraction. Chirping in time for a pulse is analogous to curving of the wavefront for an optical beam. Just as a converging beam focuses to a minimum width before it diverges, a suitably chirped pulse can reduce its width before it broadens monotonically.

3.3.2 Pulses of Arbitrary Shape

The analytic solution in Eq. (3.3.9), although useful, has only a limited validity as it applies to Gaussian-shape pulses that are affected by second-order dispersion β_2. In practice, pulse shape can be different. Moreover, third-order dispersion effects, governed by β_3, may become important close to the zero-dispersion wavelength of the fiber. Even a Gaussian pulse does not remains Gaussian in shape and develops a tail with an oscillatory structure when effects of β_3 are included [19]. Such pulses cannot be properly characterized by their FWHM. A proper measure of pulse width for pulses of arbitrary shapes is the root-mean square (RMS) width of the pulse defined as

$$\sigma_p = \left[\langle t^2\rangle - \langle t\rangle^2\right]^{1/2}, \tag{3.3.13}$$

where the angle brackets denote averaging with respect to the power profile of the pulse, that is,

$$\langle t^m\rangle = \frac{\int_{-\infty}^{\infty} t^m |A(z,t)|^2\, dt}{\int_{-\infty}^{\infty} |A(z,t)|^2\, dt}. \tag{3.3.14}$$

It turns out that σ_p can be calculated analytically for pulses of arbitrary shape, while including dispersive effects to all orders, as long as the nonlinear effects remain negligible. The derivation is based on the observation that the pulse spectrum does not change in a linear dispersive medium irrespective of what happens to the pulse shape. The first step thus consists of expressing the first and second moments in Eq. (3.3.13) in terms of the spectral amplitude $\tilde{A}(z,\omega)$ and its derivatives as

$$\langle t\rangle = \frac{-i}{N}\int_{-\infty}^{\infty} \tilde{A}^* \frac{\partial \tilde{A}}{\partial \omega}\, d\omega, \qquad \langle t^2\rangle = \frac{1}{N}\int_{-\infty}^{\infty} \left|\frac{\partial \tilde{A}}{\partial \omega}\right|^2 d\omega, \tag{3.3.15}$$

where $N \equiv \int_{-\infty}^{\infty} |\tilde{A}(z,\omega)|^2\, d\omega$ is a normalization factor related to pulse energy.

From Eq. (3.1.3), when nonlinear effects are negligible, different spectral components propagate inside the fiber according to the simple relation

$$\tilde{A}(z,\omega) = \tilde{A}(0,\omega)\exp[i\beta_L(\omega)z - i\beta_0 z], \tag{3.3.16}$$

where the propagation constant $\beta_L(\omega)$ includes dispersive effects to all orders. We substitute this relation in Eq. (3.3.15) and introduce the amplitude $S(\omega)$ and phase $\theta(\omega)$ of the input spectrum as $\tilde{A}(0,\omega) = Se^{i\theta}$. The spectral phase θ plays an important role as it is related to the frequency chirp of the pulse. Using Eq. (3.3.13), the RMS width σ_p at $z = L$ is found from the relation

$$\sigma_p^2(L) = \sigma_0^2 + [\langle\tau^2\rangle - \langle\tau\rangle^2] + 2[\langle\tau\theta_\omega\rangle - \langle\tau\rangle\langle\theta_\omega\rangle], \tag{3.3.17}$$

where the angle brackets now denote average over the input pulse spectrum such that

$$\langle f\rangle = \frac{1}{N}\int_{-\infty}^{\infty} f(\omega)S^2(\omega)\,d\omega. \tag{3.3.18}$$

In Eq. (3.3.17), σ_0 is the RMS width of input pulses, $\theta_\omega \equiv d\theta/d\omega$, and τ is the group delay for a fiber of length L defined as

$$\tau(\omega) = (d\beta_L/d\omega)L. \tag{3.3.19}$$

Equation (3.3.17) can be used for pulses of arbitrary shape, width, and chirp. It makes no assumption about the form of $\beta_L(\omega)$ and thus can be used for fiber links containing multiple fibers with arbitrary dispersion properties. A general conclusion that follows from this equation and Eq. (3.3.19) is that $\sigma_p^2(L)$ is at most a quadratic polynomial of the fiber length L. As a result, the broadening factor can be written in its most general form as

$$f_b = (1 + c_1 L + c_2 L^2)^{1/2}, \tag{3.3.20}$$

where c_1 and c_2 depend on the pulse and fiber parameters. This form applies for pulses of any shape propagating inside a fiber link with arbitrary dispersion characteristics.

As a simple application of Eq. (3.3.17), we consider the case of a rectangular-shape pulse of width $2T_0$ for which $A(0,t) = A_0$ for $|t| < T_0$ and 0 otherwise. Taking the Fourier transform of $A(0,t)$, we obtain the spectral amplitude $\tilde{A}(0,\omega)$ of such a pulse and find that

$$S(\omega) = (2A_0T_0)\,\mathrm{sinc}(\omega T_0), \qquad \theta(\omega) = 0. \tag{3.3.21}$$

Expanding $\beta_L(\omega)$ to second-order in ω, the group delay is given by $\tau(\omega) = (\beta_1 + \beta_2\omega)L$. We can now calculate all averaged quantities in Eq. (3.3.17) and find that

$$\langle\tau\rangle = \beta_1 L, \qquad \langle\tau^2\rangle = \beta_1^2 + \beta_2^2 L^2/2T_0^2, \tag{3.3.22}$$

whereas $\langle\tau\theta_\omega\rangle = 0$ and $\langle\theta_\omega\rangle = 0$. The final result for the RMS width is found to be

$$\sigma_p^2(L) = \sigma_0^2 + \tfrac{1}{2}T_0^2\xi^2 = \sigma_0^2(1 + \tfrac{3}{2}\xi^2), \tag{3.3.23}$$

where we used the relation $\sigma_0^2 = T_0^2/3$ together with $\xi = L/L_D$. Thus, the broadening factor for a rectangular pulse has the form of Eq. (3.3.20) with $c_1 = 0$ and $c_2 = \frac{3}{2}$. Noting that $c_1 = 0$ and $c_2 = 1$ for Gaussian pulses, we conclude that a rectangular pulse broadens more than a Gaussian pulse under the same conditions. This is expected in view of the sharper edges of such a pulse that produce a wider spectrum.

As a second application of Eq. (3.3.17), we use it to calculate broadening experienced by an unchirped pulse whose shape is in the form of a hyperbolic secant, that is, $A(0,t) = A_0\text{sech}(t/T_0)$. Such pulses are relevant for soliton-based lightwave systems (see Section 8.2). Taking the Fourier transform of $A(0,t)$, we find

$$S(\omega) = (\pi A_0 T_0)\,\text{sech}(\pi\omega T_0/2), \qquad \theta(\omega) = 0. \tag{3.3.24}$$

As before, using $\tau(\omega) = (\beta_1 + \beta_2\omega)L$, we can calculate all averages in Eq. (3.3.17). Utilizing the known integral $\int_{-\infty}^{\infty} x^2\text{sech}(x)\,dx = \pi^2/6$ [18], we find that

$$\langle\tau\rangle = \beta_1 L, \qquad \langle\tau^2\rangle = \beta_1^2 + \pi^2\beta_2^2 L^2/(12T_0^2), \tag{3.3.25}$$

with $\langle\tau\theta_\omega\rangle = 0$ and $\langle\theta_\omega\rangle = 0$. The RMS width of sech-shape pulses increases with distance as

$$\sigma_p^2(L) = \sigma_0^2(1 + \tfrac{1}{2}\xi^2), \tag{3.3.26}$$

where we used the relation $\sigma_0^2 = \pi^2 T_0^2/6$ together with $\xi = L/L_D$. The factor of $\frac{1}{2}$ indicates that "sech" pulses broaden less than a Gaussian pulse under the identical conditions. This is expected as the tails of a sech pulse decay slower than a Gaussian pulse.

As another application of Eq. (3.3.17), we use it to include the effects of third-order dispersion on chirped Gaussian pulses. Expanding $\beta_L(\omega)$ to third-order in ω, the group delay is now given by

$$\tau(\omega) = (\beta_1 + \beta_2\omega + \tfrac{1}{2}\beta_3\omega^2)L. \tag{3.3.27}$$

Using Eq. (3.3.7) with $\tilde{A} = Se^{i\theta}$, we obtain the following expressions for S and θ:

$$S^2(\omega) = \frac{4\pi A_0^2\sigma_0^2}{1+C^2}\exp\left(-\frac{2\omega^2\sigma_0^2}{1+C^2}\right), \quad \theta(\omega) = \frac{C\omega^2\sigma_0^2}{1+C^2} - \tan^{-1}C, \tag{3.3.28}$$

where we used $\sigma_0^2 = T_0^2/2$. All averages in Eq. (3.3.17) can be performed analytically using Eqs. (3.3.27) and (3.3.28). The final result is found to be

$$\frac{\sigma^2}{\sigma_0^2} = \left(1 + \frac{C\beta_2 L}{2\sigma_0^2}\right)^2 + \left(\frac{\beta_2 L}{2\sigma_0^2}\right)^2 + \left(\frac{\beta_3 L(1+C^2)}{4\sqrt{2}\sigma_0^3}\right)^2. \tag{3.3.29}$$

The last term represents the contribution of third-order dispersion.

3.3.3 Effects of Source Spectrum

The discussion so far has assumed that the optical source used to produce the input pulses is nearly monochromatic or, more precisely, the source spectrum (before modulation) is much narrower than the pulse spectrum. This condition is satisfied in practice for DFB lasers, but not for light-emitting diodes utilized for some applications. To account for the source spectral width, we must treat the optical field as a stochastic process and consider the coherence properties of the source. In this case, the input field should be written as $A(0,t) = A_0(t)a_p(t)$, where $a_p(t)$ represents the pulse shape and fluctuations in $A_0(t)$ produce the finite bandwidth of the source spectrum.

The effect of source fluctuations on pulse broadening can be included if we replace $\langle t \rangle$ and $\langle t^2 \rangle$ in Eq. (3.3.13) with $\langle\langle t \rangle\rangle_s$ and $\langle\langle t^2 \rangle\rangle_s$, where the outer angle brackets stand for the ensemble average over source fluctuations. It is easy to see from the definition of these moments that $S(\omega)$ in Eq. (3.3.18) becomes a convolution of the pulse and the source spectra such that

$$S(\omega) = \int_{-\infty}^{\infty} S_p(\omega - \omega_1) F(\omega_1)\, d\omega_1, \tag{3.3.30}$$

where $S_p(\omega)$ is the pulse spectrum related to Fourier transform of $a_p(t)$. The Fourier transform $F(\omega)$ of $A_0(t)$ represents a fluctuating spectral component of the field at the source. Assuming that the underlying stochastic process is stationary, its correlation function has the form

$$\langle F^*(\omega_1) F(\omega_2) \rangle_s = G(\omega_1)\delta(\omega_1 - \omega_2), \tag{3.3.31}$$

where $G(\omega)$ represents the source spectrum and the subscript s reminds us that the angle brackets denote an ensemble average over source fluctuations.

The two moments, $\langle\langle t \rangle\rangle_s$ and $\langle\langle t^2 \rangle\rangle_s$, can be calculated analytically in the special case in which the source spectrum is Gaussian and has the form

$$G(\omega) = \frac{1}{\sigma_\omega \sqrt{2\pi}} \exp\left(-\frac{\omega^2}{2\sigma_\omega^2}\right), \tag{3.3.32}$$

where σ_ω is the RMS spectral width of the source. All averages in Eq. (3.3.17) can now be performed analytically as all integrals involve only Gaussian functions. For example, from Eqs. (3.3.18) and (3.3.30)

$$\langle\langle \tau \rangle\rangle_s = \frac{1}{N} \int_{-\infty}^{\infty} d\omega \tau(\omega) \iint_{-\infty}^{\infty} S_p^*(\omega - \omega_1) S_p(\omega - \omega_2) \langle F^*(\omega_1) F(\omega_2) \rangle_s d\omega_1\, d\omega_2. \tag{3.3.33}$$

If we use Eq. (3.3.31) together with $\tau(\omega) = (\beta_1 + \beta_2 \omega + \frac{1}{2}\beta_3 \omega^2)L$, we obtain

$$\langle\langle \tau \rangle\rangle_s = \frac{L}{N} \iint_{-\infty}^{\infty} (\beta_1 + \beta_2 \omega + \tfrac{1}{2}\beta_3 \omega^2) |S_p(\omega - \omega_1)|^2 G(\omega_1)\, d\omega_1\, d\omega. \tag{3.3.34}$$

For a chirped Gaussian pulse, the pulse spectrum $S_p(\omega)$ is also Gaussian. As a result, the integral over ω_1 in Eq. (3.3.34) can be performed first, resulting in another Gaussian spectrum. The integral over ω is then straightforward and yields

$$\langle\langle t \rangle\rangle_s = L\left[\beta_1 + \frac{\beta_3}{8\sigma_0^2}(1 + C^2 + V_\omega^2)\right], \tag{3.3.35}$$

where $V_\omega = 2\sigma_\omega \sigma_0$. Repeating the same procedure for $\langle\langle t^2 \rangle\rangle_s$, we obtain the following expression for the RMS width of the pulse at the end of a fiber of length L:

$$\frac{\sigma_p^2}{\sigma_0^2} = \left(1 + \frac{C\beta_2 L}{2\sigma_0^2}\right)^2 + (1 + V_\omega^2)\left(\frac{\beta_2 L}{2\sigma_0^2}\right)^2 + (1 + C^2 + V_\omega^2)^2 \left(\frac{\beta_3 L}{4\sqrt{2}\sigma_0^3}\right)^2. \tag{3.3.36}$$

Equation (3.3.36) provides an expression for dispersion-induced broadening of Gaussian input pulses under quite general conditions. We use it in the next subsection to find the limiting bit rate of lightwave systems.

3.3.4 Limitations on the Bit Rate

The pulse-broadening formula in Eq. (3.3.36) is useful for estimating the limitations imposed on the bit rate and the system length by fiber dispersion. These limitations can be quite different depending on whether source spectral width is larger or smaller than the pulse bandwidth. For this reason, we consider the two cases separately.

Optical Sources with a Large Spectral Width

This case corresponds to $V_\omega \gg 1$ in Eq. (3.3.36). Consider a lightwave system operating away from the zero-dispersion wavelength so that the β_3 term can be neglected. The effects of frequency chirp are negligible for sources with a large spectral width. By setting $C = 0$ and using $V_\omega = 2\sigma_\omega \sigma_0$ in Eq. (3.3.36), we obtain

$$\sigma^2 = \sigma_0^2 + (\beta_2 L \sigma_\omega)^2 \equiv \sigma_0^2 + (DL\sigma_\lambda)^2, \tag{3.3.37}$$

where σ_λ is the RMS source spectral width in wavelength units. The output pulse width is thus given by

$$\sigma = (\sigma_0^2 + \sigma_D^2)^{1/2}, \tag{3.3.38}$$

where $\sigma_D \equiv |D|L\sigma_\lambda$ provides a measure of dispersion-induced broadening.

To relate σ to the bit rate, we use the requirement that the broadened pulse should remain inside its allocated bit slot, $T_B = 1/B$, where B is the bit rate. A commonly used criterion is $\sigma \leq T_B/4$; for Gaussian pulses at least 95% of the pulse energy then remains within the bit slot. With this criterion, the bit rate is limited by the condition $4B\sigma \leq 1$. In the limit $\sigma_D \gg \sigma_0$, $\sigma \approx \sigma_D = |D|L\sigma_\lambda$, and the condition becomes

$$4BL|D|\sigma_\lambda \leq 1. \tag{3.3.39}$$

This is a remarkably simple result. It can be written as $BL|D|\Delta\lambda \leq 1$, where $\Delta\lambda = 4\sigma_\lambda$ is the full spectral width containing 95% of the source power.

For a lightwave system operating exactly at the zero-dispersion wavelength, $\beta_2 = 0$ in Eq. (3.3.36). By setting $C = 0$ as before and assuming $V_\omega \gg 1$, Eq. (3.3.36) can be approximated by

$$\sigma^2 = \sigma_0^2 + \tfrac{1}{2}(\beta_3 L \sigma_\omega^2)^2 \equiv \sigma_0^2 + \tfrac{1}{2}(SL\sigma_\lambda^2)^2, \tag{3.3.40}$$

where the dispersion slope $S = (2\pi c/\lambda)^2 \beta_3$. The output pulse width can be written in the form of Eq. (3.3.38) but $\sigma_D \equiv |S|L\sigma_\lambda^2/\sqrt{2}$. As before, we can relate σ to the limiting bit rate using the condition $4B\sigma \leq 1$. When $\sigma_D \gg \sigma_0$, the limitation on the bit rate is governed by

$$\sqrt{8}BL|S|\sigma_\lambda^2 \leq 1. \tag{3.3.41}$$

As an example, consider the case of a light-emitting diode (LED) for which $\sigma_\lambda \approx 15$ nm. If we use $D = 17$ ps/(km-nm) as a typical value for standard telecommunication fibers at 1.55 μm, Eq. (3.3.39) yields $BL < 1$ (Gb/s)-km. This condition implies that LEDs can transmit a 100-Mb/s bit stream over at most 10 km. However, if the system is designed to operate at the zero-dispersion wavelength, BL can be increased to 20 (Gb/s)-km for a typical value of $S = 0.08$ ps/(km-nm^2).

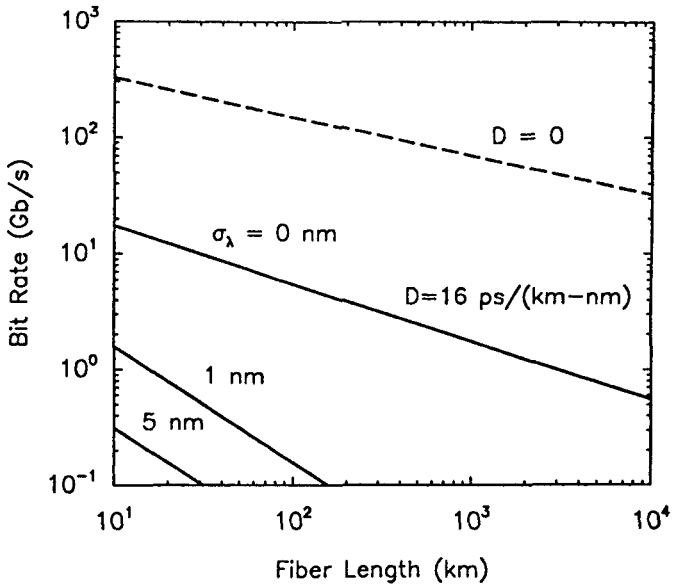

Figure 3.4: Limiting bit rate of single-mode fibers as a function of the fiber length for $\sigma_\lambda = 0$, 1, and 5 nm. The case $\sigma_\lambda = 0$ corresponds to the case of an optical source whose spectral width is much smaller than the bit rate.

Optical Sources with a Small Spectral Width

This situation corresponds to $V_\omega \ll 1$ in Eq. (3.3.36). Consider first the case in which the β_3 term can be neglected. Also assume that input pulses are unchirped and set $C = 0$ in Eq. (3.3.36). The RMS pulse width at the fiber output is then given by

$$\sigma^2 = \sigma_0^2 + (\beta_2 L/2\sigma_0)^2 \equiv \sigma_0^2 + \sigma_D^2. \tag{3.3.42}$$

Although this equation appears identical to Eq. (3.3.38), there is a major difference between the two. More specifically, σ_D in Eq. (3.3.42) depends on the initial width σ_0, whereas it is independent of σ_0 in Eq. (3.3.38). In fact, σ in Eq. (3.3.42) can be minimized by choosing an optimum value of σ_0. Setting $d\sigma/d\sigma_0 = 0$, the minimum value of σ is found to occur for $\sigma_0 = \sigma_D = (|\beta_2|L/2)^{1/2}$ and has a value $\sigma = (|\beta_2|L)^{1/2}$. The limiting bit rate is obtained using the condition $4B\sigma \leq 1$ and leads to

$$4B\sqrt{|\beta_2|L} \leq 1. \tag{3.3.43}$$

The main difference from Eq. (3.3.39) is that B scales as $L^{-1/2}$ rather than L^{-1}. Figure 3.4 compares the decrease in the bit rate with increasing L for $\sigma_\lambda = 0$, 1, and 5 nm for a fiber link with $D = 16$ ps/(km-nm). Equation (3.3.43) was used for the trace marked $\sigma_\lambda = 0$.

For a lightwave system operating close to the zero-dispersion wavelength, $\beta_2 \approx 0$ in Eq. (3.3.36). Using $V_\omega \ll 1$ and $C = 0$, the pulse width is then given by

$$\sigma^2 = \sigma_0^2 + (\beta_3 L/4\sigma_0^2)^2/2 \equiv \sigma_0^2 + \sigma_D^2. \tag{3.3.44}$$

Similar to the case of Eq. (3.3.42), σ can be minimized by optimizing the input pulse width σ_0. The minimum value of σ occurs for $\sigma_0 = (|\beta_3|L/4)^{1/3}$ and is given by

$$\sigma = \sqrt{3/2}(|\beta_3|L/4)^{1/3}. \tag{3.3.45}$$

The limiting bit rate is obtained from the condition $4B\sigma \leq 1$ and is found to be

$$B(|\beta_3|L)^{1/3} \leq 0.324. \tag{3.3.46}$$

The dispersive effects are most forgiving in this case. For a typical value of the third-order dispersion parameter, $\beta_3 = 0.1$ ps^3/km, L can exceed 340,000 km at a bit rate of 10 Gb/s. It decreases rapidly for larger bit rates since L scales with B as B^{-3} but exceeds 5,300 km even at $B = 40$ Gb/s. The dashed line in Figure 3.4 shows this case by using Eq. (3.3.46) with $\beta_3 = 0.1$ ps^3/km. The main point to note from this figure is that the performance of a lightwave system can be improved considerably by operating it near the zero-dispersion wavelength of the fiber and using optical sources with a relatively narrow spectral width.

Effects of Frequency Chirp

The input pulse in all preceding cases has been assumed to be an unchirped Gaussian pulse. In practice, optical pulses are often non-Gaussian and may exhibit considerable chirp. A super-Gaussian model has been used to study the bit-rate limitation imposed by fiber dispersion for a NRZ-format bit stream [20]. In this model, Eq. (3.3.4) is replaced with

$$A(0,t) = A_0 \exp\left[-\frac{1+iC}{2}\left(\frac{t}{T_0}\right)^{2m}\right], \tag{3.3.47}$$

where the parameter m controls the pulse shape. Chirped Gaussian pulses correspond to $m = 1$. For large value of m the pulse becomes nearly rectangular with sharp leading and trailing edges. The output pulse shape can be obtained by solving Eq. (3.3.1) numerically. The limiting bit rate–distance product BL is found by requiring that the RMS pulse width does not increase above a tolerable value.

Figure 3.5 shows the BL product as a function of the chirp parameter C for Gaussian ($m = 1$) and super-Gaussian ($m = 3$) input pulses. In both cases the fiber length L at which the pulse broadens by 20% was obtained for $T_0 = 125$ ps and $\beta_2 = -20$ ps^2/km. As expected, the BL product is smaller for super-Gaussian pulses because such pulses have sharper leading and trailing edges and thus broaden more rapidly than Gaussian pulses. The BL product is reduced dramatically for negative values of the chirp parameter C. This is due to enhanced broadening occurring when $\beta_2 C$ is positive (see Figure 3.3). Unfortunately, C is generally negative for directly modulated semiconductor lasers with a typical value of -6 at 1.55 μm. Since $BL < 100$ (Gb/s)-km under such conditions, fiber dispersion limits the bit rate to about 2 Gb/s even for $L = 50$ km. The chirp problem is usually solved for systems operating at 10 Gb/s or more by operating the laser continuously and employing an external modulator for generating the bit stream (see Section 2.3). The dispersion problem can also be alleviated to a large extent by using dispersion compensation along the fiber link, a topic we discuss next.

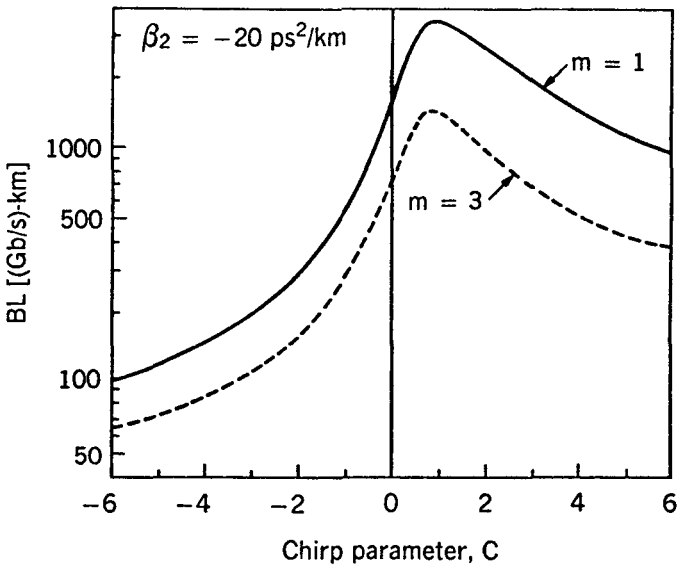

Figure 3.5: Dispersion-limited *BL* product as a function of the chirp parameter for Gaussian (solid curve) and super-Gaussian (dashed curve) input pulses. (After Ref. [20]; ©1986 OSA.)

3.3.5 Dispersion compensation

It should be evident from the discussion in this section that dispersion is a major limiting factor for any long-haul lightwave system. Fortunately, there is a simple solution to the dispersion problem, and it is often used in practice. The basic idea consists of compensating dispersion along the fiber link in a periodic fashion using fibers with opposite dispersion characteristics. Figure 3.6 shows such a fiber link made with alternating fiber sections exhibiting normal and anomalous GVD at the channel wavelength. Since β_2 is negative (anomalous GVD) for standard fibers in the 1.55-μm region, *dispersion-compensating* fibers (DCFs) with large positive values of β_2 have been developed for the sole purpose of dispersion compensation [21]–[24]. The use of DCFs provides an all-optical technique that is capable of overcoming the detrimental effects of chromatic dispersion in optical fibers, provided the average signal power is low enough that the nonlinear effects remain negligible.

The periodic arrangement of fibers shown in Figure 3.6 is referred to as a dispersion map. To understand how such a dispersion-compensation technique works, consider propagation of optical signal through one map period of length L_m consisting of two fiber segments with different dispersion parameters. Applying Eq. (3.3.2) for each fiber section consecutively, we obtain

$$A(L_m,t) = \frac{1}{2\pi}\int_{-\infty}^{\infty} \tilde{A}(0,\omega)\exp\left[\frac{i}{2}\omega^2(\beta_{21}l_1+\beta_{22}l_2) - i\omega t\right] d\omega, \tag{3.3.48}$$

where $L_m = l_1 + l_2$ and β_{2j} is the GVD parameter for the fiber segment of length l_j (j = 1 or 2). If the second fiber is chosen such that the phase term containing ω^2 vanishes,

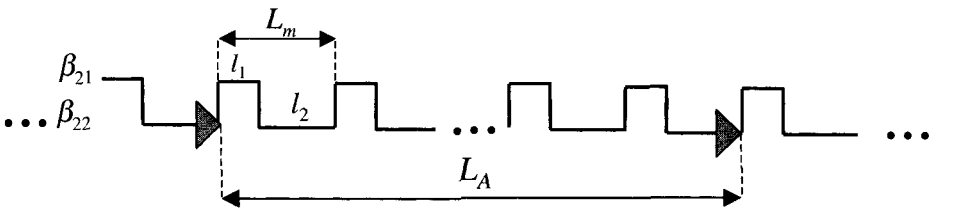

Figure 3.6: Schematic of a fiber link employing alternating fiber sections with normal and anomalous dispersions between two successive amplifiers. The lengths and dispersion parameters of two types of fibers are chosen to minimize dispersion-induced degradation of the optical bit stream.

Eq. (3.3.48) shows that $A(L_m,t) \equiv A(0,t)$, that is, the optical bit stream recovers its original shape at the end of the second fiber, no matter how much it becomes degraded in the first fiber. The condition for perfect dispersion compensation is thus given by

$$\beta_{21} l_1 + \beta_{22} l_2 = 0 \quad \text{or} \quad D_1 l_1 + D_2 l_2 = 0, \tag{3.3.49}$$

where the dispersion parameter D is related to β_2 as in Eq. (3.1.7).

Equation (3.3.49) shows that the two fibers must have dispersion parameters with opposite signs. For most lightwave systems, the transmission fiber exhibits anomalous dispersion ($D_1 > 0$) near 1.55 μm. The DCF section in that case should exhibit normal GVD ($D_2 < 0$). Moreover, its length should be chosen to satisfy

$$l_2 = -(D_1/D_2) l_1. \tag{3.3.50}$$

For practical reasons, l_2 should be as small as possible. This is possible only if the DCF has a large negative value of D_2. In practice, L_m is chosen to be the same as the amplifier spacing L_A, where as the length l_2 is a small fraction of L_A. The DCF is then a part of the amplifier module, and the two together compensate both the fiber loss and fiber dispersion simultaneously. The design of DCFs is discussed in Chapter 7 devoted to the topic of dispersion management.

3.4 Polarization-Mode Dispersion

In this section we return to the polarization issue, ignored so far in this chapter. As mentioned in Section 3.1, the polarization unit vector in Eq. (3.1.1), representing the state of polarization (SOP) of the electric field vector, does not remain constant in practical optical fibers. Rather, it changes in a random fashion along the fiber because of its fluctuating birefringence. There are two main sources of this birefringence. Geometric or form-induced birefringence is related to small departures from perfect cylindrical symmetry that occur during fiber manufacturing and produce a slightly elliptical core. Both the ellipticity and axes of the ellipse change randomly along the fiber on a length scale $\sim$10 m. The second source of birefringence has its origin in anisotropic stress produced on the fiber core during manufacturing or cabling of the fiber. This type of

birefringence can change with time because of environmental-induced changes in the position or temperature of the fiber. Such dynamic changes in fiber birefringence are relatively slow as they occur on a time scale of minutes or hours but they make the SOP of light totally unpredictable at any point inside the fiber.

Changes in the SOP of light are normally not of concern for lightwave systems because (1) information is not coded using polarization and (2) photodetectors detect the total power incident on them irrespective of the SOP of the optical signal. However, a phenomenon known as polarization-mode dispersion (PMD) induces pulse broadening whose magnitude can fluctuate with time because of environmental-induced changes in fiber birefringence. If the system is not designed with the worst-case scenario in mind, PMD-induced pulse broadening can move bits outside of their allocated time slots, resulting in errors and system failure in an unpredictable manner. The problem becomes serious as the bit rate increases and is of considerable concern for lightwave systems in which each channel operates at a bit rate of 10 Gb/s or more. For this reason, the impact of PMD on system performance has been studied extensively [25]–[30].

3.4.1 Fibers with Constant Birefringence

Before focusing on the effects of random birefringence, it is instructive to consider first fibers with constant birefringence. The discussion in this section thus applies to the so-called polarization-maintaining fibers in which a large birefringence is intentionally induced to mask the effects of small fluctuations resulting from manufacturing and environmental perturbations.

How does the phenomenon of birefringence affect pulses propagating inside an optical fiber? To answer this question, one must first note that even a single-mode fiber, in fact, supports two orthogonally polarized modes that are degenerate in all respects and propagate with the same propagation constant at a given frequency when the fiber exhibits perfect cylindrical symmetry. The main consequence of fiber birefringence is to break the degeneracy associated with these two modes such that they propagate inside the fiber with slightly different propagation constants. Mathematically, β_p is different for the two modes because the effective mode index $\bar{n}$ is not the same for them. If we represent the mode indices by $\bar{n}_x$ and $\bar{n}_y$ for the field components polarized along the x and y axes, respectively, the index difference $\Delta n = \bar{n}_x - \bar{n}_y$ provides a measure of birefringence. The two axes along which the modes are polarized are known as the *principal axes*.

When an input pulse is initially polarized along a principal axis, its SOP does not change with propagation because only one of the two polarization modes is excited. However, the phase velocity $v_p = c/\bar{n}$ and the group velocity $v_g = c/\bar{n}_g$, where $\bar{n}_g$ is the group index, are not the same for the two principal axes. It is common to choose the x direction along the principal axis with the larger mode index and call it the *slow axis*. The other axis is then referred to as the *fast axis*. When an input pulse is not polarized along a principal axis, its energy is divided into two parts as it excites both polarization modes. The fraction of energy carried by each mode depends on the input SOP of the pulse; for example, both modes are equally excited when input pulse is polarized linearly at an angle of 45° with respect to the slow axis. The two orthogonally polarized components of the pulse separate from each other and disperse along the fiber because

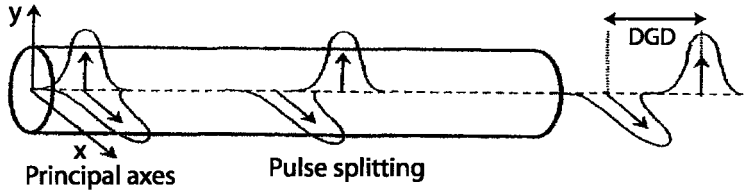

Figure 3.7: Propagation of an optical pulse in a fiber with constant birefringence. Pulse splits into its orthogonally polarized components that separate from each other because of DGD induced by birefringence.

of their different group velocities. Since the two components arrive at different times at the output end of the fiber, the pulse splits into two pulses that are orthogonally polarized. Figure 3.7 shows birefringence-induced pulse splitting schematically.

The extent of pulse splitting can be estimated from the time delay $\Delta\tau$ in the arrival of the two polarization components of the pulse at the fiber end. For a fiber of length L, $\Delta\tau$ is given by

$$\Delta\tau = \left| \frac{L}{v_{gx}} - \frac{L}{v_{gy}} \right| = L|\beta_{1x} - \beta_{1y}| = L(\Delta\beta_1), \tag{3.4.1}$$

where $\Delta\beta_1 = v_{gx}^{-1} - v_{gy}^{-1}$ is related to the difference in group velocities along the two principal SOPs [25]. The relative delay $\Delta\tau$ between the two polarization modes is called the differential group delay (DGD). The parameter $\Delta\beta_1 = \Delta\tau/L$ plays an important role as it is a measure of birefringence-induced dispersion. For polarization-maintaining fibers, $\Delta\beta_1$ can be quite large ($\sim$1 ns/km) because of their large birefringence ($\Delta n \sim 10^{-4}$). Conventional fibers exhibit much smaller birefringence ($\Delta n \sim 10^{-7}$), but its magnitude as well as orientation (directions of the principal axes) change randomly at a length scale known as the correlation length l_c (with typical values in the range of 10–100 m). For a short fiber section of length much smaller than l_c, birefringence remains constant but its DGD is below 10 fs/m.

3.4.2 Fibers with Random Birefringence

Consider a realistic long-haul lightwave system in which an optical pulse may propagate thousands of kilometers before it is converted into an electrical signal. In this situation, both the magnitude and the orientation of the birefringence vary along the fiber in a random fashion on a length scale $\sim$10 m. It is intuitively clear that the SOP of the light propagating in such fiber links will generally be elliptical and would change randomly along the fiber during propagation. The SOP will also be different for different spectral components of an optical pulse. The final polarization state is not of concern for most lightwave systems as photodetectors used inside optical receivers are insensitive to the SOP unless a coherent detection scheme is employed. What affects such systems is not the random SOP of light but pulse distortion induced by random changes in the birefringence.

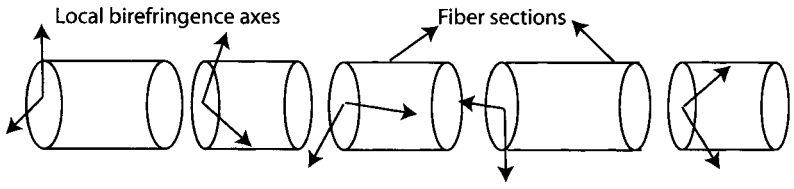

Figure 3.8: Schematic of the technique used for calculating the PMD effects. Optical fiber is divided into a large number of segments, each acting as a wave plate with different birefringence.

As seen in Figure 3.7, an input pulse splits into two orthogonally polarized components soon after it enters the fiber link. The two components begin to separate from each other at a rate that depends on the local birefringence of the fiber section. However, within a correlation length or so, the pulse enters a fiber section whose birefringence is different in both the magnitude and the orientation of the principal axes. Because of the random nature of such birefringence changes, the two components of the pulse perform a kind of random walk, each one advancing or retarding with respect to another in a random fashion. This random walk helps the pulse in the sense that the two components are not torn apart but, at the same time, the final separation $\Delta\tau$ between the two pulses becomes unpredictable, especially if birefringence fluctuates because of environmentally induced changes. The net result is that pulses appear distorted at the end of the fiber link and may even be shifted from their original location within the bit slot. When such PMD-induced distortions move pulses outside their allocated bit slot, the performance of a lightwave system is seriously compromised.

The analytical treatment of PMD is quite complex in general because of its statistical nature. A simple model divides the fiber into a large number of segments, as shown schematically in Figure 3.8. Both the degree of birefringence and the orientation of the principal axes remain constant in each section but change randomly from section to section. In effect, each fiber section is treated as a phase plate with different birefringence characteristics. One can employ the Jones-matrix formalism [31]–[33] for studying how the SOP of light at any given frequency changes with propagation inside each fiber section [25]. Propagation of each frequency component associated with an optical pulse through the entire fiber length is then governed by a composite Jones matrix obtained by multiplying individual Jones matrices for each fiber section.

It is useful to employ the "ket vector" notation of quantum mechanics for studying the PMD effects [28] and write the Jones vector associated with the optical field at a specific frequency ω in the form of a "column vector" as

$$|\tilde{A}(z,\omega)\rangle = \begin{pmatrix} \tilde{A}_x(z,\omega) \\ \tilde{A}_y(z,\omega) \end{pmatrix}, \tag{3.4.2}$$

where z represents distance within the fiber. The effect of random changes in birefringence for a fiber of length L is then governed by the matrix equation

$$|\tilde{A}(L,\omega)\rangle = \overline{T}_N \overline{T}_{N-1} \cdots \overline{T}_2 \overline{T}_1 |\tilde{A}(0,\omega)\rangle \equiv \overline{T}_c(\omega)|\tilde{A}(0,\omega)\rangle, \tag{3.4.3}$$

where $\overline{T}_j(\omega)$ is the Jones matrix of the jth section and $\overline{T}_c(\omega)$ is the composite Jones matrix of the whole fiber. It turns out that one can find two *principal states of po-*

larization (PSPs) for any fiber with the property that, when a pulse is polarized along them, the SOP at the output of fiber is independent of frequency to first order, in spite of random changes in fiber birefringence [25]. The PSPs are analogous to the slow and fast axes associated with fibers of constant birefringence, but they are in general elliptically polarized. An optical pulse polarized along a PSP does not split into two parts and maintains its shape. However, the pulse travels at different speeds for the two PSPs. The DGD can still be defined as the relative delay $\Delta\tau$ in the arrival time of pulses polarized along the two PSPs. However, it is important to stress that PSPs and $\Delta\tau$ depend not only on the birefringence properties of fiber but also on its length L and they change with L in a a random fashion.

In practice, PSPs are not known in advance, and launched pulses are rarely polarized along one of them. Each pulse then splits into two parts that are delayed with respect to each other by a random amount $\Delta\tau$. The PMD-induced pulse broadening is characterized by the RMS value of $\Delta\tau$, obtained after averaging over random birefringence changes. Several approaches have been used to calculate this average [34]–[37]. The second moment of $\Delta\tau$ turns out to be the same in all cases and is given by

$$\langle(\Delta\tau)^2\rangle \equiv \Delta\tau_{\rm RMS}^2 = 2(\Delta\beta_1)^2 l_c^2[\exp(-z/l_c) + z/l_c - 1], \tag{3.4.4}$$

where the correlation length l_c is defined as the length over which two polarization components remain correlated.

For short distances such that $z \ll l_c$, we note that $\Delta\tau_{\rm RMS} = (\Delta\beta_1)z$ from Eq. (3.4.4), as expected for a polarization-maintaining fiber. For distances $z \gg 1$ km, a reasonable estimate of pulse broadening is obtained by taking the limit $z \gg l_c$ in Eq. (3.4.4). The result is found to be

$$\Delta\tau_{\rm RMS} \approx (\Delta\beta_1)\sqrt{2l_c z} \equiv D_p\sqrt{z}, \tag{3.4.5}$$

where D_p is known as the PMD parameter. Measured values of D_p vary from fiber to fiber in the range $D_p = 0.01$–10 ps/km$^{1/2}$. Fibers installed during the 1980s had a relatively large PMD with D_p often exceeding 1 ps/km$^{1/2}$. In contrast, modern fibers are designed to have low PMD, and typically $D_p < 0.1$ ps/km$^{1/2}$ for them. Because of the $\sqrt{L}$ dependence, PMD-induced pulse broadening is relatively small compared with the GVD effects. For example, $\Delta\tau_{\rm RMS} = 1$ ps for a fiber length of 100 km, if we use $D_p = 0.1$ ps/km$^{1/2}$, and can be ignored for pulse widths >10 ps. However, PMD becomes a limiting factor for lightwave systems designed to operate over long distances at high bit rates [25]–[28].

The average in Eq. (3.4.5) denotes an ensemble average over fluctuations in the birefringence of a fiber. For a given fiber of certain length, $\Delta\tau$ has a constant value at a fixed wavelength. However, this value fluctuates from fiber to fiber in an ensemble of fibers that are identical in all respects except for random variations in their birefringence. Often, it is not practical to make extensive measurements on a large ensemble of such fibers. However, DGD also fluctuates with the wavelength of light even for one member of such an ensemble. An average of DGD over a reasonably large wavelength range provides a good approximation to the ensemble average indicated in Eq. (3.4.5), in view of the ergodic theorem valid for any stationary random process. Figure 3.9 shows experimentally measured variations in $\Delta\tau$ over a 20-nm-wide range in the

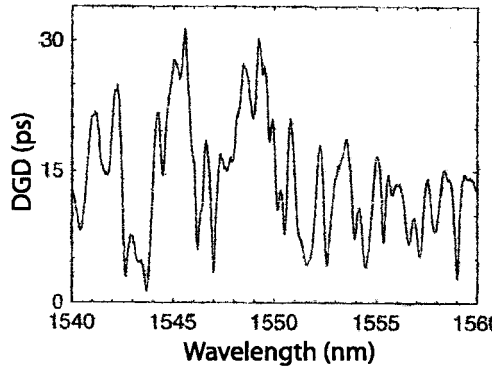

Figure 3.9: Measured variations in $\Delta\tau$ over a 20-nm-wide spectral range for a fiber with mean DGD of 14.7 ps. (After Ref. [28]; ©2002 Elsevier.)

spectral region near 1.55 μm for a fiber with the mean DGD of 14.7 ps [28]. As seen there, the measured values of DGD vary randomly from as small as 2 ps to more than 30 ps depending on the wavelength of light propagating through the fiber.

3.4.3 Jones-Matrix Formalism

In this subsection we extend the treatment of Section 3.1 to include the polarization effects and develop a vector theory of pulse propagation based on the Jones-matrix formalism [31]–[33]. To simplify the following discussion, we ignore the nonlinear effects and assume that fiber losses are polarization-independent. The polarization dependence of the signal loss or gain is discussed in Section 3.5.

In the vector case, Eq. (3.1.1) should include both polarization components of the optical field as

$$\mathbf{E}(\mathbf{r},t) = \mathrm{Re}\{[\hat{\mathbf{x}}A_x(z,t) + \hat{\mathbf{y}}A_y(z,t)]F(x,y)\exp[i\beta_{\mathrm{av}}(\omega_0)z - i\omega_0 t]\}. \tag{3.4.6}$$

The two field components have the same frequency but different propagation constants β_x and β_y because of birefringence, and β_{av} is their average value. In the frequency domain, the two polarization components evolve as

$$\frac{\partial \tilde{A}_x}{\partial z} = i[\beta_{\mathrm{av}}(\omega) + \tfrac{1}{2}\Delta\beta(\omega)], \qquad \frac{\partial \tilde{A}_y}{\partial z} = i[\beta_{\mathrm{av}}(\omega) - \tfrac{1}{2}\Delta\beta(\omega)], \tag{3.4.7}$$

where $\Delta\beta$ represents the difference between the two propagation constants. It is important to stress that both the average and the difference depend on the frequency of incident light.

To analyze pulse propagation, we consider each frequency component of the pulse separately. As in Section 3.1, we expand $\beta_{\mathrm{av}}(\omega)$ and $\Delta\beta(\omega)$ in a Taylor series around the carrier frequency ω_0 and write them in the form

$$\beta_{\mathrm{av}}(\omega) \approx \beta_0 + \beta_1(\Delta\omega) + \frac{\beta_2}{2}(\Delta\omega)^2, \qquad \Delta\beta(\omega) \approx \Delta\beta_0 + \Delta\beta_1(\Delta\omega), \tag{3.4.8}$$

where $\Delta\omega = \omega - \omega_0$. We have ignored even the quadratic term in the expansion of $\Delta\beta$; this approximation amounts to assuming that the GVD is not affected by birefringence. As before, a subscript in the expansion parameters represents the order of the derivative with respect to frequency. Following the method outlined in Section 3.1, we convert Eq. (3.4.7) to the time domain and obtain the following set of two equations for the two polarization components of the pulse:

$$\frac{\partial A_x}{\partial z} + \frac{\Delta\beta_1}{2}\frac{\partial A_x}{\partial t} + \frac{i\beta_2}{2}\frac{\partial^2 A_x}{\partial t^2} = -\frac{\alpha}{2}A_x + \frac{i}{2}\Delta\beta_0 A_x, \tag{3.4.9}$$

$$\frac{\partial A_y}{\partial z} - \frac{\Delta\beta_1}{2}\frac{\partial A_y}{\partial t} + \frac{i\beta_2}{2}\frac{\partial^2 A_y}{\partial t^2} = -\frac{\alpha}{2}A_y - \frac{i}{2}\Delta\beta_0 A_y, \tag{3.4.10}$$

where time is measured in a frame moving at the average group velocity $v_g = 1/\beta_1$. The birefringence effects appear in these equations through the parameters $\Delta\beta_0$ and $\Delta\beta_1$. The former produces a differential phase shift, while the latter leads to a temporal delay (DGD) between the two components.

Equations (3.4.9) and (3.4.10) assume that birefringence remains constant along the fiber. In the case of randomly varying birefringence, we need to consider random rotations of the birefringence axes within the fiber (see Figure 3.8). These rotations can be included in a compact form if we write Eqs. (3.4.9) and (3.4.10) in the Jones-matrix notation. Introducing the Jones vector as in Eq. (3.4.2), we obtain

$$\frac{\partial|A\rangle}{\partial z} + \frac{\Delta\beta_1}{2}\overline{M}\frac{\partial|A\rangle}{\partial t} + \frac{i\beta_2}{2}\frac{\partial^2|A\rangle}{\partial t^2} = -\frac{\alpha}{2}|A\rangle + \frac{i}{2}\Delta\beta_0\overline{M}|A\rangle, \tag{3.4.11}$$

where $\overline{M}$ is a 2×2 matrix defined as $\overline{M} = \overline{R}^{-1}\sigma_1\overline{R}$. The rotation matrix $\overline{R}$ and the Pauli spin matrices are defined as [31]

$$\overline{R} = \begin{pmatrix} \cos\psi & \sin\psi \\ -\sin\psi & \cos\psi \end{pmatrix}, \quad \sigma_1 = \begin{pmatrix} 1 & 0 \\ 0 & -1 \end{pmatrix}, \quad \sigma_2 = \begin{pmatrix} 0 & 1 \\ 1 & 0 \end{pmatrix}, \quad \sigma_3 = \begin{pmatrix} 0 & -i \\ i & 0 \end{pmatrix}, \tag{3.4.12}$$

where $\psi(z)$ is the angle by which the birefringence axes rotate as light passes a small section of fiber between z and $z+dz$. It is easy to show that the matrix $\overline{M}$ can be written in terms of the spin matrices as $\overline{M} = \sigma_1\cos 2\psi + \sigma_2 \sin 2\psi$. Since ψ changes along the fiber in a random fashion, $\overline{M}$ is a random matrix.

For discussing the PMD effects as simply as possible, we neglect the effects of GVD and set $\beta_2 = 0$ in Eq. (3.4.11). The loss term can be removed by a simple transformation as long as losses are polarization-independent. We assume this to be the case in this section and set $\alpha = 0$. Since Eq. (3.4.11) is linear, it is easier to solve it in the Fourier domain. Each frequency component $|\tilde{A}(z,\omega)\rangle$ of the Jones vector is then found to satisfy

$$\frac{\partial|\tilde{A}\rangle}{\partial z} = \frac{i}{2}(\Delta\beta_0 + \Delta\beta_1\omega)\overline{M}|\tilde{A}\rangle. \tag{3.4.13}$$

PMD is a consequence of the frequency-dependent term in this equation.

It is useful to write the solution of Eq. (3.4.13) in the form [27]

$$|\tilde{A}(z,\omega)\rangle = c_\omega\overline{W}(z)|S(z,\omega)\rangle, \tag{3.4.14}$$

where c_ω is a constant introduced to normalize $|S\rangle$ such that $\langle S|S\rangle = 1$. The random unitary matrix $\overline{W}(z)$ governs changes in the SOP of the field and is found by solving

$$\frac{\partial \overline{W}}{\partial z} = \frac{i}{2}(\Delta\beta_0)\overline{M}\,\overline{W}. \tag{3.4.15}$$

It is easy to show from Eqs. (3.4.13) through (3.4.15) that $|S(z,\omega)\rangle$ evolves as

$$\frac{\partial |S\rangle}{\partial z} = \frac{i}{2}(\Delta\beta_1)\omega\overline{W}^{-1}\overline{M}\,\overline{W}|S\rangle \equiv -i\omega\overline{B}|S\rangle, \tag{3.4.16}$$

where $\overline{B} = -(\Delta\beta_1/2)\overline{W}^{-1}\overline{M}\,\overline{W}$ is a random matrix governing birefringence fluctuations. This stochastic differential equation governs the PMD effects in the simplest form.

The origin of PMD lies in the frequency dependence of the Jones vector $|S(z,\omega)\rangle$ associated with the field component at frequency ω. This dependence can be made more explicit by studying how $|S(z,\omega)\rangle$ changes with ω at a fixed distance z. We can integrate Eq. (3.4.16) formally and write its solution as $|S\rangle = \overline{U}|S_0\rangle$, where $|S_0\rangle$ is the initial Jones vector at $z = 0$ and the transfer matrix $\overline{U}$ depends on both z and ω. If we take the frequency derivative of this equation, we obtain

$$\frac{\partial |S\rangle}{\partial \omega} = \frac{\partial \overline{U}}{\partial \omega}|S_0\rangle = \frac{\partial \overline{U}}{\partial \omega}\overline{U}^{-1}|S\rangle = -i\overline{\Omega}|S\rangle, \tag{3.4.17}$$

where $\overline{\Omega} \equiv i(\partial\overline{U}/\partial\omega)\overline{U}^{-1}$ is a matrix that shows how the SOP at a distance z evolves with frequency. We can call it the PMD matrix as it describes the PMD effects in fibers.

To connect $\overline{\Omega}$ with the concepts of PSPs and DGD introduced earlier, we first note that $\overline{U}$ is a unitary matrix, that is, $\overline{U}^{-1} = \overline{U}^{\dagger}$, where $\overline{U}^{\dagger}$ represents the adjoint matrix with the property that $U_{jk}^{\dagger} = U_{kj}^{*}$. The unitary matrix $\overline{U}$ can always be diagonalized as

$$\overline{U}|u_\pm\rangle = \exp(\pm i\theta/2)|u_\pm\rangle, \tag{3.4.18}$$

where the form of the two eigenvalues results from the property that the determinant of a unitary matrix must be 1. It is easy to show that $\overline{\Omega}$ is a Hermitian matrix ($\overline{\Omega}^{\dagger} = \overline{\Omega}$), and the eigenvalues of $\overline{\Omega}$ are real. If we denote the two eigenvectors of this matrix as $|p_+\rangle$ and $|p_-\rangle$, the eigenvalue equation can be written as

$$\overline{\Omega}|p_\pm\rangle = \pm\tfrac{1}{2}\Delta\tau|p_\pm\rangle, \tag{3.4.19}$$

where $\Delta\tau$ is the DGD of the fiber and $|p_\pm\rangle$ are the two PSPs associated with a fiber of length z. In the first-order description of PMD, one assumes that the direction of two PSPs does not change over the pulse bandwidth.

3.4.4 Stokes-Space Description

The PMD phenomenon is usually discussed in the Stokes space after introducing a Stokes vector that represents the SOP of a specific frequency component of the optical field on a sphere known as the Poincare sphere [31]–[33]. Although different notational

conventions exist in the literature, we follow the notation of [31]. The north pole of the Poincaré sphere corresponds to left-handed circular polarization in this convention.

The three-dimensional Stokes vector $\boldsymbol{S}$ is related to the two-dimensional Jones vector $|S\rangle$ through the Pauli spin matrices [26] as

$$\boldsymbol{S} = \langle S|\boldsymbol{\sigma}|S\rangle, \tag{3.4.20}$$

where $\boldsymbol{\sigma} = \sum_{j=1}^{3} \sigma_j \boldsymbol{e}_j$ is the spin vector in the Stokes space spanned by three unit vectors $\boldsymbol{e}_1$, $\boldsymbol{e}_2$, and $\boldsymbol{e}_3$. The spin vector plays an important role as it connects the Jones and Stokes formalisms. To make this connection, one makes use of the fact that an arbitrary 2×2 matrix can be written in the form

$$\overline{B} = \tfrac{1}{2}(b_0 \overline{I} + \boldsymbol{b} \cdot \boldsymbol{\sigma}), \tag{3.4.21}$$

where $\overline{I}$ is the identity matrix and $\boldsymbol{b}$ is a vector in the Stokes space. The four coefficients in this expansion can be obtained from the relations

$$b_0 = \mathrm{Tr}(\overline{B}), \qquad b_j = \mathrm{Tr}(\sigma_j \overline{B}), \tag{3.4.22}$$

where Tr stands for the trace of a matrix (the sum of diagonal components).

The first step is to convert Eq. (3.4.16) into the Stokes space using the definition in Eq. (3.4.21). If we use the well-known relations for the spin matrices [26]

$$\boldsymbol{\sigma}(\boldsymbol{a} \cdot \boldsymbol{\sigma}) = \boldsymbol{a}\overline{I} + i\boldsymbol{a} \times \boldsymbol{\sigma}, \qquad (\boldsymbol{\sigma} \cdot \boldsymbol{a})\boldsymbol{\sigma} = \boldsymbol{a}\overline{I} - i\boldsymbol{a} \times \boldsymbol{\sigma}, \tag{3.4.23}$$

where $\boldsymbol{a}$ is an arbitrary vector, the Stokes vector $\boldsymbol{S}$ is found to satisfy

$$\frac{\partial \boldsymbol{S}}{\partial z} = \omega \boldsymbol{b} \times \boldsymbol{S}, \tag{3.4.24}$$

where $\boldsymbol{b}$ is the birefringence vector whose components are related to the matrix $\overline{B}$ as indicated in Eq. (3.4.22). Equation (3.4.24) shows that, as the light of any frequency ω propagates inside the fiber, its Stokes vector rotates on the Poincaré sphere around the vector $\boldsymbol{b}$ at a rate that depends on ω as well as on the magnitude of local birefringence. For a fiber of constant birefringence, $\boldsymbol{S}$ traces a circle on the Poincaré sphere, as shown schematically in Figure 3.10(a). However, when $\boldsymbol{b}$ changes randomly along the fiber, $\boldsymbol{S}$ moves randomly over the surface of this sphere, as indicated in Figure 3.10(b). For a long fiber of length $L \gg l_c$, its motion can cover the entire surface of the Poincaré sphere. Figure 3.10 also shows changes in the SOP of light within the fiber. For fibers much longer than the correlation length, all memory of the input SOP is lost as, on average, half of the input power appears in the orthogonally polarized component.

Transformations of the Stokes vector are normally described by 4×4 Müller matrices [31]–[33]. In our case, light maintains its degree of polarization at its initial value of 1, and the length of Stokes vector does not change as it rotates on the Poincaré sphere because of birefringence fluctuations. Such rotations are governed by a transformation of the form $\boldsymbol{S}' = \overline{R}\boldsymbol{S}$, where $\overline{R}$ is a 3×3 rotation matrix. If the Jones vector changes as $|S'\rangle = \overline{U}|S\rangle$, the rotation matrix $\overline{R}$ is related to the Jones matrix $\overline{U}$ as

$$\overline{R}\boldsymbol{\sigma} = \overline{U}^{\dagger}\boldsymbol{\sigma}\overline{U}. \tag{3.4.25}$$

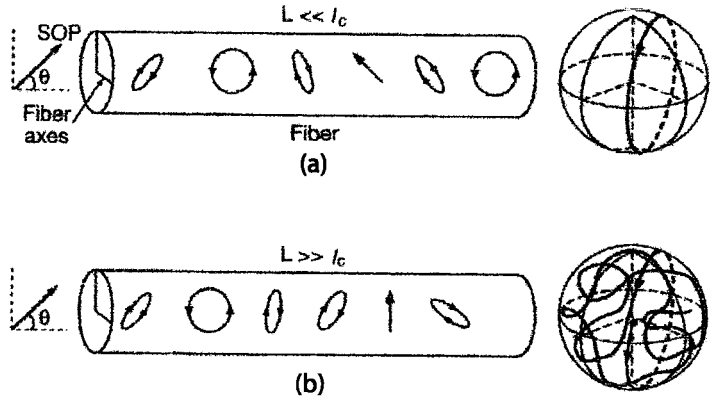

Figure 3.10: Evolution of the SOP within a fiber and the corresponding motion of the Stokes vector on the surface of the Poincaré sphere for (a) $L \ll l_c$ and (b) $L \gg l_c$. (After Ref. [25]; ©1997 Elsevier.)

The unitray matrix $\overline{U}$ can be written in terms of the Pauli matrices as

$$\overline{U} = \overline{I}\cos(\theta/2) - i\boldsymbol{u}\cdot\boldsymbol{\sigma}\sin(\theta/2) \equiv \exp[-i(\theta/2)\boldsymbol{u}\cdot\boldsymbol{\sigma}], \tag{3.4.26}$$

where $\boldsymbol{u}$ is the Stokes vector corresponding to the Jones vector $|u_-\rangle$ introduced in Eq. (3.4.18). It follows from Eq. (3.4.26) that $\overline{R}$ corresponds to a rotation of the Stokes vector on the Poincaré sphere by an angle θ around the the vector $\boldsymbol{u}$.

To describe the PMD effects, we convert Eq. (3.4.17) to the Stokes space. Noticing that this equation has the same form as Eq. (3.4.16), we can write it in the Stokes space in the form of Eq. (3.4.24). Expanding $\overline{\Omega}$ in terms of the spin matrices, noting that $\mathrm{Tr}(\overline{\Omega}) = 0$, and using $\overline{\Omega} = \frac{1}{2}\boldsymbol{\Omega}\cdot\boldsymbol{\sigma}$, we obtain

$$\frac{\partial \boldsymbol{S}}{\partial \omega} = \boldsymbol{\Omega}\times\boldsymbol{S}. \tag{3.4.27}$$

The vector $\boldsymbol{\Omega}$ is known as the PMD vector as it governs the dispersion of the output SOP of the field on the Poincaré sphere. Physically speaking, as optical frequency changes, $\boldsymbol{S}$ rotates on this sphere around the vector $\boldsymbol{\Omega}$. As defined, the PMD vector points toward the fast PSP and its magnitude $|\boldsymbol{\Omega}|$ is directly related to the DGD $\Delta\tau$ between the field components polarized along the two PSPs [25]. Figure 3.11(a) shows measured variations in the SOP at the output of a 147-km-long submarine fiber cable at a fixed input SOP as the wavelength of transmitted light is varied over a 1.5-nm range [38]. Figure 3.11(b) shows the output SOP for the same fiber over a narrow spectral range of 18 GHz for three different input SOPs (frequency changes by 2 GHz for successive dots). Even though SOP varies in a random fashion on the Poincaré sphere over a wide wavelength range, it rotates on a circle when the frequency spread is relatively small. The important point is that the axis of rotation is the same for all input SOPs. The two directions of this axis point toward the two PSPs, and the direction of the PMD vector coincides with the fast axis.

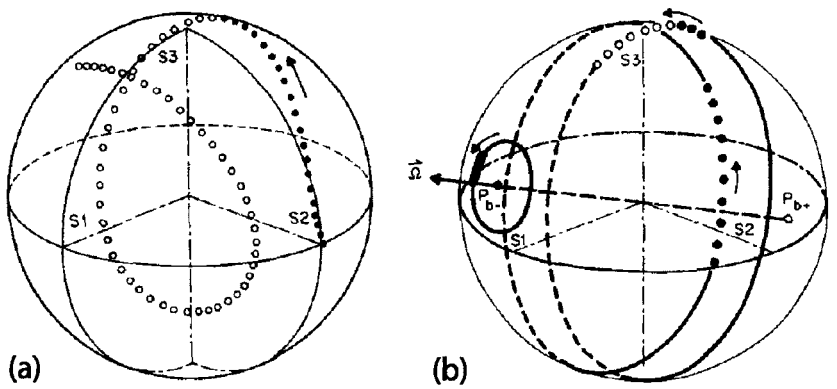

Figure 3.11: (a) Changes in the SOP of light at the output of a 147-km-long fiber at a fixed input SOP as the wavelength is varied over 1.5 nm. (b) SOP changes for the same fiber over a 18-GHz bandwidth for three different input SOPs. The frequency of input light is changed by 2 GHz for successive data points. (After Ref. [38]; ©1988 IEEE.)

To study the PMD effects, we need to know how the PMD vector changes along the fiber as its birefringence fluctuates, that is, we need an equation for the derivative of $\boldsymbol{\Omega}$ with respect to z. Such an equation can be obtained by differentiating Eq. (3.4.24) with respect to ω and Eq. (3.4.27) with respect to z and eliminating the mixed second derivative of $\boldsymbol{S}$. Using the vector identity $\boldsymbol{a}\times(\boldsymbol{b}\times\boldsymbol{c})=\boldsymbol{b}(\boldsymbol{a}\cdot\boldsymbol{c})-\boldsymbol{c}(\boldsymbol{a}\cdot\boldsymbol{b})$, we obtain

$$\frac{\partial\boldsymbol{\Omega}}{\partial z}\times\boldsymbol{S}=\boldsymbol{b}\times\boldsymbol{S}+\omega(\boldsymbol{b}\times\boldsymbol{\Omega})\times\boldsymbol{S}. \tag{3.4.28}$$

Since the preceding equation is valid for any $\boldsymbol{S}$, the PMD vector satisfies

$$\frac{\partial\boldsymbol{\Omega}}{\partial z}=\boldsymbol{b}+\omega\boldsymbol{b}\times\boldsymbol{\Omega}. \tag{3.4.29}$$

This equation contains information about birefringence fluctuations through the vector $\boldsymbol{b}$, whose three elements are random variables as they are related to the matrix elements of the random matrix $\overline{B}$ through Eq. (3.4.21). Notice that $\boldsymbol{b}$ enters Eq. (3.4.29) not only as an additive term but also as a multiplicative term, both of which induce fluctuations in the three components of the vector $\boldsymbol{\Omega}=\sum_{j=1}^{3}\Omega_j\boldsymbol{e}_j$. The DGD is related to these components as

$$\Delta\tau=|\boldsymbol{\Omega}|=(\Omega_1^2+\Omega_2^2+\Omega_3^2)^{1/2}, \tag{3.4.30}$$

and is itself a random variable. Its statistical properties are related to those of the birefringence vector $\boldsymbol{b}$ and are the subject of the following subsection.

3.4.5 Statistics of PMD

To understand how Eq. (3.4.29) affects pulse propagation in optical fibers, we first need to find the statistical properties of the PMD vector after adopting a suitable model for

birefringence fluctuations along a fiber link. In general, we should include the effects of a finite correlation length l_c associated with such fluctuations as l_c can vary over a wide range from 1 m to 1 km depending on whether the fiber is spooled or cabled [25]. In a simple but reasonably accurate model, $\boldsymbol{b}$ is treated as a three-dimensional, stationary, stochastic process whose first two moments are

$$\langle b_j(z)\rangle = 0, \qquad \langle b_j(z)b_k(z')\rangle = \tfrac{1}{3}(\Delta\beta_1)^2\delta_{jk}\exp(-|z-z'|/l_c), \tag{3.4.31}$$

where j and k take on values 1, 2, or 3 and the angle brackets denote averaging over birefringence fluctuations.

The general solution of the stochastic differential equation (3.4.29) is complicated because of the last term. However, since this term represents a rotation of $\boldsymbol{\Omega}$ in the Stokes space that does not affect the magnitude of the PMD vector, it does not influence the statistics of DGD [see Eq. (3.4.30)]. For this reason, we ignore the last term in Eq. (3.4.29) while considering the DGD statistics. The integration of Eq. (3.4.29) is then straightforward and leads to

$$\Omega_j(z) = \int_0^z b_j(z')\,dz' \approx \sum_{n=1}^{N} b_j(z_n)\Delta z \quad (j=1,2,3), \tag{3.4.32}$$

where the integral is approximated by a sum by dividing the fiber into N sections of length Δz.

Assuming that birefringence fluctuations in each section are independent, Ω_j represents the sum of a large number of independent random variables with the same statistical distribution. It follows from the central limit theorem that all three components of the PMD vector $\boldsymbol{\Omega}$ satisfy a Gaussian distribution of the form

$$p(\Omega_j) = \left[2\pi\langle\Omega_j^2\rangle\right]^{-1/2}\exp\left[-\Omega_j^2/(2\langle\Omega_j^2\rangle)\right]. \tag{3.4.33}$$

The variance $\langle\Omega_j^2\rangle$ can be found from Eqs. (3.4.32) as

$$\langle\Omega_j(z)\Omega_k(z)\rangle = \int_0^z dz' \int_0^z \langle b_j(z')b_k(z'')\rangle\,dz''. \tag{3.4.34}$$

If we use Eq. (3.4.31) and carry out the indicated integrals, we obtain

$$\langle\Omega_j(z)\Omega_k(z)\rangle = \delta_{jk}\tfrac{2}{3}(\Delta\beta_1)^2 l_c^2[\exp(-z/l_c) + z/l_c - 1]. \tag{3.4.35}$$

The probability density function $p(\Delta\tau)$ of the DGD can now be found using the relation in Eq. (3.4.30). In fact, the problem is identical to that solved by Maxwell in the nineteenth century for finding the distribution of atomic velocities in a gas at thermal equilibrium and leads to a form of $p(\Delta\tau)$ known as the Maxwellian distribution. It can be obtained by converting the joint probability density, $p(\Omega_1,\Omega_2,\Omega_3) \equiv p(\Omega_1)p(\Omega_2)p(\Omega_3)$, from Cartesian to spherical coordinates denoted by $\Delta\tau$, θ, and ϕ. Integrating over the two angles, we obtain

$$p(\Delta\tau) = \int_0^{\pi}\int_0^{2\pi} p(\Omega_1)p(\Omega_2)p(\Omega_3)(\Delta\tau)^2\sin\theta\,d\theta\,d\phi. \tag{3.4.36}$$

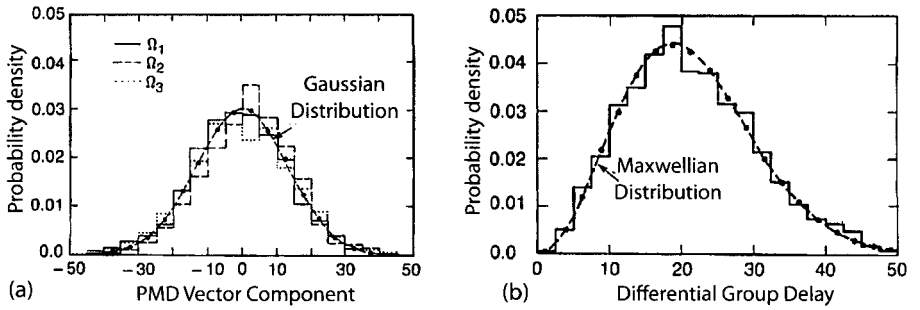

Figure 3.12: Measured histograms for individual components of the PMD vector (a) and for its magnitude $\Delta\tau$ (b) obtained using 10 km of spooled fiber. In both cases, the dashed curves show the theoretical distribution and dots show the results of numerical simulations. (After Ref. [39]; ©1991 OSA.)

Substituting $p(\Omega_j)$ from Eq. (3.4.33) and noting that the integrand does not depend on the angles, integration over the two angles produces a factor of 4π, and we obtain the Maxwellian distribution

$$p(\Delta\tau) = 3\sqrt{\frac{6}{\pi}}\frac{(\Delta\tau)^2}{\Delta\tau_{\mathrm{RMS}}^3}\exp\left[-\frac{3(\Delta\tau)^2}{2\Delta\tau_{\mathrm{RMS}}^2}\right], \tag{3.4.37}$$

where $\Delta\tau_{\mathrm{RMS}}$ is found from Eqs. (3.4.30) and (3.4.35) and is identical to that given in Eq. (3.4.4). At distances such that $z \gg l_c$, it can be approximated as indicated in Eq. (3.4.5) and increases with distance z as $\sqrt{z}$.

The mean and variance of DGD can be calculated from Eq. (3.4.37) in a closed form and are found to be

$$\langle\Delta\tau\rangle = \sqrt{\frac{8}{3\pi}}\Delta\tau_{\mathrm{RMS}}, \qquad \sigma_{\Delta\tau} = \sqrt{1-\frac{8}{3\pi}}\Delta\tau_{\mathrm{RMS}}. \tag{3.4.38}$$

As a numerical example, consider a 1,000-km long fiber link with $D_p = 0.1$ ps/$\sqrt{\text{km}}$, resulting in $\Delta\tau_{\mathrm{RMS}} = 3.16$ ps. The average value and standard deviation of DGD for such a fiber link are found to be 2.91 and 1.23 ps, respectively.

The statistical distributions found in Eqs. (3.4.33) and (3.4.37) have been observed in several experiments performed using a variety of fibers. Figure 3.12 shows (a) the histograms for the individual components of the PMD vector and (b) the histogram of the DGD, obtained using a spooled fiber of 11.6-km length [39]. In this experiment, the Stokes parameters were measured at the output end of the fiber over a 45-nm wavelength range, and they were used to deduce the wavelength dependence of the PMD vector. The solid dots show the results of numerical simulations, and dashed curves are the distributions expected from theory. Clearly, individual components of the PMD vector follow a Gaussian distribution, while the DGD $\Delta\tau$ follows the Maxwellian distribution. The agreement among theory, experiment, and simulations seen in Figure 3.12 verifies that the ensemble average at the fixed wavelength indicated in Eq. (3.4.38) can be carried out experimentally by averaging the same variable over a wide wavelength range for a single fiber.

3.4.6 PMD-Induced Pulse Broadening

Although statistical properties of DGD play an important role in understanding the PMD phenomenon, what matters from a practical perspective is the PMD-induced pulse broadening [40]–[45]. We thus need to extend the theory of Section 3.3.2 such that it include the PMD effects. This can be accomplished by replacing the scalar field amplitude $A(z,t)$ in Eq. (3.3.14) with the Jones vector $|A(z,t)\rangle$. As a result, Eq. (3.3.15) is replaced with

$$\langle t\rangle = \frac{-i}{N}\int_{-\infty}^{\infty}\langle\tilde{A}(z,\omega)|\tilde{A}_{\omega}(z,\omega)\rangle\, d\omega, \tag{3.4.39}$$

$$\langle t^2\rangle = \frac{1}{N}\int_{-\infty}^{\infty}\langle\tilde{A}_{\omega}(z,\omega)|\tilde{A}_{\omega}(z,\omega)\rangle\, d\omega, \tag{3.4.40}$$

where $N \equiv \int_{-\infty}^{\infty}\langle\tilde{A}|\tilde{A}\rangle\, d\omega$ is a normalization factor and the subscript ω stands for the frequency derivative.

Following the method outlined in Section 3.3.2, we can obtain the RMS value of pulse width, as defined in Eq. (3.3.13). The final result can be written in the form of Eq. (3.3.8), provided we add a new term σ_{PMD}^2 to it. This term represents the additional broadening induced by PMD and is given by [45]

$$\sigma_{\text{PMD}}^2 = \tfrac{1}{4}[\langle\boldsymbol{\Omega}_0\cdot\boldsymbol{\Omega}_0\rangle_s - \langle\boldsymbol{\Omega}_0\cdot\boldsymbol{S}_0\rangle_s^2] - [\langle(\tau+\theta_{\omega})(\boldsymbol{\Omega}_0\cdot\boldsymbol{S}_0)\rangle_s - \langle(\tau+\theta_{\omega})\rangle_s\langle\boldsymbol{\Omega}_0\cdot\boldsymbol{S}_0\rangle_s], \tag{3.4.41}$$

where $\boldsymbol{S}_0$ is the Stokes vector of the input field and $\boldsymbol{\Omega}_0 = \overline{R}^{-1}\boldsymbol{\Omega}$ is related to the PMD vector through the rotation matrix $\overline{R}$ introduced in Eq. (3.4.25); it is sometimes referred to as the input PMD vector [26]. We have also used the subscript s to emphasize that the average in Eq. (3.4.41) is over the input pulse spectrum, that is,

$$\langle f(\omega)\rangle_s = \frac{1}{N}\int_{-\infty}^{\infty} f(\omega)\langle\tilde{A}(0,\omega)|\tilde{A}(0,\omega)\rangle\, d\omega. \tag{3.4.42}$$

The broadening induced by PMD is not constant but fluctuates in response to birefringence fluctuations. We can average Eq. (3.4.41) over such fluctuations to obtain an average value for PMD-induced broadening. Since $\langle\boldsymbol{\Omega}_0\rangle = 0$, the average value is found to be [41]

$$\langle\sigma_{\text{PMD}}^2\rangle_b = \tfrac{1}{4}[\langle\langle\boldsymbol{\Omega}_0\cdot\boldsymbol{\Omega}_0\rangle_s\rangle_b - \langle\langle\boldsymbol{\Omega}_0\cdot\boldsymbol{S}_0\rangle_s^2\rangle_b], \tag{3.4.43}$$

where the subscript b denotes averaging over birefringence fluctuations. The double average in the first term is relatively simple to perform. The second term requires knowledge of the correlation between the PMD and Stokes vectors [45]. For an unchirped Gaussian pulse, the final result is found to be [41]

$$\langle\sigma_{\text{PMD}}^2\rangle_b = \tfrac{1}{4}[\Delta\tau_{\text{RMS}}^2 - T_0^2[(1+2\Delta\tau_{\text{RMS}}^2/3T_0^2)^{1/2} - 1]. \tag{3.4.44}$$

It is easy to see from this equation that additional broadening induced by PMD is quite small *on average* if pulse width T_0 is much larger than the RMS value of DGD. Even when $\Delta\tau_{\text{RMS}} = T_0$, the predicted broadening is only about 9%.

One may ask why PMD should be of concern if it produces an additional broadening that, on average, is below 10% in most cases of practical interest. The answer is provided by the fact that even if broadening is small on average, it may occasionally become quite large depending on the nature of PMD fluctuations. A lightwave system should operate reliably over long periods of time. Since the system would fail to perform reliably for short periods of time during which PMD fluctuations are large enough to broaden optical pulses beyond their allocated time slot, one must design the system to ensure that the probability of such an event is relatively small. This probability is referred to as the *outage probability* and it should be below 10^{-5} if one wants to ensure that system is inoperable for at most 5 min/year. It should be below 10^{-7} if the design criterion is more stringent and requires that PMD should not cause outage for more than 3 s/year. In general, one must ensure that the average DGD $\langle \Delta\tau \rangle$ of the fiber link is a small fraction of the bit slot $T_b = 1/B$, or $B\langle \Delta\tau \rangle < f_{\rm PMD}$, where $f_{\rm PMD}$ depends not only on the tolerable outage probability but also on the modulation format of the optical bit stream. Typically, $B\langle \Delta\tau \rangle$ should be below 8% for NRZ signals to maintain an outage probability below 10^{-5}, but this value increases to nearly 12% for RZ signals [28].

Similar to the case of GVD compensation discussed in Section 3.3.5, the performance of long-haul lightwave systems operating at high bit rates can be improved by employing a PMD-compensation scheme [28]. Most such schemes split the signal into two orthogonally polarized parts and adjust the delay in the two branches before combing them back. The topic of PMD compensation is discussed in Section 7.7.3 of Chapter 7 devoted to dispersion management.

3.4.7 Higher-Order PMD Effects

Equation (3.4.29) is based on the assumption that the direction of the PMD vector $\mathbf{\Omega}$ does not change significantly over the pulse bandwidth. Although such a first-order PMD description may hold well for relatively wide pulses with a narrow bandwidth, there are situations in which one must consider the higher-order PMD effects. For example, at high bit rates of 40 Gb/s or more, pulses used as bits become so short that the PSPs cannot be assumed to remain constant over the entire bandwidth of the pulse. Similarly, if first-order PMD is compensated in a lightwave system by employing PMD compensators (see Section 7.7.3), the performance of such a system would be limited by the second-order PMD effects. For this reason, the second-order PMD has been studied extensively [46]–[55].

The higher-order PMD effects can be included by expanding the PMD vector in a Taylor series around the carrier frequency ω_0 of the pulse as

$$\mathbf{\Omega}(\omega) \approx \mathbf{\Omega}(\omega_0) + \mathbf{\Omega}_\omega(\omega_0)(\omega - \omega_0) + \cdots, \tag{3.4.45}$$

where $\mathbf{\Omega}_\omega$ is the frequency derivative $d\mathbf{\Omega}/d\omega$ evaluated at $\omega = \omega_0$. This derivative governs the second-order PMD effects. Using $\mathbf{\Omega} = \Delta\tau\hat{\boldsymbol{p}}$, where $\hat{\boldsymbol{p}}$ represents a unit vector in the direction of the fast PSP, it can be written as a sum of two terms

$$\mathbf{\Omega}_\omega = \Delta\tau_\omega \hat{\boldsymbol{p}} + \Delta\tau \hat{\boldsymbol{p}}_\omega, \tag{3.4.46}$$

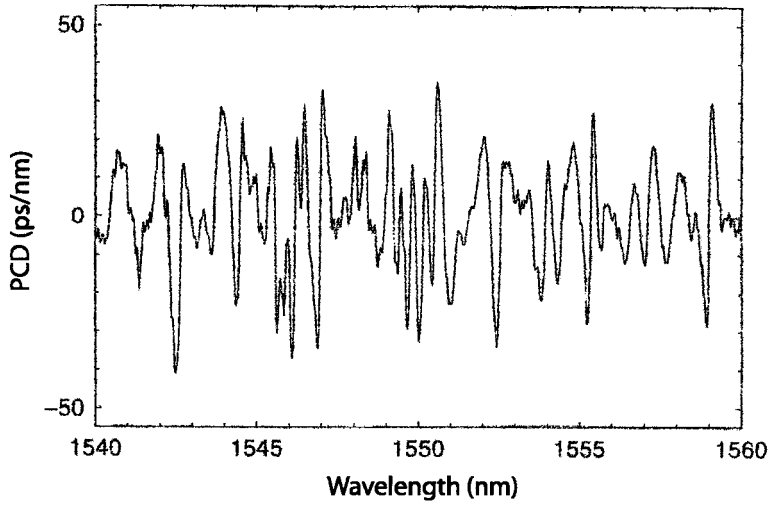

Figure 3.13: Polarization-dependent chromatic dispersion as a function of wavelength for a fiber with 14.7-ps mean DGD. (After Ref. [28]; ©2002 Elsevier.)

where the subscript ω denotes a frequency derivative. The first term is in the direction of the PMD vector, while the second term is orthogonal to it [28]. Physically, the first term describes polarization-dependent chromatic dispersion (PCD), while the second term leads to depolarization of the signal during its transmission through the fiber.

Consider first frequency dependence of the derivative $\Delta\tau_\omega \equiv d(\Delta\tau)/d\omega$. Recalling that the input signal is delayed by $\pm(\Delta\tau)/2$ when it is polarized along the two PSPs, the effective dispersion accumulated along these two directions in a fiber of length L becomes

$$\beta_2^{\pm} L = \beta_2 L \pm \tfrac{1}{2}\Delta\tau_\omega \quad \text{or} \quad D_{\pm} L = DL \pm \tfrac{1}{2}\Delta\tau_\lambda, \tag{3.4.47}$$

where $\Delta\tau_\lambda \equiv d(\Delta\tau)/d\lambda = -(2\pi c/\lambda^2)\Delta\tau_\omega$. The random nature of the second term in the preceding equation indicates that the GVD experienced by different spectral components of a pulse fluctuates around an average value. The random part $\frac{1}{2}\Delta\tau_\lambda$ is known as PCD. Figure 3.13 shows the magnitude of the PCD as a function of wavelength obtained by differentiating numerically the DGD data in Figure 3.9.

Physically, the presence of PCD implies that dispersion-induced broadening experienced by a pulse in a fiber depends on the SOP of the input pulse. In particular, the GVD takes its maximum and minimum values along the two PSPs, as indicated in Eq. (3.4.47). If the average value DL is relatively large compared with the magnitude of PCD, this is a relatively minor effect. However, as seen in Figure 3.13, PCD can be quite large when the mean DGD of the fiber exceeds 10 ps. As a result, the net fiber dispersion may take quite different values along the two PSPs, especially in dispersion-managed fiber links for which the average dispersion is kept close to zero. The resulting values D_+ and D_- of the dispersion parameter in Eq. (3.4.47) can even have opposite signs in that case. As discussed in Section 3.3.1, such a sign change for chirped input pulses indicates that pulses may compress along one of the PSPs while

experiencing broadening along the other. Such a compression of input pulses, induced by the second-order PMD effects, was first observed in a 1988 experiment [56].

Now consider the second term $\Delta\tau\hat{\boldsymbol{p}}_\omega$ in Eq. (3.4.46). It corresponds a frequency-dependent rotation of the PSPs on the Poicaré sphere by an angle $\phi(\omega)$. The rotation rate $d\phi/d\nu = 2\pi|\hat{\boldsymbol{p}}_\omega|$, where we used $\omega = 2\pi\nu$, is a measure of PSP depolarization induced by second-order PMD. This quantity is plotted in Figure 3.14 for the same fiber whose PCD is shown in Figure 3.13. Depolarization of PSPs produces considerable pulse distortion for short pulses.

Mathematically, both PCD and PSP depolarization are governed by a single random vector $\boldsymbol{\Omega}_\omega \equiv d\boldsymbol{\Omega}/d\omega$ in the Stokes space. We can use Eq. (3.4.29) to find how $\boldsymbol{\Omega}_\omega$ evolves with z along the fiber length. Differentiating this equation with respect to ω, we obtain [48]

$$\frac{\partial\boldsymbol{\Omega}_\omega}{\partial z} = \boldsymbol{b}\times\boldsymbol{\Omega} + \omega\boldsymbol{b}\times\boldsymbol{\Omega}_\omega. \tag{3.4.48}$$

This equation governs all effects produced by second-order PMD. Its statistical properties have been studied in the limit in which fiber length is much longer than the correlation length [48]. In this limit, the correlation function of $\boldsymbol{b}$ in Eq. (3.4.31) can be approximated by a delta function, and each component of $\boldsymbol{b}$ can be treated as a Markovian process with the Gaussian statistics. It turns out that the magnitude of PCD in Eq. (3.4.46), $\Delta\tau_\omega \equiv \boldsymbol{\Omega}_\omega\cdot\hat{\boldsymbol{p}}$, then has the following probability density function [50]:

$$p(\Delta\tau_\omega) = \frac{\pi}{4\mu^2}\operatorname{sech}^2\left(\frac{\pi\Delta\tau_\omega}{2\mu^2}\right), \tag{3.4.49}$$

where μ is related to the RMS and average values of DGD of the fiber as

$$\mu^2 = \frac{1}{3}\Delta\tau_{\mathrm{RMS}}^2 = \frac{\pi}{8}\langle\Delta\tau\rangle^2. \tag{3.4.50}$$

Equation (3.4.49) can be used to find any moment of the random variable $\Delta\tau_\omega$. It is easy to deduce that all odd-order moments vanish. The lowest even moment related to the variance is found to be

$$\langle(\Delta\tau_\omega)^2\rangle = \tfrac{1}{3}\mu^4 = \tfrac{1}{27}\Delta\tau_{\mathrm{RMS}}^4. \tag{3.4.51}$$

It follows from Eq. (3.4.38) that the RMS value of $\Delta\tau_\omega$ scales linearly with the fiber length L and quadratically with the PMD parameter D_p.

3.5 Polarization-Dependent Losses

The discussion of PMD in the preceding section is based on the assumption that losses of the fiber link do not depend on the SOP of the signal propagating through it. In practice, this is rarely the case, and all fiber links exhibit some polarization-dependent loss (PDL). Even though silica fibers themselves have relatively little PDL, the signal passes through a variety of optical components such as isolators, modulators, amplifiers, filters, and couplers, most of which exhibit loss (or gain in the case of optical amplifiers) whose magnitude depends on the SOP of the signal. Even though the amount of PDL

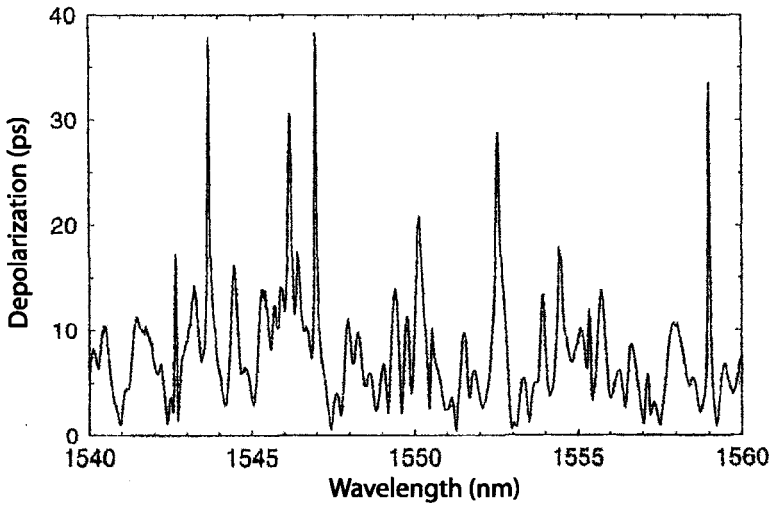

Figure 3.14: PSP depolarization as a function of wavelength for the same fiber that was used for Figure 3.13. (After Ref. [28]; ©2002 Elsevier.)

is relatively small for each component (typically ~0.1 dB), the cumulative effect of all components can produce an output signal whose power may fluctuate by a factor of 10 or more depending on its input SOP. Moreover, the combination of PDL and PMD leads not only to large random variations in the signal power but also to signal distortion that invariably affects the performance of all long-haul lightwave systems. For this reason, considerable attention has been paid to studying the PDL effects [57]–[71].

3.5.1 PDL Vector and Its Statistics

Since losses of a long, periodically amplified, fiber link depend on the SOP of the input signal, the PDL of the link is defined in terms of the maximum and minimum output powers, $P_{\max}$ and $P_{\min}$, obtained for two specific input SOPs. Mathematically, the PDL is defined as a dimensionless quantity

$$\Gamma = \frac{P_{\max} - P_{\min}}{P_{\max} + P_{\min}}, \tag{3.5.1}$$

where $0 \leq \Gamma \leq 1$. It is also common to express PDL in decibels units as

$$\rho = 10 \log \left(\frac{P_{\max}}{P_{\min}} \right) = 10 \log \left(\frac{1+\Gamma}{1-\Gamma} \right). \tag{3.5.2}$$

Both Γ and ρ are random variables for a fiber link for two reasons, First, the axes along which the loss of an optical component changes from maximum to minimum are randomly oriented for different components. Second, the SOP of the signal inside the fiber link changes in a random fashion before its arrival at each optical component because of birefringence fluctuations.

One can extend the vectorial analysis of Section 3.4.3 to include the PDL effects by allowing the quantity $\Delta\beta$ in Eq. (3.4.7) to become complex and replace it with $\Delta\beta + i\Delta\alpha$, where $\Delta\alpha(z)$ is the differential loss (or gain in the case of an optical amplifier) at a distance z at the carrier frequency ω_0. It does not change much over the pulse bandwidth and can be treated as a constant when $\Delta\beta(\omega)$ is expanded in a Taylor series appearing in Eq. (3.4.8). Following the analysis of Section 3.4.3 with this change, the Jones vector $|S\rangle$ satisfies Eq. (3.4.16) with an additional term on the right side, that is,

$$\frac{\partial|S\rangle}{\partial z} = -i(\omega\overline{B} + i\overline{\alpha})|S\rangle, \tag{3.5.3}$$

where $\overline{\alpha} = -(\Delta\alpha/2)\overline{W}^{-1}\overline{M}\,\overline{W}$ is a random Jones matrix accounting for the PDL effects.

Equation (3.5.3) shows that the output Jones vector is related as the input Jones vector $|S_0\rangle$ as $|S\rangle = \overline{U}|S_0\rangle$, but the matrix $\overline{U}$ does not remain unitary because of PDL. We can use this relation to calculate the output power as

$$P_{\text{out}} = \langle S|S\rangle = \langle S_0|\overline{U}^{\dagger}\overline{U}|S_0\rangle. \tag{3.5.4}$$

The most and least attenuated input SOPs correspond to the eigenstates of the matrix $\overline{U}^{\dagger}\overline{U}$. The corresponding output SOPs are the eigenstates of the matrix $\overline{U}\,\overline{U}^{\dagger}$ [57].

Similar to the PMD vector of Section 3.4.4, one can introduce a PDL vector by writing this matrix in the form of Eq. (3.4.21) as

$$\overline{U}\,\overline{U}^{\dagger} = a_0\bar{I} + \boldsymbol{a}\cdot\boldsymbol{\sigma}, \tag{3.5.5}$$

where the vector $\boldsymbol{a}$ points in the Stokes space in the direction of output SOP with the least attenuation. The PDL vector is then defined as $\boldsymbol{\Gamma} = \boldsymbol{a}/a_0$ and has the magnitude as indicated in Eq. (3.5.1). This PDL vector is found to satisfy the following dynamic equation [60]:

$$\frac{\partial\boldsymbol{\Gamma}}{\partial z} = \omega(\boldsymbol{b}\times\boldsymbol{\Gamma}) + \boldsymbol{\alpha} - (\boldsymbol{\alpha}\cdot\boldsymbol{\Gamma})\boldsymbol{\Gamma}, \tag{3.5.6}$$

where the vector $\boldsymbol{\alpha}$ governs differential losses and is related to the matrix $\overline{\alpha}$ through $\overline{\alpha} = \frac{1}{2}(\alpha_0\bar{I} + \boldsymbol{\alpha}\cdot\boldsymbol{\sigma})$. As seen in Eq. (3.4.22), the three components of this vector can be obtained using $\alpha_j = \text{Tr}(\sigma_j\overline{\alpha})$.

Equation (3.5.6) shows that, in general, the PMD vector is affected by both random vectors $\boldsymbol{\alpha}$ and $\boldsymbol{b}$, where $\boldsymbol{b}$ takes into account birefringence fluctuations along the fiber link. Thus, PMD and PDL are interconnected and an optical pulse is affected by the combination of the two. However, the magnitude of the PDL vector is not affected by birefringence fluctuations. This can be seen physically by noting that the term containing $\boldsymbol{b}$ in Eq. (3.5.6) represents a rotation and does not affect the magnitude of the vector $\boldsymbol{\Gamma}$. Mathematically, we note that $\Gamma^2 = \boldsymbol{\Gamma}\cdot\boldsymbol{\Gamma}$ satisfies

$$\frac{\partial\Gamma^2}{\partial z} = 2(\boldsymbol{\alpha}\cdot\boldsymbol{\Gamma})(1-\Gamma^2), \tag{3.5.7}$$

and is thus affected only by the random vector $\boldsymbol{\alpha}$.

Equation (3.5.7) has been used to obtain an analytic expression for the probability density function $P(\rho)$ of ρ [68], a scalar random variable related to Γ as indicated in Eq. (3.5.2), after assuming that each component of $\boldsymbol{\alpha}$ is a Markovian random variable with Gaussian statistics such that

$$\langle \alpha_j(z) \rangle = 0, \qquad \langle \alpha_j(z)\alpha_k(z') \rangle = \tfrac{1}{3} D_\alpha^2 \delta_{jk} \delta(z - z'), \tag{3.5.8}$$

where j and k take on values of 1, 2, or 3 and the parameter D_α measures the strength of PDL fluctuations along the fiber link. The general expression for $P(\rho)$ can be approximated by a Maxwellian distribution [65] when the total PDL is not too large ($\rho \ll 34$ dB). Under such conditions, $P(\rho)$ can be written in the form of Eq. (3.4.37) after replacing $\Delta\tau_{\text{RMS}}^2$ with $\langle \rho^2 \rangle$, where

$$\langle \rho^2 \rangle = (20/\ln 10) D_\alpha^2 z (1 + D_\alpha^2 z/9). \tag{3.5.9}$$

The parameter D_α is defined in a way similar to the PMD parameter D_p and is expressed in units of $\text{km}^{-1/2}$. The average and the variance of ρ are related to the RMS value ρ as indicated in Eq. (3.4.38).

3.5.2 PDL-Induced Pulse Distortion

As mentioned earlier, PDL also affects the pulse shape and its effects should be incorporated in the discussion of PMD-induced signal distortion. One can still introduce the PMD vector, but the presence of $\overline{\alpha}$ in Eq. (3.5.3) makes it a complex quantity. We denote the modified vector by $\boldsymbol{\Omega}_c$, where the subscript c indicates that its components are complex variables. Following the analysis of Section 3.4.5, Eq. (3.4.29) is replaced with [57]

$$\frac{\partial \boldsymbol{\Omega}_c}{\partial z} = \boldsymbol{b} + (\omega \boldsymbol{b} + i\boldsymbol{\alpha}) \times \boldsymbol{\Omega}_c, \tag{3.5.10}$$

where the presence of PDL vector $\boldsymbol{\alpha}$ governs how the PMD effects are affected by PDL. The new feature is that the matrix $\boldsymbol{\Omega}_c \cdot \boldsymbol{\sigma}$ does not remain Hermitian. As a result, its eigenvalues become complex and take the form $\pm\frac{1}{2}(\Delta\tau + i\eta_i)$, where the imaginary part η_i results from the PDL effects. Moreover, its eigenvectors are no longer orthogonal, that is, the two PSPs do not remain antiparallel in the Stokes space.

The Stokes vector $\boldsymbol{S}(z)$ representing the SOP of the field on the Poincaré sphere can still be defined as in Eq. (3.4.20), assuming that the Jones vector $|S\rangle$ has been normalized such that $\langle S|S\rangle = 1$. However, instead of Eq. (3.4.27) it satisfies the following equation [61]:

$$\frac{\partial \boldsymbol{S}}{\partial \omega} = \boldsymbol{\Omega} \times \boldsymbol{S} - (\boldsymbol{\Lambda} \times \boldsymbol{S}) \times \boldsymbol{S}, \tag{3.5.11}$$

where we have separated $\boldsymbol{\Omega}_c$ into its real and imaginary parts using $\boldsymbol{\Omega}_c = \boldsymbol{\Omega} + i\boldsymbol{\Lambda}$. The new vector $\boldsymbol{\Lambda}$ governs the impact of PDL on the PMD effects. From Eq. (3.5.10), the vectors $\boldsymbol{\Omega}$ and $\boldsymbol{\Lambda}$ are found to evolve as

$$\frac{\partial \boldsymbol{\Omega}}{\partial z} = \boldsymbol{b} + \omega \boldsymbol{b} \times \boldsymbol{\Omega} - \boldsymbol{\alpha} \times \boldsymbol{\Lambda}, \tag{3.5.12}$$

$$\frac{\partial \boldsymbol{\Lambda}}{\partial z} = \omega \boldsymbol{b} \times \boldsymbol{\Lambda} + \boldsymbol{\alpha} \times \boldsymbol{\Omega}, \tag{3.5.13}$$

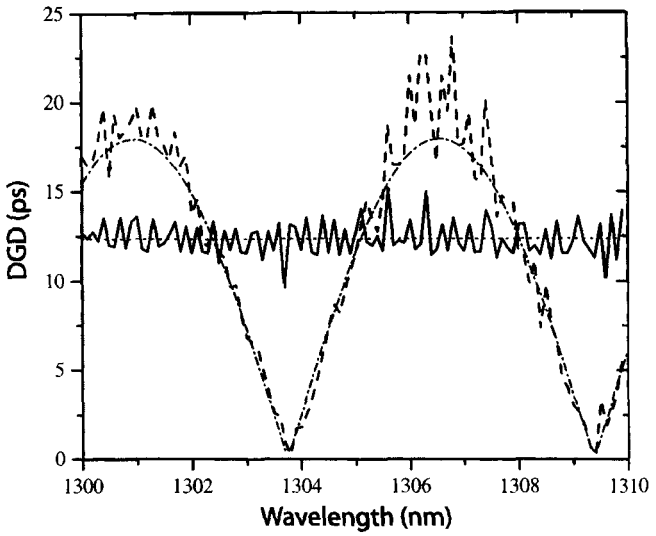

Figure 3.15: Measured DGD as a function of wavelength for a link containing a single fiber with large PDL sandwiched between two fibers with 5.65-ps DGD. The principal axes of the PDL fiber are either aligned with the other two fibers (solid curve) or rotated by 45° (dashed curve). The dotted lines show the theoretical prediction. (After Ref. [60]; ©2000 IEEE.)

These two equations can be solved analytically to find various moments of $\mathbf{\Omega}$ and $\mathbf{\Lambda}$ if one assumes that the vectors $\boldsymbol{\alpha}$ and $\boldsymbol{b}$ are parallel to each other [61]. An interesting result turns out to be $\langle \mathbf{\Omega} \cdot \mathbf{\Lambda} \rangle = 0$, that is, the two vectors are orthogonal to each other, on average. A consequence of this property is that $\langle \Omega_c^2 \rangle \equiv \langle \Omega^2 - \Gamma^2 \rangle$ is a real quantity. Moreover, it is given by Eq. (3.4.4), that is, the RMS value of Ω_c remains the same even in the presence of PDL.

From the standpoint of pulse distortion, one is interested in the RMS value of the DGD ($\Delta\tau \equiv \Omega$). It turns out that even though the RMS value of Ω_c increases only as $\sqrt{z}$ with distance, the RMS value of Ω itself can grow quadratically, or even exponentially, for sufficiently long fiber links [61]. Anomalously large values of DGD were observed in a 1997 experiment in which a single PDL fiber with 18 dB of differential loss and a DGD of 1 ps was sandwiched between two fibers exhibiting little PDL and a DGD of 5.65 ps [58]. A polarization controller was used to change the input SOP of light from a tunable laser. The DGD of the entire fiber link was measured using a polarimeter as input wavelength was varied in the wavelength range of 1,300 to 1,310 nm. Figure 3.15 shows the experimental results. The solid curve is obtained when the principal axes of all three fibers are perfectly aligned. Measured values are close to the DGD value of 12.3 ps that is expected by simply adding the individual DGDs of all three fibers. The dashed curve is obtained when the PDL fiber axis is rotated by 45°. It is evident that DGD in this case varies with wavelength widely and becomes as small as 1 ps or as large as 24 ps. Such large changes in DGD translate into compression or broadening of optical pulses. The important point from a system point of view is that the presence of PDL in a long fiber link can broaden optical pulses much more than the

value expected from the PMD alone, resulting in degradation of system performance. In practice, attempts are made to employ optical components with negligible values of PDL.

Problems

3.1 A single-mode fiber is measured to have $\lambda^2(d^2n/d\lambda^2) = 0.02$ at 0.8 μm. Calculate the dispersion parameters β_2 and D.

3.2 Show that a chirped Gaussian pulse is compressed initially inside a single-mode fiber when $\beta_2 C < 0$. Derive expressions for the minimum width and the fiber length at which the minimum occurs.

3.3 An optical communication system is operating with chirped Gaussian input pulses. Assume that $\beta_3 = 0$ and $V_\omega \ll 1$ in Eq. (3.3.36) and obtain a condition on the bit rate in terms of the parameters C, β_2, and L.

3.4 Starting from the definition $\sigma_p = [\langle t^2\rangle - \langle t\rangle^2]^{1/2}$, where the angle brackets denote average over the pulse shape, derive an expression for the RMS width σ_p for a pulse of arbitrary shape. (*Hint*: Calculate averages in the frequency domain.)

3.5 Prove that Eq. (3.3.17) leads to Eq. (3.3.11) for the broadening factor when it is applied to the case of a chirped Gaussian pulse.

3.6 Estimate the limiting bit rate for a 60-km single-mode fiber link at 1.3- and 1.55-μm wavelengths, assuming transform-limited, 50-ps (FWHM) input pulses. Assume that $\beta_2 = 0$ and -20 ps^2/km and $\beta_3 = 0.1$ ps^3/km and 0 at 1.3- and 1.55-μm wavelengths, respectively. Also assume that $V_\omega \ll 1$.

3.7 A 0.88-μm communication system transmits data over a 10-km single-mode fiber by using 10-ns (FWHM) pulses. Determine the maximum bit rate if the LED has a spectral FWHM of 30 nm. Use $D = -80$ ps/(km-nm).

3.8 Use Eq. (3.3.36) to prove that the bit rate of an optical communication system operating at the zero-dispersion wavelength is limited by $BL|S|\sigma_\lambda^2 < 1/\sqrt{8}$, where $S = dD/d\lambda$ and σ_λ is the RMS spectral width of the Gaussian source spectrum. Assume that $C = 0$ and $V_\omega \gg 1$ in the general expression of the output pulse width.

3.9 Repeat the preceding problem for the case of a single-mode semiconductor laser for which $V_\omega \ll 1$ and show that the bit rate is limited by $B(|\beta_3|L)^{1/3} < 0.324$. What is the limiting bit rate for $L = 100$ km if $\beta_3 = 0.1$ ps^3/km?

3.10 A 1.55-μm optical communication system operating at 5 Gb/s is using Gaussian pulses of width 100 ps (FWHM) chirped such that $C = -6$. What is the dispersion-limited maximum fiber length? How much will it change if the pulses were unchirped? Neglect laser linewidth and assume that $\beta_2 = -20$ ps^2/km.

3.11 Explain what is meant by PMD? What is the origin of PMD in telecommunication links and how does its presence affect a lightwave system? Utilize diagrams to support your arguments.

3.12 A 1-km-long polarization-maintaining single-mode fiber exhibits a birefringence of $\Delta n = 6 \times 10^{-4}$. Calculate the differential group delay for this fiber at 1.55 μm, assuming that the average mode index $\bar{n} = 1.45$ and $d\bar{n}/d\lambda = -0.01$ μm^{-1} at this wavelength.

3.13 What is meant by the principal states of polarization for a fiber in which birefringence fluctuates along its length? Discuss the basic idea and its implications for a lightwave system.

3.14 Using the model of birefringence fluctuations given in Eq. (3.4.31), prove that Eq. (3.4.29) leads to the Maxwellian distribution (3.4.37) for the differential group delay.

3.15 Use the Maxwellian distribution (3.4.37) to show that the mean and variance of differential group delay are given by the relations in Eq. (3.4.38).

References

[1] G. P. Agrawal, *Nonlinear Fiber Optics*, 3rd ed., Academic Press, San Diego, CA, 2001.

[2] P. Bayvel and R. Killey, in *Optical Fiber Telecommunications*, Vol. 4B, I. P. Kaminow and T. L. Koch, Eds., Academic Press, San Diego, CA, 2002, Chap. 13.

[3] G. P. Agrawal, *Applications of Nonlinear Fiber Optics*, 3rd ed., Academic Press, San Diego, CA, 2001.

[4] Y. W. Li, C. D. Hussey, and T. A. Birks, *J. Lightwave Technol.* **11**, 1812 (1993).

[5] J. Kani, M. Jinno, T. Sakamoto, S. Aisawa, M. Fukui, K. Hattori, and K. Oguchi, *J. Lightwave Technol.* **17**, 2249 (1999).

[6] Y. Mochida, N. Yamaguchi, and G. Ishikawa, *J. Lightwave Technol.* **20**, 2272 (2002).

[7] D. J. DiGiovanni, S. K. Das, L. L. Byler, W. White and R. K. Boneck, in *Optical Fiber Telecommunications*, Vol. 4A, I. P. Kaminow and T. L. Koch, Eds., Academic Press, San Diego, CA, 2002, Chap. 2.

[8] P. Audouin and J.-P. Hamaide, *IEEE Photon. Technol. Lett.* **7**, 1363 (1995).

[9] M. . Yadlowsky, E. M. Deliso, and V. L. Da Silva, *Proc. IEEE* **85**, 1765 (1997).

[10] J.-X. Cai; M. Nissov, C. R. Davidson, A. N. Pilipetskii, G. Mohs, H. Li, Y. Cai, E. A. Golovchenko, A. J. Lucero, D. G. Foursa, and N. S. Bergano, *J. Lightwave Technol.* **20**, 2247 (2002).

[11] E. Desuvire, *Erbium-Doped Fiber Amplifiers: Principles and Applications*, Wiley, New York, 1994.

[12] P. C. Becker, N. A. Olsson, and J. R. Simpson, *Erbium-Doped Fiber Amplifiers: Fundamentals and Technology*, Academic Press, San Diego, CA, 1999.

[13] E. Desuvire, D. Bayart, B. Desthieux, and S. Bigo, *Erbium-Doped Fiber Amplifiers: Device and System Development*, Wiley, New York, 2002.

[14] M. N. Islam, Ed., *Raman Amplifiers for Telecommunications: Physical Principles*, Springer, New York, 2003.

[15] C. Headley and G. P. Agrawal, Eds., *Raman Amplification in Fiber Optical Communication Systems*, Academic Press, San Diego, CA, 2004.

[16] J. Bromage, *J. Lightwave Technol.* **22**, 79 (2004).

[17] M. Born and E. Wolf, *Principles of Optics*, 7th ed., Cambridge University Press, New York, 1999, Section 8.6.

[18] A. Jeffrey and D. Zwillinger, Eds., *Table of Integrals, Series, and Products*, 6th ed., Academic Press, San Diego, CA, 2003.

[19] M. Miyagi and S. Nishida, *Appl. Opt.* **18**, 678 (1979); **18**, 2237 (1979).

[20] G. P. Agrawal and M. J. Potasek, *Opt. Lett.* **11**, 318 (1986).

[21] A. J. Antos and D. K. Smith, *J. Lightwave Technol.* **12**, 1739 (1994).

[22] M. Onishi, T. Kashiwada, Y. Ishiguro, Y. Koyano, M. Nishimura, and H. Kanamori, *Fiber Integ. Opt.* **16**, 277 (1997).

[23] J. Liu, Y. L. Lam, Y. C. Chan, Y. Zhou, and J. Yao, *Fiber Integ. Opt.* **18**, 63 (1999).

[24] L. Gruner-Nielsen, S. N. Knudsen, B. Edvold, T. Veng, D. Magnussen, C. C. Larsen, and H. Damsgaard, *Opt. Fiber Technol.* **6**, 164 (2000).

[25] C. D. Poole and J. Nagel, in *Optical Fiber Telecommunications III*, Vol. A, I. P. Kaminow and T. L. Koch, Eds., Academic Press, San Diego, CA, 1997, Chap. 6.

[26] J. P. Gordon and H. Kogelnik, *Proc. Natl. Acad. Sci. USA* **97**, 4541-4550 (2000).

[27] C. R. Menyuk, B. S. Marks, I. T. Lima, J. Zweck, Y. Sun, G. M. Carter, and D. Wang, in *Undersea Fiber Communication Systems*, J. Chesnoy, Ed., Academic Press, San Diego, CA, 2002, Chap. 7.

[28] H. Kogelnik, R. M. Jopson, and L. E. Nelson, in *Optical Fiber Telecommunications*, Vol. 4A, I. P. Kaminow and T. Li, Eds., Academic Press, San Diego, CA, 2002, Chap. 15.

[29] H. Kogelnik, L. E. Nelson, and J. P. Gordon, *J. Lightwave Technol.* **21**, 482 (2003).

[30] A. E. Willner, S. M. R. M. Nezam, L. Yan, Z. Pan, and M. C. Hauer, *J. Lightwave Technol.* **22**, 106 (2004).

[31] S. Huard, *Polarization of light*, Wiley, New York, 1997.

[32] C. Brosseau, *Fundamentals of polarized light*, Wiley, New York, 1998.

[33] D. H. Goldstein and E. Collett, *Polarized light*, Marcel Dekker, New York, 2003.

[34] F. Curti, B. Daino, G. de Marchis, and F. Matera, *J. Lightwave Technol.* **8**, 1162 (1990).

[35] N. Gisin, *Opt. Commun.* **86**, 371 (1991).

[36] G. J. Foschini and C. D. Poole, *J. Lightwave Technol.* **9**, 1439 (1996).

[37] P. K. A. Wai and C. R. Menyuk, *J. Lightwave Technol.* **14**, 148 (1996).

[38] C. D. Poole, N. S. Bergano, R. E. Wagner, and H. J. Schulte, *J. Lightwave Technol.* **6**, 1185 (1988).

[39] C. D. Poole, J. H. Winters, and J. A. Nagel, *Opt. Lett.* **16**, 372 (1991).

[40] M. Karlsson, *Opt. Lett.* **23**, 688 (1998).

[41] M. Karlsson and J. Brentel, *Opt. Lett.* **24**, 939 (1999).

[42] H. Sunnerud, M. Karlsson, and P. A. Andrekson, *IEEE Photon. Technol. Lett.* **12**, 50 (2000).

[43] S. J. Savory and F. P. Payne, *J. Lightwave Technol.* **19**, 350 (2001).

[44] J. Garnier, J. Fatome, and G. Le Meur, *J. Opt. Soc. Am. B* **19**, 1968 (2002).

[45] Q Lin and G. P. Agrawal, *J. Opt. Soc. Am. B* **20**, 192 (2003).

[46] F. Bruyère, *Opt. Fiber Technol.* **2**, 269 (1996).

[47] H. Bülow, *IEEE Photon. Technol. Lett.* **10**, 696 (1998).

[48] P. Ciprut, B. Gisin, N. Gisin, R. Passy, P. von der Weld, F. Prieto, and C. W. Zimmer, *J. Lightwave Technol.* **16**, 757 (1998).

[49] R. M. Jopson, L. E. Nelson, and H. Kogelnik, *IEEE Photon. Technol. Lett.* **11**, 1153 (1999).

[50] G. J. Foschini, R. M. Jopson, L. E. Nelson, and H. Kogelnik, *J. Lightwave Technol.* **17**, 1560 (1999).

[51] A. O. Dal Forno, A. Paradisi, R. Passy, P. von der Weid, *IEEE Photon. Technol. Lett.* **12**, 296 (2000).

[52] G. J. Foschini, L. E. Nelson, R. M. Jopson, and H. Kogelnik, *J. Lightwave Technol.* **19**, 1882 (2001).

[53] M. Wegmuller, S. Demma, C. Vinegoni, and N. Gisin, *IEEE Photon. Technol. Lett.* **14**, 630 (2002).

[54] A. Orlandini and L. Vincetti, *J. Lightwave Technol.* **21**, 1456 (2003).

[55] E. Forestieri, *J. Lightwave Technol.* **21**, 2942 (2003).

[56] C. D. Poole and C. R. Giles, *Opt. Lett.* **13**, 155 (1988).

[57] N. Gisin and B. Huttner, *Opt. Commun.* **142**, 119 (1997).

[58] B. Huttner and N. Gisin, *Opt. Lett.* **22**, 504 (1997).

[59] A. El Amari, N. Gisin, B. Perny, H. Zbinden, and C. W. Zimmer, *J. Lightwave Technol.* **16**, 332 (1998).

[60] B. Huttner, C. Geiser, and N. Gisin, *IEEE J. Sel. Topics Quantum Electron.* **6**, 317 (2000).

[61] Y. Li and A. Yariv, *J. Opt. Soc. Am. B* **17**, 1821 (2000).

[62] D. Wang and C. R. Menyuk, *J. Lightwave Technol.* **19**, 487 (2001).

[63] P. Lu, L. Chen, and X. Bao, *J. Lightwave Technol.* **19**, 856 (2001); *J. Lightwave Technol.* **20**, 1805 (2002).

[64] L.-S. Yan, Q. Yu, Y. Xie, and A. E. Willner, *IEEE Photon. Technol. Lett.* **14**, 224 (2002).

[65] A. Mecozzi and M. Shtaif, *IEEE Photon. Technol. Lett.* **14**, 313 (2002).

[66] Y. Fukuda, *J. Lightwave Technol.* **20**, 953 (2002).

[67] M. Yu, C. Kan, M. Lewis, and A. Sizmann, *IEEE Photon. Technol. Lett.* **14**, 1695 (2002).

[68] A. Galtarossa and L. Palmieri, *IEEE Photon. Technol. Lett.* **15**, 57 (2003).

[69] R. M. Craig, *J. Lightwave Technol.* **21**, 432 (2003).

[70] C. Xie and L. F. Mollenauer, *J. Lightwave Technol.* **21**, 1953 (2003).

[71] M. Shtaif and A. Mecozzi, *IEEE Photon. Technol. Lett.* **16**, 671 (2004).

Chapter 4

Nonlinear Impairments

The discussion in Chapter 3 intentionally ignored the nonlinear effects and applies to lightwave systems in which the signal power is kept small enough that the nonlinear effects, governed by the parameter γ in the NLS equation, remain negligible throughout the fiber link. This approximation can be justified for many short-haul systems (transmission distance <100 km), especially those employing light-emitting diodes as optical sources. However, the inclusion of nonlinear effects becomes essential for long-haul systems making use of a chain of cascaded optical amplifiers [1]–[6]. The reason is two-fold. First, noise added by the amplifier chain degrades the signal-to-noise ratio (SNR) to the extent that the signal cannot be recovered unless launched power levels are relatively high (typically >1 mW). Second, the nonlinear effects themselves accumulate from amplifier to amplifier and distort the optical bit stream more and more as link length increases. This chapter focuses on the impact of fiber nonlinearities in such long-haul systems. We begin with the discussion of the simplest nonlinearity—self-phase modulation—in Section 4.1 and then consider in Section 4.2 the closely related nonlinear phenomenon of cross-phase modulation. Section 4.3 deals with four-wave mixing, a nonlinear effect that becomes quite important for WDM systems. Stimulated Raman scattering is the focus of Section 4.4, whereas the phenomenon of stimulated Brillouin scattering is considered in Section 4.5. In Section 4.6 the variational and moment methods are employed for solving the NLS equation approximately. Section 4.7 focuses on the polarization effects related to residual fiber birefringence.

4.1 Self-Phase Modulation

Long-haul lightwave systems employ a chain of optical amplifiers along the fiber link for compensating fiber losses. As discussed in Section 3.2, in general one needs to solve Eq. (3.2.4) numerically to study how the nonlinear term in this equation affects the optical bit stream. To gain some physical insight and to simplify the following analysis, we neglect the noise term in this equation and eliminate the gain and loss terms with the transformation

$$A(z,t) = \sqrt{P_0 p(z)}\, U(z,t), \tag{4.1.1}$$

where P_0 is the peak power of input pulses and $U(z,t)$ governs the normalized (complex) amplitude of the optical bit stream. The function $p(z)$ takes into account changes in the average power of the signal along the fiber link and is defined such that $p(nL_A) = 1$, where L_A is the amplifier spacing and n is an integer representing the location of a specific amplifier (or a pump station in the case of distributed amplification).

With these simplifications, the use of Eq. (4.1.1) in Eq. (3.2.4) provides the following NLS equation for propagation of an optical signal along the fiber link:

$$\frac{\partial U}{\partial z} + \frac{i\beta_2}{2}\frac{\partial^2 U}{\partial t^2} = i\gamma P_0 p(z)|U|^2 U, \tag{4.1.2}$$

where $p(z)$ satisfies Eq. (3.2.6) and varies in a periodic manner. In the case of lumped amplification, $p(z)$ decreases exponentially as $e^{-\alpha z}$ between two amplifiers but increases to 1 at the location of each lumped amplifier. It is not easy to solve Eq. (4.1.2) analytically except in some simple cases. To gain some physical insight, we first consider the case in which dispersive effects are negligible and set $\beta_2 = 0$ in Eq. (4.1.2).

4.1.1 Nonlinear Phase Shift

In terms of the normalized amplitude $U(z,T)$, Eq. (4.1.2) in the limit $\beta_2 = 0$ reduces to

$$\frac{\partial U}{\partial z} = \frac{ip(z)}{L_{\rm NL}}|U|^2 U, \tag{4.1.3}$$

where the nonlinear length is defined as $L_{\rm NL} = (\gamma P_0)^{-1}$. Similar to the concept of the dispersion length introduced in Section 3.3, the nonlinear length provides a length scale over which the nonlinear effects become relevant for optical fibers. If we use $\gamma = 2\ {\rm W}^{-1}/{\rm km}$ as a typical value, the nonlinear length $L_{\rm NL}$ equals 100 km for an optical signal with 5-mW peak power and scales inversely with P_0.

Equation (4.1.3) can be solved by substituting $U = V\exp(i\phi_{\rm NL})$ and separating its real and imaginary parts. This procedure yields

$$\frac{\partial V}{\partial z} = 0, \qquad \frac{\partial \phi_{\rm NL}}{\partial z} = \frac{p(z)}{L_{\rm NL}}V^2. \tag{4.1.4}$$

As the amplitude V does not change along the fiber length L, the phase equation can be integrated analytically to obtain the general solution

$$U(L,t) = U(0,t)\exp[i\phi_{\rm NL}(L,t)], \tag{4.1.5}$$

where $U(0,t)$ is the field amplitude at $z = 0$ and

$$\phi_{\rm NL}(L,t) = |U(0,t)|^2(L_{\rm eff}/L_{\rm NL}). \tag{4.1.6}$$

The effective length $L_{\rm eff}$ is defined as

$$L_{\rm eff} = \int_0^L p(z)\,dz = N_A\int_0^{L_A} p(z)\,dz, \tag{4.1.7}$$

where we assumed that the fiber link consists of N_A sections, each of length L_A.

Equation (4.1.5) shows that the nonlinear term in the NLS equation gives rise to an intensity-dependent phase shift. This phenomenon is referred to as *self-phase modulation* (SPM) because the signal propagating inside a nonlinear medium modulates its own phase; it was first observed inside an optical fiber in a 1978 experiment [7]. The nonlinear phase shift $\phi_{\rm NL}$ in Eq. (4.1.6) increases with the link length L. The quantity $L_{\rm eff}$ plays the role of an effective length that is smaller than L because of fiber losses. In the case of lumped amplification, $p(z) = \exp(-\alpha z)$ in each fiber section. The integral in Eq. (4.1.6) can be performed analytically in this case, and the effective link length is given by

$$L_{\rm eff} = L[1 - \exp(-\alpha L_A)]/(\alpha L_A) \approx N_A/\alpha, \tag{4.1.8}$$

if we assume that amplifier spacing is large enough that $\exp(-\alpha L_A)$ can be neglected in comparison to 1. In the absence of fiber losses, $\alpha = 0$, and $L_{\rm eff} = L$.

The time-dependent nature of the optical signal implies that the SPM-induced phase shift changes with time. Consider a single 1 bit within an RZ bit stream. The maximum phase shift $\phi_{\rm max}$ occurs at the pulse center assumed to be located at $t = 0$. Since U is normalized such that $|U(0,0)| = 1$,

$$\phi_{\rm max} = L_{\rm eff}/L_{\rm NL} = \gamma P_0 L_{\rm eff}. \tag{4.1.9}$$

As seen in Section 3.3, a temporally varying phase for an optical field implies that the instantaneous carrier frequency differs across the pulse from its central value ω_0. The frequency shift $\delta\omega$ is itself time-dependent and is given by

$$\delta\omega(t) = -\frac{\partial \phi_{\rm NL}}{\partial t} = -\left(\frac{L_{\rm eff}}{L_{\rm NL}}\right)\frac{\partial}{\partial t}|U(0,t)|^2, \tag{4.1.10}$$

where the minus sign is due to the choice of the factor $\exp(-i\omega_0 t)$ in Eq. (3.1.1). The time dependence of $\delta\omega$ is referred to as frequency chirping. The chirp induced by SPM increases in magnitude with the transmitted distance. In other words, new frequency components are generated continuously as the optical signal propagates down the fiber. These SPM-generated frequency components broaden the spectrum of the bit stream from its initial width at $z = 0$. Such a spectral broadening is undesirable because it not only increases the signal bandwidth but can also distort the pulse shape when dispersive effects are included.

As discussed in Section 2.2.3, for any realistic lightwave system the input field $U(0,t)$ in Eq. (4.1.10) is composed of a random sequence of 0 and 1 bits and can be written as $U(0,t) = \sum b_n U_p(t - nT_b)$, where $U_p(t)$ represents pulse shape, T_b is the bit duration, and the random variable b_n takes on values of 0 or 1. Using this form in Eq. (4.1.6), the SPM-induced phase shift can be written as

$$\phi_{\rm NL}(L,t) \approx (L_{\rm eff}/L_{\rm NL})\sum_k b_k^2 |U_p(t - kT_b)|^2, \tag{4.1.11}$$

where we assumed that optical pulses in the neighboring bit slots do not overlap appreciably. Since $b_k = 0$ for 0 bits, the nonlinear phase shift occurs for only 1 bits and has the same magnitude for each of them. In fact, the form of $\phi_{\rm NL}$ mimics the bit pattern

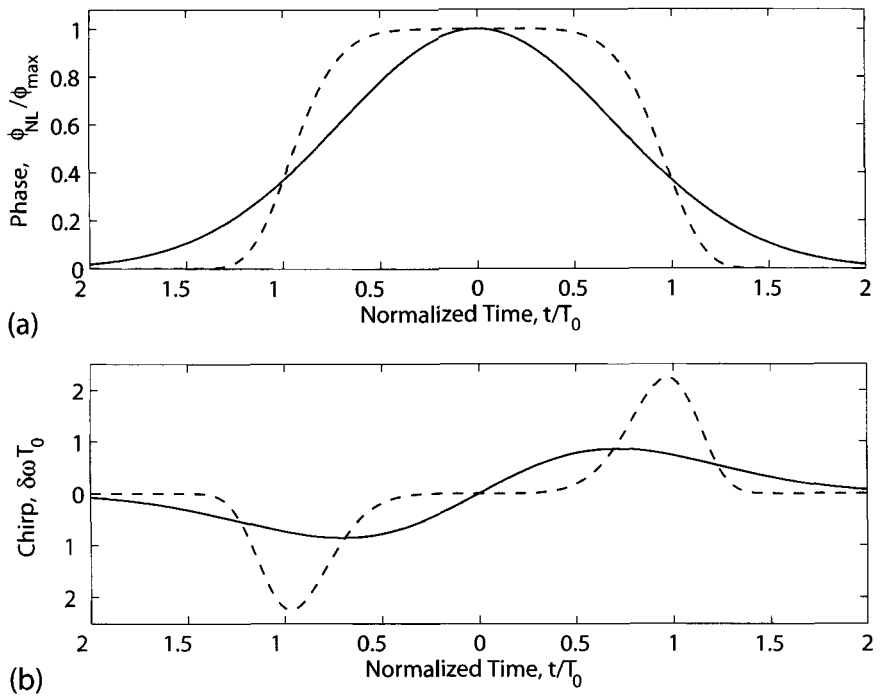

Figure 4.1: Temporal variation of (a) SPM-induced phase shift ϕ_{NL} and (b) frequency chirp $\delta\omega$ for Gaussian (solid curves) and super-Gaussian (dashed curves) pulses.

of the launched signal. In what follows, we consider a single 1 bit and retain only the $k = 0$ term in Eq. (4.1.11). We should stress that one cannot use this simple form of the nonlinear phase shift when optical pulses in neighboring bit slots overlap considerably. This is the case for pseudo-linear systems designed such that the dispersion spreads each optical pulse over several bit slots. The XPM interaction between two overlapping pulses then leads to new effects referred to as the intrachannel nonlinear effects (see Chapter 8).

The magnitude of SPM-induced chirp depends on the pulse shape. Consider, for example, the case of a super-Gaussian pulse for which the incident field is given in Eq. (3.3.47). The SPM-induced chirp $\delta\omega(t)$ for such a pulse is obtained from Eq. (4.1.10) and has the form

$$\delta\omega(t) = \frac{2m}{T_0}\frac{L_{\text{eff}}}{L_{\text{NL}}}\left(\frac{t}{T_0}\right)^{2m-1}\exp\left[-\left(\frac{t}{T_0}\right)^{2m}\right], \tag{4.1.12}$$

where T_0 is the pulse width. The integer $m = 1$ for a Gaussian pulse. For larger values of m, pulses representing 1 bits become nearly rectangular and develop steeper leading and trailing edges. This change in pulse shape affects the SPM-induced phase shift considerably. Figure 4.1 shows variations of (a) nonlinear phase shift ϕ_{NL} and (b) SPM-induced frequency chirp $\delta\omega$ across the pulse at a distance $L_{\text{eff}} = L_{\text{NL}}$ for Gaussian

($m = 1$) and super-Gaussian ($m = 3$) pulses. As ϕ_{NL} is directly proportional to $|U(0,t)|^2$ in Eq. (4.1.6), its temporal profile is identical to that of the pulse intensity. The chirp profile $\delta\omega(t)$ exhibits several interesting features. First, $\delta\omega$ is negative near the leading edge (red shift) but becomes positive near the trailing edge (blue shift) of the pulse. Second, frequency chirp is linear and positive (up-chirp) over a large central region of the Gaussian pulse. Third, it is considerably larger for pulses with steeper leading and trailing edges. Fourth, super-Gaussian pulses behave differently than Gaussian pulses because the chirp occurs only near pulse edges and does not vary in a linear fashion.

4.1.2 Spectral Broadening and Narrowing

The main consequence of SPM-induced chirp is that the spectrum of an optical bit stream becomes broader as the signal travels down the fiber link. Such spectral broadening is undesirable for any lightwave system as it can enhance dispersion-induced degradation of the signal, and may force one to increase the channel spacing.

The magnitude of SPM-induced spectral broadening can be estimated from the peak value of $\delta\omega$ in Figure 4.1. Mathematically, we can calculate the peak value by maximizing $\delta\omega(t)$ in Eq. (4.1.12). By setting its time derivative to zero, the maximum value of $\delta\omega$ is found to be

$$\delta\omega_{max} = mf(m)\phi_{max}/T_0, \tag{4.1.13}$$

where ϕ_{max} is given in Eq. (4.1.9) and $f(m)$ is defined as

$$f(m) = 2\left(1 - \frac{1}{2m}\right)^{1-1/2m} \exp\left[-\left(1 - \frac{1}{2m}\right)\right]. \tag{4.1.14}$$

The numerical value of f depends on m only slightly; $f = 0.86$ for $m = 1$ and tends toward 0.74 for large values of m relevant for super-Gaussian pulses.

To obtain a spectral broadening factor, the width parameter T_0 should be related to the initial spectral width $\Delta\omega_0$ of the pulse. For an unchirped Gaussian pulse, $\Delta\omega_0 = T_0^{-1}$ from Eq. (3.3.8). Equation (4.1.13) then becomes (with $m = 1$)

$$\delta\omega_{max} = 0.86\Delta\omega_0\phi_{max}, \tag{4.1.15}$$

showing that the spectral broadening factor is approximately given by the numerical value of the maximum phase shift ϕ_{max}. Since $\phi_{max} > 10$ possible for long fiber links, it is evident that SPM can broaden the signal spectrum considerably.

The shape of the pulse spectrum $S(\omega)$ at a distance L is obtained by taking the Fourier transform of Eq. (4.1.5). Using $S(\omega) = |\tilde{U}(L,\omega)|^2$, we obtain

$$S(\omega) = \left|\int_{-\infty}^{\infty} U(0,t)\exp[i\phi_{NL}(L,t) + i(\omega - \omega_0)t]\,dt\right|^2, \tag{4.1.16}$$

where $\phi_{NL}(L,t)$ is given in Eq. (4.1.6). It is evident from this equation that $S(\omega)$ depends not only on the pulse shape but also on whether input pulses are chirped. Figure 4.2 shows the influence of input chirp on the spectrum of Gaussian pulses after they

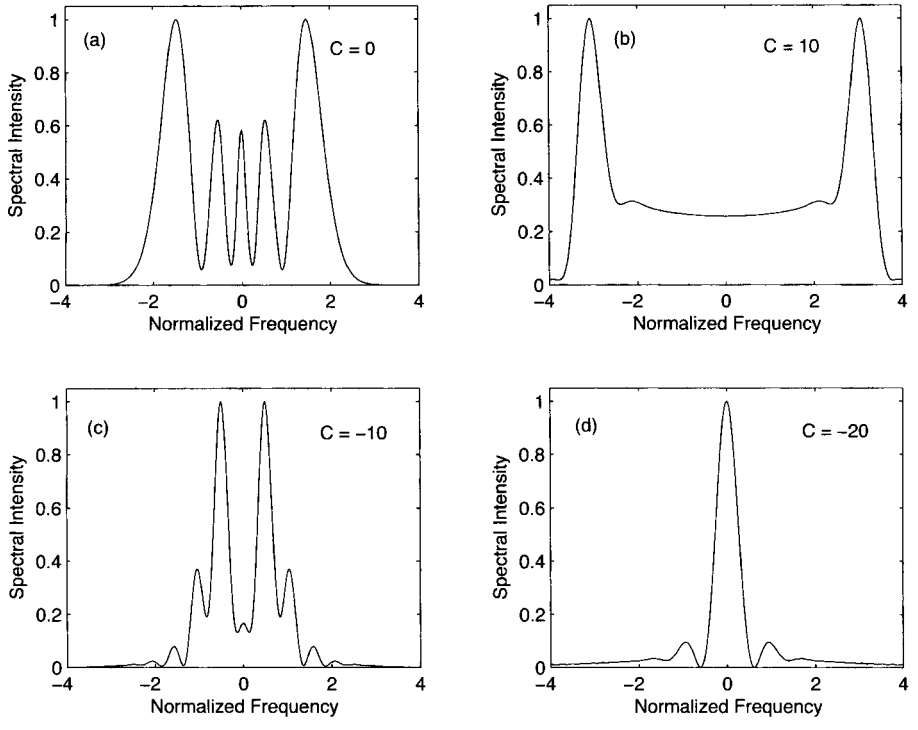

Figure 4.2: Comparison of output spectra for Gaussian pulses for four values of chirp parameter C when fiber length and peak powers are chosen such that $\phi_{\max} = 4.5\pi$. Spectrum broadens for $C < 0$ but becomes narrower for $C < 0$ when compared with that of the input pulse.

have propagated inside a fiber such that $\phi_{\max} = 4.5\pi$; fiber losses as well as dispersive effects are ignored for this illustration. The most notable feature of Figure 4.2(a) is that SPM-induced spectral broadening is accompanied by an oscillatory structure. For unchirped pulses, the spectrum consists of multiple peaks such that the two outermost peaks are the most intense. The number of peaks depends on $\phi_{\max}$ and increases linearly with it. For $C > 0$, spectral broadening increases and the oscillatory structure becomes less pronounced, as seen in Figure 4.2(b).

It is clear from Figure 4.2 that the sign of the chirp parameter C plays a critical role. In fact, a negatively chirped pulse undergoes *spectral narrowing* through SPM, as seen clearly in parts (c) and (d) of Figure 4.2. The spectrum contains a central dominant peak for $C = -20$ and narrow further as C decreases. This behavior can be understood from Eq. (4.1.16) by noting that the SPM-induced phase shift is partially cancelled by the input chirp when C is negative. If we employ the approximation that $\phi_{\rm NL}(t) \approx \phi_{\max}(1 - t^2/T_0^2)$ near the pulse center for Gaussian pulses, the SPM-induced chirp is nearly cancelled for $C = -2\phi_{\max}$. This approximation provides a rough estimate of the value of C for which narrowest spectrum occurs for a given value of $\phi_{\max}$.

From a practical perspective, SPM-induced spectral broadening should be con-

trolled for any long-haul lightwave system. The maximum phase shift in Eq. (4.1.9) determines the spectral broadening factor. As a rough design guideline, the SPM effects become important only when $\phi_{\max} > 1$. For short-haul systems, this condition is rarely satisfied at typical peak power levels used ($\sim$1 mW). The situation changes when fiber losses are compensated using optical amplifiers because the SPM effects then accumulate over the entire link. Typically, amplifier spacing is large enough that αL_A exceeds 3, and we can use $L_{\text{eff}} \approx N_A/\alpha$ from Eq. (4.1.8) for a system designed with N_A amplifiers. The condition $\phi_{\max} < 1$ is satisfied if

$$P_0 < \alpha/(\gamma N_A). \tag{4.1.17}$$

If we use typical values of α and γ for 1.55-μm lightwave systems, the peak power is limited to below 1 mW for a fiber links containing 30 amplifiers. Clearly, SPM can be a major limiting factor for long-haul lightwave systems.

4.1.3 Effects of Fiber Dispersion

The preceding discussion is oversimplified as it ignores the dispersive effects completely. In a real lightwave system, dispersive and nonlinear effects act on the optical bit stream simultaneously. Unfortunately, it is not easy to solve Eq. (4.1.2) analytically except in some simple cases. For example, in the specific case of $p = 1$ and β_2 constant but negative, this equation reduces to a standard NLS equation and has solutions in the form of solitons—pulses that maintain their shape and width in spite of dispersion. This case is discussed in Section 4.6. Physically speaking, by choosing the input pulse shape and peak power appropriately, SPM-induced chirp can be made just large enough to cancel the chirp induced by dispersion.

Another special case is that of rectangular-shape pulses propagating in a fiber with positive β_2 (normal GVD). Using the transformation

$$U(z,t) = \sqrt{\rho(z,t)}\exp\left[i\int_0^t v(z,t)\,dt\right] \tag{4.1.18}$$

in Eq. (4.1.2), the pulse-propagation problem reduces to a fluid-dynamics problem in which the variables ρ and v play, respectively, the role of local density and velocity of a fluid [10]. In the optical case, these variables represent the local intensity and chirp of the pulse. As this problem is identical to the hydrodynamic problem of "breaking a dam," it can be solved analytically in the limit of small dispersion. The resulting solution is useful for lightwave systems employing the NRZ format and provides considerable physical insight [11]–[13].

An important question is how the SPM-induced chirp affects broadening of optical pulses in the presence of dispersion. The broadening factor can be estimated, without requiring a complete solution of Eq. (4.1.2), using various approximations [14]–[20]. A variational approach was used as early as 1983 [14]. A split-step approach, in which the effects of SPM and GVD are considered separately, also provides a reasonable estimate of pulse broadening [15]. In an extension of this technique, the SPM-induced chirp is treated as an effective chirp parameter at the input end [18]. A perturbative approach in which the nonlinear term in Eq. (4.1.2) is treated as being relatively small

can also be employed to calculate σ_p^2 defined in Eq. (3.3.13). For a symmetric pulse, $\langle t \rangle = 0$, and σ_p^2 is approximately given by [20]

$$\sigma_p^2(z) = \sigma_L^2(z) + \gamma P_0 f_s \int_0^z \beta_2(z_1) \left[\int_0^{z_1} p(z_2)\, dz_2 \right] dz_1, \tag{4.1.19}$$

where σ_L^2 is the RMS width expected in the linear case ($\gamma = 0$). The shape of the input pulse enters through the parameter f_s, defined as

$$f_s = \frac{\int_{-\infty}^{\infty} |U(0,t)|^4\, dt}{\int_{-\infty}^{\infty} |U(0,t)|^2\, dt}. \tag{4.1.20}$$

For a Gaussian pulse with $U(0,t) = \exp[-\frac{1}{2}(t/T_0)^2]$, $f_s = 1/\sqrt{2} \approx 0.7$. For a square pulse, $f_s = 1$.

As an example, consider the case of a uniform-GVD fiber with distributed amplification such that the pulse energy remains nearly constant. Using $p(z) = 1$ with constant β_2 in Eq. (4.1.19), we obtain the simple expression

$$\sigma_p^2(z) = \sigma_L^2(z) + \tfrac{1}{2} f_s \gamma P_0 \beta_2 z^2. \tag{4.1.21}$$

This equation shows that the SPM enhances pulse broadening in the normal-GVD regime but leads to pulse compression in the anomalous-GVD regime. This behavior can be understood by noting that the SPM-induced chirp is positive in nature ($C > 0$). As a result, the pulse goes through a contraction phase when $\beta_2 < 0$. Figure 4.3 shows the pulse-broadening factor σ_p/σ_0 over one dispersion length for three input power levels by solving Eq. (4.1.2) for a super-Gaussian input $U(0,t) = \exp[-\frac{1}{2}(t/T_0)^{2m}]$ with $m = 2$ and $p = 1$. As the input peak power increases, the pulse initially contracts because of the SPM effects, attains a minimum value at a certain value of the peak power, and then begins to increase rapidly. In practical terms, the input power should be optimized properly if we want to take advantage of the soliton-like effects for NRZ systems [21].

4.1.4 Modulation Instability

Modulation instability is a well-known phenomenon [4]. It refers to an inherent instability of the CW solution of the NLS equation (4.1.2) in the anomalous-GVD regime of a fiber link. It is easy to deduce that this equation has a CW solution in the form $U(z) = \exp(i\phi_{\mathrm{NL}})$, where ϕ_{NL} is the nonlinear phase shift induced by SPM. Thus, a CW signal should propagate through the fiber unchanged except for acquiring a power-dependent phase shift (and reduced power because of fiber losses).

Before reaching this conclusion, however, one must ask whether the CW solution is stable against small perturbations. To answer this question, we perturb the CW solution slightly such that

$$U = (1 + a)\exp(i\phi_{\mathrm{NL}}) \tag{4.1.22}$$

and examine evolution of the perturbation $a(z,t)$ using a linear stability analysis. Substituting Eq. (4.1.22) in Eq. (4.1.2) and linearizing in a, we obtain

$$i\frac{\partial a}{\partial z} = \frac{\beta_2}{2}\frac{\partial^2 a}{\partial t^2} - \gamma P_0 (a + a^*), \tag{4.1.23}$$

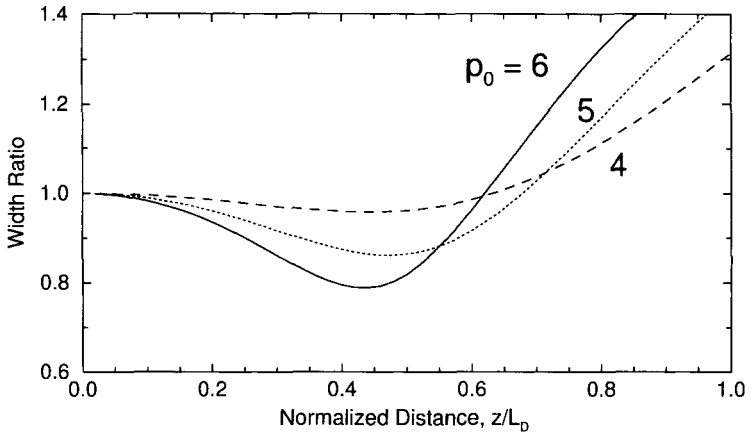

Figure 4.3: Width ratio σ_p/σ_0 as a function of propagation distance for a super-Gaussian pulse ($m = 2$) at three input peak powers labeled using $p_0 = \gamma P_0 L_D$.

where for simplicity we set $p = 1$, assuming that losses are perfectly compensated through distributed amplification.

The linear equation (4.1.23) can be solved easily in the frequency domain. However, because of the a^* term, the Fourier components at frequencies Ω and $-\Omega$ are coupled. Thus, we should consider its solution in the form

$$a(z,t) = a_1 \exp[i(Kz - \Omega t)] + a_2 \exp[-i(Kz - \Omega t)], \tag{4.1.24}$$

where K and Ω are the wave number and the frequency of perturbation, respectively. Equations (4.1.23) and (4.1.24) provide a set of two homogeneous equations for the two constants a_1 and a_2. This set has a nontrivial solution only when K and Ω satisfy the following dispersion relation:

$$K = \pm\tfrac{1}{2}|\beta_2\Omega|[\Omega^2 + \mathrm{sgn}(\beta_2)\Omega_c^2]^{1/2}, \tag{4.1.25}$$

where $\mathrm{sgn}(\beta_2) = \pm 1$ depending on the sign of β_2, and

$$\Omega_c^2 = \frac{4\gamma P_0}{|\beta_2|} = \frac{4}{|\beta_2| L_{\mathrm{NL}}}. \tag{4.1.26}$$

Because of the factor $\exp[i(\beta_0 z - \omega_0 t)]$ that has been factored out in Eq. (3.1.1), the actual wave number and the frequency of perturbation are $\beta_0 \pm K$ and $\omega_0 \pm \Omega$, respectively. With this in mind, the two terms in Eq. (4.1.24) represent two different frequency components. These frequency components correspond to two spectral sidebands that are generated when modulation instability occurs.

The dispersion relation (4.1.25) shows that steady-state stability depends on whether light experiences normal or anomalous GVD inside the fiber. In the case of normal GVD ($\beta_2 > 0$), K is real for all Ω, and the steady state is stable against small perturbations. By contrast, in the case of anomalous GVD ($\beta_2 < 0$), K becomes imaginary

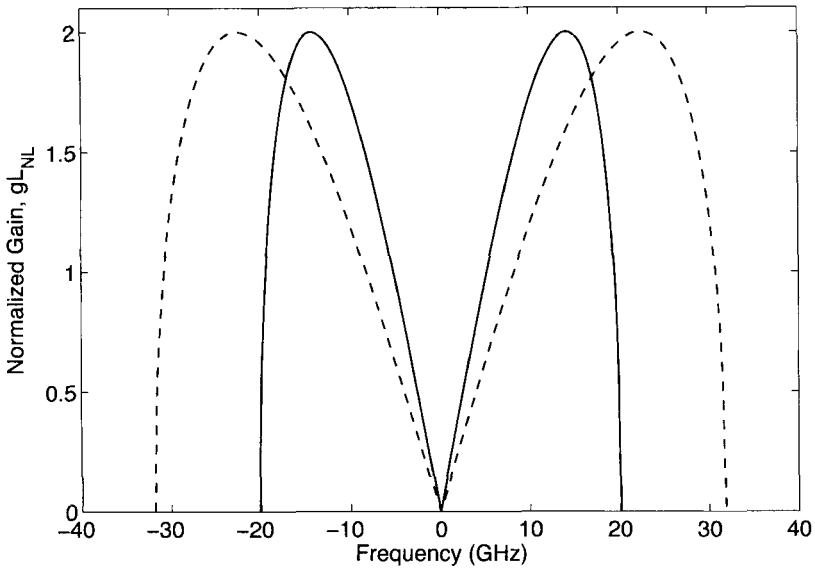

Figure 4.4: Gain spectra of modulation instability for $L_{NL} = 20$ km (dashed curve) and 50 km (solid curve) for an optical fiber with $\beta_2 = -5$ ps^2/km.

for $|\Omega| < \Omega_c$, and the perturbation $a(z,t)$ grows exponentially with z. As a result, the CW solution is unstable for $\beta_2 < 0$. This instability leads to a spontaneous temporal modulation of the CW beam, and it can transform the beam into a pulse train [22]–[24].

The gain spectrum of modulation instability is obtained from Eq. (4.1.25) by setting $\text{sgn}(\beta_2) = -1$ and $g(\Omega) = 2\,\text{Im}(K)$, where the factor of 2 converts g to power gain. The gain exists only if $|\Omega| < \Omega_c$ and is given by

$$g(\Omega) = |\beta_2 \Omega|(\Omega_c^2 - \Omega^2)^{1/2}. \tag{4.1.27}$$

Figure 4.4 shows the gain spectra for two values of nonlinear lengths (20 and 50 km) for an optical fiber with $\beta_2 = -5$ ps^2/km. As an example, $L_{NL} = 50$ km at a power level of 10 mW if we use a realistic value of $\gamma = 2$ W^{-1}/km. The gain spectrum is symmetric with respect to $\Omega = 0$ such that $g(\Omega)$ vanishes at $\Omega = 0$. The gain becomes maximum at two frequencies given by

$$\Omega_{\max} = \pm \frac{\Omega_c}{\sqrt{2}} = \pm \left(\frac{2\gamma P_0}{|\beta_2|} \right)^{1/2}, \tag{4.1.28}$$

with a peak value

$$g_{\max} \equiv g(\Omega_{\max}) = \tfrac{1}{2}|\beta_2|\Omega_c^2 = 2\gamma P_0, \tag{4.1.29}$$

where Eq. (4.1.26) was used to relate Ω_c to P_0. The peak gain is independent of the GVD parameter β_2 and increases linearly with the incident power.

At first sight, it may appear that modulation instability is not likely to occur in a lightwave system in which the optical signal is in the form of a pulse train. In fact,

it affects the performance of periodically amplified lightwave systems in two different ways. First, for systems utilizing the NRZ-format, optical pulses occupy the entire time slot and can be several bits long depending on the bit pattern. As a result, the situation is quasi-CW-like. As early as 1990, numerical simulations indicated that performance of a 6,000-km-long system, operating at bit rates >1 Gb/s with 100-km amplifier spacing, would be severely affected by modulation instability if the signal propagates in the anomalous-GVD regime and is launched with peak power levels in excess of a few milliwatts [25].

Second, modulation instability can be seeded by the broadband noise added by optical amplifiers (over the entire gain bandwidth or over the bandwidth of optical filters when they are used to reduce noise). The growth of this noise can degrade the SNR considerably at the receiver end [26]–[36]. Such degradation can occur in both the normal- and anomalous-dispersion regimes of the fiber link [31]. In the case of anomalous GVD, spectral components of noise falling within the gain spectrum of modulation instability are amplified by it, resulting in considerable degradation of the SNR [33]–[36]. Such SPM-induced SNR reduction has been observed experimentally. In a 10-Gb/s system, considerable degradation in system performance was noticed after a transmission distance of only 455 km [34]. We discuss the SNR-degradation issue in Chapter 6 devoted to amplifier noise.

4.2 Cross-Phase Modulation

The preceding discussion assumed implicitly that only a single channel was being transmitted through the fiber link. In the case of WDM systems, pulse trains of different wavelengths propagate simultaneously inside optical fibers. Since pulses belonging to different channels travel at different speeds, they overlap from time to time. Whenever that happens, a nonlinear phenomenon known as cross-phase modulation (XPM) induces an additional phase shift, that is, the phase of the pulse is affected not only by SPM but also by XPM. The XPM effects are quite important for WDM lightwave systems since the phase of each optical channel is affected by both the average power and the bit pattern of all other channels. Fiber dispersion converts phase variations into amplitude fluctuations that affect the SNR and introduce timing jitter. For this reason, an understanding of the interplay between XPM and GVD is of considerable importance for WDM systems [37]–[51].

4.2.1 XPM-Induced Phase Shift

To see the origin of XPM as clearly as possible, it is instructive to consider the case of a two-channel lightwave system. The total optical field in Eq. (3.1.12) in this case can be written as

$$A(z,t) = A_1(z,t)\exp(-i\Omega_1 t) + A_2(z,t)\exp(-i\Omega_2 t), \tag{4.2.1}$$

where $\Omega_m = \omega_m - \omega_0$, ω_m is the carrier frequency of the mth channel, and ω_0 is the reference carrier frequency that was used in deriving Eq. (4.1.2). If we choose ω_0 to

coincide with one of the channel frequencies, say, ω_1, then $\Omega_1 = 0$ and Ω_2 corresponds to channel spacing.

Substituting Eq. (4.2.1) in Eq. (3.1.12) and equating the terms oscillating at frequencies Ω_1 and Ω_2 on both sides, we obtain two coupled NLS equations:

$$\frac{\partial A_1}{\partial z} + \Omega_1 \beta_2 \frac{\partial A_1}{\partial t} + \frac{i\beta_2}{2}\frac{\partial^2 A_1}{\partial t^2} = i\gamma(|A_1|^2 + 2|A_2|^2)A_1 + \frac{i}{2}\beta_2 \Omega_1^2 A_1, \quad (4.2.2)$$

$$\frac{\partial A_2}{\partial z} + \Omega_2 \beta_2 \frac{\partial A_2}{\partial t} + \frac{i\beta_2}{2}\frac{\partial^2 A_2}{\partial t^2} = i\gamma(|A_2|^2 + 2|A_1|^2)A_2 + \frac{i}{2}\beta_2 \Omega_2^2 A_2. \quad (4.2.3)$$

The second term in these equations represents the group-velocity mismatch and results from the fact that the time in the original NLS equation is measured in a frame moving with the group velocity at the reference frequency ω_0. The nonlinear parameter γ is assumed to be nearly the same for both channels (it is slightly different as it scales linearly with the channel frequency). In deriving the coupled NLS equations, we neglected the terms oscillating at frequencies $2\Omega_1 - \Omega_2$ and $2\Omega_2 - \Omega_1$. These terms result from another nonlinear phenomenon known as four-wave mixing (FWM). The contribution of FWM cannot be ignored when more than two channels are involved and is considered in Section 4.3.

As seen from Eqs. (4.2.2) and (4.2.3), the single nonlinear term of the form $|A|^2A$ gives rise to two nonlinear terms when two channels are considered separately. The first term is responsible for SPM because it depends on the power of the channel under consideration. The second term is due to XPM because it induces a nonlinear phase shift proportional to the power of the second copropagating channel. When more than two channels are involved, this nonlinear term involves all other copropagating channels. In fact, it is easy to show that for an M-channel WDM system Eqs. (4.2.2) and (4.2.3) are replaced with a set of M nonlinearly coupled equations of the form

$$\frac{\partial A_j}{\partial z} + \Omega_j \beta_2 \frac{\partial A_j}{\partial t} + \frac{i\beta_2}{2}\frac{\partial^2 A_j}{\partial t^2} = i\gamma\Big(|A_j|^2 + 2\sum_{m\neq j}|A_m|^2\Big)A_j + \frac{i}{2}\beta_2 \Omega_j^2 A_j, \quad (4.2.4)$$

where $j = 1$ to M and we have ignored all FWM terms.

In general, this set of M nonlinear equations should be solved numerically. It can be solved analytically in the CW case or when the dispersive effects are ignored. Setting $\beta_2 = 0$ in Eq. (4.2.4) and integrating over z, we obtain the result $A_j(L) = \sqrt{P_j}\exp(i\phi_j)$, where P_j is the input power and the nonlinear phase shift resulting from the combination of SPM and XPM is given by

$$\phi_j = \gamma L_{\text{eff}}\Big(P_j + 2\sum_{m\neq j} P_m\Big), \quad (4.2.5)$$

where L_{eff} is given in Eq. (4.1.8).

The CW solution applies approximately for NRZ-format systems operating at relatively low bit rates. The phase ϕ_j of a specific channel would vary from bit to bit depending on the bit patterns of neighboring channels. In the worst case in which all channels have 1 bits in their time slots simultaneously, the XPM-induced phase shift is

largest. If the input power is assumed to be the same for each channel, this maximum value is given by

$$\phi_{\max} = N_A(\gamma/\alpha)(2M-1)P_{\text{ch}}, \tag{4.2.6}$$

where L_{eff} was replaced by N_a/α from Eq. (4.1.8) assuming $\alpha L_A \gg 1$. The XPM-induced phase shift increases linearly both with M and N_A and can become quite large for long-haul WDM systems.

The XPM-induced phase shift was first measured in 1984 in a two-channel configuration [37]. Light from two semiconductor lasers operating near 1.3 and 1.5 μm was injected into a 15-km-long fiber. The phase shift at 1.5 μm, induced by the copropagating 1.3-μm wave, was measured using an interferometer. A value of $\phi_{\max} = 0.024$ was found for $P_{\text{ch}} = 1$ mW. This value is in good agreement with the predicted value of 0.022 from Eq. (4.2.6). As a rough estimate of the importance of the XPM effects for WDM systems, if we use the condition $\phi_{\max} < 1$ in Eq. (4.2.6) together with $N_A = 1$, the channel power is restricted to

$$P_{\text{ch}} < \alpha/[\gamma(2M-1)]. \tag{4.2.7}$$

For typical values of α and γ, P_{ch} should be below 10 mW even for five channels and it reduces to below 1 mW for more than 50 channels.

4.2.2 Effects of Group-Velocity Mismatch

The preceding analysis overestimates the XPM-induced phase shift because it neglects the time-dependent nature of the optical signal. In practice, each channel carries an optical bit stream in which the location of pulses representing 1 bits is data-dependent (or pseudo-random). Moreover, pulses belonging to different channels travel at different speeds and walk through each other at a rate that depends on their wavelength difference. Since XPM can occur only when pulses overlap in the time domain, the phase shift induced by it is reduced considerably by the walk-off effects.

A simple way to understand the critical role played by the group-velocity mismatch is to consider a pump-probe configuration in which one of the channels is in the form of a weak CW field. This channel acts as probe whose phase is modulated by the "pump" channel containing an optical bit stream. Equations (4.2.2) and (4.2.3) can be readily adopted for this case. Let A_1 play the role of the pump and A_2 that of the CW probe. Also assume that the reference frequency is chosen such that $\Omega_2 = 0$ so that Ω_1 equals the channel spacing. If we assume that dispersion-induced pulse broadening is negligible and neglect the second-derivative terms, Eqs. (4.2.2) and (4.2.3) reduce to

$$\frac{\partial A_1}{\partial z} + \delta\frac{\partial A_1}{\partial t} = i\gamma|A_1|^2A_1 + \frac{i}{2}\beta_2\Omega_1^2A_1 - \frac{\alpha}{2}A_1, \tag{4.2.8}$$

$$\frac{\partial A_2}{\partial z} = 2i\gamma|A_1|^2A_2 - \frac{\alpha}{2}A_2, \tag{4.2.9}$$

where the parameter $\delta = \Omega_1\beta_2$ represents a group-velocity mismatch between the pump and probe and the probe power is assumed to be much smaller than the pump. We have added a loss term in these equations to account for fiber losses, assumed to be the same at the pump and probe wavelengths.

Equations (4.2.8) and (4.2.9) can be solved analytically to find the XPM-induced phase shift on the probe. The solution of the pump equation (4.2.8) is straightforward once we note that the pump phase does not play any role. Introducing $A_1 = \sqrt{P_1}\exp(i\phi_1)$, we find that the pump power $P_1(z,t)$ satisfies

$$\frac{\partial P_1}{\partial z} + \delta\frac{\partial P_1}{\partial t} + \alpha A_1 = 0, \tag{4.2.10}$$

and has the solution

$$P_1(z,t) = P_{\text{in}}(t-\delta z)\exp(-\alpha z), \tag{4.2.11}$$

where $P_{\text{in}}(t)$ represents the temporal power profile of the input bit stream launched into the pump channel. It is relatively simple to incorporate the effects of periodic amplification in Eq. (4.2.11). In fact, we only need to replace the factor $\exp(-\alpha z)$ in this equation with the power-variation factor $p(z)$ introduced in Section 4.1.

The probe equation can also be easily solved. For a fiber of length L, the solution takes the simple form

$$A_2(z) = A_2(0)\exp(-\alpha L/2 + i\phi_{\text{XPM}}), \tag{4.2.12}$$

where the XPM-induced phase shift is given by

$$\phi_{\text{XPM}}(t) = 2\gamma\int_0^L P_{\text{in}}(t-\delta z)e^{-\alpha z}dz. \tag{4.2.13}$$

In the case of a CW pump, we recover the maximum phase shift obtained earlier. However, for a time-dependent pump the phase shift is affected considerably by the group-velocity mismatch governed by the parameter δ.

A simple way to understand the role of group-velocity mismatch is to consider a pump modulated sinusoidally at a frequency ω_m as $P_{\text{in}}(t) = P_0 + p_m\cos(\omega_m t)$ and ask how the XPM-induced phase shift of the probe changes with the modulation frequency ω_m. Writing this phase shift in the form $\phi_{\text{XPM}} = \phi_0 + \phi_m\cos(\omega_m t + \psi)$, it is easy to show that $\phi_0 = 2\gamma P_0 L_{\text{eff}}$ and ϕ_m is given by [41]

$$\phi_m(\omega_m) = 2\gamma p_m L_{\text{eff}}\sqrt{\eta_{\text{XPM}}}, \tag{4.2.14}$$

where η_{XPM} is a measure of the XPM efficiency and is given by

$$\eta_{\text{XPM}}(\omega_m) = \frac{\alpha^2}{\alpha^2+\omega_m^2\delta^2}\left[1 + \frac{4\sin^2(\omega_m\delta L/2)e^{-\alpha L}}{(1-e^{-\alpha L})^2}\right]. \tag{4.2.15}$$

The quantity ψ represents a phase lag that also depends on δ, among other parameters.

The important feature of Eq. (4.2.14) is that $\phi_m(\omega_m)$ depends not only on the modulation frequency ω_m but also on the channel spacing Ω_1 through the parameter δ. Figure 4.5 shows the XPM index, defined as the ratio ϕ_m/p_m, as a function of ω_m for two different channel spacings, assuming that the 25-km-long single-mode fiber has a dispersion of 16.4 ps/(km-nm) and losses of 0.21 dB/km. Experimental results agree reasonably well with the theoretical predictions based on Eq. (4.2.14). This equation can be easily generalized to include the effects of periodic signal amplification.

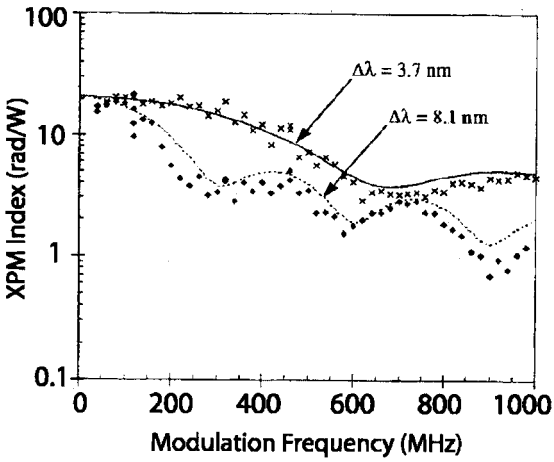

Figure 4.5: Measured (symbols) and calculated (solid line) values of the XPM index for a standard 25-km-long fiber as a function of modulation frequency for two values of channel spacing. (After Ref. [41]; ©1996 IEEE.)

4.2.3 Effects of Group-Velocity Dispersion

Strictly speaking, the XPM-induced phase shift should not affect system performance if the GVD effects were negligible because optical receivers respond to only channel powers and ignore all phase changes. However, chromatic dispersion of optical fibers converts pattern-dependent phase shifts to power fluctuations, resulting in a lower SNR at the receiver. For this reason, XPM is a major source of nonlinear impairment for most WDM lightwave systems. This subsection focuses on the XPM-induced SNR degradation.

The conversion from time-dependent phase changes to power fluctuations can be understood qualitatively by noting that time-dependent phase changes are equivalent to frequency chirping. As was seen in Section 3.2, chirping of optical pulses within an optical bit stream affects dispersion-induced broadening of the optical signal. The new feature is that the temporal dependence of the phase shift (or the frequency chirp) of any channel depends on the bit patterns of all other copropagating channels since XPM can occur only when 1 bits are present simultaneously in at least two channels. Moreover, since pulses in different channels travel at different speeds because of the group-velocity mismatch, the XPM-induced interaction between two channels depends on the channel spacing.

Focusing again on the pump-probe configuration used earlier, we include the GVD effects in the probe equation (4.2.9) by adding a second-derivative term as

$$\frac{\partial A_2}{\partial z} + \frac{i\beta_2}{2}\frac{\partial^2 A_2}{\partial t^2} = 2i\gamma P_1(z,t)A_2 - \frac{\alpha}{2}A_2, \tag{4.2.16}$$

where $P_1(z,t)$ is the pump power given in Eq. (4.2.11). For simplicity of discussion, dispersion-induced broadening of pump pulses is still neglected.

The probe equation (4.2.16) can be solved in the Fourier domain because of its linear nature. However, since both P_1 and A_2 change with time, the solution is complicated and involves a convolution in the frequency domain. It is useful to treat the XPM-induced phase shift as a small perturbation and write the solution of Eq. (4.2.16) as $A_2(z,t) = A_u(z) + a(z,t)$, where $A_u(z)$ is the unperturbed solution in the absence of XPM and $a(z,t)$ represents XPM-induced perturbation of the probe. Substituting this relation in Eq. (4.2.16), $a(z,t)$ is found to satisfy

$$\frac{\partial a}{\partial z} + \frac{i\beta_2}{2}\frac{\partial^2 a}{\partial t^2} + \frac{\alpha}{2}a = 2i\gamma P_1(z,t)A_u(z), \tag{4.2.17}$$

where we neglected a small term on the right side and kept only the unperturbed part of the probe field. This equation can be easily solved in the Fourier domain. For a fiber-link of length L, it has the solution

$$\tilde{a}(L,\omega) = 2i\gamma \int_0^L \tilde{P}_1(z,\omega)A_u(z)\exp\left[\tfrac{1}{2}(i\beta_2\omega^2 - \alpha)(L-z)\right] dz, \tag{4.2.18}$$

where $\tilde{P}_1(z,\omega)$ is the Fourier transform of the pump power $P_1(z,t)$ in Eq. (4.2.11) and is related to the input spectrum $P_1(0,\omega)$ as

$$\tilde{P}_1(z,\omega) = \tilde{P}_1(0,\omega)\exp(-\alpha z + i\omega\delta z). \tag{4.2.19}$$

The XPM-induced change $\widetilde{\delta P}$ in the probe power at a specific frequency ω can now be calculated by noting that $\widetilde{\delta P} = A_u^*\tilde{a} + A_u\tilde{a}^*$. It is common to introduce a power transfer function $H_{XPM}(\omega)$ for XPM-induced power fluctuations through the relation

$$\widetilde{\delta P}(\omega)/|A_u(L)|^2 = H_{XPM}(\omega)P_1(0,\omega)/P_0, \tag{4.2.20}$$

where P_0 is the average power of the pump channel. Using Eqs. (4.2.18) and (4.2.19), this transfer function can be calculated analytically in a closed form and is found to be [43]–[46]

$$H_{XPM}(\omega) = 2\gamma P_0[F(\delta,\beta_2) - F(\delta,-\beta_2)], \tag{4.2.21}$$

where the function F depends on the two dispersion parameters δ and β_2 as

$$F(\delta,\beta_2) = \exp(-i\beta_2\omega^2 L/2)\left(\frac{1-\exp[i(\delta\omega + \beta_2\omega^2/2 + i\alpha)L]}{\delta\omega + \beta_2\omega^2/2 + i\alpha}\right). \tag{4.2.22}$$

The measurements of power transfer function $H_{XPM}(\omega)$ provide a convenient way to quantify the XPM effects in a fiber link. As an example, Figure 4.6(a) shows how it varies with the modulation frequency ω for a 114-km-long fiber (single span) with $\alpha = 2.5$ dB/km, the zero-dispersion wavelength at 1,520.2 nm, and a dispersion slope at this wavelength of 0.075 ps/(km-nm^2). The pump channel had an average power level of 11.5 dBm at a wavelength of 1,560.6 nm, while the probe was shifted from this wavelength by 0.8 or 1.6 nm. Figure 4.6(b) is obtained under the same conditions except that a second fiber of 116-km length has been added. In both cases, solid lines show the predictions based on Eqs. (4.2.21). Clearly, the preceding simple theory

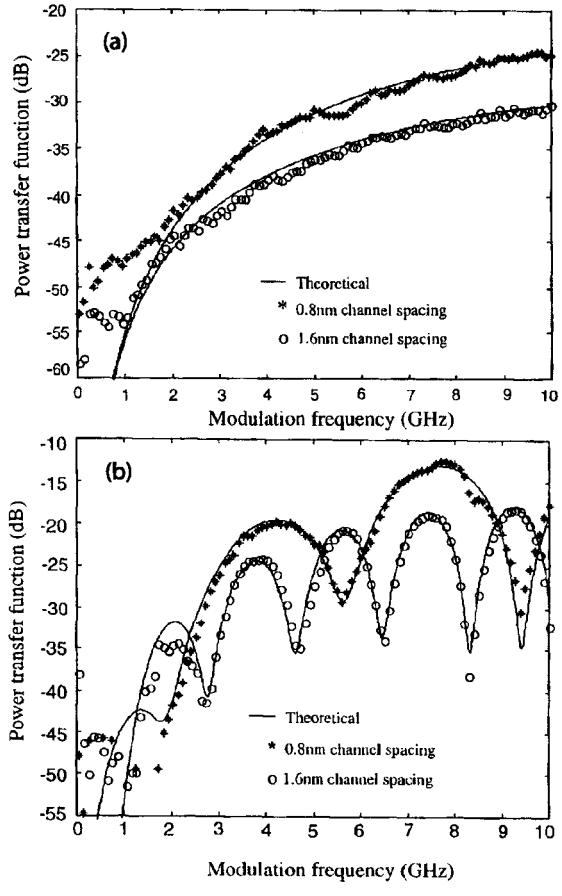

Figure 4.6: Power transfer function as a function of modulation frequency for (a) 114-km and (b) 230-km fiber links and two different channel spacings. In each case, solid curves show a theoretical fit to the experimental data. (After Ref. [46]; ©1999 IEEE.)

provides a reasonable description of XPM-induced power fluctuations in spite of the approximations made. In general, fluctuations are smaller for a wider channel separation. This is easily understood by noting that a wider channel spacing introduces a larger mismatch between the pump and probe group velocities. As a result, the length of the fiber over which pulses in two channels overlap is reduced.

As seen in Figure 4.6, XPM-induced power variations can become quite large even for a link length of 200 km or so. The important question is how much the power of a CW probe fluctuates when the probe is copropagated with the pump channel containing a realistic optical bit stream. Figure 4.7 shows XPM-induced fluctuations on a CW probe launched with a pump channel modulated at 10 Gb/s using the NRZ format (bottom trace). Although the fluctuation level is close to 0.1% for a single 130-km-long span (middle trace), probe power fluctuates by as much as 6% for the 320-km

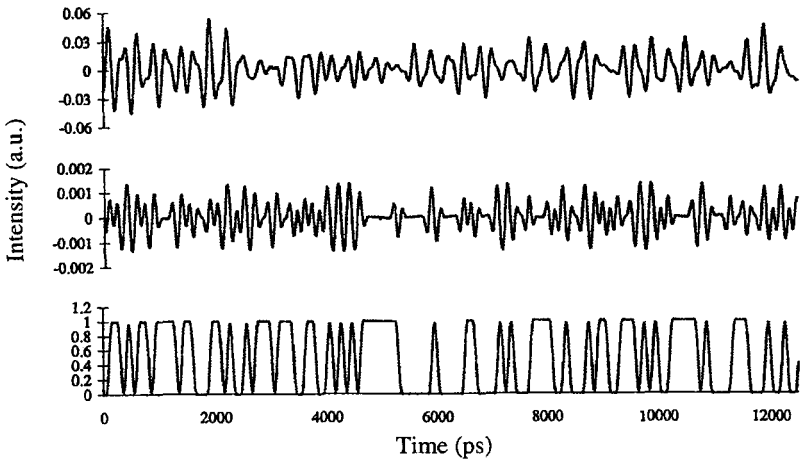

Figure 4.7: XPM-induced power fluctuations on a CW probe for 130-km (middle) and 320-km (top) fiber links with dispersion management. The NRZ bit stream in the pump channel responsible for fluctuations is shown in the bottom trace. (After Ref. [46]; ©1999 IEEE.)

fiber link (top trace). Clearly, such XPM-induced fluctuations will become intolerable for long-haul lightwave systems whose length may exceed 1,000 km.

The combination of GVD and XPM can also lead to timing jitter in WDM systems. We can use the results of Section 4.1 to understand the origin of timing jitter. As a faster-moving pulse belonging to one channel collides with and passes through a specific pulse in another channel, its leading edge arrives first and is followed by the trailing edge after the two have completely overlapped. Since the frequency chirp induced by XPM depends on the derivative of the power profile [see Eq. (4.1.10)], it shifts the pulse spectrum first toward red and then toward blue. In a lossless fiber, collisions of two pulses are perfectly symmetric, resulting in no net spectral shift at the end of the collision. In a loss-managed system, with lumped amplifiers placed periodically along the link, power variations make collisions between pulses of different channels asymmetric, resulting in a net frequency shift that depends on the channel spacing. Such frequency shifts lead to timing jitter (the speed of a channel depends on its frequency because of GVD) since their magnitude depends on the bit pattern as well as on channel wavelengths (see Section 8.4).

4.2.4 Control of XPM Interaction

Since XPM affects the performance of all WDM systems, a lightwave system must be designed to control its impact so that it can operate reliably. In practice, the dominant contribution to XPM affecting the performance of a specific channel comes from the two channels that are its nearest neighbors in the spectral domain. The XPM interaction between neighboring channels can always be reduced by increasing the channel spacing. A larger channel spacing increases the mismatch between the group velocities at which pulses in each channel propagate through the fiber link. As a result, pulses

cross each other so fast that they overlap for a relatively short duration, resulting in a much reduced XPM interaction. This scheme is effective but it reduces the spectral efficiency as channels must be spaced farther apart. XPM effects can also be reduced by lowering channel powers. However, a reduction in the channel power also lowers the SNR at the receiver. In practice, channel powers cannot be reduced below a critical value set by the SNR requirements.

A simple scheme, often employed in practice, controls the state of polarization (SOP) with which each channel is launched into the fiber link [52]. More specifically, individual channels are launched such that any two neighboring channels are orthogonally polarized. In practice, even- and odd-numbered channels are grouped together and their SOPs are made orthogonal before launching them into the fiber link. This scheme is sometimes referred to as the polarization channel interleaving technique. The XPM interaction between two orthogonally polarized does not vanish but its strength is reduced significantly. Mathematically, the analysis is complicated because one must take into account the vector nature of the electromagnetic field within the fiber [4]. It turns out that the coupled NLS equations, Eqs. (4.2.2) and (4.2.3), can still be used, provided the factor of 2 appearing in the XPM term is replaced with 2/3. It is this reduction in the XPM strength that reduces the magnitude of the XPM-induced phase shift and improves the system performance when neighboring channels of a WDM system are orthogonally polarized.

It may appear surprising that such a scheme works in spite of birefringence fluctuations that change the SOP of each channel and produce polarization-mode dispersion (PMD). Indeed, the SOP of all channels changes in a random fashion along the fiber in any realistic lightwave system. The vector theory of XPM capable of including the PMD effects (see Section 4.7) shows that the XPM-induced crosstalk is reduced considerably even for two copolarized channels simply because the channels do not remain copolarized as they propagate within the fiber link [53]. For the same reason, the effectiveness of polarization-interleaving technique is reduced. However, this technique is still useful in practice for dense WDM systems in which any two neighboring channels differ in their wavelengths by a relative small amount (typically <1 nm). Because of a small difference in the carrier frequencies, the SOPs of the two neighboring channels can remain nearly orthogonal over relatively long distances, and XPM effects can be reduced by launching alternate channels with orthogonal SOPs [52].

4.3 Four-Wave Mixing

Four-wave mixing (FWM) becomes a major source of interchannel crosstalk whenever more than two channels are transmitted simultaneously over the same fiber, and it has been studied extensively in the context of WDM lightwave systems [54]–[67]. On a fundamental level, FWM can be viewed as a scattering process in which two photons of energies $\hbar\omega_1$ and $\hbar\omega_2$ are destroyed, and their energy appears in the form of two new photons of energies $\hbar\omega_3$ and $\hbar\omega_4$ such that the total energy is conserved. Such a process becomes efficient when a phase-matching condition stemming from the requirement of momentum conservation is satisfied.

It is easy to see why FWM would degrade the performance of a WDM system if it remains uncontrolled. The FWM process can generate a new wave at the frequency $\omega_{\rm FWM} = \omega_i + \omega_j - \omega_k$, whenever three waves of frequencies ω_i, ω_j, and ω_k copropagate inside the fiber. For an M-channel system, i, j, and k vary from 1 to M, resulting in a large combination of new frequencies generated through FWM. In the case of equally spaced channels, most new frequencies coincide with the existing channel frequencies and interfere coherently with the signals in those channels. This interference depends on the bit pattern and leads to considerable fluctuations in the detected signal at the receiver. When channels are not equally spaced, most FWM components fall in between the channels and their power acts as background noise. System performance is affected in both cases but the degradation is much more severe for equally spaced channels because of the coherent nature of resulting interchannel crosstalk.

4.3.1 FWM Efficiency

To see the origin of FWM, we extend the discussion of Section 4.2 to the case of a multichannel lightwave system and write the total optical field $A(z,t)$ in the NLS equation (3.1.12) as

$$A(z,t) = \sum_{m=1}^{M} A_m(z,t)\exp(-i\Omega_m t), \tag{4.3.1}$$

where $\Omega_m = \omega_m - \omega_0$, ω_m is the carrier frequency of the mth channel, and ω_0 is the reference carrier frequency that was used in deriving the NLS equation. As before, we substitute Eq. (4.3.1) in Eq. (3.1.12) and collect all terms oscillating at a specific frequency. The resulting equation for the mth channel takes the form

$$\frac{\partial A_m}{\partial z} + \Omega_j\beta_2\frac{\partial A_m}{\partial t} + \frac{i\beta_2}{2}\frac{\partial^2 A_m}{\partial t^2} = \frac{i}{2}\beta_2\Omega_m^2 A_m - \frac{\alpha}{2}A_m + i\gamma\Big(|A_m|^2 + 2\sum_{j\neq m}^{M}|A_j|^2\Big)A_m + i\gamma\sum_i\sum_j\sum_k A_i A_j A_k^*. \tag{4.3.2}$$

In the last term that takes into account FWM among various channels, the triple sum is restricted to only those frequency combinations that satisfy the FWM condition $\omega_m = \omega_i + \omega_j - \omega_k$. Fiber losses have been added to this equation for completeness.

An exact analysis of the FWM process in optical fibers requires a numerical approach. However, considerable physical insight can be gained by considering a single FWM term in the triple sum in Eq. (4.3.2) and focusing on the quasi-CW case so that time-derivative terms can be set to zero. If we neglect the phase shifts induced by SPM and XPM, assume that the three channels participating in the FWM process remain nearly undepleted, and eliminate the remaining β_2 term through the transformation $A_m = B_m\exp(i\beta_2\Omega_m^2 z/2 - \alpha z/2)$, the amplitude B_m of the FWM component is governed by

$$\frac{dB_m}{dz} = i\gamma B_i B_j B_k^*\exp(-\alpha z - i\Delta k z), \tag{4.3.3}$$

where the linear phase mismatch depends on the dispersion parameter as

$$\Delta k = \beta_2(\Omega_m^2 + \Omega_k^2 - \Omega_i^2 - \Omega_j^2). \tag{4.3.4}$$

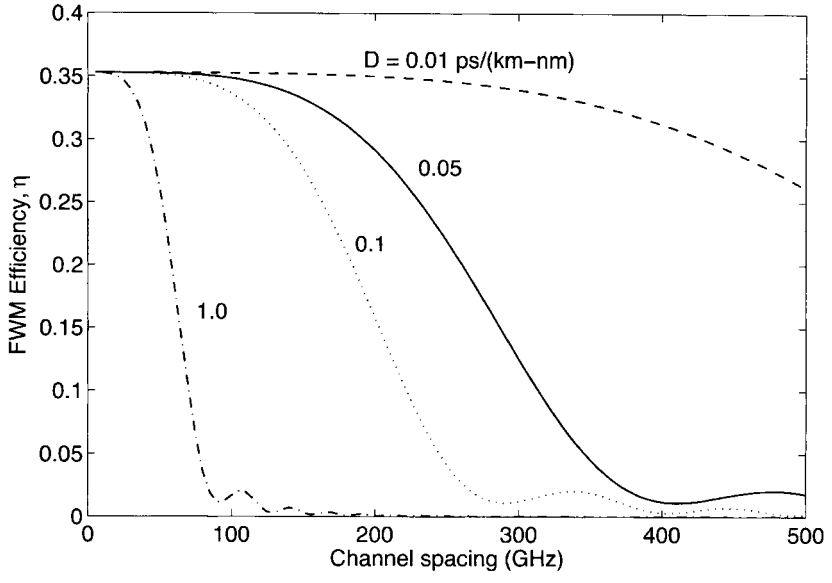

Figure 4.8: FWM efficiency plotted as a function of channel spacing for 25-km-long fibers with different dispersion characteristics. Fiber loss is assumed to be 0.2 dB/km in all cases.

Equation (4.3.3) can be easily integrated to obtain $B_m(z)$. The power transferred to the FWM component in a fiber of length L is given by [54]

$$|A_m(L)|^2 = \eta_{\text{FWM}}(\gamma L)^2 P_i P_j P_k e^{-\alpha L}, \tag{4.3.5}$$

where $P_j = |A_j(0)|^2$ is the power launched initially into the jth channel and η_{FWM} is the FWM efficiency defined as

$$\eta_{\text{FWM}} = \left| \frac{1 - \exp[-(\alpha + i\Delta k)L]}{(\alpha + i\Delta k)L} \right|^2. \tag{4.3.6}$$

The FWM efficiency η_{FWM} depends on the channel spacing through the phase mismatch Δk given in Eq. (4.3.4). Using the FWM condition, $\Omega_m = \Omega_i + \Omega_j - \Omega_k$, this mismatch can also be written as

$$\Delta k = \beta_2(\Omega_i - \Omega_k)(\Omega_j - \Omega_k) \equiv \beta_2(\omega_i - \omega_k)(\omega_j - \omega_k). \tag{4.3.7}$$

In the case of degenerate FWM for which both pump photons come from the same channel ($\Omega_i = \Omega_j$), the phase mismatch is given by $\Delta k = \beta_2(2\pi\Delta\nu_{\text{ch}})^2$, where $\Delta\nu_{\text{ch}}$ is the channel spacing. Figure 4.8 shows how η_{FWM} varies with $\Delta\nu_{\text{ch}}$ for several values of dispersion parameter D, related to β_2 as $D = (-2\pi c/\lambda_0^2)\beta_2$, using $\alpha = 0.2$ dB/km and $\lambda_0 = 1.55$ μm for a 25-km-long fiber. The FWM efficiency is relatively large for low-dispersion fibers even when channel spacing exceeds 100 GHz. In contrast, it nearly vanishes even for $\Delta\nu_{\text{ch}} = 50$ GHz when $D > 2$ ps/(km-nm).

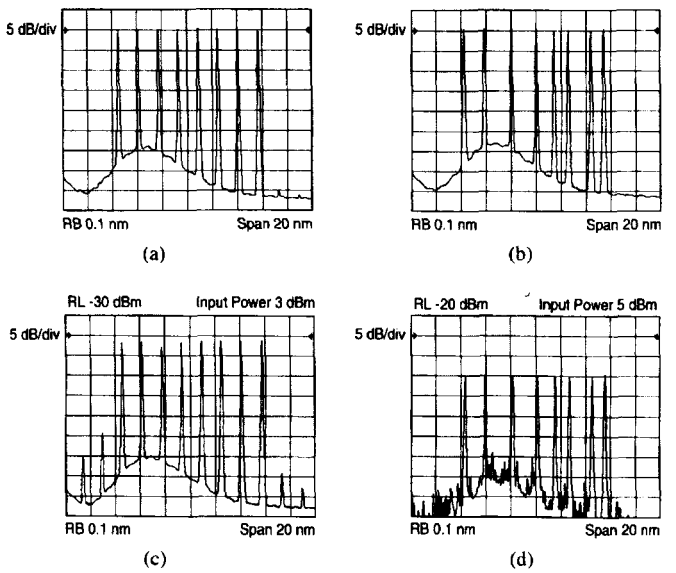

Figure 4.9: Input (a) and output (c) optical spectra for eight equally spaced channels launched with 3-dBm powers. Input (b) and output (d) optical spectra in the case of unequal channel spacings when launched power per channel is 5 dBm. (After Ref. [59]; ©1995 IEEE.)

If the dispersion parameter of the transmission fiber is relatively large ($|\beta_2| > 5$ ps^2/km), $\eta_{\rm FWM}$ nearly vanishes for typical channel spacings of 50 GHz or more used for WDM systems. In contrast, $\eta_{\rm FWM} \approx (\alpha L)^{-2}$ close to the zero-dispersion wavelength of the fiber as seen from Eq. (4.3.6) in the limit $\Delta k = 0$ and $\alpha L \gg 1$. Under such conditions, considerable power is transferred from each channel to several FWM components, especially when channel powers are relatively high. Figure 4.9(c) shows, as an example, the optical spectrum measured at the output of a 137-km-long fiber link (composed of dispersion-shifted fibers with the zero-dispersion wavelength near 1,540 nm) when eight channels, each with 2-mW average power, are launched into it [59]. This spectrum should be compared with the input spectrum shown in Figure 4.9(a). Multiple spectral components generated through FWM can be seen clearly in the output spectrum. Since the number of FWM components for an M-channel WDM system increases as $M^2(M-1)/2$ for an M-channel WDM system, the total power transferred from each channel to all FWM components can be quite large. In the case of equal channel powers, P_m increases as $P_{\rm ch}^3$. This cubic dependence of the FWM component limits the channel powers to below 1 mW when low-dispersion fibers are used for which the FWM is nearly phase-matched.

4.3.2 Control of FWM

The main issue from a system standpoint is how FWM affects the performance of a WDM system. When all channels are spaced equally in the frequency domain, it

follows from the FWM condition ($\omega_m = \omega_i + \omega_j - \omega_k$) that the frequencies of most FWM components will coincide with the channel frequencies. Under such conditions, FWM effects are not apparent in the spectral domain, as seen in Figure 4.9(c), except for uneven channel powers. However, their presence leads to an enhanced noise level in the time domain.

The origin of noise enhancement can be understood physically by noting that one or more FWM components interfere with the signal in a specific channel in a coherent fashion if they have the same carrier frequency. If channel powers were constant with time, this interference will not be a major problem since each channel that loses power through FWM also receives some power from neighboring channels, thereby roughly balancing the power transfer. However, the situation is much more complicated for channels containing optical bit streams that are neither synchronized in time nor have identical bit patterns. Moreover, these bit streams travel though the fiber at slightly different speeds because of the group-velocity mismatch. FWM can only occur when optical pulses are present simultaneously in the same time slot in at least two channels. Since near coincidence of bits in different channels occurs in a random fashion, FWM manifests as fluctuations in the power level of each channel, and the level of such fluctuations increases for low-dispersion fibers because FWM efficiency is enhanced for them.

A simple scheme for reducing the FWM-induced degradation consists of designing WDM systems with unequal channel spacings [59]. Figures 4.9(b) and 4.9(d) show the input and output optical spectra for an eight-channel WDM system when channel wavelengths are adjusted to ensure that none of the FWM components falls within the channel bandwidths. Similar to the case of equal channel spacings, new FWM components are generated but they do not interfere with the signal in a coherent fashion and thus do not degrade the SNR significantly. The average power of each channel is reduced because of FWM, but the reduction is nearly the same for all channels. In a 1999 experiment, this technique was used to transmit 22 channels, each operating at 10 Gb/s, over 320 km of dispersion-shifted fiber with 80-km amplifier spacing [66]. Channel spacings ranged from 125 to 275 GHz in the wavelength range of 1,532 to 1,562 nm and were determined using a periodic allocation scheme [68]. The zero-dispersion wavelength of the fiber was close to 1,548 nm, resulting in near phase matching of many FWM components. Nonetheless, the system performed quite well, because of unequal channel spacings, resulting in less than 1.5-dB power penalty for all channels.

The use of a nonuniform channel spacing is not always practical since many WDM components, such as Fabry–Perot filters and arrayed waveguide gratings (see Chapter 8 of LT1), operate on the assumption that channels are spaced apart equally. Also, such a scheme is spectrally inefficient, as the bandwidth of the resulting WDM signal is considerably larger compared with the case of equally spaced channels [59].

A practical solution is offered by the dispersion-management technique discussed in Section 3.3.4. In this scheme, fibers with normal and anomalous GVD are combined to form a periodic dispersion map such that GVD is locally high all along the fiber link, even though its average value is relatively low and can even be zero. As a result, the FWM efficiency η_F is negligible in each fiber section. As early as 1993, eight channels at 10 Gb/s could be transmitted over 280 km through dispersion management [69]. By 1996, the use of dispersion management had become quite common for FWM suppres-

sion in WDM systems because of its practical simplicity. FWM can also be suppressed by using fibers whose GVD varies along the fiber length [70].

Modulation instability can enhance the effects of FWM for certain specific values of channel spacing even when dispersion management is used and local GVD is relatively high [63]. The reason can be understood by noting that SPM and XPM, ignored in deriving Eq. (4.3.5), can produce phase matching even when $\beta_2 \neq 0$. It is possible to extend the preceding analysis and include the phase shifts induced by SPM and XPM [4]. It turns out that Eq. (4.3.5) can still be used but the phase-mismatch factor Δk in Eq. (4.3.7) is replaced with [65]

$$\Delta k \approx \beta_2(\omega_i - \omega_k)(\omega_j - \omega_k) + \gamma(P_i + P_j - P_k)[1 - \exp(-\alpha L_{\text{eff}})]/(\alpha L_{\text{eff}}). \quad (4.3.8)$$

Clearly, Δk may become close to zero for some FWM terms, depending on the channel powers and spacings, when β_2 is in the anomalous-GVD regime of the fiber. The corresponding FWM process will then become phase-matched, resulting in significant FWM efficiency.

One can understand such a FWM enhancement as follows. If the frequency at which the gain of modulation instability peaks nearly coincides with the channel spacing in a WDM system, modulation-instability sidebands will overlap with the neighboring channels. As a result, the FWM process will become enhanced resonantly in spite of the large value of the GVD parameter. We can estimate the channel spacing $\delta\nu_{\text{ch}}$ for which such resonant FWM is expected to occur using Eq. (4.1.28). Settimg the channel spacing equal to the gain-peak frequency, we obtain

$$\Omega_s = 2\pi\delta\nu_{\text{ch}} = (2\gamma P_{\text{ch}}/|\beta_2|)^{1/2}. \quad (4.3.9)$$

As a rough estimate, $\delta\nu_{\text{ch}} \approx 10$ GHz when $P_{\text{ch}} = 5$ mW, $\beta_2 = -5$ ps^2/km, and $\gamma = 2$ W^{-1}/km. Since channel spacing in modern WDM systems is typically 50 GHz or more, resonance enhancement of FWM can easily be avoided. However, it may become of concern for dense WDM systems designed with a channel spacing close to 10 GHz.

As discussed in Chapters 9 and 10 of LT1, FWM can be quite beneficial for certain applications related to lightwave systems. It is often used for demultiplexing individual channels when time-division multiplexing is used in the optical domain. It can also be employed for applications such as wavelength conversion and fast optical switching. FWM is sometimes used for generating a spectrally inverted signal through the process of *optical phase conjugation*. As discussed in Chapter 7, the phase-conjugation technique can be used for dispersion compensation. Fiber-optic parametric amplifiers (see Section 3.3 of LT1) constitute another application of FWM. In all such applications of FWM, the fiber-based device is pumped using one or two lasers whose wavelengths are chosen judiciously in the vicinity of the zero-dispersion wavelength of the fiber to enhance FWM efficiency.

4.4 Stimulated Raman Scattering

Rayleigh scattering, a major source of fiber losses, is an example of elastic scattering in which the frequency of scattered light remains unchanged. In contrast, the frequency is

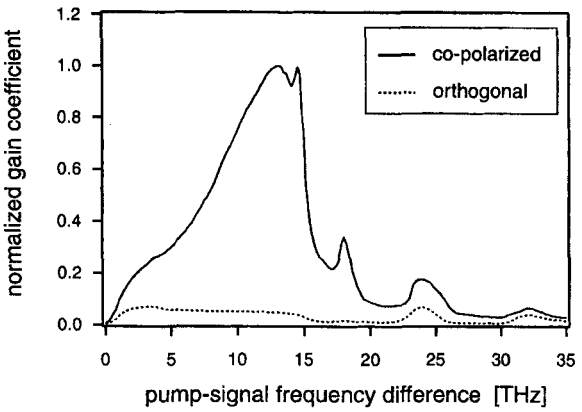

Figure 4.10: Raman gain coefficient (peak value normalized to 1) for silica fibers as a function of difference in the carrier frequency of the pump and signal when the two are copolarized (solid curve) or orthogonally polarized (dotted curve). The peak value is about 6×10^{-14} m/W for a pump near 1.5 μm. (After Ref. [95]; ©2004 IEEE.)

shifted downward during inelastic scattering. Raman and Brillouin processes provide two examples of inelastic scattering. Both of them can be understood as the conversion of a photon to a lower-energy photon such that the energy difference appears in the form of a phonon. The main difference between the two is that optical phonons (related to vibrations of silica molecules) participate in Raman scattering, whereas acoustic phonons participate in Brillouin scattering. The two processes are not of much concern for lightwave systems at low channel powers because the amount of power loss through spontaneous scattering is relatively small. However, they become stimulated at high power levels and affect the performance of lightwave systems considerably. This section focuses on stimulated Raman scattering (SRS).

4.4.1 Raman-Gain Spectrum

As discussed in Section 1.6.5 of LT1, the SRS process generates a Stokes wave from noise when the launched power exceeds a certain value. It can also amplify a signal when it is launched into the fiber together with a pump that supplies energy for the amplification process. SRS was first observed in optical fibers in 1972 using optical pulses with high peak powers [71]. Since then, the impact of SRS on the performance of lightwave systems has been studied extensively [72]–[92]. As discussed in Section 3.2, the SRS process is also beneficial for lightwave systems as it can be used to amplify WDM channels through distributed Raman amplification [93]–[95].

How much power is transferred from the pump to signal depends on the frequency spacing between them as well as on the fiber material. The Raman-gain spectrum of silica fibers shown in Figure 4.10 is extremely broad and spans a frequency range wider than 20 THz. The Raman gain also depends on the relative state of polarization of the pump and signal fields. It is largest when the two are copolarized (solid curve) and nearly vanishes if they are orthogonally polarized (dotted curve). The Raman shift,

corresponding to the location of the main peak in Figure 4.10, is close to 13 THz for silica fibers. The peak value of the Raman gain g_R at this frequency depends on the pump wavelength and is about 6×10^{-14} m/W in the wavelength region near 1.5 μm. When only the pump is launched into the fiber, a Stokes wave is generated from noise and its power grows exponentially when the pump power exceeds a certain value known as the Raman threshold. The frequency of the Stokes wave is downshifted from that of the pump by the Raman shift ν_R.

4.4.2 Raman Threshold

The SRS process in optical fibers is governed by the following set of two coupled nonlinear equations [4]:

$$\frac{dI_s}{dz} = g_R(\Omega) I_p I_s - \alpha_s I_s, \tag{4.4.1}$$

$$\frac{dI_p}{dz} = -\frac{\omega_p}{\omega_s} g_R(\Omega) I_p I_s - \alpha_p I_p, \tag{4.4.2}$$

where I_s and I_p are the intensities and α_s and α_p are fiber losses for the Stokes and pump waves at the carrier frequencies ω_s and ω_p, respectively. Noting that the quantity $I_j/(\hbar\omega_j)$ represents photon flux for a beam at frequency ω_j, these equations are like the rate equations that include the rates at which photons appear in or disappear from each beam. The term containing $g_R(\Omega)$, where $\Omega = \omega_p - \omega_s$ is the Raman shift, describes the conversion of pump photons to Stokes photons. As seen from Figure 4.10, the magnitude of g_R depends not only on Ω but also on whether the Stokes and pump are copolarized or orthogonally polarized.

Equations (4.4.1) and (4.4.2) are difficult to solve in general because of their nonlinear nature. However, they can be solved easily if we assume that the pump is so intense compared with the Stokes that its depletion can be ignored. If we neglect the g_R term in Eq. (4.4.2) and substitute its solution in Eq. (4.4.1), we obtain

$$dI_s/dz = g_R I_0 \exp(-\alpha_p z) I_s - \alpha_s I_s, \tag{4.4.3}$$

where I_0 is the pump intensity at $z = 0$. The preceding equation can be easily solved for a fiber of length L to obtain

$$I_s(L) = I_s(0) \exp(g_R I_0 L_{\text{eff}} - \alpha_s L), \tag{4.4.4}$$

where $L_{\text{eff}} = (1 - e^{-\alpha L})/\alpha$ is the effective fiber length introduced earlier.

In the case of a lightwave system, the impact of SRS depends on whether a single or multiple channels are being transmitted. In a single-channel system, a Stokes wave is not present initially, and it must be generated from noise. Even though SRS builds up from spontaneous Raman scattering occurring throughout the fiber length, this process is equivalent to injecting one fictitious photon per mode at the input end of the fiber [72]. Thus, we can calculate the Stokes power by considering amplification of each frequency component of energy $\hbar\omega$ as in Eq. (4.4.4) and then integrating over the entire bandwidth of the Raman-gain spectrum. This process results in the integral

$$P_s(L) = \int_{-\infty}^{\infty} \hbar\omega \exp[g_R(\omega_p - \omega) I_0 L_{\text{eff}} - \alpha_s L]\, d\omega, \tag{4.4.5}$$

where the frequency dependence of g_R results from the gain spectrum in Figure 4.10. Even though the functional form of $g_R(\Omega)$ is not known, the integral in Eq. (4.4.5) can be evaluated approximately using the method of steepest descent because the main contribution to the integral comes from a narrow region around the gain peak. The result is found to be [4]

$$P_s(L) = P_{s0}^{\text{eff}} \exp[g_R(\Omega_R) I_0 L_{\text{eff}} - \alpha_s L], \tag{4.4.6}$$

where the effective input power at $z = 0$ is given by

$$P_{s0}^{\text{eff}} = \hbar\omega_s \left(\frac{2\pi}{I_0 L_{\text{eff}}}\right)^{1/2} \left(\frac{\partial^2 g_R}{\partial \omega^2}\right)_{\omega=\omega_s}^{-1/2}. \tag{4.4.7}$$

The Raman threshold is defined as the input pump power at which the Stokes power becomes equal to the pump power at the fiber output [72], or

$$P_s(L) = P_p(L) \equiv P_0 \exp(-\alpha_p L), \tag{4.4.8}$$

where $P_0 = I_0 A_{\text{eff}}$ is the input pump power and A_{eff} is the effective core area. Using Eq. (4.4.6) in Eq. (4.4.8) and assuming $\alpha_s \approx \alpha_p$, the threshold condition becomes

$$P_{s0}^{\text{eff}} \exp(g_R P_0 L_{\text{eff}} / A_{\text{eff}}) = P_0. \tag{4.4.9}$$

The solution of this equation provides the pump power required to reach the Raman threshold. Assuming a Lorentzian shape for the Raman-gain spectrum, the threshold power can be estimated from the simple relation [72]

$$\frac{g_R P_{th} L_{\text{eff}}}{A_{\text{eff}}} \approx 16. \tag{4.4.10}$$

As before, we can replace L_{eff} with $1/\alpha$ for long fiber lengths used in lightwave systems. Using $g_R \approx 6 \times 10^{-14}$ m/W, P_{th} is about 500 mW in the spectral region near 1.55 μm. Since channel powers are limited to below 10 mW because of other nonlinear processes, SRS is not of much concern for single-channel systems.

The situation is quite different for WDM systems transmitting multiple channels spaced apart by 100 GHz or so. The same fiber in which channels propagate then acts as a distributed Raman amplifier such that each channel is amplified by all channels with a shorter wavelength as long as the wavelength difference is within the Raman-gain bandwidth. The shortest-wavelength channel is depleted most as it can pump all other channels simultaneously. Such an energy transfer among channels can be detrimental for system performance since it depends on the bit pattern—it occurs only when 1 bits are present in both channels simultaneously. The signal-dependent amplification leads to power fluctuations, resulting in a reduced SNR. Raman crosstalk can be avoided if channel powers are made so small that Raman amplification is negligible over the fiber-link length. This issue is discussed in Chapter 9 devoted to WDM systems.

4.5 Stimulated Brillouin Scattering

As discussed in Section 1.6.4 of LT1, SBS differs from SRS in several ways. First, it generates a Stokes wave only in the backward direction. Second, the Brillouin-gain spectrum of silica fibers is extremely narrow and typically spans a frequency range of less than 50 MHz. Third, the Brillouin shift ν_B, corresponding to the location of the gain peak, is only about 11 GHz for silica fibers in the wavelength region near 1.55 μm. The Brillouin shift depends on the acoustic velocity and scales inversely with the pump wavelength. Fourth, the peak value of the Brillouin gain g_B is larger by more than a factor of 100 compared with that of the Raman gain, a feature that makes SBS to occur at relatively low power levels. SBS in optical fibers was first observed in 1972 and has been studied extensively since then because of its implications for lightwave systems [96]–[101].

4.5.1 Brillouin Threshold

At low pump powers (<1 mW or so), not much power is reflected by spontaneous Brillouin scattering in the form of a Stokes wave. However, the situation changes when the power level exceeds a threshold value. The power of the Stokes wave grows exponentially beyond the SBS threshold. In fact, the fiber appears to act as a mirror far above this threshold because most of the pump power is reflected backward.

The SBS process in optical fibers is governed by a set of two coupled nonlinear equations that resembles Eqs. (4.4.1) and (4.4.2) with some minor differences and can be written as [4]:

$$-\frac{dI_s}{dz} = g_B(\Omega) I_p I_s - \alpha_s I_s, \tag{4.5.1}$$

$$\frac{dI_p}{dz} = -g_B(\Omega) I_p I_s - \alpha_p I_p, \tag{4.5.2}$$

where the Stokes is assumed to travel backward. Two simplifications are made in writing theses equations in view of the relatively small frequency difference between the pump and Stokes. First, we assume $\alpha_s = \alpha_p \equiv \alpha$. Second, we set the factor ω_p/ω_s appearing in Eq. (4.4.2) equal to 1. We also assume that the Stokes and pump are copolarized.

Similar to the SRS case, Eqs. (4.5.1) and (4.5.2) can be solved easily if we assume that the pump is so intense compared with the Stokes that its depletion can be ignored. If we neglect the g_B term in Eq. (4.5.2) and substitute the solution in Eq. (4.4.1), we obtain

$$dI_s/dz = -g_R I_0 \exp(-\alpha_p z) I_s + \alpha_s I_s, \tag{4.5.3}$$

where I_0 is the pump intensity at $z = 0$. This equation can be easily solved for a fiber of length L to obtain

$$I_s(0) = I_s(L) \exp(g_B P_0 L_{\text{eff}}/A_{\text{eff}} - \alpha L), \tag{4.5.4}$$

where L_{eff} is the effective fiber length and we used $P_0 = I_0 A_{\text{eff}}$, where P_0 is the input pump power. Note that the Stokes wave grows exponentially in the backward direction from an initial seed injected at the fiber output end at $z = L$.

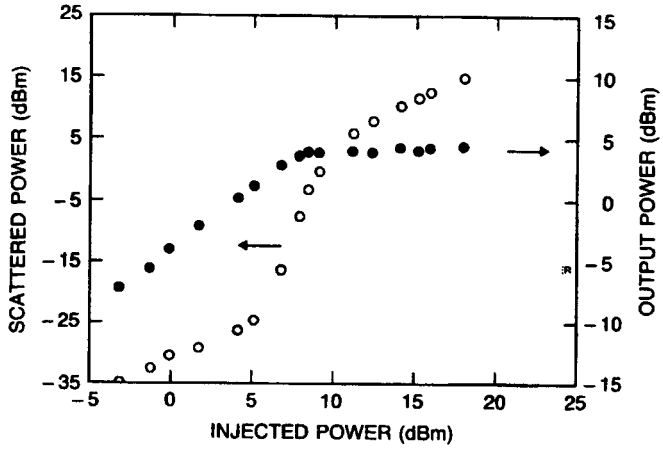

Figure 4.11: Transmitted (solid circles) and reflected (empty circles) powers as a function of input power injected into a 13-km-long fiber. (After Ref. [99], ©1992 IEEE.)

One can now follow a method similar to that used in the SRS case to find a fictitious input field at $z = L$. For a CW pump with a relatively narrow spectrum, the threshold power P_{th} is found from the condition [72]

$$g_B(\nu_B)P_{\text{th}}L_{\text{eff}}/A_{\text{eff}} \approx 21, \tag{4.5.5}$$

where $g_B(\nu_B)$ is the peak value of the Brillouin gain with a Lorentzian spectral profile [4]

$$g_B(\nu) = \frac{g_B(\nu_B)}{1+4(\nu-\nu_B)^2/(\Delta\nu_B)^2}, \tag{4.5.6}$$

and the Brillouin-gain bandwidth $\Delta\nu_B$ is related inversely to the decay time of acoustic phonons ($\sim$100 ns). Both the Brillouin shift ν_B and the gain bandwidth $\Delta\nu_B$ can vary from fiber to fiber because of the presence of dopants in the fiber core. For long fibers such that $\alpha L \gg 1$, one can use $L_{\text{eff}} \approx 1/\alpha \approx 21.74$ km when $\alpha = 0.2$ dB/km. Using $g_B \approx 5 \times 10^{-11}$ m/W and $A_{\text{eff}} = 50\ \mu\text{m}^2$ as typical values, the threshold power P_{th} for the SBS onset can be as low as 1 mW for CW signals in the wavelength region near 1.55 μm [97].

Figure 4.11 shows how the transmitted and reflected powers change for a 13-km-long dispersion-shifted fiber as the injected CW power is increased from 0.5 to 50 mW. At low power levels, the reflected signal consists of only 4% of input power and has its origin in the Fresnel reflection at the fiber–air interface occurring when light is coupled to the fiber. The Brillouin threshold is reached at a power level of about 5 mW. The reflected power increases rapidly after this threshold and consists of mostly SBS-generated Stokes radiation. No more than 3 mW could be transmitted through the fiber in this experiment after the onset of SBS.

The SBS threshold increases for CW beams whose spectral width is larger than the Brillouin-gain bandwidth that varies from fiber to fiber to some extent but falls typically in the range of $\Delta\nu_B$ = 20 to 50 MHz. It also increases when short optical pulses

propagate through the fiber because of their relatively wide bandwidth. In lightwave systems, the optical signal is in the form of a bit stream that consists of pulses whose widths depend on the bit rate as well as on the modulation format employed. Considerable attention has been paid to estimating the Brillouin threshold and quantifying the SBS limitations for practical lightwave systems [102]–[107]. The Brillouin threshold of an optical bit stream is higher than that of a CW signal, but the amount by which the threshold power increases depends on the modulation format used for data transmission.

Calculation of the Brillouin threshold for an optical bit stream is quite involved as it requires a time-dependent analysis [102]. Considerable simplification occurs if the bit rate B is assumed to be much larger than the Brillouin-gain line width $\Delta\nu_B$. Even with this assumption, the analysis is complicated by the fact that the 1 and 0 bits do not follow a fixed pattern. A simple approach assumes that the situation is equivalent to that of a CW pump whose spectrum corresponds to that caused by a random bit pattern. This is justified by noting that the backward nature of the SBS-generated Stokes wave tends to average out time-dependent fluctuations. A surprising result of such an approximate analysis is that the Brillouin threshold increases by about a factor of 2 irrespective of the actual bit rate of the system. As a result, input powers of up to about 10 mW can be injected into a fiber link without the onset of SBS. Since channel powers rarely exceed 5 mW in most WDM lightwave systems for various other reasons, SBS is not of much practical concern for such systems. In particular, it does not produce interchannel crosstalk unless the same fiber link is used to transmit WDM signals in both directions. Even then, the two counterpropagating channels have to be separated in frequency by precisely the Brillouin shift (about 11 GHz) before any crosstalk can occur.

In modern WDM systems, fiber losses are compensated periodically using optical amplifiers. An important question is how amplifiers affect the SBS process. If the Stokes wave were amplified by amplifiers, it would accumulate over the entire link and grow enormously. Fortunately, periodically amplified lightwave systems commonly employ an optical isolator within each amplifier unit that blocks the passage of the Stokes wave. However, the SBS growth between two amplifiers is still undesirable for two reasons. First, it removes power from the signal once the signal power exceeds the threshold level. Second, it induces large fluctuations in the remaining signal, resulting in degradation of the SNR [100]. For these reasons, channel powers are invariably kept below the SBS threshold and are limited in practice to below 10 mW.

4.5.2 Control of SBS

Some applications require launch powers in excess of 10 mW. An example is provided by the shore-to-island fiber links designed to transmit information over several hundred kilometers without employing in-line amplifiers or repeaters [108]–[110]. Input power levels in excess of 50 mW are needed for distances >300 km. One must raise the Brillouin threshold before such power levels can be transmitted through the fiber link, and several schemes have been proposed for this purpose [111]–[118]. These schemes rely on increasing either the Brillouin-gain bandwidth $\Delta\nu_B$ or the spectral width of optical carrier. The former has a value in the range of 20 to 50 MHz for silica fibers, while

the latter is typically <10 MHz for DFB lasers used commonly for systems operating at bit rates above 2 Gb/s. The bandwidth of an optical carrier can be increased by modulating its phase at a frequency much lower than the bit rate. Typically, the modulation frequency $\Delta\nu_m$ is chosen in the range of 200 to 400 MHz. Since the effective Brillouin gain is reduced by a factor of $(1 + \Delta\nu_m/\Delta\nu_B)$ (see Section 1.6.4 of LT1), the SBS threshold increases by the same factor. The launched power can be increased by more than a factor of 10 by the phase-modulation technique.

If the Brillouin-gain bandwidth $\Delta\nu_B$ of the fiber itself can be increased from its nominal value of 20 to 50 MHz to more than 200 MHz, the SBS threshold can be increased without requiring a phase modulator. One technique applies sinusoidal strain along the fiber length for this purpose. The applied strain changes the Brillouin shift ν_B by a few percent in a periodic manner. The resulting Brillouin-gain spectrum is much broader than that occurring for a fixed value of ν_B. The strain can be applied during cabling of the fiber. In one fiber cable, $\Delta\nu_B$ was found to increase from 50 MHz to 400 MHz [114]. The Brillouin shift ν_B can also be changed by making the core radius nonuniform along the fiber length since the longitudinal acoustic frequency depends on the core radius [115]. The same effect can be realized by changing the dopant concentration along the fiber length. In a 1996 experiment, this technique increased the SBS threshold of one fiber by 7 dB [116]. A side effect of varying the core radius or the dopant concentration is that the GVD parameter β_2 also changes along the fiber length. It is possible to vary the two simultaneously in such a way that β_2 remains relatively uniform [118].

4.6 Nonlinear Pulse Propagation

Among the five nonlinear effects discussed so far, SRS and SBS are avoided in practice by lowering channel powers to below 5 mW or so. FWM can also be nearly eliminated by managing fiber dispersion or channel spacings. The remaining two, SPM and XPM, are harder to control unless channel powers are made so small that the entire fiber link acts as a linear medium. This is not feasible for long-haul systems because the noise added by amplifiers degrades the SNR as the link length increases.

The effects of SPM, XPM, as well as FWM can be included by solving the NLS equation (4.1.2) numerically. However, considerable physical insight is gained if this equation can be solved approximately in an analytic or semianalytic fashion. In this section we consider the simplest single-channel case and employ two analytic techniques for solving the NLS equation.

4.6.1 Moment Method

The moment method was used as early as 1971 for nonlinear optical systems [119]. It can be used to solve the NLS equation (4.1.2) approximately, provided one can assume that the pulse maintains a specific shape as it propagates down a fiber link even though its amplitude, width, and chirp change continuously [120]–[122]. This assumption holds reasonably well in many cases of practical interest. For example, it was seen in Section 3.3 that a Gaussian pulse maintains its shape in a linear dispersive medium

even though its amplitude, width, and chirp change during propagation. Let us assume that the Gaussian shape remains approximately valid when the nonlinear effects are relatively weak.

The basic idea behind the moment method is to treat the optical pulse like a particle whose energy E, RMS width σ, and chirp C are defined as

$$E = \int_{-\infty}^{\infty} |U|^2 dt, \qquad \sigma^2 = \frac{1}{E}\int_{-\infty}^{\infty} t^2 |U|^2 dt, \tag{4.6.1}$$

$$C = \frac{i}{E}\int_{-\infty}^{\infty} t\left(U^*\frac{\partial U}{\partial t} - U\frac{\partial U^*}{\partial t}\right) dt. \tag{4.6.2}$$

As the pulse propagates inside the fiber, these parameters change. To find how they evolve with z, we differentiate Eqs. (4.6.1) and (4.6.2) with respect to z and use Eq. (4.1.2). After some algebra, we find that $dE/dz = 0$ but σ^2 and C satisfy

$$\frac{d\sigma^2}{dz} = \frac{\beta_2}{E}\int_{-\infty}^{\infty} t^2 \mathrm{Im}\left(U^*\frac{\partial^2 U}{\partial t^2}\right) dt, \tag{4.6.3}$$

$$\frac{dC}{dz} = \frac{2\beta_2}{E}\int_{-\infty}^{\infty}\left|\frac{\partial U}{\partial t}\right|^2 dt + \frac{\gamma P_0}{E}p(z)\int_{-\infty}^{\infty}|U|^4 dt. \tag{4.6.4}$$

In the case of a chirped Gaussian pulse, the field $U(z,t)$ at any distance z has the form

$$U(z,t) = a\exp[-\tfrac{1}{2}(1+iC)(t/T)^2 + i\phi], \tag{4.6.5}$$

where all four pulse parameters, a, C, T, and ϕ, are functions of z. The phase ϕ does not appear in Eqs. (4.6.3) and (4.6.4). Even though it changes with z, it does not affect other pulse parameters and can be ignored. The peak amplitude a is related to the energy as $E = \sqrt{\pi}a^2 T$. Since E does not change with z, we can replace it with its initial value $E_0 = \sqrt{\pi}T_0$. The width parameter T is related to the RMS width σ of the pulse as $T = \sqrt{2}\sigma$. Using Eq. (4.6.5) and performing integrals in Eqs. (4.6.3) and (4.6.4), the width T and chirp C are found to change with z as

$$\frac{dT}{dz} = \frac{\beta_2 C}{T}, \tag{4.6.6}$$

$$\frac{dC}{dz} = (1+C^2)\frac{\beta_2}{T^2} + \gamma P_0 \frac{p(z)}{\sqrt{2}}\frac{T_0}{T}. \tag{4.6.7}$$

This set of two first-order differential equations can be used to find how the nonlinear effects modify the width and chirp of the pulse.

Considerable physical insight can be gained from Eqs. (4.6.6) and (4.6.7). The SPM phenomenon does not affect the pulse width directly as the nonlinear parameter γ appears only in the chirp equation (4.6.7). The two terms on the right side of this equation originate from dispersive and nonlinear effects, respectively. They have the same sign for normal GVD ($\beta_2 > 0$). Since SPM-induced chirp in this case adds to the GVD-induced chirp, we expect SPM to increase the rate of pulse broadening. In contrast, when GVD is anomalous ($\beta_2 < 0$), the two terms on the right side of Eq. (4.6.7) have opposite signs, and the pulse broadening should be reduced in the presence

of SPM because of smaller values of C in Eq. (4.6.6). In fact, this equation can be integrated to obtain the following general relation between pulse width and chirp:

$$T^2(z) = T_0^2 + 2\int_0^z \beta_2(z)C(z)\,dz. \tag{4.6.8}$$

The equation shows explicitly that the pulse compresses whenever the quantity $\beta_2 C < 0$, a result obtained earlier in Section 3.3.

4.6.2 Variational Method

The variational method is well known from classical mechanics and is used in many different contexts [123]–[125]. It was applied as early as 1983 to the problem of pulse propagation inside optical fibers [14]. Mathematically, it makes use of the Lagrangian $\mathscr{L}$ defined as

$$\mathscr{L} = \int_{-\infty}^{\infty} \mathscr{L}_d(q,q^*)\,dt, \tag{4.6.9}$$

where the Lagrangian density $\mathscr{L}_d$ is a function of the generalized coordinate $q(z)$ and $q^*(z)$, both of which evolve with z. Minimization of the "action" functional, $\mathscr{S} = \int \mathscr{L}\,dz$, requires that $\mathscr{L}_d$ satisfy the Euler–Lagrange equation

$$\frac{\partial}{\partial t}\left(\frac{\partial \mathscr{L}_d}{\partial q_t}\right) + \frac{\partial}{\partial z}\left(\frac{\partial \mathscr{L}_d}{\partial q_z}\right) - \frac{\partial \mathscr{L}_d}{\partial q} = 0, \tag{4.6.10}$$

where q_t and q_z denote the derivative of q with respect to t and z, respectively.

The variational method makes use of the fact that the NLS equation (4.1.2) can be derived from the Lagrangian density

$$\mathscr{L}_d = \frac{i}{2}\left(U^*\frac{\partial U}{\partial z} - U\frac{\partial U^*}{\partial z}\right) + \frac{\beta_2}{2}\left|\frac{\partial U}{\partial t}\right|^2 + \tfrac{1}{2}\gamma P_0 p(z)|U|^4, \tag{4.6.11}$$

with U^* acting as the generalized coordinate q in Eq. (4.6.10). If we assume that the pulse shape is known in advance in terms of a few parameters, the time integration in Eq. (4.6.9) can be performed analytically to obtain the Lagrangian $\mathscr{L}$ in terms of these pulse parameters. In the case of a chirped Gaussian pulse of the form given in Eq. (4.6.5), we obtain

$$\mathscr{L} = \frac{\beta_2 E}{4T^2}(1+C^2) + \frac{\gamma p(z)E^2}{\sqrt{8\pi}T} + \frac{E}{4}\left(\frac{dC}{dz} - \frac{2C}{T}\frac{dT}{dz}\right) - E\frac{d\phi}{dz}, \tag{4.6.12}$$

where $E = \sqrt{\pi}a^2 T$ is the pulse energy.

The final step is to minimize the action $\mathscr{S} = \int \mathscr{L}(z)\,dz$ with respect to the four pulse parameters. This step results in the reduced Euler–Lagrange equation

$$\frac{d}{dz}\left(\frac{\partial \mathscr{L}}{\partial q_z}\right) - \frac{\partial \mathscr{L}}{\partial q} = 0, \tag{4.6.13}$$

where $q_z = dq/dz$ and q represents one of the pulse parameters. If we use $q = \phi$ in Eq. (4.6.13), we obtain $dE/dz = 0$. This equation indicates that the energy E remains

constant, as expected. Using $q = E$ in Eq. (4.6.13), we obtain the following equation for pulse phase ϕ:

$$\frac{d\phi}{dz} = \frac{\beta_2}{2T^2} + \frac{5\gamma p(z)E}{4\sqrt{2\pi}T}. \tag{4.6.14}$$

We can follow the same procedure to obtain equations for T and C. In fact, using $q = C$ and T in Eq. (4.6.13), we find that pulse width and chirp satisfy the same two equations, namely Eqs. (4.6.6) and (4.6.7) obtained earlier with the moment method. Thus, the two approximate methods lead to identical results in the case of the NLS equation.

4.6.3 Specific Analytic Solutions

As a simple application of the moment or variational method, consider first the case of a low-energy pulse propagating in a constant-dispersion fiber with negligible nonlinear effects. Recalling that $(1+C^2)/T^2$ is related to the spectral width of the pulse that does not change in a linear medium, we can replace this quantity with its initial value $(1+C_0^2)/T_0^2$, where T_0 and C_0 are input values at $z = 0$. Since the second term is negligible in Eq. (4.6.7), it can be integrated easily and provides the solution

$$C(z) = C_0 + s(1+C_0^2)z/L_D, \tag{4.6.15}$$

where $s = \text{sgn}(\beta_2)$ and $L_D = T_0^2/|\beta_2|$ is the dispersion length. Using this solution in Eq. (4.6.8), we find that the pulse width changes as

$$T^2(z) = T_0^2[1 + 2sC_0(z/L_D) + (1+C_0^2)(z/L_D)^2]. \tag{4.6.16}$$

It is easy to verify that these expressions agree with those obtained in Section 3.3.1 by solving the pulse propagation equation directly.

To solve Eqs. (4.6.6) and (4.6.7) in the nonlinear case, we make two approximations. First, we assume that fiber losses are compensated such that $p(z) = 1$ (ideal distributed amplification). Second, the nonlinear effects are weak enough that the chirp at any distance z can be written as $C = C_L + C'$, where the nonlinear part $C' \ll C_L$. It is easy to see that the linear part is given by Eq. (4.6.15), while the nonlinear part satisfies

$$\frac{dC'}{dz} = \frac{\gamma P_0}{\sqrt{2}}\frac{T_0}{T}. \tag{4.6.17}$$

Dividing Eqs. (4.6.6) and (4.6.17), we obtain

$$\frac{dC'}{dT} = \frac{\gamma P_0 T_0}{\sqrt{2}\beta_2 C} \approx \frac{\gamma P_0 T_0}{\sqrt{2}\beta_2 C_L}, \tag{4.6.18}$$

where we replaced C with C_L as $C' \ll C_L$. This equation is now easy to solve, and the result can be written as

$$C'(z) = \frac{\gamma P_0 T_0}{\sqrt{2}\beta_2 C_L}(T - T_0). \tag{4.6.19}$$

Once $C = C_L + C'$ is known, the pulse width can be found from Eq. (4.6.8).

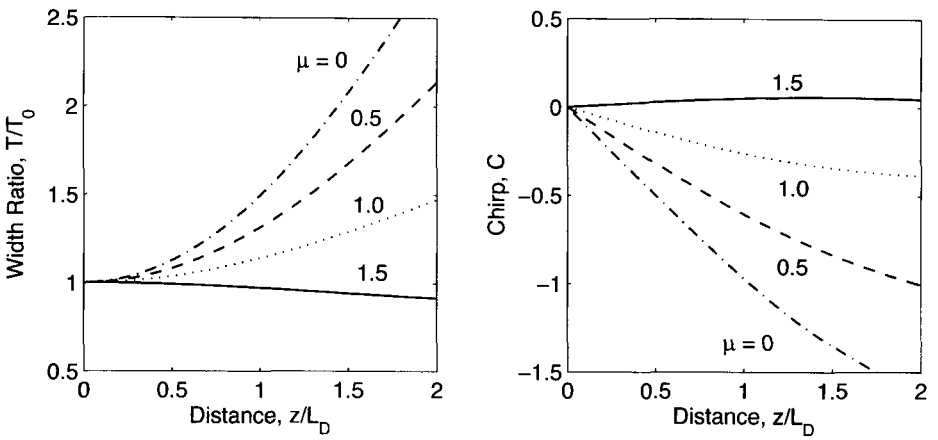

Figure 4.12: Width ratio T/T_0 and chirp C as a function of propagation distance z for an input Gaussian pulse with parameters such that $\gamma P_0 L_D = 0.1$. The solid and dashed curves show the exact and approximate solutions, respectively.

The preceding analytic solution can only be used when the parameter μ, defined as $\mu = \gamma P_0 L_D = L_D/L_{\rm NL}$, is less than 0.3 or so. However, one can easily solve Eqs. (4.6.6) and (4.6.7) numerically for any value of μ. Figure 4.12 shows changes in T/T_0 and C as a function of z/L_D for several values of μ assuming that input pulses are unchirped ($C_0 = 0$) and propagate in the region of anomalous regime ($s = -1$). In the linear case ($\mu = 0$), pulse broadens rapidly and develops considerable chirp, and the results reduce to those obtained in Section 3.3.1. However, as the nonlinear effects increase and μ becomes larger, pulse broadens less and less. Eventually, it even begins to compress, as seen in Figure 4.12 for $\mu = 1.5$.

The behavior seen in Figure 4.12 can be understood in terms of the SPM-induced chirp as follows. As seen from Eq. (4.6.7), the two terms on its right side have opposite signs when $\beta_2 < 0$. As a result, SPM tends to cancel the dispersion-induced chirp, and reduces pulse broadening. For a certain value of the nonlinear parameter μ, the two terms nearly cancel, and pulse width does not change much with propagation. For even larger values of μ, pulse may even compress, at least initially. In the case of normal dispersion ($s = 1$), the two terms on the right side have the same sign. Since SPM enhances the dispersion-induced chirp, pulse broadens even faster than that expected in the absence of SPM. Clearly, the anomalous-dispersion regime is useful for lightwave systems as the nonlinear effects in this case help to control pulse broadening. As discussed in Section 8.2, the results seen in Figure 4.12 point to the possibility of soliton formation. It should be stressed that Eqs. (4.6.6) and (4.6.7) are only approximately valid in this regime because of a "sech" shape associated with solitons.

To show how the combination of SPM and GVD can lead to the formation of solitons, we replace Eq. (4.6.7) with

$$U(z,t) = a\,\mathrm{sech}(t/T)\exp[-iC(t/T)^2 + i\phi]. \tag{4.6.20}$$

We can now use the moment method, or the variational method, to study how pulse parameters evolve with z. For example, when we employ the variational method, we obtain the following expression for the Lagrangian:

$$\mathscr{L} = \frac{\beta_2 E}{6T^2}\left(1+\frac{\pi^2}{4}C^2\right) + \frac{\gamma p(z)E^2}{6T} + \frac{\pi^2 E}{24}\left(\frac{dC}{dz} - \frac{2C}{T}\frac{dT}{dz}\right) - E\frac{d\phi}{dz}. \tag{4.6.21}$$

Using $q = C$ and T in Eq. (4.6.13) with this form of $\mathscr{L}$, we find that the pulse width still satisfies Eq. (4.6.6), but the chirp equation (4.6.7) is modified slightly to become

$$\frac{dC}{dz} = \left(C^2 + \frac{4}{\pi^2}\right)\frac{\beta_2}{T^2} + \gamma P_0 p(z)\frac{4}{\pi^2}\frac{T_0}{T}. \tag{4.6.22}$$

It is useful to introduce a normalized time variable as $\tau = T/T_0$ and write the chirp equation in the form

$$L_D\frac{dC}{dz} = \left(C^2 + \frac{4}{\pi^2}\right)\frac{s}{\tau^2} + \gamma P_0 L_D \frac{4}{\pi^2 \tau}, \tag{4.6.23}$$

where L_D is the dispersion length and we have set $p(z) = 1$, assuming ideal distributed amplification. If the pulse is unchirped initially, $C = 0$ and $\tau = 1$ at $z = 0$. Equation (4.6.23) shows that $dC/dz = 0$ in the case of anomalous dispersion ($s = -1$) if the peak power of the pulse satisfies the condition $\gamma P_0 L_D = L_D/L_{\rm NL} = 1$. Thus, $C(z)$ remains zero during propagation, and $T(z) = T_0$ from Eq. (4.6.6). Under such conditions, a sech-shape pulse maintains its width in spite of the SPM and GVD because the chirps induced by them cancel precisely. This pulse is known as a soliton and its formation requires that dispersive and nonlinear lengths be equal ($L_D = L_{\rm NL}$). In terms of the fiber and pulse parameters, the peak power of the pulse should be chosen such that $P_0 = |\beta_2|/(\gamma T_0^2)$.

4.7 Polarization Effects

In this section we return to the polarization issue. So far in this chapter, we have assumed that the state of polarization (SOP) of the electric field vector remains unchanged inside the nonlinear dispersive medium in which optical pulses are propagating. As discussed in Section 3.4, this is not really the case in optical fibers. Because of a fluctuating residual birefringence of fibers, the SOP of any optical field changes inside the fiber in a random fashion. Since most nonlinear effects depend on the SOPs of the interacting fields, their impact on the optical signal is also affected by the residual birefringence of fibers.

4.7.1 Vector NLS equation

To find a vectorial form of the NLS equation, we follow the Jones-matrix formalism of Section 3.4.3 and write the optical field in the form of Eq. (3.4.6). In the linear case ($\gamma = 0$), the Jones vector $|A\rangle$ satisfies Eq. (3.4.11). We need to add the nonlinear terms

to this equation to obtain the vector NLS equation. Such a equation has been studied in the context of solitons [126]–[138].

Both SPM and XPM have their origin in the third-order nonlinear response of the medium in which light is propagating. If we neglect the nuclear contribution, and consider only the fast electronic response, the third-order nonlinear polarization has the general form [4]

$$\boldsymbol{P}^{(3)}(\boldsymbol{r},t) = \varepsilon_0 \chi^{(3)} \vdots \boldsymbol{E}(\boldsymbol{r},t)\boldsymbol{E}(\boldsymbol{r},t)\boldsymbol{E}(\boldsymbol{r},t), \tag{4.7.1}$$

where ε_0 is the vacuum permittivity, $\boldsymbol{E}$ is the electric field vector, and the tensor $\chi^{(3)}$ represents the third-order susceptibility. Writing $\boldsymbol{E}$ in terms of the Jones vector as

$$\boldsymbol{E}(\boldsymbol{r},t) = \mathrm{Re}[F(x,y)|A(z,t)\rangle \exp(i\beta_{\mathrm{av}} z - i\omega_0 t)], \tag{4.7.2}$$

and making use of the symmetry properties of the $\chi^{(3)}$ tensor [139], we obtain

$$\boldsymbol{P}^{(3)}(\boldsymbol{r},t) = \frac{\varepsilon_0}{4}\chi^{(3)}_{1111}|F(x,y)|^3 [2\langle A|A\rangle + |A^*\rangle\langle A^*|]\,|A\rangle. \tag{4.7.3}$$

We can now use Maxwell's equations and follow the treatment of Section 3.4 to obtain the following vectorial form of the NLS equation:

$$\frac{\partial|A\rangle}{\partial z} + \frac{\Delta\beta_1}{2}\sigma_1\frac{\partial|A\rangle}{\partial t} + \frac{i\beta_2}{2}\frac{\partial^2|A\rangle}{\partial t^2} + \frac{\alpha}{2}|A\rangle - \frac{i}{2}\Delta\beta_0\sigma_1|A\rangle = i\gamma\left(\langle A|A\rangle|A\rangle - \frac{1}{3}\langle A|\sigma_3|A\rangle\sigma_3|A\rangle\right), \tag{4.7.4}$$

where $\Delta\beta_0$ and $\Delta\beta_1$ are defined as in Eq. (3.4.8), σ_1 is the Pauli matrix given in Eq. (3.4.12), and we make use of the identity [53]

$$|A^*\rangle\langle A^*| = |A\rangle\langle A| - \langle A|\sigma_3|A\rangle\sigma_3. \tag{4.7.5}$$

The nonlinear parameter $\gamma = n_2\omega_0/(cA_{\mathrm{eff}})$ is defined, as before, with $n_2 = 3\chi^{(3)}_{1111}/(8n_c)$, n_c being the refractive index of the fiber core. The two terms on the right side of Eq. (4.7.4) account for the nonlinear effects. They include the XPM-induced nonlinear coupling between the two polarization components of the optical field. This coupling represents the new feature when polarization effects are included. Whereas only SPM effects occur in the scalar case, XPM coupling between the orthogonally polarized components of the same field must be considered in the vector case.

Fiber birefringence is assumed to be constant in deriving Eq. (4.7.4). To include its random variations, we need to work in a rotating frame and introduce the transformation $|A\rangle = \overline{R}|A'\rangle$, where $\overline{R}$ is a random rotation matrix given in Eq. (3.4.12). In the rotating frame, as seen in Eq. (3.4.11), each Pauli matrix σ_j in Eq. (4.7.4) is replaced with a random matrix $\overline{M}_j = \overline{R}^{-1}\sigma_j\overline{R}$. The term containing $\Delta\beta_0$ only changes the phase in a random fashion and can be eliminated by another transformation $|A'\rangle = \overline{W}|A''\rangle$, where $\overline{W}$ represents a unitary matrix obtained by solving Eq. (3.4.15). With these two transformations, Eq. (4.7.4) reduces to

$$\frac{\partial|A\rangle}{\partial z} + \frac{\Delta\beta_1}{2}\bar{r}_1\frac{\partial|A\rangle}{\partial t} + \frac{i\beta_2}{2}\frac{\partial^2|A\rangle}{\partial t^2} + \frac{\alpha}{2}|A\rangle = i\gamma\left(\langle A|A\rangle|A\rangle - \frac{1}{3}\langle A|\bar{r}_3|A\rangle\bar{r}_3|A\rangle\right), \tag{4.7.6}$$

where $\overline{r}_j = \overline{W}^{-1}\overline{M}_j\overline{W}$ is a random unitary matrix, and for simplicity of notation, we have dropped the primes over $|A\rangle$.

4.7.2 Manakov Equation

Equation (4.7.6) is the vector NLS equation governing pulse propagation in a realistic fiber in which residual birefringence varies randomly along the fiber length. It includes not only the dispersive and nonlinear effects but also the PMD effects. It must be solved numerically in general. Even a numerical solution is not easy to obtain because of different length scales associated with the PMD, GVD, and SPM phenomena. Birefringence in a typical optical fiber varies on a length scale of 10 to 100 m, while the dispersive and nonlinear effects vary on length scales ranging from 10 to 100 km. Thus, one must use a step size of <1 m even when the fiber link length exceeds 1,000 km, requiring a long computation time. Moreover, as Eq. (4.7.6) is a stochastic equations, it must be solved hundreds of times before any averages can be computed. The net result is that a direct integration of Eq. (4.7.6) is rarely practical.

The vast disparity among various length scales permits one to employ an approximate approach for solving Eq. (4.7.6). The underlying idea makes use of the observation that birefringence fluctuations change the SOP of the optical field on such a short length scale that the tip of the Stokes vector associated with the field covers nearly the entire Poincaré sphere after a few kilometers. As a result, if the nonlinear length L_{NL} exceeds 10 km or so, one can average the nonlinear terms in Eq. (4.7.6) over birefringence fluctuations [127]. The averaging procedure involves writing the random unitary matrix $\overline{r}_3$ in terms of the two angles θ and ϕ that specify the position of the Stokes vector on the Poincaré sphere and average over them. The result is found to be [129]

$$\overline{\langle A|\overline{r}_3|A\rangle\overline{r}_3|A\rangle} = \frac{1}{3}\langle A|A\rangle|A\rangle, \tag{4.7.7}$$

where an overbar indicates averaging over both θ and ϕ. Using Eq. (4.7.7) in Eq. (4.7.6), we obtain

$$\frac{\partial|A\rangle}{\partial z} + \frac{\Delta\beta_1}{2}\overline{r}_1\frac{\partial|A\rangle}{\partial t} + \frac{i\beta_2}{2}\frac{\partial^2|A\rangle}{\partial t^2} + \frac{\alpha}{2}|A\rangle = \frac{8}{9}i\gamma\langle A|A\rangle|A\rangle. \tag{4.7.8}$$

It is clear from Eq. (4.7.8) that the main effect of rapid random variations in the SOP of the optical field is to reduce the nonlinear parameter γ by a factor of 8/9. Note that the nonlinear term still couples the orthogonally polarized components A_x and A_y of the field through XPM. This can be seen by noting that $\langle A|A\rangle = |A_x|^2 + |A_y|^2$. An interesting feature is that the strength of the SPM and XPM effects is the same in Eq. (4.7.8), even though it differs by a factor of 2/3 in the case of fibers with constant birefringence.

Equation (4.7.8) still includes the PMD effects through the $\Delta\beta_1$ term that leads to different group velocities for the two orthogonally polarized components of a pulse. Because $\overline{r}_1$ is a random matrix, the speed difference between them varies in a random fashion. It is found, both theoretically and experimentally, that the XPM-induced coupling between the two polarization components reduces the impact of PMD [134]–[138]. This is especially so for modern fibers with relatively low values of the PMD

parameter. Under such conditions, one can ignore the PMD term, at least to the first order. If we also introduce the normalization indicated in Eq. (4.1.1), we obtain

$$\frac{\partial|U\rangle}{\partial z}+\frac{i\beta_2}{2}\frac{\partial^2|U\rangle}{\partial t^2}=\frac{8}{9}i\gamma P_0 p(z)\langle U|U\rangle|U\rangle. \tag{4.7.9}$$

This deterministic equation is known as the Manakov equation [140] who first found its soliton-like solutions in the case of $p(z)=1$. It turns out that, when SPM and XPM have equal strengths, this set of two coupled NLS equations is integrable through the inverse scattering method.

Problems

4.1 Solve the NLS equation

$$\frac{\partial A}{\partial z}+\frac{i\beta_2}{2}\frac{\partial^2 A}{\partial t^2}=i\gamma|A|^2A-\frac{\alpha}{2}A,$$

in the limit of zero dispersion ($\beta_2=0$) and derive an expression for the SPM-induced nonlinear phase shift for pulses of arbitrary shape. How is this shift affected by fiber losses?

4.2 Apply the result of Problem 4.1 to input pulses with $A(0,t)=\sqrt{P_0}\,\mathrm{sech}(t/T_0)$ and plot the frequency chirp as a function of time at the output of a 25-km-long fiber. Assume $\alpha=0.2$ dB/km, $\gamma=2$ W^{-1}/km, and 5-ps pulses (FWHM) with 20-mW peak power.

4.3 A 1.55-μm continuous-wave signal with 6-dBm power is launched into a fiber with 50-μm^2 effective mode area. After what fiber length would the nonlinear phase shift induced by SPM become 2π? Assume $\bar{n}_2=2.6\times10^{-20}$ m^2/W and neglect fiber losses.

4.4 Calculate the power launched into a 40-km-long single-mode fiber for which the SPM-induced nonlinear phase shift becomes 180°. Assume $\lambda=1.55$ μm, $A_{\mathrm{eff}}=40$ μm^2, $\alpha=0.2$ dB/km, and $\bar{n}_2=2.6\times10^{-20}$ m^2/W.

4.5 Find the maximum frequency shift occurring because of the SPM-induced chirp imposed on a Gaussian pulse of 20-ps width (FWHM) and 5-mW peak power after it has propagated 100 km. Use the fiber parameters of the preceding problem but assume $\alpha=0$.

4.6 Calculate numerically the spectrum of a Gaussian pulse of 10-ps width (FWHM) with 10-mW peak power after it has propagated 200, 400, 600, 800, and 1,000 km inside a fiber link with $\alpha=0.2$ dB/km and $\gamma=2$ W^{-1}/km. Assume that fiber losses are fully compensated after every 50 km.

4.7 Starting from the NLS equations, derive the coupled set of two equations, Eqs. (4.2.2) and (4.2.3), when two channels are launched into the same fiber.

4.8 Solve Eqs. (4.2.8) and (4.2.9) analytically and show that the solution for the probe is indeed given by Eq. (4.2.12).

4.9 Plot the XPM-induced phase shift given in Eq. (4.2.13) at the output of a 30-km-long fiber when the pump pulse is Gaussian in shape with 10-ps width (FWHM) and 50-mW peak power. Assume $\alpha = 0.2$ dB/km, $\gamma = 2$ W^{-1}/km, $\beta_2 = -4$ ps^2/km, and a channel spacing of 1 nm. Comment on the shape of the phase profile.

4.10 Explain what is meant by FWM in the context of a WDM lightwave system. How many new frequencies will be generated by FWM in the case of a four-channel system?

4.11 Why does FWM require phase matching? Consider two channels with spacing $\Delta\nu$, producing an idler wave at the frequency $\omega_4 = 2\omega_1 - \omega_2$. Prove that phase mismatch in this case is given by $\Delta k = \beta_2(2\pi\Delta\nu)^2$, where β_2 is the dispersion at the pump frequency ω_1.

4.12 Explain how FWM affects the performance of a WDM system. Describe two techniques that can be used in practice to reduce the impact of FWM.

4.13 A silica fiber is used as a Raman amplifier by launching the pump and signal beams simultaneously into it. Solve Eqs. (4.4.1) and (4.4.2), assuming that the pump is so intense that it remains undepleted, and derive an expression for the signal gain at the fiber output.

4.14 Calculate the threshold power for stimulated Brillouin scattering for a 50-km fiber link operating at 1.3 μm and having a loss of 0.5 dB/km. How much does the threshold power change if the operating wavelength is changed to 1.55 μm, where the fiber loss is only 0.2 dB/km? Assume that $A_{\text{eff}} = 50\ \mu\text{m}^2$ and $g_B = 5 \times 10^{-11}$ m/W at both wavelengths.

4.15 Use the three moments defined in Eqs. (4.6.1) and (4.6.2) for a chirped Gaussian pulse and derive Eqs. (4.6.6) and (4.6.7).

4.16 Apply the moment method with U given in Eqs. (4.6.20) and show that the width and chirp satisfy Eqs. (4.6.6) and (4.6.22).

4.17 Use the Lagrangian density given in in Eq. (4.6.11) and prove by performing all integrals that the Lagrangian is given by Eq. (4.6.12) for a chirped Gaussian pulse.

4.18 Repeat the same procedure with U given in Eqs. (4.6.20) and show that the Lagrangian is given by Eq. (4.6.21) for a chirped sech pulse.

References

[1] A. R. Chraplyvy, *J. Lightwave Technol.* **8**, 1548 (1990).

[2] F. Forghieri, R. W. Tkach, and A. R. Chraplyvy, in *Optical Fiber Telecommunications*, Vol. 3A, I. P. Kaminow and T. L. Koch, Eds., Academic Press, San Diego, CA, 1997, Chap. 8.

[3] E. Iannone, F. Matera, A. Mecozzi, and M. Settembre, *Nonlinear Optical Communication Networks*, Wiley, New York, 1998.

[4] G. P. Agrawal, *Nonlinear Fiber Optics*, 3rd ed., Academic Press, San Diego, CA, 2001.

[5] G. P. Agrawal, *Fiber-Optic Communication Systems*, 3rd ed., Wiley, New York, 2002.
[6] P. Bayvel and R. Killey, in *Optical Fiber Telecommunications*, Vol. 4B, I. P. Kaminow and T. L. Koch, Eds., Academic Press, San Diego, CA, 2002, Chap. 13.
[7] R. H. Stolen and C. Lin, *Phys. Rev. A* **17**, 1448 (1978).
[8] F. Shimizu, *Phys. Rev. Lett.* **19**, 1097 (1967).
[9] R. Cubeddu, R. Polloni, C. A. Sacchi, and O. Svelto, *Phys. Rev. A* **2**, 1955 (1970).
[10] Y. Kodama and S. Wabnitz, *Opt. Lett.* **20**, 2291 (1995).
[11] Y. Kodama and S. Wabnitz, *Electron. Lett.* **31**, 1761 (1995).
[12] Y. Kodama, S. Wabnitz, and K. Tanaka *Opt. Lett.* **21**, 719 (1996).
[13] A. M. Kamchatnov and H. Steudel, *Opt. Commun.* **162**, 162 (1999).
[14] D. Anderson, *Phys. Rev. A* **27**, 3135 (1983).
[15] M. J. Potasek, G. P. Agrawal, and S. C. Pinault, *J. Opt. Soc. Am. B* **3**, 205 (1986).
[16] D. Marcuse, *J. Lightwave Technol.* **10**, 17 (1992).
[17] P. A. Bélanger and N. Bélanger, *Opt. Commun.* **117**, 56 (1995).
[18] N. Kikuchi and S. Sasaki, *J. Lightwave Technol.* **13**, 868 (1995).
[19] M. Florjanczyk and R. Tremblay, *J. Lightwave Technol.* **13**, 1801 (1995).
[20] Q. Yu and C. Fan, *J. Lightwave Technol.* **15**, 444 (1997).
[21] M. J. Potasek and G. P. Agrawal, *Electron. Lett.* **22**, 759 (1986).
[22] A. Hasegawa, *Opt. Lett.* **9**, 288 (1984).
[23] K. Tajima, *J. Lightwave Technol.* **4**, 900 (1986).
[24] K. Tai, A. Hasegawa, and A. Tomita, *Phys. Rev. Lett.* **56**, 135 (1986).
[25] J. P. Hamide, P. Emplit, and J. M. Gabriagues, *Electron. Lett.* **26**, 1452 (1990).
[26] D. Mracuse, *J. Lightwave Technol.* **9**, 356 (1991).
[27] M. Murakami and S. Saito, *IEEE Photon. Technol. Lett.* **4**, 1269 (1992).
[28] K. Kikuchi, *IEEE Photon. Technol. Lett.* **5**, 221 (1993).
[29] F. Matera, A. Mecozzi, M. Romagnoli, and M. Settembre, *Opt. Lett.* **18**, 1499 (1993).
[30] A. Mecozzi, *J. Opt. Soc. Am. B* **11**, 462 (1994).
[31] M. Yu, G. P. Agrawal, and C. J. McKinstrie, *J. Opt. Soc. Am. B* **12**, 1126 (1995).
[32] N. J. Smith and N. J. Doran, *Opt. Lett.* **21**, 570 (1996).
[33] C. Lorattanasane and K. Kikuchi, *IEEE J. Quantum Electron.* **33**, 1084 (1997).
[34] R. A. Saunders, B. A. Patel, and D. Garthe, *IEEE Photon. Technol. Lett.* **9**, 699 (1997).
[35] R. Q. Hui, M. O'Sullivan, A. Robinson, and M. Taylor, *J. Lightwave Technol.* **15**, 1071 (1997).
[36] E. Ciaramella and M. Tamburrini, *IEEE Photon. Technol. Lett.* **11**, 1608 (1999).
[37] A. R. Chraplyvy and J. Stone, *Electron. Lett.* **20**, 996 (1984).
[38] G. P. Agrawal, P. L. Baldeck, and R. R. Alfano, *Phys. Rev. A* **40**, 5063 (1989).
[39] J. Wang and K. Petermann, *J. Lightwave Technol.* **10**, 96 (1992).
[40] D. Marcuse, A. R. Chraplyvy, and R. W. Tkach, *J. Lightwave Technol.* **12**, 885 (1994).
[41] T. K. Chiang, N. Kagi, M. E. Marhic, and L. G. Kazovsky, *J. Lightwave Technol.* **14**, 249 (1996).
[42] M. Shtaif and M. Eiselt, *IEEE Photon. Technol. Lett.* **10**, 979 (1998); M. Shtaif, *Opt. Lett.* **23**, 1191 (1998).
[43] G. Belloti, M. Varani, C. Francia, and A. Bononi, *IEEE Photon. Technol. Lett.* **10**, 1745 (1998).
[44] A. V. T. Cartaxo, *J. Lightwave Technol.* **17**, 178 (1999).
[45] L. Rapp, *J. Opt. Commun.* **20**, 29 (1999); *J. Opt. Commun.* **20**, 144 (1999).

[46] R. Hui, K. R. Demarest, and C. T. Allen, *J. Lightwave Technol.* **17**, 1018 (1999).
[47] S. Bigo, G. Bellotti, and M. W. Chbat, *IEEE Photon. Technol. Lett.* **11**, 605 (1999).
[48] M. Eiselt, M. Shtaif, and L. D. Garettt, *IEEE Photon. Technol. Lett.* **11**, 748 (1999).
[49] L. E. Nelson, R. M. Jopson, A. H. Gnauck, and A. R. Chraplyvy, *IEEE Photon. Technol. Lett.* **11**, 907 (1999).
[50] S. Betti and M. Giaconi, *IEEE Photon. Technol. Lett.* **13**, 305 (2001); *IEEE Photon. Technol. Lett.* **13**, 1304 (2001).
[51] H. J. Thiele, R. I. Killey, and P. Bayvel, *Opt. Fiber Technol.* **8**, 71 (2002).
[52] D. I. Kovsh, L. Liu, B. Bakhshi, A. N. Pilipetskii, E. A. Golovchenko, and N. S. Bergano, *IEEE J. Sel. Topics Quantum Electron.* **8**, 597 (2002).
[53] Q. Lin and G. P. Agrawal, *J. Lightwave Technol.* **22**, 977 (2004); *IEEE J. Quantum Electron.* **40**, 958 (2004).
[54] N. Shibata, R. P. Braun, and R. G. Waarts, *IEEE J. Quantum Electron.* **23**, 1205 (1987).
[55] M. W. Maeda, W. B. Sessa, W. I. Way, A. Yi-Yan, L. Curtis, R. Spicer, and R. I. Laming, *J. Lightwave Technol.* **8**, 1402 (1990).
[56] K. Inoue, *Opt. Lett.* **17**, 801 (1992); *J. Lightwave Technol.* **10**, 1553 (1992); *J. Lightwave Technol.* **12**, 1023 (1994).
[57] K. Inoue, K. Nakanishi, K. Oda, and H. Toba, *J. Lightwave Technol.* **12**, 1423 (1994).
[58] K. Inoue and H. Toba, *J. Lightwave Technol.* **13**, 88 (1995).
[59] F. Forghieri, R. W. Tkach, and A. R. Chraplyvy, *J. Lightwave Technol.* **13**, 889 (1995).
[60] A. Yu and M. J. O'Mahony, *IEE Proc.* **142**, 190 (1995).
[61] H. Taga, *J. Lightwave Technol.* **14**, 1287 (1996).
[62] W. Zeiler, F. Di Pasquale, P. Bayvel, and J. E. Midwinter, *J. Lightwave Technol.* **14**, 1933 (1996).
[63] D. F. Grosz, C. Mazzali, S. Celaschi, A. Paradisi, and H. L. Fragnito, *IEEE Photon. Technol. Lett.* **11**, 379 (1999).
[64] M. Eiselt, *J. Lightwave Technol.* **17**, 2261 (1999).
[65] S. Song, C. T. Allen, K. R. Demarest, and R. Hui, *J. Lightwave Technol.* **17**, 2285 (1999).
[66] H. Suzuki, S. Ohteru, and N. Takachio, *IEEE Photon. Technol. Lett.* **11**, 1677 (1999).
[67] S. Betti, M. Giaconi, and M. Nardini, *IEEE Photon. Technol. Lett.* **15**, 1079 (2003).
[68] J. S. Lee, D. H. Lee, and C. S. Park, *IEEE Photon. Technol. Lett.* **10**, 825 (1998).
[69] A. R. Chraplyvy, A. H. Gnauck, R. W. Tkach, and R. M. Derosier, *IEEE Photon. Technol. Lett.* **5**, 1233 (1993).
[70] K. Nakajima, M. Ohashi, K. Shiraki, T. Horiguchi, K. Kurokawa, and Y. Miyajima, *J. Lightwave Technol.* **17**, 1814 (1999).
[71] R. H. Stolen, E. P. Ippen, and A. R. Tynes, *Appl. Phys. Lett.* **20**, 62 (1972).
[72] R. G. Smith, *Appl. Opt.* **11**, 2489 (1972).
[73] A. Tomita, *Opt. Lett.* **8**, 412 (1983).
[74] A. R. Chraplyvy, *Electron. Lett.* **20**, 58 (1984).
[75] D. Cotter and A. M. Hill, *Electron. Lett.* **20**, 185 (1984).
[76] A. M. Hill, D. Cotter, and I. Wright, *Electron. Lett.* **20**, 247 (1984).
[77] J. Hegarty, N. A. Olsson, and M. McGlashan-Powell, *Electron. Lett.* **21**, 395 (1985).
[78] M. S. Kao and J. Wu, *J. Lightwave Technol.* **7**, 1290 (1989).
[79] M. S. Kao, *Electron. Lett.* **26**, 1034 (1990).
[80] S. Chi and S. C. Wang, *Electron. Lett.* **26**, 1509 (1990).
[81] J. C. Palais, T. Y. Lin, and S. Tariq, *Fiber Integ. Opt.* **10**, 75 (1991).

[82] A. R. Chraplyvy and R. W. Tkach, *IEEE Photon. Technol. Lett.* **5**, 666 (1993).
[83] F. Forghieri, R. W. Tkach, and A. R. Chraplyvy, *IEEE Photon. Technol. Lett.* **7**, 101 (1995).
[84] Z. Wang, A. Li, C. J. Mahon, G. Jacobsen, and E. Bodtker, *IEEE Photon. Technol. Lett.* **7**, 1492 (1995).
[85] S. Tariq and J. C. Palais, *J. Lightwave Technol.* **11**, 1914 (1993); *Fiber Integ. Opt.* **15**, 335 (1996).
[86] Y. Zhao, J. S. Wang, W. Zhou, H. Y. Tam, and M. S. Demokan, *Microwave Opt. Tech. Lett.* **12**, 111 (1996).
[87] D. N. Christodoulides and R. B. Jander, *IEEE Photon. Technol. Lett.* **8**, 1722 (1996).
[88] J. Wang, X. Sun, and M. Zhang, *IEEE Photon. Technol. Lett.* **10**, 540 (1998).
[89] M. Zirngibl, *Electron. Lett.* **34**, 789 (1998).
[90] M. E. Marhic, F. S. Yang, and L. G. Kazovsky, *J. Opt. Soc. Am. B* **15**, 957 (1998).
[91] S. Bigo, S. Gauchard. A Bertaina, and J. P. Hamaide, *IEEE Photon. Technol. Lett.* **11**, 671 (1999).
[92] A. G. Grandpierre, D. N. Christodoulides, and J. Toulouse, *IEEE Photon. Technol. Lett.* **11**, 1271 (1999).
[93] M. N. Islam, Ed., *Raman Amplifiers for Telecommunications*, Springer, New York, 2003.
[94] C. Headley and G. P. Agrawal, Eds., *Raman Amplification in Fiber Optical Communication Systems*, Academic Press, San Diego, CA, 2005.
[95] J. Bromage, *J. Lightwave Technol.* **22**, 79 (2004).
[96] E. P. Ippen and R. H. Stolen, *Appl. Phys. Lett.* **21**, 539 (1972).
[97] D. Cotter, *Electron. Lett.* **18**, 495 (1982); *J. Opt. Commun.* **4**, 10 (1983).
[98] T. Sugie, *J. Lightwave Technol.* **9**, 1145 (1991); *IEEE Photon. Technol. Lett.* **5**, 102 (1992).
[99] X. P. Mao, R. W. Tkach, A. R. Chraplyvy, R. M. Jopson, and R. M. Derosier, *IEEE Photon. Technol. Lett.* **4**, 66 (1992).
[100] D. A. Fishman and J. A. Nagel, *J. Lightwave Technol.* **11**, 1721 (1993).
[101] T. Sugie, *Opt. Quantum Electron.* **27**, 643 (1995).
[102] D. Cotter, *Electron. Lett.* **18**, 504 (1982).
[103] R. G. Waarts and R. P. Braun, *Electron. Lett.* **21**, 1114 (1985).
[104] Y. Aoki, K. Tajima, and I. Mito, *J. Lightwave Technol.* **6**, 710 (1988).
[105] E. Lichtman, *Electron. Lett.* **27**, 759 (1991).
[106] A. Hirose, Y. Takushima, and T. Okoshi, *J. Opt. Commun.* **12**, 82 (1991).
[107] T. Sugie, *J. Lightwave Technol.* **9**, 1145 (1991); *IEEE Photon. Technol. Lett.* **5**, 102 (1993).
[108] Y. K. Park, O. Mizuhara, L. D. Tzeng, J.-M. P. Delavaux, T. V. Nguyen, M.-L. Kao, P. D. Yeates, and J. Stone, *IEEE Photon. Technol. Lett.* **5**, 79 (1993).
[109] G. Grandpierre, O. Gautheron, L. Pierre, J.-P. Thiery, and P. Kretzmeyer, *IEEE Photon. Technol. Lett.* **5**, 531 (1993).
[110] Y. Miyamoto, T. Kataoka, A. Sano, K. Hagimoto, A. Aida, and Y. Kobayashi, *Electron. Lett.* **30**, 797 (1994).
[111] D. Cotter, *Electron. Lett.* **18**, 638 (1982).
[112] M. Tsubokawa, S. Seikai, T. Nakashima, and N. Shibata, *Electron. Lett.* **22**, 473 (1986).
[113] A. Hadjifotiou and G. A. Hill, *IEE Proc.* **133**, Pt. J, 256 (1986).
[114] N. Yoshizawa and T. Imai, *J. Lightwave Technol.* **11**, 1518 (1993).
[115] K. Shiraki, M. Ohashi, and M. Tateda, *Electron. Lett.* **31**, 668 (1995).
[116] K. Shiraki, M. Ohashi, and M. Tateda, *J. Lightwave Technol.* **14**, 50 (1996).
[117] M. M. Howerton, W. K. Burns, and G. K. Gopalakrishnan, *J. Lightwave Technol.* **14**, 417 (1996).

[118] K. Tsujikawa, K. Nakajima, Y. Miyajima, and M. Ohashi, *IEEE Photon. Technol. Lett.* **10**, 1139 (1998).

[119] S. N. Vlasov, V. A. Petrishchev, and V. I. Talanov, *Radiophys. Quantum Electron.* 14, 1062 (1971).

[120] V. S. Grigoryan, C. R. Menyuk, and R. M. Mu, *J. Lightwave Technol.* **17**, 1347 (1999).

[121] C. J. McKinstrie, J. Santhanam and G. P. Agrawal, *J. Opt. Soc. Am. B* **19**, 640 (2002).

[122] J. Santhanam and G. P. Agrawal, *IEEE J. Sel. Topics Quantum Electron.* **8**, 632 (2002); *Opt. Commun.* **222**, 413 (2003).

[123] M. Struwe, *Variational Methods*, Springer-Verlag, New York, 1990.

[124] B. Malomed, in *Progress in Optics*, Vol. 43, E. Wolf, Ed., North-Holland, Amsterdam, 2002, Chap. 2.

[125] R. K. Nesbet, *Variational Principles and Methods in Theoretical Physics and Chemistry*, Cambridge University Press, New York, 2003.

[126] L. F. Mollenauer, K. Smith, J. P. Gordon, and C. R. Menyuk, *Opt. Lett.* **9**, 1219 (1989).

[127] S. G. Evangelides, L. F. Mollenauer, J. P. Gordon, and N. S. Bergano, *J. Lightwave Technol.* **10**, 28 (1992).

[128] T. Ueda and W. L. Kath, *Physica D* **55**, 166 (1992); *J. Opt. Soc. Am. B* **11** 818 (1994).

[129] P. K. A. Wai and C. R. Menyuk, *J. Lightwave Technol.* **14**, 148 (1996).

[130] M. Matsumoto, Y. Akagi, and A. Hasegawa, *J. Lightwave Technol.* **15**, 584 (1997).

[131] D. Marcuse, C. R. Menyuk, and P. K. A. Wai, *J. Lightwave Technol.* **15**, 1735 (1997).

[132] T. L. Lakoba and D. J. Kaup, *Phys. Rev. E* **56**, 6147 (1997).

[133] C. A. Eleftherianos, D. Syvridis, T. Sphicopoulos, and C. Caroubalos, *Opt. Commun.* **154**, 14 (1998).

[134] H. Sunnerud, C. Xie, M. Karlsson, P. A. Andrekson, *J. Lightwave Technol.* **19**, 1453 (2001).

[135] C. Xie, M. Karlsson, P. A. Andrekson, H. Sunnerud, and J. Li, *IEEE J. Sel. Topics Quantum Electron.* **8**, 575 (2002)

[136] H. Sunnerud, M. Karlsson, P. A. Andrekson, *J. Lightwave Technol.* **20**, 2204 (2002).

[137] A. Levent, S. G. Rajeev, F. Yaman, and G. P. Agrawal, *Phys. Rev. Lett.* **90**, 013902 (2003).

[138] A. Hasegawa, *Physica D* **188**, 241 (2004).

[139] R. W. Boyd, *Nonlinear Optics*, 2nd ed., Academic Press, San Diego, CA, 2003.

[140] S. V. Manakov, *Sov. Phys. JETP* **38**, 248 (1974).

Chapter 5

Signal Recovery and Noise

An optical bit stream that has been degraded by the linear and nonlinear mechanisms during its transmission through the fiber link eventually reaches an optical receiver, which converts it into an electrical form and attempts to recover the original coded information. However, the distorted nature of the optical signal, and the noise added by optical amplifiers and the receiver, make it nearly impossible to recover the original bit stream with 100% accuracy. For this reason, the performance of a lightwave system is characterized in terms of the bit-error rate (BER). This chapter focuses on noise sources and their impact on BER and receiver sensitivity. Section 5.1 deals with shot and thermal noises that must be taken into account for any receiver. The signal-to-noise ratio (SNR) of the electrical signal generated at the receiver is considered in Section 5.2. The concept of receiver sensitivity is introduced in Section 5.3, where we obtain a simple expression for the BER and relate it to an important parameter known as the Q factor. Degradation of receiver sensitivity caused by a number of unavoidable processes is discussed in Section 5.4. The topic of forward error correction is addressed in Section 5.5.

5.1 Noise Sources

Optical receivers convert incident optical power P_{in} into an electric current using a photodetector [1]–[5]. The conversion process is linear in nature and would lead to a current that is directly proportional to the incident optical power, $I = R_d P_{\text{in}}$, in the absence of noise, where R_d is the responsivity of the photodetector. However, this is not the case in practice. Two fundamental noise mechanisms, known as *shot* noise and *thermal* noise [6]–[8], produce fluctuations in the current even when the incident optical signal has a constant power. Of course, additional noise is generated if P_{in} is itself fluctuating because of noise produced by optical amplifiers. This section focuses on shot and thermal noises; optical amplifier noise, a dominant source of noise for long-haul systems, is considered in Chapter 6. To simplify the following discussion, we assume that P_{in} is constant and consider its time dependence in Section 5.3.

5.1.1 Shot Noise

Shot noise is a consequence of the fact that an electric current consists of a stream of electrons that are generated at random times. It was first studied by Schottky [9] in 1918 and has been thoroughly investigated since then [6]–[8]. Even when power incident on a photodetector is constant, photons are absorbed, and electron-hole pairs are generated, at random time intervals. We can write the current in the form [10]

$$I(t) = \sum_{n=1}^{N_e} q h_c(t - t_n) \equiv \bar{I} + i_s(t), \tag{5.1.1}$$

where q is the magnitude of electron charge, t_n is the arrival time of the nth photon, and the sum is over the total number of electrons, N_e, generated over a fixed time interval T_d. The response function $h_c(t)$ governs the shape of the current pulse produced by each absorbed photon and is normalized such that $\int_0^{T_d} h_c(t)\,dt = 1$. The duration of each current pulse is much shorter than T_d, and $h_c(t)$ behaves like a delta function for most photodetectors.

In Eq. (5.1.1), $\bar{I}$ is the average photocurrent. We can calculate its value as

$$\bar{I} = \sum_n q\langle h_c(t - t_n)\rangle = \sum_n \frac{q}{T_d}\int_0^{T_d} h_c(t - t_n)\,dt = q \equiv qR_e, \tag{5.1.2}$$

where we performed the average by noting that the probability of a photon being absorbed in the time interval dt is dt/T_d and $R_e = N_e/T_d$ represents the average rate of electron generation. Noting that $R_e = \eta R_{\text{ph}}$, where η is the quantum efficiency of the photodetector and R_{ph} is the average rate of photon arrival related to the incident power as $R_{\text{ph}} = P_{\text{in}}/h\nu_0$, we obtain the well-known result $\bar{I} = R_d P_{\text{in}}$ with $R_d = \eta q/h\nu_0$ is the responsivity of the photodetector and $h\nu_0$ is the photon energy.

The fluctuating part of current, $i_s(t) = I(t) - \bar{I}$, is responsible for the shot noise. Its average vanishes by definition but has a finite variance. Mathematically, $i_s(t)$ is a stationary random process whose statistical properties reflect the *Poisson statistics* associated with photon streams [11]. In practice, $i_s(t)$ can be assumed to follow the Gaussian statistics whenever the number of photons involved is not too small. It should be stressed that shot noise is not generated at the receiver. On a fundamental level, shot noise has its origin in the quantum nature of light and is related to vacuum fluctuations [12]. In this sense, shot noise is a manifestation of the intrinsic quantum nature of light and it sets the minimum noise level for any photodetector.

The autocorrelation function of $i_s(t)$ can also be calculated from Eq. (5.1.1) as

$$\langle i_s(t) i_s(t+\tau)\rangle = q^2 \sum_m \sum_n \left[\langle h_c(t - t_m) h_c(t - t_n + \tau)\rangle - \langle h_c(t - t_m)\rangle\langle h_c(t - t_n + \tau)\rangle\right]. \tag{5.1.3}$$

Since arrival times of photons are uncorrelated, only the $m = n$ terms contribute in the double sum, assuming that the incident optical signal is coherent [12]. If we approximate $h_c(t)$ with a delta function, the autocorrelation function can be written as

$$\langle i_s(t) i_s(t+\tau)\rangle = \int_{-\infty}^{\infty} S_s(f)\exp(2\pi i f\tau)\,df, \tag{5.1.4}$$

where $S_s(f) = q\bar{I}$ is the spectral density of shot noise. Equation (5.1.4) represents an example of the Wiener–Khintchine theorem, applicable to any stationary stochastic process [8]. The spectral density of shot noise is frequency-independent (an example of *white noise*). Note that $S_s(f)$ is the *two-sided* spectral density, as negative frequencies are included in Eq. (5.1.4). If only positive frequencies are considered by changing the lower limit of integration to zero, the *single-sided* spectral density becomes $2q\bar{I}$.

The noise variance is obtained by setting $\tau = 0$ in Eq. (5.1.4), that is,

$$\sigma_s^2 = \langle i_s^2(t) \rangle = 2\int_0^{\Delta f} S_s(f)\, df = 2q\bar{I}\Delta f, \tag{5.1.5}$$

where the integration range is restricted over the *effective* noise bandwidth Δf of the receiver. The contribution of the dark current can be included in Eq. (5.1.5) by replacing $\bar{I}$ with $\bar{I} + I_d$ so that

$$\sigma_s^2 = 2q(\bar{I} + I_d)\Delta f. \tag{5.1.6}$$

The quantity σ_s represents the root-mean-square (RMS) value of the noise current induced by shot noise. As a numerical example, $\sigma_s = 1.4\ \mu$A, when $\bar{I} = 1$ mA, $I_d \ll \bar{I}$, and $\Delta f = 6$ GHz.

5.1.2 Thermal Noise

At a finite temperature, electrons move randomly inside any conductor. Such thermal motion of electrons inside a resistor manifests as a fluctuating current even in the absence of an applied voltage. The load resistor in the front end of an optical receiver adds such fluctuations to the current generated by the photodiode. This noise is referred to as thermal noise [10]. It is also called *Johnson noise* [13] or *Nyquist noise* [14], after the two scientists who first studied it in 1928, and represents an example of the fluctuation–dissipation theorem [12], according to which loss (or gain) is always accompanied with fluctuations. As electrical energy is dissipated by a resistor, the current flowing through the circuit exhibits additional fluctuations.

Thermal noise can be included by writing the current in the form

$$I(t) = \bar{I} + i_s(t) + i_T(t), \tag{5.1.7}$$

where $i_T(t)$ is a current fluctuation induced by thermal noise. Mathematically, $i_T(t)$ is modeled as a stationary Gaussian random process. It vanishes on average but its variance is finite. Similar to the case of shot noise, one can relate the autocorrelation function of $i_T(t)$ to the spectral energy $S_T(f)$ through the Fourier-transform relation given in Eq. (5.1.4). The one-sided spectral density of thermal noise is well known [6]. Using this result, the two-sided spectral density of thermal noise is given by

$$S_T(f) = \frac{2hf}{R_L[\exp(hf/k_BT) - 1]} \approx \frac{2k_BT}{R_L}, \tag{5.1.8}$$

where k_B is the Boltzmann constant, T is the absolute temperature (in Kelvin), and R_L is the load resistor. The frequency-independent form of S_T holds as long as $hf/(k_BT) \ll 1$ and is valid for all receivers with bandwidths below 100 GHz. As one would have

expected, S_T depends on the thermal energy k_BT associated with electrons at a finite temperature. This energy is about 4×10^{-21} J (or 25 meV) at room temperature, if we use $k_B = 1.38 \times 10^{-23}$ J/K.

The autocorrelation function of $i_T(t)$ is given by Eq. (5.1.4) if we replace the subscript s by T. The noise variance is obtained by setting $\tau = 0$ and becomes

$$\sigma_T^2 = \langle i_T^2(t) \rangle = 2 \int_0^{\Delta f} S_T(f)\, df = (4k_BT/R_L)\Delta f, \tag{5.1.9}$$

where Δf is the effective noise bandwidth. Note that σ_T^2 does not depend on the average current $\bar{I}$, whereas σ_s^2 does.

Equation (5.1.9) includes thermal noise generated in the load resistor. A receiver contains many other electrical components, some of which add additional thermal noise. For example, noise is invariably added by electrical amplifiers. The amount of noise added depends on the receiver design (see Chapter 7 of LT1) and the type of amplifiers used [4]. A simple approach accounts for the thermal noise of amplifiers in terms of a *noise figure* F_n introduced by modifying Eq. (5.1.9) as

$$\sigma_T^2 = (4k_BT/R_L)F_n\Delta f. \tag{5.1.10}$$

Physically, F_n represents the factor by which thermal noise is enhanced by electrical amplifiers used within the receiver.

For a perfect optical signal, total current noise can be obtained by adding the contributions of shot and thermal noises. Since $i_s(t)$ and $i_T(t)$ in Eq. (5.1.7) are independent random processes with approximately Gaussian statistics, the total variance of current fluctuations, $\Delta I = I - \bar{I} = i_s + i_T$, can be obtained by simply adding individual variances. The result is

$$\sigma^2 = \langle (\Delta I)^2 \rangle = \sigma_s^2 + \sigma_T^2 = 2q(\bar{I} + I_d)\Delta f + (4k_BT/R_L)F_n\Delta f. \tag{5.1.11}$$

We use this equation in the next section for calculating the electrical SNR at the receiver.

5.2 Signal-to-Noise Ratio

The performance of an optical receiver depends on the signal-to-noise ratio (SNR). The SNR of an electrical signal is defined as

$$\text{SNR} = \frac{\text{average signal power}}{\text{noise power}} = \frac{\bar{I}^2}{\sigma^2}. \tag{5.2.1}$$

The SNR depends on whether a *p–i–n* photodiode or an avalanche photodiode (APD) is used within the receiver (see Chapter 7 of LT1). We consider the two types of receivers separately.

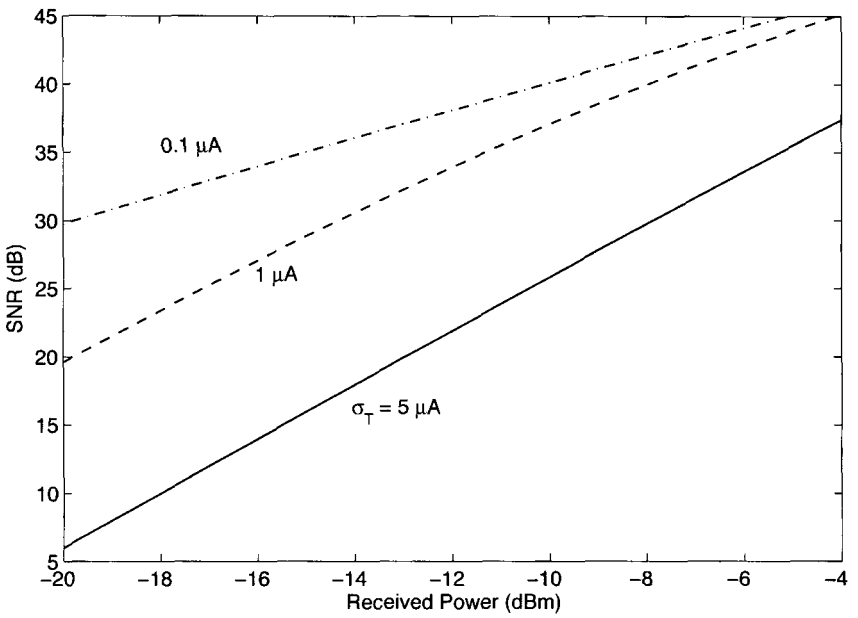

Figure 5.1: Increase in SNR with received power P_{in} for three values of σ_T for a receiver with a bandwidth of 30 GHz.

5.2.1 Receivers with a *p–i–n* Photodiode

In the case of a *p–i–n* photodiode, we use Eq. (5.1.11) in Eq. (5.2.1) together with $\bar{I} = R_d P_{\text{in}}$. The SNR is related to the incident optical power as

$$\text{SNR} = \frac{R_d^2 P_{\text{in}}^2}{2q(R_d P_{\text{in}} + I_d)\Delta f + 4(k_B T/R_L)F_n \Delta f}, \tag{5.2.2}$$

where $R_d = \eta q / h\nu_0$ is the responsivity of the *p–i–n* photodiode for photons of energy $h\nu_0$ and η is its quantum efficiency. Figure 5.1 shows the dependence of *SNR* on received power P_{in} for three values of σ_T for a receiver with $R_d = 1$ A/W, $I_d \approx 0$, and a bandwidth of 30 GHz. Thermal noise dominates for $\sigma_T = 5$ μA but it is almost negligible, and shot noise dominates when $\sigma_T = 0.1$ μA. In the intermediate case of $\sigma_T = 1$ μA, the magnitudes of shot and thermal noises are comparable. In the following discussion, we consider the two limits separately.

In most cases of practical interest, thermal noise dominates over shot noise ($\sigma_T^2 \gg \sigma_s^2$). Neglecting the shot-noise term in Eq. (5.2.2), the SNR becomes

$$\text{SNR} = \frac{R_L R_d^2 P_{\text{in}}^2}{4k_B T F_n \Delta f}. \tag{5.2.3}$$

The SNR varies as P_{in}^2 in the thermal-noise limit and can be improved considerably by increasing the optical power reaching the receiver. It can also be improved by increasing the load resistance. The effect of thermal noise is often quantified through a

quantity called the *noise-equivalent power* (NEP). The NEP is defined as the minimum optical power per unit bandwidth required to produce SNR = 1 and is given by

$$\text{NEP} = \frac{P_{\text{in}}}{\sqrt{\Delta f}} = \left(\frac{4k_B T F_n}{R_L R_d^2}\right)^{1/2}. \tag{5.2.4}$$

Typical values of NEP are in the range of 1 to 10 pW/Hz$^{1/2}$. The advantage of specifying NEP for a *p–i–n* receiver is that one does not need to know details of the receiver design. The optical power needed to realize a specific value of SNR can be obtained from the relation $P_{\text{in}} = (\text{NEP}\sqrt{\Delta f})\text{SNR}$.

Consider the opposite limit in which the receiver performance is dominated by shot noise ($\sigma_s^2 \gg \sigma_T^2$). Since σ_s^2 increases linearly with P_{in}, the shot-noise limit can be realized by making incident optical power large. The dark current I_d can be neglected in that situation. Equation (5.2.2) then provides the following expression for SNR:

$$\text{SNR} = \frac{RP_{\text{in}}}{2q\Delta f} = \frac{\eta P_{\text{in}}}{2h\nu_0 \Delta f}. \tag{5.2.5}$$

The SNR increases linearly with P_{in} in the shot-noise limit and depends only on the quantum efficiency η, the bandwidth Δf, and the photon energy $h\nu_0$.

The SNR given in Eq. (5.2.5) can be written in terms of the number of photons N_p contained in a single "1" bit. If we use for the energy contained in a bit of duration $T_b \equiv 1/B$ the relation

$$E_p = N_p h\nu_0 = P_{\text{in}}/B, \tag{5.2.6}$$

where B is the bit rate, we obtain $P_{\text{in}} = N_p h\nu_0 B$. If we choose $\Delta f = B/2$ (a typical value for the receiver bandwidth), the SNR is simply given by ηN_p. In the shot-noise limit, a SNR of 20 dB can be realized when $N_p \approx 100$ and $\eta \approx 1$. By contrast, several thousand photons are required to obtain an SNR of 20 dB when thermal noise dominates the receiver. As a reference, for a 1.55-μm receiver operating at 10 Gb/s, $N_p = 100$ when $P_{\text{in}} \approx 130$ nW.

5.2.2 APD Receivers

Optical receivers that employ an APD generally provide a higher SNR for the same incident optical power. The improvement is due to the internal gain (see Section 7.3 of LT1) that increases the photocurrent by a multiplication factor M so that

$$\bar{I} = MR_d P_{\text{in}} = R_{\text{APD}} P_{\text{in}}, \tag{5.2.7}$$

where $R_{\text{APD}} \equiv MR_d$ is the APD responsivity, enhanced by a factor of M compared with that of *p–i–n* photodiodes. The SNR would improve by a factor of M^2 if the receiver noise were unaffected by the internal gain mechanism of APDs. Unfortunately, this is not the case, and the SNR improvement is considerably less than M^2.

Enhancement of Shot Noise

Thermal noise remains the same for APD receivers, as it originates in the electrical components that are not part of the APD. This is not the case for shot noise. As

discussed in Section 7.3 of LT1, APD gain results from the generation of secondary electron–hole pairs through the process of impact ionization. Since such pairs are generated at random times, an additional contribution is added to the shot noise associated with the generation of primary electron–hole pairs. In effect, the multiplication factor itself is a random variable, and M appearing in Eq. (5.2.7) represents the average APD gain. The shot noise for APDs can be written in the form [15]

$$\sigma_s^2 = 2qM^2F_A(R_dP_{\text{in}} + I_d)\Delta f, \tag{5.2.8}$$

where F_A is called the *excess noise factor* and is given by

$$F_A(M) = k_AM + (1 - k_A)(2 - 1/M). \tag{5.2.9}$$

The dimensionless parameter $k_A = \alpha_h/\alpha_e$ if $\alpha_h < \alpha_e$ but is defined as $k_A = \alpha_e/\alpha_h$ when $\alpha_h > \alpha_e$, where α_e and α_h represent the impact ionization coefficients for electrons and holes, respectively. By definition, $0 < k_A < 1$. In general, F_A increases with M monotonically. However, although F_A is at most 2 for $k_A = 0$ and increases with M sublinearly for small values of k_A, it continues increasing linearly ($F_A = M$) when $k_A = 1$. Clearly, the ratio k_A should be as small as possible for a low-noise APD [16].

If the avalanche-gain process were noise-free ($F_A = 1$), both $\bar{I}$ and σ_s would increase by the same factor M, and the SNR would be unaffected, as far as the shot-noise contribution is concerned. It is the dominance of thermal noise in practical receivers that makes APDs attractive. By adding the contributions of both the shot and thermal noises, the SNR of an APD receiver can be written as

$$\text{SNR} = \frac{(MR_dP_{\text{in}})^2}{2qM^2F_A(R_dP_{\text{in}} + I_d)\Delta f + 4(k_BT/R_L)F_n\Delta f}, \tag{5.2.10}$$

where Eqs. (5.1.10), (5.2.7), and (5.2.8) were used. Figure 5.2 shows the dependence of SNR on received power P_{in} for three values of APD gain M with $\sigma_T = 1$ μA using the same receiver parameters used in Figure 5.1 and assuming that $k_A = 0.7$ for the APD. This value of k_A is realistic for InGaAs APDs designed to operate in the spectral region near 1.55 μm.

Several points are noteworthy from Figure 5.2. Noting that $M = 1$ case corresponds to the use of a *p–i–n* photodiode, it is evident that the SNR is in fact degraded for an APD receiver when input powers are relatively large. Some improvement in SNR occurs only for low input power levels below -20 dBm. The reason behind this behavior is related to the enhancement of shot noise in APD receivers. At low power levels, thermal noise dominates over shot noise, and the APD gain helps. However, as the APD gain increases, shot noise begins to dominate over thermal noise, and APD performs worse than a *p–i–n* photodiode under the same operating conditions. To make this point clear, we consider the two limits separately.

In the thermal-noise limit ($\sigma_s \ll \sigma_T$), the SNR becomes

$$\text{SNR} = (R_LR_d^2/4k_BTF_n\Delta f)M^2P_{\text{in}}^2 \tag{5.2.11}$$

and is improved, as expected, by a factor of M^2 compared with that of *p–i–n* receivers [see Eq. (5.2.3)]. By contrast, in the shot-noise limit ($\sigma_s \gg \sigma_T$), the SNR is given by

$$\text{SNR} = \frac{R_dP_{\text{in}}}{2qF_A\Delta f} = \frac{\eta P_{\text{in}}}{2h\nu_0F_A\Delta f} \tag{5.2.12}$$

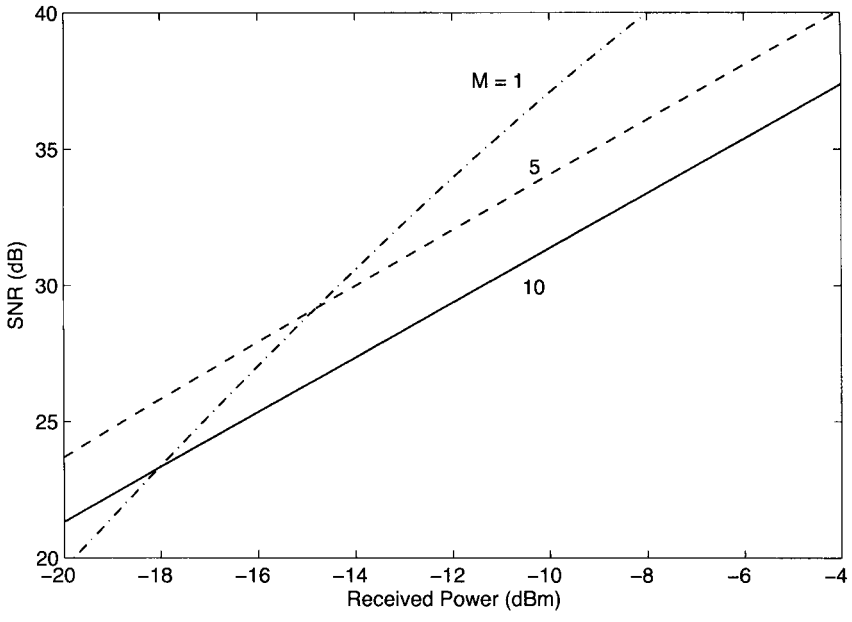

Figure 5.2: Increase in SNR with received power P_{in} for three values of APD gain M for a receiver with a bandwidth of 30 GHz. The $M = 1$ case corresponds to a *p–i–n* photodiode.

and is reduced by the excess noise factor F_A compared with that of *p–i–n* receivers.

Optimum APD Gain

Equation (5.2.10) and Figure 5.2 indicate that for a given P_{in}, the SNR of APD receivers is maximum for an optimum value M_{opt} of the APD gain M. It is easy to show that the SNR is maximum when M_{opt} satisfies the following cubic polynomial:

$$k_A M_{\text{opt}}^3 + (1 - k_A) M_{\text{opt}} = \frac{4k_B T F_n}{qR_L(R_d P_{\text{in}} + I_d)}. \tag{5.2.13}$$

The optimum value M_{opt} depends on a large number of the receiver parameters such as the dark current, the responsivity R_d, and the ionization-coefficient ratio k_A. However, it is independent of receiver bandwidth. The most notable feature of Eq. (5.2.13) is that M_{opt} decreases with an increase in P_{in}. Figure 5.3 shows the variation of M_{opt} with P_{in} for several values of k_A using typical parameter values for a 1.55-μm InGaAs receiver: $R_L = 1$ kΩ, $F_n = 2$, $R_d = 1$ A/W, and $I_d = 2$ nA.

The optimum APD gain is quite sensitive to the ionization-coefficient ratio k_A. For $k_A = 0$, M_{opt} decreases inversely with P_{in}, as inferred readily from Eq. (5.2.13) after noting that the contribution of I_d is negligible in practice. By contrast, M_{opt} varies as $P_{\text{in}}^{-1/3}$ for $k_A = 1$, and this form of dependence appears to hold even for k_A as small as 0.01 as long as $M_{\text{opt}} > 10$. In fact, by neglecting the second term in Eq. (5.2.13), M_{opt}

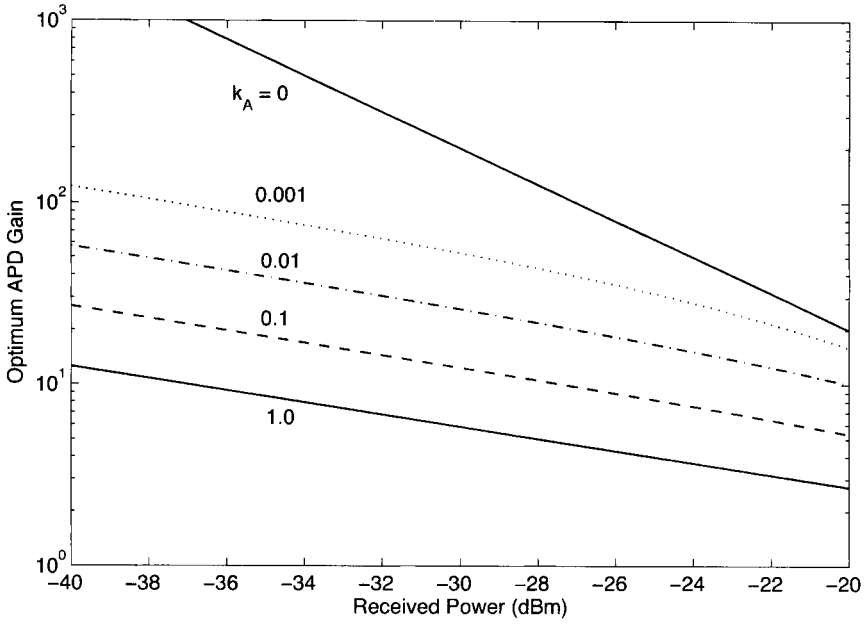

Figure 5.3: Optimum APD gain M_{opt} as a function of the incident optical power P_{in} for several values of k_A. Parameter values correspond to a typical 1.55-μm InGaAs APD receiver.

is well approximated by

$$M_{\text{opt}} \approx \left[\frac{4k_B T F_n}{k_A q R_L (R_d P_{\text{in}} + I_d)}\right]^{1/3} \tag{5.2.14}$$

for k_A in the range of 0.01 to 1. This expression shows the critical role played by the ionization-coefficient ratio k_A. In the case of silicon APDs, for which $k_A \ll 1$, M_{opt} can be as large as 100. By contrast, M_{opt} is in the neighborhood of 10 for InGaAs receivers, with $k_A \approx 0.7$.

5.3 Receiver Sensitivity

Receiver sensitivity is an important parameter for any lightwave system. Among a group of optical receivers, a receiver is said to be more sensitive if it achieves the same performance with less optical power incident on it. The performance criterion for digital receivers is governed by the BER, defined as the probability of incorrect identification of a bit by the decision circuit of the receiver. For example, a BER of 2×10^{-9} corresponds to 2 errors per billion bits, on average. Modern high-speed lightwave system transmit data at a bit rate of 10 Gb/s or more per channel. Such systems often require the BER to be below 10^{-12}, or even 10^{-15}. The receiver sensitivity is defined as the minimum average power $\bar{P}_{\text{rec}}$ required by the receiver to operate reliably below a specific BER.

5.3.1 Bit-Error Rate

To calculate the BER, we consider the electrical bit stream generated at the receiver in the form of a time-varying current $I(t)$ that has been corrupted by noise. Figure 5.4(a) shows schematically the fluctuating signal received by the decision circuit of the receiver. A clock-recovery circuit provides information about the duration of each bit slot. Depending on the design, the receiver may integrate the signal over the bit slot, or sample it periodically at the decision instant t_D set at the center of the bit slot.

As seen in Figure 5.4(a), the sampled value I fluctuates from bit to bit around an average value of I_1 or I_0 depending on whether the bit corresponds to 1 or 0 in the bit stream. The decision circuit compares the sampled value with a threshold value I_D and calls it bit 1 if $I > I_D$ or bit 0 if $I < I_D$. An error occurs if $I < I_D$ for bit 1 because of noise. An error also occurs if $I > I_D$ for bit 0. Both sources of errors can be included by defining the *error probability* as

$$\text{BER} = p(1)P(0/1) + p(0)P(1/0), \tag{5.3.1}$$

where $p(1)$ and $p(0)$ are the probabilities of receiving bits 1 and 0, respectively, $P(0/1)$ is the probability of deciding 0 when 1 is transmitted, and $P(1/0)$ is the probability of deciding 1 when 0 is transmitted. Since 1 and 0 bits are equally likely to occur in any realistic bit stream, $p(1) = p(0) = 1/2$, and the BER becomes

$$\text{BER} = \tfrac{1}{2}[P(0/1) + P(1/0)]. \tag{5.3.2}$$

Figure 5.4(b) shows how $P(0/1)$ and $P(1/0)$ depend on the probability density function $p(I)$ of the sampled value I. The functional form of $p(I)$ depends on the statistics of noise sources responsible for current fluctuations. Thermal noise i_T in Eq. (5.1.7) is well described by Gaussian statistics with zero mean and variance σ_T^2. The statistics of shot-noise contribution i_s in Eq. (5.1.7) is also approximately Gaussian for *p–i–n* receivers, although that is not the case for APDs [15]–[17]. A common approximation treats i_s as a Gaussian random variable for both *p–i–n* and APD receivers but with different variances given by Eqs. (5.1.6) and (5.2.8), respectively. Since the sum of two Gaussian random variables is also a Gaussian random variable, the sampled value I follows a Gaussian distribution with variance $\sigma^2 = \sigma_s^2 + \sigma_T^2$.

It is important to note that both the average and the variance are different for 1 and 0 bits since $\bar{I}$ in Eq. (5.1.7) equals I_1 or I_0, depending on the bit received. If σ_1^2 and σ_0^2 are the corresponding variances, the conditional error probabilities are given by

$$P(0/1) = \frac{1}{\sigma_1\sqrt{2\pi}} \int_{-\infty}^{I_D} \exp\left(-\frac{(I-I_1)^2}{2\sigma_1^2}\right) dI = \frac{1}{2}\,\text{erfc}\left(\frac{I_1 - I_D}{\sigma_1\sqrt{2}}\right), \tag{5.3.3}$$

$$P(1/0) = \frac{1}{\sigma_0\sqrt{2\pi}} \int_{I_D}^{\infty} \exp\left(-\frac{(I-I_0)^2}{2\sigma_0^2}\right) dI = \frac{1}{2}\,\text{erfc}\left(\frac{I_D - I_0}{\sigma_0\sqrt{2}}\right), \tag{5.3.4}$$

where $\text{erfc}(x)$ stands for the complementary error function defined as [18]

$$\text{erfc}(x) = \frac{2}{\sqrt{\pi}} \int_x^{\infty} \exp(-y^2)\, dy. \tag{5.3.5}$$

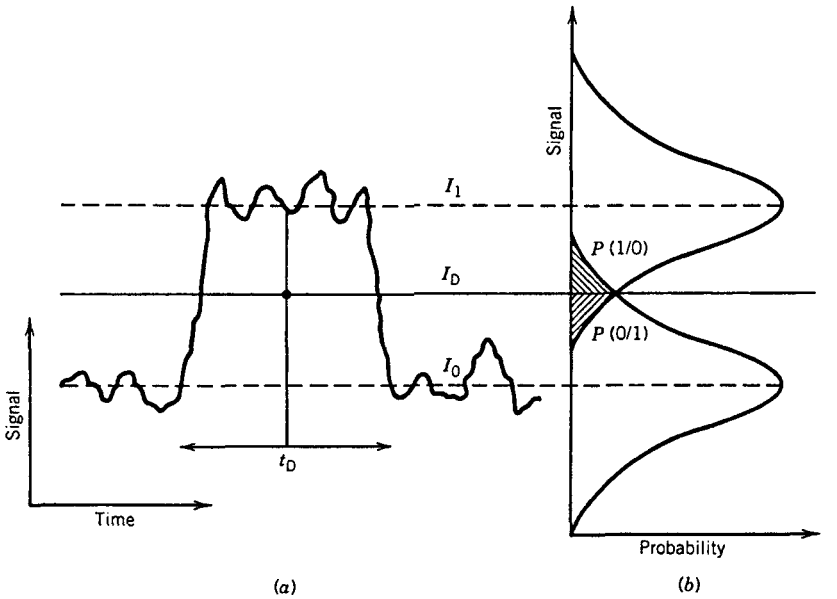

Figure 5.4: (a) Fluctuating signal generated at the receiver. (b) Gaussian probability densities of 1 and 0 bits. The dashed region shows the probability of incorrect identification.

By substituting Eqs. (5.3.3) and (5.3.4) in Eq. (5.3.2), the BER is given by

$$\text{BER} = \frac{1}{4}\left[\text{erfc}\left(\frac{I_1 - I_D}{\sigma_1\sqrt{2}}\right) + \text{erfc}\left(\frac{I_D - I_0}{\sigma_0\sqrt{2}}\right)\right]. \tag{5.3.6}$$

Equation (5.3.6) shows that the BER depends on the decision threshold I_D. Figure 5.5 shows how BER varies with I_D/I_1 for three values of the ratio I_1/σ_1, assuming that $I_0 = 0$ and $\sigma_1 \approx \sigma_0$. In practice, I_D is optimized to minimize the BER. We can find the optimum value of I_D by taking the derivative of Eq. (5.3.6) with respect to I_D and setting it to zero. The BER becomes minimum when I_D is chosen such that

$$\frac{(I_D - I_0)^2}{2\sigma_0^2} = \frac{(I_1 - I_D)^2}{2\sigma_1^2} + \ln\left(\frac{\sigma_1}{\sigma_0}\right). \tag{5.3.7}$$

The last term in this equation is negligible in most cases of practical interest, and I_D is approximately obtained from

$$(I_D - I_0)/\sigma_0 = (I_1 - I_D)/\sigma_1 \equiv Q. \tag{5.3.8}$$

An explicit expression for I_D is

$$I_D = \frac{\sigma_0 I_1 + \sigma_1 I_0}{\sigma_0 + \sigma_1}. \tag{5.3.9}$$

When $\sigma_1 = \sigma_0$, $I_D = (I_1 + I_0)/2$, which corresponds to setting the decision threshold in the middle. This is the situation for most *p–i–n* receivers whose noise is dominated

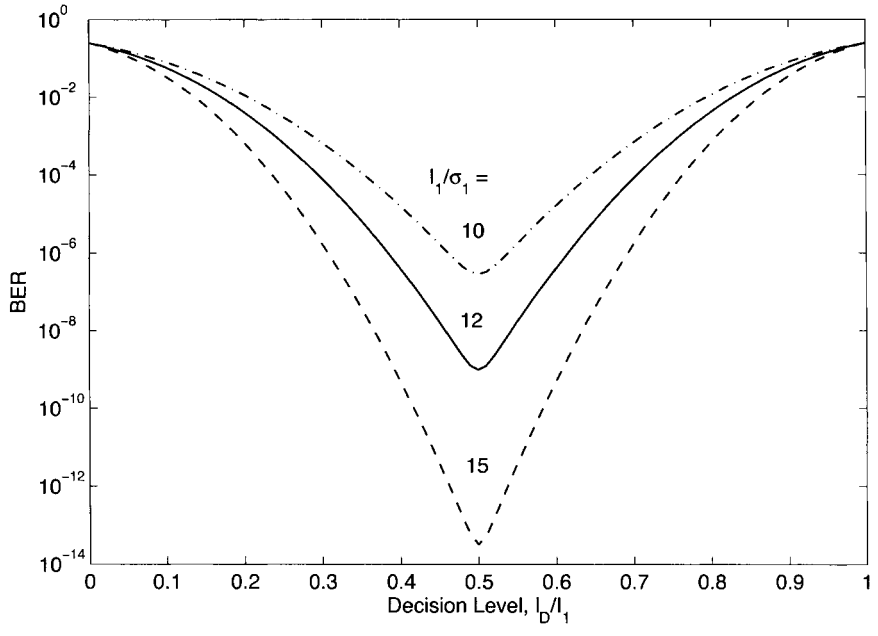

Figure 5.5: Variation of BER with I_D/I_1 for three values of I_1/σ_1.

by thermal noise ($\sigma_T \gg \sigma_s$) and is independent of the average current. In contrast, shot noise is larger for 1 bits as σ_s^2 varies linearly with the average current. In the case of APD receivers, the BER should be minimized by setting the decision threshold in accordance with Eq. (5.3.9).

The BER with the optimum setting of the decision threshold is obtained by using Eqs. (5.3.6) and (5.3.8) and depends only on the Q factor as

$$\text{BER} = \frac{1}{2}\,\text{erfc}\left(\frac{Q}{\sqrt{2}}\right) \approx \frac{\exp(-Q^2/2)}{Q\sqrt{2\pi}}. \tag{5.3.10}$$

The Q factor is obtained from Eqs. (5.3.8) and (5.3.9) and is given by

$$Q = \frac{I_1 - I_0}{\sigma_1 + \sigma_0}. \tag{5.3.11}$$

The approximate form of BER in Eq. (5.3.10) is obtained by using the asymptotic expansion [18] of $\text{erfc}(Q/\sqrt{2})$ and is reasonably accurate for $Q > 3$. Figure 5.6 shows how BER varies with the Q factor. The BER improves as Q increases and becomes lower than 10^{-9} for $Q > 6$. The Q factor plays an important role as it is a kind of SNR that determines the BER uniquely.

It is possible to relate Q to the electrical SNR. The relation is particularly simple when the receiver noise is dominated by thermal noise (as is the case for *p–i–n* photodiodes) and is thus the same for all bits. Using $\sigma_1 \approx \sigma_0 = \sigma_T$ with $I_0 = 0$, we obtain

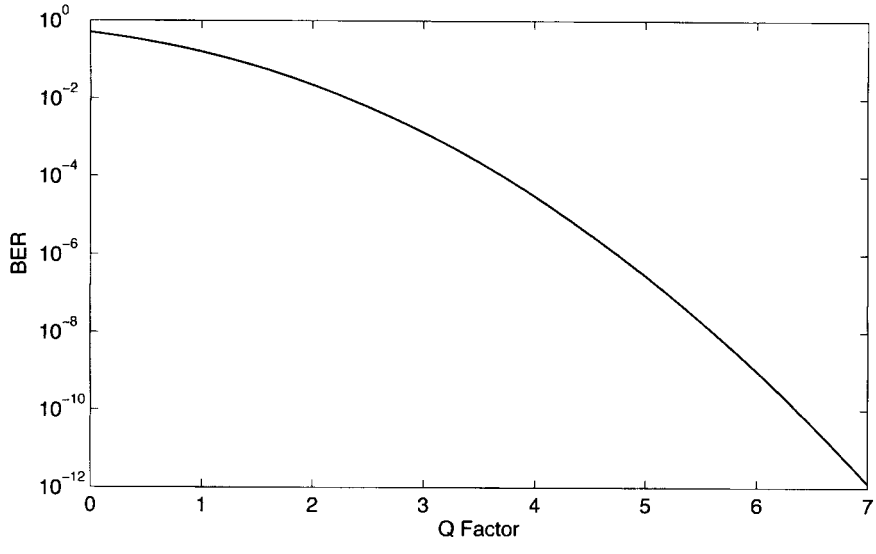

Figure 5.6: Bit-error rate versus the Q factor.

SNR = $4Q^2$. The requirement $Q = 6$ translates into an SNR of 144 or 21.6 dB. Since SNR scales as Q^2, it is common to define the Q^2 factor on the decibel scale as

$$Q^2(\text{in dB}) = 20 \log_{10} Q. \tag{5.3.12}$$

In this notation, a BER of 10^{-9} requires $Q^2 = 15.56$ dB, and this value increases to 16.9 dB at a BER of 10^{-12}.

5.3.2 Minimum Average Power

Equation (5.3.10) can be used to calculate the minimum average power that a receiver needs to operate reliably with a BER below a specified value. For this purpose the Q factor should be related to the incident optical power. For simplicity, consider the case in which 0 bits carry no optical power so that $P_0 = 0$, and hence $I_0 = 0$. The power P_1 required for 1 bits is related to I_1 as

$$I_1 = MR_d P_1 = 2MR_d \bar{P}_{\text{rec}}, \tag{5.3.13}$$

where $\bar{P}_{\text{rec}}$ is the average received power defined as $\bar{P}_{\text{rec}} = (P_1 + P_0)/2$. The APD gain M is included in Eq. (5.3.13) for generality. The case of p–i–n receivers can be recovered by setting $M = 1$.

The RMS noise currents σ_1 and σ_0 should include the contributions of both shot and thermal noises and can be written as

$$\sigma_1 = (\sigma_s^2 + \sigma_T^2)^{1/2} \quad \text{and} \quad \sigma_0 = \sigma_T, \tag{5.3.14}$$

where σ_s^2 and σ_T^2 are given by Eqs. (5.2.8) and (5.1.10), respectively. Neglecting the contribution of dark current, the noise variances become

$$\sigma_s^2 = 2qM^2F_AR_d(2\bar{P}_{\text{rec}})\Delta f, \tag{5.3.15}$$

$$\sigma_T^2 = (4k_BT/R_L)F_n\Delta f. \tag{5.3.16}$$

Using Eqs. (5.3.11) through (5.3.14), the Q factor is given by

$$Q = \frac{I_1}{\sigma_1 + \sigma_0} = \frac{2MR_d\bar{P}_{\text{rec}}}{(\sigma_s^2 + \sigma_T^2)^{1/2} + \sigma_T}. \tag{5.3.17}$$

For a specified value of BER, Q is determined from Eq. (5.3.10) and the receiver sensitivity $\bar{P}_{\text{rec}}$ is found from Eq. (5.3.17). A simple analytic expression for $\bar{P}_{\text{rec}}$ is obtained by solving Eq. (5.3.17) for a given value of Q and is given by [3]

$$\bar{P}_{\text{rec}} = \frac{Q}{R_d}\left(qF_AQ\Delta f + \frac{\sigma_T}{M}\right). \tag{5.3.18}$$

Equation (5.3.18) shows how $\bar{P}_{\text{rec}}$ depends on various receiver parameters and how it can be optimized. Consider first the case of a *p–i–n* receiver by setting $M = 1$. Since thermal noise σ_T generally dominates for such a receiver, $\bar{P}_{\text{rec}}$ is given by the simple expression

$$(\bar{P}_{\text{rec}})_{\text{pin}} \approx Q\sigma_T/R_d. \tag{5.3.19}$$

From Eq. (5.3.16), σ_T^2 depends not only on receiver parameters such as R_L and F_n but also on the bit rate through the receiver bandwidth Δf (typically $\Delta f = B/2$). Thus, $\bar{P}_{\text{rec}}$ increases as $\sqrt{B}$ in the thermal-noise limit. As an example, consider a 1.55-μm *p–i–n* receiver with $R_d = 1$ A/W. If we use $\sigma_T = 100$ nA as a typical value and $Q = 6$ corresponding to a BER of 10^{-9}, the receiver sensitivity is given by $\bar{P}_{\text{rec}} = 0.6\ \mu$W or -32.2 dBm.

Equation (5.3.18) shows how receiver sensitivity improves with the use of APD receivers. If thermal noise remains dominant, $\bar{P}_{\text{rec}}$ is reduced by a factor of M, and the received sensitivity is improved by the same factor. However, shot noise increases considerably for APD, and Eq. (5.3.18) should be used in the general case in which shot-noise and thermal-noise contributions are comparable. Similar to the case of SNR discussed in Section 4.4.3, the receiver sensitivity can be optimized by adjusting the APD gain M. By using F_A from Eq. (5.2.9) in Eq. (5.3.18), it is easy to verify that $\bar{P}_{\text{rec}}$ is minimum for an optimum value of M given by [3]

$$M_{\text{opt}} = k_A^{-1/2}\left(\frac{\sigma_T}{Qq\Delta f} + k_A - 1\right)^{1/2} \approx \left(\frac{\sigma_T}{k_AQq\Delta f}\right)^{1/2}, \tag{5.3.20}$$

and the minimum value is given by

$$(\bar{P}_{\text{rec}})_{\text{APD}} = (2q\Delta f/R_d)Q^2(k_AM_{\text{opt}} + 1 - k_A). \tag{5.3.21}$$

The improvement in receiver sensitivity obtained by the use of an APD can be estimated by comparing Eqs. (5.3.19) and (5.3.21). It depends on the ionization-coefficient

ratio k_A and is larger for APDs with a smaller value of k_A. For InGaAs APD receivers, the sensitivity is typically improved by 6 to 8 dB; such an improvement is sometimes called the APD advantage. Note that $\bar{P}_{\text{rec}}$ for APD receivers increases linearly with the bit rate B ($\Delta f \approx B/2$), in contrast with its $\sqrt{B}$ dependence for p–i–n receivers. The linear dependence of $\bar{P}_{\text{rec}}$ on B is a general feature of shot-noise-limited receivers. For an ideal receiver with no thermal noise ($\sigma_T = 0$), the receiver sensitivity is obtained by setting $M = 1$ in Eq. (5.3.18) and is given by

$$(\bar{P}_{\text{rec}})_{\text{ideal}} = (q\Delta f/R_d)Q^2. \tag{5.3.22}$$

5.3.3 Quantum Limit of Photodetection

A question one may ask is related to the quantum limit of the photodetection process. Assuming that a perfect optical signal is incident on an ideal receiver only limited by shot noise, how many photons per bit are needed for recovering the signal reliably? In this subsection we address this question.

We assume that zero bits carry no power, and thus $I_0 = 0$. In the absence of thermal noise, $\sigma_0 \approx 0$ since shot noise also vanishes for the "0" bit if the dark-current contribution is neglected for an ideal receiver. From the definition of the Q factor in Eq. (5.2.11), we find that

$$Q = I_1/\sigma_1 = (\text{SNR})^{1/2}. \tag{5.3.23}$$

As shown earlier, SNR $\approx \eta N_p$ in the shot-noise limit, where N_p is the number of photons contained in each 1 bit [see Eq. (5.2.5) and the following discussion]. By using $Q = (\eta N_p)^{1/2}$ in Eq. (5.3.10), the BER is given by

$$\text{BER} = \tfrac{1}{2}\,\text{erfc}\left(\sqrt{\tfrac{1}{2}\eta N_p}\right). \tag{5.3.24}$$

For a receiver with 100% quantum efficiency ($\eta = 1$), BER $= 1 \times 10^{-9}$ when $N_p = 36$. As 0 bits contain no photons and 1 and 0 bits occur half of the time on average, the average number of photons per bit is 18 from Eq. (5.3.24).

It turns out that this conclusion is incorrect. The BER expression, Eq. (5.3.24), is not totally accurate since its derivation is based on the Gaussian approximation for the noise statistics. When the number of photons is relatively small, one should use the Poisson statistics. The probability of generating m electron–hole pairs when N_p photons are incident on an ideal receiver is given by the Poisson distribution [11]

$$P_m = \exp(-N_p)N_p^m/m!. \tag{5.3.25}$$

Let us use this result to find the BER for an ideal receiver.

The BER can be calculated by using Eqs. (5.3.2) and (5.3.25). For an ideal detector (no thermal noise, no dark current, and 100% quantum efficiency), $\sigma_0 = 0$, as shot noise vanishes in the absence of incident power. As a result, the decision threshold can be set quite close to the 0-level signal. Indeed, for an ideal receiver, 1 bits can be identified without error as long as even one photon is detected. An error is made only if a 1 bit fails to produce even a single electron–hole pair. The probability $P(1/0)$ that a

1 is identified when 0 is received is zero since no electron–hole pair is generated when $N_p = 0$. The probability P(0/1) is obtained by setting $m = 0$ in Eq. (5.3.25), since a 0 is decided in that case even though 1 is received. Since $P(0/1) = \exp(-N_p)$, the BER is given by the simple expression

$$\text{BER} = \tfrac{1}{2} \exp(-N_p). \tag{5.3.26}$$

For BER $< 10^{-9}$, N_p must exceed 20, that is, each 1 bit must contain at least 20 photons to be detected with a BER $< 10^{-9}$. Thus, the average number of photons/bit (including 0 bits) is only 10, and not 18, as found before from Eq. (5.3.24). This discrepancy illustrates that one must examine all approximations carefully when a small number of photons is involved. It also shows that the noise statistics play an important role, and Eq. (5.3.10) should be used with care if the total noise cannot be treated as a Gaussian stochastic process.

It is important to stress that the quantum limit is rarely reached in practical receivers employing direct detection because their noise is dominated by thermal noise (unless the receiver is cooled to temperature levels near absolute zero). Most receivers operate away from the quantum limit by 20 dB or more. This is equivalent to saying that the average number of photons/bit typically exceeds 1,000 in practical receivers.

5.4 Sensitivity Degradation

The discussion of receiver sensitivity in Section 5.3 includes thermal noise but is still overly simplified in many respects. In particular, the analysis assumes that the optical signal incident on the receiver consists of an ideal bit stream such that 1 bits consist of an optical pulse of constant energy, while no energy is contained in 0 bits. In practice, an optical signal deviates from this ideal situation even at the transmitter end. Moreover, it can be degraded during its transmission through the fiber link. An example of such degradation is provided by dispersion-induced pulse broadening. The minimum average optical power required by the receiver increases because of such nonideal conditions. This increase in the required power is referred to as the *power penalty*. In this section, we focus on several sources of power penalties that can lead to sensitivity degradation. The impact of noise added by optical amplifiers is discussed in Chapter 6.

5.4.1 Finite Extinction Ratio

A simple source of a power penalty is related to the energy contained in 0 bits. Some power is emitted by most transmitters even in the off state. In the case of a directly modulated semiconductor laser, the off-state power P_0 depends on the bias level. In the case of a external modulators. P_0 depends on the on–off contrast of the modulator. In both cases, the *extinction ratio* is defined as

$$r_{\text{ex}} = P_0/P_1. \tag{5.4.1}$$

The power penalty can be obtained from Eq. (5.3.11). For a p–i–n receiver $I_1 = R_d P_1$ and $I_0 = R_d P_0$ (APD gain can be included by replacing R_d with MR_d). Using

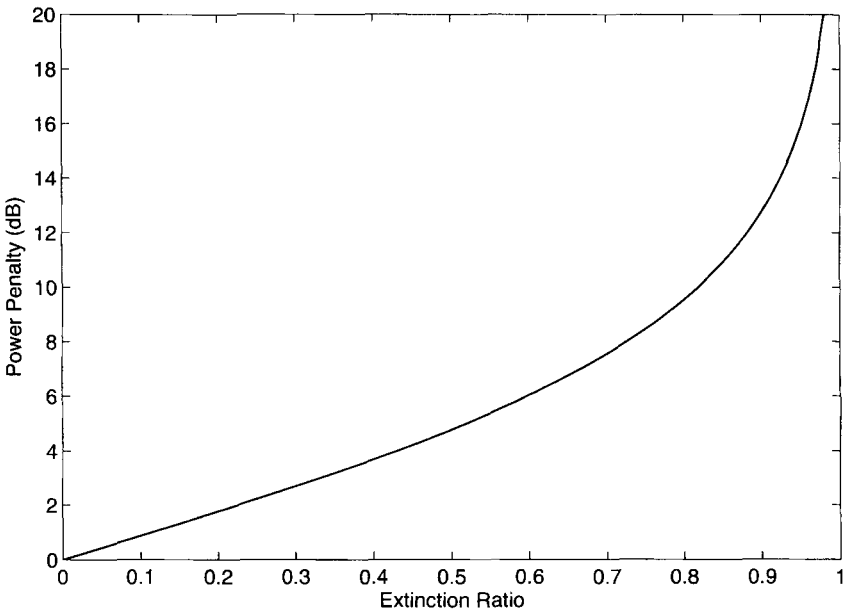

Figure 5.7: Power penalty as a function of the extinction ratio r_{ex}.

$\bar{P}_{rec} = (P_1 + P_0)/2$ for the receiver sensitivity, the Q factor is given by

$$Q = \left(\frac{1 - r_{ex}}{1 + r_{ex}}\right) \frac{2R_d \bar{P}_{rec}}{\sigma_1 + \sigma_0}. \tag{5.4.2}$$

In general, σ_1 and σ_0 depend on $\bar{P}_{rec}$ because of the dependence of the shot-noise contribution on the received optical signal. However, both of them can be approximated by σ_T when receiver performance is dominated by thermal noise. By using $\sigma_1 \approx \sigma_0 \approx \sigma_T$ in Eq. (5.4.2), $\bar{P}_{rec}$ is given by

$$\bar{P}_{rec}(r_{ex}) = \left(\frac{1 + r_{ex}}{1 - r_{ex}}\right) \frac{\sigma_T Q}{R_d}. \tag{5.4.3}$$

This equation shows that $\bar{P}_{rec}$ increases when $r_{ex} \neq 0$.

The power penalty is defined as the ratio $\delta_{ex} = \bar{P}_{rec}(r_{ex})/\bar{P}_{rec}(0)$. It can be expressed in decibel (dB) units as

$$\delta_{ex} = 10 \log_{10}\left(\frac{\bar{P}_{rec}(r_{ex})}{\bar{P}_{rec}(0)}\right) = 10 \log_{10}\left(\frac{1 + r_{ex}}{1 - r_{ex}}\right). \tag{5.4.4}$$

Figure 5.7 shows how the power penalty increases with r_{ex}. A 1-dB penalty occurs for $r_{ex} = 0.12$ and increases to 4.8 dB for $r_{ex} = 0.5$. In practice, most lightwave systems are designed with r_{ex} below 0.05, and the corresponding power penalty is negligible (<0.4 dB). However, it may become significant for a directly modulated semiconductor

laser biased above threshold. An expression for $\bar{P}_{\rm rec}(r_{\rm ex})$ can be obtained for APD receivers by including the APD gain and the shot-noise contribution to σ_0 and σ_1 in Eq. (5.4.2). The optimum APD gain is lower than that in Eq. (5.3.20) when $r_{\rm ex} \neq 0$. The sensitivity is also reduced because of this lower optimum gain. Typically, the power penalty for an APD receiver is larger by about a factor of 2 for the same value of $r_{\rm ex}$.

5.4.2 Intensity Noise of Lasers

In practice, light emitted by any laser exhibits power fluctuations. Such fluctuations, called intensity noise, have been discussed in Section 5.3.4 of LT1 in the context of semiconductor lasers. An optical receiver converts power fluctuations into current fluctuations, which add to those resulting from shot and thermal noises. As a result, the receiver SNR is degraded and is lower than that given in Eq. (5.2.10). An exact analysis is complicated as it involves the calculation of photocurrent statistics [12]. A simple approach consists of adding a third term to the current variance given in Eq. (5.1.11) and writing it as

$$\sigma^2 = \sigma_s^2 + \sigma_T^2 + \sigma_I^2, \tag{5.4.5}$$

where σ_I^2 is related to the variance of power fluctuations as

$$\sigma_I = R_d \langle (\Delta P_{\rm in}^2) \rangle^{1/2} = R_d P_{\rm in} r_I. \tag{5.4.6}$$

The parameter r_I, defined as $r_I = \langle (\Delta P_{\rm in}^2) \rangle^{1/2} / P_{\rm in}$, is a measure of the noise level of the optical signal. It is related to the *relative intensity noise* (RIN) of the laser as

$$r_I^2 = \int_{-\infty}^{\infty} {\rm RIN}(f)\, df, \tag{5.4.7}$$

where ${\rm RIN}(f)$ represents the intensity-noise spectrum. As discussed in Section 5.3.4 of LT1, r_I is simply the inverse of the SNR of light emitted by the transmitter. Typically, the transmitter SNR is better than 20 dB, and $r_I < 0.01$.

As a result of the dependence of σ_0 and σ_1 on the parameter r_I, the parameter Q in Eq. (5.3.11) is reduced in the presence of intensity noise. Since Q should have the same value to maintain a specific BER, it is necessary to increase the received power. This is the origin of the power penalty induced by intensity noise. To simplify the following analysis, the extinction ratio is assumed to be zero, so that $I_0 = 0$ and $\sigma_0 = \sigma_T$. Using $I_1 = RP_1 = 2R\bar{P}_{\rm rec}$ and Eq. (5.4.5) for σ_1, Q is given by

$$Q = \frac{2R\bar{P}_{\rm rec}}{(\sigma_T^2 + \sigma_s^2 + \sigma_I^2)^{1/2} + \sigma_T}, \tag{5.4.8}$$

where

$$\sigma_s = (4qR\bar{P}_{\rm rec}\Delta f)^{1/2}, \qquad \sigma_I = 2r_I R\bar{P}_{\rm rec}, \tag{5.4.9}$$

and σ_T is given by Eq. (5.1.10). Equation (5.4.8) is easily solved to obtain the following expression for the receiver sensitivity:

$$\bar{P}_{\rm rec}(r_I) = \frac{Q\sigma_T + Q^2 q\Delta f}{R(1 - r_I^2 Q^2)}. \tag{5.4.10}$$

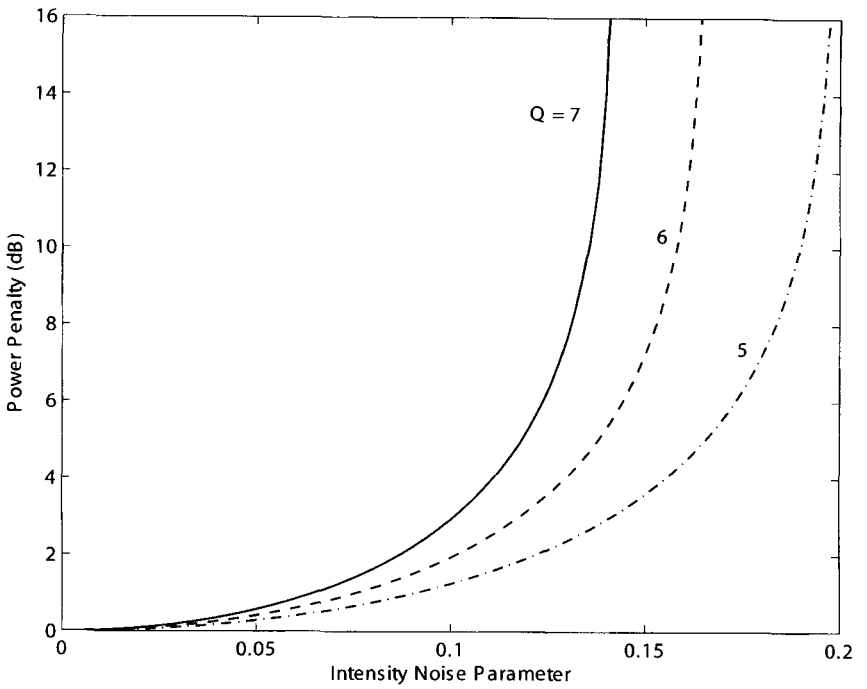

Figure 5.8: Power penalty as a function of the intensity noise parameter r_I.

The power penalty, defined as the increase in $\bar{P}_{\text{rec}}$ when $r_I \neq 0$, is given by

$$\delta_I = 10 \log_{10}[\bar{P}_{\text{rec}}(r_I)/\bar{P}_{\text{rec}}(0)] = -10 \log_{10}(1 - r_I^2 Q^2). \tag{5.4.11}$$

Figure 5.8 shows power penalty as a function of r_I for $Q = 5$, 6, and 7. The penalty is negligible for $r_I < 0.01$ as δ_I is below 0.02 dB. Since this is the case for most optical transmitters, the effect of transmitter noise is negligible in practice. The power penalty is almost 2 dB for $r_I = 0.1$ and becomes infinite when $r_I = Q^{-1} = 0.167$. An infinite power penalty implies that the receiver cannot operate at the specific BER even if the received optical power is increased indefinitely. In Figure 5.6, an infinite power penalty corresponds to a saturation of the BER curve above a specific error level, a feature referred to as the BER floor. In this respect, the effect of intensity noise is qualitatively different than the extinction ratio, for which the power penalty remains finite for all values of r_{ex} such that $r_{\text{ex}} < 1$.

The preceding analysis assumes that the intensity noise at the receiver end is the same as at the transmitter end. This is not the case when optical signal propagates through a long fiber link. The noise added by in-line optical amplifiers often becomes a limiting factor for long-haul lightwave systems. This issue is discussed in Chapter 6.

5.4.3 Dispersive Pulse Broadening

Dispersion-induced pulse broadening affects the receiver performance in two ways. First, a part of the pulse energy spreads beyond the allocated bit slot and leads to intersymbol interference. Second, the pulse energy within the bit slot is reduced when the optical pulse broadens. Such a decrease in pulse energy reduces the SNR at the decision circuit. As the SNR should remain constant to maintain the system performance, the receiver requires more average power. This is the origin of dispersion-induced power penalty δ_d.

An exact calculation of δ_d is difficult, as it depends on many details such as the extent of pulse shaping at the receiver. A rough estimate is obtained by following the analysis of Section 3.3.1, where broadening of Gaussian pulses is discussed. Equation (3.3.9) shows that the optical pulse remains Gaussian, but its peak power is reduced by a pulse-broadening factor given in Eq. (3.3.10). If we define the power penalty δ_d as the increase (in decibels) in the received power that would compensate the peak-power reduction, δ_d is given by

$$\delta_d = 10 \log_{10} b_f, \tag{5.4.12}$$

where b_f is the pulse broadening factor. As in Section 3.3.4, we consider the case of broadband and narrowband optical sources separately.

Consider first a lightwave system designed with a relatively broadband optical source. The broadening factor f_b in this case is given in Eq. (3.3.38) and has the form

$$b_f = \sigma/\sigma_0 = [1 + (DL\sigma_\lambda/\sigma_0)^2]^{1/2}, \tag{5.4.13}$$

where σ_λ is the RMS width of the source spectrum. The RMS width σ_0 of the optical pulse at the transmitter end is a design parameter. It can be related to the duty cycle d_c of RZ pulses as $4\sigma_0 = d_c T_b$, where $T_b \equiv 1/B$ is the duration of the bit slot at a given bit rate B. Using $\sigma_0 = d_c/(4B)$ in Eq. (5.4.13) and using Eq. (5.4.12), the power penalty becomes

$$\delta_d = 5 \log_{10}[1 + (4BLD\sigma_\lambda/d_c)^2]. \tag{5.4.14}$$

This result should be compared with the condition (3.3.40) found in Section 3.3.4. If we assume that input pulses are wide enough to occupy the entire bit slot ($d_c = 1$), the power penalty is negligible for $4BLD\sigma_\lambda \ll 1$, becomes 1.5 dB when $4BLD\sigma_\lambda = 1$, and increases rapidly beyond that.

In the case of a long-haul system designed with a narrowband source and chirp-free pulses, the broadening factor f_b is obtained from Eq. (3.3.43). If we use again $\sigma_0 = d_c/(4B)$, the power penalty is given by

$$\delta_d = 5 \log_{10}[1 + (8\beta_2 B^2 L/d_c^2)^2]. \tag{5.4.15}$$

Figure 5.9 shows power penalty as a function of the dimensionless parameter combination $\mu = |\beta_2| B^2 L$ for three values of d_c. Although the power penalty is negligible for values of $\mu < 0.05$ and $d_c > 0.5$, it increases rapidly as μ increases and exceeds 5 dB for $\mu = 0.1$ and $d_c = 0.5$. It is thus important to keep μ below 0.1. As an example, the operating distance of a 10-Gb/s lightwave system is limited to below 50 km because of dispersion when standard fibers are used with $|\beta_2| \approx 20$ ps^2/km, but this value can be

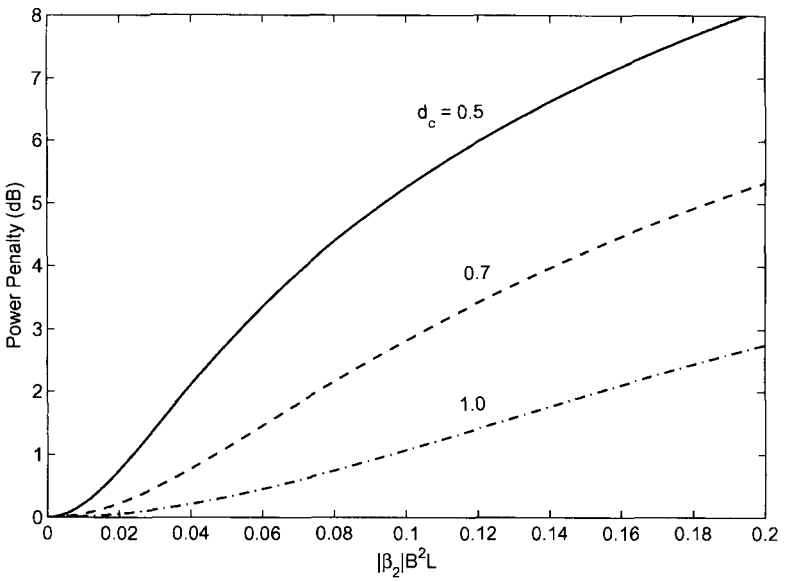

Figure 5.9: Dispersion-induced power penalty function as a function of $\mu = |\beta_2|B^2L$ for three values of duty cycle associated with an RZ bit stream.

increased considerably through dispersion management. It should be stressed that Eq. (5.4.15) provides only a rough estimate as its derivation is based on the assumptions of a Gaussian pulse shape.

5.4.4 Frequency Chirping

The preceding discussion of dispersion-induced power penalty assumed that the input pulses were unchirped. An initial chirp on optical pulses is known to limit the performance of 1.55-μm lightwave systems when directly modulated semiconductor lasers are used to generate the digital bit stream [19]–[32]. As discussed in Section 3.3, frequency chirping can enhance the dispersion-induced broadening of optical pulses and thus may degrade the performance of a long-haul lightwave system more than that expected when unchirped pulses are employed.

An exact calculation of the chirp-induced power penalty δ_c is difficult because frequency chirp depends on both the shape and the width of the optical pulse [21]–[24]. However, if we assume a Gaussian pulse shape and a linear chirp, the analysis of Section 3.3.3 can be used to estimate the chirp-induced power penalty. If we use Eq. (3.3.11) for the pulse broadening factor in Eq. (5.4.12) together with $T_0 = \sqrt{2}d_c/(4B)$, the power penalty is given by

$$\delta_c = 5\log_{10}[(1 + 8C\beta_2 B^2 L/d_c^2)^2 + (8\beta_2 B^2 L/d_c^2)^2]. \tag{5.4.16}$$

Figure 5.10 shows the chirp-induced power penalty as a function of $|\beta_2|B^2L$ for several values of the chirp parameter C with $d_c = 1$. The parameter β_2 is taken to be

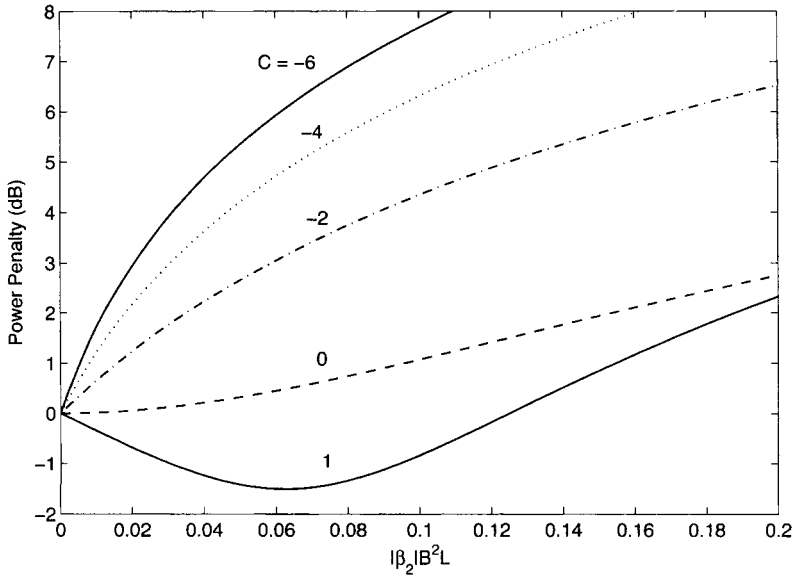

Figure 5.10: Chirp-induced power penalty as a function of $|\beta_2|B^2L$ for several values of the chirp parameter C. Gaussian pulses are assumed to be linearly chirped.

negative, as is the case for 1.55-μm lightwave systems. The $C = 0$ curve corresponds to the case of a chirp-free pulse. Power penalty is negligible (<0.1 dB) in this ideal case as long as $|\beta_2|B^2L < 0.05$. However, the penalty can exceed 5 dB if the transmitted pulses are chirped such that $C = -6$ (a typical value for semiconductor lasers). To keep the penalty below 0.1 dB, the system should be designed with $|\beta_2|B^2L < 0.002$. For standard optical fibers with $\beta_2 \approx -20$ ps^2/km, B^2L is limited to 100 (Gb/s)^2-km, indicating that even at $B = 2.5$ Gb/s, the transmission distance is limited to below 16 km because of frequency chirping. Interestingly, system performance can be improved by ensuring that $\beta_2 C < 0$. As discussed in Section 3.3, each optical pulse then undergoes an initial compression phase. As C is negative for semiconductor lasers, fibers with "normal" dispersion ($\beta_2 > 0$) can provide better performance whenever directly modulated semiconductor lasers are employed. For this reason, fibers with normal GVD are often employed in metropolitan area networks. Alternatively, one can make use of dispersion compensation and ensure that the average value of β_2 is close to zero.

5.4.5 Timing Jitter

The decision circuit of a receiver is designed to sample the signal at the peak of the voltage pulse. As discussed in Section 7.5.3 of LT1, the decision instant is determined by a clock-recovery circuit. Because of the noisy nature of the input to this circuit, sampling time may fluctuate from bit to bit. Such fluctuations represent an example of electrical *timing jitter* [33]–[36]. As discussed in Section 6.5, noise produced by optical amplifiers can produce optical timing jitter. In both cases, the SNR is degraded

because timing jitter leads to additional fluctuations in the sampled value of the signal. This can be understood by noting that if the bit is not sampled at the bit center, or it has moved from the bit center, the sampled value is reduced by an amount that depends on the timing jitter Δt. The SNR is reduced as a result of jitter-induced fluctuations. It can be maintained at its original value only by increasing the optical power. This increase corresponds to the power penalty induced by timing jitter.

An exact calculation of the jitter-induced power penalty δ_j is complicated because it depends on details of the receiver design. A rough estimate of the tolerable value of timing jitter is obtained by assuming Gaussian statistics for Δt with the probability density

$$p(\Delta t) = \frac{1}{\sigma_t \sqrt{2\pi}} \exp\left(-\frac{\Delta t^2}{2\sigma_t^2}\right), \tag{5.4.17}$$

where σ_t is the RMS value (standard deviation) of Δt. The BER can be calculated by following the analysis of Section 5.3.1. If we assume that an error occurs whenever the pulse has moved out of the bit slot, we need to find the accumulated probability for $|\Delta t|$ to exceed $T_b/2$, where $T_b \equiv 1/B$ is the bit slot. This probability is found to be

$$\text{BER} = 2\int_{T_b/2}^{\infty} p(\Delta t)\, d(\Delta t) = \text{erfc}\left(\frac{T_b}{2\sqrt{2}\sigma_t}\right) \approx \frac{4\sigma_t}{\sqrt{2\pi}T_b} \exp\left(-\frac{T_b^2}{8\sigma_t^2}\right), \tag{5.4.18}$$

where erfc stands for the complimentary error function defined in Eq. (5.3.5). To reduce the BER below 10^{-9}, σ_t should be less than 8% of the bit slot T_b. Thus, a tolerable value of the jitter is 8 ps for 10-Gb/s systems and reduces to only 2 ps for 40-Gb/s systems.

The preceding estimate is relatively crude as it focuses on errors induced by jitter alone. We can improve on it by considering how the Q factor is affected by timing jitter. For simplicity, consider a *p–i–n* receiver dominated by thermal noise and assume a zero extinction ratio. Using $I_0 = 0$ in Eq. (5.3.11), the Q factor is given by

$$Q = \frac{I_1 - \langle \Delta i_j \rangle}{(\sigma_T^2 + \sigma_j^2)^{1/2} + \sigma_T}, \tag{5.4.19}$$

where $\langle \Delta i_j \rangle$ is the average value and σ_j is the RMS value of the current fluctuation Δi_j induced by timing jitter Δt. If $S_p(t)$ governs the shape of the current pulse,

$$\Delta i_j = I_1[S_p(0) - S_p(\Delta t)], \tag{5.4.20}$$

where the ideal sampling instant is taken to be $t = 0$. Clearly, σ_j depends on the shape of the electrical pulse at the decision circuit, which in turn depends on the filters used within the receiver. One choice corresponds to $S_p(t) = \cos^2(\pi Bt/2)$, where B is the bit rate [24], as receivers are often designed to mimic this shape. Rather then considering a specific pulse shape, we approximate S_p by a parabola as $S_p(t) = 1 - \frac{1}{2}(c_p Bt)^2$, where c_p governs the pulse curvature near $t = 0$. Since Δt is likely to be much smaller than T_b, this approximation holds for any pulse shape and leads to a current fluctuation of the form

$$\Delta i_j = (c_p B \Delta t)^2 I_1. \tag{5.4.21}$$

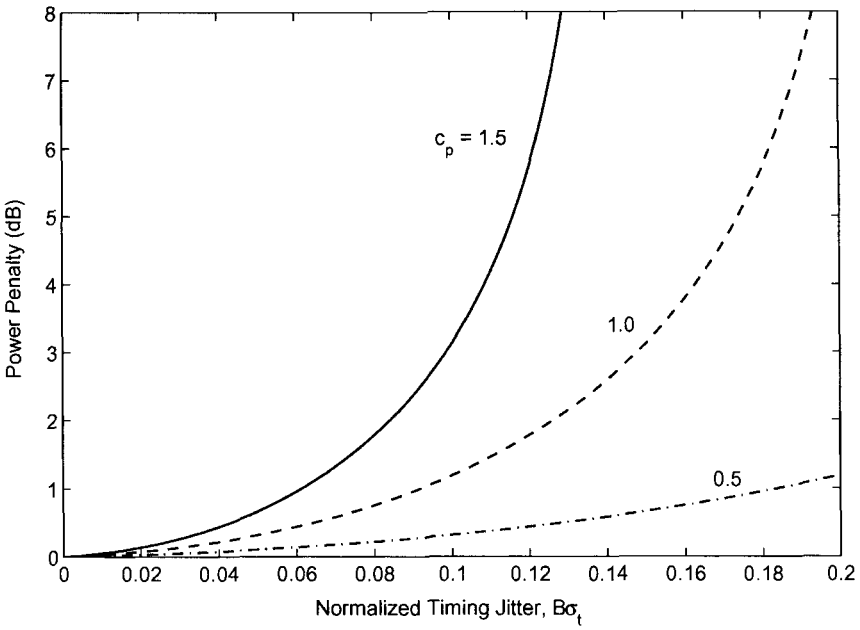

Figure 5.11: Power penalty versus timing-jitter parameter $B\sigma_t$.

To calculate $\langle \Delta i_j \rangle$ and σ_j, we first need to find the probability density function $p(\Delta i_j)$ using Eq. (5.4.17). Noting that Δi_j is proportional to $(\Delta t)^2$ and using the relation $p(\Delta i_j)\, d\Delta i_j = p(\Delta t)\, d\Delta t$, we obtain

$$p(\Delta i_j) = \frac{1}{\sqrt{\pi b \Delta i_j I_1}} \exp\left(-\frac{\Delta i_j}{b I_1}\right), \tag{5.4.22}$$

where $b = (c_p B\sigma_t)^2$. Using this equation, we find the first two moments of Δi_j and obtain

$$\langle \Delta i_j \rangle = bI_1/2, \qquad \sigma_j = bI_1/\sqrt{2}. \tag{5.4.23}$$

Using Eqs. (5.4.19) and (5.4.23) and noting that $I_1 = 2R_d \bar{P}_{\text{rec}}$, the receiver sensitivity is given by

$$\bar{P}_{\text{rec}}(b) = \left(\frac{\sigma_T Q}{R_d}\right) \frac{1 - b/2}{(1-b/2)^2 - b^2 Q^2/2}. \tag{5.4.24}$$

The power penalty, defined as the increase in $\bar{P}_{\text{rec}}$ when $b \neq 0$, is given by

$$\delta_j = 10 \log_{10}\left(\frac{\bar{P}_{\text{rec}}(b)}{\bar{P}_{\text{rec}}(0)}\right) = 10 \log_{10}\left(\frac{1 - b/2}{(1-b/2)^2 - b^2 Q^2/2}\right). \tag{5.4.25}$$

Figure 5.11 shows how the power penalty varies with the parameter $B\sigma_t$ for three values of the parameter c_p to maintain a BER below 10^{-9} ($Q = 6$). As seen there, pulse curvature near the center of the bit slot plays an important role. In all cases, the

power penalty increases with an increase in timing jitter and becomes infinitely large at a certain value of $B\sigma_t$. The tolerable value $B\sigma_t$ depends on c_p and decreases as c_p increases. In most receivers, the filter bandwidth is smaller than the bit rate, and the electrical pulse is wider than the bit slot. As a result, $c_p < 1$ in practice. The power penalty in this case can be kept negligible (below 0.5 dB) if the jitter is such that $B\sigma_t < 8\%$, although it increases rapidly beyond $B\sigma_t > 12\%$. It is interesting to note that this conclusion is in agreement with the prediction based on Eq. (5.4.18). We should stress that even Eq. (5.4.25) is based on the use of Gaussian statistics for the receiver current. As evident from Eq. (5.4.22), jitter-induced current fluctuations are not Gaussian in nature. A more accurate calculation shows that Eq. (5.4.25) underestimates the power penalty [35].

5.4.6 Eye-Closure Penalty

An alternative measure of system performance is provided by the extent the "eye opening" in the eye diagram is affected by the dispersive and nonlinear effects accumulated inside the fiber link. As discussed in Section 7.5.2 of LT1, an electrical filter with a bandwidth smaller than the bit rate is used inside the receiver to reshape pulses before they reach the decision circuit. When successive combinations of two or three bits are overlapped within the same temporal window, the resulting pattern observed on an oscilloscope looks like an open eye for an NRZ-format bit stream diagram. When the RZ format or one of its variants is employed, the pattern still has the appearance of an eye even though the top horizontal rail is missing. Even in the case of the DPSK format, the eye diagram retains its shape. The top row in Figure 5.12 shows the measured eye diagrams at 40 Gb/s in the case of NRZ, CSRZ, NRZ-DPSK, and RZ-DPSK formats under back-to-back conditions in which the transmitter is connected to the receiver with virtually no fiber in between. In each case, the thickness of curves is due to receiver noise.

As the optical bit stream is transmitted through a fiber link, the accumulation of dispersive and nonlinear effects distorts optical pulses. These distortions manifest in the eye diagram through a reduced opening of the eye. The bottom row in Figure 5.12 shows the measured eye diagrams at 40 Gb/s after a 263-km-long fiber link for the same four modulation formats [37]. As seen there, eye opening is reduced for all formats. Since the decision threshold is set in the center of the open portion of the eye, any reduction in eye opening indicates an increase in the BER. This observation relates eye closure to the BER and suggests that its magnitude can provide a measure of the system performance. More precisely, the eye-closure penalty is quantified (in dB) as

$$\delta_{\text{eye}} = -10 \log_{10} \left(\frac{\text{eye opening after transmission}}{\text{eye opening before transmission}} \right). \tag{5.4.26}$$

Before Eq. (5.4.26) can be used, we need to clarify what one means by eye opening. Ideally, the eye amplitude peaks in the center of the bit slot and it provides an appropriate measure of eye opening. However, in practice, timing jitter makes it difficult to sample each pulse precisely at the location where pulse amplitude is maximum. If we allow an uncertainty of up to 10% on each side of the decision threshold, we should

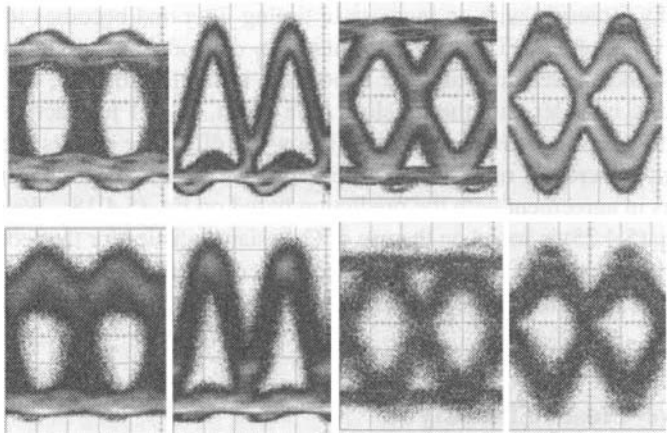

Figure 5.12: Measured eye diagrams at 40 Gb/s under back-to-back conditions (top row) and after a 263-km-long fiber link (bottom row). In both cases successive traces corresponds to NRZ, CSRZ, NRZ-DPSK, and RZ-DPSK formats, respectively. (After Ref. [37]; ©2004 IEEE.)

consider a rectangle of the largest area with a base of $0.2T_b$, where T_b is the duration of the bit slot, that can be fitted within the open portion of the eye. The height of this rectangle then measures eye opening. This approach is commonly adopted for numerical simulations.

5.5 Forward Error Correction

As seen in the preceding section, receiver sensitivity and the BER of a lightwave system are degraded by many factors that are not always controllable in practice. Depending on details of the system design and objectives, it is entirely possible that a specified BER cannot be achieved. Under such conditions, the use of an error-correction scheme remains the only viable alternative.

Error control is not a new concept and is employed widely in electrical systems dealing with the transfer of digital data from one device to another [38]–[41]. The techniques used for controlling errors can be divided into two groups. In one group, errors are detected but not corrected. Rather, each packet of bits received with errors is retransmitted. This approach is suitable when data bits are transmitted in the form of packets (as is the case for the protocol used by the Internet) and they do not arrive at the destination in a synchronous fashion. In the other group, errors are detected as well as corrected at the receiver end without any retransmission of bits. This approach is referred to as forward error correction (FEC) and is best suited for lightwave systems operating with a synchronous protocol such as SONET or SDH.

Historically, lightwave systems did not employ FEC until the use of in-line optical amplifiers became common [42]–[44]. The use of FEC accelerated with the advent of WDM technology. As early as 1996, FEC was employed for a WDM system designed to operate over more than 425 km without any in-line amplifier or regenerator [45].

Since then, the FEC technique has been used in many WDM systems and is now considered almost routine [46]–[52]. This section provides only basic information about FEC; we refer to recent literature for further details [53]–[56].

5.5.1 Error-Correcting Codes

The basic idea behind any error-control technique is to add extra bits to the signal at the transmitter end in a judicial manner using a suitable coding algorithm [38]–[41]. A simple example is provided by the so-called parity bit that is added to the 7-bit ASCII code. In this example, the parity bit is chosen to be 0 or 1 depending on whether the number of 1 bits in the 7-bit sequence is even or odd. If a single bit is in error at the receiving end, an examination of the parity bit reveals the error.

The situation is somewhat different in the case of an optical bit stream, but the basic idea remains the same. An encoder within the transmitter adds additional control bits using a suitable code. At the receiver end, a decoder uses these control bits to detect errors, while correcting them simultaneously. How many errors can be corrected depends on the coding scheme employed. In general, more errors can be corrected by adding more control bits to the signal. Clearly, there is a limit to this process since the bit rate of the signal increases after the decoder. If B_e is the effective bit rate after coding a signal at the bit rate B, the *FEC overhead* associated with the error-correcting code is $B_e/B - 1$. The concept of *redundancy* is also used for FEC codes as the bits added by the coding scheme do not carry any information. Redundancy of a code is defined as $\rho = 1 - B/B_e$.

Many different types of error-correcting codes have been developed, often classified under names such as linear, cyclic, Hamming, Reed–Solomon, convolutional, product, and turbo codes [53]. Among these, Reed–Solomon (RS) codes have attracted most attention in the context of lightwave systems [54]. An RS code is denoted as RS(n,k), where k is the size of a packet of bits that is converted through coding into a larger packet with n bits. The value of n is chosen such that $n = 2^m - 1$, where m is an integer. The RS code recommended by ITU for submarine applications uses $m = 8$ and is written as RS(255, 239). The FEC overhead for this code is only 6.7%. Many other RS codes can be used if a higher overhead is permitted. For example, the code RS(255, 207) has an overhead of 23.2% but it allows for more robust error control. The choice of the code depends on the level of improvement in the BER required for the system to operate reliably. It is common to quantify this improvement through the *coding gain*, a concept we discuss next.

5.5.2 Coding Gain

Coding gain is a measure of the improvement in BER realized through FEC. Since BER is related to the Q factor as indicated in Eq. (5.3.10), it is often expressed in terms of the equivalent value of Q that corresponds to the BER realized after the FEC decoder. The coding gain in decibel units is defined as [54]

$$G_c = 20 \log_{10}(Q_c/Q), \tag{5.5.1}$$

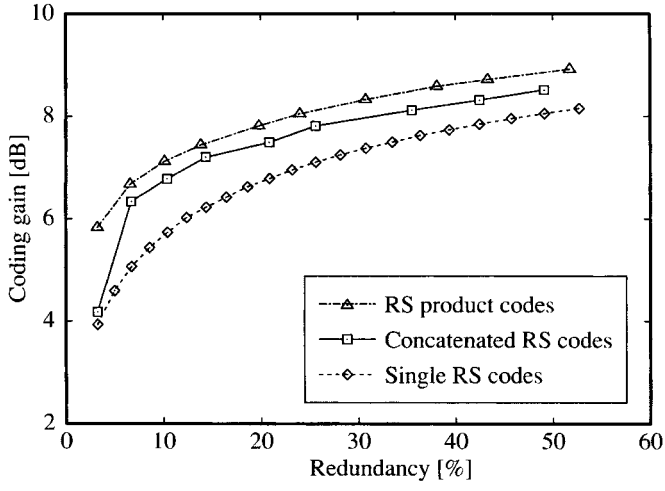

Figure 5.13: Coding gain as a function of code redundancy (overhead) for single, concatenated, and product-type RS codes. (After Ref. [54]; ©2002 IEEE.)

where Q_c and Q are related to the BERs obtained with and without FEC as

$$\text{BER}_c = \tfrac{1}{2}\,\text{erfc}(Q_c/\sqrt{2}), \qquad \text{BER} = \tfrac{1}{2}\,\text{erfc}(Q/\sqrt{2}). \tag{5.5.2}$$

The reason that the factor of 20 is used in place of 10 is related to the definition of Q_{dB} in Eq. (5.3.12). As an example, if the FEC decoder improves the BER from its original value of 10^{-3} to 10^{-9}, the value of Q increases from about 3 to 6, resulting in a coding gain of 6 dB. The coding gain is sometimes defined in terms of the SNR [53]. The two definitions differ by a small amount of $10\log_{10}(B_e/B)$.

As one would expect, the magnitude of coding gain increases with the FEC overhead (or redundancy). The dashed line in Figure 5.13 shows this behavior. The coding gain is about 5.5 dB for 10% overhead and increases sublinearly, reaching only 8 dB even for a 50% overhead. It can be improved by concatenating two or more RS codes or by employing the RS product codes, but in all cases the coding gain begins to saturate as overhead increases. In the case of a RS product code, more than 6 dB of coding gain can be realized with only 5% overhead. The basic idea behind an RS product code is shown in Figure 5.14. As seen there, a block of data with k^2 bits is converted into n^2 bits by applying the same RS(n,k) code both along the rows and columns. As a result, the overhead of $n^2/k^2 - 1$ for a RS product code is larger, but it also allows more error control.

5.5.3 Optimum Coding Overhead

While implementing FEC for a lightwave system, one faces a dilemma. As the overhead is increased to realize more coding gain, the bit rate of the optical signal increases. Since the Q factor realized at the receiver depends on the bit rate, its value before the

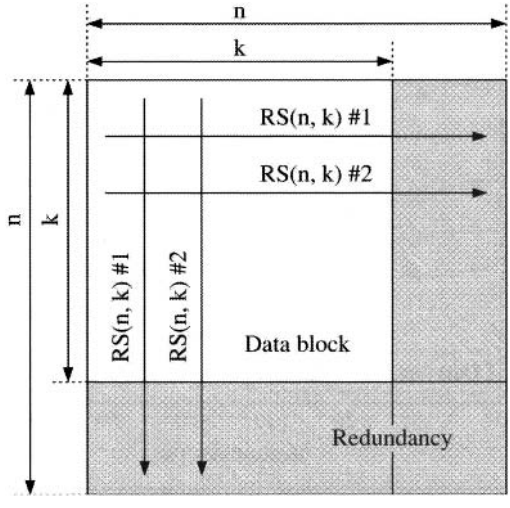

Figure 5.14: Schematic illustration of a RS product code. The same code is applied along the rows and columns of a block of bits. (After Ref. [54]; ©2002 IEEE.)

FEC decoder is reduced, and the BER is actually worse than that expected in the absence of FEC. The decoder improves it but not as much as one would like because it first has to overcome the degradation caused by the increased bit rate. In fact, if an aggressive FEC scheme with a large overhead is employed, it is possible that the BER is degraded so much that the system is not operable even with the FEC scheme. In other words, there exists an optimum range of the coding overhead for every system designed to operate at a specific bit rate over a certain distance.

Numerical simulations have been used to show that such an optimum range for the coding overhead indeed exists [54]. Figure 5.15(a) shows the value of the Q factor before the decoder as a function of the redundancy (or overhead) for a 25-channel WDM system designed to operate over more than 5,000 km with $B = 40$ Gb/s per channel. The effective values of Q_c after the decoder are shown in part (b). In the absence of FEC, the system cannot operate beyond 3,000 km. With FEC, the Q factor becomes worse as the overhead increases because of the enhanced bit rate. However, the system can operate over a distance of 5,000 km over a wide range of overhead between 7 and 40%. The transmission distance can be increased to 6,000 km, but the overhead range over which the system can operate shrinks to below 25%. However, distance cannot be increased any further no matter what coding overhead is employed. The reason for this behavior is apparent from Figure 5.15(a). As seen there, Q^2 is about 9 dB in the absence of FEC at a distance of 6,400 km. With FEC, this value drops to below 8 dB for a 20% overhead and drops sharply afterward as the overhead is increased further. Since a coding gain of more than 8 dB is not possible for the simple RS code used in the example of Figure 5.15, one cannot increase Q_c^2 above 15.6 dB, the value needed to realize a BER of less than 10^{-9}.

Most lightwave systems currently employ the RS(255, 239) code that has been recommended by ITU for submarine applications. It allows for a coding gain of up to

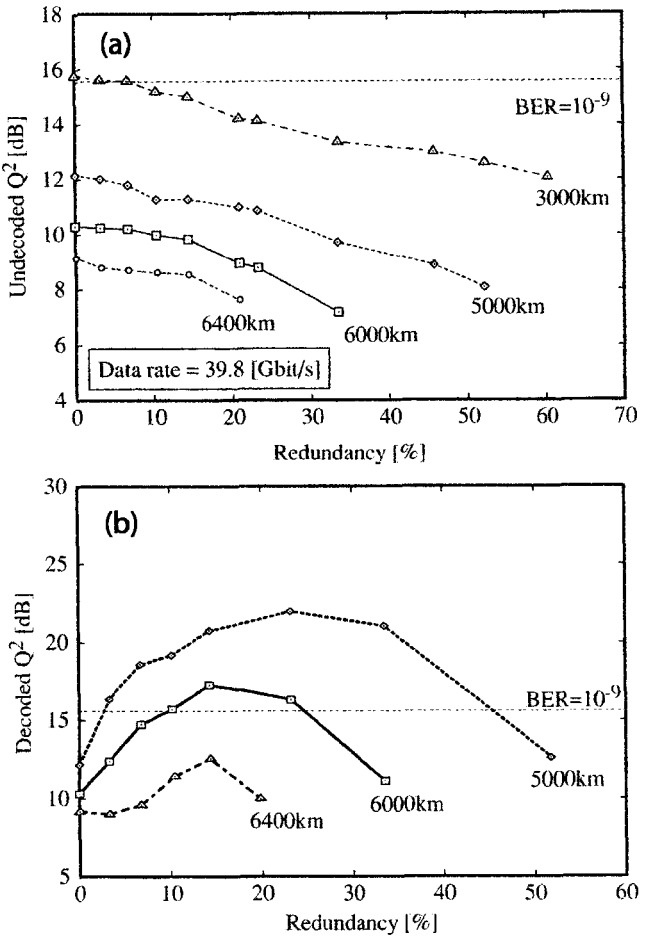

Figure 5.15: Numerically simulated Q factors (a) before and (b) after the FEC decoder as a function of code redundancy for a WDM system with 25 channels, each at 40 Gb/s. (After Ref. [54]; ©2002 IEEE.)

6 dB with an overhead of 6.7%. The coding gain can be increased by about 1.2 dB if the FEC coder employs the RS(255, 223) scheme with an overhead of 14.3%. Concatenation of two RS(255, 239) codes also improves the coding gain by 1.2 dB at a somewhat reduced overhead of 13.8%. An enhanced version of the FEC chip also became available commercially in 2002. It can improve the coding gain by 2 dB while keeping the overhead close to 7%. In a 2003 experiment, the required optical SNR for a 10-7-Gb/s duobinary signal transmitted over 200 km was reduced from >23 dB to 15 dB with the standard RS(255, 223) code [57]. This value was further reduced to only 13 dB when the enhanced FEC was employed. In another experiment, a similar increase in the coding gain was observed even when a 40-Gb/s signal was transmitted with the RZ-DPSK format [58].

Problems

5.1 Consider a 0.8-μm receiver with a silicon p–i–n photodiode. Assume 20 MHz bandwidth, 65% quantum efficiency, 1 nA dark current, 8 pF junction capacitance, and 3 dB amplifier noise figure. The receiver is illuminated with 5 μW of optical power. Determine the noise currents due to shot noise, thermal noise, and amplifier noise. Also calculate the signal-to-noise ratio.

5.2 The receiver of Problem 5.1 is used in a digital communication system that requires a signal-to-noise ratio of at least 20 dB. What is the minimum required power when receiver performance is limited by (a) shot noise and (b) thermal noise? Also calculate the noise-equivalent power in the two cases.

5.3 The excess noise factor of avalanche photodiodes is often approximated by M^x instead of Eq. (5.2.9). Find the range of M for which Eq. (5.2.9) can be approximated within 10% by $F_A(M) = M^x$ by choosing $x = 0.3$ for Si, 0.7 for InGaAs, and 1.0 for Ge. Use $k_A = 0.02$ for Si, 0.35 for InGaAs, and 1.0 for Ge.

5.4 Derive Eq. (5.2.13). Plot M_{opt} versus k_A by solving the cubic polynomial on a computer by using $R_L = 1$ kΩ, $F_n = 2$, $R = 1$ A/W, $P_{\text{in}} = 1$ μW, and $I_d = 2$ nA. Compare the results with the approximate analytic solution given by Eq. (5.2.14) and comment on its validity.

5.5 Derive an expression for the optimum value of M for which the signal-to-noise ratio becomes maximum by using $F_A(M) = M^x$ in Eq. (5.2.10).

5.6 Prove that the bit-error rate given in Eq. (5.3.6) is minimum when the decision threshold is set close to a value given by Eq. (5.3.9).

5.7 A 1.3-μm digital receiver is operating at 100 Mb/s and has an effective noise bandwidth of 60 MHz. The p–i–n photodiode has negligible dark current and 90% quantum efficiency. The load resistance is 100 Ω and the amplifier noise figure is 3 dB. Calculate the receiver sensitivity corresponding to a BER of 10^{-9}. How much does it change if the receiver is designed to operate reliably up to a BER of 10^{-12}?

5.8 Calculate the receiver sensitivity (at a BER of 10^{-9}) for the receiver in Problem 5.7 in the shot-noise and thermal-noise limits. How many photons are incident during bit 1 in the two limits if the optical pulse can be approximated by a square pulse?

5.9 Derive an expression for the optimum gain M_{opt} of an APD receiver that would maximize the receiver sensitivity by taking the excess-noise factor as M^x. Plot M_{opt} as a function of x for $\sigma_T = 0.2$ μA and $\Delta f = 1$ GHz and estimate its value for InGaAs APDs.

5.10 Derive an expression for the sensitivity of an APD receiver when the signal has a finite extinction ratio and both shot noise and thermal noise contribute to the receiver sensitivity. You can neglect the dark current.

5.11 Derive an expression for the intensity-noise-induced power penalty of a p–i–n receiver by taking into account a finite extinction ratio. Shot-noise and intensity-

noise contributions can both be neglected compared with the thermal noise in the off state but not in the on state.

5.12 Use the result of the preceding problem to plot the power penalty as a function of the intensity-noise parameter r_I [see Eq. (5.4.6) for its definition] for several values of the extinction ratio. When does the power penalty become infinite? Explain the meaning of an infinite power penalty.

5.13 Derive an expression for the timing-jitter-induced power penalty by assuming a parabolic pulse shape $I(t) = \bar{I}(1 - B^2t^2)$ and a Gaussian jitter distribution with a standard deviation τ_j. You can assume that the receiver performance is dominated by thermal noise. Calculate the tolerable value of $B\tau$ that would keep the power penalty below 1 dB.

5.14 Explain how the FEC technique is implemented in practice for improving the performance of a lightwave system. Define the FEC overhead and the redundancy and calculate their values if the effective bit rate of a 40-Gb/s is 45 Gb/s.

5.15 Explain the meaning of coding gain associated with an FEC technique. How much coding gain is realized if the FEC decoder improves the BER from 10^{-5} to 10^{-12}

References

[1] S. D. Personick, *Bell Syst. Tech. J.* **52**, 843 (1973); **52**, 875 (1973).

[2] T. P. Lee and T. Li, in *Optical Fiber Telecommunications I*, S. E. Miller and A. G. Chynoweth, Eds., Academic Press, San Diego, CA, 1979, Chap. 18.

[3] R. G. Smith and S. D. Personick, in *Semiconductor Devices for Optical Communications*, H. Kressel, Ed., Springer, New York, 1980.

[4] B. L. Kasper, in *Optical Fiber Telecommunications II*, S. E. Miller and I. P. Kaminow, Eds., Academic Press, San Diego, CA, 1988, Chap. 18.

[5] S. B. Alexander, *Optical Communication Receiver Design*, Vol. TT22, SPIE Press, Bellingham, WA, 1995.

[6] W. R. Bennett, *Electrical Noise*, McGraw-Hill, New York, 1960.

[7] D. K. C. MacDonald, *Noise and Fluctuations: An Introduction*, Wiley, New York, 1962.

[8] F. N. H. Robinson, *Noise and Fluctuations in Electronic Devices and Circuits*, Oxford University Press, Oxford, 1974.

[9] W. Schottky, *Ann. Phys.* **57**, 541 (1918).

[10] H. A. Haus, *Electromagnetic Noise and Quantum Optical Measurements*, Springer, New York, 2000, Chap. 4.

[11] B. E. A. Saleh and M. Teich, *Fundamentals of Photonics*, Wiley, New York, 1991, Chap. 11.

[12] L. Mandel and E. Wolf, *Coherence and Quantum Optics*, Cambridge University Press, New York, 1995, Chap. 9.

[13] J. B. Johnson, *Phys. Rev.* **32**, 97 (1928).

[14] H. Nyquist, *Phys. Rev.* **32**, 110 (1928).

[15] R. J. McIntyre, *IEEE Trans. Electron. Dev.* **13**, 164 (1966); **19**, 703 (1972).

[16] P. P. Webb, R. J. McIntyre, and J. Conradi, *RCA Rev.* **35**, 235 (1974).

[17] P. Balaban, *Bell Syst. Tech. J.* **55**, 745 (1976).

[18] M. Abramowitz and I. A. Stegun, Eds., *Handbook of Mathematical Functions*, Dover, New York, 1970.

[19] D. A. Frisch and I. D. Henning, *Electron. Lett.* **20**, 631 (1984).

[20] R. A. Linke, *Electron. Lett.* **20**, 472 (1984); *IEEE J. Quantum Electron.* **21**, 593 (1985).

[21] T. L. Koch and J. E. Bowers, *Electron. Lett.* **20**, 1038 (1984).

[22] F. Koyama and Y. Suematsu, *IEEE J. Quantum Electron.* **21**, 292 (1985).

[23] A. H. Gnauck, B. L. Kasper, R. A. Linke, R. W. Dawson, T. L. Koch, T. J. Bridges, E. G. Burkhardt, R. T. Yen, D. P. Wilt, J. C. Campbell, K. C. Nelson, and L. G. Cohen, *J. Lightwave Technol.* **3**, 1032 (1985).

[24] G. P. Agrawal and M. J. Potasek, *Opt. Lett.* **11**, 318 (1986).

[25] P. J. Corvini and T. L. Koch, *J. Lightwave Technol.* **5**, 1591 (1987).

[26] J. J. O'Reilly and H. J. A. da Silva, *Electron. Lett.* **23**, 992 (1987).

[27] S. Yamamoto, M. Kuwazuru, H. Wakabayashi, and Y. Iwamoto, *J. Lightwave Technol.* **5**, 1518 (1987).

[28] D. A. Atlas, A. F. Elrefaie, M. B. Romeiser, and D. G. Daut, *Opt. Lett.* **13**, 1035 (1988).

[29] K. Hagimoto and K. Aida, *J. Lightwave Technol.* **6**, 1678 (1988).

[30] H. J. A. da Silva, R. S. Fyath, and J. J. O'Reilly, *IEE Proc.* **136**, Pt. J, 209 (1989).

[31] J. C. Cartledge and G. S. Burley, *J. Lightwave Technol.* **7**, 568 (1989).

[32] J. C. Cartledge and M. Z. Iqbal, *IEEE Photon. Technol. Lett.* **1**, 346 (1989).

[33] G. P. Agrawal and T. M. Shen, *Electron. Lett.* **22**, 450 (1986).

[34] J. J. O'Reilly, J. R. F. DaRocha, and K. Schumacher, *IEE Proc.* **132**, Pt. J, 309 (1985).

[35] K. Schumacher and J. J. O'Reilly, *Electron. Lett.* **23**, 718 (1987).

[36] T. M. Shen, *Electron. Lett.* **22**, 1043 (1986).

[37] D. Sandel, S. Bhandare, A. F. Abas, B. Milivojevic, R. Noé, M. Guy, and M. Lapointe, *IEEE Photon. Technol. Lett.* **16**, 2568 (2004).

[38] J. Baylis, *Error-Correcting Codes: A Mathematical Introduction*, Chapman and Hall, New York, 1998.

[39] I. S. Reed and X. Chen, *Error-Control Coding for Data Networks*, Kluwer, Norwell, MA, 1999.

[40] S. Gravano, *Introduction to Error-Control Code*, Oxford University Press, New York, 2001.

[41] W. C. Huffman, *Fundamentals of Error-Correcting Codes*, Cambridge University Press, New York, 2003.

[42] S. Yamamoto, H. Takahira, and M. Tanaka, *Electron. Lett.* **30**, 254 (1994).

[43] J. L. Pamart, E. Lefranc, S. Morin, G. Balland, Y. C. Chen, T. M. Kissell, J. L. Miller, *Electron. Lett.* **30**, 342 (1994).

[44] J. E. J. Alphonsus, P. B. Hansen, L. Eskildsen, D. A. Truxal, S. G. Grubb, D. J. DiGiovanni, T. A Strasser, and E. C. Beck, *IEEE Photon. Technol. Lett.* **7**, 1495 (1995).

[45] S. Sian, S. M. Webb, K. M. Guild, and D. R. Terrence, *Electron. Lett.* **32**, 50 (1996).

[46] E. Brandon, J.-P. Blondel, G. Grandpierre, and A. Lombard, *IEEE Photon. Technol. Lett.* **10**, 168 (1998).

[47] Y. Yamada, S.-I. Nakagawa, K. Takashina, T. Kawazawa, H. Taga, and K. Goto, *Electron. Lett.* **35**, 2212 (1999).

[48] B. Zhu, S. N. Knudsen, L. E. Nelson, D. W. Peckham, M. O. Pedersen, and S. Stulz, *Electron. Lett.* **37**, 1467 (2001).

[49] Y. Yamada, S.-I. Nakagawa, Y. Kurosawa, T. Kawazawa, H. Taga, and K. Goto, *Electron. Lett.* **38**, 328 (2002).

[50] J. X. Cai, M. Nissov, C. R. Davidson, A. N. Pilipetskii, G. Mohs, H. Li, Y. Cai, E. A. Golovchenko, A. J. Lucero, D. G. Foursa, and N. S. Bergano, *J. Lightwave Technol.* **20**, 2247 (2002).

[51] H. Suzuki, N. Takachio, H. Masuda, and K. Iwatsuki, *J. Lightwave Technol.* **21**, 973 (2003).

[52] C. Rasmussen, T. Fjelde, J. Bennike, F. Liu, S. Dey, B. Mikkelsen, P. Mamyshev, P. Serbe, P. vanderWagt, Y. Akasaka, D. Harris, D. Gapontsev, V. Ivshin, and P. Reeves-Hall, *J. Lightwave Technol.* **22**, 203 (2004).

[53] P. V. Kumar, M. Z. Win, H.-F. Lu, and C. N. Georghiades, in *Optical Fiber Telecommunications*, Vol. 4B, I. P. Kaminow and T. L. Koch, Eds., Academic Press, San Diego, CA, 2002, Chap. 17.

[54] A. Agata, K. Tanaka, and N. Edagawa, *J. Lightwave Technol.* **20**, 2189 (2002).

[55] B. V. Vasic, I. B. Djordjevic, and R. Kostuk, *J. Lightwave Technol.* **21**, 438 (2003).

[56] I. B. Djordjevic, S. Sankaranarayanan, and B. V. Vasic, *J. Lightwave Technol.* **22**, 695 (2004).

[57] X. Liu, Z. Zheng, N. Kaneda, X. Wei, M. Tayahi, M. Movassaghi, S. Radic, S. Chandrasekhar, and D. Levy, *IEEE Photon. Technol. Lett.* **15**, 1162 (2003).

[58] N. W. Spellmeyer, J. C. Gottschalk, D. O. Caplan, and M. L. Stevens, *IEEE Photon. Technol. Lett.* **16**, 1579 (2004).

Chapter 6

Optical Amplifier Noise

As seen in Chapter 5, it is not possible to recover the original information without errors even in a perfect lightwave system because of the shot noise that is always present. In practice, several other noise sources set the bit-error rate (BER) that can be realized in a realistic system. For example, thermal noise cannot be avoided at room temperature, and it sets the ultimate limit for most short-haul lightwave systems. The situation is somewhat different for long-haul systems in which the optical signal is amplified periodically for compensating fiber losses. Each optical amplifier adds noise that becomes so large when multiple amplifiers are used that system performance is dominated by this source of noise, rather than thermal noise. This chapter focuses on amplifier noise and how it can be controlled in practice to design lightwave systems that can operate reliably over thousands of kilometers. We begin in Section 6.1 with a discussion of the origin of noise in lumped and distributed amplifiers. Section 6.2 shows how the noise added by amplifiers affects the optical SNR of the signal. The electrical SNR at the receiver is discussed in Section 6.3, where we also introduce the concept of noise figure for optical amplifiers. Section 6.4 focuses on the BER and the Q factor that can be realized at the receiver end of a long-haul lightwave system designed with a chain of in-line optical amplifiers. Section 6.5 considers how the dispersive and nonlinear effects influence an optical signal that is corrupted with noise periodically at multiple amplifiers. The topics discussed include the growth of noise through modulation instability and random changes in the energy, frequency, and position (timing jitter) of optical pulses induced by amplifier noise. Section 6.6 shows how the combination of amplifier noise and fiber nonlinearities affects the BER and the Q factor.

6.1 Origin of Amplifier Noise

As discussed in Section 3.2, optical amplifiers used for lightwave systems can be classified into two categories known as lumped and distributed amplification. Erbium-doped fiber amplifiers (EDFAs) fall into the category of lumped amplification, whereas Raman amplification falls into the later category. The impact of noise is not the same for these two types of amplifiers. For this reason, we consider them separately.

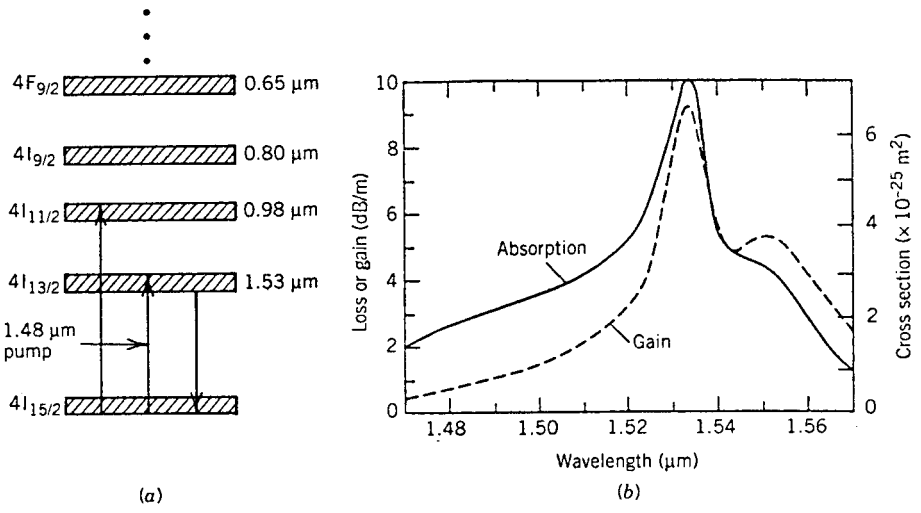

Figure 6.1: (a) Energy bands (shaded regions) of erbium ions in silica fibers. Numbers on the right show the wavelengths corresponding to energy gaps. (b) Absorption and gain spectra of an EDFA whose core was codoped with germania.

6.1.1 EDFA Noise

EDFAs makes use of a rare-earth element (erbium) that is doped into the fiber core during the manufacturing process [1]–[3]. When erbium is incorporated into the amorphous silica-glass matrix, it is ionized triply. Figure 6.1(a) shows a few energy levels of Er^{3+} ions. The amorphous nature of silica broadens all energy levels into bands. The energy separation between the two lowest bands corresponds to a wavelength range from 1.46 to 1.62 μm that happens to coincide with the low-loss region of silica fibers. These two bands are used for amplifying a WDM signal occupying the C and L bands. Figure 6.1(b) shows the absorption and gain spectra for atomic transitions occurring between them. The gain is possible only if more ions are in the excited state $^4I_{13/2}$ than in the ground state. Such population inversion is realized by pumping the erbium-doped fiber optically with a laser operating continuously at a suitable wavelength. Any of the higher-energy bands can be used for pumping an EDFA. The excited state $^4I_{11/2}$ is often employed for this purpose, and a semiconductor laser emitting light in the spectral region near 980 nm is used for pumping EDFAs. However, as seen in Figure 6.1(b), EDFAs exhibit significant absorption near 1.48 μm. This makes it possible to pump an EDFA in this region, while amplifying signals in the 1.55-μm region.

Amplification occurs when erbium ions in the excited state emit coherent light through stimulated emission. Occasionally, however, an excited ion can decay to the ground state through a process known as spontaneous emission and emit a photon of nearly the same energy as signal photons but with an arbitrary phase. In free space, such spontaneously emitted photons can be emitted in any direction with an arbitrary state of polarization and can have their energies anywhere within the gain spectrum of erbium ions. In the case of optical fibers, spontaneous emission occurs in all modes

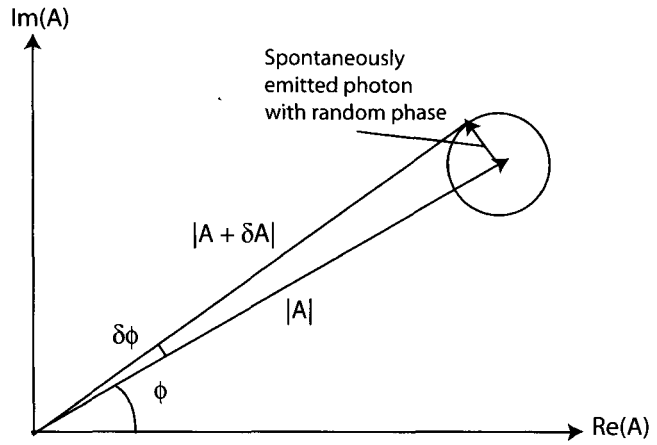

Figure 6.2: Schematic illustration of amplitude and phase perturbations produced by a single spontaneous emitted photon. The tip of the small arrow can be anywhere on the circle depending on the phase of this photon.

supported by the fiber (guided and unguided). Clearly, some of these photons would appear from time to time in the same fiber mode occupied by the signal field. As shown schematically in Figure 6.2, each such spontaneously emitted photon perturbs both the amplitude A and the phase ϕ of the optical field in a a random fashion. These random perturbations of the signal are the source of amplifier noise in EDFAs.

The important question is how much noise is added by an optical amplifier. The noise properties of optical amplifiers have been studied extensively since the early 1960s [4]–[9]. On a fundamental level, spontaneous emission has its origin in vacuum fluctuations, and one must carry out a quantum-mechanical analysis of the amplification process to find the magnitude of amplifier noise [10]–[14]. Semiclassically, we can account for the noise by adding a Langevin-noise source term to the field equation governing signal propagation within the amplifier. Since the NLS equation describes wave propagation inside optical fibers, it can be generalized to include the gain and noise of optical amplifiers as

$$\frac{\partial A}{\partial z} + \frac{i\beta_2}{2}\frac{\partial^2 A}{\partial t^2} = i\gamma|A|^2 A + \frac{1}{2}(g_0 - \alpha)A + f_n(z,t), \tag{6.1.1}$$

where $g_0 = \sigma_e N_2 - \sigma_a N_1$ is the gain coefficient, σ_e and σ_a are the emission and absorption cross sections, and N_1 and N_2 are the erbium-ion densities in the two lowest-energy states (see Figure 6.1).

The last term $f_n(z,t)$ in Eq. (6.1.1) accounts for the fluctuations induced by spontaneous emission and is responsible for the amplifier-added noise. It vanishes on average, that is, $\langle f_n(z,t)\rangle = 0$, where angle brackets denote the ensemble average over the random process. If this process is assumed to be Markovian with Gaussian statistics, its statistical properties are completely described by the correlation function [14]

$$\langle f_n^*(z,t) f_n(z',t')\rangle = n_{sp} h\nu_0 g_0 \delta(z-z')\delta(t-t'), \tag{6.1.2}$$

where $h\nu_0$ is the photon energy and the spontaneous-emission factor n_{sp} is defined as

$$n_{sp} = \sigma_e N_2/(\sigma_e N_2 - \sigma_a N_1). \tag{6.1.3}$$

The two delta functions in Eq. (6.1.2) ensure that all spontaneous-emission events are independent of each other both in time and at different points along the amplifier length. The form of Eq. (6.1.2) represents an example of the fluctuation-dissipation theorem [15] and is consistent with the quantum treatment of amplifier noise. It can be justified by noting that $n_{sp}g_0 \equiv \sigma_e N_2$ corresponds to the rate of spontaneous emission (per unit length) into each mode supported by the fiber.

In the case of lumped amplifiers, the length l_a of each amplifier is much shorter than the spacing L_A between two amplifiers. Since $l_a < 0.1$ km typically, neither loss, nor dispersion, nor nonlinearities are important within the amplifier, and one can set α, β_2, and γ to zero in Eq. (6.1.1). The resulting equation can be integrated over the amplifier length l_a with the result of

$$A_{out}(t) = \sqrt{G}A_{in}(t) + a_n(t), \tag{6.1.4}$$

where $G \equiv \exp(g_0 l_a)$ is the amplifier gain and $a_n(t)$ represents amplified spontaneous emission (ASE) at the output of the amplifier such that

$$a_n(t) = \int_0^{l_a} f_n(z,t) \exp\left[\tfrac{1}{2} g_0 (l_a - z)\right] dz. \tag{6.1.5}$$

The statistical properties of $a_n(t)$ can be obtained from those of $f_n(z,t)$. As Eq. (6.1.5) represents a linear transformation, $a_n(t)$ remains a Gaussian process. Moreover, since $\langle f_n(z,t)\rangle = 0$, $a_n(t)$ also vanishes on average. Similarly, using Eq. (6.1.2), the second moment of $a_n(t)$ is found to be

$$\langle a_n(t) a_n(t')\rangle = S_{ASE}\delta(t-t'), \qquad S_{ASE} = n_{sp} h\nu_0 (G-1), \tag{6.1.6}$$

where S_{ASE} is the power spectral density of ASE noise. The same form of spectral density is found in a quantum treatment of optical amplifiers [9].

It is important to note that $a_n(t)$ in Eq. (6.1.4) represents only the portion of ASE that is coupled to the mode occupied by the signal. The total noise power is obtained by adding the contributions of all possible modes and can be quite large as one must add up noise over the entire bandwidth of the amplifier. An optical filter is often placed just after the amplifier to reduce the noise power. If that is the case, noise is added only over the filter bandwidth, and the ASE power becomes

$$P_{ASE} = 2\int_{-\infty}^{\infty} S_{ASE} H_f(\nu - \nu_0)\, d\nu \approx 2 S_{ASE} \Delta\nu_o, \tag{6.1.7}$$

where H_f is the transfer function, ν_0 is the center frequency, and $\Delta\nu_o$ is the effective bandwidth of the optical filter. The factor of 2 takes into account the fact that even a single-mode fiber supports two orthogonally polarized modes; only half the power appears in the noise component that is copolarized with the optical signal.

6.1.2 Distributed Amplification

In the case of distributed amplification, Eq. (6.1.1) should be solved along the entire fiber link after $g_0(z)$ has been determined for a given pumping scheme. We focus on the case of distributed Raman amplification [16]–[18] and assume that $g_0(z)$ is known in terms of the pump power injected at the pumping stations. The new feature is that the gain produced by stimulated Raman scattering is not constant along the fiber length, and its z-dependence must be accounted for. The origin of noise $f_n(z,t)$ is also different and is related to *spontaneous* Raman scattering, rather than spontaneous emission between two atomic energy states.

It is not easy to solve Eq. (6.1.1) in the general case. However, if we neglect the dispersive and nonlinear effects by setting $\beta_2 = 0$ and $\gamma = 0$, the resulting equation can be easily integrated along the amplifier length L to obtain

$$A(L,t) = \sqrt{G(L)}A(0,t) + a_n(t), \tag{6.1.8}$$

where the total accumulated noise is given by

$$a_n(t) = \sqrt{G(L)} \int_0^L \frac{f_n(z,t)}{\sqrt{G(z)}}\, dz, \tag{6.1.9}$$

and the net gain at a distance z is obtained from

$$G(z) = \exp\left(\int_0^z [g_0(z') - \alpha]\, dz' \right). \tag{6.1.10}$$

It is easy to show that $a_n(t)$ vanishes on average and its second moment is given by

$$\langle a_n(t) a_n(t') \rangle = G(L) \int_0^L dz \int_0^L dz' \frac{\langle f_n(z,t) f_n(z',t') \rangle}{\sqrt{G(z)G(z')}} = S_{\text{ASE}} \delta(t - t'), \tag{6.1.11}$$

where the spectral density of ASE noise is defined as

$$S_{\text{ASE}} = n_{\text{sp}} h \nu_0 G(L) \int_0^L \frac{g_0(z)}{G(z)}\, dz. \tag{6.1.12}$$

The spontaneous-emission factor n_{sp} in this expression has a different meaning than that encountered in the case of EDFAs. In contrast with the case of EDFAs, no electronic transitions are involved during the Raman-amplification process. Rather, noise in Raman amplifiers is produced by spontaneous Raman scattering, whose magnitude is affected by phonon population in the first vibrational state of silica molecules and depends on the temperature of the fiber. More precisely, n_{sp} is given by [18]

$$n_{\text{sp}}(\Omega) = 1 + \frac{1}{\exp(\hbar\Omega / k_B T) - 1} \equiv \frac{1}{1 - \exp(-\hbar\Omega / k_B T)}, \tag{6.1.13}$$

where $\Omega = 2\pi(\nu_p - \nu_0)$ is the Raman shift, ν_p is the pump frequency, k_B is the Boltzmann constant, and T denotes the absolute temperature of the fiber. At room temperature $n_{\text{sp}} = 1.14$ when Ω is close to 13 THz near the Raman-gain peak.

Similar to the case of lumped amplifiers, the total ASE power is obtained by adding contributions over the entire Raman-gain bandwidth, or the bandwidth of an optical filter when such a filter is used. Assuming this to be the case, the total ASE power after the amplifier is given by

$$P_{\text{ASE}} = 2\int_{-\infty}^{\infty} S_{\text{ASE}} H_f(\nu - \nu_0)\, d\nu = 2S_{\text{ASE}}\Delta\nu_o, \tag{6.1.14}$$

where $\Delta\nu_o$ is the bandwidth of the optical filter and the factor of 2 includes both polarization components.

6.2 Optical SNR

The ASE noise added by each amplifier to the signal reduces the SNR of the amplified signal. As was seen in Chapter 5, the SNR for lightwave systems is usually considered in the electrical domain after the signal has been converted into an electric form using a photodetector. However, the concept of optical SNR, defined as the ratio of optical power to the ASE power, is also useful as it can provide design guidelines. In this section we focus on the optical SNR and consider electrical SNR in the next section.

6.2.1 Lumped Amplification

In a chain of cascaded lumped amplifiers (see Figure 3.1), ASE accumulates from amplifier to amplifier and can build up to high levels [2]. The ASE power added by any amplifier is attenuated in succeeding fiber sections, but it is also amplified by all following amplifiers. The net effect is that one can simply add the ASE powers of all amplifiers at the end of a fiber link. Assuming that all amplifiers are spaced apart by the same distance L_A and are operated with the same gain $G = \exp(\alpha L_A)$, the total ASE power for a chain of N_A amplifiers is given by

$$P_{\text{ASE}}^{\text{tot}} = 2N_A S_{\text{ASE}}\Delta\nu_o = 2n_{\text{sp}} h\nu_0 N_A (G-1)\Delta\nu_o, \tag{6.2.1}$$

where, as before, the factor of 2 takes into account the unpolarized nature of ASE and $\Delta\nu_o$ is the bandwidth of the optical filter.

Clearly, ASE power can become quite large for large values of G and N_A. A side effect of high ASE levels is that, at some point, ASE begins to saturate amplifiers. Then, signal power is reduced while, at the same time, noise power keeps on increasing, resulting in severe degradation of the SNR. The ASE power can be controlled, and SNR can be improved, by reducing the amplifier spacing L_A. At first sight, this approach appears counterintuitive since it increases the number N_A of amplifiers. However, noting that $N_A = L_T/L_A = \alpha L_T/\ln G$ for a link of total length L_T, we find that $P_{\text{ASE}}^{\text{tot}}$ scales with G as $(G-1)/\ln G$, and can be lowered by simply reducing the gain G of each amplifier. Thus, increasing the number of amplifiers while reducing their separation is an effective technique for controlling ASE noise. This feature explains why distributed amplification helps to improve the performance of a lightwave system.

In the case of lumped amplification, one wants to minimize the number of amplifiers for economical reasons. In this situation, the system should be designed with an

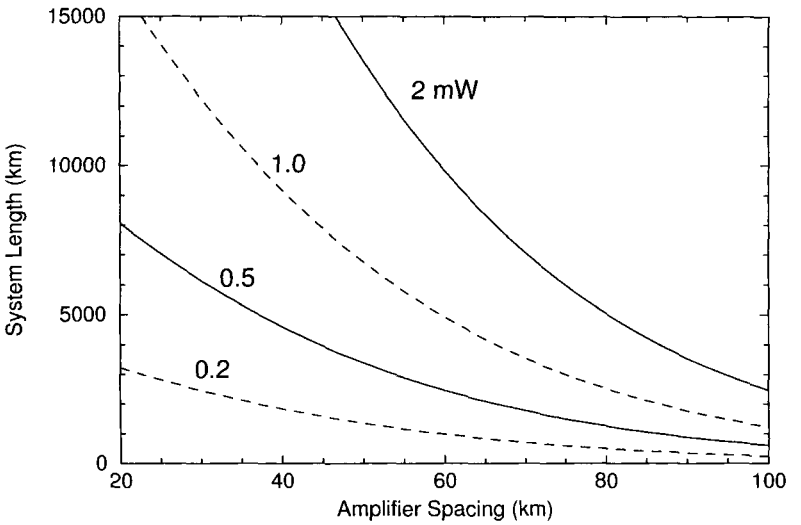

Figure 6.3: Maximum ASE-limited system length as a function of amplifier spacing L_A for several values of average signal power launched into a periodically amplified fiber link.

amplifier spacing that is relatively large but still small enough to operate the system reliably and to realize a target value of optical SNR. From Eq. (6.2.1), the optical SNR can be written as

$$\text{SNR}_o = \frac{P_{\text{in}}}{P_{\text{ASE}}^{\text{tot}}} = \frac{P_{\text{in}} \ln G}{2n_{\text{sp}} h\nu_0 \Delta\nu_o \alpha L_T (G-1)}, \tag{6.2.2}$$

where P_{in} is the input average power. Figure 6.3 shows the total system length L_T as a function of L_A for several values of input powers using $\alpha = 0.2$ dB/km, $n_{\text{sp}} = 1.6$, $\Delta\nu_o = 100$ GHz, and assuming that an optical SNR of 20 is required for the system to function properly. For a given input power, amplifier spacing L_A becomes smaller as the system length increases. Although amplifier spacing can be improved by increasing the input power P_{in}, in practice, the maximum power that can be launched is limited by the onset of various nonlinear effects discussed in Chapter 4. Typically, P_{in} is limited to close to 1 mW. At such power levels, L_A should be in the range of 40 to 50 km for submarine lightwave systems with lengths of 6,000 km or more, but it can be increased to 80 km or so for terrestrial systems with link lengths under 3,000 km.

6.2.2 Distributed Amplification

In the case of distributed amplification, pump power is injected periodically at pump stations spaced apart by L_A and is chosen such that the signal power recovers at each pump station to its input value, that is, $P_s(nL_A) = P_{in}$. One can use an approach similar to that employed for lumped amplifiers for calculating the optical SNR and finding the optimum pump-station spacing. The optical SNR of the amplified signal in this case

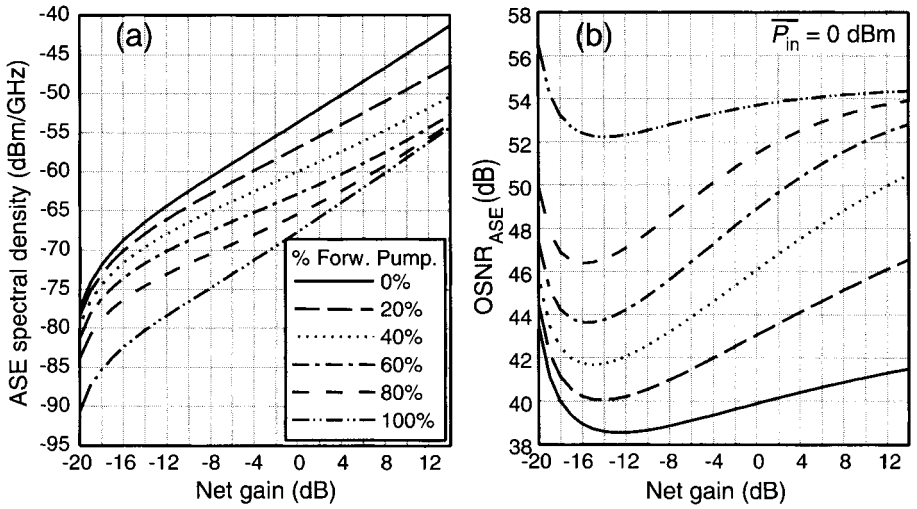

Figure 6.4: (a) ASE spectral density and (b) optical SNR as a function of net gain for a 100-km-long, bidirectionally pumped, distributed Raman amplifier when $P_{\text{in}} = 1$ mW. The fraction of pump power in the forward direction varies from 0 to 100%. (After Ref. [16]; ©2003 Springer.)

takes the form

$$\text{SNR}_o = \frac{P_s(L_T)}{N_A P_{\text{ASE}}} = \frac{P_{in}}{2N_A S_{\text{ASE}} \Delta\nu_o}, \tag{6.2.3}$$

where $L_T = N_A L_A$ is the link length, N_A is the number of pump stations, and S_{ASE} is given in Eq. (6.1.12).

A new feature of distributed amplification is that the pump power can be injected in the forward, backward, or both directions. Since the functional form of gain $g(z)$ depends on the pumping scheme, and S_{ASE} in Eq. (6.1.12) depends on $g(z)$, we can control the optical SNR to some extent by adopting a suitable pumping scheme. Figure 6.4 shows how (a) ASE spectral density and (b) optical SNR vary with the net gain $G(L)$ for several different pumping schemes, assuming that a 1-mW input signal is transmitted through a 100-km-long, bidirectionally pumped, distributed Raman amplifier [16]. The fraction of forward pumping varies from 0 to 100%. Fiber losses are 0.26 and 0.21 dB/km at the pump and signal wavelength, respectively. Other parameters used were $n_{\text{sp}} = 1.13$, $h\nu_0 = 0.8$ eV, and $g_R = 0.68$ W^{-1}/km. The optical SNR is highest in the case of purely forward pumping (about 54 dB or so), but it degrades by as much as 15 dB as the fraction of backward pumping is increased from 0 to 100%. This can be understood by noting that the ASE generated near the input end experiences accumulated losses over the full length of the fiber in the case of forward pumping, whereas it experiences only a fraction of such losses in the case of backward pumping.

Figure 6.4(b) shows the optical SNR for a single 100-km-long section but it illustrates clearly the benefits of distributed amplification. If N_A such sections are employed to form a long-haul fiber link, SNR is reduced by a factor of N_A, as seen from Eq. (6.2.3). Even when $N_A = 100$ and the total link length $L_T = 10{,}000$ km, SNR$_o$ remains

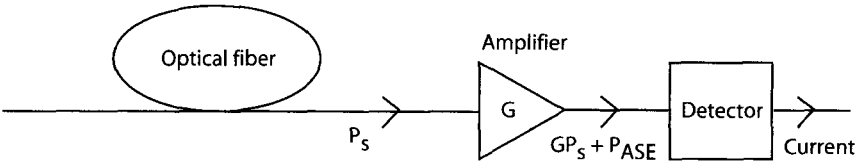

Figure 6.5: Schematic of the optical preamplification scheme. An amplifier is placed just before the detector to improve receiver sensitivity. The amplifier adds ASE to the signal and generates additional noise in the receiver current.

larger than 20 dB. Such high values of optical SNR are difficult to maintain for long fiber links when EDFAs are used.

6.3 Electrical SNR

Optical SNR, although useful for design purposes, is not what governs the BER at the receiver. In this section, we focus on the electrical SNR of the current generated when an ASE-degraded optical signal is incident on a photodetector. For simplicity of discussion, we use the configuration shown in Figure 6.5 and assume that a single optical amplifier is used before the receiver to amplify a low-power signal before it is detected. This configuration is sometimes used to improve the receiver sensitivity through optical preamplifcation.

6.3.1 ASE-Induced Current Fluctuations

When the contribution of ASE noise to the signal field E_s is included, the photocurrent generated at the receiver can be written as

$$I = R_d(|\sqrt{G}E_s + E_{\rm cp}|^2 + |E_{\rm op}|^2) + i_s + i_T, \tag{6.3.1}$$

where G is the amplifier gain, i_s and i_T are current fluctuations induced by the shot noise and thermal noise, respectively, $E_{\rm cp}$ is the part of the ASE copolarized with the signal, and $E_{\rm op}$ is the orthogonally polarized part of the ASE. It is necessary to separate the ASE into two parts because only the copolarized part of the ASE can beat with the signal.

The ASE-induced current noise has its origin in the beating of E_s with $E_{\rm cp}$ and the beating of ASE with itself. To understand this beating phenomenon more clearly, notice that the ASE occurs over a broader bandwidth than the signal bandwidth $\Delta\nu_s$. It is useful to divide the ASE bandwidth $\Delta\nu_o$ into M bins, each of bandwidth $\Delta\nu_s$, and write $E_{\rm cp}$ in the form

$$E_{\rm cp} = \sum_{m=1}^{M} (S_{\rm ASE}\Delta\nu_s)^{1/2} \exp(i\phi_m - i\omega_m t), \tag{6.3.2}$$

where ϕ_m is the phase of the noise component at the frequency $\omega_m = \omega_l + m(2\pi\Delta\nu_s)$ and ω_l is the lower boundary of the filter passband. The spectral density of ASE for a

lumped amplifier is given in Eq. (6.1.6). A form identical to that of Eq. (6.3.2) applies for E_{op}.

Using $E_s = \sqrt{P_s}\exp(i\phi_s - i\omega_s t)$ and E_{cp} from Eq. (6.3.2) in Eq. (6.3.1) and including all beating terms, the current I can be written in the form

$$I = R_d G P_s + i_{\text{sig-sp}} + i_{\text{sp-sp}} + i_s + i_T, \tag{6.3.3}$$

where $i_{\text{sig-sp}}$ and $i_{\text{sp-sp}}$ represent current fluctuations resulting from signal–ASE and ASE–ASE beating, respectively, and are given by

$$i_{\text{sig-sp}} = 2R_d(GP_s S_{\text{ASE}}\Delta\nu_s)^{1/2}\sum_{m=1}^{M}\cos[(\omega_s - \omega_m)t + \phi_m - \phi_s], \tag{6.3.4}$$

$$i_{\text{sp-sp}} = 2R_d S_{\text{ASE}}\Delta\nu_s\sum_{m=1}^{M}\sum_{n=1}^{M}\cos[(\omega_n - \omega_m)t + \phi_m - \phi_n]. \tag{6.3.5}$$

Since these two noise currents fluctuate rapidly with time, we need to find their averages and variances. It is easy to see that $\langle i_{\text{sig-sp}}\rangle$ vanishes. However, $\langle i_{\text{sp-sp}}\rangle$ has a finite value resulting from the terms in the double sum for which $m = n$. This average value is given by

$$\langle i_{\text{sp-sp}}\rangle = 2R_d S_{\text{ASE}}\Delta\nu_s M = 2R_d S_{\text{ASE}}\Delta\nu_o \equiv R_d P_{\text{ASE}}. \tag{6.3.6}$$

Variances of the two noise currents can also be calculated by squaring them and averaging over time. We write the final result directly as details are available in several texts [1]–[3]:

$$\sigma^2_{\text{sig-sp}} = 4R_d^2 G P_s S_{\text{ASE}}\Delta f, \tag{6.3.7}$$

$$\sigma^2_{\text{sp-sp}} = 4R_d^2 S^2_{\text{ASE}}\Delta f(\Delta\nu_o - \Delta f/2), \tag{6.3.8}$$

where Δf is the effective noise bandwidth of the receiver (see Section 5.1). The total variance σ^2 of current fluctuations can be written as [6]

$$\sigma^2 = \sigma^2_{\text{sig-sp}} + \sigma^2_{\text{sp-sp}} + \sigma_s^2 + \sigma_T^2, \tag{6.3.9}$$

where σ_T^2 is due to thermal noise and the shot-noise variance has an additional contribution resulting from the average in Eq. (6.3.6), that is,

$$\sigma_s^2 = 2q[R_d(GP_s + P_{\text{ASE}})]\Delta f, \tag{6.3.10}$$

where $P_{\text{ASE}} = 2S_{\text{ASE}}\Delta\nu_o$ is the total ASE power entering the receiver.

6.3.2 Impact of ASE on SNR

We can now calculate the electrical SNR at the receiver. Noting from Eq. (6.3.3) that $\langle I\rangle = R_d(GP_s + P_{\text{ASE}})$, the SNR is given by

$$\text{SNR}_e = \frac{\langle I\rangle^2}{\sigma^2} = \frac{R_d^2(GP_s + P_{\text{ASE}})^2}{\sigma^2_{\text{sig-sp}} + \sigma^2_{\text{sp-sp}} + \sigma_s^2 + \sigma_T^2}. \tag{6.3.11}$$

The important question is whether the SNR_e is improved or degraded because of signal amplification before its detection. To answer this question, we compare Eq. (6.3.11) with the SNR realized in the absence of optical amplifier. Setting $G = 1$ and $P_{\text{ASE}} = 0$, this SNR is given by

$$\text{SNR}'_e = \frac{R_d^2 P_s^2}{\sigma_s^2 + \sigma_T^2}. \tag{6.3.12}$$

Consider first the case of an ideal receiver with no thermal noise and 100% quantum efficiency so that $R_d = q/h\nu_0$. In this case, SNR without an amplifier is given by $\text{SNR}'_e = P_s/(2h\nu_0\Delta f)$. When an optical amplifier is used, the current variance is dominated by $\sigma^2_{\text{sig-sp}}$. Neglecting $\sigma^2_{\text{sp-sp}}$ and P_{ASE} in Eq. (6.3.11), the SNR is found to be

$$\text{SNR}_e = \frac{GP_s}{(4S_{\text{ASE}} + 2h\nu_0)\Delta f}. \tag{6.3.13}$$

Using S_{ASE} from Eq. (6.3.3), we find that the optical amplifier degrades the electrical SNR by a factor of

$$F_o = \frac{\text{SNR}'_e}{\text{SNR}_e} = 2n_{\text{sp}}\left(1 - \frac{1}{G}\right) + \frac{1}{G}. \tag{6.3.14}$$

In analogy with an electrical amplifier, F_o is known as the noise figure of an optical amplifier. In the limit of large gain ($G \gg 1$), SNR is degraded by a factor of $F_o = 2n_{\text{sp}}$. Even when a perfect amplifier with $n_{\text{sp}} = 1$ is employed, SNR is reduced by a factor of 2 or 3 dB. This is a well-known feature of all amplifiers and is expected on physical grounds [9].

The above conclusion holds for an ideal receiver, limited only by the quantum noise. In practice, thermal noise exceeds shot noise by a large amount, and it should be included before concluding that an optical amplifier always degrades the electrical SNR. Neglecting shot noise in Eq. (6.3.12) and retaining only the dominant term $\sigma^2_{\text{sig-sp}}$ in Eq. (6.3.11), we find that

$$\frac{\text{SNR}_e}{\text{SNR}'_e} = \frac{G\sigma_T^2}{4R_d^2 P_s S_{\text{ASE}}\Delta f}. \tag{6.3.15}$$

As this ratio can be made quite large by lowering P_s and increasing the amplifier gain G, electrical SNR can be improved by 20 dB or more compared with its value possible without amplification. This apparent contradiction can be understood by noting that the receiver noise, dominated by $\sigma^2_{\text{sig-sp}}$, is so large in magnitude that thermal noise can be neglected in comparison to it. In other words, optical preamplification of the signal helps to mask the thermal noise, resulting in an improved SNR. In fact, if we retain only the dominant noise term, the electrical SNR of the amplified signal becomes

$$\text{SNR}_e = \frac{GP_s}{4S_{\text{ASE}}\Delta f} = \frac{GP_s\Delta\nu_o}{2P_{\text{ASE}}\Delta f}. \tag{6.3.16}$$

This should be compared with the optical SNR of GP_s/P_{ASE}. As seen in Eq. (6.3.16), electrical SNR is higher by a factor of $\Delta\nu_o/(2\Delta f)$ under identical conditions since ASE noise contributes only over the receiver bandwidth Δf that is much narrower than the filter bandwidth $\Delta\nu_o$.

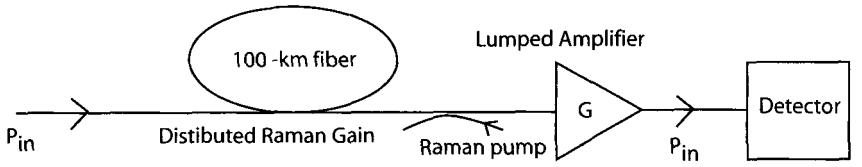

Figure 6.6: Schematic illustration of a hybrid scheme in which fiber losses are compensated by combining a lumped amplifier with partial Raman amplification of the signal within the fiber span through backward pumping.

6.3.3 Noise Figure of Distributed Amplifiers

The concept of noise figure can be easily extended to the case of distributed amplification. Equation (6.3.13) remains valid for a distributed amplifier provided the ASE spectral density is calculated from Eq. (6.1.12). Because of gain variations along the amplifier length, noise figure is given by

$$F_o = 2n_{sp}\int_0^L \frac{g_0(z)}{G(z)}\,dz + \frac{1}{G(L)}. \tag{6.3.17}$$

This equation provides reasonably small noise figures for "lumped" Raman amplifiers for which fiber length is $\sim$1 km, and the net signal gain exceeds 10 dB.

When the same fiber used for signal transmission is employed for distributed amplification, the length of each fiber section typically exceeds 50 km, and pumping is such that net gain $G(z) < 1$ over most of the fiber length. In this case, F_o predicted by Eq. (6.3.17) is relatively large and can exceed 15 dB depending on the span length. This does not mean distributed amplifiers are more noisy than lumped amplifiers. To resolve this apparent contradiction, consider the hybrid scheme shown in Figure 6.6. Losses of 100-km-long fiber span (with a loss of 0.2 dB/km) are compensated using a scheme in which a lumped amplifier with 5-dB noise figure is combined with Raman amplification realized within the fiber span through backward pumping. The on–off gain G_R of the Raman amplifier (defined as the increase in the output fiber as the pump is turned on) can be varied in the range of 0 to 20 dB by adjusting the pump power. Clearly, $G_R = 0$ and 20 dB correspond to the cases of pure lumped and pure distributed amplifications, respectively.

The solid line in Figure 6.7 shows how the noise figure of such a hybrid combination changes as G_R is varied from 0 to 20 dB [18]. When $G_R = 0$ (no pumping), Eq. (6.3.17) shows that the passive fiber has a noise figure of 20 dB. This is not surprising since any fiber loss reduces signal power and thus degrades the SNR. As the signal is amplified inside a lumped amplifier, an additional 5-dB degradation occurs, resulting in a total noise figure of 25 dB in Figure 6.7. This value decreases as G_R increases, reaching a level of about 17.5 dB for $G_R = 20$ dB (no lumped amplification). The dashed line shows the noise figure of the Raman-pumped fiber span alone as predicted by Eq. (6.3.17). The total noise figure is higher because the lumped amplifier adds some noise if span losses are only partially compensated by the Raman amplifier. The

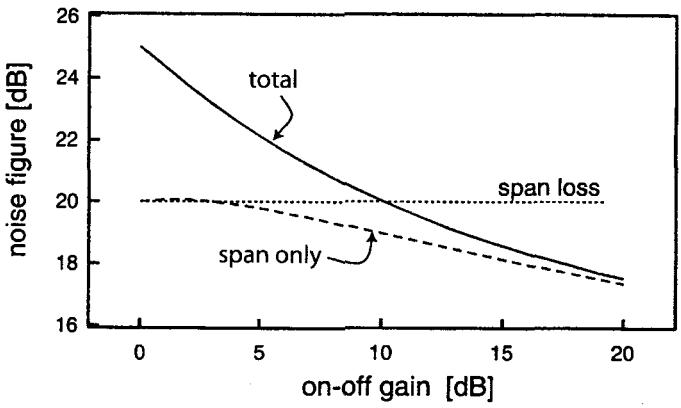

Figure 6.7: Total noise figure as a function of the on–off gain when 20-dB losses (dotted line) of a 100-km-long fiber span are compensated using a hybrid amplification scheme. The dashed line shows the noise figure of Raman-pumped fiber span alone. (After Ref. [18]; ©2004 IEEE.)

important point is that total noise figure drops below the 20-dB level (dotted line) when the Raman gain exceeds a certain value.

To emphasize the noise advantage of distributed amplifiers, it is common to introduce the concept of an *effective* noise figure using the definition $F_{\text{eff}} = F_o \exp(-\alpha L)$, where α is the fiber-loss parameter at the signal wavelength. In decibel units, $F_{\text{eff}} = F_o - \mathscr{L}$, where $\mathscr{L}$ is the span loss in dB. Using Eq. (6.3.17) and $g(z) = g_R P_p(z)$, where g_R is the Raman-gain coefficient and P_p is the pump power, the effective noise figure of a distributed Raman amplifier can be written as

$$F_{\text{eff}} = \frac{e^{-\alpha L}}{G(L)} \left(2n_{\text{sp}} g_R G(L) \int_0^L \frac{P_p(z)}{G(z)} dz + 1 \right), \tag{6.3.18}$$

where $G(z)$ is the net gain given in Eq. (6.1.10). When all fiber losses are compensated through distributed amplification, $G(L) = 1$. As seen from Figure 6.7, $F_{\text{eff}} < 1$ (or negative on the decibel scale) by definition. It is this feature of distributed amplification that makes it so attractive for long-haul WDM lightwave systems. For the example shown in Figure 6.7, $F_{\text{eff}} \approx -2.5$ dB when pure distributed amplification is employed. However, the noise advantage is more than 7.5 dB when noise figures are compared for lumped and distributed amplification schemes.

The effective noise figure of a Raman amplifier depends on the pumping scheme used because, as discussed in Section 3.2, $P_p(z)$ can be quite different for forward, backward, and bidirectional pumping. In general, forward pumping provides the highest SNR, and the smallest noise figure, because most of the Raman gain is then concentrated toward the input end of the fiber where power levels are high. However, backward pumping is often employed in practice because of other considerations such as the transfer of pump noise to signal and the effects of residual fiber birefringence.

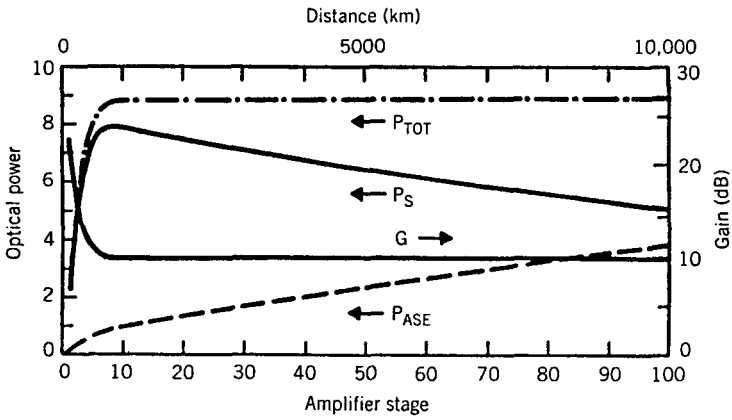

Figure 6.8: Variation of the signal power P_s and the ASE power P_{ASE} along a cascaded chain of optical amplifiers. The total power P_{TOT} becomes nearly constant after a few amplifiers. (After Ref. [20]; ©1991 IEEE.)

6.3.4 Noise Buildup in an Amplifier Chain

As mentioned earlier, long-haul lightwave systems require cascading of multiple optical amplifiers in a periodic fashion. The buildup of ASE noise is the most critical factor for such systems for two reasons. First, in a cascaded chain of optical amplifiers (see Figure 3.1), the ASE accumulates over many amplifiers and degrades the SNR as the number of amplifiers increases [19]–[22]. Second, as the level of ASE grows, it begins to saturate optical amplifiers and reduce the gain of amplifiers located further down the fiber link. The net result is that the signal level drops while the ASE level increases. Numerical simulations show that the system is self-regulating in the sense that the total power obtained by adding the signal and ASE powers ($P_{\text{TOT}} = P_s + P_{\text{ASE}}$) remains relatively constant. Figure 6.8 shows this self-regulating behavior for a cascaded chain of 100 amplifiers with 100-km spacing and 35-dB small-signal gain. The power launched by the transmitter is 1 mW. The other parameters are $n_{\text{sp}} = 1.3$ and $G_0 \exp(-\alpha L_A) = 3$. The signal and ASE powers become comparable after 10,000 km. Clearly, ASE-induced gain saturation should be avoided as much as possible. We assume this to be the case in the following discussion.

To estimate the SNR associated with a long-haul lightwave system, we assume that all amplifiers are spaced apart by a constant distance L_A, and the amplifier gain $G \equiv \exp(\alpha L_A)$ is just large enough to compensate for fiber losses in each fiber section. The total ASE power for a chain of N_A amplifiers is then given by Eq. (6.2.1) and can be used to find the optical SNR using $\text{SNR}_o = P_{\text{in}}/P_{\text{ASE}}$. To calculate the electrical SNR, we need to find the current variance at the receiver. If we assume that the receiver noise is dominated by the signal–ASE beat noise and include only this dominant contribution, the electrical SNR is found to be

$$\text{SNR}_e = \frac{R_d^2 P_{\text{in}}^2}{N_A \sigma_{\text{sig-sp}}^2} = \frac{P_{\text{in}}}{4 N_A S_{\text{ASE}} \Delta f}, \tag{6.3.19}$$

where we used Eq. (6.3.7). This equation shows that the electrical SNR is reduced by a factor of N_A simply because ASE noise is increased by that factor. However, one should not conclude from this equation that the system designed to operate over a total length L_T can be improved by placing fewer amplifiers along the link. The reason is related to the fact that each amplifier would have to operate with a higher gain G. Since S_{ASE} in Eq. (6.1.6) scales linearly with $G-1$, the noise level of each amplifier would increase. In fact, as discussed earlier in Section 6.2.1, reducing the number of amplifiers makes the situation worse. The appropriate design solution is to employ more amplifiers, each with a lower gain. This can be understood by noting that N_A scales with gain as $N_A = L_T/L_A = \alpha L_T/\ln G$. As a result, SNR_e scales with G as $\ln(G)/(G-1)$ and can be improved by reducing G or L_A. The results shown in Figure 6.3 also apply here because the optical and electrical SNRs are related to each other as $\text{SNR}_e/\text{SNR}_o = \Delta\nu_o/(2\Delta f)$.

6.4 Receiver Sensitivity and Q Factor

So far in this chapter, we have considered only a constant-power input signal even though optical signal in any realistic lightwave system is in the form of a pseudo-random bit stream consisting of 0 and 1 bits. This section focuses on such a realistic situation and evaluates the effects of amplifier noise on the BER and the receiver sensitivity.

6.4.1 Bit-Error Rate

The calculation of BER for lightwave systems employing optical amplifiers follows the approach outlined in Section 5.3.1. More specifically, BER is given by Eq. (5.3.2). However, the conditional probabilities $P(0/1)$ and $P(1/0)$ require knowledge of the probability density function (PDF) for the current I corresponding to symbols 0 and 1. Strictly speaking, the PDF does not remain Gaussian when optical amplifiers are used, and one should employ a more complicated form of the PDF for calculating the BER [23]–[25]. However, the results are much simpler if the actual PDF is approximated by a Gaussian. We assume this to be the case in this subsection.

With the Gaussian approximation for the receiver noise, we can use the analysis of Section 5.3.1 to find that the BER is given by Eq. (5.3.11), and the Q factor can still be defined as

$$Q = \frac{I_1 - I_0}{\sigma_1 + \sigma_0}. \tag{6.4.1}$$

However, the noise currents σ_1 and σ_0 should now include the beating terms introduced in Section 6.3.1 and are obtained using

$$\sigma_1^2 = \sigma_{\text{sig-sp}}^2 + \sigma_{\text{sp-sp}}^2 + \sigma_s^2 + \sigma_T^2, \qquad \sigma_0^2 = \sigma_{\text{sp-sp}}^2 + \sigma_T^2. \tag{6.4.2}$$

In the case of 0 bits, σ_s^2 and $\sigma_{\text{sig-sp}}^2$ can be neglected as these two noise contributions are signal-dependent and nearly vanish for 0 bits if we assume a high extinction ratio for the bit stream. As the Q factor specifies the BER completely, one can realize a BER

below 10^{-9} by ensuring that Q exceeds 6. The value of Q should exceed 7 if the BER needs to be below 10^{-12}.

Several other approximations can be made while calculating the Q fcator. A comparison of Eqs. (6.3.7) and (6.3.10) shows that σ_s^2 can be neglected in comparison with $\sigma_{\text{sig-sp}}^2$ in most cases of practical interest. The thermal noise σ_T^2 can also be neglected in comparison with the dominant beating term whenever the average optical power at the receiver is relatively large (>0.1 mW). The noise currents σ_1 and σ_0 are then well approximated by

$$\sigma_1 = (\sigma_{\text{sig-sp}}^2 + \sigma_{\text{sp-sp}}^2)^{1/2}, \qquad \sigma_0 = \sigma_{\text{sp-sp}}. \tag{6.4.3}$$

An important question is how receiver sensitivity is affected by optical amplification. Since the thermal noise does not appear in Eq. (6.4.3), one would expect that receiver performance would not be limited by it, and one may need much fewer photons per bit compared with thousands of photons required when thermal noise dominates.This is indeed the case, as also observed during the 1990s in several experiments that required about 100 to 150 photons/bit [26]–[29]. On the other hand, as discussed in Section 5.3.3, only 10 photns/bit are needed, on average, in the quantum limit. Even though we do not expect this level of performance when optical amplifiers are used because of the additional noise introduced by them, it is useful to inquire about the minimum number of photons in this case.

To calculate the receiver sensitivity, we assume for simplicity that no energy is contained in 0 bits so that $I_0 \approx 0$. Clearly, $I_1 = 2R_d\bar{P}_{\text{rec}}$, where $\bar{P}_{\text{rec}}$ is the average power incident on the receiver. Using Eq. (6.3.7) and (6.3.8) in Eq. (6.4.3) together with Eq. (6.4.1), we obtain

$$\bar{P}_{\text{rec}} = h\nu_0 F_o \Delta f[Q^2 + Q(\Delta\nu_o/\Delta f - \tfrac{1}{2})^{1/2}]. \tag{6.4.4}$$

The receiver sensitivity can be written in terms of the average number of photons/bit, $\bar{N}_p$, by using the relation $\bar{P}_{\text{rec}} = \bar{N}_p h\nu_0 B$. If we accept $\Delta f = B/2$ as a typical value of the receiver bandwidth, $\bar{N}_p$ is given by

$$\bar{N}_p = \tfrac{1}{2}F_o[Q^2 + Q(r_f - \tfrac{1}{2})^{1/2}], \tag{6.4.5}$$

where $r_f = \Delta\nu_o/\Delta f$ is the factor by which the optical filter bandwidth exceeds the receiver bandwidth.

Equation (6.4.5) is a remarkably simple expression for the receiver sensitivity. It shows clearly why amplifiers with a small noise figure must be used; the receiver sensitivity degrades as F_o increases. It also shows how narrowband optical filters can improve the receiver sensitivity by reducing r_f. Figure 6.9 shows $\bar{N}_p$ as a function of r_f for several values of the noise figure F_o using $Q = 6$, a value required to maintain a BER of 10^{-9}. The minimum value of F_o is 2 for an ideal amplifier. The minimum value of r_f is also 2 since $\Delta\nu_o$ should be wide enough to pass a signal at the bit rate B. Using $Q = 6$ with $F_o = 2$ and $r_f = 2$, the best receiver sensitivity from Eq. (6.4.5) is $\bar{N}_p$ = 43.3 photons/bit. This value should be compared with $\bar{N}_p = 10$, the value obtained for an ideal receiver operating in the quantum-noise limit (see Section 5.3.3). Of course, $\bar{N}_p = 10$ is never realized in practice because of thermal noise; typically, $\bar{N}_p$ exceeds 1,000 without optical amplifiers.

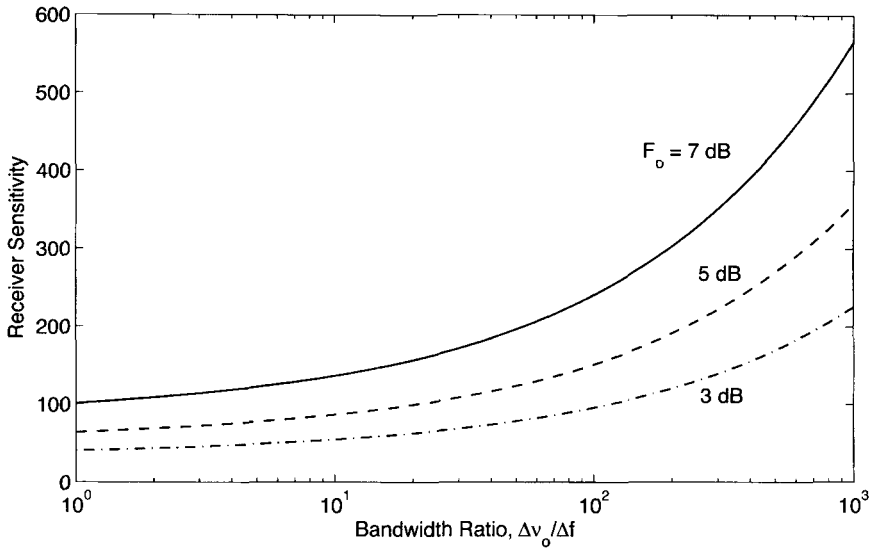

Figure 6.9: Receiver sensitivity $\bar{N}_p$ as a function of optical filter bandwidth (normalized to the receiver bandwidth) for several values of amplifier-noise figure F_o.

6.4.2 Non-Gaussian Receiver Noise

As mentioned earlier, even though the ASE itself has a Gaussian PDF, the detector current generated at the receiver does not follow Gaussian statistics. The reason can be understood from Eq. (6.3.1). If we neglect the last two terms, retain only the ASE-related terms, and assume no net amplification of the signal at the end of an amplifier chain, the detector current becomes

$$I = R_d(|E_s + E_{\rm cp}|^2 + |E_{\rm op}|^2), \tag{6.4.6}$$

where $E_{\rm cp}$ and $E_{\rm op}$ represent the copolarized and orthogonally polarized parts of the ASE noise. The orthogonal part can be suppressed by placing a polarizer in front of the receiver. If we use Eq. (6.3.2), we can write the current as

$$I = I_s + 2\sqrt{I_N I_s}\sum_{m=1}^{M} c_m + I_N \sum_{m=1}^{pM}(c_m^2 + s_m^2), \tag{6.4.7}$$

where $I_s = R_d|E_s|^2$ is the current in the absence of noise and $I_N = R_d S_{\rm ASE}\Delta\nu_s$ is the noise current induced by ASE within the signal bandwidth. We have also introduced two real random variables c_m and s_m as $c_m + is_m = \exp(i\phi_m)$, where ϕ_m represents a randomly varying phase. The integer $p = 1$ or 2 depending on whether a polarizer is placed or not placed in front of the receiver.

As seen in Eq. (6.4.7), I is a function of a large number of random variables, each of which follows Gaussian statistics. In the absence of ASE–ASE beating, I would have a Gaussian PDF since it represents a linear combination of Gaussian variable. However,

this beating term cannot be ignored, and the statistics of I are generally non-Gaussian. It turns out that the PDF can be obtained in an analytic form for both 0 and 1 symbols [23]–[25]. In the case of 0 bits, $I_s = 0$, and the PDF is found to be

$$p_0(I) = \frac{I^{pM-1}}{(pM-1)!I_N^{pM}} \exp\left(-\frac{I}{I_N}\right). \tag{6.4.8}$$

The PDF expression is somewhat more complicated in the case of 1 bits. Using $I_s = I_1$, it can be written as

$$p_1(I) = \frac{1}{I_N}\left(\frac{I}{I_1}\right)^{\frac{1}{2}(pM-1)} \exp\left(-\frac{I+I_1}{I_N}\right) \mathscr{I}_{pM-1}\left(-\frac{2\sqrt{II_1}}{I_N}\right), \tag{6.4.9}$$

where $\mathscr{I}_k$ represents the modified Bessel function of order k. The two conditional probabilities appearing in Eq. (5.3.2) can now be calculated numerically for a given value of the decision level I_D. The resulting BER is then minimized to find the optimum value of the decision level. The average number of photons/bit required to maintain a BER below 10^{-9} is about 40 when Eqs. (6.4.8) and (6.4.9) are used. This value is lower by about 0.3 dB compared with the value of 43.3 found earlier with the Gaussian approximation for the two PDFs.

Experimental measurements agree with the theoretical predictions based on Eqs. (6.4.8) and (6.4.9). Figure 6.10 compares the experimental and predicted PDFs for a receiver with an electrical bandwidth of 7 GHz when a cascade of three EDFAs provided a net signal gain of around 32 dB [25]. The optical filter had a bandwidth of 1.3 nm in this experiment. In the absence of signal, receiver noise is dominated by ASE–ASE beating, and the PDF is far from Gaussian. However, deviations are relatively small in the case of 1 bits because the noise level is dominated by signal–ASE beating. As mentioned earlier, a Gaussian distribution is expected in the absence of ASE–ASE beating. In general, the Gaussian approximation holds better as the bandwidth of optical filter increases and M becomes large.

The use of Gaussian PDF is questionable for predicting the decision threshold I_D at which BER becomes minimum [3]. However, in practice, I_D is determined experimentally by adjusting it until the "eye" in the eye diagram is as wide open as possible. This procedure is equivalent to finding the minimum BER based on Eqs. (6.4.8) and (6.4.9). The BER predicted by a Gaussian PDF with this choice of I_D is reasonably close to the actual answer. For this reason, the Gaussian approximation is often used in practice for calculating the receiver sensitivity. In particular, one can employ Eq. (6.4.1) for calculating the Q factor and use it to judge the system performance.

6.4.3 Relation between Q Factor and Optical SNR

The Q parameter that appears in the calculation of BER and the optical SNR calculated in Section 6.2 are related to each other. To show this relationship in a simple form, we consider a lightwave system dominated by amplifier noise and assume that 0 bits carry no energy (except ASE). Then, $I_0 \approx 0$ and $I_1 = R_d P_1$, where P_1 is the peak power level during each 1 bit. Using the definition of total ASE power in Eq. (6.1.14) together with

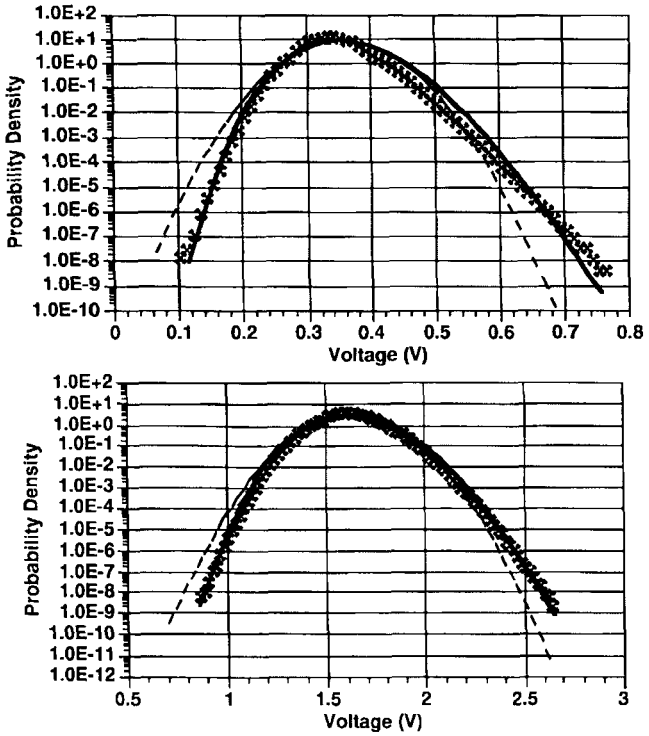

Figure 6.10: Measured (symbols) and predicted (solid line) PDFs for 0 bits (top) and 1 bits (bottom). In each case, a dashed line shows the Gaussian approximation. (After Ref. [25]; ©1997 IEEE.)

Eqs. (6.3.7) and (6.3.8), we obtain

$$\sigma^2_{\text{sig-sp}} = 2R_d\sqrt{P_1 P_{\text{ASE}}}/M, \qquad \sigma^2_{\text{sp-sp}} = P^2_{\text{ASE}}/M, \tag{6.4.10}$$

where we assumed $M = \Delta\nu_o/\Delta f \gg 1$.

Using the two variances from Eq. (6.4.10) in Eq. (6.4.3), we can obtain σ_1 and σ_0. If we calculate Q with the help of Eq. (6.4.1), the result is found to be [23]

$$Q = \frac{\text{SNR}_o\sqrt{M}}{\sqrt{2\text{SNR}_o + 1} + 1}, \tag{6.4.11}$$

where $\text{SNR}_o \equiv P_1/P_{\text{ASE}}$ is the optical SNR. This relation can be easily inverted to find

$$\text{SNR}_o = \frac{2Q^2}{M} + \frac{2Q}{\sqrt{M}}. \tag{6.4.12}$$

These equations show that $Q = 6$ can be realized for relatively low values of optical SNR. For example, we only need $\text{SNR}_o = 7.5$ when $M = 16$ to maintain $Q = 6$. Figure

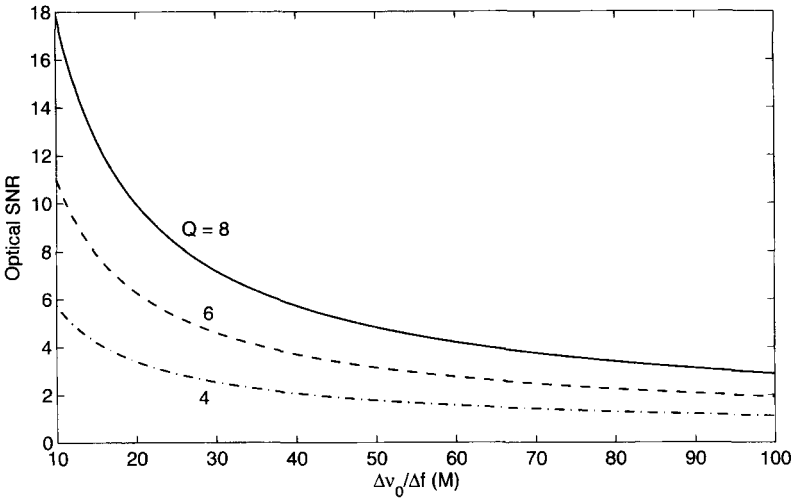

Figure 6.11: Required optical SNR as a function of M for several values of the Q factor.

6.11 shows how optical SNR varies with M for values of Q in the range of 4 to 8. As seen there, the required optical SNR increases rapidly as M is reduced below 10.

In some receivers, an electrical filter known as the integrate-and-dump filter is employed before the decision circuit. Such receivers use pulse energy defined as $E_p = \int_{-\infty}^{\infty} |A(L,t)|^2 dt$ for distinguishing between 0 and 1 bits, where $A(L,t)$ is the optical field at the end of the fiber link. The ASE noise added by amplifiers induces fluctuations in E_p that affect the BER at the receiver. We consider such energy fluctuations in the following section.

6.5 Role of Dispersive and Nonlinear Effects

So far in this chapter we have considered amplifier noise without paying attention to how this noise interacts with the dispersive and nonlinear effects that also occur as an optical signal propagates along the fiber link. In reality, ASE noise propagates with the signal and is affected also by the same dispersive and nonlinear mechanisms that affect the optical signal. In this section, we consider the general problem and show that ASE noise can be enhanced considerably if the conditions are suitable for modulation instability to occur. ASE noise also affects optical pulses and induces not only energy fluctuations but also timing jitter by shifting each pulse in a random fashion from its original location within the bit slot.

6.5.1 Noise Growth through Modulation Instability

Consider a long-haul lightwave system with lumped amplifiers placed periodically along the link. Each amplifier adds ASE noise that propagates with the signal in multi-

ple fiber sections. In a purely linear system, the noise power would not change. However, the nonlinear term in the NLS equation (6.1.1) couples the ASE and signal and modifies the signal through the three nonlinear effects, SPM, XPM, and FWM, discussed in Chapter 4. For a lightwave system operating close to the zero-dispersion wavelength of the fiber, FWM is of considerable concern [30], but SPM and XPM do not affect the system performance much [31]. The situation changes in the presence of fiber dispersion because conventional FWM is then not phase-matched and becomes negligible. However, the phenomenon of modulation instability (see Section 4.1.4) degrades the system performance by amplifying the ASE noise and converting phase fluctuations into intensity noise [32]–[40]. Conceptually, modulation instability is related to a FWM process that is phase-matched by the nonlinear effects [41]. The ASE noise seeds the FWM process and amplifies those spectral components of noise that lie within the gain bandwidth of modulation instability.

To study how ASE noise is affected by modulation instability, we need to solve Eq. (6.1.1). As was done in Section 3.2.3, it is helpful to employ the transformation $A(z,t) = \sqrt{p(z)}B(z,t)$ and write Eq. (6.1.1) in terms of $B(z,t)$ as

$$\frac{\partial B}{\partial z} + \frac{i\beta_2}{2}\frac{\partial^2 B}{\partial t^2} = i\gamma p(z)|B|^2 B + f_n(z,t)/\sqrt{p(z)}, \tag{6.5.1}$$

where $p(z)$ denotes variations in the peak power of the signal along the fiber link and is defined such that $p(z_m) = 1$, where z_m is the location of the mth amplifier. In the case of lumped amplifiers, the noise term $f_n = 0$ in each fiber section because noise is generated only within amplifiers. However, this noise term should be retained for distributed Raman amplification. We focus on the case of lumped amplifiers in the following discussion and set $p(z) = \exp(-\alpha z)$.

In general, one must solve Eq. (6.5.1) numerically as both the signal and ASE noise are time-dependent. Some insight in the noise amplification process can be gained by assuming that a CW signal with power P_0 enters the fiber with noise superimposed on it. We can then write the solution of Eq. (6.5.1) in the form

$$B(z,t) = [\sqrt{P_0} + a(z,t)]\exp(i\phi_{\rm NL}), \tag{6.5.2}$$

where $\phi_{\rm NL} = \gamma P_0 \int_0^z e^{-\alpha z}\,dz$ is the SPM-induced nonlinear phase shift. Substituting Eq. (6.5.2) in Eq. (6.5.1) and assuming that noise is much weaker than the signal ($|a|^2 \ll P_0$), we obtain

$$\frac{\partial a}{\partial z} + \frac{i\beta_2}{2}\frac{\partial^2 a}{\partial t^2} = i\gamma P_0 e^{-\alpha z}(a + a^*). \tag{6.5.3}$$

The linear equation (6.5.3) is easier to solve in the Fourier domain because it reduces to the following set of two ordinary differential equations:

$$\frac{db_1}{dz} = \frac{i}{2}\beta_2\Omega^2 b_1 + i\gamma P_0 e^{-\alpha z}(b_1 + b_2^*), \tag{6.5.4}$$

$$\frac{db_2}{dz} = \frac{i}{2}\beta_2\Omega^2 b_2 + i\gamma P_0 e^{-\alpha z}(b_2 + b_1^*), \tag{6.5.5}$$

where $b_1(z) = \tilde{a}(z,\Omega)$, $b_2(z) = \tilde{a}(z,-\Omega)$, $\tilde{a}$ represents the Fourier transform of a, and $\Omega = \omega_n - \omega_0$ represents the shift of the noise frequency ω_n from the signal carrier frequency ω_0. These equations show that SPM couples the spectral components of ASE

noise located symmetrically around ω_0. When Ω falls within the gain bandwidth of modulation instability (see Figure 4.4), the corresponding noise components are amplified. In the FWM picture, two photons of energy $\hbar\omega_0$ from the signal are converted into two new photons with energies $\hbar(\omega_0+\Omega)$ and $\hbar(\omega_0-\Omega)$.

The coupled equations (6.5.4) and (6.5.5) can be solved easily when fiber losses are negligible ($\alpha = 0$) so that the last term is z-independent [32]. It can also be solved when $\alpha \neq 0$ but the solution involves the Hankel functions [35] or modified Bessel functions of complex order and argument [39]. An approximate solution is obtained when $e^{-\alpha z}$ is replaced with its average value L_{eff}/L [34], where L is the fiber length and L_{eff} is the effective length introduced in Section 4.1. In a more accurate approach, fiber is divided into multiple segments [37]. Propagation through each segment of length h is governed by a transfer matrix [32]

$$\begin{pmatrix} b_1(z_n+h) \\ b_2(z_n+h) \end{pmatrix} = \begin{pmatrix} M_{11} & M_{12} \\ M_{21} & M_{22} \end{pmatrix} \begin{pmatrix} b_1(z_n) \\ b_2(z_n) \end{pmatrix}, \tag{6.5.6}$$

where the matrix elements are given by

$$M_{11} = [\exp(ik_1h) - r_1r_2\exp(ik_2h)]/(1-r_1r_2), \tag{6.5.7}$$

$$M_{22} = [\exp(ik_2h) - r_1r_2\exp(ik_1h)]/(1-r_1r_2), \tag{6.5.8}$$

$$M_{12} = r_2[\exp(ik_2h) - \exp(ik_1h)]/(1-r_1r_2), \tag{6.5.9}$$

$$M_{21} = r_1[\exp(ik_1h) - \exp(ik_2h)]/(1-r_1r_2). \tag{6.5.10}$$

The four parameters appearing in these expression depend on the dispersion and nonlinear parameter combinations $d = \beta_2\Omega^2$ and $\mu = \gamma P_0 e^{-\alpha z_n}$ as

$$k_1 = [(\mu+d)^2 - \mu^2]^{1/2}, \quad k_2 = -[(\mu+d)^2 - \mu^2]^{1/2} \tag{6.5.11}$$

$$r_1 = (k_1 - d)/\mu - 1, \qquad r_2 = -(k_2+d)/\mu - 1. \tag{6.5.12}$$

The matrix elements M_{mn} are constants in each fiber segment but change from segment to segment. The solution at the end of fiber is obtained by multiplying individual matrices. The effects of dispersion compensation can be easily incorporated by changing the values of β_2 for specific segments. To calculate the buildup of ASE noise in a long chain of amplifiers, one must add additional noise after each amplifier, propagate it in subsequent fiber sections, and sum the contribution for all amplifiers. This procedure allows one to calculate the optical spectrum as well as the relative intensity noise (RIN) spectrum at the receiver end [37]. Figure 6.12 shows an example of a numerically simulated optical spectrum at the end of a 2,500-km fiber link with 50 amplifiers placed 50 km apart [40]. A 1-mW signal at the 1.55-μm wavelength is transmitted through a fiber link using parameter values of $\beta_2 = -1$ ps^2/km, $\gamma = 2$ W^{-1}/km, and $\alpha = 0.22$ dB/km. Optical filters with a 8-nm passband filter the ASE after every amplifier. The broad pedestal represents the ASE spectrum expected even in the absence of nonlinear effects. The double-peak structure near the signal wavelength is due to modulation instability. The weak satellite peaks result from the nonlinear index grating formed by periodic variations of signal power along the fiber link.

From the standpoint of system performance, what matters most is the signal–ASE beating at the photodetector. It is possible to calculate the factor F_v by which the

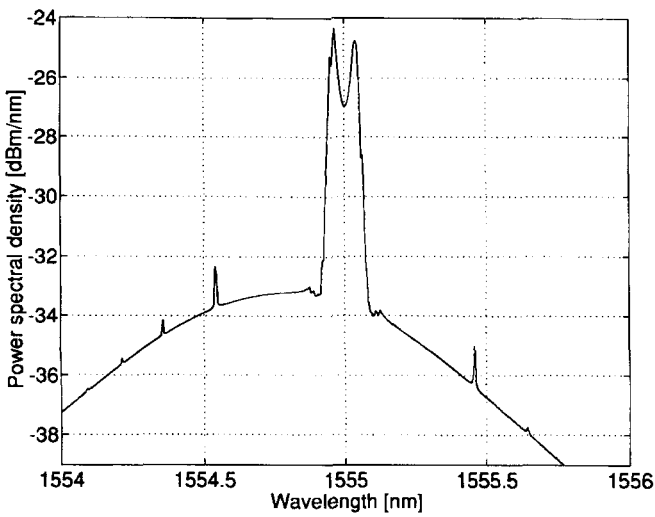

Figure 6.12: Optical spectrum showing effects of modulation instability at the end of a 2,500-km fiber link consisting of 50 amplifiers. (After Ref. [40]; ©1999 IEEE.)

noise variance $\sigma^2_{\text{sig-sp}}$ changes because of the dispersive and nonlinear effects occurring within the fiber link [37]. Figure 6.13 shows how F_v changes with the launched input power for a lightwave system consisting of four 100-km-long sections with $\alpha = 0.2$ dB/km and $\gamma = 1.2$ W^{-1}/km. The receiver bandwidth varies in the range of 2 to 30 GHz. Fiber dispersion is either (a) anomalous with $D = 2$ ps/(km-nm) or (b) normal with $D = -2$ ps/(km-nm). In the case of anomalous dispersion, noise variance is always enhanced; the enhancement factor increases both with receiver bandwidth and launched input power and can exceed a value of 10. In contrast, when link dispersion is normal, noise may increase or decrease depending on system parameters, but change is relatively small (within 30% or so). The large enhancement of the signal–ASE beat noise in the case of anomalous dispersion is directly related to the impact of modulation instability. Experimental results for a lightwave system operating at 10 Gb/s exhibited performance degradation after a transmission distance of only 455 km [36]. The system performance improved considerably when link dispersion was partially compensated.

6.5.2 Noise-Induced Signal Degradation

We next focus on the degradation of optical signal as it propagates through the link while ASE noise is added by amplifiers periodically. For this purpose we consider a single pulse representing bit 1 in a fixed time slot and ask how its energy and position are affected by noise. Although changes in pulse energy are expected, ASE can also induce timing jitter in a bit stream by shifting optical pulses from their original location within the time slot in a random fashion. Such a jitter was first studied in 1986 in the context of solitons and is called the Gordon–Haus jitter [42]. It was recognized later that timing jitter occurs in any lightwave system employing optical amplifiers and it

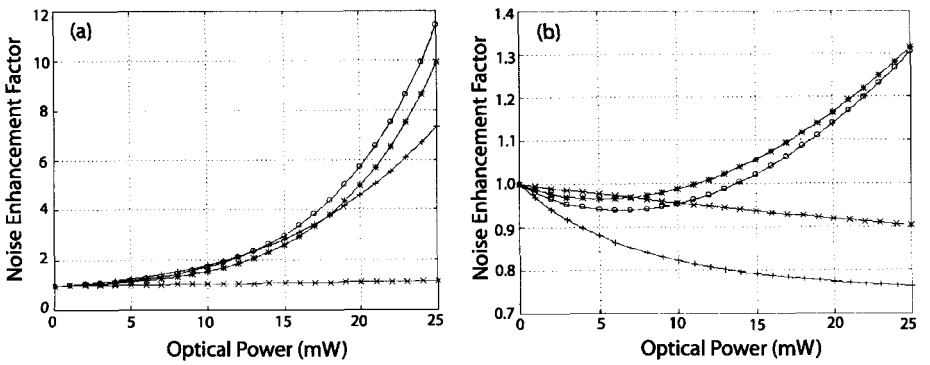

Figure 6.13: Noise-enhancement factor F_v as a function of input optical power in the cases of (a) anomalous and (b) normal dispersion for Δf = 2 GHz (crosses), 8 GHz (crosses), 20 GHz (crosses), and 30 GHz (crosses). In each case, the fiber link consists of four 100-km-long sections. (After Ref. [37]; ©1997 IEEE.)

imposes a fundamental limitation on all long-haul systems [43]–[49].

The physical origin of ASE-induced jitter can be understood by noting that optical amplifiers affect not only the amplitude but also the phase of the amplified signal, as apparent from Eq. (6.1.1) or Figure 6.2. Time-dependent variations in the optical phase shift the signal frequency from the carrier frequency ω_0 by a small amount after each amplifier. Since the group velocity of an optical pulse depends on its carrier frequency (because of dispersion), the speed at which a pulse propagates through the fiber is affected by each amplifier in a random fashion. Such speed changes produce random shifts in the pulse position at the receiver and are responsible for the ASE-induced timing jitter.

In general, one should solve Eq. (6.5.1) numerically to study how much signal is affected by noise. However, such a Monte–Carlo approach is quite cumbersome in practice as this equation should be solved multiple times to collect a large enough statistical sample. The moment method, discussed in Section 4.6.1, allows one to perform the average over ASE noise analytically. We need to extend this method and introduce two new moments q and Ω, representing pulse position within the bit slot and shift in the carrier frequency, respectively, and defined as [45]

$$q(z) = \frac{1}{E}\int_{-\infty}^{\infty} t|B(z,t)|^2\,dt, \tag{6.5.13}$$

$$\Omega(z) = \frac{i}{2E}\int_{-\infty}^{\infty}\left(B^*\frac{\partial B}{\partial t} - B\frac{\partial B^*}{\partial t}\right)dt, \tag{6.5.14}$$

where $E(z) \equiv \int_{-\infty}^{\infty}|B(z,t)|^2\,dt$ is related to pulse energy. Noting that fiber losses have been removed from Eq. (6.5.1), we expect E to remain constant along the fiber in the absence of ASE noise.

Differentiating E, q, and Ω with respect to z and using Eq. (6.5.1), we find that they

change in each passive fiber section as [46]

$$\frac{dE}{dz} = 0, \qquad \frac{dq}{dz} = \beta_2 \Omega, \qquad \frac{d\Omega}{dz} = 0. \tag{6.5.15}$$

A simple integration shows that while pulse energy E and frequency Ω do not change during propagation, pulse position shifts if the pulse enters the fiber with a finite value of Ω. This is easily understood if we recall from Section 3.2 that Eq. (6.5.1) is written in a frame moving with the group velocity v_g of the pulse, that is, the center of the pulse remains stationary as long as the carrier frequency ω_0 remains fixed. However, if this frequency shifts by Ω, the group velocity changes, and the pulse center shifts by $q(z) = \beta_2 \Omega z$.

Consider now what happens when pulse enters the kth amplifier along the fiber link. Because of ASE added by the amplifier, E, Ω, and q change by random amounts δE_k, $\delta \Omega_k$, and δq_k, respectively. If we include these random changes, Eqs. (6.5.15) take the form

$$\frac{dE}{dz} = \sum_k \delta E_k \, \delta(z - z_k), \tag{6.5.16}$$

$$\frac{dq}{dz} = \beta_2 \Omega + \sum_k \delta q_k \, \delta(z - z_k), \tag{6.5.17}$$

$$\frac{d\Omega}{dz} = \sum_k \delta \Omega_k \, \delta(z - z_k), \tag{6.5.18}$$

where the sum is over the total number of amplifiers encountered by the pulse before it arrives at z. These equations show that frequency fluctuations induced by amplifiers manifest as position fluctuations because of GVD; some jitter occurs even when $\beta_2 = 0$. Clearly, ASE-induced timing jitter would be large for fibers with large dispersion and can be reduced by operating a lightwave system near the zero-dispersion wavelength of the fiber.

Before proceeding further, we need to consider the statistics of fluctuations δE_k, δq_k, and $\delta \Omega_k$. Let $B(z_k, t)$ be the field entering the kth amplifier. After amplification, this field can be written as $B(z_k, t) + b_k(t)$, where $b_k(t)$ is the ASE-induced change in the optical field. As discussed in Section 6.1, $b_k(t)$ vanishes on average but its correlation function is given by

$$\langle b_j^*(t) b_k(t') \rangle = S_{\text{ASE}} \delta_{jk} \delta(t - t'), \tag{6.5.19}$$

where S_{ASE} is the spectral density of ASE given in Eq. (6.1.6) and δ_{jk} indicates that fluctuations at two different amplifiers are not correlated. We can calculate the change in E, q, and Ω occurring after the kth amplifier by applying Eqs. (6.5.13) and (6.5.14) at the end of that amplifier. We then obtain the following relations:

$$E_k + \delta E_k = \int_{-\infty}^{\infty} |B + b_k|^2 \, dt, \tag{6.5.20}$$

$$(q_k + \delta q_k)(E_k + \delta E_k) = \int_{-\infty}^{\infty} t |B + b_k|^2 \, dt, \tag{6.5.21}$$

$$(\Omega_k + \delta \Omega_k)(E_k + \delta E_k) = \frac{i}{2} \int_{-\infty}^{\infty} (B^* + b_k^*) \frac{\partial (B + b_k)}{\partial t} \, dt + \text{c.c.}, \tag{6.5.22}$$

where q_k, Ω_k, and E_k are the pulse parameters before entering the amplifier. After some simplifications, these equations reduce to

$$\delta E_k = \int_{-\infty}^{\infty} (B^* b_k + B b_k^* + |b_k|^2)\, dt, \tag{6.5.23}$$

$$\delta q_k = \frac{1}{E_k} \int_{-\infty}^{\infty} (t-q)(B^* b_k + B b_k^*)\, dt, \tag{6.5.24}$$

$$\delta \Omega_k = \frac{i}{E_k} \int_{-\infty}^{\infty} b_k^* \left(\frac{\partial B}{\partial t} + i\Omega_k B \right) dt + \text{c.c.} \tag{6.5.25}$$

We can now perform the average over the random variable b_k using Eq. (6.5.19) together with $\langle b_k \rangle = 0$. Random variables δq_k and $\delta \Omega_k$ vanish on average, but $\langle \delta E_k \rangle = S_{\text{ASE}}$. Their correlation function and variances can also be calculated with the help of Eq. (6.5.19) and are found to be

$$\langle (\delta q_k)^2 \rangle = \frac{2S_{\text{ASE}}}{E_k^2} \int_{-\infty}^{\infty} (t-q_k)^2 |V(z_k,t)|^2\, dt, \tag{6.5.26}$$

$$\langle (\delta \Omega_k)^2 \rangle = \frac{2S_{\text{ASE}}}{E_k^2} \int_{-\infty}^{\infty} \left| \frac{\partial V}{\partial t} \right|^2 dt, \tag{6.5.27}$$

$$\langle \delta q_k\, \delta \Omega_k \rangle = \frac{iS_{\text{ASE}}}{2E_k^2} \int_{-\infty}^{\infty} (t-q_k) V \frac{\partial V^*}{\partial t}\, dt + \text{c.c.}, \tag{6.5.28}$$

where $V = B\exp[i\Omega_k(t-q_k)]$. These equations apply for any pulse shape. However, they requite a knowledge of the optical field $B(z,t)$ at each amplifier. In the most general case, this field can be obtained by solving Eq. (6.5.1) numerically (without the noise term). Such a semianalytic approach is quite useful in practice as it solves the NLS equation numerically only once while performing the average over ASE noise in an analytic fashion [45].

6.5.3 Noise-Induced Energy Fluctuations

As a simple application of the moment method, we calculate the variance of pulse-energy fluctuations. As noted before, $\langle \delta E_k \rangle = S_{\text{ASE}}$. Calculating $\langle \delta E_k^2 \rangle$ from Eq. (6.5.23) and performing the average with the help of Eq. (6.5.19), we obtain the relatively simple result

$$\langle \delta E_k^2 \rangle = 2S_{\text{ASE}} E_k + S_{\text{ASE}}^2. \tag{6.5.29}$$

If we use the definition of energy variance

$$\sigma_E^2 = \langle \delta E_k^2 \rangle - \langle \delta E_k \rangle^2, \tag{6.5.30}$$

the standard deviation $\sigma_E \equiv (2S_{\text{ASE}} E_k)^{1/2}$ depends on the pulse energy E_k before the amplifier. As a numerical example, after an amplifier with 20 dB gain and $n_{\text{sp}} = 1.5$ (noise figure about 4.8 dB), 1-pJ input pulses have a relative fluctuation level σ_E/E of about 0.6% in the spectral region near 1.55 μm.

The important question is how this noise accumulates along the fiber link. We can calculate energy variance for a long fiber link with multiple amplifiers by considering

what happens to pulse energy in the fiber section before the kth amplifier. As seen from Eq. (6.5.15), E remains unchanged within a passive fiber as losses have been removed from Eq. (6.5.1). This leads to a recurrence relation $E_k = E_{k-1} + \delta E_k$ that can be used to obtain the final energy at the end of the last amplifier in the form

$$E_f = E_0 + \sum_{k=1}^{N_A} \delta E_k, \tag{6.5.31}$$

where E_0 is the input pulse energy and N_A is the number of amplifiers along the fiber link assumed to be spaced apart equally.

The average value is found from Eq. (6.5.31) to be

$$\langle E_f \rangle = E_0 + \sum_{k=1}^{N_A} \langle \delta E_k \rangle = E_0 + N_A S_{\text{ASE}}. \tag{6.5.32}$$

The second moment can also be calculated as

$$\langle E_f^2 \rangle = E_0^2 + 2E_0 \sum_{k=1}^{N_A} \langle \delta E_k \rangle + \sum_{k=1}^{N_A} \sum_{j=1}^{N_A} \langle \delta E_j \delta E_k \rangle. \tag{6.5.33}$$

Using the fact that fluctuations at each amplifier follow an independent random process and thus are uncorrelated, we obtain

$$\langle E_f^2 \rangle = E_0^2 + 4N_A S_{\text{ASE}} E_0 + N_A^2 S_{\text{ASE}}^2. \tag{6.5.34}$$

The standard deviation of energy fluctuations follows from Eqs. (6.5.30), (6.5.32), (6.5.34) and is given by

$$\sigma_E = \sqrt{2N_A S_{\text{ASE}} E_0}. \tag{6.5.35}$$

As expected on physical grounds, σ_E scales with the number of amplifiers as $\sqrt{N_A}$, or with the link length as $\sqrt{L_T}$ since $L_T = N_A L_A$ for an amplifier spacing of L_A. Even for a relatively long fiber link with 100 cascaded amplifiers, the level of energy fluctuations remains below 10% for typical parameter values.

6.5.4 Noise-Induced Frequency Fluctuations

We can follow the same procedure to calculate the variance of frequency fluctuations at the end of N_A amplifiers. However, even though we were able to calculate energy variance without knowing the actual pulse shape, this is not so in the case of frequency fluctuations or timing jitter. Let us assume that optical pulses representing 1 bits are in the form of a chirped Gaussian pulse and that nonlinear effects are relatively weak so that each pulse is affected mostly by fiber dispersion. As seen in Section 3.2, each pulse maintains its Gaussian shape on propagation but its parameters change. The optical field associated with a single pulse can be written as

$$B(z,t) = a \exp[-(1+iC)(t-q)^2/2T^2 + i\phi - i\Omega(t-q)], \tag{6.5.36}$$

where the amplitude a, phase ϕ, frequency Ω, position q, chirp C, and width T all are functions of z. As discussed in Section 4.6, we can use the the moment method to find the pulse parameters at the location of each amplifier.

Using the Gaussian form of $B(z,t)$ from Eq. (6.5.36) in Eqs. (6.5.26) through (6.5.28), we can perform the time integration analytically. The variances and cross-correlation of δq_k and $\delta\Omega_k$ at the location of the ith amplifier are then found to be [46]

$$\langle(\delta\Omega_k)^2\rangle = (S_{\mathrm{ASE}}/E_k)[(1+C_k^2)/T_k^2], \tag{6.5.37}$$

$$\langle(\delta q_k)^2\rangle = (S_{\mathrm{ASE}}/E_k)T_k^2, \qquad \langle\delta\Omega_k\,\delta q_k\rangle = (S_{\mathrm{ASE}}/E_k)C_k, \tag{6.5.38}$$

where E_k, C_k, and T_k are the energy, chirp, and width at $z = z_k$.

The final step is to write these parameters in terms of the input pulse parameters E_0, C_0, and T_0. The pulse energy E_k can be replaced with E_0 if each amplifier compensates all losses of the preceding fiber section. The pulse width and chirp are found from Section 3.3 or 4.6 to be

$$T_k = T_0\left[\left(1+kC_0\frac{d_a}{T_0^2}\right)^2 + k^2\frac{d_a^2}{T_0^4}\right]^{1/2}, \qquad C_k = C_0 + k(1+C_0^2)\frac{d_a}{T_0^2}, \tag{6.5.39}$$

where $d_a = \int_0^{L_A}\beta_2(z)\,dz$ is the net accumulated dispersion in each fiber section. Using Eq. (6.5.39) in Eqs. (6.5.37) and (6.5.38), we obtain

$$\langle(\delta\Omega_k)^2\rangle = (S_{\mathrm{ASE}}/E_0)[(1+C_0^2)/T_0^2], \tag{6.5.40}$$

$$\langle(\delta q_k)^2\rangle = (S_{\mathrm{ASE}}T_0^2/E_0)[(1+kC_0d_a/T_0^2)^2 + (kd_a/T_0^2)^2], \tag{6.5.41}$$

$$\langle\delta\Omega_k\,\delta q_k)\rangle = (S_{\mathrm{ASE}}/E_0)[C_0 + k(1+C_0^2)d_a/T_0^2]. \tag{6.5.42}$$

The variance of frequency fluctuations is found by integrating Eq. (6.5.18), and the total frequency shift at the end of the last amplifier is found to be $\Omega_f = \sum_{k=1}^{N_A}\delta\Omega_k$. In contrast with the case of energy fluctuations, the average value $\langle\Omega_f\rangle = 0$. The variance is found to be

$$\sigma_\Omega^2 = \langle\Omega_f^2\rangle = \sum_{k=1}^{N_A}\sum_{j=1}^{N_A}\langle\delta\Omega_j\delta\Omega_k\rangle = N_A\langle(\delta\Omega_k)^2\rangle. \tag{6.5.43}$$

Using $\langle(\delta\Omega_k)^2\rangle$ from Eq. (6.5.42), the standard deviation of frequency fluctuations for initially unchirped Gaussian pulses is given by

$$\sigma_\Omega = [N_AS_{\mathrm{ASE}}/(E_0T_0^2)]^{1/2} = \sigma_E/(\sqrt{2}E_0T_0). \tag{6.5.44}$$

As a numerical estimate, if we assume a 5% fluctuation level in the pulse energy, $\sigma_\Omega = 3.5\times10^9\ \mathrm{s}^{-1}$ for $T_0 = 10$ ps. Thus, even for a relatively long link, the level of frequency fluctuations remains below 1 GHz. However, as discussed next, such small fluctuations can still produce considerable timing jitter.

6.5.5 Noise-Induced Timing Jitter

We now proceed to calculate the timing jitter at the end of a fiber link with a cascaded chain of N_A amplifiers. Equation (6.5.17) can be integrated in a straightforward manner to obtain the total jitter at the end of the fiber link as

$$q_f = \sum_{n=1}^{N_A} \delta q_n + d_a \sum_{n=1}^{N_A} \sum_{k=1}^{n-1} \delta\Omega_k, \tag{6.5.45}$$

where $d_a = \bar{\beta}_2 L_A$ is the accumulated dispersion in each fiber section with average dispersion $\bar{\beta}_2$. Timing jitter is calculated from this equation using

$$\sigma_t^2 = \langle q_f^2 \rangle - \langle q_f \rangle^2, \tag{6.5.46}$$

where angle brackets denote averaging over the random variables δq_k and $\delta\Omega_k$. Since both of them vanish on average, it follows that $\langle q_f \rangle = 0$. However, the variance σ_t^2 remains finite.

Rather than using Eq. (6.5.45) and dealing with triple and quadruple sums, it is simpler to consider what happens between two amplifiers and obtain two recurrence relations. From Eqs. (6.5.17) and (6.5.18), we find that

$$q_{k+1} = q_k + d_a \delta\Omega_k + \delta q_{k+1}, \qquad \Omega_{k+1} = \Omega_k + \delta\Omega_{k+1}. \tag{6.5.47}$$

Using the fact that fluctuations at two amplifiers are not correlated, it easy to deduce from these recurrence relations that

$$\langle q_{k+1}^2 \rangle = \langle q_k^2 \rangle + d_a^2 \langle \Omega_k^2 \rangle + 2 d_a \langle \Omega_k q_k \rangle + \langle (\delta q_{k+1})^2 \rangle, \tag{6.5.48}$$

$$\langle \Omega_{k+1}^2 \rangle = \langle \Omega_k^2 \rangle + \langle (\delta\Omega_{k+1})^2 \rangle, \tag{6.5.49}$$

$$\langle \Omega_{k+1} q_{k+1} \rangle = \langle \Omega_k q_k \rangle + d_a \langle \Omega_k^2 \rangle + \langle \delta\Omega_{k+1}\, \delta q_{k+1} \rangle. \tag{6.5.50}$$

Timing jitter at the end of the last amplifier is found from Eq. (6.5.48) to be

$$\sigma_t^2 = d_a^2 \sum_{k}^{N_A-1} \langle \Omega_k^2 \rangle + 2 d_a \sum_{k}^{N_A-1} \langle \Omega_k q_k \rangle + \sum_{k}^{N_A} \langle (\delta q_k)^2 \rangle. \tag{6.5.51}$$

Using Eqs. (6.5.40) through (6.5.42) for the three moments appearing in this equation, the final result turns out to be relatively simple and has the form [46]

$$\sigma_t^2 = (S_{\rm ASE}/E_0) T_0^2 N_A [(1 + (C_0 + N_A d_a / T_0^2)^2]. \tag{6.5.52}$$

In the case of perfect dispersion compensation such that $d_a = 0$, the jitter variance increases linearly with the number of amplifiers. In contrast, when $d_a \neq 0$, it increases with N_A in a cubic fashion. For such long-haul systems, the dominant term in Eq. (6.5.19) varies as $N_A^3 d_a^2$. This is a general feature of ASE-induced jitter resulting from frequency fluctuations [42]. The cubic dependence of timing jitter on system length shows that even relatively small frequency fluctuations can induce enough jitter for long-haul systems that they may become inoperable, especially when fiber dispersion is not compensated.

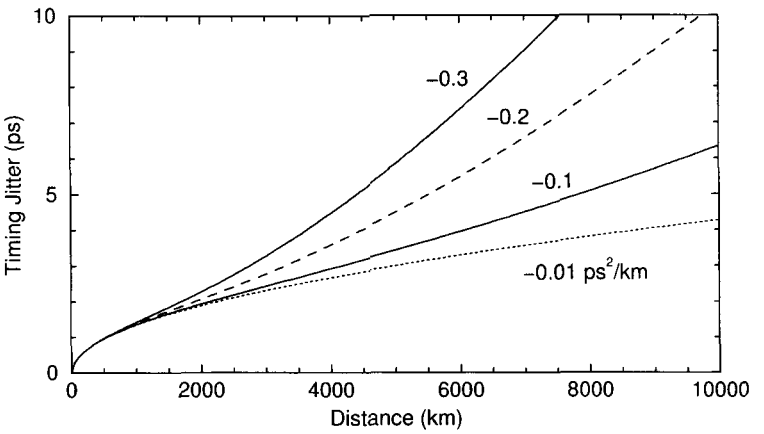

Figure 6.14: ASE-induced timing jitter as a function of system length for several values of the average dispersion $\bar{\beta}_2$.

Residual dispersion of a fiber link can lead to considerable timing jitter in CRZ systems, as seen from Eq. (6.5.52). Figure 6.14 shows the timing jitter as a function of the total system length $L_T = N_A L_A$ for a 10-Gb/s system using four values of $\bar{\beta}_2$ with $T_m = 30$ ps, $L_A = 50$ km, $C_0 = 0.2$, and $S_{\rm ASE}/E_0 = 10^{-4}$. The ASE-induced jitter becomes a significant fraction of the pulse width for values of $|\bar{\beta}_2|$ as small as 0.2 ps^2/km because of the cubic dependence of σ_t^2 on the system length L_T. Such jitter would lead to large power penalties, as discussed in Section 5.4.5, if left uncontrolled.

6.5.6 Jitter Reduction through Distributed Amplification

As seen earlier in this chapter, the use of distributed amplification lowers the noise level in lightwave systems. One would thus expect timing jitter to be reduced if Raman amplification is employed in place of lumped amplifiers. This indeed turns out to be the case [49].

The mathematical treatment of timing jitter is more complex in the case of distributed amplification as one must take into account the z dependence of the Raman gain and use the integral form of the spectral density of ASE noise given in Eq. (6.1.12). Similarly, the sum over the number of amplifiers in Eqs. (6.5.16) through (6.5.18) is replaced with an integral. These equations can still be integrated to calculate the variance of the random variable q following the method used in [50]. In the case of Gaussian pulses, σ_t^2 is given by the following expression:

$$\begin{aligned}\sigma_t^2 = {} & \frac{2h\nu_0}{E_0}\int_0^z \beta_2(z_1)\,dz_1 \int_0^{z_1} \beta_2(z_2)\,dz_2 \int_0^{z_2} g(z')n_{sp}(z')\frac{1+C^2(z')}{G(z')T^2(z')}\,dz' \\ & + \frac{h\nu_0}{E_0}\int_0^z \beta_2(z_1)\,dz_1 \int_0^{z_1} g(z')n_{sp}(z')G^{-1}(z')C(z')\,dz' \\ & + \frac{h\nu_0}{E_0}\int_0^z g(z')n_{sp}(z')G^{-1}(z')T^2(z')\,dz'. \end{aligned} \tag{6.5.53}$$

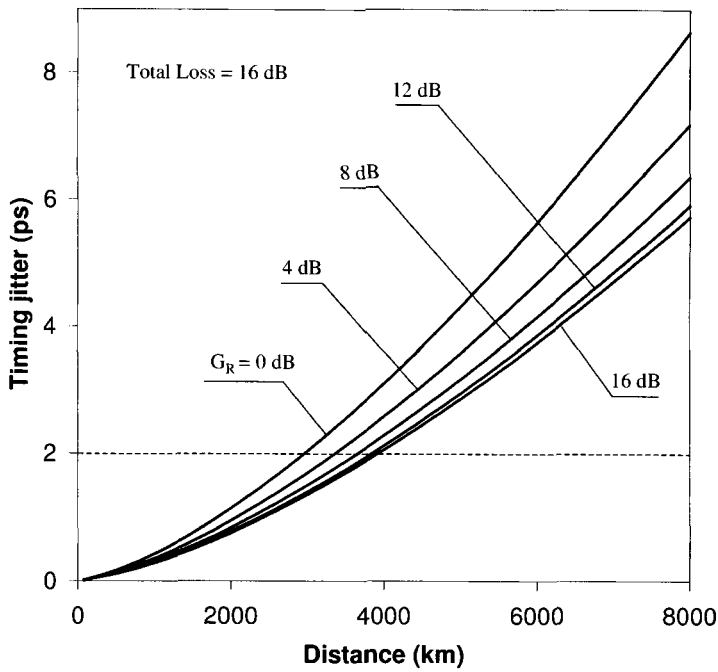

Figure 6.15: ASE-induced timing jitter as a function of system length for a 40-Gb/s lightwave system employing a hybrid amplification scheme. Total losses are 16 dB over each 80-km section. The contribution of Raman gain G_R is varied from 0 to 16 dB. The dashed line shows the tolerable value of timing jitter. (After Ref. [50]; ©2002 IEEE.)

The three terms in this equations have the same origin as the three terms in Eq. (6.5.51) found in the case of lumped amplifiers. The first and third terms result from frequency and position fluctuations induced by ASE, while the second term is due to their correlations.

Equation (6.5.53) can be used for fiber links employing dispersion management. We apply it to a lightwave system designed to operate at 40 Gb/s while employing a hybrid Raman amplification in which only a part of fiber losses is compensated with lumped amplifiers spaced 80-km apart. Remaining losses are compensated through distributed Raman amplification realized by pumping each 80-km section backward. Dispersion of the fiber is alternated in a periodic fashion using 5-km sections with $\beta_2 = 3.9$ and -4.1 ps^2/km, resulting in an average dispersion of -0.1 ps^2/km. Each fiber section has $\alpha = 0.2$ dB/km and $\gamma = 2.5$ W^{-1}/km. Input pulse parameters (the width T_0, chirp C_0, and energy E_0) are chosen to ensure that Gaussian pulses can propagate stably over long distances (see Chapter 7). Figure 6.15 shows how timing jitter grows with distance as the Raman gain G_R is varied from 0 to 16 dB to compensate for 16-dB losses of each 80-km section [50]. The $G_R = 0$ case corresponds to pure lumped amplification. In contrast, no lumped amplifiers are employed in the case of $G_R = 16$ dB. Timing jitter is maximum for $G_R = 0$ and begins to decrease even when losses are only partially

compensated through Raman amplification. It reduces by about 40% when all losses are compensated through distributed amplification.

From a system perspective, a decrease in timing jitter allows the system to operate over longer distances. The dashed line in Figure 6.15 shows the tolerable level of timing jitter for a 40-Gb/s system (8% of the 25-ps bit slot). When lumped amplifiers are used, the system cannot operate even over a distance of 3,000 km. However, the limiting distance increases by more than 25% when distributed Raman amplification is employed. Even when a system can be designed to operate with lumped amplifiers, the use of distributed amplification allows one to increase amplifier spacing [49], an option that may lower the system cost.

6.6 Periodically Amplified Lightwave Systems

Many single-channel experiments performed during the early 1990s employed a chain of cascaded in-line optical amplifiers for increasing the length of long-haul fiber links [51]–[56]. These experiments showed that fiber dispersion becomes the limiting factor in periodically amplified lightwave systems. Indeed, the experiments were feasible only because the system was operated close to the zero-dispersion wavelength of the fiber link. Moreover, the residual dispersion was tailored along the link in such a way that the total dispersion over the entire link length was quite small at the operating wavelength. By 1992, total system length could be increased to beyond 10,000 km with such dispersion-management techniques. In a 1992 experiment [54], a 2.5-Gb/s signal was transmitted over 10,073 km using 199 EDFAs. An effective transmission distance of 21,000 km at 2.5 Gb/s and of 14,300 km at 5 Gb/s was demonstrated using a recirculating fiber loop [57].

A rough estimate of dispersion-limited system length can be obtained if launched power is assumed to be low enough that one can neglect the nonlinear effects during signal transmission. Since amplifiers compensate only for fiber losses, dispersion limitations discussed in Section 3.3.4 and shown in Figure 3.5 apply for each channel of a WDM system if L is replaced by L_T. From Eq. (3.3.44), the dispersion limit for systems making use of standard fibers ($\beta_2 \approx -20$ ps^2/km at 1.55 μm) is $B^2 L_T < 3{,}000$ (Gb/s)^2-km: System length is limited to below 30 km at 10 Gb/s for such fibers. An increase by a factor of 20 can be realized by using dispersion-shifted fibers with $|\beta_2| \approx 1$ ps^2/km. To extend the distance to beyond 6,000 km at 10 Gb/s, average GVD along the link should be smaller than $|\bar{\beta}_2| = 0.1$ ps^2/km.

6.6.1 Numerical Approach

The preceding estimate is crude since it does not include the impact of nonlinear effects discussed in Chapter 4. Even though power levels are kept relatively modest for each channel, the nonlinear effects can become quite important because of their accumulation over long distances. For single-channel systems, the most dominant nonlinear phenomenon that limits the system performance is SPM. An estimate of power limitation imposed by the SPM can be obtained from Eq. (4.1.17). If we use $\alpha = 0.2$ dB/km

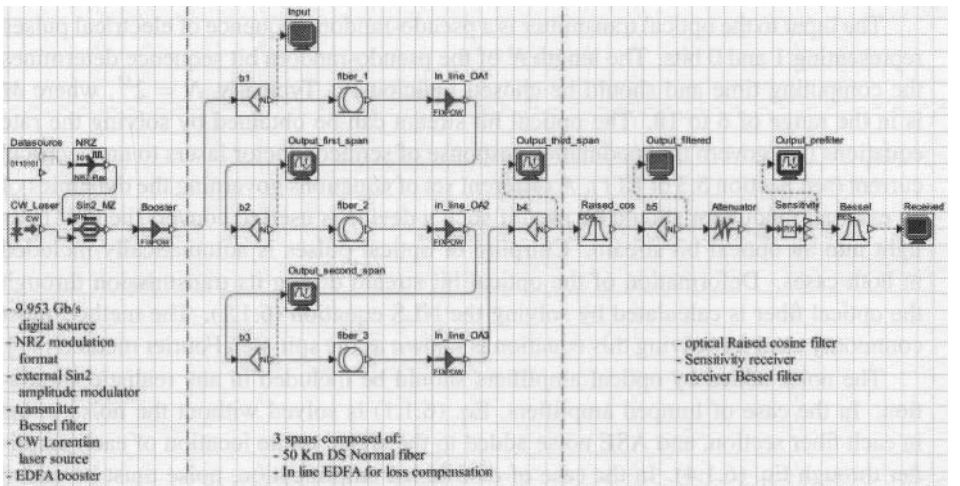

Figure 6.16: Layout of a typical lightwave system for modeling based on the software package OptSim.

and $\gamma = 2\ \mathrm{W}^{-1}/\mathrm{km}$ as typical values, and assume that the fiber link contains 100 amplifiers with 50-km spacing, the input power should be below 0.25 mW (−6 dBm) for the resulting 5,000-km-long system. Such power levels may not be high enough to maintain the required Q factor when ASE noise accumulated over 100 amplifiers is taken into account. The only solution would then be to decrease the number of the cascaded amplifiers.

An analytic estimate of the SPM-limited distance provides only a rough guideline as it ignores not only fiber dispersion but also the accumulation of ASE noise along the link. In reality, the nonlinear and dispersive act on the noisy optical signal simultaneously, and their mutual interplay is quite important. For this reason, the most practical approach for designing modern lightwave system consists of solving the NLS equation (6.1.1) directly using a suitable numerical technique. Numerical simulations indeed show that the accumulation of the nonlinear effects often limits the system length in practical lightwave systems and requires optimization of various design parameters such as amplifier spacing, input power launched into fiber, and dispersion properties of fibers used to construct the transmission link [58]–[74]. Indeed, several software packages dealing with the design of lightwave systems are available commercially. One such package, marketed by the RSoft Design Group and called OptSim 4.0, is provided on the compact disk enclosed with this book (see Appendix B).

The main advantage of a computer-aided design technique for designing modern lightwave systems is that such an approach is capable of optimizing the whole system and can provide the optimum values of various system parameters such that the design objectives are met at a minimum cost. Figure 6.16 illustrates the various steps involved in the simulation process. The approach consists of generating an optical bit pattern at the transmitter, transmitting it through the fiber link, detecting it at the receiver, and then analyzing it through the tools such as the eye diagram and the Q factor.

The input to the optical transmitter is a pseudo-random sequence of electrical pulses, representing 1 and 0 bits. The length N of the pseudo-random bit sequence determines the computing time and should be chosen judiciously. Typically, $N = 2^M$, where M is in the range of 6 to 10. The optical bit stream can be obtained by solving the rate equations that govern the modulation response of semiconductor lasers to an electrical current (see Section 5.3 of LT1). A different set of equations governing the dynamics of an external modulator should be used if such a device is used to convert the CW laser light into an optical bit stream. Chirping of optical pulses is automatically included in both cases. Deformation of the optical bit stream during its transmission through the optical fiber is calculated by solving the NLS equation (6.1.1). The method most commonly used for solving this equation is known as the spit-step Fourier method [41].

The noise added by optical amplifiers should be included in any realistic simulation. In the case of lumped amplifiers, Eq. (6.1.1) is solved without the noise terms in each fiber section, and ASE noise added to the signal at the location of each amplifier through Eq. (6.1.4). In the case of distributed amplification, noise must be added throughout the fiber length and it should satisfy the correlation function given in Eq. (6.1.2).

There are two equivalent techniques for adding ASE noise to the signal during numerical simulations. In one case, noise is added in the time domain, while ensuring that it follows Gaussian statistics and has a correlation function that satisfies Eq. (6.1.2) in the distributed case and Eq. (6.1.6) in the lumped case. The delta function $\delta(t-t')$ appearing in these equations requires that noise be uncorrelated in time. Because of a finite temporal resolution Δt in any numerical simulation, the delta function must be replaced with a rectangular-shape function whose width is Δt and height is $1/\Delta t$ so that the requirement $\int_{-\infty}^{-\infty} \delta(t)\,dt = 1$ is satisfied. In an alternative approach, noise is added in the frequency domain. In the case of lumped amplification, Eq. (6.1.4) is replaced by

$$\tilde{A}_{\text{out}}(\nu) = \sqrt{G}\tilde{A}_{\text{in}}(\nu) + \tilde{a}_n(\nu), \tag{6.6.1}$$

where a tilde represents the Fourier transform. The noise $\tilde{a}_n(\nu)$ is assumed to be frequency-independent (white noise) over the whole amplifier bandwidth, or the filter bandwidth if an optical filter is used after each amplifier. Mathematically, $\tilde{a}_n(\nu)$ is a complex Gaussian random variable whose real and imaginary parts have the spectral density $S_{\text{ASE}}/2$.

After adding noise at each amplifier, the NLS equation is solved in the following fiber section, and the procedure is repeated until the last amplifier is reached. A suitable receiver model converts optical signal into the electric domain and filters it using a filter whose bandwidth Δf is close to but smaller than the bit rate B (typically $\Delta f/B$ = 0.6–0.8). The resulting electric bit stream is used to find the instantaneous values of currents, I_0 and I_1, for 0 and 1 bits, respectively, by sampling it at the center of each bit slot. An eye diagram is also constructed using the filtered bit stream. The system performance is quantified through the Q factor, defined in Eq. (5.3.11) and related directly to the BER through Eq. (5.3.10). The calculation of the Q factor requires that the NLS equation be solved a large number of times with different seeds for the amplifier noise. Such an approach can be used to investigate trade-offs that would optimize overall system performance.

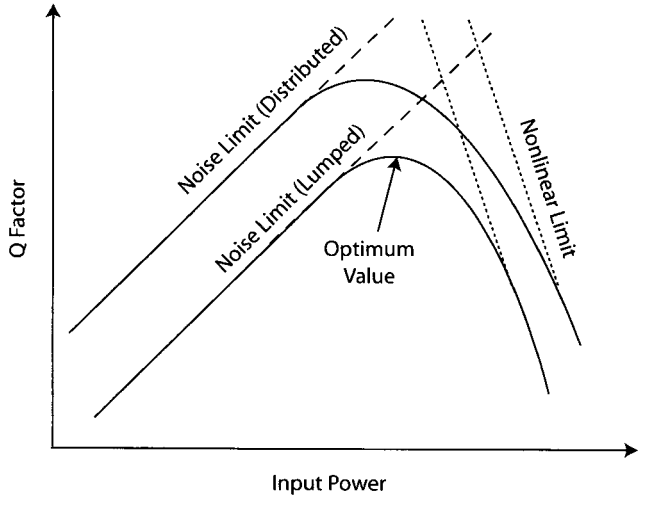

Figure 6.17: Schematic illustration of Q-factor variations with launched power in long-haul systems employing lumped or distributed amplification. The dashed and dotted lines show the ASE and nonlinear limits, respectively.

Computer-aided design has another important role to play. A long-haul lightwave system may contain many repeaters, both optical and electrical. Transmitters, receivers, and amplifiers used at repeaters, although chosen to satisfy nominal specifications, are never identical. Similarly, fiber cables are constructed by splicing many different pieces (with a typical length of 4 to 8 km) that have slightly different loss and dispersion characteristics. The net result is that many system parameters vary around their nominal values. For example, the dispersion parameter D, responsible not only for pulse broadening but also for other sources of power penalty, can vary significantly in different sections of the fiber link because of variations in the zero-dispersion wavelength and the transmitter wavelength. A statistical approach is often used to estimate the effect of such inherent variations on the performance of a realistic lightwave system. The idea behind such an approach is that it is extremely unlikely that all system parameters would take their worst-case values at the same time. Thus, repeater spacing can be increased well above its worst-case value if the system is designed to operate reliably at the specific bit rate with a high probability (say, 99.9%).

6.6.2 Optimum Launched Power

The importance of computer-aided design for fiber-optic communication systems became apparent during the 1990s with the advent of optical amplifiers. Amplifiers not only added ASE noise to the signal but also allow the dispersive and nonlinear effects to accumulate over long lengths. Moreover, amplifier noise often forces one to increase the channel power to more than 1 mW in order to maintain a high SNR (and a high Q factor consistent with the BER requirements). Since noise limits the Q factor at low power levels whereas nonlinear effects limit it at high power levels, it is evident that

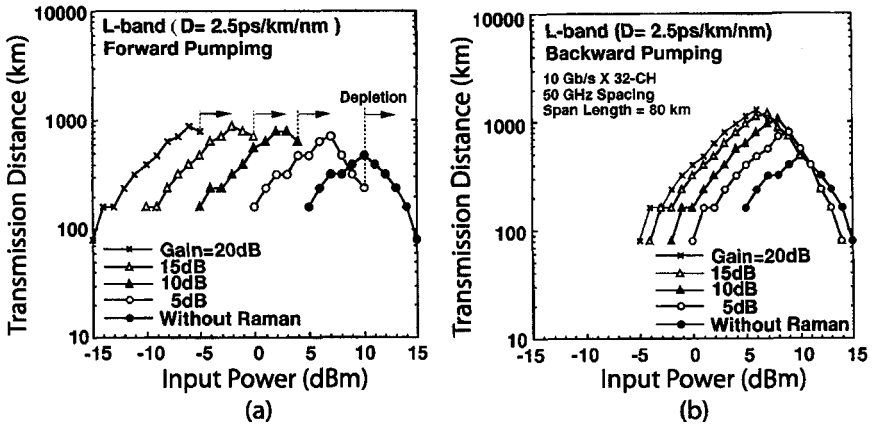

Figure 6.18: Maximum transmission distance as a function of input power when losses are compensated using a hybrid amplification scheme. The Raman gain is varied from 0 to 20 dB in the cases of (a) forward and (b) backward pumping. Arrows mark the maximum power at which pump depletion becomes significant. (After Ref. [73]; ©2001 IEEE.)

a lightwave system would have the largest value of Q at an optimum value of the average power launched into the fiber at the input end. Figure 6.17 shows schematically how the Q factor varies with the average input power for a long-haul lightwave system limited by the nonlinear effects. The Q factor increases initially with launched power, reaches a peak value, and then decreases with a further increase in the power because of the onset of the nonlinear effects.

Figure 6.17 also illustrates why the use of distributed amplification, in place of lumped amplifiers, improves system performance. Since the level of ASE noise is lower in the case of distributed amplification, such systems exhibit a higher optical SNR (or the Q factor) at a given power level (dashed line). As a result, the power level at which Q peaks is smaller compared with the lumped case. From a practical perspective, one can trade off a higher Q with a larger transmission distance. In other words, distributed amplification helps to increase the link length. This feature is shown in Figure 6.18, where numerical results are shown for a 32-channel WDM system [73] by plotting the maximum possible transmission distance as a function of input power assuming that a value of $Q = 7$ must be maintained at the end to ensure a BER below 10^{-12}. The fiber link is divided into 80-km sections, and the 20-dB loss of each section is compensated using a forward or backward pumping configuration.

Several features of Figure 6.18 are noteworthy. As expected from Figure 6.17, transmission distance is maximum at an optimum value of input power. This optimum value is largest (about 10 mW), and the distance is smallest (about 480 km) in the case of pure lumped amplification. As the amount of Raman gain increases, the optimum power is reduced and transmission distance increases. The same signal can be transmitted over more than 1,000 km when all losses are compensated through Raman amplification. The optimum value of input power drops below -5 dBm in the case of forward pumping. The more than two-fold increase in the link length with the use of

Raman amplification is due to a reduced ASE noise that is added to the signal during its transmission.

Some terrestrial lightwave systems serving the backbone of a wide-area network should operate over more than 3,000 km (called ultra-long-haul systems). This can be realized by employing forward error correction because the minimum value of Q required at the receiver then drops to close to 3 (rather than being 7, as assumed in Figure 6.18). Indeed, by 2004, a WDM system with 128 channels, each channel operating at 10 Gb/s, was able to transmit information over 4,000 km when it was designed to compensate losses through forward Raman pumping in each 100-km section of dispersion-shifted fibers [75]. Even when standard fibers were employed, the system could be operated over 3,200 km with a pump-station spacing of 80 km. In both cases, it was necessary to employ forward error correction with 7% overhead. The average power launched into the fiber link was only -5 dBm. Such low power was enough to maintain an optical SNR of more than 15 dB for all channels because of a low noise level associated with distributed Raman amplification in the forward-pumping configuration. It was also important to compensate for fiber dispersion along the fiber link. In general, system performance can be improved with dispersion management. We turn to this issue in Chapter 7.

Problems

6.1 Why do amplifiers always add noise to the amplified signal? What is the origin of noise in EDFAs and Raman amplifiers?

6.2 Starting with the differential equation $\partial q/\partial z = g_0 A + f_n(z,t)$ and Eq. (6.1.2), prove that the spectral density of ASE noise added by a lumped amplifier of length l_a is given by $S_{\text{ASE}} = n_{\text{sp}} h \nu_0 [\exp(g_0 l_a) - 1]$.

6.3 Repeat the preceding problem for a distributed amplifier for which g_0 is a function of z and prove that the noise spectral density is given by Eq. (6.1.12).

6.4 Derive an expression for the optical SNR at the end of a fiber link containing N_A amplifiers spaced apart by a distance L_A. Assume that an optical filter of bandwidth $\Delta\nu_o$ is used to control the ASE noise.

6.5 Calculate the optical SNR at the output end of a 4,000-km lightwave system designed using 50 EDFAs with 4.5-dB noise figure. Assume a fiber-cable loss of 0.25 dB/km at 1.55 μm, an input power of 1 mW, and a 2-nm-bandwidth for the optical filter.

6.6 Explain the concept of noise figure for an optical amplifier. Use Eq. (6.3.9) for the total variance of current fluctuations and prove that the minimum noise figure is 3 dB for an ideal amplifier with high gain ($G \gg 1$) and complete inversion ($n_{\text{sp}} = 1$).

6.7 Derive an expression for the noise figure of a distributed Raman amplifier, assuming that the pump power varies along the fiber length. Discuss physically whether forward or backward pumping would result in a lower noise figure.

6.8 What is meant by the effective noise figure of a distributed Raman amplifier? Why is this noise figure always negative on a decibel scale?

6.9 Write a computer program capable of calculating the noise figure of a distributed Raman amplifier using Eq. (6.3.17). Use it to reproduce the noise-figure curves shown in Figure 6.7. You are allowed to consult Ref. [18].

6.10 Calculate the receiver sensitivities at a BER of 10^{-9} and 10^{-12} by using Eq. (6.4.4). Assume that the receiver operates at 1.55 μm with a 8-GHz bandwidth. The preamplifier has a noise figure of 4 dB, and a 1-nm optical filter is installed between the preamplifier and the detector.

6.11 Solve Eqs. (6.5.4) and (6.5.5) in the case $\alpha = 0$ for a fiber of length L and show that the result can be written in a matrix form of Eqs. (6.5.6). Give explicit expressions for all matrix elements in terms of fiber parameters. You are allowed to consult [32].

6.12 Use the definitions of moments in Eqs. (6.5.13) and (6.5.14) and prove that q and Ω evolve with z as indicated in Eqs. (6.5.17) and (6.5.18).

6.13 Use Eqs. (6.5.19) and (6.5.20) and prove that energy fluctuations at the end of N_A cascaded amplifiers have the variance $\sigma_E^2 = 2N_A S_{\text{ASE}} E_0$, where E_0 is the input pulse energy. Assume that each amplifier fully compensates losses of the preceding fiber section.

6.14 Use the results of the preceding problem to calculate the noise level σ_E/E_0 for a 1.55-μm fiber link consisting of 50 amplifiers spaced 80-km apart. Assume a noise figure of 4.8 dB for each amplifier and fiber losses of 0.25 dB/km.

6.15 Why does ASE induce timing jitter in lightwave systems? Starting from Eq. (6.5.45), prove that timing jitter is indeed given by Eq. (6.5.52).

6.16 Start the OptSim software and load Example 6.B. Change input power in the range of 0.1 to 10 mW and construct a graph showing the Q factor as a function of input power. Explain the shape of this curve in physical terms.

References

[1] E. Desuvire, *Erbium-Doped Fiber Amplifiers: Principles and Applications*, Wiley, New York, 1994.

[2] P. C. Becker, N. A. Olsson, and J. R. Simpson, *Erbium-Doped Fiber Amplifiers: Fundamentals and Technology*, Academic Press, San Diego, CA, 1999.

[3] E. Desuvire, D. Bayart, B. Desthieux, and S. Bigo, *Erbium-Doped Fiber Amplifiers: Device and System Development*, Wiley, New York, 2002.

[4] H. Heffner, *Proc. IRE* **50**, 1604 (1962).

[5] H. A. Haus and J. A. Mullen, *Phys. Rev.* **128**, 2407 (1962).

[6] N. A. Olsson, *J. Lightwave Technol.* **7**, 1071 (1989).

[7] G. L. Cairolaro, P. Franco, M. Mifrio, and G. L. Pierobon, *IEEE J. Quantum Electron.* **31**, 1114 (1995).

[8] S. Donati and G. Giuliani, *IEEE J. Quantum Electron.* **33**, 1481 (1997).

[9] Y. Yamamoto and K. Inoue, *J. Lightwave Technol.* **21**, 2695 (2003).

[10] K. Shimoda, H. Takahasi, and C. H. Townes, *J. Phys. Soc. Jpn.* **12**, 686 (1957).
[11] M. Lax, *IEEE J. Quantum Electron.* **3**, 37 (1966).
[12] R. Loudon and T. J. Shepard, *Opt. Acta* **31**, 1243 (1984).
[13] P. Diament and M. Teich, *IEEE J. Quantum Electron.* **28**, 132 (1992); T. Li and M. C. Teich, *IEEE J. Quantum Electron.* **29**, 2569 (1993).
[14] H. A. Haus, *Electromagnetic Noise and Quantum Optical Measurements*, Springer, New York, 2000, Chap. 6
[15] L. Mandel and E. Wolf, *Coherence and Quantum Optics*, Cambridge University Press, New York, 1995, Chap. 17.
[16] J. Bromage, P. J. Winzer, and R. J. Essiambre, in *Raman Amplifiers for Telecommunications*, M. N. Islam, Ed., Springer, New York, 2003, Chap. 15.
[17] C. Headley and G. P. Agrawal, Eds., *Raman Amplification in Fiber Optical Communication Systems*, Academic Press, San Diego, CA, 2005.
[18] J. Bromage, *J. Lightwave Technol.* **22**, 79 (2004).
[19] Y. Yamamoto and T. Mukai, *Opt. Quantum Electron.* **21**, S1 (1989).
[20] C. R. Giles and E. Desurvire, *J. Lightwave Technol.* **9**, 147 (1991).
[21] G. R. Walker, N. G. Walker, R. C. Steele, M. J. Creaner, and M. C. Brain, *J. Lightwave Technol.* **9**, 182 (1991).
[22] S. Ryu, S. Yamamoto, H. Taga, N. Edagawa, Y. Yoshida, and H. Wakabayashi, *J. Lightwave Technol.* **9**, 251 (1991).
[23] D. Marcuse, *J. Lightwave Technol.* **8**, 1816 (1990); *J. Lightwave Technol.* **9**, 505 (1991).
[24] P. A. Humblet and M. Azizoglu, *J. Lightwave Technol.* **9**, 1576 (1991).
[25] B. Chan and J. Conradi, *J. Lightwave Technol.* **15**, 680 (1997).
[26] T. Saito, Y. Sunohara, K. Fukagai, S. Ishikawa, N. Henmi, S. Fujita, and Y. Aoki, *IEEE Photon. Technol. Lett.* **3**, 551 (1991).
[27] A. H. Gnauck and C. R. Giles, *IEEE Photon. Technol. Lett.* **4**, 80 (1992).
[28] J. Nakagawa, T. Mizuochi, K. Takano, K. Motoshima, K. Shimizu, and T. Kitayama, *Electron. Lett.* **32**, 48 (1996).
[29] P. B. Hansen, A. J. Stentz, L. Eskilden, S. G. Grubb, T. A. Strasser, J. R. Pedrazzani, *Electron. Lett.* **32**, 2164 (1996).
[30] D. Marcuse, *J. Lightwave Technol.* **9**, 356 (1991).
[31] A. Mecozzi, *J. Opt. Soc. Am. B* **11**, 462 (1994).
[32] M. Yu, G. P. Agrawal, and C. J. McKinstrie, *J. Opt. Soc. Am. B* **12**, 1126 (1995).
[33] M. O. van Deventer, S. Wingstrand, B. Hermansson, A. Bolle, P. Jalderot, C. Backdahl, and J. Karlsson, *Opt. Fiber Technol.* **2**, 183 (1996).
[34] C. Lorattanasane and K. Kikuchi, *IEEE J. Quantum Electron.* **33**, 1084 (1997).
[35] A. Carena, V. Curri, R. Gaudino, P. Poggiolini, and S. Benedetto, *IEEE Photon. Technol. Lett.* **9**, 535 (1997).
[36] R. A. Saunders, B. A. Patel, and D. Garthe, *IEEE Photon. Technol. Lett.* **9**, 699 (1997).
[37] R. Q. Hui, M. O'Sullivan, A. Robinson, and M. Taylor, *J. Lightwave Technol.* **15**, 1071 (1997).
[38] M. Midrio, *J. Opt. Soc. Am. B* **14**, 2910 (1997).
[39] E. Ciaramella and M. Tamburrini, *IEEE Photon. Technol. Lett.* **11**, 1608(1999).
[40] M. Norgia, G. Giuliani, and S. Donati, *J. Lightwave Technol.* **17**, 1750 (1999).
[41] G. P. Agrawal, *Nonlinear Fiber Optics*, 3rd ed., Academic Press, San Diego, CA, 2001.
[42] J. P. Gordon and H. A. Haus, *Opt. Lett.* **11**, 665 (1986).
[43] R. J. Essiambre and G. P. Agrawal, *J. Opt. Soc. Am. B* **14**, 314 (1997).

[44] E. Iannone, F. Matera, A. Mecozzi, and M. Settembre, *Nonlinear Optical Communication Networks*, Wiley, New York, 1998, Chap. 5.
[45] V. S. Grigoryan, C. R. Menyuk, and R. M. Mu, *J. Lightwave Technol.* **17**, 1347 (1999).
[46] J. Santhanam, C. J. McKinstrie, T. I. Lakoba, and G. P. Agrawal, *Opt. Lett.* **26**, 1131 (2001).
[47] C. J. McKinstrie, J. Santhanam, and G. P. Agrawal, *J. Opt. Soc. Am. B* **19**, 640 (2002).
[48] J. Santhanam and G. P. Agrawal, *IEEE J. Sel. Topics Quantum Electron.* **7**, 632 (2002).
[49] E. Poutrina and G. P. Agrawal, *IEEE Photon. Technol. Lett.* **14**, 39 (2002).
[50] E. Poutrina and G. P. Agrawal, *J. Lightwave Technol.* **20**, 762 (2002).
[51] N. Edagawa, Y. Toshida, H. Taga, S. Yamamoto, K. Mochizuchi, and H. Wakabayashi, *Electron. Lett.* **26**, 66 (1990).
[52] S. Saito, T. Imai, and T. Ito, *J. Lightwave Technol.* **9**, 161 (1991).
[53] S. Saito, *J. Lightwave Technol.* **10**, 1117 (1992).
[54] T. Imai, M. Murakami, T. Fukuda, M. Aiki, and T. Ito, *Electron. Lett.* **28**, 1484 (1992).
[55] M. Murakami, T. Kataoka, T. Imai, K. Hagimoto, and M. Aiki, *Electron. Lett.* **28**, 2254 (1992).
[56] H. Taga, M. Suzuki, N. Edagawa, Y. Yoshida, S. Yamamoto, S. Akiba, and H. Wakabayashi, *Electron. Lett.* **28**, 2247 (1992).
[57] N. S. Bergano, J. Aspell, C. R. Davidson, P. R. Trischitta, B. M. Nyman, and F. W. Kerfoot, *Electron. Lett.* **27**, 1889 (1991).
[58] F. Matera and M. Settembre, *J. Lightwave Technol.* **14**, 1 (1996).
[59] X. Y. Zou, M. I. Hayee, S. M. Hwang, and A. E. Willner, *J. Lightwave Technol.* **14**, 1144 (1996).
[60] K. Inser and K. Petermann, *IEEE Photon. Technol. Lett.* **8**, 443 (1996); D. Breuer and K. Petermann, *IEEE Photon. Technol. Lett.* **9**, 398 (1997).
[61] F. Forghieri, P. R. Prucnal, R. W. Tkach, and A. R. Chraplyvy, *IEEE Photon. Technol. Lett.* **9**, 1035 (1997).
[62] F. Matera and M. Settembre, *Fiber Integ. Opt.* **15**, 89 (1996); *J. Opt. Commun.* **17**, 1 (1996); *Opt. Fiber Technol.* **4**, 34 (1998).
[63] S. Bigo, A. Bertaina, M. W. Chbat, S. Gurib, J. Da Loura, J. C. Jacquinot, J. Hervo, P. Bousselet, S. Borne, D. Bayart, L. Gasca, and J. L. Beylat, *IEEE Photon. Technol. Lett.* **10**, 1045 (1998).
[64] D. Breuer, K. Obermann, and K. Petermann, *IEEE Photon. Technol. Lett.* **10**, 1793 (1998).
[65] M. I. Hayee and A. E. Willner, *IEEE Photon. Technol. Lett.* **11**, 991 (1999).
[66] A. Sahara, H. Kubota, and M. Nakazawa, *Opt. Commun.* **160**, 139 (1999).
[67] R. Lebref, A. Ciani, F. Matera, and M. Tamburrini, *Fiber Integ. Opt.* **18**, 245 (1999).
[68] F. M. Madani and K. Kikuchi, *J. Lightwave Technol.* **17**, 1326 (1999).
[69] J. Kani, M. Jinno, T. Sakamoto, S. Aisawa, M. Fukui, K. Hattori, and K. Oguchi, *J. Lightwave Technol.* **17**, 2249 (1999).
[70] C. M. Weinert, R. Ludwig, W. Pieper, H. G. Weber, D. Breuer, K. Petermann, and F. Kuppers, *J. Lightwave Technol.* **17**, 2276 (1999).
[71] A. J. Lowery, O. Lenzmann, I. Koltchanov, R. Moosburger, R. Freund, A. Richter, S. Georgi, D. Breuer, and H. Hamster, *IEEE J. Sel. Topics Quantum Electron.* **6**, 282 (2000).
[72] F. Matera and M. Settembre, *IEEE J. Sel. Topics Quantum Electron.* **6**, 308 (2000).
[73] N. Takachio and H. Suzuki, *J. Lightwave Technol.* **19**, 60 (2001).
[74] M. Suzuki and N. Edagawa, *J. Lightwave Technol.* **21**, 916 (2003).
[75] D. F. Grosz, A. Agarwal, S. Banerjee, D. N. Maywar, and A. P. Küng, *J. Lightwave Technol.* **21**, 423 (2004).

Chapter 7

Dispersion Management

As seen from Chapter 6, optical amplifiers solve the loss problem but make the dispersion problem worse as dispersive effects can accumulate over long distances (see Section 3.3). Indeed, long-haul lightwave systems are often limited by the dispersive and nonlinear effects rather than fiber losses. As mentioned in Section 3.3.5, the dispersion problem can be managed in practice through a dispersion-compensation scheme. This chapter focuses on several techniques that can be employed for dispersion management. Section 7.1 explains the basic idea behind dispersion management. Section 7.2 is devoted to special kinds of fibers developed for compensating dispersion in long-haul links. Several types of dispersion-equalizing filters are discussed in Section 7.3. The use of fiber gratings for dispersion management is considered in Section 7.4. The technique of optical phase conjugation, also known as midspan spectral inversion, is discussed in Section 7.5. In Section 7.6 we focus on several techniques employed at the transmitter or receiver end for managing the dispersion of medium-haul links. Section 7.7 is devoted to dispersion management in high-speed systems in which each channel operates at 40 Gb/s or more. The compensation of polarization-mode dispersion (PMD) is also discussed in this section.

7.1 Dispersion Problem and Its Solution

All long-haul lightwave systems employ single-mode optical fibers in combination with distributed feedback (DFB) semiconductor lasers, capable of operating in a single longitudinal mode with a narrow line width (<0.1 GHz). As discussed in Section 3.3.4, the performance of such systems is often limited by pulse broadening induced by group-velocity dispersion (GVD) of silica fibers. Direct modulation of a DFB laser chirps optical pulses representing 1 bits in an optical bit stream and broadens their spectrum enough that this technique cannot be used at bit rates above 2.5 Gb/s.

Lightwave systems operating at single-channel bit rates as high as 40-Gb/s have been designed by using external modulators that avoid spectral broadening induced by frequency chirping. Under such conditions, the GVD-limited transmission distance at

a given bit rate B is obtained from Eq. (3.3.44) and can be written as

$$L < \frac{1}{16|\beta_2|B^2} = \frac{\pi c}{8\lambda^2|D|B^2}, \tag{7.1.1}$$

where β_2 is the GVD parameter related to the commonly used dispersion parameter D of the fiber through Eq. (3.1.7), c is the speed of light in vacuum, and λ is the channel wavelength. The numerical value of D depends on the operating wavelength λ. For "standard" telecommunication fibers D is about 16 ps/(km-nm) near $\lambda = 1.55$ μm. Equation (7.1.1) predicts that L cannot exceed 30 km at a bit rate of 10 Gb/s when such fibers are used for designing lightwave systems.

The existing worldwide fiber-cable network, installed during the 1980s, consists of more than 50 million kilometers of standard fiber. This fiber was suitable for second- and third-generation systems designed to operate at bit rates of up to 2.5 Gb/s with repeater spacing of under 80 km (without optical amplifiers). However, the same fiber could not be used for upgrading the existing transmission links to fourth-generation systems (operating at 10 Gb/s and employing optical amplifiers for loss compensation) because of the 30-km dispersion limit set by Eq. (7.1.1). Although it is possible to manufacture dispersion-shifted fibers, installation of new fibers is a costly solution to the dispersion problem, and it is not a viable alternative in practice. For this reason, several dispersion-management schemes were developed during the 1990s to address the upgrade problem [1]–[3].

One may think that the dispersion problem can be solved for new fiber links by employing dispersion-shifted fibers and operating the link close to the zero-dispersion wavelength of this fiber so that $|D| \approx 0$. Under such conditions, system performance is limited by third-order dispersion (TOD). The dashed line in Figure 3.5 shows the maximum possible transmission distance at a given bit rate B when $D = 0$. Indeed, such a system can operate over more than 1,000 km even at a bit rate of 40 Gb/s. However, this solution is not practical for WDM systems because of four-wave mixing (FWM). As discussed in Section 4.3, the nonlinear phenomenon of FWM becomes quite efficient for low values of the dispersion parameter D and limits performance of any system operating close to the zero-dispersion wavelength of the fiber. For this reason, some form of dispersion management is employed for all long-haul WDM systems [2]–[4].

The basic idea behind any dispersion-management scheme is quite simple and can be understood from the pulse-propagation equation (3.1.11) used in Section 3.3 for studying the impact of fiber dispersion. We set $\alpha = 0$ in this equation, assuming that losses have been compensated with amplifiers. We ignore the nonlinear term for the moment, assuming that signal power is low enough that all nonlinear effects can be neglected. Setting $\gamma = 0$ in Eq. (3.1.11), we obtain the following linear equation:

$$\frac{\partial A}{\partial z} + \frac{i\beta_2}{2}\frac{\partial^2 A}{\partial t^2} - \frac{\beta_3}{6}\frac{\partial^3 A}{\partial t^3} = 0, \tag{7.1.2}$$

where β_3 governs the effects of TOD. This equation is easily solved with the Fourier-transform method (see Section 3.3.1) and has the solution

$$A(z,t) = \frac{1}{2\pi}\int_{-\infty}^{\infty} \tilde{A}(0,\omega)\exp\left(\frac{i}{2}\beta_2\omega^2 z + \frac{i}{6}\beta_3\omega^3 z - i\omega t\right) d\omega, \tag{7.1.3}$$

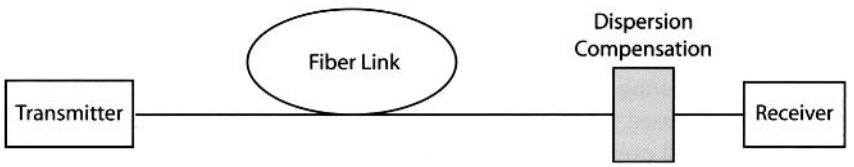

Figure 7.1: Schematic of a dispersion-compensation scheme in which an optical filter is placed before the receiver.

where $\tilde{A}(0,\omega)$ is the Fourier transform of $A(0,t)$.

Dispersion-induced degradation of the optical signal is caused by the z-dependent phase factor acquired by spectral components of the pulse during propagation inside the fiber. Indeed, one can think of fiber as an optical filter with the transfer function

$$H_f(z,\omega) = \exp(i\beta_2\omega^2 z/2 + i\beta_3\omega^3 z/6). \tag{7.1.4}$$

All dispersion-management schemes implement an optical dispersion-compensating "filter" whose transfer function $H(\omega)$ is chosen such that it cancels the phase factor associated with the fiber. As seen from Eq. (7.1.3), if $H(\omega) = H_f^*(L,\omega)$, the output signal can be restored to its input form at the end of a fiber link of length L. Moreover, if nonlinear effects are negligible, such a filter can be placed at the transmitter end, or at the receiver end, or somewhere along the fiber link.

Consider the simplest situation shown schematically in Figure 7.1, where a dispersion-compensating filter is placed just before the receiver. From Eq. (7.1.3), the optical field after the filter is given by

$$A(L,t) = \frac{1}{2\pi}\int_{-\infty}^{\infty} \tilde{A}(0,\omega)H(\omega)\exp\left(\frac{i}{2}\beta_2\omega^2 L + \frac{i}{6}\beta_3\omega^3 L - i\omega t\right)d\omega. \tag{7.1.5}$$

Expanding the phase of $H(\omega)$ in a Taylor series and retaining up to the cubic term, we obtain

$$H(\omega) = |H(\omega)|\exp[i\phi(\omega)] \approx |H(\omega)|\exp[i(\phi_0 + \phi_1\omega + \tfrac{1}{2}\phi_2\omega^2 + \tfrac{1}{6}\phi_3\omega^3)], \tag{7.1.6}$$

where $\phi_m = d^m\phi/d\omega^m (m = 0,1,\ldots)$ is evaluated at the carrier frequency ω_0. The constant phase ϕ_0 and the time delay ϕ_1 do not affect the pulse shape and can be ignored. The spectral phase introduced by the fiber can be compensated by choosing an optical filter such that $\phi_2 = -\beta_2 L$ and $\phi_3 = -\beta_3 L$. The signal will be restored perfectly only if $|H(\omega)| = 1$ and other higher-order terms in Eq. (7.1.6) are negligible. The same optical filter can also reduce amplifier noise if its bandwidth is chosen suitably.

7.2 Dispersion-Compensating Fibers

Optical filters whose transfer function has the form $H(\omega) = H_f^*(L,\omega)$ are not easy to design. The simplest solution is to use an especially designed fiber as an optical filter because it automatically has the desired form of the transfer function. This solution

was suggested as early as 1980 [5] and it provides an all-optical, fiber-based solution to the dispersion problem. During the 1990s, a special kind of fiber, known as the *dispersion-compensating fiber* (DCF), was developed for this purpose [6]–[11]. Such fibers are routinely used for upgrading old fiber links from 2.5 Gb/s to 10 Gb/s. Such a scheme works well even when the nonlinear effects are not negligible as long as the average optical power launched into the fiber link is optimized properly.

7.2.1 Conditions for Dispersion Compensation

Consider the situation shown in Figure 7.1 and assume that the optical bit stream propagates through two fiber segments of lengths L_1 and L_2, the second of which is the DCF. Each fiber has a transfer function of the form given in Eq. (7.1.4). After passing through the two fibers, the optical field is given by

$$A(L,t) = \frac{1}{2\pi}\int_{-\infty}^{\infty} \tilde{A}(0,\omega) H_{f1}(L_1,\omega) H_{f2}(L_2,\omega) \exp(-i\omega t)\, d\omega, \tag{7.2.1}$$

where $L = L_1 + L_2$ is the total length. If the DCF is designed such that the the product of the two transfer functions is 1, the pulse will fully recover its original shape at the end of DCF. If β_{2j} and β_{3j} are the GVD and TOD parameters for the two fiber segments ($j = 1, 2$), the conditions for perfect dispersion compensation are

$$\beta_{21} L_1 + \beta_{22} L_2 = 0, \qquad \beta_{31} L_1 + \beta_{32} L_2 = 0. \tag{7.2.2}$$

These conditions can be written in terms of the dispersion parameter D and the dispersion slope S (defined in Section 3.1) as

$$D_1 L_1 + D_2 L_2 = 0, \qquad S_1 L_1 + S_2 L_2 = 0. \tag{7.2.3}$$

The first condition is sufficient for compensating dispersion of a single channel since the TOD does not affect the bit stream much until pulse widths become shorter than 1 ps. Consider the upgrade problem for fiber links made with standard telecommunication fibers. Such fibers have $D_1 \approx 16$ ps/(km-nm) near the 1.55-μm wavelength within the C band. Equation (7.2.3) shows that a DCF must exhibit normal GVD ($D_2 < 0$). For practical reasons, L_2 should be as small as possible. This is possible only if the DCF has a large negative value of D_2. As an example, if we use $D_1 = 16$ ps/(km-nm) and assume $L_1 = 50$ km, we need a 10-km-long DCF when $D_2 = -80$ ps/(km-nm). This length can be reduced to 6.7 km if the DCF is designed to have $D_2 = -120$ ps/(km-nm). In practice, DCFs with larger values of $|D_2|$ are preferred to minimize extra losses incurred inside a DCF (that must be compensated using an optical amplifier).

Consider now a WDM system. The second condition in Eq. (7.2.3) must be satisfied if the same DCF must compensate dispersion over the entire bandwidth of a WDM system. The reason can be understood by noting that the dispersion parameters D_1 and D_2 in Eq. (7.2.3) are wavelength-dependent. As a result, the single condition $D_1 L_1 + D_2 L_2 = 0$ is replaced with a set of conditions

$$D_1(\lambda_n) L_1 + D_2(\lambda_n) L_2 = 0 \quad (n = 1, \ldots, N), \tag{7.2.4}$$

where λ_n is the wavelength of the nth channel and N is the number of channels within the WDM signal. In the vicinity of the zero-dispersion wavelength of a fiber, D varies with the wavelength almost linearly. Writing $D_j(\lambda_n) = D_j^c + S_j(\lambda_n - \lambda_c)$ in Eq. (7.2.4), where D_j^c is the value at the wavelength λ_c of the central channel, the dispersion slope of the DCF should satisfy

$$S_2 = -S_1(L_1/L_2) = S_1(D_2/D_1), \tag{7.2.5}$$

where we used the condition (7.2.3) for the central channel. This equation shows that the ratio S/D, called the *relative* dispersion slope, for the DCF should be equal to the value obtained for the transmission fiber.

If we use typical values, $D \approx 16$ ps/(km-nm) and $S \approx 0.05$ ps/(km-nm^2), we find that the ratio S/D is positive and about 0.003 nm^{-1} for standard fibers. Since D must be negative for a DCF, its dispersion slope S should be negative as well. Moreover, its magnitude should satisfy Eq. (7.2.5). For a DCF with $D \approx -100$ ps/(km-nm), the dispersion slope should be about -0.3 ps/(km-nm^2). The use of *negative-slope* DCFs offers the simplest solution to the problem of dispersion-slope compensation for WDM systems with a large number of channels. Indeed, such DCFs were developed and commercialized during the 1990s for dense WDM systems [12]–[15]. In a 1995 experiment [12], 8 channels with 1.6-nm spacing, each operating at 20 Gb/s, were transmitted over 232 km of standard fiber by using multiple DCFs. The residual dispersion for each channel was relatively small ($\sim$100 ps/nm for the entire span). In another experiment, 10 channels, each operating at 10 Gb/s, were transmitted over 6,000 km by employing a dispersion-slope compensator [13]. In a 2001 experiment, broadband DCFs were used to transmit a 1-Tb/s WDM signal (101 channels, each operating at 10 Gb/s) over 9,000 km [15].

7.2.2 Dispersion Maps

It is not necessary to employ just two fiber sections as shown in Figure 7.1. In general, a fiber link may contain multiple types of fibers with different dispersion characteristics. The main impact of dispersion management from a mathematical standpoint is that the dispersion coefficients β_2 and β_3 appearing in Eq. (7.1.2) become z-dependent as they change from one fiber section to the next. As long as the nonlinear effects remain negligible, we can still solve this equation. If we neglect the TOD effects for simplicity, the solution given in Eq. (7.1.3) is modified to become

$$A(z,t) = \frac{1}{2\pi}\int_{-\infty}^{\infty} \tilde{A}(0,\omega)\exp\left(\frac{i}{2}d_a(z)\omega^2 - i\omega t\right)d\omega, \tag{7.2.6}$$

where $d_a(z) = \int_0^z \beta_2(z')\,dz'$ represents the total accumulated dispersion up to a distance z. Dispersion management requires that $d_a(L) = 0$ at the end of the fiber link so that $A(L,t) = A(0,t)$. In practice, the accumulated dispersion of a fiber link is quantified through $\bar{d}_a(z) = \int_0^z D(z')\,dz'$. It is related to d_a as $\bar{d}_a = (-2\pi c/\lambda^2)d_a$.

Figure 7.2 shows three possible schemes for managing dispersion in long-haul fiber links. In each case, the accumulated dispersion is shown along the fiber link in a schematic fashion. In the first configuration, known as *precompensation*, the dispersion

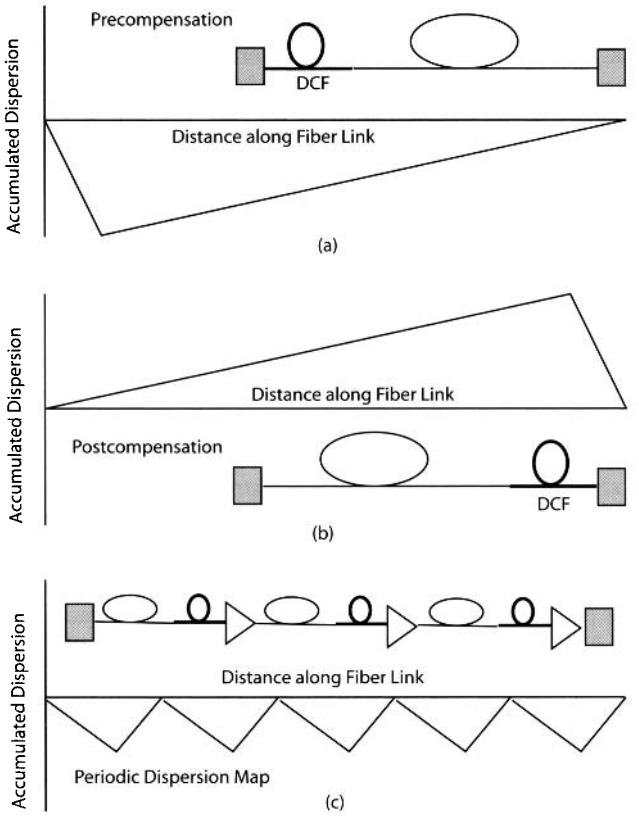

Figure 7.2: Schematic of three dispersion-management schemes: (a) precompensation, (b) post-compensation, and (c) periodic compensation. In each case, accumulated dispersion is shown along the link length.

accumulated over the entire link is compensated at the transmitter end. In the second configuration, known as *postcompensation*, a DCF of appropriate length is placed at the receiver end. In the third configuration, known as *periodic compensation*, dispersion is compensated in a periodic fashion all along the link. Each of these configurations is referred to as a dispersion map, as it provides a visual map of dispersion variations along the link length. One can construct a variety of dispersion maps by combining several different fibers.

A natural question is which dispersion map is the best from a system's standpoint. For a truly linear system (no nonlinear effects), all three schemes shown in Figure 7.2 are identical. In fact, any dispersion map for which $d_a(L) = 0$ at the end of a fiber link of length L would recover the original bit stream, no matter how much it became distorted along the way. However, nonlinear effects are always present, although their impact depends on the power launched into the fiber link. As discussed in Chapter 6, the launched power should often exceed 1 mW for long-haul links to overcome the impact of ASE noise. The nonlinear effects cannot be neglected under such condi-

tions. It turns out that the three configurations shown in Figure 7.2 behave differently when nonlinear effects are included, and the system performance can be improved by adopting an optimized dispersion map. We discuss this issue in Chapter 8.

7.2.3 DCF Designs

There are two basic approaches to designing DCFs. In one case, the DCF supports a single mode and is fabricated with a relatively small value of the fiber parameter V. In the other approach, the V parameter is increased beyond the single-mode limit ($V > 2.405$) so that the DCF supports two or more modes. We consider both designs in this section.

In the single-mode design, the V parameter of the fiber is close to 1. This is accomplished by reducing the core size and modifying the refractive-index profile through doping of the core and cladding regions. As discussed in Section 1.3.3 of LT1, the fundamental mode of the fiber is weakly confined for $V \approx 1$. As a large fraction of the mode propagates inside the cladding region, the waveguiding contribution to total dispersion is enhanced considerably, resulting in large negative values of D. A depressed-cladding design is often used in practice for making DCFs [6]. Values of D below -100 ps/(km-nm) can be realized by narrowing the central core and adjusting the design parameters of the depressed cladding region surrounding the core [11]. Dispersion slope S near 1,550 nm can also be made negative and varied considerably by adjusting the design parameters to match the ratio S/D of the DCF to different types of transmission fibers.

Unfortunately, such DCFs suffer from two problems, both resulting from their relatively narrow core diameter. First, they exhibit relatively high losses because a considerable fraction of the fundamental fiber mode resides in the cladding region (α = 0.4–0.6 dB/km). The ratio $|D|/\alpha$ is often used as a figure of merit for characterizing various DCFs [6]. Clearly, this ratio should be as large as possible, and values >250 ps/(nm-dB) have been realized in practice. Second, the effective core area A_{eff} is only 20 μm^2 or so for DCFs. As the nonlinear parameter $\gamma \equiv 2\pi n_2/(\lambda A_{\text{eff}})$ is larger by about a factor of 4 for DCFs compared with its value for standard fibers, the optical intensity is also larger at a given input power, and the nonlinear effects are enhanced considerably inside DCFs [11].

A practical solution for upgrading the existing terrestrial lightwave systems operating over standard fibers consists of adding a DCF module (with 6–8 km of DCF) to optical amplifiers spaced apart by 60 to 80 km. The DCF compensates for GVD, while the amplifier takes care of fiber losses. This scheme is quite attractive but suffers from the loss and nonlinearity problems. Insertion losses of a DCF module often exceed 5 dB. These losses can be compensated by increasing the amplifier gain, but only at the expense of enhanced amplified spontaneous emission (ASE). As input power should be kept relatively low to avoid the nonlinear effects, the transmission distance is limited by ASE noise.

Several new designs have been proposed to solve the problems associated with a standard DCF. In one design, shown schematically in Figure 7.3(a), the DCF is designed with two concentric cores, separated by a ring-shaped cladding region [7]. The relative core-cladding index difference is larger for the inner core ($\Delta_i \approx 2\%$) compared

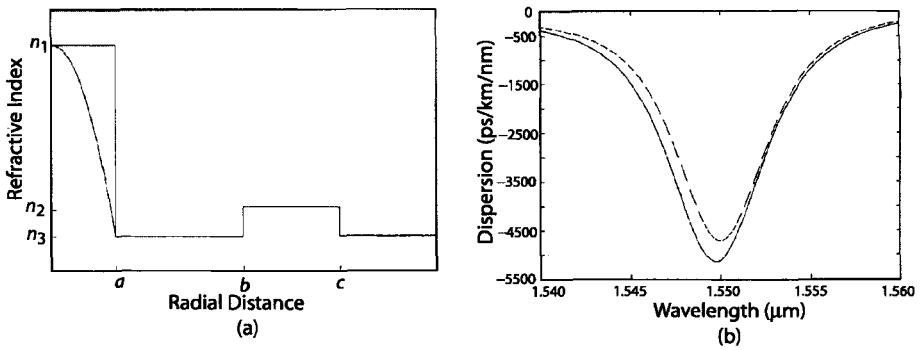

Figure 7.3: (a) Refractive-index profiles of two DCFs designed with two concentric cores. (b) Dispersion parameter as a function of wavelength for the same two designs. (After Ref. [7]; ©1996 IEEE.)

with the outer core ($\Delta_o \approx 0.3\%$), but the core sizes are chosen such that each core supports a single mode. The three size parameters a, b, and c and the three refractive indices n_1, n_2, and n_3 can be optimized to design DCFs with desired dispersion characteristics. The solid curve in Figure 7.3(b) shows the calculated values of D in the 1.55-μm region for a specific design with $a = 1$ μm, $b = 15.2$ μm, $c = 22$ μm, $\Delta_i = 2\%$, and $\Delta_o = 0.3\%$. The dashed curve corresponds to a parabolic index profile for the inner core. The mode diameter for both designs is about 9 μm, a value close to that of standard fibers. However, as shown in Figure 7.3(b), the dispersion parameter can be as large as $-5{,}000$ ps/(km-nm) for such DCFs. It has proven difficult to realize such high values of D experimentally. Nevertheless, a DCF with $D = -1{,}800$ ps/(km-nm) was fabricated by 2000 [10]. For this value of D, a length of <1 km is enough to compensate dispersion accumulated over 100 km of standard fiber. Insertion losses are negligible for such small lengths.

The problems associated with a single-mode DCF can also be solved by using a *two-mode fiber* designed with values of V such that the fiber supports the LP_{01} and LP_{11} modes ($V \approx 2.5$). These fibers have almost the same loss as the single-mode fiber but can be designed such that the dispersion parameter D for the LP_{11} mode has large negative values [16]–[19]. Indeed, values of D close to -770 ps/(km-nm) were measured as early as 1994 for elliptical-core DCFs [16]. A 1-km length of such a DCF can compensate the GVD accumulated over 45 km, while adding relatively little to the total link loss or nonlinear degradation.

The use of a two-mode DCF requires a mode-conversion device capable of transferring optical signal from the fundamental mode to a higher-order mode supported by the DCF. Several such all-fiber devices have been developed [20]–[22]. The all-fiber nature of the mode-conversion device is important to keep the insertion loss of the device to an acceptable level. Additional requirements on a mode converter are that it should be polarization-insensitive and should operate over a broad bandwidth. Almost all practical mode-conversion devices use a two-mode fiber with a fiber grating that provides coupling between the two modes (see Section 2.2 of LT1). The grating

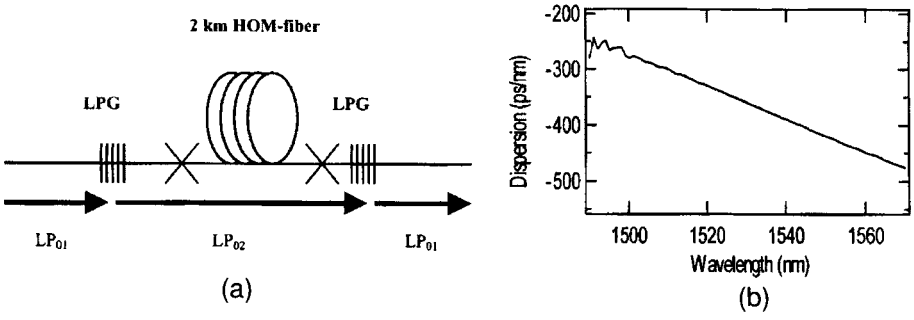

Figure 7.4: (a) Schematic of a DCF made using a higher-order mode (HOM) fiber and two long-period gratings (LPGs). (b) Measured wavelength dependence of the dispersion parameter for such a DCF. (After Ref. [18]; ©2001 IEEE.)

period Λ is chosen to match the effective-index difference $\delta\bar{n}$ between the two modes ($\Lambda = \lambda/\delta\bar{n}$) and is typically $\sim$100 μm. Such gratings are called long-period fiber gratings [22].

The LP_{11} mode is inherently polarization sensitive, and its use requires polarization controllers in front of each dispersion-compensating module. This problem can be solved by using fibers oscillating in a few modes and employing the higher-order LP_{02} mode for dispersion compensation. Figure 7.4(a) shows schematically such a DCF spliced in between two long-period fiber gratings that convert the LP_{01} mode into LP_{02} mode at the input end and then back into the LP_{01} mode at the output end [18]. The mode converters are designed to be >99% efficient over the entire C band. The measured dispersion characteristics of such a 2-km-long DCF are shown in Figure 7.4(b). The parameter D has a value of -420 ps/(km-nm) near 1,550 nm and this value changes considerably with wavelength because of a large dispersion slope associated with this fiber. This feature allows for broadband dispersion compensation by ensuring that the ration S/D of the DCF is close to the fiber used for transmitting data. Other useful features of such a DCF are that the device is polarization-insensitive, exhibits relatively low insertion losses (<3.7 dB), and offers dispersion compensation over the entire C band. Such devices were close to reaching the commercial stage in 2004.

Another approach to DCF design makes use of photonic-crystal fibers [23]–[25]. Such fibers contain a two-dimensional array of air holes around a central core that modifies their dispersion characteristics substantially, depending on the size of air holes and the spacing among them. Figure 7.5(a) shows a scanning-electron-microscope (SEM) image of the cross section of such a fiber [23]. Estimated values of the dispersion parameter D for this fiber at a wavelength of 1.55 μm are shown in Figure 7.5(b) as a function of the core diameter. Values as large as $-2{,}000$ ps/(km-nm) are possible with a suitable design. Broadband dispersion compensation can be realized by tailoring the size and spacing of air holes [23]. A dual-core photonic-crystal fiber can provide even larger values of $|D|$ but only over a narrower bandwidth [25].

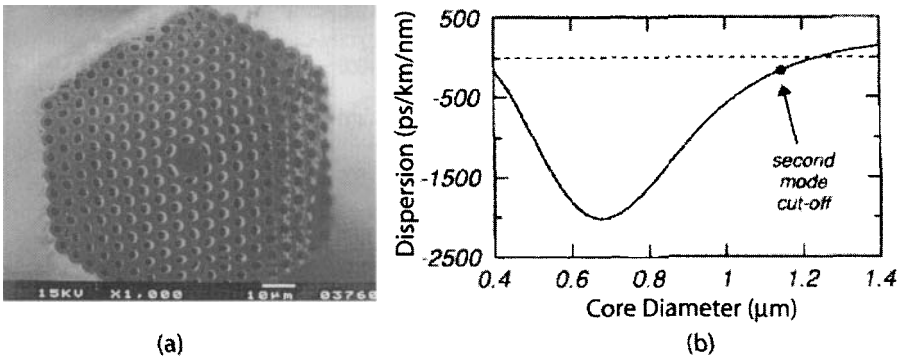

Figure 7.5: (a) SEM image of a photonic-crystal fiber with air holes surrounding a central core. (b) Dispersion parameter at 1.55 μm as a function of core diameter. (After Ref. [23]; ©1999 IEEE.)

7.2.4 Reverse-Dispersion Fibers

Two problems associated with the conventional DCFs (relatively large losses and a small core area) can also be overcome by using new kinds of fibers, known as *reverse-dispersion* fibers. Such fibers were developed during the late 1990s [26]–[30] and are designed such that both D and dispersion slope S have values similar to those of standard single-mode fibers but with opposite signs. As seen from Eq. (7.2.3), both conditions can be satisfied using a periodic dispersion map in which two fiber sections have nearly the same length.

The use of a reverse-dispersion fiber has several advantages compared with traditional DCFs. They all stem from the fact that the core size of reverse-dispersion fibers is significantly larger than that of DCFs. As a result, such fibers exhibit a lower loss, a larger effective core area, and a lower value of the PMD parameter. When a long-haul fiber link is constructed by alternating normal- and reverse-dispersion fibers, each of length $L_A/2$ where L_A is the amplifier spacing, the entire link can have nearly zero net dispersion over the entire C band [26]. Such a design is useful for WDM systems because the local value of $|D|$ is quite large all along the fiber, a situation that helps to suppress four-wave mixing among neighboring channels almost entirely [27].

In an extension of this basic idea, the lengths of two fiber sections with positive and negative dispersion are reduced to below 10 km such that the map period L_m becomes a small fraction of the amplifier spacing L_A. This technique is referred to as *short-period* or *dense* dispersion management and offers some distinct advantages. First, the length of fiber drawn from a single perform is close to 5 km. One can thus construct a fiber cable by combining two types of fibers with opposite dispersion characteristics. Such a fiber cable with 4.5-km section lengths was used in a 2000 WDM transmission experiment [30]. Second, it allows the use of dispersion-managed solitons at high bit rates (see Section 8.3). Transmission at 11 Tb/s was realized using reverse-dispersion fibers in an experiment that transmitted 273 channels, each operating at 40 Gb/s, over the C, L, and S bands simultaneously [31].

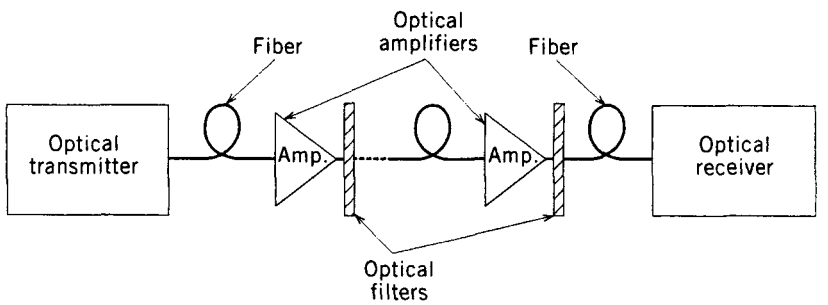

Figure 7.6: Dispersion management in a long-haul fiber link using optical filters after each amplifier. Filters compensate for GVD and can also reduce amplifier noise.

7.3 Dispersion-Equalizing Filters

A shortcoming of commonly used DCFs is that a relatively long length (>5 km) is required to compensate for the GVD acquired over 50 to 60 km of standard fiber. Losses encountered within each DCF add considerably to the total link loss, especially in the case of long-haul applications. For this reason, several other all-optical schemes have been developed for dispersion management. Most of them can be classified under the category of dispersion-equalizing filters. Figure 7.6 shows schematically how a compact optical filter can be combined with the amplifier module such that both fiber losses and GVD are compensated simultaneously in a periodic fashion. Moreover, the optical filter can also reduce the amplifier noise if its bandwidth is much smaller than the amplifier bandwidth.

7.3.1 Gires–Tournois Filters

As discussed in Section 8.1 of LT1, any interferometer acts as an optical filter because it is sensitive to the frequency of input light by its very nature and exhibits frequency-dependent transmission and reflection characteristics. A simple example is provided by the Fabry–Perot interferometer. The only problem from the standpoint of dispersion compensation is that the transfer function of a Fabry–Perot filter affects both the amplitude and phase of passing light. As seen from Eq. (7.1.4), a dispersion-equalizing filter should affect the phase of light but not its amplitude.

This problem is easily solved by using a *Gires–Tournois* (GT) interferometer, which is simply a Fabry–Perot interferometer whose back mirror has been made 100% reflective. The transfer function of a GT filter can be obtained by considering multiple round trips inside its cavity and is given by [32]

$$H_{\mathrm{GT}}(\omega) = H_0 \frac{-r + \exp(i\omega T_r)}{1 - r\exp(-i\omega T_r)}, \tag{7.3.1}$$

where the constant H_0 takes into account all losses, $|r|^2$ is the front-mirror reflectivity, and T_r is the round-trip time within the filter cavity. If losses are constant over the

signal bandwidth, $|H_{GT}(\omega)|$ is frequency-independent, and only the spectral phase is modified by such a filter.

However, the phase $\phi(\omega)$ of $H_{GT}(\omega)$ is far from ideal. It is a periodic function, peaking at frequencies that correspond to longitudinal modes of the cavity. In the vicinity of each peak, a spectral region exists in which phase variations are nearly quadratic in ω. The group delay, defined as $\tau_g = d\phi(\omega)/d\omega$, is also a periodic function. The quantity $\phi_2 \equiv d\tau_g/d\omega$, related to the slope of the group delay, represents the total dispersion of the GT filter. At frequencies corresponding to the longitudinal modes, ϕ_2 is given by

$$\phi_2 = 2T_r^2 r(1-r)/(1+r)^3. \tag{7.3.2}$$

As an example, for a 2-cm-thick GT filter designed with $r = 0.8$, $\phi_2 \approx 2{,}200$ ps^2. This filter can compensate the GVD acquired over 110 km of standard fiber.

Several experiments have shown the potential of GT filters as a compact dispersion compensator. In a 1991 experiment, such a device was used to transmit a 8-Gb/s signal over 130 km of standard fiber [33]. The GT filter had a 1-mm-long cavity with 70% reflectivity for the front mirror. The relatively high insertion loss of 8 dB was compensated by using an optical amplifier. However, 6-dB losses were due to the 3-dB fiber coupler that was used to separate the reflected signal from the incident signal. This amount can be reduced to below 1 dB using an optical circulator (see Section 2.4.3 of LT1). The micro-electro-mechanical system (MEMS) technology has also been employed for fabricating a GT filter whose cavity length can be adjusted electronically [34]. When such a device is used in the off-axis configuration, one can avoid using a circulator by physically separating the input and output fibers.

A GT filter can compensate dispersion for multiple channels simultaneously because, as seen in Eq. (7.3.1), it exhibits a periodic response at frequencies that correspond to the longitudinal modes of the underlying Fabry–Perot cavity. However, the periodic nature of the transfer function also indicates that ϕ_2 in Eq. (7.3.2) is the same for all channels. In other words, a GT filter cannot compensate for the dispersion slope of the transmission fiber without suitable design modifications. Several schemes have been proposed for dispersion slope compensation [35]–[37]. In one approach, two or more cavities are coupled such that the entire device acts as a composite GT filter [35]. In another design, GT filters are cascaded in series. In a 2004 experiment, cascaded GT filters were used to compensate dispersion of 40 channels (each operating at 10 Gb/s) over a length of 3,200 km [36]. Another interesting approach employs two fiber gratings that act as two mirrors of a GT filter. Since reflectivity is distributed over the grating length, such a device is referred to as a distributed GT filter [37].

Figure 7.7 shows the basic idea behind the dispersion slope compensation schematically in the case of two cascaded GT filters. A four-port circulator forces the input WDM signal to pass through the two filters in a sequential fashion. Two filters have different cavity lengths and mirror reflectivities, resulting in group-delay profiles whose peaks are slightly shifted and have different amplitudes. This combination results in a composite group-delay profile that exhibits different slopes (and hence a different effective dispersion parameter D) near each peak. Changes in D occurring from one peak to the next can be designed to satisfy the slope condition in Eq. (7.3.1) by choosing the filter parameters appropriately.

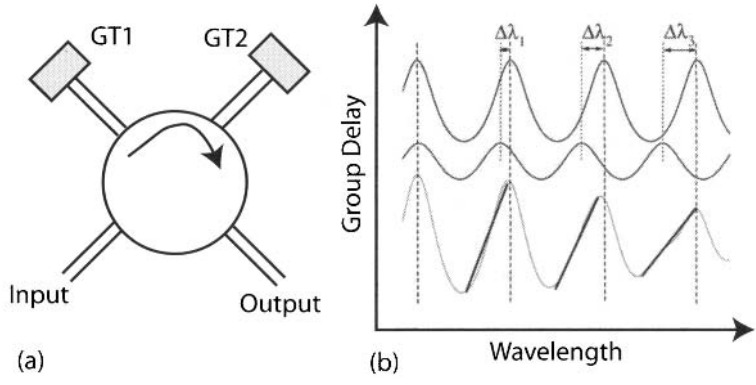

Figure 7.7: (a) Schematic illustration of dispersion slope compensation using two cascaded GT filters. (b) Group delay as a function of wavelength for two GT filters and the resulting total group delay (gray curve). Dark lines show the slope of group delay.

7.3.2 Mach–Zehnder Filters

A Mach–Zehnder (MZ) interferometer can also act as an optical filter. As discussed in Section 8.1.2 of LT1, an all-fiber MZ interferometer can be constructed by connecting two directional couplers in series. The first coupler splits the input signal into two parts, which acquire different phase shifts if optical path lengths are different, before they interfere at the second coupler. The signal may exit from either of the two output ports depending on its frequency and the arm lengths. In the case of two 3-dB couplers, the transfer function for the cross port is given by [38]

$$H_{\mathrm{MZ}}(\omega) = \tfrac{1}{2}[1 + \exp(i\omega\tau)], \tag{7.3.3}$$

where τ is the extra delay in the longer arm of the MZ interferometer.

If we compare Eq. (7.3.3) with Eq. (7.1.4), we can conclude that a single MZ interferometer is not suitable for dispersion compensation. However, it turned out that a cascaded chain of several MZ interferometers acts as an excellent dispersion-equalizing filter [39]. Such filters have been fabricated in the form of a *planar lightwave circuit* using silica waveguides on a silicon substrate [40]–[45]. Figure 7.8(a) shows a specific circuit design schematically. This device was 52×71 mm^2 in size and exhibited a chip loss of 8 dB [40]. It consisted of 12 couplers with asymmetric arm lengths that were cascaded in series. A chromium heater was deposited on one arm of each MZ interferometer to provide thermo-optic control of the optical phase. The main advantage of such a device is that its dispersion-equalization characteristics can be controlled by changing the arm lengths and the number of MZ interferometers.

The operation of the MZ filter can be understood from the unfolded view shown in Figure 7.8(b). The device is designed such that the higher-frequency components propagate in the longer arm of the MZ interferometers. As a result, they experience more delay than the lower-frequency components taking the shorter route. The relative delay introduced by such a device is just the opposite of that introduced by a standard fiber

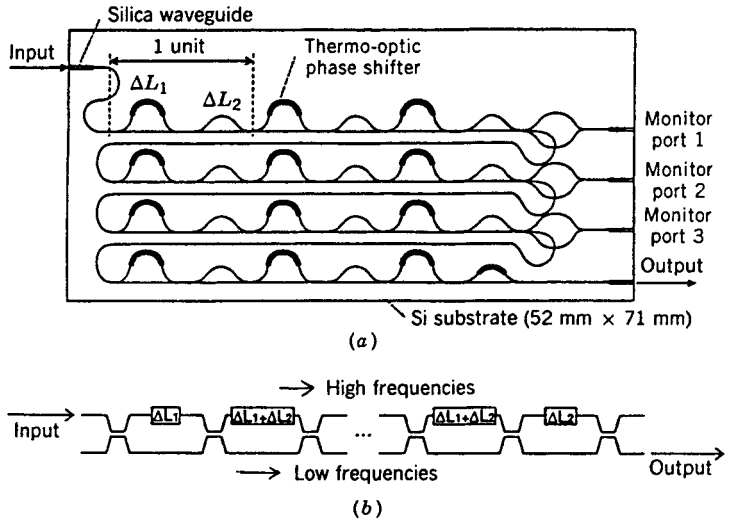

Figure 7.8: (a) A planar lightwave circuit made of a chain of Mach–Zehnder interferometers; (b) unfolded view of the device. (After Ref. [40]; ©1994 IEEE.)

exhibiting anomalous dispersion near 1.55 μm. The transfer function $H(\omega)$ can be obtained analytically and is used to optimize the device design and performance [41]. In a 1994 implementation [42], a planar lightwave circuit with only five MZ interferometers provided a relative delay of 836 ps/nm. Such a device is only a few centimeters long, but it is capable of compensating dispersion acquired over 50 km of fiber. Its main limitations are a relatively narrow bandwidth ($\sim$10 GHz) and sensitivity to input polarization. However, it acts as a programmable optical filter whose GVD as well as the operating wavelength can be adjusted. In one device, the GVD could be varied from $-1,006$ to 834 ps/nm [43].

It is not easy to compensate for the dispersion slope of the fiber with a single MZ chain. A simple solutions is to demultiplex the WDM signal, employ a MZ chain

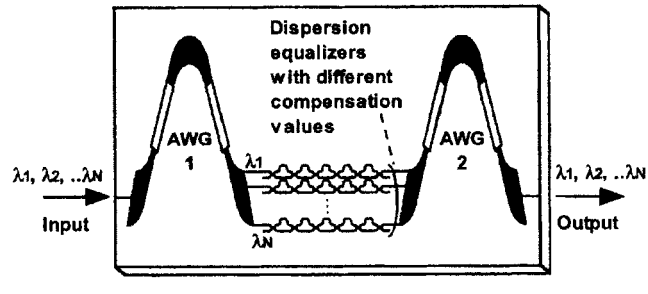

Figure 7.9: A planar lightwave circuit capable of compensating both the dispersion and dispersion slope. A separate MZ chain is employed for each WDM channel. (After Ref. [45]; ©2003 IEEE.)

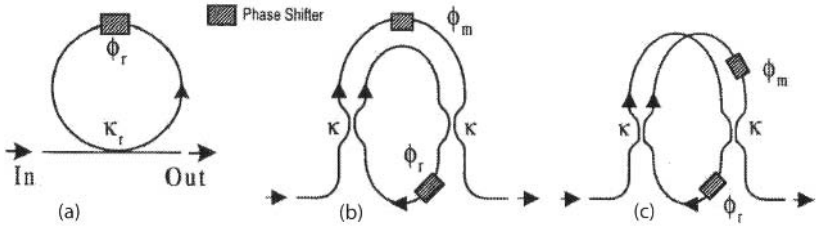

Figure 7.10: Three designs for all-pass fliters based on ring resonators: (a) A simple ring resonator with a built-in phase shifter; (b) an asymmetric MZ configuration; (c) a symmetric MZ configuration. (After Ref. [51]; ©1999 IEEE.)

designed suitably for each channel, and then multiplex the WDM channels back. Although this process sounds too complicated to be practical, all components can be integrated on a single chip using the silica-on-silicon technology [45]. Figure 7.9 shows the schematic of such a planar lightwave circuit. The use of a separate MZ chain for each channel allows the flexibility that the device can be tuned to match dispersion experienced by each channel.

7.3.3 Other All-Pass Filters

It is possible to design several other types of filters that affect the signal phase but leave the signal amplitude intact. Such filters are known as all-pass filters (as they pass all of the optical power incident on them) and have attracted considerable attention within the context of dispersion compensation [46]–[49]. As discussed in Section 2.3.1 of LT1, a ring resonator constitutes a simple example of an all-pass filter. Indeed, ring resonators have been employed for this purpose since 1998 [50]–[52].

Figure 7.10 shows schematically three designs that use directional couplers and phase shifters to form a ring resonator [51]. Although a single ring can be employed for dispersion compensation, cascading of multiple rings increases the amount of dispersion. More complicated designs combine a MZ interferometer with a ring. The resulting device can compensate even the dispersion slope of a fiber. Such devices have been fabricated using the silica-on-silicon technology (see Section 4.3.3 of LT1). With this technology, the phase shifters seen in Figure 7.10 are incorporated using thin-film chromium heaters. One such device exhibited dispersion that ranged from -378 to $-3{,}026$ ps/nm depending on the channel wavelength.

In general, all-pass filters such as those shown in Figure 7.10 suffer from a narrow bandwidth over which dispersion can be compensated. The amount of dispersion can be increased by using multiple stages but the bandwidth is reduced even further. A solution is provided by the filter architectures shown in Figure 7.11 [49]. In configuration (a), the WDM signal is split into individual channels using a demultiplexer and an array of dispersive elements, followed by delay lines and phase shifters, is used to compensate the dispersion of each channel by the desired amount. Individual channels are then multiplexed back. Configuration (b) uses a mirror to employ the same devoice for multiplexing and demultiplexing purposes. In configuration (c) movable mirrors

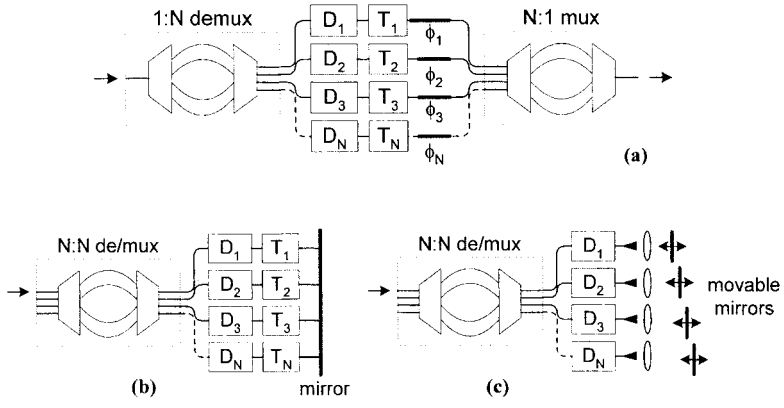

Figure 7.11: Three architectures for all-pass filters: (a) a transmissive filter with controllable dispersion for each channel through optical delay lines and phase shifters; (b) a reflective filter with a fixed mirror; (c) a reflective filter with moving mirrors acting as delay lines. (After Ref. [49]; ©2003 IEEE.)

are used to act as delay lines. Such designs, although more complicated, provide the most flexibility.

7.4 Fiber Bragg Gratings

The optical filters discussed in Section 7.3 are often fabricated using planar silica waveguides. Although such devices are compact, they suffer from high insertion losses, resulting from an inefficient coupling of light between an optical fiber and a planar waveguide. Insertion losses can be reduced by using a fiber-based optical filter.

As discussed in Section 2.2 of LT1, a fiber Bragg grating acts as an optical filter because of the existence of a *stop band*—a spectral region over which most of the incident light is reflected back. The stop band is centered at the *Bragg wavelength* related to the grating period Λ as $\lambda_B = 2\bar{n}\Lambda$, where $\bar{n}$ is the average mode index. The periodic nature of index variations couples the forward- and backward-propagating waves at wavelengths close to the Bragg wavelength and, as a result, provides frequency-dependent reflectivity to the incident signal over a bandwidth determined by the grating strength. In essence, a fiber grating acts as a reflection filter. Although the use of such gratings for dispersion compensation was proposed in the 1980s [53], it was only during the 1990s that fabrication technology advanced enough to make their use practical [22].

7.4.1 Constant-Period Gratings

In the simplest type of grating, the refractive index varies along the grating length in a periodic fashion as

$$n(z) = \bar{n} + n_g \cos(2\pi z/\Lambda), \tag{7.4.1}$$

where $\bar{n}$ is the average value of the refractive index and n_g is the modulation depth (typically, $n_g \sim 10^{-4}$ and $\Lambda \sim 0.5\ \mu$m). Bragg gratings are analyzed using two coupled-mode equations that describe the coupling between the forward- and backward-propagating waves at a given frequency $\omega = 2\pi c/\lambda$. These equations have the form [22]

$$dA_f/dz = i\delta A_f + i\kappa A_b, \tag{7.4.2}$$

$$dA_b/dz = -i\delta A_b - i\kappa A_f, \tag{7.4.3}$$

where A_f and A_b are the field amplitudes of the two waves and

$$\delta = \frac{2\pi}{\lambda} - \frac{2\pi}{\lambda_B}, \qquad \kappa = \frac{\pi n_g \Gamma}{\lambda_B}. \tag{7.4.4}$$

Physically, δ represents detuning from the Bragg wavelength, κ is the coupling coefficient, and Γ is the confinement factor.

The coupled-mode equations can be solved analytically owing to their linear nature (see Section 2.2.4 of LT1). Most of the input light is reflected when optical frequency is close to the Bragg wavelength. The transfer function of the grating, acting as a reflective filter, is found to be [38]

$$H(\omega) = \frac{A_b(0)}{A_f(0)} = \frac{i\kappa \sin(qL_g)}{q\cos(qL_g) - i\delta \sin(qL_g)}, \tag{7.4.5}$$

where $q^2 = \delta^2 - \kappa^2$ and L_g is the grating length. When incident wavelength falls in the region $-\kappa < \delta < \kappa$, q becomes imaginary, and most of the light is reflected back by the grating (reflectivity becomes nearly 100% for $\kappa L_g > 3$). This region constitutes the stop band of the grating.

As before, the dispersion characteristics of the grating are related to the frequency dependence of the phase of $H(\omega)$. It is easy to show that the phase is nearly linear inside the stop band. Thus, grating-induced dispersion exists mostly outside the stop band, a region in which grating transmits most of the incident signal. In this region ($|\delta| > \kappa$), the dispersion parameters of a fiber grating are given by [38]

$$\beta_2^g = -\frac{\mathrm{sgn}(\delta)\kappa^2/v_g^2}{(\delta^2 - \kappa^2)^{3/2}}, \qquad \beta_3^g = \frac{3|\delta|\kappa^2/v_g^3}{(\delta^2 - \kappa^2)^{5/2}}, \tag{7.4.6}$$

where v_g is the group velocity. Grating dispersion is anomalous ($\beta_2^g < 0$) on the high-frequency or "blue" side of the stop band, where δ is positive and the carrier frequency exceeds the Bragg frequency. In contrast, dispersion becomes normal ($\beta_2^g > 0$) on the low-frequency or "red" side of the stop band. The red side can be used for compensating the dispersion of standard fibers near 1.55 μm ($\beta_2 \approx -21$ ps^2/km). Since β_2^g can exceed 1,000 ps^2/cm, a single 2-cm-long grating can compensate dispersion accumulated over 100 km of fiber. However, higher-order dispersion of the grating, nonuniform transmission, and rapid variations of $|H(\omega)|$ close to stop-band edges make constant-period fiber gratings far from being practical for dispersion compensation.

An *apodization technique* is used in practice to improve the grating response [22]. In an apodized grating, the index change n_g is nonuniform across the grating, resulting

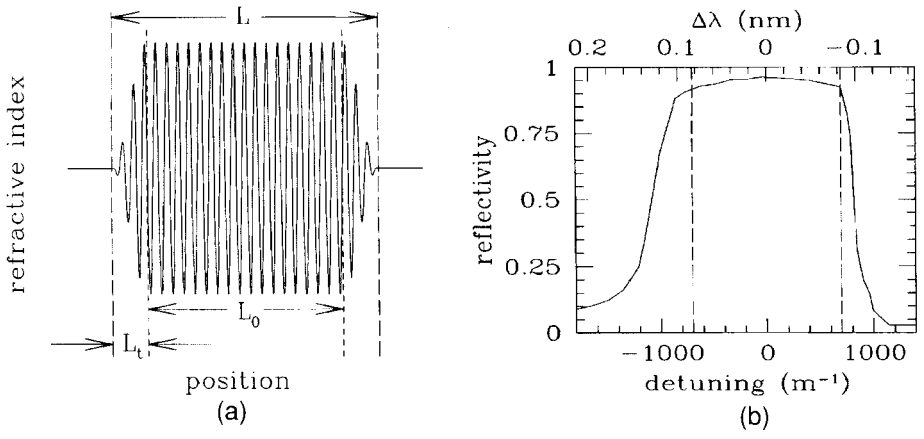

Figure 7.12: (a) Schematic variation of the refractive index in an apodized fiber grating. The length L_t of tapering region is chosen to be a small faction of the total grating length L. (b) Measured reflectivity spectrum for such a 7.5-cm-long grating. (After Ref. [54]; ©1999 OSA.)

in a z-dependent κ. Typically, as shown in Figure 7.12(a), κ is uniform in the central region of length L_0 and tapers down to zero at both ends over a short length L_t for a grating of length $L \equiv L_0 + 2L_t$. Figure 7.12(b) shows the measured reflectivity spectrum of an apodized 7.5-cm-long grating [54]. The reflectivity exceeds 90% within the stop band designed to be about 0.17-nm wide. The sharp drop in the reflectivity at both edges of the stop band is due to apodization. In another approach, the grating is fabricated such that κ varies linearly over its entire length. In a 1996 experiment, such an 11-cm-long grating was used to compensate the GVD acquired by a 10-Gb/s signal over 100 km of standard fiber [55]. The coupling coefficient $\kappa(z)$ varied smoothly from 0 to 6 cm^{-1} over the grating length. Such a grating compensated GVD over 106 km for a 10-Gb/s signal with only a 2-dB power penalty at a bit-error rate (BER) of 10^{-9}. In the absence of the grating, the penalty was infinitely large because of the existence of a BER floor.

Tapering of the coupling coefficient along the grating length can also be used for dispersion compensation when the signal wavelength lies within the stop band, and the grating acts as a reflection filter. Numerical solutions of the coupled-mode equations for a uniform-period grating for which $\kappa(z)$ varies linearly from 0 to 12 cm^{-1} over the 12-cm length show that such a grating exhibits a V-shaped group-delay profile, centered at the Bragg wavelength. It can be used for dispersion compensation if the wavelength of the incident signal is offset from the center of the stop band such that the signal spectrum sees a linear variation of the group delay. Such a 8.1-cm-long grating was capable of compensating the GVD acquired over 257 km of standard fiber by a 10-Gb/s signal [56]. Although uniform gratings have been used for dispersion compensation [55]–[58], they suffer from a relatively narrow stop band (typically $<$0.1 nm) and cannot be used at high bit rates. This shortcoming can be overcome by using chirped gratings, a topic we turn to next.

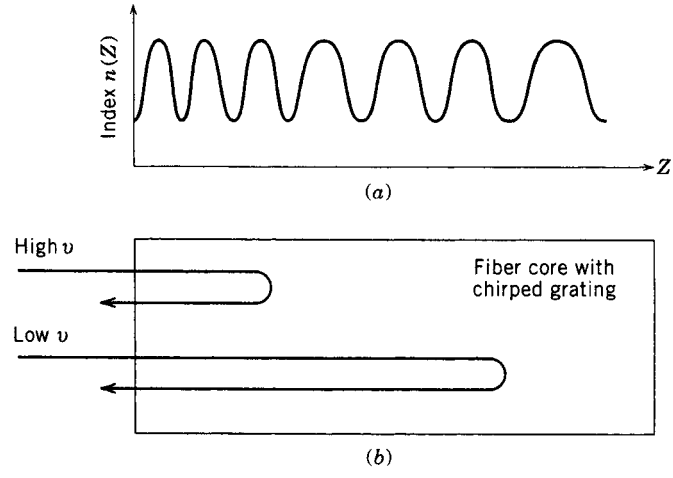

Figure 7.13: Dispersion compensation by a linearly chirped fiber grating: (a) index profile $n(z)$ along the grating length; (b) reflection of low and high frequencies at different locations within the grating because of variations in the Bragg wavelength.

7.4.2 Chirped Fiber Gratings

Chirped fiber gratings have a relatively broad stop band and were proposed for dispersion compensation as early as 1987 [59]. The optical period $\bar{n}\Lambda$ in a chirped grating is not constant but changes over its length. Since the Bragg wavelength ($\lambda_B = 2\bar{n}\Lambda$) also varies along the grating length, different frequency components of an incident optical pulse are reflected at different points, depending on where the Bragg condition is satisfied locally. In essence, the stop band of a chirped fiber grating results from overlapping of many mini stop bands, each shifted as the Bragg wavelength shifts along the grating. The resulting stop band can be more than 10 nm wide, depending on the grating length. Such gratings can be fabricated using several different methods [22].

It is easy to understand the operation of a chirped fiber grating from Figure 7.13, where the low-frequency components of a pulse are delayed more because of increasing optical period (and the Bragg wavelength). This situation corresponds to anomalous GVD. The same grating can provide normal GVD if it is flipped (or if the light is incident from the right). Thus, the optical period $\bar{n}\Lambda$ of the grating should decrease for it to provide normal GVD. From this simple picture, the dispersion parameter D_g of a chirped grating of length L_g can be determined by using the relation $T_R = D_g L_g \Delta\lambda$, where T_R is the round-trip time inside the grating and $\Delta\lambda$ is the difference in the Bragg wavelengths at the two ends of the grating. Since $T_R = 2\bar{n}L_g/c$, the grating dispersion is given by a remarkably simple expression

$$D_g = 2\bar{n}/(c\Delta\lambda). \tag{7.4.7}$$

As an example, $D_g \approx 5 \times 10^7$ ps/(km-nm) for a grating bandwidth $\Delta\lambda = 0.2$ nm. Because of such large values of D_g, a 10-cm-long chirped grating can compensate for the GVD acquired over 300 km of standard fiber.

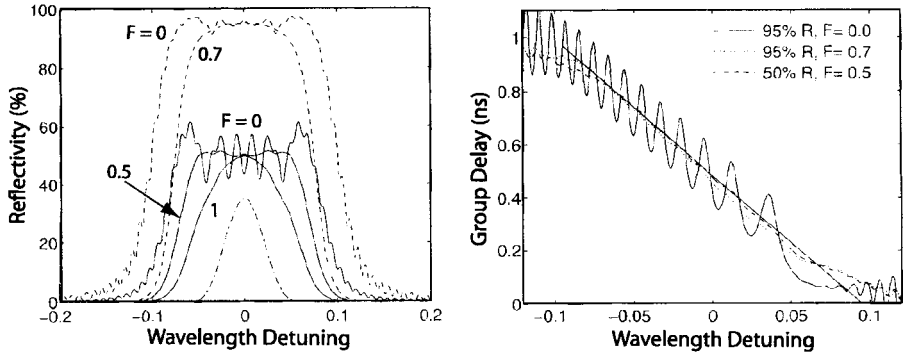

Figure 7.14: (a) Reflectivity and (b) group delay as a function of wavelength for linearly chirped fiber gratings with 50% (solid curves) or 95% (dashed curves) reflectivities and different values of apodization fraction F. The innermost curve shows for comparison the spectrum of a 100-ps pulse. (After Ref. [65]; ©1996 IEEE.)

Chirped fiber gratings were employed for dispersion compensation during the 1990s in several transmission experiments [60]–[64]. In a 10-Gbs/s experiment, a 12-cm-long chirped grating was used to compensate dispersion accumulated over 270 km of fiber [61]. Later, the transmission distance was increased to 400 km using a 10-cm-long apodized chirped fiber grating [62]. This represents a remarkable performance by an optical filter that is only 10 cm long. When compared to DCFs, fiber gratings offer lower insertion losses and do not enhance the nonlinear degradation of the signal.

It is necessary to apodize chirped gratings to avoid group-delay ripples that affect system performance. Mathematically, Eq. (7.4.1) for index variations across the grating takes the following form for an apodized chirped grating:

$$n(z) = \bar{n} + n_g a_g(z) \cos[2\pi(z/\Lambda_0)(1 + C_g z)], \tag{7.4.8}$$

where $a_g(z)$ is the apodization function, Λ_0 is the value of the grating period at $z = 0$, and C_g is the rate at which this period changes with z. The apodization function is chosen such that $a_g = 0$ at the two grating ends but becomes 1 in the central part of the grating. The fraction F of the grating length over which a_g changes from 0 to 1 plays an important role. Figure 7.14 shows the reflectivity and the group delay (related to the phase derivative $d\phi/d\omega$) calculated as a function of wavelength by solving the coupled-mode equations for several 10-cm-long gratings with different values of peak reflectivities and the apodization fraction F. The chirp rate $C_g = 6.1185 \times 10^{-4}$ m^{-1} was constant in all cases [65]. The modulation depth n_g was chosen such that the grating bandwidth was wide enough to fit a 10-Gb/s signal within its stop band. Dispersion characteristics of such gratings can be further optimized by choosing the apodization profile $a_g(z)$ appropriately [66].

It is evident from Figure 7.14 that apodization reduces ripples in both the reflectivity and group-delay spectra. Since the group delay should vary with wavelength linearly to produce a constant GVD across the signal spectrum, it should be as ripple-free as possible. However, if the entire grating length is apodized ($F = 1$), the reflectivity ceases

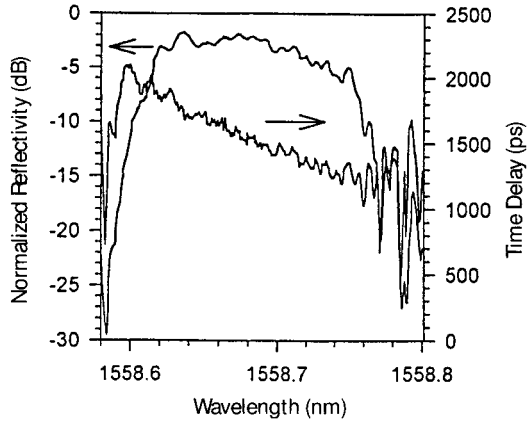

Figure 7.15: Measured reflectivity and time delay for a linearly chirped fiber grating with a bandwidth of 0.12 nm. (After Ref. [64]; ©1996 IEEE.)

to be constant across the pulse spectrum, an undesirable situation. Also, reflectivity should be as large as possible to reduce insertion losses. In practice, gratings with 95% reflectivity and $F = 0.7$ provide the best compromise for 10-Gb/s systems [65]. Figure 7.15 shows the measured reflectivity and group delay spectra for a 10-cm-long grating whose bandwidth of 0.12 nm is chosen to ensure that a 10-Gb/s signal fits within its stop band [64]. The slope of the group delay (about 5,000 ps/nm) is a measure of the dispersion-compensation capability of the grating. Such a grating can recover a 10-Gb/s signal by compensating the GVD acquired over 300 km of the standard fiber.

It is clear from Eq. (7.4.7) that D_g of a chirped grating is ultimately limited by the bandwidth $\Delta\lambda$ over which GVD compensation is required, which in turn is determined by the bit rate B. This creates a dilemma because as the stop-band bandwidth is increased to accommodate a high-bit-rate signal, the grating dispersion D_g decreases. Cascading of two or more gratings can solve this problem to some extent. In a 1996 experiment [63], two chirped fiber gratings were cascaded in series to compensate fiber dispersion over 537 km. In another 1996 experiment, the transmission distance of a 10-Gb/s signal was extended to 700 km by using a 10-cm-long chirped grating in combination with a phase-alternating duobinary scheme [64].

A drawback of chirped fiber gratings is that they work as a reflection filter. A 3-dB fiber coupler can be used to separate the reflected signal from the incident one. However, its use imposes a 6-dB loss that adds to other insertion losses. An optical circulator reduces insertion losses to below 2 dB. Several other techniques can be used. For example, two or more fiber gratings can be combined to form a transmission filter that provides dispersion compensation with relatively low insertion losses [67]. A single grating can be converted into a transmission filter by introducing a phase shift in the middle of the grating [68]. A Moiré grating, constructed by superimposing two chirped gratings formed on the same piece of fiber, also has a transmission peak within its stop band [69]. The bandwidth of such transmission filters is relatively small.

A major drawback of fiber gratings is that transfer function exhibits a single peak in

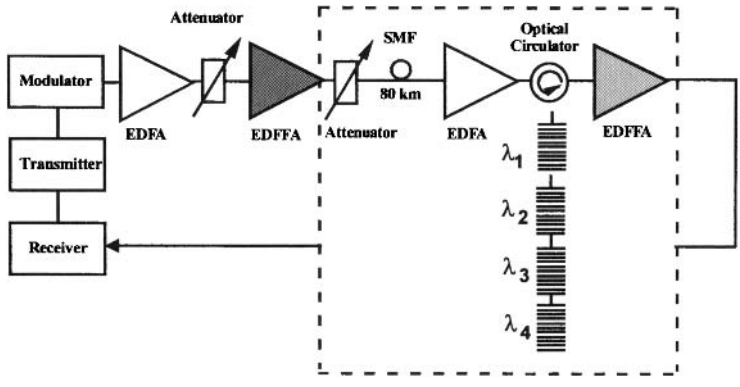

Figure 7.16: Cascaded gratings used for dispersion compensation in a WDM system. (After Ref. [74]; ©1999 IEEE.)

contrast with the optical filters discussed in Section 7.3. Thus, a single grating cannot compensate the dispersion of several WDM channels unless its design is modified. Several different approaches can be used to solve this problem.

A chirped fiber grating can have a stop band as wide as 10 nm if it is made long enough. Such a grating can be used in a WDM system if the number of channels is small enough that the total signal bandwidth fits inside its stop band. In a 1999 experiment, a 6-nm-bandwidth chirped grating was used for a four-channel WDM system, each channel operating at 40 Gb/s [70]. When the WDM-signal bandwidth is much larger than that, one can use several cascaded chirped gratings in series such that each grating reflects one channel and compensates its dispersion [71]–[75]. The advantage of this technique is that the gratings can be tailored to match the dispersion experienced by each channel, resulting in automatic dispersion-slope compensation. Figure 7.16 shows the cascaded-grating scheme schematically for a four-channel WDM system [74]. Every 80 km, a set of four gratings compensates the GVD for all channels, while two optical amplifiers take care of all losses. By 2000, this approach was applied to a 32-channel WDM system with 18-nm bandwidth [75]. Six chirped gratings, each with a 6-nm-wide stop band, were cascaded to compensate GVD for all channels simultaneously.

7.4.3 Sampled Gratings

The cascaded-gratings approach becomes cumbersome as the number of channels in a WDM system becomes large. A new kind of fiber grating, referred to as the *sampled grating*, has been developed to solve this problem. Such devices have double periodicity and are also known as *superstructure gratings*. Fiber-based superstructure gratings were first made in 1994 [76]. Since then, they have attracted considerable attention for dispersion compensation [77]–[84].

A sampled or superstructure grating consists of multiple subgratings separated from each other by a section of uniform index (each subgrating is a sample, hence the name

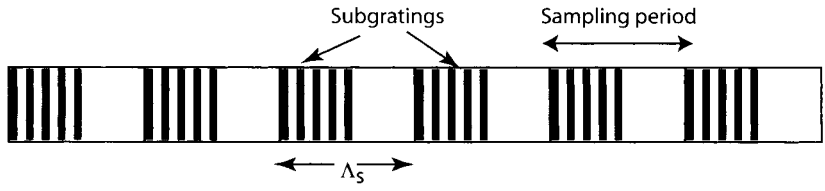

Figure 7.17: Schematic of a sampled grating. Darkened areas indicate regions with a higher refractive index.

"sampled" grating). Figure 7.17 shows a sampled grating schematically. In practice, such a structure can be realized by blocking certain regions through an amplitude mask during fabrication of a long grating such that $\kappa = 0$ in the blocked regions. It can also be made by etching away parts of an existing grating. In both cases, $\kappa(z)$ varies periodically along z. It is this periodicity that modifies the stop band of a uniform grating. If the average index $\bar{n}$ also changes with the same period, both δ and κ become periodic in the coupled-mode equations. The solution of these equation shows that a sampled grating has multiple stop bands separated from each other by a constant amount. The frequency spacing $\Delta\nu_p$ among neighboring reflectivity peaks is set by the sample period Λ_s as $\Delta\nu_p = c/(2n_g\Lambda_s)$ and is controllable during the fabrication process. Moreover, if each subgrating is chirped, the dispersion characteristics of each reflectivity peak are governed by the amount of chirp introduced.

A sampled grating is characterized by a periodic sampling function $S(z)$. The sampling period Λ_s of about 1 mm is chosen so that $\Delta\nu_p$ is close to 100 GHz (typical channel spacing for WDM systems). In the simplest kind of grating, the sampling function is a "rect" function such that $S(z) = 1$ over a section of length $f_s\Lambda_s$ and 0 over the remaining portion of length $(1 - f_s)\Lambda_s$. However, this is not the optimum choice because it leads to a transfer function in which each peak is accompanied by multiple subpeaks. The reason is related to the fact that the shape of the reflectivity spectrum is governed by the Fourier transform of $S(z)$. This can be seen by multiplying n_g in Eq. (7.4.1) with $S(z)$ and expanding $S(z)$ in a Fourier series to obtain

$$n(z) = \bar{n} + n_g \,\mathrm{Re}\{\sum_m F_m \exp[2i(\beta_0 + m\beta_s)z]\}, \tag{7.4.9}$$

where F_m is the Fourier coefficient, $\beta_0 = \pi/\Lambda_0$ is the Bragg wave number, and β_s is related to the sampling period Λ_s as $\beta_s = \pi/\Lambda_s$. In essence, a sampled grating behaves as a collection of multiple gratings whose stop bands are centered at wavelengths $\lambda_m = 2\pi/\beta_m$, where $\beta_m = \beta_0 + m\beta_s$ and m is an integer. The peak reflectivity associated with different stop bands is governed by the Fourier coefficient F_m.

A multipeak transfer function with nearly constant reflectivity for all peaks can be realized by adopting a sampling function of the form $S(z) = \sin(az)/az$, where a is a constant. Such a "sinc" shape function was used in 1998 to fabricate 10-cm-long gratings with up to 16 reflectivity peaks separated by 100 GHz [78]. A 1999 experiment used such a sampled grating for a four-channel WDM system [79]. As the number of channels increases, it becomes more and more difficult to compensate the GVD of all channels at the same time because such a grating does not compensate for

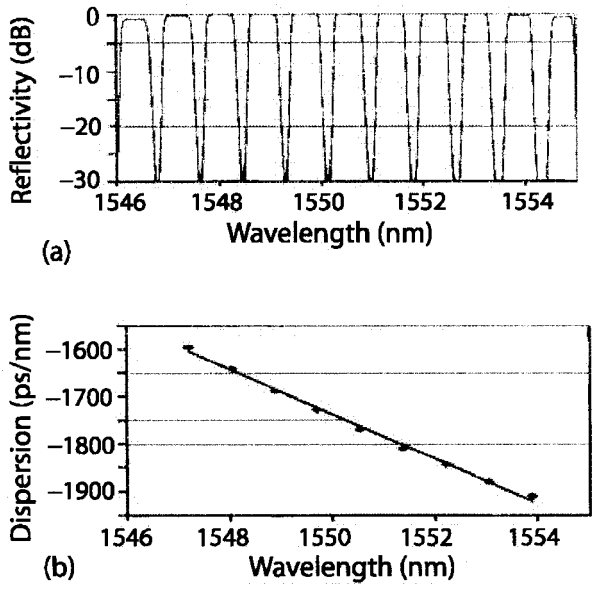

Figure 7.18: (a) Reflection and (b) dispersion characteristics of a chirped sampled grating designed for 8 channels spaced apart by 100 GHz. (After Ref. [80]; ©1999 IEEE.)

the dispersion slope of the fiber. This problem can be solved by introducing a chirp in the sampling period Λ_s, in addition to the chirping of the grating period Λ [80]. In practice, a linear chirp is used. The amount of chirp depends on the dispersion slope of the fiber as $\delta\Lambda_s/\Lambda_s = |S/D|\Delta\lambda_{\rm ch}$, where $\Delta\lambda_{\rm ch}$ is the channel bandwidth and $\delta\Lambda_s$ is the change in the sampling period over the entire grating length. Figure 7.18 shows the reflection and dispersion characteristics of a 10-cm-long sampled grating designed for 8 WDM channels with 100-GHz spacing. For this grating, each subgrating was 0.12 mm long and the 1-mm sampling period was changed by only 1.5% over the 10-cm grating length.

The preceding approach becomes impractical as the number N of WDM channels increases because it requires a large index modulation (n_g grows linearly with N). A solution is offered by sampled gratings in which the sampling function $S(z)$ modifies the phase of κ, rather than changing its amplitude; the modulation depth in this case grows only as $\sqrt{N}$. The phase-sampling technique has been used with success for making tunable semiconductor lasers [85]. Recently, it has been applied to fiber gratings [81]–[84]. In contrast with the case of amplitude sampling, index modulations exist over the entire grating length. However, the phase of modulation changes in a periodic fashion with a period Λ_s that itself is chirped along the grating length. Mathematically, index variations can be written in the form [83]

$$n(z) = \bar{n} + n_g \mathrm{Re}\{\exp[2i\pi(z/\Lambda_0) + i\phi_s(z)]\}, \tag{7.4.10}$$

where n_g is the constant modulation amplitude, Λ_0 is the average grating period, and the phase $\phi_s(z)$ varies in a periodic fashion. By expanding $\exp(i\phi_s)$ in a Fourier series,

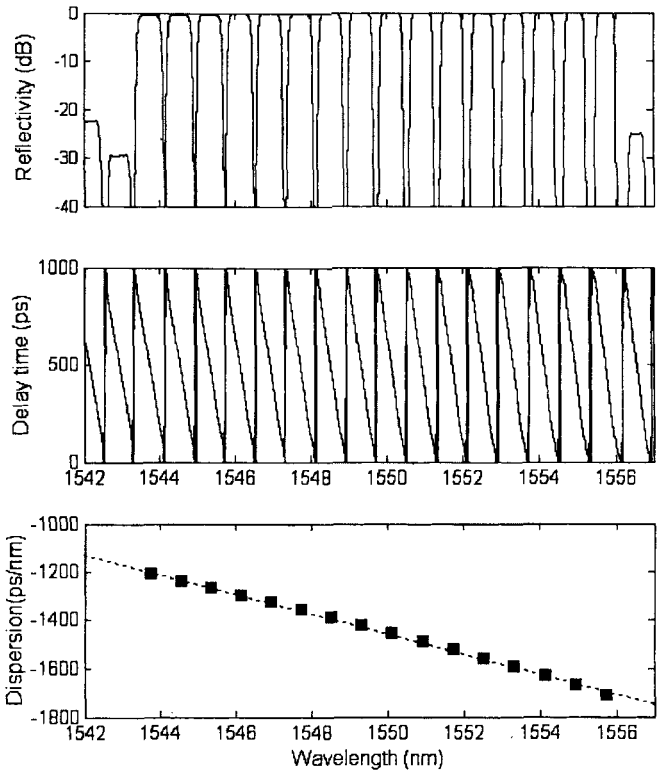

Figure 7.19: Reflectivity, group delay, and dispersion of a phase-sampled grating designed for 16 WDM channels. (After Ref. [83]; ©2003 IEEE.)

$n(z)$ can be written in the form of Eq. (7.4.9), where F_m depends on how the phase $\phi_s(z)$ varies in each sampling period. The shape of the reflectivity spectrum and dispersion characteristics of the grating can be tailored by controlling F_m and by varying the magnitude of chirp in the grating and sampling periods [83].

As an example, Figure 7.19 shows calculated values of the reflectivity, group delay, and dispersion as a function of wavelength for a 10-cm-long grating designed with $n_g = 4 \times 10^{-4}$ and $\Lambda_s = 1$ mm. The sampling period is chirped such that it is reduced by 2.1% over the grating length. The grating period was also chirped at a rate of 0.07 nm/cm. The phase profile $\phi(z)$ over one sampling period was optimized to ensure a relativity constant reflectivity over the entire channel bandwidth. Such a grating can compensate both the dispersion and dispersion slope of a fiber for 16 WDM channels with 100-GHz spacing.

7.5 Optical Phase Conjugation

Although the use of optical phase conjugation (OPC) for dispersion compensation was proposed in 1979 [86], it was only in 1993 that the OPC technique was first imple-

mented experimentally [87]–[90]. It has attracted considerable attention since then [91]–[113]. In contrast to other optical schemes discussed in this chapter, the OPC is a nonlinear optical technique. This section describes the principle behind it and discusses its implementation in practical lightwave systems.

7.5.1 Principle of Operation

The simplest way to understand how OPC can compensate the GVD is to take the complex conjugate of Eq. (7.1.2) and obtain

$$\frac{\partial A^*}{\partial z} - \frac{i\beta_2}{2}\frac{\partial^2 A^*}{\partial t^2} - \frac{\beta_3}{6}\frac{\partial^3 A^*}{\partial t^3} = 0. \tag{7.5.1}$$

A comparison of Eqs. (7.1.2) and (7.5.1) shows that the phase-conjugated field A^* propagates with the sign reversed for the GVD parameter β_2. This observation suggests immediately that, if the optical field is phase-conjugated in the middle of the fiber link, as shown in Figure 7.20(a), second-order dispersion (GVD) accumulated over the first half will be compensated exactly in the second half of the fiber link. As the β_3 term does not change sign on phase conjugation, OPC cannot compensate for the TOD. In fact, it is easy to show by keeping the higher-order terms in the Taylor expansion in Eq. (3.1.6) that OPC compensates for all even-order dispersion terms, while leaving the odd-order terms unaffected.

The effectiveness of midspan OPC for dispersion compensation can also be verified by using Eq. (7.1.3) with $\beta_3 = 0$. The optical field just before OPC is obtained by substituting $z = L/2$ in this equation. The propagation of the phase-conjugated field A^* in the second-half section then yields

$$A^*(L,t) = \frac{1}{2\pi}\int_{-\infty}^{\infty} \tilde{A}^*\left(\frac{L}{2},\omega\right)\exp\left(\frac{i}{4}\beta_2 L\omega^2 - i\omega t\right)d\omega, \tag{7.5.2}$$

where $\tilde{A}^*(L/2,\omega)$ is the Fourier transform of $A^*(L/2,t)$ and is given by

$$\tilde{A}^*(L/2,\omega) = \tilde{A}^*(0,-\omega)\exp(-i\omega^2\beta_2 L/4). \tag{7.5.3}$$

By substituting Eq. (7.5.3) in Eq. (7.5.2), one finds that $A(L,t) = A^*(0,t)$. Thus, except for a phase reversal induced by the OPC, the input field is completely recovered, and the pulse shape is restored to its input form. Since the signal spectrum after OPC becomes the mirror image of the input spectrum, the OPC technique is also referred to as *midspan spectral inversion*.

7.5.2 Compensation of Self-Phase Modulation

As discussed in Section 4.1, the nonlinear phenomenon of SPM leads to the chirping of the transmitted signal that manifests itself through broadening of the signal spectrum. Although this chirp can be used to advantage in soliton-based systems (see Section 8.2), in most lightwave systems the SPM-induced nonlinear effects degrade the signal quality, especially when the signal is propagated over long distances using multiple optical amplifiers.

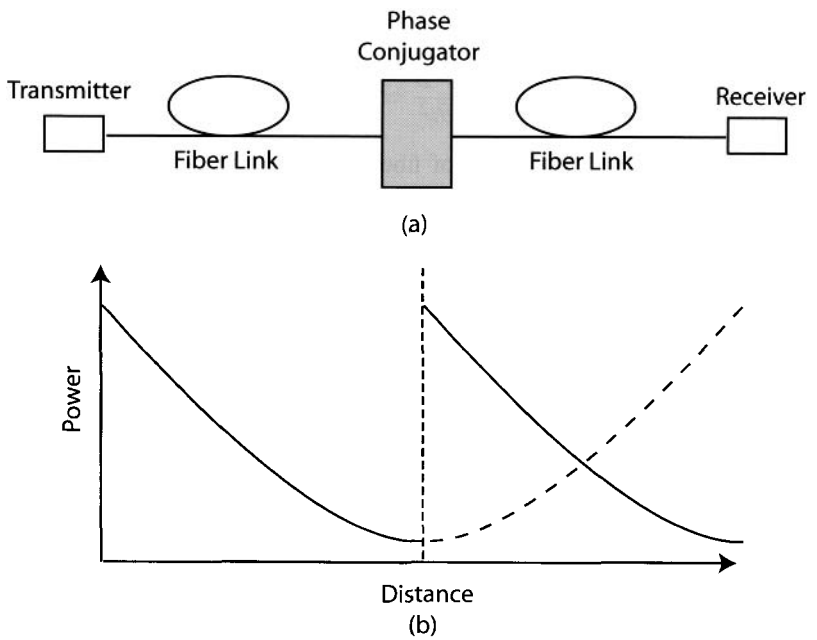

Figure 7.20: (a) Schematic of dispersion management through midspan phase conjugation. (b) Power variations inside the fiber link when an amplifier boosts the signal power at the phase conjugator. The dashed line shows the power profile required for SPM compensation.

The OPC technique differs from all other dispersion-compensation schemes in one important way: Under certain conditions, it can compensate simultaneously for both the GVD and SPM. This feature of OPC was noted in the early 1980s [114] and attracted considerable attention after 1993 [99]. It is easy to show that both the GVD and SPM are compensated perfectly in the absence of fiber losses. Pulse propagation in a lossy fiber is governed by Eq. (3.1.12) or by

$$\frac{\partial A}{\partial z} + \frac{i\beta_2}{2}\frac{\partial^2 A}{\partial t^2} = i\gamma|A|^2 A - \frac{\alpha}{2}A, \tag{7.5.4}$$

where α accounts for fiber losses. When $\alpha = 0$, A^* satisfies the same equation when we take the complex conjugate of Eq. (7.5.4) and change z to $-z$. In other words, the propagation of A^* is equivalent to sending the signal backward and undoing distortions induced by β_2 and γ. As a result, midspan OPC can compensate for both SPM and GVD simultaneously.

Fiber losses destroy this important property of midspan OPC. The reason is intuitively obvious if we note that the SPM-induced phase shift is power-dependent. As a result, much larger phase shifts are induced in the first half of the link than the second half, and OPC cannot compensate for the nonlinear effects. Equation (7.5.4) can be used to study the impact of fiber losses. By making the substitution

$$A(z,t) = B(z,t)p(z), \tag{7.5.5}$$

Eq. (7.5.4) can be written as

$$\frac{\partial B}{\partial z} + \frac{i\beta_2}{2}\frac{\partial^2 B}{\partial t^2} = i\gamma p(z)|B|^2 B, \tag{7.5.6}$$

where $p(z) = \exp(-\alpha z)$. The effect of fiber losses is mathematically equivalent to the loss-free case but with a z-dependent nonlinear parameter. By taking the complex conjugate of Eq. (7.5.6) and changing z to $-z$, it is easy to see that perfect SPM compensation can occur only if $p(z) = \exp(\alpha z)$ after phase conjugation ($z > L/2$). A general requirement for the OPC technique to work is $p(z) = p(L - z)$. This condition cannot be satisfied when $\alpha \neq 0$.

One may think that the problem can be solved by amplifying the signal after OPC so that the signal power becomes equal to the input power before it is launched in the second-half section of the fiber link. Although such an approach reduces the impact of SPM, it does not lead to perfect compensation of it. The reason can be understood by noting that the propagation of a phase-conjugated signal is equivalent to propagating a *time-reversed* signal [115]. Thus, perfect SPM compensation can occur only if the power variations are symmetric around the midspan point where the OPC is performed so that $p(z) = p(L - z)$ in Eq. (7.5.6). Optical amplification does not satisfy this property. Figure 7.20(b) shows the actual and required forms of $p(z)$. One can come close to SPM compensation if the signal is amplified often enough that the power does not vary by a large amount during each amplification stage. This approach is, however, not practical because it requires closely spaced amplifiers. The use of distributed Raman amplification with bidirectional pumping can also help because it can provide $p(z)$ close to 1 over the entire span.

Perfect compensation of both GVD and SPM can be realized by employing dispersion-decreasing fibers in which $|\beta_2|$ decreases along the fiber length. To see how such a scheme can be implemented, assume that β_2 in Eq. (7.5.6) is a function of z. By making the transformation

$$\xi = \int_0^z p(z)\, dz, \tag{7.5.7}$$

Eq. (7.5.6) can be written as [99]

$$\frac{\partial B}{\partial \xi} + \frac{i}{2} b(\xi)\frac{\partial^2 B}{\partial t^2} = i\gamma |B|^2 B, \tag{7.5.8}$$

where $b(z) = \beta_2(z)/p(z)$. Both GVD and SPM are compensated if $b(\xi) = b(\xi_L - \xi)$, where ξ_L is the value of ξ at $z = L$. This condition is automatically satisfied when $\beta_2(z)$ decreases in exactly the same way as $p(z)$ so that their ratio remains constant. Since $p(z)$ decreases exponentially, both GVD and SPM can be compensated in a dispersion-decreasing fiber whose GVD decreases as $e^{-\alpha z}$. This approach is quite general and applies even when in-line amplifiers are used.

7.5.3 Generation of Phase-Conjugated Signal

The implementation of the midspan OPC technique requires a nonlinear optical element that generates the phase-conjugated signal. The most commonly used method

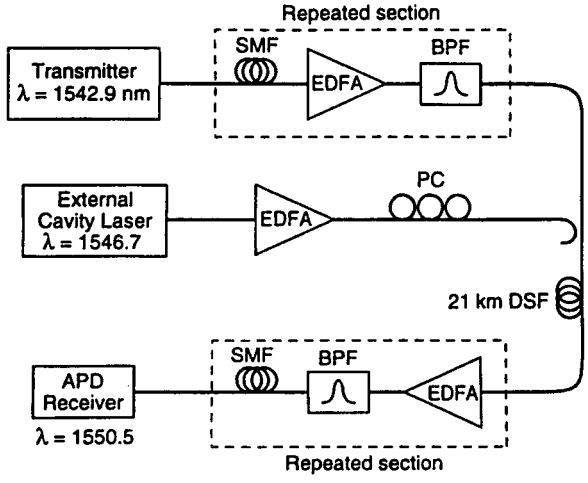

Figure 7.21: Experimental setup for dispersion compensation through midspan spectral inversion in a 21-km-long dispersion-shifted fiber. (After Ref. [88]; ©1993 IEEE.)

makes use of *four-wave mixing* (FWM) in a nonlinear medium. Since the optical fiber itself is a nonlinear medium [116], a simple approach is to use a few-kilometer-long fiber, designed especially to maximize the FWM efficiency. As discussed in Section 4.3, the use of FWM requires lunching of a pump beam at a frequency ω_p that is shifted from the signal frequency ω_s by a small amount ($\sim$0.5 THz). Such a device acts as a parametric amplifier and amplifies the signal, while also generating an idler at the frequency $\omega_c = 2\omega_p - \omega_s$ if the phase-matching condition is satisfied. The idler beam carries the same information as the signal but its phase is reversed with respect to the signal and its spectrum is inverted.

The phase-matching condition can be approximately satisfied if the zero-dispersion wavelength of the OPC fiber is chosen to nearly coincide with the pump wavelength. This was the approach adopted in a 1993 experiment [87] in which a 1,546-nm signal was phase-conjugated using FWM in a 23-km-long fiber pumped at 1,549 nm. A 6-Gb/s signal could be transmitted over 152 km by compensating dispersion through OPC in the middle of the fiber link. In another 1993 experiment [88], a 10-Gb/s signal was transmitted over 360 km with the setup shown in Figure 7.21. The midspan OPC was performed in a 21-km-long fiber by using a pump laser whose wavelength was tuned exactly to the zero-dispersion wavelength of the fiber. The pump and signal wavelengths differed by 3.8 nm, and a bandpass filter was used to separate the phase-conjugated signal from the pump.

Several factors need to be considered while implementing the midspan OPC technique in practice. First, since the signal wavelength changes from ω_s to $\omega_c = 2\omega_p - \omega_s$ at the phase conjugator, the GVD parameter β_2 becomes different in the second-half section. As a result, perfect compensation occurs only if the phase conjugator is slightly offset from the midpoint of the fiber link. The exact location L_p can be determined by using the condition $\beta_2(\omega_s)L_p = \beta_2(\omega_c)(L - L_p)$, where L is the total link length. By

expanding $\beta_2(\omega_c)$ in a Taylor series around the signal frequency ω_s, L_p is found to be

$$\frac{L_p}{L} = \frac{\beta_2 + \delta_c \beta_3}{2\beta_2 + \delta_c \beta_3}, \tag{7.5.9}$$

where $\delta_c = \omega_c - \omega_s$ is the frequency shift of the signal induced by the OPC technique. For a typical wavelength shift of 6 nm, the phase-conjugator location changes by about 1%. The effect of residual dispersion and SPM in the phase-conjugation fiber itself can also affect the placement of a phase conjugator [96].

A second factor that needs to be addressed is that the FWM process in optical fibers is polarization-sensitive. As signal polarization is not controlled in optical fibers, it varies at the OPC in a random fashion. Such random variations affect FWM efficiency and make the standard FWM technique unsuitable for practical purposes. Fortunately, the FWM scheme can be modified to make it polarization-insensitive. In one approach, two orthogonally polarized pump beams at different wavelengths, located symmetrically on the opposite sides of the zero-dispersion wavelength λ_{ZD} of the fiber, are used [90]. This scheme has another advantage: The phase-conjugate wave can be generated at the frequency of the signal itself by choosing λ_{ZD} such that it coincides with the signal frequency. Polarization-insensitive OPC can also be realized by using a single pump in combination with a fiber grating and an *orthoconjugate mirror* [92], but the device works in the reflective mode and requires separation of the conjugate wave from the signal through an optical circulator.

Low efficiency of the OPC process can be of concern. In early experiments, the conversion efficiency η_c was below 1%, making it necessary to amplify the phase-conjugated signal [88]. However, the FWM process is not inherently a low-efficiency process and, in principle, it can even provide net gain [116]. Indeed, analysis of the FWM equations shows that η_c can be increased considerably by increasing the pump power; it can even exceed 100% by optimizing the power levels and the wavelength difference of the the pump and signal [94]. High pump powers require suppression of stimulated Brillouin scattering through modulation of pump phases. In a 1994 experiment, 35% conversion efficiency was realized with this technique [91].

The FWM process in a semiconductor optical amplifier (SOA) can also be used to generate the phase-conjugated signal. This approach was first used in a 1993 experiment to demonstrate the transmission of a 2.5-Gb/s signal over 100 km of standard fiber [89]. Later, in a 1995 experiment the same approach was used for transmitting a 40-Gb/s signal over 200 km of standard fiber [95]. The possibility of highly nondegenerate FWM inside SOAs was suggested in 1987, and this technique is used extensively in the context of wavelength conversion [117]. Its main advantage is that the phase-conjugated signal can be generated in a device of 1-mm length. The conversion efficiency is also typically higher than that of FWM in an optical fiber because of amplification, although this advantage is offset by the relatively large coupling losses resulting from the need to couple the signal back into the fiber. By a proper choice of the pump-signal detuning, conversion efficiencies of more than 100% (net gain for the phase-conjugated signal) have been realized through FWM in SOAs [118].

Periodically poled lithium-niobate (PPLN) waveguides have been used to make a compact, wideband, spectral inverter [102]. The phase-conjugated signal in such a

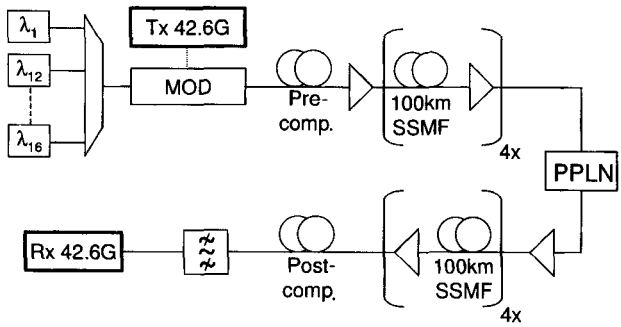

Figure 7.22: Experimental setup of a 16-channel WDM system, employing a PPLN-based phase conjugator to transmit data over 800 km of standard fiber. (After Ref. [113]; ©2004 IEEE.)

device is generated through two cascaded second-order nonlinear processes that are quasi-phase-matched through periodic poling of the crystal. Such an OPC device exhibited only 7-dB insertion losses and was capable of compensating the dispersion of four 10-Gb/s channels simultaneously over 150 km of standard fiber.

The OPC technique has been used for dispersion compensation in several recent experiments [107]–[113]. In a 1999 experiment, a FWM-based phase conjugator was used to compensate the GVD of a 40-Gb/s signal over 140 km of standard fiber. In the absence of OPC, the 40-Gb/s signal cannot be transmitted over more than 7 km, as dictated by Eq. (7.1.1). An SOA was used in a 2002 experiment to transmit the 80-Gb/s signal over 208 km of standard fiber [110]. In a 2004 WDM experiment, a PPLN-based phase conjugator was used to demonstrate the transmission of 16 channels (each operating at 40 Gb/s) over 800 km of standard fiber [113]. Amplifier spacing was 100 km and a single PPLN device was used midway after 4 amplifiers. Figure 7.22 shows the experimental setup schematically. A single pump at a wavelength of 1,546.12 nm phase-conjugated all 16 WDM channels as it inverted the signal spectrum around the pump wavelength. The BER of all channels was below 10^{-5}, a value small enough that the system can work reliably with forward error correction.

Most of the experimental work on dispersion compensation has considered transmission distances of several hundred kilometers. For long-haul applications, one may ask whether the OPC technique can compensate the GVD acquired over thousands of kilometers. This question has been studied mainly through numerical simulations. In one set of simulations, a 10-Gb/s signal could be transmitted over 6,000 km when the average launch power was kept below 3 mW to reduce the effects of fiber nonlinearity [97]. In another study, the amplifier spacing was found to play an important role; transmission over 9,000 km was feasible by keeping the amplifiers 40 km apart [100]. The choice of the operating wavelength with respect to the zero-dispersion wavelength was also critical. In the anomalous-dispersion region ($\beta_2 < 0$), periodic variations of the signal power along the fiber link can lead to the generation of additional sidebands through an instability known as *sideband instability* [119]. This instability can be avoided if the dispersion parameter is relatively large [$D > 10$ ps/(km-nm)]. This is the case for standard fibers near 1.55 μm. In general, the maximum transmission

distance depends on many factors such as FWM efficiency, input power, and amplifier spacing and may decrease to below 3,000 km, depending on the operating parameters [98]. If a suitably designed periodic dispersion map is used in combination with OPC, it is possible to suppress the sideband instability and increase the transmission distance to beyond 10,000 km [105].

The use of OPC for long-haul lightwave systems requires periodic use of optical amplifiers and phase conjugators. These two optical elements can be combined into one by using parametric amplifiers, which not only generate the phase-conjugated signal through the FWM process but also amplify it. The analysis of such a long-haul system shows that 20- to 30-ps input pulses can travel over thousands of kilometers despite a high GVD; the total transmission distance can exceed 10,000 km for dispersion-shifted fibers with $\beta_2 = -2$ ps^2/km near 1.55 μm [120]. However, the phase-conjugation technique has yet to be employed in a commercial lightwave system.

7.6 Other Schemes

For medium-haul lightwave systems (with link lengths $\sim$100 km), several other techniques can be employed for dispersion compensation. Most of them modify the characteristics of input pulses at the transmitter before they are launched into the fiber link. Others process the electronic signal at the receiver end to minimize distortions induced by dispersion. We consider such schemes in this section.

7.6.1 Prechirp Technique

The underlying idea behind prechirping can be understood from Eq. (7.1.3). It consists of changing the spectral amplitude $\tilde{A}(0,\omega)$ of input pulses in such a way that GVD-induced degradation is eliminated, or at least reduced substantially. Clearly, if the spectral amplitude is modified as

$$\tilde{A}(0,\omega) \rightarrow \tilde{A}(0,\omega)\exp(-i\omega^2\beta_2 L/2 - i\beta_3\omega^3 L/6), \tag{7.6.1}$$

where L is the link length, GVD will be compensated exactly, and the pulse will retain its shape at the fiber output. Unfortunately, it is not easy to implement Eq. (7.6.1) in practice. Often, one can ignore the cubic term proportional to β_3, as it is relatively small. The quadratic term is then introduced by chirping the input pulse suitably. Since frequency chirp is applied at the transmitter end, this scheme is referred to as the prechirp technique.

We can use Figure 3.3 to understand how prechirping helps. As discussed in Section 3.3, for values of C such that $\beta_2 C < 0$, a chirped Gaussian pulse compresses initially before its width increases. Clearly, a suitably chirped pulse can propagate over longer distances before it broadens outside its allocated bit slot. As a rough estimate of the improvement, assume that pulse broadening by a factor of up to $\sqrt{2}$ is tolerable. Using Eq. (3.3.11) with $b_f = \sqrt{2}$, the maximum transmission distance is found to be

$$L = \frac{C + \sqrt{1+2C^2}}{1+C^2} L_D, \tag{7.6.2}$$

where $L_D = T_0^2/|\beta_2|$ is the dispersion length. For unchirped Gaussian pulses, $C = 0$ and $L = L_D$. However, L increases by 36% for $C = 1$. The maximum improvement by a factor of $\sqrt{2}$ occurs for $C = 1/\sqrt{2}$. These features clearly illustrate that the prechirp technique requires careful optimization. Even though the pulse shape is rarely Gaussian in practice, the prechirp technique can increase the transmission distance by 50% or more. As early as 1986, a super-Gaussian model suitable for nonreturn-to-zero (NRZ) transmission predicted such an improvement [121].

The prechirp technique was considered during the 1980s in the context of directly modulated semiconductor lasers [121]–[123]. Such lasers chirp the pulse automatically through the carrier-induced index changes. Unfortunately, the chirp parameter C is negative for directly modulated semiconductor lasers. Since β_2 in the 1.55-μm wavelength region is also negative for standard fibers, the condition $\beta_2 C < 0$ is not satisfied. In fact, as seen in Figure 3.3, the chirp induced by direct modulation reduces the transmission distance drastically when standard fibers are used. In contrast, if dispersion-shifted fibers with normal GVD ($\beta_2 > 0$) are employed, the same chirp helps to improve the system performance.

In the case of external modulation, optical pulses are nearly chirp-free. The prechirp technique in this case imposes a frequency chirp with a positive value of the chirp parameter C so that the condition $\beta_2 C < 0$ is satisfied. Several schemes have been proposed for this purpose [124]–[130]. In a simple approach shown schematically in Figure 7.23, the carrier frequency of the DFB laser is first modulated (FM) before the laser output is passed to an external modulator for amplitude modulation (AM). The resulting optical signal exhibits simultaneous AM and FM [127]. From a practical standpoint, the FM of the optical carrier can be realized by modulating the current injected into the DFB laser by a small amount ($\sim$1 mA). Although such a direct modulation of the DFB laser also modulates the optical power sinusoidally, the magnitude is small enough that it does not interfere with the detection process.

It is clear from Figure 7.23 that the FM of the optical carrier, followed by external AM, generates a signal that consists of chirped pulses. The amount of chirp can be determined as follows. Assuming that the pulse shape is Gaussian, the optical signal can be written as

$$E(0,t) = A_0 \exp(-t^2/T_0^2) \exp[-i\omega_0(1 + \delta \sin \omega_m t)t], \tag{7.6.3}$$

where the carrier frequency ω_0 of the pulse is modulated sinusoidally at the frequency ω_m with a modulation depth δ. Near the pulse center, $\sin(\omega_m t) \approx \omega_m t$, and Eq. (7.6.3) becomes

$$E(0,t) \approx A_0 \exp\left[-\frac{1+iC}{2}\left(\frac{t}{T_0}\right)^2\right] \exp(-i\omega_0 t), \tag{7.6.4}$$

where the chirp parameter C is given by

$$C = 2\delta \omega_m \omega_0 T_0^2. \tag{7.6.5}$$

Both the sign and magnitude of the chirp parameter C can be controlled by changing the FM parameters δ and ω_m.

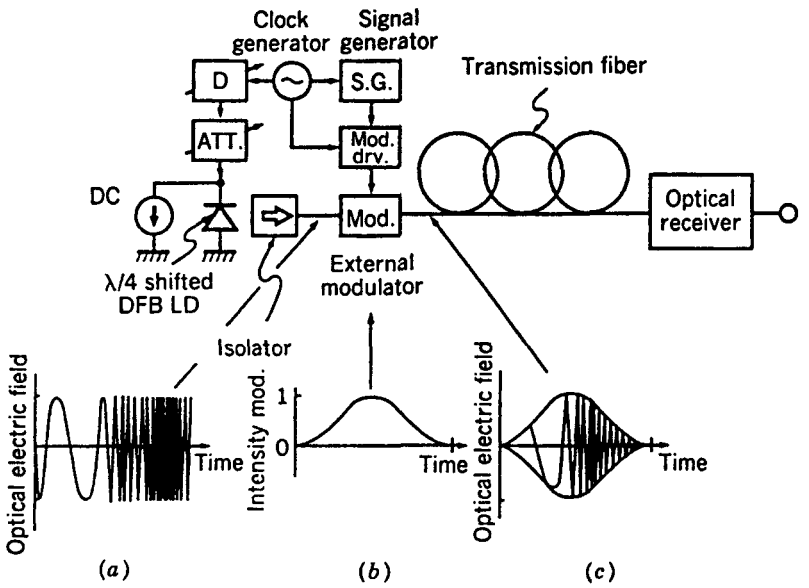

Figure 7.23: Schematic of the prechirp technique used for dispersion compensation: (a) FM output of the DFB laser; (b) pulse shape produced by external modulator; and (c) prechirped pulse used for signal transmission. (After Ref. [127]; ©1994 IEEE.)

Phase modulation of the optical carrier also leads to a positive chirp, as can be verified by replacing Eq. (7.6.3) with

$$E(0,t) = A_0 \exp(-t^2/T_0^2) \exp[-i\omega_0 t + i\delta \cos(\omega_m t)] \tag{7.6.6}$$

and using $\cos x \approx 1 - x^2/2$. An advantage of the phase-modulation technique is that the external modulator itself can modulate the carrier phase. The simplest solution is to employ an external modulator whose refractive index can be changed electronically in such a way that it imposes a frequency chirp with $C > 0$ [124]. As early as 1991, a 5-Gb/s signal was transmitted over 256 km [125] using a $LiNbO_3$ modulator such that values of C were in the range of 0.6 to 0.8. These experimental values are in agreement with the Gaussian-pulse theory on which Eq. (7.6.2) is based. Other types of semiconductor modulators, such as an electroabsorption modulator [126] or a Mach–Zehnder (MZ) modulator [128], can also chirp the optical pulse with $C > 0$, and have been used to demonstrate transmission beyond the dispersion limit [129]. With the development of DFB lasers integrated with an electroabsorption modulator, the implementation of the prechirp technique has become quite practical. In a 1996 experiment, a 10-Gb/s NRZ signal was transmitted over 100 km of standard fiber using such a transmitter [130].

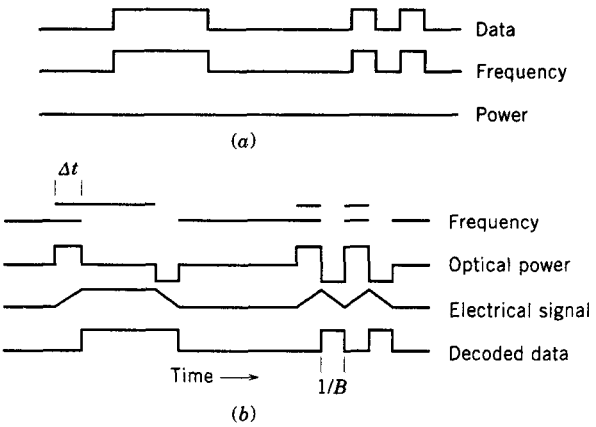

Figure 7.24: Dispersion compensation using FSK coding: (a) Optical frequency and power of the transmitted signal; (b) frequency and power of the received signal and the electrically decoded data. (After Ref. [131]; ©1994 IEEE.)

7.6.2 Novel Coding Techniques

The dispersion problem can also be alleviated to some extent by adopting a suitable modulation format. In one approach, referred to as *dispersion-supported transmission*, a frequency-shift keying (FSK) format is used for signal transmission [131]–[135]. The FSK signal is generated by switching the laser wavelength by a constant amount $\Delta\lambda$ between 1 and 0 bits while leaving the power unchanged. During propagation inside the fiber, the two wavelengths travel at slightly different speeds. The time delay between the 1 and 0 bits is determined by the wavelength shift $\Delta\lambda$ and is given by $\Delta T = DL\Delta\lambda$. The wavelength shift $\Delta\lambda$ is chosen such that $\Delta T = 1/B$. Figure 7.24 shows schematically how the one-bit delay produces a three-level optical signal at the receiver. In essence, because of fiber dispersion, the FSK signal is converted into a signal whose amplitude is modulated. The signal can be decoded at the receiver by using an electrical integrator in combination with a decision circuit [131].

Several transmission experiments have shown the usefulness of the dispersion-supported transmission scheme [131]–[133]. All these experiments were concerned with increasing the transmission distance of a 1.55-μm lightwave system operating at 10 Gb/s or more over the standard fibers. In 1994, the transmission of a 10-Gb/s signal over 253 km of standard fiber was realized [131]. By 1998, in a 40-Gb/s field trial, the signal was transmitted over 86 km of standard fiber [133]. These values should be compared with the prediction of Eq. (7.1.1). Clearly, the transmission distance can be improved by a large factor by employing the FSK technique when the system is properly designed [135].

Another approach to increasing the transmission distance consists of transmitting an optical signal whose bandwidth at a given bit rate is smaller compared with that of the standard on–off coding technique. One scheme makes use of *duobinary coding* [136]. This coding scheme reduces the signal bandwidth by 50% by adding two successive bits in the digital bit stream, thus forming a three-symbol duobinary code

at half the bit rate. Since both the 01 and 10 combinations add to 1, the signal phase must be modified to distinguish between the two. Since the GVD-induced degradation depends on signal bandwidth, transmission distance is considerably larger for a duobinary signal [137]–[142].

In a 1994 experiment designed to compare the binary and duobinary schemes, a 10-Gb/s signal could be transmitted over distances 30 to 40 km longer by replacing binary coding with duobinary coding [137]. The duobinary scheme can be combined with the prechirping technique. Indeed, transmission of a 10-Gb/s signal over 160 km of a standard fiber was realized in 1994 by combining duobinary coding with an external modulator capable of producing a frequency chirp with $C > 0$ [137]. Since chirping increases the signal bandwidth, it is hard to understand why it would help. It appears that phase reversals occurring in practice when a duobinary signal is generated are primarily responsible for improvement realized with duobinary coding [138]. A new dispersion-management scheme, called the *phase-shaped* binary transmission, has been proposed to take advantage of phase reversals [139]. The use of duobinary transmission increases signal-to-noise requirements and requires decoding at the receiver. Despite these shortcomings, it is useful for upgrading the existing terrestrial lightwave systems to bit rates of 10 Gb/s and more [140]–[142].

7.6.3 Nonlinear Prechirp Techniques

A simple nonlinear prechirp technique, demonstrated in 1989, amplifies the transmitter output using a semiconductor optical amplifier (SOA) operating in the gain-saturation regime [143]–[147]. As discussed in Section 5.5.4 of LT1, gain saturation leads to time-dependent variations in the carrier density, which, in turn, chirp the amplified pulse through changes in the refractive index. The amount of chirp depends on the input pulse shape and is nearly linear over most of the pulse. The SOA not only amplifies the pulse but also chirps it such that the chirp parameter $C > 0$. Because of this chirp, the input pulse can be compressed in a fiber with $\beta_2 < 0$. Such a compression was observed in an experiment in which 40-ps input pulses were compressed to 23 ps when they were propagated over 18 km of standard fiber [143].

The potential of this technique for dispersion compensation was demonstrated in a 1989 experiment by transmitting a 16-Gb/s signal over 70 km of fiber [144]. Figure 7.25 compares the streak-camera traces of the signal obtained with and without dispersion compensation. From Eq. (7.1.1), in the absence of amplifier-induced chirp, the transmission distance at 16 Gb/s is limited to about 14 km for a fiber with $D = 15$ ps/(km-nm). The use of the amplifier in the gain-saturation regime increased the transmission distance five-fold, a feature that makes this approach to dispersion compensation quite attractive. It has the added benefit that it can compensate for the coupling and insertion losses that invariably occur in a transmitter by amplifying the signal before it is launched into the optical fiber. Moreover, this technique can be used for the simultaneous compensation of fiber losses and GVD if SOAs are used as in-line amplifiers [147].

A nonlinear medium can also be used to prechirp the pulse. As discussed in Section 4.1, the nonlinear phenomenon of SPM chirps an optical pulse as it propagates down a fiber. Thus, a simple prechirp technique consists of passing the transmitter output

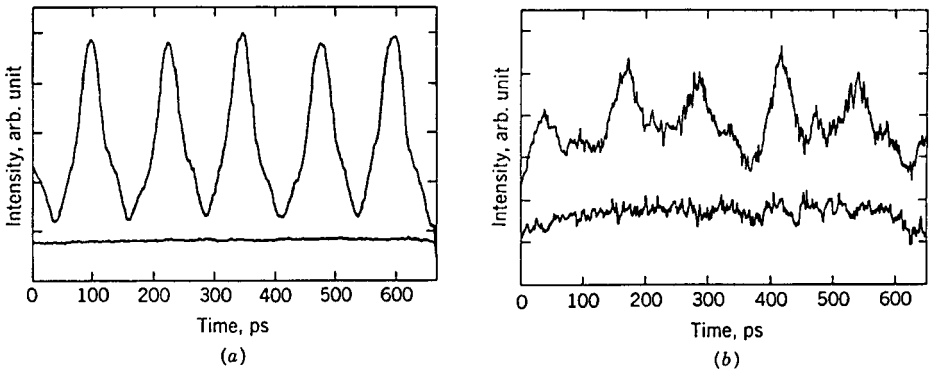

Figure 7.25: Streak-camera traces of the 16-Gb/s signal transmitted over 70 km of standard fiber (a) with and (b) without SOA-induced chirp. Bottom trace shows the background level in each case. (After Ref. [144]; ©1989 IEE.)

through a fiber of suitable length before launching it into the communication link. From Eq. (4.1.5), the phase of the optical signal is modulated by SPM as

$$A(0,t) = \sqrt{P(t)}\exp[i\gamma L_m P(t)], \tag{7.6.7}$$

where $P(t)$ is the power of the pulse and L_m is the length of the nonlinear fiber. In the case of Gaussian pulses for which $P(t) = P_0\exp(-t^2/T_0^2)$, the chirp is nearly linear, and Eq. (7.6.7) can be approximated by

$$A(0,t) \approx \sqrt{P_0}\exp\left[-\frac{1+iC}{2}\left(\frac{t}{T_0}\right)^2\right]\exp(-i\gamma L_m P_0), \tag{7.6.8}$$

where the chirp parameter is given by $C = 2\gamma L_m P_0$. For $\gamma > 0$, the chirp parameter C is positive, and is thus suitable for dispersion compensation. The transmission fiber itself can be used for chirping the pulse. This approach was suggested in a 1986 study; it indicated the possibility of doubling the transmission distance by optimizing the average power of the input signal [148].

7.6.4 Electronic Compensation Techniques

Electronic techniques can be used for compensation of GVD within the receiver. The philosophy behind this approach is that even though the optical signal has been degraded by GVD, one may be able to equalize the effects of dispersion electronically if the fiber acts as a *linear system*. It is relatively easy to compensate for dispersion if a heterodyne receiver is used for signal detection. Such a receiver first converts the optical signal into a microwave signal at the intermediate frequency ω_{IF} while preserving both the amplitude and phase information. A microwave bandpass filter whose impulse response is governed by the transfer function

$$H(\omega) = \exp[-i(\omega - \omega_{IF})^2\beta_2 L/2], \tag{7.6.9}$$

where L is the fiber length, should restore the signal to its original form. This conclusion follows from the standard theory of linear systems. This technique is most practical for dispersion compensation in coherent lightwave systems [149]. In a 1992 experiment, a 31.5-cm-long *microstrip line* was used for dispersion equalization [150]. Its use made it possible to transmit an 8-Gb/s signal over 188 km of standard fiber. In a 1993 experiment, the technique was extended to homodyne detection [151], and a 6-Gb/s signal could be recovered at the receiver after propagating over 270 km of standard fiber. Microstrip lines can be designed to compensate for GVD acquired over fiber lengths as long as 4,900 km for a lightwave system operating at a bit rate of 2.5 Gb/s [152].

An electronic dispersion equalizer can be used in the case of direct-detection receivers. A linear electronic circuit cannot compensate GVD in this case. The problem lies in the fact that all phase information is lost during direct detection as a photodetector responds to optical intensity only. As a result, no linear equalization technique can recover a signal that has spread outside its allocated bit slot. Nevertheless, several nonlinear equalization techniques have been developed that permit recovery of the degraded signal [153]–[156]. In one method, the decision threshold, normally kept fixed at the center of the eye diagram, is varied from bit to bit depending on the preceding bits. In another, the decision about a given bit is made after examining the analog waveform over a multiple-bit interval surrounding the bit in question [153]. The main difficulty with all such techniques is that they require electronic logic circuits, which must operate at the bit rate and whose complexity increases exponentially with the number of bits over which an optical pulse has spread because of GVD-induced pulse broadening. Nevertheless, electronic equalization at bit rates of up to 10 Gb/s has been realized [157]–[159]. As discussed later, an electronic equalizer can also be used for PMD compensation.

7.7 High-Speed Lightwave Systems

Although most commercial WDM lightwave systems operate each channel at 10 Gb/s, the bit rate of individual channels could be boosted to 40 Gb/s by 2002, and efforts were underway to increase the channel bit rate to 160 Gb/s and beyond. For such high-speed systems, the management of channel dispersion poses additional problems. In this section we focus on several relevant issues.

7.7.1 Tunable Dispersion Compensation

It is difficult to attain full GVD compensation for all channels in a WDM system. A small amount of residual dispersion remains uncompensated and often becomes a concern for long-haul systems. For a link of length L, this residual dispersion is given by $d_r = \int_0^L D(z)\,dz$, where $D(z)$ denotes local dispersion along the link. In laboratory experiments, a postcompensation technique is often adopted in which the residual dispersion for individual channels is compensated by adding adjustable lengths of a DCF at the receiver end (dispersion trimming). This technique is not suitable for commercial WDM systems for several reasons. First, the exact amount of channel-dependent

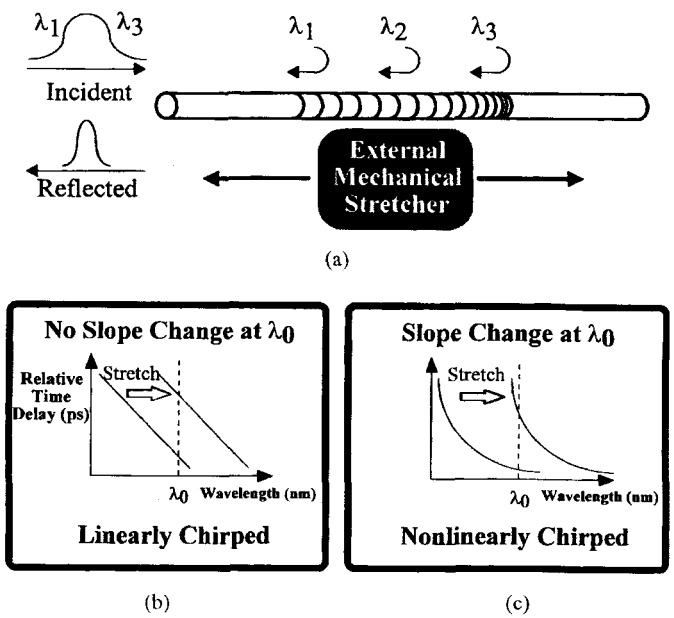

Figure 7.26: (a) Schematic of tunable dispersion compensation by stretching a nonlinearly chirped fiber grating. Group delay as a function of wavelength for (b) linearly and (c) nonlinearly chirped fiber gratings. (After Ref. [160]; ©1999 IEEE.)

residual dispersion is not always known because of uncontrollable variations in the dispersion of fiber segments forming the transmission path. Second, even the path length may change in reconfigurable optical networks. Third, as the single-channel bit rate increases toward 40 Gb/s and beyond, the tolerable value of the residual dispersion becomes so small that even temperature-induced changes in GVD become a concern. For these reasons, the best approach may be to adopt a tunable dispersion-compensation scheme that allows the GVD control for each channel in a dynamic fashion.

Several techniques for tunable dispersion compensation have been developed and used for system experiments [160]–[177]. Most of them make use of a fiber Bragg grating whose dispersion is tuned by changing the optical period $\bar{n}\Lambda$ of the grating. In one scheme, the grating is made with a nonlinear chirp (Bragg wavelength increases nonlinearly along the grating length) that can be changed by stretching the grating with a piezoelectric transducer [160]. Figure 7.26 shows schematically why a nonlinear chirp is required for tuning dispersion. In a linearly chirped grating, the slope of group delay (responsible for dispersion) at a given wavelength does not change with stretching. However, this slope can be changed by a large factor when the chirp is nonlinear. Mathematically, stress-induced changes in the mode index $\bar{n}$ change the local Bragg wavelength as $\lambda_B(z) = 2\bar{n}(z)\Lambda(z)$. For such a grating, Eq. (7.4.7) is replaced by

$$D_g(\lambda) = \frac{d\tau_g}{d\lambda} = \frac{2}{c}\frac{d}{d\lambda}\left(\int_0^{L_g} \bar{n}(z)\,dz\right), \tag{7.7.1}$$

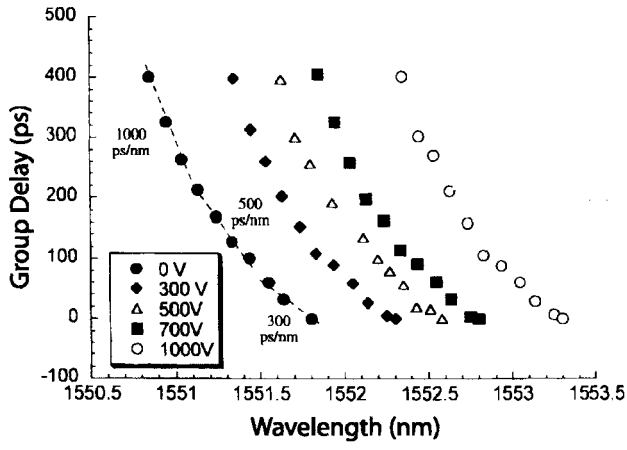

Figure 7.27: Group delay as a function of wavelength at several applied voltages for a nonlinearly chirped fiber grating. (After Ref. [160]; ©1999 IEEE.)

where τ_g is the group delay and L_g is the grating length. The value of D_g at any wavelength can be altered by changing the mode index $\bar{n}$ (through heating or stretching), resulting in tunable dispersion characteristics for the Bragg grating.

The stretching technique has been used with success since 1999 to tune the dispersion provided by a nonlinearly chirped fiber grating [160]. The grating is placed on a mechanical stretcher and a piezoelectric transducer is used to stretch it by applying an external voltage. Figure 7.27 shows the group-delay characteristics of a 5-cm-long grating as the voltage is changed from 0 to 1,000 V. For a fixed channel wavelength, d_a can be changed from -300 to $-1{,}000$ ps/nm by changing the voltage, resulting in a tuning range of 700 ps/nm. The same technique can be extended to provide tunable compensation for multiple channels by using a sampled grating with nonlinear chirp. However, it suffers from a relatively large third-order dispersion that affects each channel. This problem can be solved by cascading two identical gratings in a fashion such that their chirps are opposite in nature [167].

In a different approach to realizing tunable dispersion, the grating is made with either no chirp or with a linear chirp, and a temperature gradient is used to produce a controllable chirp. Such distributed heating requires a thin-film heater deposited on the outer surface of the fiber whose core contains the grating. In a simple technique [162], film thickness is changed along the grating length to create a temperature gradient when a constant voltage is applied across the film. Figure 7.28(a) shows the reflection spectra of a 8-cm-long grating at three voltage levels. The total dispersion, calculated from the group delay $\tau_g(\lambda)$, is displayed in Figure 7.28(b) as a function of applied voltage. The grating is initially unchirped and has a narrow stop band that shifts and broadens as the grating is chirped through nonuniform heating. Physically, the Bragg wavelength λ_B changes along the grating because the optical period $\bar{n}(z)\Lambda$ becomes z-dependent when a temperature gradient is established along the grating. The total dispersion $D_g L_g$ can be changed in the range of -500 to $-2{,}200$ ps/nm by this approach. Such gratings can

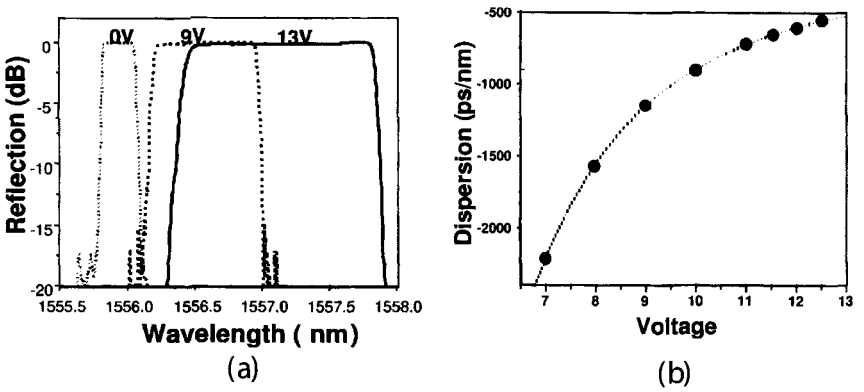

Figure 7.28: (a) Reflection spectrum and (b) total GVD as a function of voltage for a fiber grating with temperature gradient. The inset shows $\tau_g(\lambda)$ at several voltages. (After Ref. [162]; ©2000 IEEE; reprinted with permission.)

be used to provide tunable dispersion for 10-Gb/s systems.

A segmented thin-film heater is also used for creating a temperature gradient as it provides better temperature control along the grating length. Figure 7.29 shows the design of such a device schematically [165]. The thin-film heater consists of 32 chromium heating elements formed on the silica substrate on which the grating is mounted. Each heating element is 60 μm wide and 1.245 mm long. The spacing between two neighboring elements is only 5 μm, as seen in the inset. Six Peltier elements under the silica substrate maintain the center wavelength of the grating as the temperature distri-

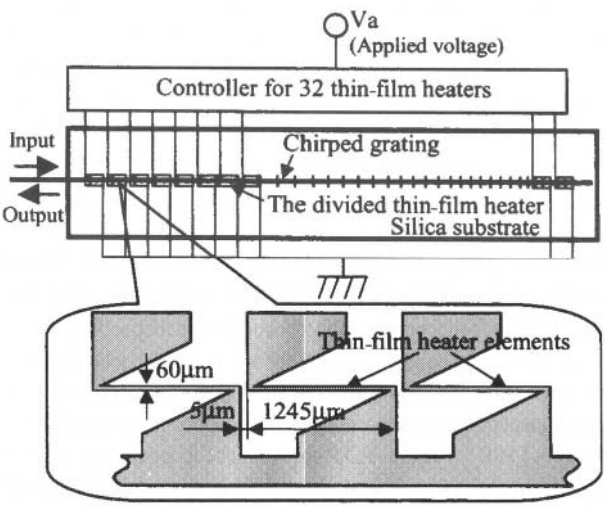

Figure 7.29: Schematic of a device used for tunable dispersion compensation. A chirped fiber grating is heated using 32 thin-film segments. (After Ref. [165]; ©2001 IEEE.)

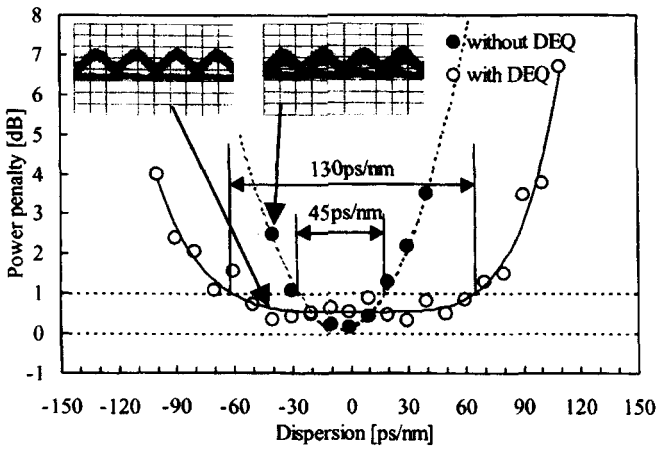

Figure 7.30: Measured power penalties in a 40-Gb/s experiment as a function of residual dispersion. Solid and dashed curves show results with (filled circles) and without (empty circles) the dispersion equalizer (DEQ). Recorded eye diagrams are also shown at two data points indicated by arrows. (After Ref. [165]; ©2001 IEEE.)

bution is changed by applying different voltages to each element. Both the dispersion and dispersion slope of such a device can be controlled electronically. In contrast to the stretching technique that requires large voltages, only a few volts are required to change the dispersion slope from $+100$ to -300 ps/nm^2.

Such a tunable device was used for a system operating at 40 Gb/s. Figure 7.30 shows the measured power penalties as a function of residual dispersion. The dashed curve shows the behavior expected in the absence of tunable grating. Accumulated dispersion should be within ± 30 ps/nm for less than 1-dB penalty. As shown by the solid curve, this tolerable range can be more than doubled by employing the chirped grating with tunable dispersion [165]. The two eye diagrams shown as an inset were obtained for a net dispersion of -40 ps/nm. They clearly indicate the improvement in the system performance that can be realized with tunable dispersion compensation.

A different kind of device, known as a virtually imaged phased array, can also provide tunable dispersion [178]–[180]. It is based on free-space optics; Figure 7.31 shows its design schematically. Dispersed signal is first collimated and focused using a cylindrical lens onto a tilted glass plate with 100% and $\approx$98% reflecting layers on the front and back surfaces [178]. This arrangement creates multiple beams that appear to diverge from an array of virtual images. Interference among these beams produces output at an angle that varies with wavelength. Light is then focused on a three-dimensional mirror that provides controllable wavelength-dependent group delay by just moving the mirror along one axis [180]. Figure 7.31 shows (a) the insertion loss and (b) group delay of such a dispersion compensator as the GVD is varied from -800 to $+800$ ps/nm. It was used in 2002 to realize the transmission of 88 WDM channels, each operating at 43 Gb/s, over 600 km of fiber whose dispersion varied from 7.9 to 9.7 ps/(km-nm) in the wavelength range of 1,550 to 1,580 nm.

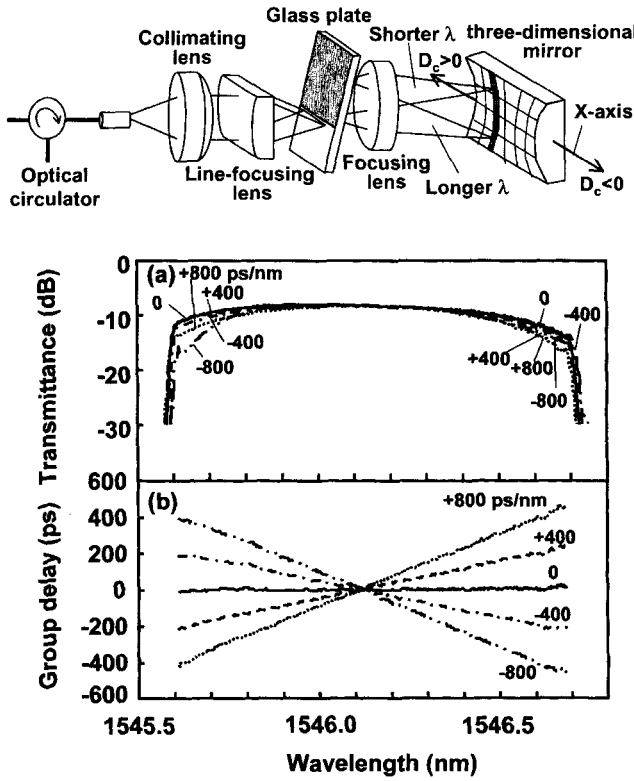

Figure 7.31: Schematic of a virtually imaged phased array providing tunable dispersion compensation. (a) Insertion loss and (b) group delay versus wavelength as dispersion is varied from −800 to +800 ps/nm. (After Ref. [180]; ©2002 IEEE.)

7.7.2 Higher-Order Dispersion Management

When the bit rate of a single channel exceeds 40 Gb/s (through the used of time-division multiplexing, e.g.), the third- and higher-order dispersive effects begin to influence the optical signal. For example, the bit slot at a bit rate of 160 Gb/s is only 6.25 ps wide. An RZ optical signal at such a high bit rate consists of pulses of width <5 ps. Equation (3.3.46) can be used to estimate the maximum transmission distance L, limited by the TOD β_3, when the second-order dispersion (GVD) is fully compensated. The result is found to be

$$L \leq 0.034(|\beta_3|B^3)^{-1}. \tag{7.7.2}$$

This limitation is shown in Figure 3.4 by the dashed line. At a bit rate of 200 Gb/s, L is limited to about 50 km and drops to only 3.4 km at 500 Gb/s if we use a typical value of $\beta_3 = 0.08$ ps^3/km. Clearly, it is essential to develop devices that can compensate for both the GVD and TOD simultaneously when the single-channel bit rate exceeds 100 Gb/s [181]–[195].

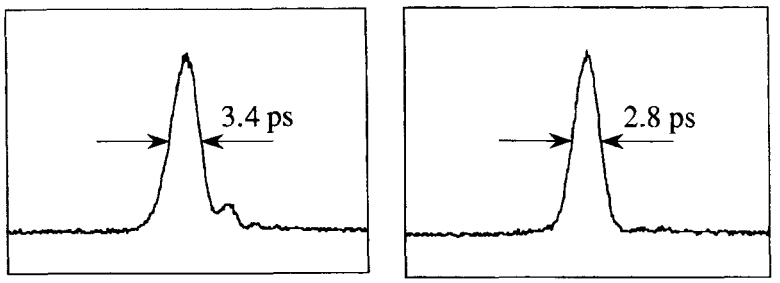

Figure 7.32: Pulse shapes after a 2.1-ps input pulse has propagated over 100 km of dispersion-shifted fiber ($\beta_2 = 0$). Left and right traces compare the improvement realized by compensating the third-order dispersion. (After Ref. [182]; ©1998 IEEE.)

The simplest solution to TOD compensation is provided by DCFs designed to have a negative dispersion slope so that both β_2 and β_3 have opposite signs in comparison with the standard fibers. The necessary conditions for designing such fibers is given in Eq. (7.2.5). Thus, the DCFs used for the compensation of dispersion slope in WDM systems also provide control of third-order dispersion for each channel. The only problem with DCFs is that their dispersion characteristics are not easily tunable. As a result, system performance can be easily compromised if link dispersion changes because of temperature or other environmental changes.

The tunable compensation of dispersion slope is possible through optical filters. Planar lightwave circuits based on cascaded MZ interferometric filters have proved quite successful because of the programmable nature of such filters. As early as 1996, such a filter was designed to have a dispersion slope of -15.8 ps/nm^2 over a 170-GHz bandwidth and used to compensate third-order dispersion over 300 km of a dispersion-shifted fiber with $\beta_3 \approx 0.05$ ps/(km-nm^2) at the operating wavelength [182]. Figure 7.32 compares the pulse shapes at the fiber output observed with and without β_3 compensation when a 2.1-ps pulse was transmitted over 100 km of such a fiber. The equalizing filter eliminates the oscillatory tail and reduces the width of the main peak from 3.4 to 2.8 ps. The residual increase in the pulse width from its input value of 2.1 ps is partly due to PMD.

Chirped fiber gratings are often preferred in practice because of their all-fiber nature. Long fiber gratings ($\sim$1 m) were developed by 1997 for this purpose [183]. In 1998, a nonlinearly chirped fiber grating was capable of compensating the TOD over 6 nm for distances as long as 60 km [184]. The cascading of several chirped gratings can provide a dispersion compensator that has arbitrary dispersion characteristics and is capable for compensating dispersion to all higher orders. Figure 7.33(a) shows a simple configuration for compensating the TOD β_3 of a fiber [185]. Two identical chirped fiber gratings are cascaded through an optical circulator, but one of them is flipped over so that their chirps are opposite in nature. As the group-delay slopes are equal but of opposite signs for the two gratings, the combination provides no net GVD. However, their TOD contributions add up to produce a nearly parabolic shape for the relative group delay, as shown in Figure 7.33(b).

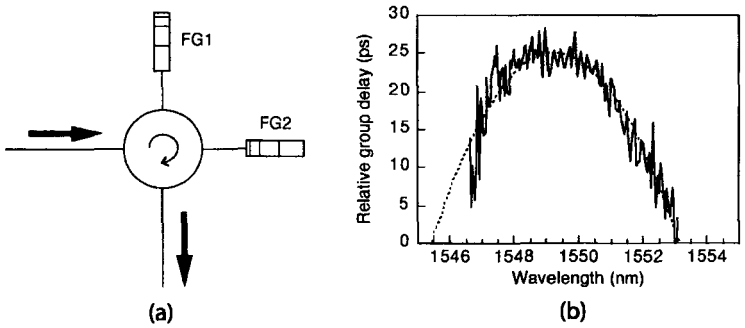

Figure 7.33: (a) Compensation of third-order dispersion by cascading two identical fiber gratings (FG). (b) Resulting group delay (solid curve) with a parabola (dotted curve) superimposed on it. (After Ref. [185]; ©2000 IEEE.)

An arrayed-waveguide grating [186] or a sampled fiber grating [80] can also compensate for second- and third-order dispersions simultaneously. Although a nonlinearly chirped sampled grating can provide tunable dispersion for several channels simultaneously [189], its bandwidth is still limited. An arrayed-waveguide grating in combination with a spatial phase filter can provide dispersion-slope compensation over a bandwidth as large as 8 THz and should be suitable for 40-Gb/s multichannel systems [190]. The feasibility of transmitting a 100-Gb/s signal over 10,000 km has also been investigated using midspan optical phase conjugation in combination with third-order dispersion compensation [191].

Tunable compensation of dispersion slope can also be realized by integrating a segmented thin-film heater with a chirped fiber grating. The device design is similar to that shown in Figure 7.34. In a 2004 experiment, a 4-cm-long grating was heated in a distributed fashion using 32 thin-film segments. A DCF module was used after the grating to ensure that accumulated second-order dispersion was zero at the center wavelength of the channel. It was possible to vary the dispersion slope from -20 to $+20$ ps/nm^2 by adjusting temperature distribution along the grating.

In a different approach, two fiber gratings, linearly or nonlinearly chirped by applying a strain, were cascaded in series through an optical circulator [194]. Both gratings were mounted on a substrate that could be bent by moving a block, as shown in Figure 7.34. It was possible to change only the dispersion slope from nearly 0 to -58 ps/nm^2 over a bandwidth of 1.7 nm without affecting the Bragg wavelength of the grating.

Several experiments have explored the possibility of transmitting a single channel at bit rates of more than 200 Gb/s [196]–[200]. In a 1996 experiment [196], a 400-Gb/s signal was transmitted by managing the fiber dispersion and transmitting 0.98-ps pulses inside a 2.5-ps time slot. Without compensation of the third-order dispersion, the pulse broadened to 2.3 ps after 40 km and exhibited a long oscillatory tail extending over 6 ps, a characteristic feature of the third-order dispersion [116]. With partial compensation of third-order dispersion, the oscillatory tail disappeared, and the pulse width reduced to 1.6 ps, making it possible to recover the 400-Gb/s data with high accuracy. Optical pulses as short as 0.4 ps were used in 1998 to realize a bit rate of 640 Gb/s [197]. In a

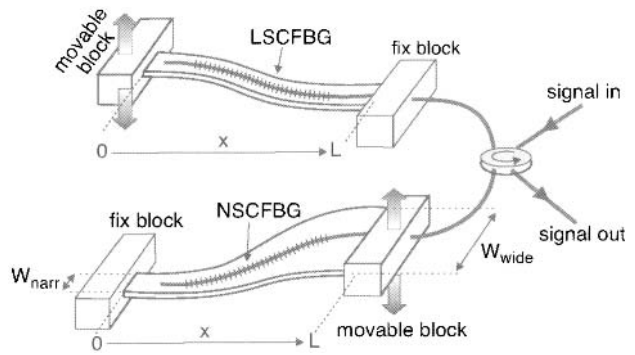

Figure 7.34: Schematic of a device used for tunable dispersion-slope compensation. A linearly strain-chirped fiber Bragg grating (LSCFBG) is cascaded with another that is nonlinearly chirped (NSCFBG) using an optical circulator. (After Ref. [194]; ©2004 IEEE.)

2001 experiment, the bit rate was extended to 1.28 Tb/s by transmitting 380-fs pulses over 70 km of fiber [200]. The propagation of such short pulses requires compensation of second-, third-, and fourth-order dispersions simultaneously. It turns out that if sinusoidal phase modulation of the right kind is applied to the linearly chirped pulse before it is transmitted through a GVD-compensated fiber, it can compensate for both the third- and fourth-order dispersions.

7.7.3 PMD Compensation

As discussed in Section 3.4, PMD leads to distortion of optical pulses because of random variations in the birefringence of an optical fiber along its length. This distortion occurs in addition to GVD-induced pulse broadening. The use of dispersion management can eliminate GVD-induced broadening but does not affect the PMD-induced degradation of an optical signal. For this reason, PMD has become a major source of concern for modern dispersion-managed lightwave systems [201]–[214].

Before considering the techniques used for PMD compensation, it is important to obtain an order-of-magnitude estimate of the maximum link length for uncompensated systems. Equation (3.4.5) shows that the RMS value of the differential group delay (DGD) for a link of length L is given by $\Delta\tau_{\rm RMS} = D_p\sqrt{L}$, where D_p is the PMD parameter and $\Delta\tau$ is the DGD along the two principal states of polarization (PSPs). It is important to note that the instantaneous value of $\Delta\tau$ fluctuates with time over a wide range because of temperature and other environmental factors [202]. If $\Delta\tau$ exceeds the bit slot, the system will stop functioning properly; this is referred to as fading or *outage* in analogy with a similar effect occurring in radio systems [201].

The performance of a PMD-limited system is quantified using the concept of the outage probability, which should be below a prescribed value (often set near 10^{-5} or 5 min/year) for most systems [201]. An accurate estimate of outage probability is of considerable interest and it often requires extensive numerical simulations [205]–[214]. In general, outage probability depends on the modulation format used for transmitting

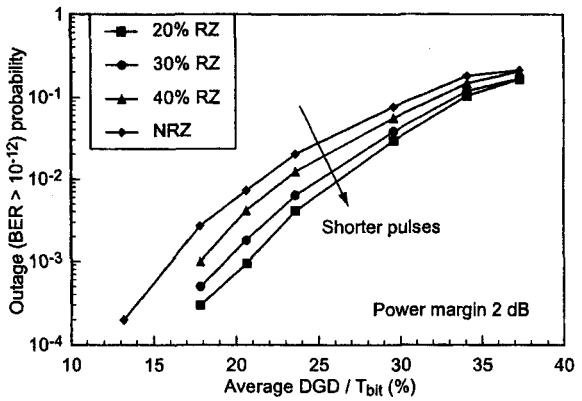

Figure 7.35: Outage probability as a function of average DGD (normalized to bit slot) for NRZ and RZ formats. Duty cycle is varied from 20 to 40% in the case of RZ pulses. (After Ref. [209]; ©2002 IEEE.)

the signal across a fiber link. Figure 7.35 shows outage probability as a function of average DGD for the NRZ and RZ formats assuming that outage occurs when the power penalty exceeds 2 dB to maintain a BER of 10^{-12}. In general, the performance is better for the RZ format with shorter pulses. The main conclusion is that the RMS value $\Delta\tau_{\text{RMS}}$ of DGD should only be a small fraction of the bit slot at a given bit rate B. The exact value of this fraction varies in the range of 0.1 to 0.15 depending on the modulation format and other design details of a lightwave system. If we use 10% as a conservative criterion for this ratio and use $B\Delta\tau_{\text{RMS}} = 0.1$, the system length and the bit rate are related to the PMD parameter D_p of the fiber by the condition

$$B^2L < (10D_p)^{-2}. \tag{7.7.3}$$

We can use this condition to estimate the maximum PMD-limited distance over which a system can operate at a given bit rate B. In the case of "old" fiber links installed using standard fibers, the condition (7.7.3) becomes $B^2L < 10^4$ (Gb/s)^2-km, if we use $D_p = 1$ ps/$\sqrt{\text{km}}$ as a representative value. Such fibers require PMD compensation at $B = 10$ Gb/s when the link length exceeds even 100 km. In contrast, modern fibers have typically D_p below 0.1 ps/$\sqrt{\text{km}}$. For systems designed using such fibers, B^2L can exceed 10^6 (Gb/s)^2-km. As a result, PMD compensation is not necessary at 10 Gb/s but may be required at 40 Gb/s if the link length exceeds 600 km. It should be stressed that Eq. (7.7.3) provides only an order-of-magnitude estimate. Moreover, this condition can be relaxed when the technique of forward error correction (FEC) is employed at the receiver. Indeed, system length can be increased considerably with the use of FEC [209].

The preceding discussion shows that PMD can limit the performance of long-haul systems when the channel bit rate is close to 10 Gb/s or more. For this reason, techniques for compensating PMD attracted attention as early as 1994 and have continued to evolve since then [215]–[227]. They can be classified as being optical or electrical. Figure 7.36 shows the basic idea behind the electrical and optical PMD compensation

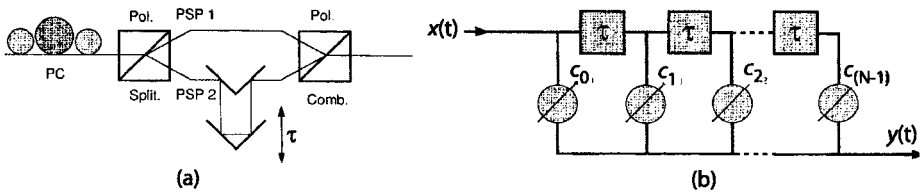

Figure 7.36: Schematic illustration of (a) optical and (b) electrical PMD compensators. (After Ref. [219]; ©2000 Elsevier.)

schemes. An electrical PMD equalizer corrects for the PMD effects within the receiver using a transversal filter. The filter splits the electrical signal $x(t)$ into a number of branches using multiple tapped delay lines and then combines the output as

$$y(t) = \sum_{m=0}^{N-1} c_m x(t - m\tau), \tag{7.7.4}$$

where N is the total number of taps, τ is the delay time, and c_m is the tap weight for the mth tap. Tap weights are adjusted in a dynamic fashion using a control algorithm in such a way that the system performance is improved [219]. The error signal for the control electronics is often based on the closing of the "eye" at the receiver. Such an electrical technique cannot eliminate the PMD effects completely as it does not consider the PMD-induced delay between the two PSPs. On the positive side, it corrects for all sources of degradation that lead to eye closing.

An optical PMD compensator also makes use of a delay line. It can be inserted periodically all along the fiber link (at the amplifier locations, e.g.) or just before the receiver. Typically, the PMD-distorted signal is separated into two components along the PSPs using a polarization controller (PC) followed by a polarization beam splitter; the two components are combined, as seen in Figure 7.36(a), after introducing an adjustable delay in one branch through a variable delay line. A feedback loop is still needed to obtain an error signal that is used to adjust the polarization controller in response to the environmental changes in the fiber PSPs. The success of this technique depends on the ratio $L/L_{\rm PMD}$ for a fiber of length L, where $L_{\rm PMD} = (T_0/D_p)^2$ and T_0 is the pulse width [228]. Considerable improvement is expected as long as this ratio does not exceed 4. Because $L_{\rm PMD}$ is close to 10,000 km for $D_p \approx 0.1$ ps/$\sqrt{\rm km}$ and $T_0 = 10$ ps, such a PMD compensator can work over transoceanic distances for 10-Gb/s systems.

Several other all-optical techniques can be used for PMD compensation [221]–[224]. Examples include $LiNbO_3$-based distributed compensator [223], ferroelectric liquid crystals, twisted polarization-maintaining fibers [218], optical all-pass filters [226], and birefringent chirped fiber gratings. Figure 7.37 shows how a grating-based PMD compensator works [217]. Because of a large birefringence, the two field components polarized along the slow and fast axis have different Bragg wavelengths and experience slightly shifted stop bands. As a result, they are reflected at different places within the grating and undergo a differential group delay that can compensate for the PMD-induced group delay. The delay is wavelength-dependent because of the chirped nature of the grating. Moreover, it can be tuned over several nanometers by stretching

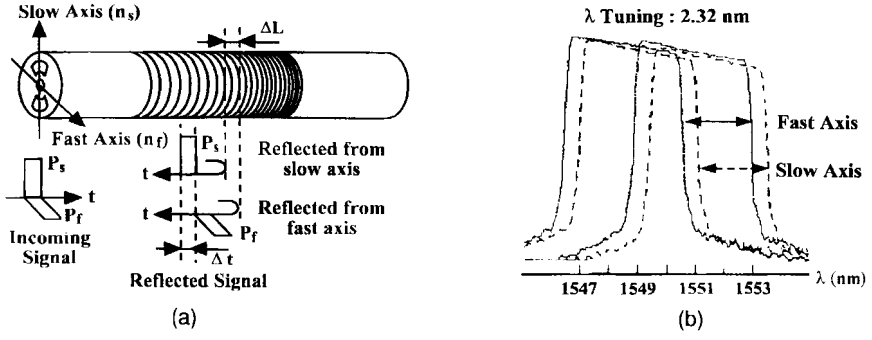

Figure 7.37: Tunable PMD compensation provided by a birefringent chirped fiber grating. (a) The origin of differential group delay; (b) stop-band shift induced by stretching the grating. (After Ref. [160]; ©1999 IEEE.)

the grating [160]. Such a device can provide tunable PMD compensation and is suited for WDM systems.

A distributed PMD compensator fabricated on a $LiNbO_3$ chip is attractive because of its integrated nature, resulting in a compact device. It has been used for PMD compensation in a 40-Gb/s system designed with the RZ-DPSK format [223]. Figure 7.38 shows the experimental setup used. A polarization scrambler at the transmitter end makes it possible to estimate the instantaneous value of DGD through an arrival-time detection technique implemented within the receiver. This value is used to create an electrical signal that controls the $LiNbO_3$ PMD compensator. A section of this com-

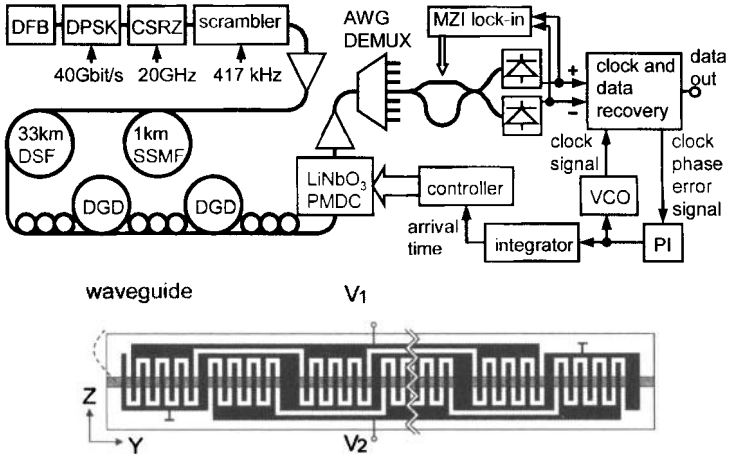

Figure 7.38: Experimental setup for the 40-Gb/s system employing a $LiNbO_3$ chip for PMD compensation together with a polarization scrambler at the transmitter and a phase-locked loop at the receiver. Comb-shaped electrodes used on the $LiNbO_3$ chip are also shown. (After Ref. [223]; ©2004 IEEE.)

pensator is shown in Figure 7.38. It employs comb-shaped electrodes that are used to covert the optical signal propagating inside the birefringent waveguide between the TE and TM modes supported by that waveguide. The electrode period is about 22 μm, a value that corresponds to the TE–TM beat length at the signal wavelength near 1,550 nm.

It should be stressed that most PMD compensators help to mitigate only the first-order PMD effects. At high bit rates, optical pulses are short enough, and their spectrum becomes wide enough, that the PSPs cannot be assumed to remain constant over the whole pulse spectrum. Higher-order PMD effects become of concern for lightwave systems operating at bit rates of 40 Gb/s or more. The compensation of second- and even third-order PMD may be necessary in some cases. In most cases, a first-order PMD compensator can increase the tolerable value of DGD by more than a factor of 3, resulting in a substantial increase in the transmission distance for PMD-compensated systems. In practice, a single PMD compensator cannot be used for all WDM channels. Rather, a separate PMD compensator is required for each channel. This fact makes PMD compensation along the fiber link a costly proposition for WDM systems. An optical compensator just before the receiver or an electrical PMD equalizer built into the receiver provides the most practical solution.

Problems

7.1 What is the dispersion-limited transmission distance for a 1.55-μm lightwave system making use of direct modulation at 10 Gb/s? Assume that frequency chirping broadens the Gaussian-shape pulse spectrum by a factor of 6 from its transform-limited width. Use $D = 17$ ps/(km-nm) for fiber dispersion.

7.2 How much improvement in the dispersion-limited transmission distance is expected if an external modulator is used in place of direct modulation for the lightwave system of Problem 7.1?

7.3 Solve Eq. (7.1.2) by using the Fourier transform method. Use the solution to find an analytic expression for the pulse shape after a Gaussian input pulse has propagated to $z = L$ in a fiber with $\beta_2 = 0$.

7.4 Use the results of preceding problem and plot the pulse shape after a Gaussian pulse with a full width at half-maximum (FWHM) of 1 ps is transmitted over 20 km of dispersion-shifted fiber with $\beta_2 = 0$ and $\beta_3 = 0.08$ ps^3/km. How would the pulse shape change if the sign of β_3 is inverted?

7.5 Use Eq. (7.1.3) to plot the pulse shapes for $C = -1$, 0, and 1 when 50-ps (FWHM) chirped Gaussian pulses are transmitted over 100 km of standard fiber with $D = 16$ ps/(km-nm). You can neglect third-order dispersion.

7.6 The transfer function of an optical filter is given by

$$H(\omega) = \exp[-(1 + ib)\omega^2/\omega_f^2].$$

What is the impulse response of this filter? Use Eq. (7.1.5) to find the pulse shape at the filter output when an unchirped Gaussian pulse is launched at the

input end of a fiber of length L. How would you optimize the filter to minimize the effect of fiber dispersion?

7.7 Use the results of the preceding problem to compare the pulse shapes before and after the filter when 30-ps (FWHM) Gaussian pulses are propagated over 100 km of fiber with $\beta_2 = -20$ ps^2/km. Assume that the filter bandwidth is the same as the pulse spectral width and that the filter parameter b is optimized. What is the optimum value of b?

7.8 Prove by using Eq. (7.1.5) that a DCF can provide dispersion compensation over the entire C band when the ratio S/D for the DCF is matched to that of the fiber used to construct the transmission link.

7.9 Derive Eq. (7.3.1) by considering multiple round trips inside a Fabry–Perot filter whose back mirror is 100% reflecting.

7.10 Solve Eqs. (7.4.2) and (7.4.3) and show that the transfer function of a Bragg grating is indeed given by Eq. (7.4.5).

7.11 Write a computer program to solve Eqs. (7.4.2) and (7.4.3) for chirped fiber gratings for which both δ and κ vary with z. Use it to plot the amplitude and phase of the reflectivity of a grating in which the period varies linearly by 0.01% over the 10-cm length. Assume $\kappa L = 4$ and the Bragg wavelength of 1.55 μm at the input end of the grating.

7.12 Use the dispersion relation $q^2 = \delta^2 - \kappa^2$ of a Bragg grating to show that the second- and third-order dispersion parameters of the grating are given by Eq. (7.4.6).

7.13 Explain how a chirped fiber grating compensates for GVD. Derive an expression for the GVD parameter of such a grating when the grating period varies linearly by $\delta\Lambda$ over the grating length L.

7.14 A 5-cm-long sampled grating is designed with a sampling period of 1 mm. Each period contains a 0.4-mm-long subgrating with 0.5-μm modulation period. Plot the reflectivity spectrum by solving Eqs. (7.4.2) and (7.4.3) with $\kappa = 0.6$ cm^{-1}.

7.15 Explain how midspan OPC compensates for fiber dispersion. Show that the OPC process inverts the signal spectrum.

7.16 Prove that both SPM and GVD can be compensated through midspan OPC only if the fiber loss $\alpha = 0$. Show also that the simultaneous compensation of SPM and GVD can occur when $\alpha \neq 0$ if GVD decreases along the fiber length. What is the optimum GVD profile for such a fiber?

7.17 Prove that the phase conjugator should be located at a distance given in Eq. (7.5.9) when the frequency ω_c of the phase-conjugated field does not coincide with the signal frequency ω_s.

7.18 The prechirp technique is used for dispersion compensation in a 10-Gb/s lightwave system operating at 1.55 μm and transmitting the 1 bits as chirped Gaussian pulses of 40-ps width (FWHM). Pulse broadening by up to 50% can be tolerated. What is the optimum value of the chirp parameter C, and how far can the signal be transmitted for this optimum value? Use $D = 17$ ps/(km-nm).

7.19 The prechirp technique of preceding Problem is implemented through frequency modulation of the optical carrier. Determine the modulation frequency for a maximum change of 10% from the average value.

7.20 Repeat the preceding problem for the case in which the prechirp technique is implemented through sinusoidal modulation of the carrier phase.

7.21 Start the OptSim package and open Example 7.A. Vary the DCF length from 0 to 30 km in each span and plot the Q factor. Also show the eye diagrams for DCF lengths of 10, 20, and 30 km.

7.22 Start the OptSim package and open Example 7.B. Compare the eye diagrams with and without fiber grating. If the fiber length were 150 km, what parameter of the grating would you change for perfect compensation?

References

[1] A. Gnauck and R. Jopson, in *Optical Fiber Telecommunications*, Vol. 3A, I. P. Kaminow and T. L. Koch, Eds., Academic Press, San Diego, CA, 1997, Chap. 7.

[2] J. Zyskind, R. Barry, G. Pendock, M. Cahill, and J. Ranka, in *Optical Fiber Telecommunications*, Vol. 4B, I. P. Kaminow and T. Li, Eds., Academic Press, San Diego, CA, 2002, Chap. 7.

[3] A. E. Willner and B. Hoanca, in *Optical Fiber Telecommunications IV*, Vol. 4B, I. P. Kaminow and T. Li, Eds., Academic Press, San Diego, CA, 2002, Chap. 14.

[4] M. Suzuki and N. Edagawa, *J. Lightwave Technol.* **21**, 916 (2003).

[5] C. Lin, H. Kogelnik, and L. G. Cohen, *Opt. Lett.* **5**, 476 (1980).

[6] A. J. Antos and D. K. Smith, *J. Lightwave Technol.* **12**, 1739 (1994).

[7] K. Thyagarajan, R. K. Varshney, P. Palai, A. K. Ghatak, and I. C. Goyal, *IEEE Photon. Technol. Lett.* **8**, 1510 (1996).

[8] M. Onishi, T. Kashiwada, Y. Ishiguro, Y. Koyano, M. Nishimura, and H. Kanamori, *Fiber Integ. Opt.* **16**, 277 (1997).

[9] J. Liu, Y. L. Lam, Y. C. Chan, Y. Zhou, and J. Yao, *Fiber Integ. Opt.* **18**, 63 (1999).

[10] J.-L. Auguste, R. Jindal, J.-M. Blondy, M. Clapeau, J. Marcou, B. Dussardier, G. Monnom, D. B. Ostrowsky, B. P. Pal, and K. Thyagarajan, *Electron. Lett.* **36**, 1689 (2000).

[11] L. Gruner-Nielsen, S. N. Knudsen, B. Edvold, T. Veng, D. Magnussen, C. C. Larsen, and H. Damsgaard, *Opt. Fiber Technol.* **6**, 164 (2000).

[12] R. W. Tkach, R. M. Derosier, A. H. Gnauck, A. M. Vengsarkar, D. W. Peckham, J. J. Zyskind, J. W. Sulhoff, and A. R. Chraplyvy, *IEEE Photon. Technol. Lett.* **7**, 1369 (1995).

[13] H. Taga, M. Suzuki, N. Edagawa, S. Yamamoto, and S. Akiba, *IEEE J. Quantum Electron.* **34**, 2055 (1998).

[14] C. D. Chen, T. Kim, O. Mizuhara, T. V. Nguyen, K. Ogawa, R. E. Tench, L. D. Tzeng, and P. D. Yeates, *Electron. Lett.* **35**, 648 (1999).

[15] B. Bakhshi, M. F. Arend, M. Vaa, W. W. Patterson, R. L. Maybach, and N. S. Bergano, Paper PD2, *Proc. Optical Fiber Commun. Conf.*, Optical Society of America, Washington, DC, 2001.

[16] C. D. Poole, J. M. Wiesenfeld, D. J. DiGiovanni, and A. M. Vengsarkar, *J. Lightwave Technol.* **12** 1746 (1994).

[17] M. Eguchi, M Koshiba, and Y. Tsuji, *J. Lightwave Technol.* **14**, 2387 (1996).

[18] S. Ramachandran, B. Mikkelsen, L. C. Cowsar, M. F. Yan, G. Raybon, L. Boivin, M. Fishteyn, W. A. Reed, P. Wisk, D. Brownlow, R. G. Huff, and L. Gruner-Nielsen, *IEEE Photon. Technol. Lett.* **13**, 632 (2001).

[19] M. Eguchi, *J. Opt. Soc. Am. B* **18**, 737 (2001).

[20] R. C. Youngquist, J. L. Brooks, and H. J. Shaw, *Opt. Lett.* **9**, 177 (1984).

[21] C. D. Poole, C. D. Townsend, and K. T. Nelson, *J. Lightwave Technol.* **9**, 598 (1991).

[22] R. Kashyap, *Fiber Bragg Gratings*, Academic Press, San Diego, CA, 1999.

[23] T. A. Birks, D. Mogilevtsev, J. C. Knight, and P. St.J. Russell, *IEEE Photon. Technol. Lett.* **11**, 674 (1999).

[24] L. P. Shen, W.-P. Huang, G. X. Chen, and S. S. Jian, *IEEE Photon. Technol. Lett.* **15**, 540 (2003).

[25] Y. Ni, L. Zhang, L. An, J. Peng, and C. Fan, *IEEE Photon. Technol. Lett.* **16**, 1516 (2004).

[26] K. Yonenga and Y. Miyamoyo, *Proc. Optical Fiber Commun. Conf.*, Paper FD4, Optical Society of America, Washington, DC, 1998.

[27] K. Nakajima, M. Ohashi, K. Shiraki, T. Horiguchi, K. Kurokawa, and Y. Miyajima, *J. Lightwave Technol.* **17**, 1814 (1999).

[28] T. Tsuritani, K. Tanaka, M. Edagawa, and M. Suzuki, *Electron. Lett.* **36**, 447 (2000).

[29] S. N. Knudsen, M. O Pedersen, and L. Gruner-Nielsen, *Electron. Lett.* **36**, 2067 (2000).

[30] H. S. Chung, H. Kim, S. E. Jin, E. S. Son, D. W. Kim, K. M Lee, H. Y. Park, and Y. C. Chung, *IEEE Photon. Technol. Lett.* **12**, 1397 (2000).

[31] K. Fukuchi, T. Kasamatsu, M. Morie, R. Ohhira, T. Ito, K. Sekiya, D. Ogasahara, and T. Ono, Paper PD24, *Proc. Optical Fiber Commun. Conf.*, Optical Society of America, Washington, DC, 2001.

[32] L. J. Cimini, L. J. Greenstein, and A. A. M. Saleh, *J. Lightwave Technol.* **8**, 649 (1990).

[33] A. H. Gnauck, C. R. Giles, L. J. Cimini, J. Stone, L. W. Stulz, S. K. Korotoky, and J. J. Veselka, *IEEE Photon. Technol. Lett.* **3**, 1147 (1991).

[34] C. K. Madsen, J. A. Walker, J. E. Ford, K. W. Goossen, T. N. Nielsen, and G. Lenz, *IEEE Photon. Technol. Lett.* **12**, 651 (2000).

[35] M. Jablonski, Y. Takushima, and K. Kikuchi, *J. Lightwave Technol.* **19**, 1194 (2001).

[36] D. Yang, C. Lin, W. Chen, and G. Barbarossa, *IEEE Photon. Technol. Lett.* **16**, 299 (2004).

[37] X. Shu, K. Chisholm, and K. Sugden, *IEEE Photon. Technol. Lett.* **16**, 1092 (2004).

[38] G. P. Agrawal, *Applications of Nonlinear Fiber Optics*, Academic Press, San Diego, CA, 2001.

[39] T. Ozeki, *Opt. Lett.* **17**, 375 (1992).

[40] K. Takiguchi, K. Okamoto, S. Suzuki, and Y. Ohmori, *IEEE Photon. Technol. Lett.* **6**, 86 (1994).

[41] M. Sharma, H. Ibe, and T. Ozeki, *J. Lightwave Technol.* **12**, 1759 (1994).

[42] K. Takiguchi, K. Okamoto, and K. Moriwaki, *IEEE Photon. Technol. Lett.* **6**, 561 (1994).

[43] K. Takiguchi, K. Okamoto, and K. Moriwaki, *J. Lightwave Technol.* **14**, 2003 (1996).

[44] K. Takiguchi, S. Kawanishi, H. Takara, A. Himeno, and K. Hattori, *J. Lightwave Technol.* **16**, 1647 (1998).

[45] K. Takiguchi, K. Okamoto, T. Goh, and M. Itoh, *J. Lightwave Technol.* **21**, 2463 (2003).

[46] C. K. Madsen and L. H. Zhao, *Optical Filter Design and Analysis: A Signal Processing Approach*, Wiley, New York, 1999.

[47] G. Lenz and C. K. Madsen, *J. Lightwave Technol.* **17**, 1248 (1999).

[48] C. K. Madsen, *J. Lightwave Technol.* **18**, 880 (2000).

[49] C. K. Madsen, *J. Lightwave Technol.* **21**, 2412 (2003).

[50] C. K. Madsen and G. Lenz, *IEEE Photon. Technol. Lett.* **10**, 994 (1998).

[51] C. K. Madsen, G. Lenz, A. J. Bruce, M. A. Capuzzo, L. T. Gomez, and R. E. Scotti, *IEEE Photon. Technol. Lett.* **11**, 1623 (1999).

[52] O. Schwelb, *J. Lightwave Technol.* **22**, 1380 (2004).

[53] D. K. W. Lam, B. K. Garside, and K. O. Hill, *Opt. Lett.* **7**, 291 (1982).

[54] B. J. Eggleton, C. M. de Sterke, and R. E. Slusher, *J. Opt. Soc. Am. B* **16**, 587 (1999).

[55] B. J. Eggleton, T. Stephens, P. A. Krug, G. Dhosi, Z. Brodzeli, and F. Ouellette, *Electron. Lett.* **32**, 1610 (1996).

[56] T. Stephens, P. A. Krug, Z. Brodzeli, G. Dhosi, F. Ouellette, and L. Poladian, *Electron. Lett.* **32**, 1599 (1996).

[57] N. M. Litchinister, B. J. Eggleton, and D. B. Pearson, *J. Lightwave Technol.* **15**, 1303 (1997).

[58] K. Hinton, *J. Lightwave Technol.* **15**, 1411 (1997).

[59] F. Ouellette, *Opt. Lett.* **12**, 622, 1987.

[60] K. O. Hill, S. Thériault, B. Malo, F. Bilodeau, T. Kitagawa, D. C. Johnson, J. Albert, K. Takiguchi, T. Kataoka, and K. Hagimoto, *Electron. Lett.* **30**, 1755 (1994).

[61] P. A. Krug, T. Stephens, G. Yoffe, F. Ouellette, P. Hill, and G. Dhosi, *Electron. Lett.* **31**, 1091 (1995).

[62] W. H. Loh, R. I. Laming, X. Gu, M. N. Zervas, M. J. Cole, T. Widdowson, and A. D. Ellis, *Electron. Lett.* **31**, 2203 (1995).

[63] W. H. Loh, R. I. Laming, N. Robinson, A. Cavaciuti, F. Vaninetti, C. J. Anderson, M. N. Zervas, and M. J. Cole, *IEEE Photon. Technol. Lett.* **8**, 944 (1996).

[64] W. H. Loh, R. I. Laming, A. D. Ellis, and D. Atkinson, *IEEE Photon. Technol. Lett.* **8**, 1258 (1996).

[65] D. Atkinson, W. H. Loh, J. J. O'Reilly, and R, I. Laming, *IEEE Photon. Technol. Lett.* **8**, 1085 (1996).

[66] K. Ennser, M. N. Zervas, and R. I. Laming, *IEEE J. Quantum Electron.* **34**, 770 (1998).

[67] S. V. Chernikov, J. R. Taylor, and R. Kashyap, *Opt. Lett.* **20**, 1586 (1995).

[68] G. P. Agrawal and S. Radic, *IEEE Photon. Technol. Lett.* **6**, 995 (1994).

[69] L. Zhang, K. Sugden, I. Bennion, and A. Molony, *Electron. Lett.* **31**, 477 (1995).

[70] A. H. Gnauck, J. M. Wiesenfeld, L. D. Garrett, R. M. Derosier, F. Forghieri, V. Gusmeroli, and D. Scarano, *IEEE Photon. Technol. Lett.* **11**, 1503 (1999).

[71] L. D. Garrett, A. H. Gnauck, F. Forghieri, V. Gusmeroli, and D. Scarano, *IEEE Photon. Technol. Lett.* **11**, 484 (1999).

[72] K. Hinton, *Opt. Fiber Technol.* **5**, 145 (1999).

[73] X. F. Chen, Z. B. Ma, C. Guang, Y. Meng, and X. L. Yang, *Microwave Opt. Tech. Lett.* **23**, 352 (1999).

[74] I. Riant, S. Gurib, J. Gourhant, P. Sansonetti, C. Bungarzeanu, and R. Kashyap, *IEEE J. Sel. Topics Quantum Electron.* **5**, 1312 (1999).

[75] L. D. Garrett, A. H. Gnauck, R. W. Tkach, B. Agogliati, L. Arcangeli, D. Scarano, V. Gusmeroli, C. Tosetti, G. Di Maio, and F. Forghieri, *IEEE Photon. Technol. Lett.* **12**, 356 (2000).

[76] B. J. Eggleton, P. A. Krug, L. Poladian, and F. Ouellette, *Electron. Lett.* **30**, 1620 (1994).

[77] F. Ouellette, P. A. Krug, T. Stephens, G. Dhosi, and B. Eggleton, *Electron. Lett.* **31**, 899 (1995).

[78] M. Ibsen, M. K. Durkin, M. J. Cole, and R. I. Laming, *IEEE Photon. Technol. Lett.* **10**, 842 (1998).

[79] M. Ibsen, A. Fu, H. Geiger, and R. I. Laming, *Electron. Lett.* **35**, 982 (1999).

[80] W. H. Loh, F. Q. Zhou, and J. J. Pan, *IEEE Photon. Technol. Lett.* **11**, 1280 (1999).

[81] J. E. Rothenberg, H. Li, Y. Li, J. Popelek, Y. Wang, R. B. Wilcox, and J. Zweiback, *IEEE Photon. Technol. Lett.* **14**, 1309 (2002).

[82] A. V. Buryak, K. Y. Kolossovski, and D. Y. Stepanov, *IEEE J. Quantum Electron.* **39**, 91 (2003).

[83] H. J. Lee and G. P. Agrawal, *IEEE Photon. Technol. Lett.* **15**, 1091 (2003).

[84] H. Li, Y. Sheng, Y. Li, and J. E. Rothenberg, *J. Lightwave Technol.* **21**, 2074 (2003).

[85] H. Ishii, F. Kano, Y. Tohmori, Y.Kondo, T. Tamamura, and Y.Yoshikuni, *IEEE J. Sel. Topics Quantum Electron.* **1**, 401 (1995).

[86] A. Yariv, D. Fekete, and D. M. Pepper, *Opt. Lett.* **4**, 52 (1979).

[87] S. Watanabe, N. Saito, and T. Chikama, *IEEE Photon. Technol. Lett.* **5**, 92 (1993).

[88] R. M. Jopson, A. H. Gnauck, and R. M. Derosier, *IEEE Photon. Technol. Lett.* **5**, 663 (1993).

[89] M. C. Tatham, G. Sherlock, and L. D. Westbrook, *Electron. Lett.* **29**, 1851 (1993).

[90] R. M. Jopson and R. E. Tench, *Electron. Lett.* **29**, 2216 (1993).

[91] S. Watanabe and T. Chikama, *Electron. Lett.* **30**, 163 (1994).

[92] C. R. Giles, V. Mizrahi, and T. Erdogan, *IEEE Photon. Technol. Lett.* **7**, 126 (1995).

[93] M. E. Marhic, N. Kagi, T.-K. Chiang, and L. G. Kazovsky, *Opt. Lett.* **20**, 863 (1995).

[94] S. Wabnitz, *IEEE Photon. Technol. Lett.* **7**, 652 (1995).

[95] A. D. Ellis, M. C. Tatham, D. A. O. Davies, D. Nesser, D. G. Moodie, and G. Sherlock, *Electron. Lett.* **31**, 299 (1995).

[96] M. Yu, G. P. Agrawal, and C. J. McKinstrie, *IEEE Photon. Technol. Lett.* **7**, 932 (1995).

[97] X. Zhang, F. Ebskamp, and B. F. Jorgensen, *IEEE Photon. Technol. Lett.* **7**, 819 (1995).

[98] X. Zhang and B. F. Jorgensen, *Electron. Lett.* **32**, 753 (1996).

[99] S. Watanabe and M. Shirasaki, *J. Lightwave Technol.* **14**, 243 (1996).

[100] C. Lorattanasane and K. Kikuchi, *J. Lightwave Technol.* **15**, 948 (1997).

[101] S. F. Wen, *J. Lightwave Technol.* **15**, 1061 (1997).

[102] M. H. Chou, I. Brener, G. Lenz, R. Scotti, E. E. Chaban, J. Shmulovich, D. Philen, S. Kosinski, K. R. Parameswaran, and M. M. Fejer, *IEEE Photon. Technol. Lett.* **12**, 82 (2000).

[103] H. C. Lim and K. Kikuchi, *IEEE Photon. Technol. Lett.* **13**, 481 (2001).

[104] J. Herrera, F. Ramos, and J. Marti, *J. Lightwave Technol.* **29**, 1688 (2002).

[105] P. Kaewplung, T. Angkaew, and K. Kikuchi, *J. Lightwave Technol.* **21**, 1465 (2003).

[106] G. L. Woods, P. Papaparaskeva, M. Shtaif, I. Brener, and D. A. Pitt, *IEEE Photon. Technol. Lett.* **16**, 677 (2004).

[107] S. Y. Set, R. Girardi, E. Riccardi, B. E. Olsson, M. Puleo, M. Ibsen, R. I. Laming, P. A. Andrekson, F. Cisternino, and H. Geiger, *Electron. Lett.* **35**, 581 (1999).

[108] T. Merker, P. Meissner, and U. Feiste, *IEEE J. Sel. Topics Quantum Electron.* **6**, 258 (2000).

[109] D. Kunimatsu, C. Q. Xu, M. D. Pelusi, X. Wang, K. Kikuchi, H. Ito, and A. Suzuki, *IEEE Photon. Technol. Lett.* **12**, 1621 (2000).

[110] J. Inoue, H. Sotobayashi, W. Chujo, and H. Kawaguchi, *Electron. Lett.* **38**, 819 (2002).

[111] C. Peucheret, B. Zsigri, P. A. Andersen, K. S. Berg, A. Tersigni, P. Jeppesen, K. P. Hansen, and M. D. Nielsen, *Electron. Lett.* **39**, 919 (2003).

[112] J. Inoue and F. Kubota, *Electron. Lett.* **39**, 1842 (2003).
[113] S. L. Jansen, S. Spalter, G.-D. Khoe, H. de Waardt, H. E. Escobar, L Marshall, and M. Sher, *IEEE Photon. Technol. Lett.* **16**, 1763 (2004).
[114] R. A. Fisher, B. R. Suydam, and D. Yevick, *Opt. Lett.* **8**, 611 (1983).
[115] R. A. Fisher, Ed., *Optical Phase Conjugation*, Academic Press, San Diego, CA, 1983.
[116] G. P. Agrawal, *Nonlinear Fiber Optics*, 3rd ed., Academic Press, San Diego, CA, 2001.
[117] G. P. Agrawal, in *Semiconductor Lasers: Past, Present, Future*, G. P. Agrawal, Ed., AIP Press, Woodbury, NY, 1995, Chap. 8.
[118] A. D'Ottavi, F. Martelli, P. Spano, A. Mecozzi, and S. Scotti, *Appl. Phys. Lett.* **68**, 2186 (1996).
[119] F. Matera, A. Mecozzi, M. Romagnoli, and M. Settembre, *Opt. Lett.* **18**, 1499 (1993).
[120] R. D. Li, P. Kumar, W. L. Kath, and J. N. Kutz, *IEEE Photon. Technol. Lett.* **5**, 669 (1993).
[121] G. P. Agrawal and M. J. Potasek, *Opt. Lett.* **11**, 318 (1986).
[122] R. Olshansky and D. Fye, *Electron. Lett.* **20**, 80 (1984).
[123] T. L. Koch and R. C. Alferness, *J. Lightwave Technol.* **3**, 800 (1985).
[124] F. Koyoma and K. Iga, *J. Lightwave Technol.* **6**, 87 (1988).
[125] A. H. Gnauck, S. K. Korotky, J. J. Veselka, J. Nagel, C. T. Kemmerer, W. J. Minford, and D. T. Moser, *IEEE Photon. Technol. Lett.* **3**, 916 (1991).
[126] E. Devaux, Y. Sorel, and J. F. Kerdiles, *J. Lightwave Technol.* **11**, 1937 (1993).
[127] N. Henmi, T. Saito, and T. Ishida, *J. Lightwave Technol.* **12**, 1706 (1994).
[128] J. C. Cartledge, H. Debrégeas, and C. Rolland, *IEEE Photon. Technol. Lett.* **7**, 224 (1995).
[129] J. A. J. Fells, M. A. Gibbon, I. H. White, G. H. B. Thompson, R. V. Penty, C. J. Armistead, E. M. Kinber, D. J. Moule, and E. J. Thrush, *Electron. Lett.* **30**, 1168 (1994).
[130] K. Morito, R. Sahara, K. Sato, and Y. Kotaki, *IEEE Photon. Technol. Lett.* **8**, 431 (1996).
[131] B. Wedding, B. Franz, and B. Junginger, *J. Lightwave Technol.* **12**, 1720 (1994).
[132] B. Wedding, K. Koffers, B. Franz, D. Mathoorasing, C. Kazmierski, P. P. Monteiro, and J. N. Matos, *Electron. Lett.* **31**, 566 (1995).
[133] W. Idler, B. Franz, D. Schlump, B. Wedding, and A. J. Ramos, *Electron. Lett.* **35**, 2425 (1998).
[134] K. Perlicki and J. Siuzdak, *Opt. Quantum Electron.* **31**, 243 (1999).
[135] J. A. V. Morgado and A. V. T. Cartaxo, *IEE Proc. Optoelect.* **148**, 107 (2001).
[136] M. Schwartz, *Information, Transmission, Modulation, and Noise*, 4th ed., McGraw-Hill, New York, 1990, Sec. 3.10.
[137] G. May, A. Solheim, and J. Conradi, *IEEE Photon. Technol. Lett.* **6**, 648 (1994).
[138] D. Penninckx, L. Pierre, J.-P. Thiery, B. Clesca, M. Chbat, and J.-L. Beylat, *Electron. Lett.* **32**, 1023 (1996).
[139] D. Penninckx, M. Chbat, L. Pierre, and J.-P. Thiery, *IEEE Photon. Technol. Lett.* **9**, 259 (1997).
[140] K. Yonenaga and S. Kuwano, *J. Lightwave Technol.* **15**, 1530 (1997).
[141] T. Ono, Y. Yano, K. Fukuchi, T. Ito, H. Yamazaki, M. Yamaguchi, and K. Emura, *J. Lightwave Technol.* **16**, 788 (1998).
[142] W. Kaiser, T. Wuth, M. Wichers, and W. Rosenkranz, *IEEE Photon. Technol. Lett.* **13**, 884 (2001).
[143] G. P. Agrawal and N. A. Olsson, *Opt. Lett.* **14**, 500 (1989).
[144] N. A. Olsson, G. P. Agrawal, and K. W. Wecht, *Electron. Lett.* **25**, 603 (1989).
[145] N. A. Olsson and G. P. Agrawal, *Appl. Phys. Lett.* **55**, 13 (1989).
[146] G. P. Agrawal and N. A. Olsson, *IEEE J. Quantum Electron.* **25**, 2297 (1989).

[147] G. P. Agrawal and N. A. Olsson, U.S. Patent 4,979,234 (1990).
[148] M. J. Potasek and G. P. Agrawal, *Electron. Lett.* **22**, 759 (1986).
[149] K. Iwashita and N. Takachio, *J. Lightwave Technol.* **8**, 367 (1990).
[150] N. Takachio, S. Norimatsu, and K. Iwashita, *IEEE Photon. Technol. Lett.* **4**, 278 (1992).
[151] K. Yonenaga and N. Takachio, *IEEE Photon. Technol. Lett.* **5**, 949 (1993).
[152] S. Yamazaki, T. Ono, and T. Ogata, *J. Lightwave Technol.* **11**, 603 (1993).
[153] J. H. Winters and R. D. Gitlin, *IEEE Trans. Commun.* **38**, 1439 (1990).
[154] J. H. Winters, *J. Lightwave Technol.* **8**, 1487 (1990).
[155] J. C. Cartledge, R. G. McKay, and M. C. Nowell, *J. Lightwave Technol.* **10**, 1105 (1992).
[156] J. H. Winters, *Proc. SPIE* **1787**, 346 (1992).
[157] F. Cariali, F. Martini, P. Chiappa, and R. Ballentin, *Electron. Lett.* **36**, 889 (2000).
[158] X. Zhao and F. S. Choa, *IEEE Photon. Technol. Lett.* **14**, 1187 (2002).
[159] J. Wang and J. M. Kahn *J. Lightwave Technol.* **22**, 362 (2004); *IEEE Photon. Technol. Lett.* **16**, 1397 (2004).
[160] A. E. Willner, K. M. Feng, J. Cai, S. Lee, J. Peng, and H. Sun, *IEEE J. Sel. Topics Quantum Electron.* **5**, 1298 (1999).
[161] M. J. Erro, M. A. G. Laso, D. Benito, M. J. Garde, and M. A. Muriel, *IEEE J. Sel. Topics Quantum Electron.* **5**, 1332 (1999).
[162] B. J. Eggleton, A. Ahuja, P. S.Westbrook, J. A. Rogers, P. Kuo, T. N. Nielsen, and B. Mikkelsen, *J. Lightwave Technol.* **18**, 1418 (2000).
[163] B. J. Eggleton, B. Mikkelsen, G. Raybon, A. Ahuja, J. A. Rogers, P. S. Westbrook, T. N. Nielsen, S. Stulz, and K. Dreyer, *IEEE Photon. Technol. Lett.* **12**, 1022 (2000).
[164] T. Inui, T. Komukai, and M. Nakazawa, *Opt. Commun.* **190**, 1 (2001).
[165] S. Matsumoto, T. Ohira, M. Takabayashi, K. Yoshiara, and T. Sugihara, *IEEE Photon. Technol. Lett.* **13**, 827 (2001).
[166] L. M. Lunardi, D. J. Moss, S. Chandrasekhar, L. L. Buhl, M. Lamont, S. McLaughlin, G. Randall, P. Colbourne, S. Kiran, and C. A. Hulse, *J. Lightwave Technol.* **20**, 2136 (2002).
[167] Z. Pan, Y. W. Song, C. Yu, Y. Wang, Q. Yu, J. Popelek, H. Li, Y. Li, and A. E. Willner, *J. Lightwave Technol.* **20**, 2239 (2002).
[168] Y. W. Song, Z. Pan, S. M. R. Motaghian Nezam, C. Yu, Y. Wang, D. Starodubov, V. Grubsky, J. E. Rothenberg, J. Popelek, H. Li, Y. Li, R. Caldwell, R. Wilcox, and A. E. Willner, *J. Lightwave Technol.* **20**, 2259 (2002).
[169] S. Ramachandran, S. Ghalmi, S. Chandrasekhar, I. Ryazansky, M. F. Yan, F. V. Dimarcello, W. A. Reed, and P. Wisk, *IEEE Photon. Technol. Lett.* **15**, 727 (2003).
[170] D. J. Moss, M. Lamont, S. McLaughlin, G. Randall, P. Colbourne, S. Kiran, and C. A. Hulse, *IEEE Photon. Technol. Lett.* **15**, 730 (2003).
[171] T. Sano, T. Iwashima, M. Katayama, T. Kanie, M. Harumoto, M. Shigehara, H. Suganuma, and M. Nishimura, *IEEE Photon. Technol. Lett.* **15**, 1109 (2003).
[172] X. Shu, K. Sugden, P. Rhead, J. Mitchell, I. Felmeri, G. Lloyd, K. Byron, Z. Huang, I. Khrushchev, and I. Bennion, *IEEE Photon. Technol. Lett.* **15**, 1111 (2003).
[173] M. Sumetsky, N. M. Litchinitser, P. S. Westbrook, P. I. Reyes, B. J. Eggleton, Y. Li, R. Deshmukh, C. Soccolich, F. Rosca, J. Bennike, F. Liu, and S. Dey, *Electron. Lett.* **39**, 1196 (2003).
[174] D. Gauden, E. Goyat, A. Mugnier, P. Lesueur, P. Yvernault, and D. Pureur, *IEEE Photon. Technol. Lett.* **15**, 1387 (2003).
[175] N. Q. Ngo, S. Y. Li, R. T. Zheng, S. C. Tjin, and P. Shum, *J. Lightwave Technol.* **21**, 1568 (2003).

[176] X. Chen, X. Xu, M, Zhou, D. Jiang, X. Li, J. Feng, and S. Xie, *IEEE Photon. Technol. Lett.* **16**, 188 (2004).

[177] J. Kim, J. Bae, Y.-G. Han, S. H. Kim, J.-M. Jeong, and S. B. Lee, *IEEE Photon. Technol. Lett.* **16**, 849 (2004).

[178] M. Shirasaki, *IEEE Photon. Technol. Lett.* **9**, 1598 (1997).

[179] M. Shirasaki, A. N. Akhter, and C. Lin, *IEEE Photon. Technol. Lett.* **11**, 1443 (1999)

[180] H. Ooi, K. Nakamura, Y. Akiyama, T. Takahara, T. Terahara, Y. Kawahata, H. Isono, and G, Ishikawa, *J. Lightwave Technol.* **20**, 2196 (2002).

[181] M. Onishi, T. Kashiwada, Y. Koyano, Y. Ishiguro, M. Nishimura, and H. Kanamori, *Electron. Lett.* **32**, 2344 (1996).

[182] K. Takiguchi, S. Kawanishi, H. Takara, A. Himeno, and K. Hattori, *J. Lightwave Technol.* **16**, 1647 (1998).

[183] M. Durkin, M. Ibsen, M. J. Cole, and R. I. Laming, *Electron. Lett.* **33**, 1891 (1997).

[184] T. Komukai and M. Nakazawa, *Opt. Commun.* **154**, 5 (1998).

[185] T. Komukai, T. Inui, and M. Nakazawa, *IEEE J. Quantum Electron.* **36**, 409 (2000).

[186] H. Tsuda, K. Okamoto, T. Ishii, K. Naganuma, Y. Inoue, H. Takenouchi, and T. Kurokawa, *IEEE Photon. Technol. Lett.* **11**, 569 (1999).

[187] M. J. Erro, M. A. G. Laso, D. Benito, M. J. Garde, and M. A. Muriel, *Fiber Integ. Opt.* **19**, 367 (2000).

[188] A. H. Gnauck, L. D. Garrett, Y. Danziger, U. Levy, and M. Tur, *Electron. Lett.* **36**, 1946 (2000).

[189] Y. Xie, S. Lee, Z. Pan, J. X. Cai, A. E. Willner, V. Grubsky, D. S. Starodubov, E. Salik, and J. Feinberg, *IEEE Photon. Technol. Lett.* **12**, 1417 (2000).

[190] H. Takenouchi, T. Ishii, and T. Goh, *Electron. Lett.* **37**, 777 (2001).

[191] P. Kaewplung, R. Angkaew, and K. Kikuchi, *IEEE Photon. Technol. Lett.* **13**, 293 (2001).

[192] M. Kato, N. Yoshizawa, T. Sugie, and K. Okamoto, *IEEE Photon. Technol. Lett.* **13**, 463 (2001).

[193] T. Inui, T. Komukai, M. Nakazawa, K. Suzuki, K. R. Tamura, K. Uchiyama, and T. Morioka, *IEEE Photon. Technol. Lett.* **14**, 540 (2002).

[194] C. S. Goh, S. Y. Set, and K. Kikuchi, *IEEE Photon. Technol. Lett.* **16**, 524 (2004).

[195] S. Matsumoto, M. Takabayashi, K. Yoshiara, T. Sugihara, T. Miyazaki, and F. Kubota, *IEEE Photon. Technol. Lett.* **16**, 1095 (2004).

[196] S. Kawanishi, H. Takara, T. Morioka, O. Kamatani, K. Takiguchi, T. Kitoh, and M. Saruwatari, *Electron. Lett.* **32**, 916 (1996).

[197] M. Nakazawa, E. Yoshida, T. Yamamoto, E. Yamada, and A. Sahara, *Electron. Lett.* **34**, 907 (1998).

[198] T. Yamamoto, E. Yoshida, K. R. Tamura, K. Yonenaga, and M. Nakazawa, *IEEE Photon. Technol. Lett.* **12**, 355, (2000).

[199] M. D. Pelusi, X. Wang, F. Futami, K. Kikuchi, and A. Suzuki, *IEEE Photon. Technol. Lett.* **12**, 795 (2000).

[200] M. Nakazawa, T. Yamamaoto, and K. R. Tamura, *Electron. Lett.* **36**, 2027 (2000); T. Yamamoto and M. Nakazawa, *Opt. Lett.* **26**, 647 (2001).

[201] C. D. Poole and J. Nagel, in *Optical Fiber Telecommunications III*, Vol. A, I. P. Kaminow and T. L. Koch, Eds., Academic Press, San Diego, CA, 1997, Chap. 6.

[202] M. Karlsson, J. Brentel, and P. A. Andrekson, *J. Lightwave Technol.* **18**, 941 (2000).

[203] H. Kogelnik, R. M. Jopson, and L. E. Nelson, in *Optical Fiber Telecommunications*, Vol. 4A, I. P. Kaminow and T. Li, Eds., Academic Press, San Diego, CA, 2002, Chap. 15.

[204] A. E. Willner, S. M. Reza, M. Nezam, L. Yan, Z. Pan, and M. C. Hauer, *J. Lightwave Technol.* **22**, 106 (2004).

[205] H. Bülow, *IEEE Photon. Technol. Lett.* **10**, 696 (1998).

[206] R. Khosravani and A. E. Willner, *IEEE Photon. Technol. Lett.* **13**, 296 (2001).

[207] A. Djupsjobacka, *IEEE Photon. Technol. Lett.* **13**, 660 (2001).

[208] P. Lu, L. Chen, and X. Bao, *J. Lightwave Technol.* **20**, 1805 (2002).

[209] H. Sunnerud, M. Karlsson, C. Xie, and P. A. Andrekson, *J. Lightwave Technol.* **20**, 2204 (2002).

[210] J. N. Damask, G. Gray, P. Leo, G. Simer, K. Rochford, and D. Veasey, *IEEE Photon. Technol. Lett.* **15**, 48 (2003).

[211] J. Kissing, T. Gravemann, and E. Voges, *IEEE Photon. Technol. Lett.* **15**, 611 (2003).

[212] P. J. Winzer, H. Kogelnik, and K. Ramanan, *IEEE Photon. Technol. Lett.* **16**, 449 (2004).

[213] E. Forestieri and G. Prati, *J. Lightwave Technol.* **22**, 988 (2004).

[214] G. Biondini, W. L. Kath, and C. R. Menyuk, *J. Lightwave Technol.* **22**, 1201 (2004).

[215] T. Takahashi, T. Imai, and M. Aiki, *Electron. Lett.* **30**, 348 (1994).

[216] C. Francia, F. Bruyère, J. P. Thiéry, and D. Penninckx, *Electron. Lett.* **35**, 414 (1999).

[217] S. Lee, R. Khosravani, J. Peng, V. Grubsky, D. S. Starodubov, A. E. Willner, and J. Feinberg, *IEEE Photon. Technol. Lett.* **11**, 1277 (1999).

[218] R. Noé, D. Sandel, M. Yoshida-Dierolf, S. Hinz, V. Mirvoda, A. Schopflin, C. Gungener, E. Gottwald, C. Scheerer, G. Fischer, T. Weyrauch, and W. Haase, *J. Lightwave Technol.* **17**, 1602 (1999).

[219] T. Merker, N. Hahnenkamp, and P. Meissner, *Opt. Commun.* **182**, 135 (2000).

[220] H. Y. Pua, K. Peddanarappagari, B. Zhu, C. Allen, K. Demarest, and R. Hui, *J. Lightwave Technol.* **18**, 832 (2000).

[221] H. Sunnerud, C. Xie, M. Karlsson, R. Samuelsson, and P. A. Andrekson, *J. Lightwave Technol.* **20**, 368 (2002).

[222] D. Sandel, V. Mirvoda, S. Bhandare, F. Wüst, and R. Noé, *J. Lightwave Technol.* **21**, 1198 (2003).

[223] R. Noé, D. Sandel, and V. Mirvoda, *IEEE J. Sel. Topics Quantum Electron.* **10**, 341 (2004).

[224] S. Lanne and E. Corbel, *J. Lightwave Technol.* **22**, 1033 (2004).

[225] I. T. Lima, A. O Lima, G. Biondini, C. R. Menyuk, and W. L. Kath, *J. Lightwave Technol.* **22**, 1023 (2004).

[226] C. K. Madsen, M. Cappuzzo, E. J. Laskowski, E. Chen, L. Gomez, A. Griffin, A. Wong-Foy, S. Chandrasekhar, L. Stulz, and L. Buhl, *J. Lightwave Technol.* **22**, 1041 (2004).

[227] H. F. Haunstein, W. Sauer-Greff, A. Dittrich, K. Sticht, and R. Urbansky, *J. Lightwave Technol.* **22**, 1169 (2004).

[228] D. Mahgerefteh and C. R. Menyuk, *IEEE Photon. Technol. Lett.* **11**, 340 (1999).

Chapter 8

Nonlinearity Management

The use of dispersion compensation solves the dispersion problem to a large extent, just as optical amplifiers solve the loss problem for lightwave systems. However, as discussed in Section 6.5, noise added by optical amplifiers forces one to launch into a fiber link an average power level close to 1 mW or more for each channel. At such power levels, several nonlinear effects discussed in Chapter 4 cannot be ignored, and they impact considerably on the performance of a long-haul lightwave system. In fact, along with amplifier noise, the nonlinear nature of optical fibers is the ultimate limiting factor for such systems. In this chapter we focus on the techniques used to manage the nonlinear effects. Section 8.1 shows how nonlinear effects limit a long-haul fiber link and introduces the two main techniques used to reduce their impact. Section 8.2 focuses on the formation of optical soliton in fibers with constant dispersion and how they can be used to advantage for transmitting information. In soliton-based systems, optical pulses representing 1 bits are much shorter than the bit slot, and their shape inside the fiber is maintained by carefully balancing the dispersive and nonlinear effects. Dispersion-managed solitons are considered in Section 8.3 with an emphasis on dispersion maps that ensure the periodic evolution of such solitons over long link lengths. Section 8.4 deals with pseudo-linear systems in which fiber dispersion is used to broaden short optical pulses so much that their peak power is reduced by a large factor over most of the fiber link. Overlapping of neighboring pulses still produces intrachannel nonlinear effects, and the techniques used for controlling them are discussed in Section 8.5. The focus of Section 8.6 is a single high-speed channel. Interchannel nonlinear effects are discussed in Chapter 9, which is devoted to WDM systems.

8.1 Role of Fiber Nonlinearity

As discussed in Chapter 7, the use of dispersion management in combination with optical amplifiers can extend the transmission distance to several thousand kilometers. If the optical signal is regenerated electronically every 300 to 400 km, such a system works well as the nonlinear effects do not accumulate over long lengths. In contrast, if the signal is maintained in the optical domain by cascading many amplifiers, several

nonlinear effects discussed in Chapter 4, such as self-phase modulation (SPM), cross-phase modulation (XPM), and four-wave mixing (FWM), would ultimately limit the system performance [1]. Indeed, the impact of nonlinear effects on the performance of dispersion-managed systems has been investigated since the early 1990s [2]–[25]. In this section we study how the nonlinear effects influence a dispersion-managed system and how their impact can be minimized with a suitable choice of system parameters.

8.1.1 System Design Issues

In the absence of nonlinear effects, the use of dispersion management ensures that each pulse is confined to its bit slot when the optical signal arrives at the receiver, even if pulses have spread over multiple slots during their transmission. Moreover, it is immaterial whether dispersion is compensated at the transmitter end, receiver end, or periodically within the fiber link. Any dispersion map can be used as long as the accumulated group-velocity dispersion (GVD) $d_a(L) \equiv \int_0^L \beta_2(z)\,dz = 0$ at the end of a link of length L. The performance of such a system is only limited by the signal-to-noise ratio (SNR) degradation induced by amplifier noise. Since SNR can be improved by increasing input optical power, link length can be made arbitrarily long in principle.

As discussed in Section 6.6, the nonlinear effects are not negligible for long-haul systems when power levels exceed a few milliwats. As a result, the transmission distance is limited by the nonlinear effects. Moreover, an optimum power level exists at which bit-error rate (BER) is the lowest and the system performs best. Dispersion management is essential for long-haul systems to ensure that the system is not limited by GVD-induced pulse broadening. However, different dispersion maps can lead to different Q factors at the receiver end even when $d_a(L) = 0$ for all of them [2]. This is so because the dispersive and nonlinear effects do not act on the signal independently. As a result, degradation induced by the nonlinear effects depends on the local value of $d_a(z)$ at any distance z within the fiber link.

The major nonlinear phenomenon affecting the performance of a single channel is the SPM. As in earlier chapters, the propagation of an optical bit stream inside a dispersion-managed system is governed by the nonlinear Schrödinger (NLS) equation. From Eq. (6.1.1), it can be written as

$$i\frac{\partial A}{\partial z} - \frac{\beta_2}{2}\frac{\partial^2 A}{\partial t^2} + \gamma|A|^2 A = \frac{i}{2}(g_0 - \alpha)A, \tag{8.1.1}$$

where we have ignored the noise term to simplify the following discussion. In a dispersion-managed system the three fiber parameters (β_2, γ, and α) are functions of z because of their different values in two or more fiber sections used to form the dispersion map. The gain parameter g_0 is also a function of z because of loss management. Its functional form depends on whether a lumped or a distributed amplification scheme is employed.

In general, Eq. (8.1.1) is solved numerically to study the performance of dispersion-managed systems. As was done in Sections 3.2.3 and 6.5.1, it is useful to eliminate the gain and loss terms in this equation with the transformation $A(z,t) = \sqrt{P_0 p(z)}\,U(z,t)$

and write it in terms of $U(z,t)$ as

$$i\frac{\partial U}{\partial z} - \frac{\beta_2}{2}\frac{\partial^2 U}{\partial t^2} + \gamma P_0 p(z)|U|^2 U = 0, \tag{8.1.2}$$

where P_0 is the input peak power and $p(z)$ governs variations in the peak power of the signal along the fiber link through

$$p(z) = \exp\left(\int_0^z [g_0(z) - \alpha(z)]\, dz\right). \tag{8.1.3}$$

If losses are compensated in a periodic fashion, $p(z_m) = 1$, where $z_m = mL_A$ is the location of the mth amplifier and L_A is the amplifier spacing. In the case of lumped amplifiers, $g_0 = 0$ within the fiber link, and $p(z) = \exp[-\int_0^z \alpha(z)\, dz]$. Equation (8.1.2) shows that the effective nonlinear parameter $\gamma_e(z) \equiv \gamma p(z)$ is also z-dependent because of changes in the signal power induced by fiber losses and optical amplifiers. In particular, when lumped amplifiers are used, the nonlinear effects are strongest just after signal amplification and become negligible in the tail end of each fiber section between two amplifiers.

There are two major design issues for any dispersion-managed system: What is the optimum dispersion map and which modulation format provides the best performance? Both of these issues have been studied by solving the NLS equation (8.1.2) numerically [4]–[25]. Although attention was initially focused on the NRZ format, the performance of RZ and NRZ formats was compared starting in 1996, both numerically and experimentally, under realistic operating conditions [8]–[14]. As an example, Figure 8.1 shows the numerical results for the (a) NRZ and (b) RZ formats by plotting the maximum transmission distance L at which eye opening is reduced by 1 dB at the receiver of a 40-Gb/s system as average launched power is increased [8]. The periodic dispersion map consisted of 50 km of standard fiber with $D = 16$ ps/(km-nm), $\alpha = 0.2$ dB/km, and $\gamma = 1.31$ W^{-1}/km, followed by 10 km of dispersion-compensating fiber (DCF) with $D = -80$ ps/(km-nm), $\alpha = 0.5$ dB/km, and $\gamma = 5.24$ W^{-1}/km. Optical amplifiers with 6-dB noise figure were placed 60 km apart and compensated total fiber losses within each map period. The duty cycle was 50% in the case of the RZ format.

As discussed earlier and evident from Figure 8.1, distance can be continuously increased in the absence of amplifier noise by decreasing the launched power (open squares). However, when noise is included, an optimum power level exists for which the link length is maximum. This distance is less than 400 km when the NRZ format is employed but becomes larger by about a factor of 3 when the RZ format is implemented with a 50% duty cycle. The reason behind this improvement can be understood by noting that the dispersion length is relatively small (<5 km) for RZ pulses propagating inside a standard fiber. As a result, RZ-format pulses spread quickly and their peak power is reduced considerably compared with the NRZ case. This reduction in the peak power lowers the impact of SPM.

Figure 8.1 also shows how the buildup of nonlinear effects within DCFs affects the system performance. In the case of RZ format, maximum distance is below 900 km at an input power level of -4 dBm because of the DCF-induced nonlinear degradation (filled squares). Not only DCFs have a larger nonlinear parameter because of their

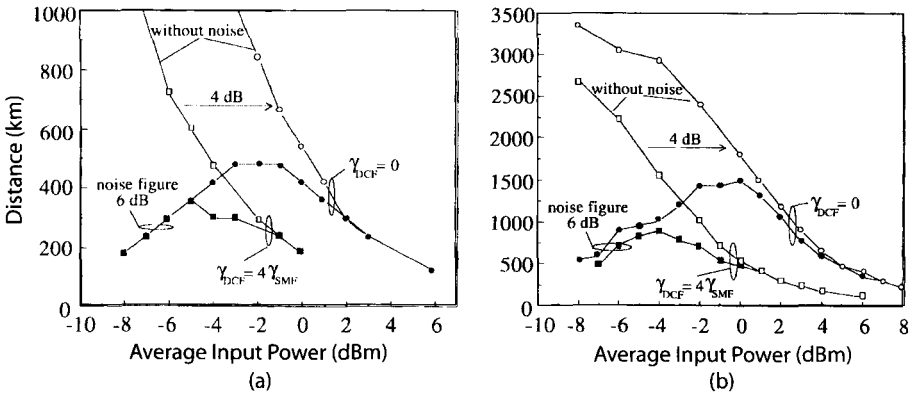

Figure 8.1: Maximum transmission distance as a function of average input power for a 40-Gb/s dispersion-managed system designed with the (a) NRZ and (b) RZ formats. The filled and empty symbols show numerical data obtained with and without amplifier noise, respectively. (After Ref. [8]; ©1997 IEEE.)

smaller core size, pulses are also compressed inside them to their original width, resulting in much higher peak powers. If the nonlinear effects can be suppressed within DCF, maximum distance can be increased close to 1,500 km by launching higher powers. This improvement can be realized in practice by using an alternate dispersion-compensating device requiring shorter lengths (such as a two-mode DCF or a fiber grating). In the case of NRZ format, the link length is limited to below 500 km even when nonlinear effects are negligible within DCFs.

As seen from Figure 8.1, the nonlinear effects play an important role in dispersion-managed systems whenever a DCF is used because its smaller core size enhances optical intensities (manifested through a larger value of the γ parameter). Placement of the amplifier after the DCF helps since the signal is then weak enough that the nonlinear effects are less important in spite of a small core area of DCFs. The optimization of system performance using different dispersion maps has been the subject of intense study. In a 1994 experiment, a 1,000-km-long fiber loop containing 31 fiber amplifiers was used to study three different dispersion maps [2]. The maximum transmission distance of 12,000 km at a bit rate of 5 Gb/s was realized for the case in which short sections of normal-GVD fibers were used to compensate for the anomalous GVD of long sections. In a 1995 experiment, the transmission distance of a 80-Gb/s signal, obtained by multiplexing eight 10-Gb/s channels with 0.8-nm channel spacing, was found to be limited to 1,171 km because of the onset of various nonlinear effects [3].

The choice between the RZ and NRZ formats is not always so obvious as it depends on many other design parameters. As early as 1995, an experiment as well as numerical simulations indicated that a 10-Gb/s signal can be transmitted over 2,245 km using the NRZ format with 90-km amplifier spacing, provided the link dispersion is not fully compensated [6]. A similar conclusion was reached in a 1999 experiment in which RZ and NRZ formats were compared for a 10-Gb/s system [14]. Figure 8.2 shows the recirculating loop used in this experiment. Because of cost considerations, most labora-

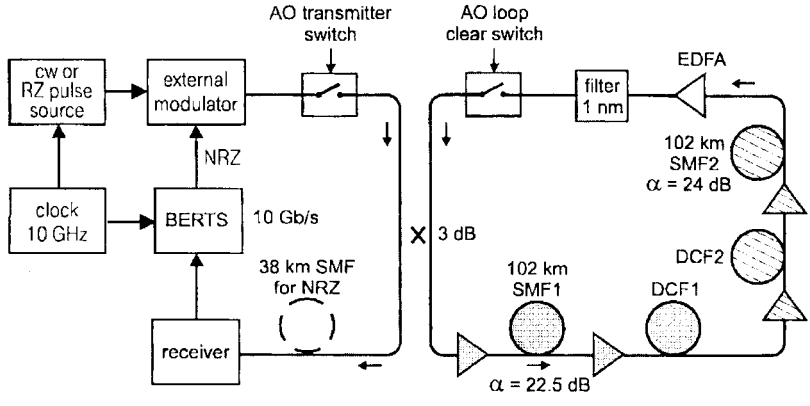

Figure 8.2: Recirculating fiber loop used to demonstrate the transmission of a 10-Gb/s signal over 2,040 km of standard fiber. Two acousto-optic (AO) switches control the timing of signal into and out of the loop. BERTS stands for bit-error-rate test set. (After Ref. [14]; ©1999 IEEE.)

tory experiments employ a fiber loop in which the optical signal is forced to recirculate many times to simulate a long-haul lightwave system. Two optical switches determine how long a pseudo-random bit stream circulates inside the loop before it reaches the receiver. The loop length and the number of round trips set the total transmission distance. The loop shown in Figure 8.2 contains two 102-km sections of standard fiber and two 20-km DCFs. A filter with a 1-nm bandwidth reduces the buildup of broadband ASE noise. The 10-Gb/s signal could be transmitted over 2,040 km with both the RZ and NRZ formats when launched power was properly optimized. However, it was necessary to add a 38-km section of standard fiber in front of the receiver in the NRZ case so that dispersion was not fully compensated.

Perfect compensation of GVD in each map period is not generally the best solution in the presence of nonlinear effects. A numerical approach is generally used to optimize the design of dispersion-managed lightwave systems [4]–[13]. In general, local GVD should be kept relatively large, while minimizing the average dispersion for all channels. In a 1998 experiment, a 40-Gb/s signal was transmitted over 2,000 km of standard fiber using a novel dispersion map [15]. The distance could be increased to 16,500 km at a lower bit rate of 10 Gb/s by placing an optical amplifier right after the DCF within the recirculating fiber loop [16]. Since the nonlinear effects were not negligible, it is believed that soliton properties played an important role in this experiment (see Section 8.2).

A systematic study based on the NLS equation (8.1.2) shows that although the NRZ format can be used at 10 Gb/s, the RZ format is superior in most practical situations for lightwave systems operating at bit rates of 40 Gb/s or higher [8]–[20]. Even at 10 Gb/s, the RZ format can be used to design systems that are capable of transmitting data over a distance of up to 10,000 km over standard fibers [22]. Such a performance is not realizable with the NRZ format. For this reason, the focus of this chapter is high-speed systems designed with the RZ format.

8.1.2 Semianalytic Approach

Although the NLS equation (8.1.2) must be solved numerically for a realistic modeling of lightwave systems, considerable insight can be gained by adopting a semianalytic approach in which the dispersive and nonlinear effects are considered for a single optical pulse representing an isolated 1 bit. In this case, Eq. (8.1.2) can be reduced to solving a set of two ordinary differential equations using a variational approach [17]. As discussed in Section 4.6, the moment method can also be employed for this purpose. Both methods assume that each optical pulse maintains its shape even though its amplitude, width, and chirp may change during propagation. As was seen in Section 3.3, a chirped Gaussian pulse maintains its functional form in the linear case ($\gamma = 0$). If the nonlinear effects are relatively weak in each fiber section locally compared with the dispersive effects, the pulse is likely to retain its Gaussian shape approximately even when nonlinear effects are included.

At a distance z inside the fiber, the envelope of a chirped Gaussian pulse has the form

$$U(z,t) = a \exp[-\tfrac{1}{2}(1+iC)t^2/T^2 + i\phi], \tag{8.1.4}$$

where a is the amplitude, T is the width, C is the chirp, and ϕ is the phase. All four parameters vary with z. As discussed in Section 4.6, the variational or the moment method can be used to obtain four ordinary differential equations governing the evolution of these four parameters with z. The phase equation can be ignored as it is not coupled to the other three equations. The amplitude equation can be integrated to find that the product a^2T does not vary with z and is related to the input pulse energy E_0 as $E_0 = \sqrt{\pi} P_0 a^2(z) T(z) = \sqrt{\pi} P_0 T(0)$ as $a(0) = 1$. Thus, we only need to solve the following two coupled equations:

$$\frac{dT}{dz} = \frac{\beta_2(z)C}{T}, \tag{8.1.5}$$

$$\frac{dC}{dz} = (1+C^2)\frac{\beta_2(z)}{T^2} + \frac{\gamma(z)p(z)E_0}{\sqrt{2\pi}T}. \tag{8.1.6}$$

Details of loss and dispersion managements appear in these equations through the z dependence of three parameters β_2, γ, and p. Equations (8.1.5) and (8.1.6) require values of three pulse parameters at the input end, namely the width T_0, chirp C_0, and energy E_0, before they can be solved. The pulse energy E_0 is related to the average power launched into the fiber link through the relation $P_{\text{av}} = \frac{1}{2}BE_0 = (\sqrt{\pi}/2)P_0(T_0/T_b)$, where T_b is the duration of bit slot at the bit rate B.

Consider first the linear case by setting $\gamma(z) = 0$. In this case, E_0 plays no role because pulse-propagation details are independent of the initial pulse energy. As shown in Section 4.6.1, Eqs. (8.1.5) and (8.1.6) can be solved analytically in the linear case and have the following general solution:

$$T^2(z) = T_0^2 + 2\int_0^z \beta_2(z)C(z)\,dz, \qquad C(z) = C_0 + \frac{1+C_0^2}{T_0^2}\int_0^z \beta_2(z)\,dz, \tag{8.1.7}$$

where details of the dispersion map are included through $\beta_2(z)$. This solution looks complicated but it is easy to perform integrations for a two-section dispersion map.

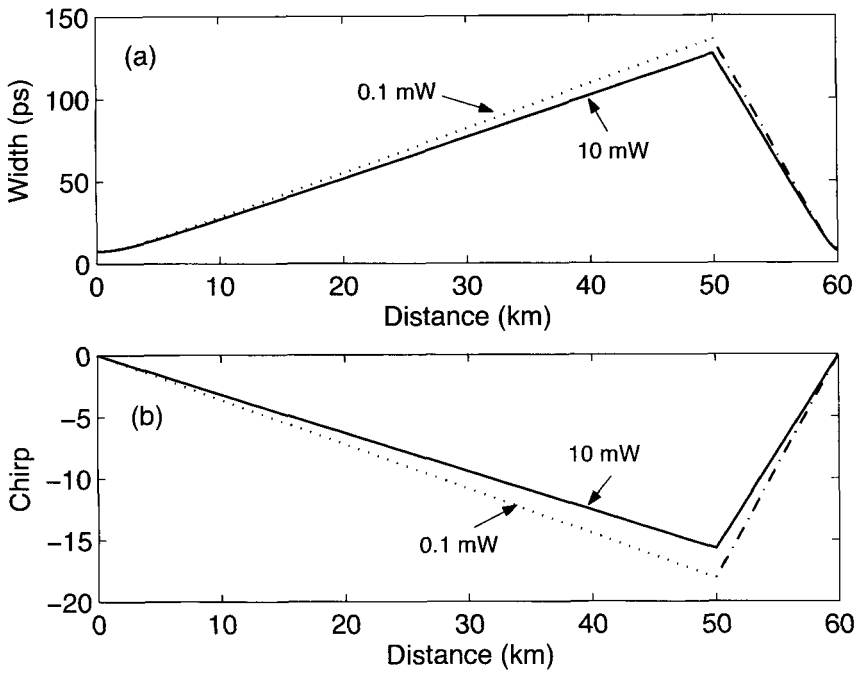

Figure 8.3: (a) Pulse width and (b) chirp at the end of successive amplifiers for several values of average input power for the 40-Gb/s system with a periodic dispersion map used in Figure 8.1.

The values of T and C at the end of the map period $z = L_{\text{map}}$ are given by

$$T_1 = T_0[(1 + C_0 d)^2 + d^2]^{1/2}, \qquad C_1 = C_0 + (1 + C_0^2)d, \tag{8.1.8}$$

where the dimensionless parameter d is defined as

$$d = \frac{1}{T_0^2}\int_0^{L_{\text{map}}} \beta_2(z)\, dz = \frac{\bar{\beta}_2 L_{\text{map}}}{T_0^2}, \tag{8.1.9}$$

and $\bar{\beta}_2$ is the average value of the dispersion parameter over the map period L_{map}.

As is evident from Eq. (8.1.8), the final pulse parameters depend only on the average dispersion, and not on details of the dispersion map, when nonlinear effects are negligible. This is exactly what one would expect when the theory of Section 3.3 is applied to a linear system. If the dispersion map is designed such that $\bar{\beta}_2 = 0$, both T and C return to their input values at $z = L_{\text{map}}$. In the case of a periodic dispersion map, each pulse would recover its original shape after each map period if $d = 0$. However, when the average GVD of the dispersion-managed link is not zero, T and C change after each map period, and pulse evolution is not periodic.

To study how the nonlinear effects governed by the γ term in Eq. (8.1.8) affect the pulse parameters, we can solve Eqs. (8.1.5) and (8.1.6) numerically. Figure 8.3 shows the evolution of pulse width and chirp over the first 60-km span for an isolated pulse in

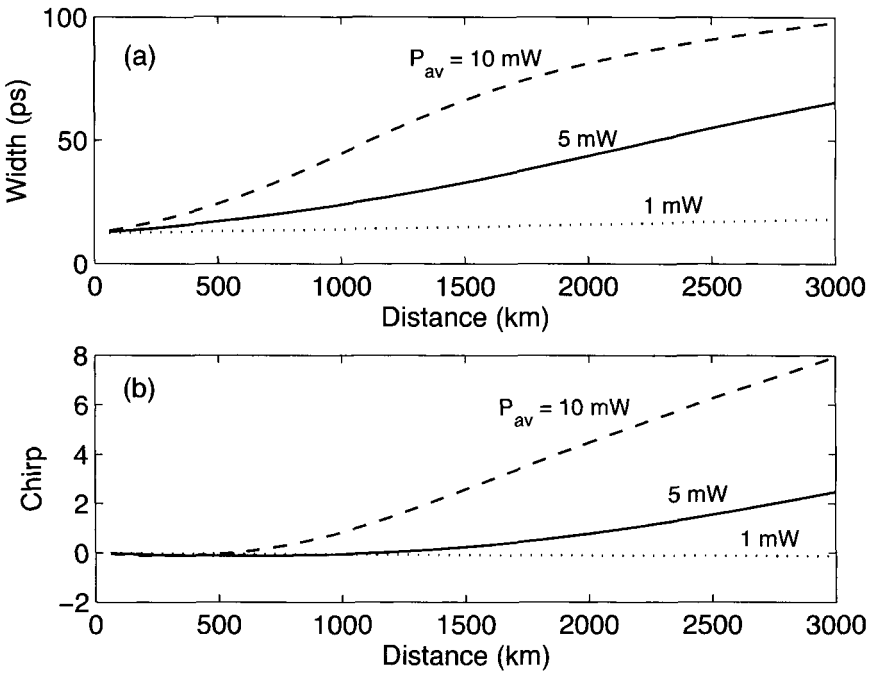

Figure 8.4: (a) Pulse width and (b) chirp at the end of successive amplifiers for three values of average input power for a 40-Gb/s system with the periodic dispersion map used in Figure 8.1.

a 40-Gb/s bit stream using the same two-section dispersion map employed for Figure 8.1 (50-km standard fiber followed with 10 km of DCF). Solid lines represent 10-mW launched power. Dotted lines show the low-power case for comparison. In the first 50-km section, pulse broadens by a factor of about 15, but it is compressed back in the DCF because of dispersion compensation. Although the nonlinear effects modify both the pulse width and chirp, changes are not large even for a 10-mW launched power. In particular, the width and chirp are almost recovered after the first 60-km span.

The situation changes considerably if the pulse is allowed to propagate over many map periods. Figure 8.4 shows the pulse width and chirp after each amplifier (spaced 60-km apart) over a distance of 3,000 km (50 map periods). At a relatively low power level of 1 mW, the input values are almost recovered after each map period as dispersion is fully compensated. However, as the launched power is increased beyond 1 mW, the nonlinear effects start to dominate, and the pulse width and chirp begin to deviate considerably from their input values, in spite of dispersion compensation. Even for $P_{av} = 5$ mW, pulse width becomes larger than the bit slot after a distance of about 1,000 km, and the situation is worse for $P_{av} = 10$ mW. Thus, the optimum power level is close to 1 mW if the objective is to minimize the impact of nonlinear effects. This conclusion is in agreement with the results shown in Figure 8.1 and obtained by solving the NLS equation directly, after including the effect of amplifier noise.

8.1.3 Soliton and Pseudo-linear Regimes

As the preceding discussion shows, when the nonlinear term in Eq. (8.1.6) is not negligible, pulse parameters do not return to their input values after each map period even for perfect dispersion compensation ($d = 0$). Eventually, the buildup of nonlinear distortion affects each pulse within the optical bit stream so much that the system cannot operate beyond a certain distance. As seen in Figure 8.1, this limiting distance can be under 500 km depending on the system design. For this reason, the management of nonlinear effects is an important issue for long-haul lightwave systems. It turns out that the parameters associated with a dispersion map (length and GVD of each section) can be controlled to manage the nonlinearity problem. Two main techniques have evolved, and systems employing them are said to operate in the *pseudo-linear* and *soliton* regimes.

It was noted in several experiments that a nonlinear system performs best when GVD compensation is only 90 to 95% so that some residual dispersion remains after each map period. In fact, if the input pulse is initially chirped such that $\bar{\beta}_2 C < 0$, the pulse at the end of the fiber link may even be shorter than the input pulse. This behavior is expected for a linear system (see Section 3.3) and follows from Eq. (8.1.8) for $C_0 d < 0$. It also persists for weakly nonlinear systems. This observation has led to the adoption of the chirped RZ (CRZ) format for dispersion-managed fiber links.

To understand how the system and fiber parameters affect the evolution of an optical signal inside a fiber link, consider a lightwave system in which dispersion is compensated only at the transmitter and receiver ends. Since fiber parameters are constant over most of the link, it is useful to introduce the dispersion and nonlinear length scales as

$$L_D = T_0^2/|\beta_2|, \qquad L_{\rm NL} = (\gamma P_0)^{-1}, \tag{8.1.10}$$

respectively. Introducing a normalized time τ as $\tau = t/T_0$, the NLS equation (8.1.2) can be written in the form

$$iL_D \frac{\partial U}{\partial z} - \frac{s}{2}\frac{\partial^2 U}{\partial \tau^2} + \frac{L_D}{L_{\rm NL}} p(z)|U|^2 U = 0, \tag{8.1.11}$$

where $s = \text{sign}(\beta_2) = \pm 1$, depending on the sign of β_2. If we use $\gamma = 2\ \text{W}^{-1}/\text{km}$ as a typical value, the nonlinear length $L_{\rm NL} \sim 100$ km at peak-power levels in the range of 2 to 4 mW. In contrast, the dispersion length L_D can vary over a wide range (from $\sim$1 to 10,000 km), depending on the bit rate of the system and the type of fibers used to construct it. As a result, one can encounter the following three situations.

If $L_D \gg L_{\rm NL}$ and link length $L < L_D$, the dispersive effects play a minor role, but the nonlinear effects cannot be ignored when $L > L_{\rm NL}$. This is the situation for systems operating at a bit rate of 2.5 Gb/s or less. For example, L_D exceeds 1,000 km at $B = 2.5$ Gb/s even for standard fibers with $\beta_2 = -21\ \text{ps}^2/\text{km}$ and can exceed 10,000 km for dispersion-shifted fibers. Such systems can be designed to operate over long distances by reducing the peak power and increasing the nonlinear length accordingly. The use of a dispersion map is also helpful for this purpose.

If L_D and $L_{\rm NL}$ are comparable and much shorter than the link length, both the dispersive and nonlinear terms are equally important in the NLS equation (8.1.11).

This is often the situation for 10-Gb/s systems operating over standard fibers because L_D becomes $\sim$100 km when T_0 is close to 50 ps. The use of optical solitons is most beneficial in the regime in which L_D and L_{NL} have similar magnitudes. A soliton-based system confines each pulse tightly to its original bit slot by employing the RZ format with a low duty cycle and maintains this confinement through a careful balance of frequency chirps induced by GVD and SPM. Since GVD is used to offset the impact of nonlinear effects, dispersion is never fully compensated in soliton-based systems. It will be seen in Section 8.2 that solitons can be formed only in the anomalous-GVD regime. A dispersion map can still be used but the average dispersion of the fiber link should be controlled. Solitons formed under such conditions are known as dispersion-managed solitons and are covered in Section 8.3.

If $L_D \ll L_{NL}$, we enter a new regime in which dispersive effects dominate locally, and the nonlinear effects can be treated in a perturbative manner. This situation is encountered in lightwave systems whose individual channels operate at a bit rate of 40 Gb/s or more. The bit slot is only 25 ps at 40 Gb/s. If T_0 is $<$10 ps and standard fibers are employed, L_D is reduced to below 5 km. A lightwave system operating under such conditions is said to operate in the pseudo-linear regime. In such systems, input pulses broaden so rapidly that they spread over several neighboring bits. The extreme broadening reduces their peak power by a large factor. Since the nonlinear term in the NLS equation (8.1.2) scales with the peak power, its impact is considerably reduced. Interchannel nonlinear effects (discussed in Chapter 9) are reduced considerably in pseudo-linear systems because of an averaging effect that produces a nearly constant total power in all bit slots. In contrast, overlapping of neighboring pulses enhances the *intrachannel* nonlinear effects. As nonlinear effects remain important, such systems are called *pseudo-linear* [26]. Of course, pulses must be compressed back at the receiver end to ensure that they occupy their original time slot before the optical signal arrives at the receiver. This can be accomplished by compensating the accumulated dispersion with a DCF or another dispersion-equalizing filter. Section 8.4 is devoted to pseudo-linear systems.

8.2 Solitons in Optical Fibers

The existence of solitons in optical fibers is the result of a balance between the chirps induced by GVD and SPM, both of which limit the system performance when acting independently. One can develop an intuitive understanding of how such a balance is possible by following the analysis of Section 3.3. As shown there, the GVD broadens an optical pulse during its propagation inside an optical fiber, except when the pulse is initially chirped in the right way (see Figure 3.3). More specifically, a chirped pulse can be compressed during the early stage of propagation whenever β_2 and the chirp parameter C happen to have opposite signs so that $\beta_2 C$ is negative. As discussed in Section 4.1, SPM imposes a chirp on the optical pulse such that $C > 0$. If $\beta_2 < 0$, the condition $\beta_2 C < 0$ is readily satisfied. Moreover, as the SPM-induced chirp is power-dependent, it is not difficult to imagine that under certain conditions, SPM and GVD may cooperate in such a way that the SPM-induced chirp is just right to cancel

the GVD-induced broadening of the pulse. The optical pulse would then propagate undistorted in the form of a soliton.

8.2.1 Properties of Optical Solitons

To find the conditions under which solitons can form, we use $s = -1$ in Eq. (8.1.11), assuming that pulses are propagating in the region of anomalous GVD, and set $p(z) = 1$, a condition requiring perfect distributed amplification. Introducing a normalized distance as $\xi = z/L_D$, Eq. (8.1.11) can be written as

$$i\frac{\partial U}{\partial \xi} + \frac{1}{2}\frac{\partial^2 U}{\partial \tau^2} + N^2|U|^2U = 0, \tag{8.2.1}$$

where the parameter N is defined as

$$N^2 = \frac{L_D}{L_{\rm NL}} = \frac{\gamma P_0 T_0^2}{|\beta_2|}. \tag{8.2.2}$$

It represents a dimensionless combination of the pulse and fiber parameters. Even the single parameter N appearing in Eq. (8.2.1) can be removed by introducing $u = NU$ as a renormalized amplitude. With this change, the NLS equation takes on its canonical form

$$i\frac{\partial u}{\partial \xi} + \frac{1}{2}\frac{\partial^2 u}{\partial \tau^2} + |u|^2u = 0. \tag{8.2.3}$$

The NLS equation (8.2.3) belongs to a special class of nonlinear partial differential equations that can be solved exactly with a mathematical technique known as the *inverse scattering method* [27]–[29]. It was first solved in 1971 by this method [30]. The main result can be summarized as follows. When an input pulse having an initial amplitude

$$u(0, \tau) = N\,\mathrm{sech}(\tau) \tag{8.2.4}$$

is launched into the fiber, its shape remains unchanged during propagation when $N = 1$ but follows a periodic pattern for integer values of $N > 1$ such that the input shape is recovered at $\xi = m\pi/2$, where m is an integer.

An optical pulse whose parameters satisfy the condition $N = 1$ is called the *fundamental soliton*. Pulses corresponding to other integer values of N are called *higher-order solitons*. The parameter N represents the order of the soliton. Noting that $\xi = z/L_D$, the soliton period z_0, defined as the distance over which higher-order solitons recover their original shape, is given by

$$z_0 = \frac{\pi}{2}L_D = \frac{\pi}{2}\frac{T_0^2}{|\beta_2|}. \tag{8.2.5}$$

The *soliton period* z_0 and *soliton order* N play an important role in the theory of optical solitons. Figure 8.5 shows the evolution of a third-order soliton over one soliton period by solving the NLS equation (8.2.1) numerically with $N = 3$. The pulse shape changes considerably but returns to its original form at $z = z_0$. Only a fundamental soliton

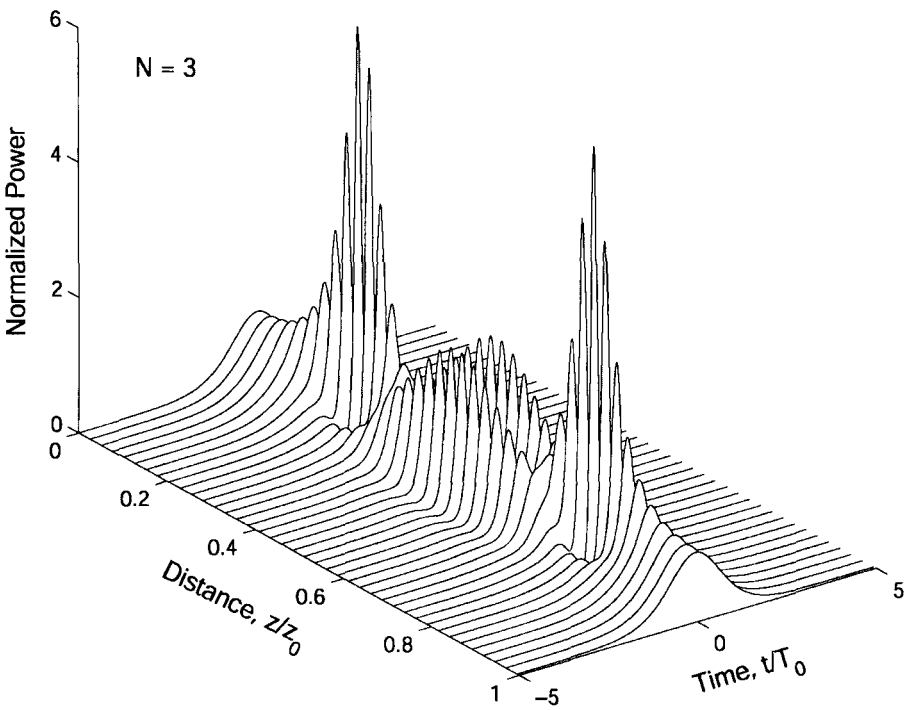

Figure 8.5: Evolution of a third-order soliton over one soliton period. The power profile $|u|^2$ is plotted as a function of z/L_D.

maintains its shape during propagation inside optical fibers. In a 1973 study, Eq. (8.2.1) was solved numerically to show that optical solitons can form in optical fibers [31].

The solution corresponding to the fundamental soliton can be obtained by solving Eq. (8.2.3) directly, without recourse to the inverse scattering method. The approach consists of assuming that a solution of the form

$$u(\xi,\tau) = V(\tau)\exp[i\phi(\xi)] \tag{8.2.6}$$

exists, where V must be independent of ξ for Eq. (8.2.6) to represent a fundamental soliton that maintains its shape during propagation. The phase ϕ can depend on ξ but is assumed to be time-independent. When Eq. (8.2.6) is substituted in Eq. (8.2.3) and the real and imaginary parts are separated, we obtain two real equations for V and ϕ. These equations show that ϕ should be of the form $\phi(\xi) = K\xi$, where K is a constant. The function $V(\tau)$ is then found to satisfy the nonlinear differential equation

$$\frac{d^2V}{d\tau^2} = 2V(K - V^2). \tag{8.2.7}$$

This equation can be solved by multiplying it with $2(dV/d\tau)$ and integrating over τ. The result is found to be

$$(dV/d\tau)^2 = 2KV^2 - V^4 + C, \tag{8.2.8}$$

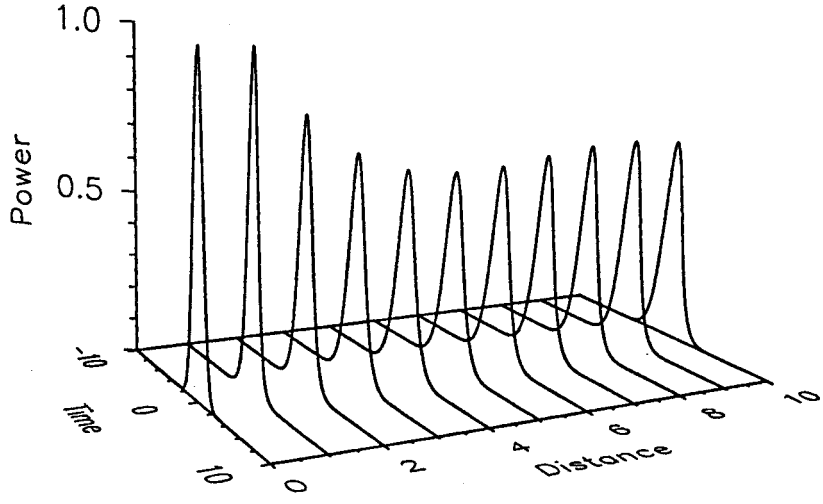

Figure 8.6: Evolution of a Gaussian pulse with $N = 1$ over the range $\xi = 0$ to 10. The pulse evolves toward the fundamental soliton by changing its shape, width, and peak power.

where C is a constant of integration. Using the boundary condition that both V and $dV/d\tau$ should vanish for any optical pulse at $|\tau| \to \infty$, C can be set to zero.

The constant K in Eq. (8.2.8) is determined using the boundary condition that $V = 1$ and $dV/d\tau = 0$ at the soliton peak, assumed to occur at $\tau = 0$. Its use provides $K = \frac{1}{2}$, resulting in $\phi = \xi/2$. Equation (8.2.8) is easily integrated to obtain $V(\tau) = \text{sech}(\tau)$. We have thus found the well-known "sech" solution [27]–[29]

$$u(\xi, \tau) = \text{sech}(\tau) \exp(i\xi/2) \tag{8.2.9}$$

for the fundamental soliton by integrating the NLS equation directly. It shows that the input pulse acquires a phase shift $\xi/2$ as it propagates inside the fiber, but its amplitude remains unchanged. It is this property of a fundamental soliton that makes it an ideal candidate for optical communications. In essence, the effects of fiber dispersion are exactly compensated by the fiber nonlinearity when the input pulse has a "sech" shape and its width and peak power are related by Eq. (8.2.2) in such a way that $N = 1$.

An important property of optical solitons is that they are remarkably stable against perturbations. Thus, even though the fundamental soliton requires a specific shape and a certain peak power corresponding to $N = 1$ in Eq. (8.2.2), it can be created even when the pulse shape and the peak power deviate from the ideal conditions. Figure 8.6 shows the numerically simulated evolution of a Gaussian input pulse for which $N = 1$ but $u(0, \tau) = \exp(-\tau^2/2)$. As seen there, the pulse adjusts its shape and width as it propagates down the fiber in an attempt to become a fundamental soliton and attains a "sech" profile for $\xi \gg 1$. Similar behavior is observed when N deviates from 1. It turns out that the Nth-order soliton can form when the input value of N is in the range $N - \frac{1}{2}$ to $N + \frac{1}{2}$ [32]. In particular, the fundamental soliton can be excited for values of N in the range of 0.5 to 1.5.

It may seem mysterious that an optical fiber can force any input pulse to evolve toward a soliton. A simple way to understand this behavior is to think of optical solitons as the temporal modes of a nonlinear waveguide. Higher intensities in the pulse center create a temporal waveguide by increasing the refractive index only in the central part of the pulse. Such a waveguide supports temporal modes just as the core-cladding index difference leads to spatial modes of optical fibers. When the input pulse does not match a temporal mode precisely but it is close to it, most of the pulse energy can still be coupled to that temporal mode. The rest of the energy spreads in the form of *dispersive waves*. It will be seen later that such dispersive waves affect system performance and should be minimized by matching the input conditions as close to the ideal requirements as possible. When solitons adapt to perturbations adiabatically, perturbation theory developed specifically for solitons can be used to study how the soliton amplitude, width, frequency, speed, and phase evolve along the fiber.

The NLS equation can be solved with the inverse scattering method even when an optical fiber exhibits normal dispersion [33]. The intensity profile of the resulting solutions exhibits a dip in a uniform background, and it is the dip that remains unchanged during propagation inside an optical fiber [34]. For this reason, such solutions of the NLS equation are called *dark* solitons. Even though dark solitons were observed during the 1980s and their properties have been studied thoroughly [35]–[42], most experiments have employed bright solitons with a "sech" shape. In the following discussion we focus on the fundamental soliton given in Eq. (8.2.9).

8.2.2 Loss-Managed Solitons

As seen in the preceding section, solitons use SPM to maintain their width even in the presence of fiber dispersion. However, this property holds only if soliton energy is maintained inside the fiber. It is not difficult to see that a decrease in pulse energy because of fiber losses would produce soliton broadening simply because a reduced peak power weakens the SPM effect necessary to counteract the GVD. When optical amplifiers are used periodically for compensating fiber losses, soliton energy changes in a periodic fashion. Such energy variations are included in the NLS equation (8.1.11) through the periodic function $p(z)$. In the case of lumped amplifiers, $p(z)$ decreases exponentially between two amplifiers and can vary by 20 dB or more over each period. The important question is whether solitons can maintain their shape and width in spite of such large energy fluctuations. It turns out that solitons can remain stable over long distances, provided amplifier spacing L_A is kept much smaller than the dispersion length L_D [43].

In general, changes in soliton energy are accompanied by changes in pulse width. Large rapid variations in $p(z)$ can destroy a soliton if its width changes rapidly through the emission of dispersive waves. The concept of the *path-averaged* soliton [43] makes use of the fact that solitons evolve little over a distance that is short compared with the dispersion length (or soliton period). Thus, when $L_A \ll L_D$, the width of a soliton remains virtually unchanged even if its peak power varies considerably in each section between two amplifiers. In effect, one can replace $p(z)$ by its average value $\bar{p}$ in Eq. (8.1.11) when $L_A \ll L_D$. Noting that $\bar{p}$ is just a constant that modifies γP_0, we recover the standard NLS equation.

From a practical viewpoint, a fundamental soliton can be excited if the input peak power P_s (or energy) of the path-averaged soliton is chosen to be larger by a factor of $1/\bar{p}$. If we introduce the amplifier gain as $G = \exp(\alpha L_A)$ and use $\bar{p} = L_A^{-1} \int_0^{L_A} e^{-\alpha z} dz$, the energy enhancement factor for loss-managed solitons is given by

$$f_{\rm LM} = \frac{P_s}{P_0} = \frac{1}{\bar{p}} = \frac{\alpha L_A}{1 - \exp(-\alpha L_A)} = \frac{G \ln G}{G - 1}. \tag{8.2.10}$$

Thus, soliton evolution in lossy fibers with periodic lumped amplification is identical to that in lossless fibers provided (1) amplifiers are spaced such that $L_A \ll L_D$ and (2) the launched peak power is larger by a factor $f_{\rm LM}$. As an example, $G = 10$ and $f_{\rm LM} \approx 2.56$ when $L_A = 50$ km and $\alpha = 0.2$ dB/km.

The condition $L_A \ll L_D$ is somewhat vague for designing soliton systems. The question is how close L_A can be to L_D before the system may fail to work. The semi-analytic approach of Section 8.1.2 can be extended to study how fiber losses affect the evolution of solitons. However, we should replace Eq. (8.1.4) with

$$U(z,t) = a\,\mathrm{sech}(t/T)\exp[-iCt^2/T^2 + i\phi], \tag{8.2.11}$$

to ensure that the "sech" shape of a soliton is maintained. Using the variational or the moment method from Section 4.6, we obtain the following two coupled equations:

$$\frac{dT}{dz} = \frac{\beta_2 C}{T}, \tag{8.2.12}$$

$$\frac{dC}{dz} = \left(\frac{4}{\pi^2} + C^2\right)\frac{\beta_2}{T^2} + \frac{2\gamma p(z) E_0}{\pi^2 T}, \tag{8.2.13}$$

where $E_0 = 2P_0T_0$ is the input pulse energy. A comparison with Eqs. (8.1.5) and (8.1.6) obtained for Gaussian pulses shows that the width equation remains unchanged; the chirp equation also has the same form but different coefficients.

As a simple application, let us use the moment method for finding the soliton-formation condition in the ideal case of $p(z) = 1$. If the pulse is initially unchirped, both derivatives in Eqs. (8.2.12) and (8.2.13) vanish at $z = 0$ if β_2 is negative and the pulse energy is chosen to be $E_0 = 2|\beta_2|/(\gamma T_0)$. Under such conditions, the width and chirp of the pulse will not change with z, and the pulse will form a fundamental soliton. Using $E_0 = 2P_0T_0$, it is easy to see that this condition is equivalent to setting $N = 1$ in Eq. (8.2.2).

Consider now what happens when $p(z) = \exp(-\alpha z)$ in each fiber section of length L_A in a periodic fashion. Figure 8.7 shows how the soliton width changes at successive amplifiers for several values of L_A in the range 25 to 100 km, assuming $L_D = 100$ km. Such values of dispersion length are realized for a 10-Gb/s soliton system, for example, when $T_0 = 20$ ps and $\beta_2 = -4$ ps^2/km. When amplifier spacing is 25 km, both the width and chirp remain close to their input values. As L_A is increased to 50 km, they oscillate in a periodic fashion, and oscillation amplitude increases as L_A increases. For example, the width can change by more than 10% when $L_A = 75$ km. The oscillatory behavior can be understood by performing a linear stability analysis of Eqs. (8.2.12) and (8.2.13). However, if L_A/L_D exceeds 1 considerably, the pulse width starts to

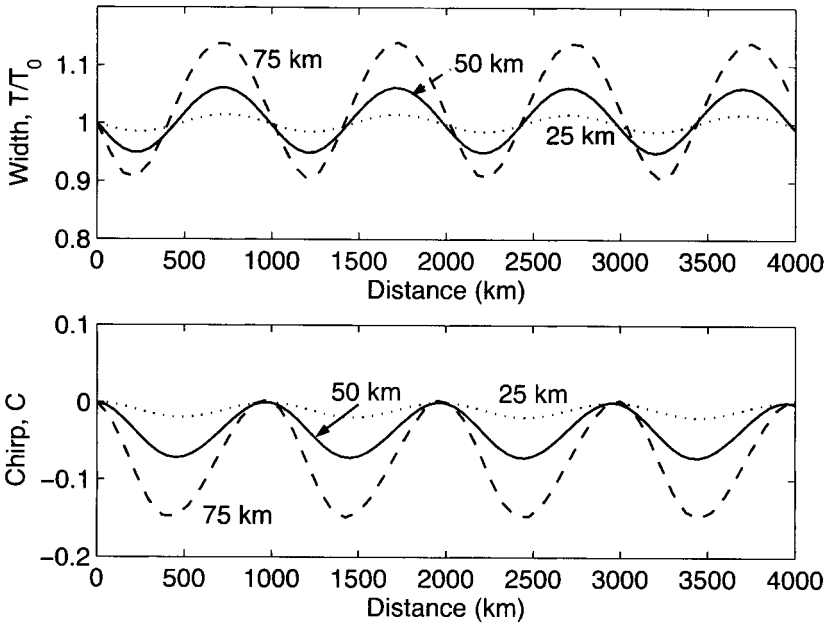

Figure 8.7: Evolution of pulse with T and chirp C along the fiber length for three amplifier spacings (25, 50, and 75 km) when $L_D = 100$ km.

increase exponentially in a monotonic fashion. Figure 8.7 shows that $L_A/L_D \leq 0.5$ is a reasonable design criterion when lumped amplifiers are used for loss management.

The variational equations such as Eqs. (8.2.12) and (8.2.13) only serve as a guideline, and their solutions are not always trustworthy, because they completely ignore the dispersive radiation generated as solitons are perturbed. For this reason, it is important to verify their predictions through direct numerical simulations of the NLS equation itself. Figure 8.8 shows the evolution of a loss-managed soliton over a distance of 10,000 km, assuming that solitons are amplified every 50 km. When the input pulse width corresponds to a dispersion length of 200 km, the soliton is preserved quite well even after 10,000 km because the condition $L_A \ll L_D$ is well satisfied. However, if the dispersion length is reduced to 25 km, the soliton is unable to sustain itself because of the excessive emission of dispersive waves.

How does the limitation on amplifier spacing affect the design of soliton systems? The condition $L_A < L_D$ can be related to the width T_0 through $L_D = T_0^2/|\beta_2|$. The resulting condition is

$$T_0 > \sqrt{|\beta_2| L_A}. \tag{8.2.14}$$

The pulse width T_0 must be a small fraction of the bit slot $T_b = 1/B$ to ensure that the neighboring solitons are well separated. Mathematically, the soliton solution in Eq. (8.2.9) is valid only when a single pulse propagates by itself. It remains approximately valid for a train of pulses only when individual solitons are well isolated. This requirement can be used to relate the soliton width T_0 to the bit rate B using $T_b = 2q_0 T_0$, where

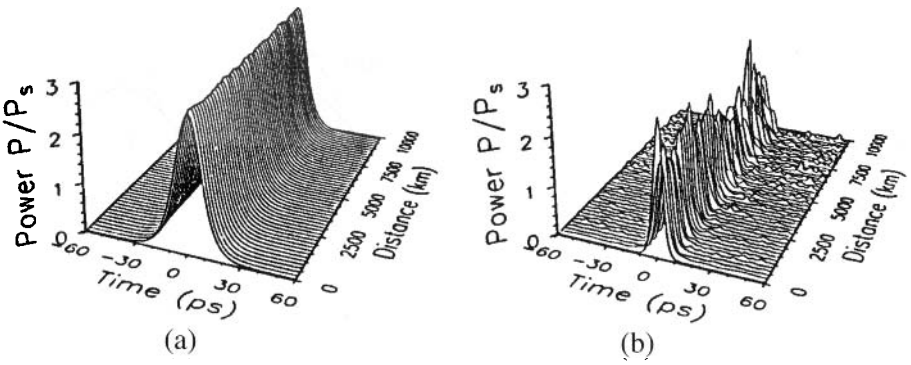

Figure 8.8: Evolution of loss-managed solitons over 10,000 km for (a) $L_D = 200$ km and (b) 25 km with $L_A = 50$ km, $\alpha = 0.22$ dB/km, and $\beta_2 = -0.5$ ps^2/km.

$2q_0$ is a measure of separation between two neighboring pulses in an optical bit stream. Typically, q_0 exceeds 4 to ensure that pulse tails do not overlap significantly. Using $T_0 = (2q_0B)^{-1}$ in Eq. (8.2.14), we obtain the following design criterion:

$$B^2 L_A < (4q_0^2|\beta_2|)^{-1}. \tag{8.2.15}$$

Choosing typical values, $\beta_2 = -2$ ps^2/km, $L_A = 50$ km, and $q_0 = 5$, we obtain $T_0 > 10$ ps and $B < 10$ GHz. Clearly, the use of path-averaged solitons imposes a severe limitation on both the bit rate and the amplifier spacing for soliton communication systems. To operate even at 10 Gb/s, one must reduce either q_0 or L_A if β_2 is kept fixed. Both of these parameters cannot be reduced much below the values used in obtaining the preceding estimate.

A partial solution to this problem was suggested in 2000 when it was proposed that one could prechirp the soliton to relax the condition $L_A \ll L_D$, even though the standard soliton solution in Eq. (8.2.9) has no chirp [44]. The basic idea consists of finding a periodic solution of Eqs. (8.2.12) and (8.2.13) that repeats itself at each amplifier using the periodic boundary conditions

$$T(z = L_A) = T_0, \qquad C(z = L_A) = C_0. \tag{8.2.16}$$

The input pulse energy E_0 and input chirp C_0 can be used as two adjustable parameters. A perturbative solution of Eqs. (8.2.12) and (8.2.13) shows that the pulse energy must be increased by a factor close to the energy enhancement factor $f_{\rm LM}$ in Eq. (8.2.10). At the same time, the input chirp that provides a periodic solution is related to this factor as

$$C_0 = \frac{4}{\pi^2}\left[\frac{1}{2} - \frac{(f_{\rm LM} - 1)}{\ln G}\right]. \tag{8.2.17}$$

Numerical results based on the NLS equation show that with a proper prechirping of input solitons, amplifier spacing can exceed $2L_D$. However, dispersive waves eventually destabilize a soliton over long fiber lengths when L_A is made significantly larger than the dispersive length.

The condition $L_A \ll L_D$ can also be relaxed considerably by employing distributed amplification. As discussed in Section 3.2, a distributed-amplification scheme is superior to lumped amplification because its use provides a nearly lossless fiber by compensating losses locally at every point along the fiber link. Historically, distributed Raman amplification of solitons was proposed in 1984 [45] and was used by 1985 in an experiment [46]. A 1988 experiment transmitted solitons over 4,000 km using periodic Raman amplification [47]. This experiment used a 42-km recirculating fiber loop whose loss was exactly compensated by injecting pump light from a 1.46-μm color-center laser. Solitons were allowed to circulate many times along the fiber loop and their width was monitored after each round trip. The 55-ps solitons could be circulated along the loop up to 96 times without a significant increase in their pulse width, indicating soliton recovery over 4,000 km. The distance could be increased to 6,000 km with further optimization. This experiment was the first to demonstrate that solitons could be transmitted over transoceanic distances in principle. The main drawback was that Raman amplification required pump lasers emitting more than 500 mW of power near 1.46 μm. It was not possible to obtain such high powers from semiconductor lasers in 1988, and the color-center lasers used in the experiment were too bulky to be useful for practical lightwave systems.

Starting in 1989, lumped amplifiers were used for loss-managed soliton systems. In a 1991 experiment, 2.5-Gb/s solitons were transmitted over 12,000 km by using a 75-km recirculating loop containing three amplifiers, spaced apart by 25 km [48]. In this experiment, the bit rate–distance product of $BL = 30$ (Tb/s)-km was limited mainly by the timing jitter induced by amplifier noise. During the 1990s, several schemes for reducing the timing jitter were discovered and employed for improving the performance of soliton systems [49]–[51]. Even the technique of Raman amplification was revived in 1999 and has become quite common for both the soliton and nonsoliton systems.

8.3 Dispersion-Managed Solitons

The preceding discussion of solitons assumed that the GVD was constant along the fiber link. However, dispersion management is employed commonly for modern WDM lightwave systems as it helps in suppressing FWM among channels. It turns out that solitons can form even when the GVD parameter β_2 varies along the link length but their properties are quite different. This section is devoted to such dispersion-managed solitons. We first consider dispersion-decreasing fibers and then focus on fiber links with periodic dispersion maps.

8.3.1 Dispersion-Decreasing Fibers

An interesting scheme proposed in 1987 relaxes completely the restriction $L_A \ll L_D$ imposed normally on loss-managed solitons by employing a new kind of fiber in which GVD varies along the fiber length [52]. Such fibers are called *dispersion-decreasing* fibers (DDFs) and are designed such that the decreasing GVD counteracts the reduced SPM experienced by solitons weakened from fiber losses.

Soliton evolution in a DDF is governed by Eq. (8.1.2) except that β_2 is a continuous function of z. Introducing the normalized distance and time variables as

$$\xi = T_0^{-2} \int_0^z \beta_2(z)\, dz, \qquad \tau = t/T_0, \tag{8.3.1}$$

we can write this equation in the form

$$i\frac{\partial U}{\partial \xi} + \frac{1}{2}\frac{\partial^2 U}{\partial \tau^2} + N^2(z)|U|^2 U = 0, \tag{8.3.2}$$

where $N^2(z) = \gamma P_0 T_0^2 p(z)/|\beta_2(z)|$. If the GVD profile is chosen such that $|\beta_2(z)| = |\beta_2(0)|p(z)$, N becomes a constant, and Eq. (8.3.2) reduces the standard NLS equation obtained earlier with $p(z) = 1$. As a result, fiber losses have no effect on a soliton in spite of its reduced energy when DDFs are used. More precisely, lumped amplifiers can be placed at any distance and are not limited by the condition $L_A \ll L_D$, provided the GVD decreases exponentially in the fiber section between two amplifiers as

$$|\beta_2(z)| = |\beta_2(0)| \exp(-\alpha z). \tag{8.3.3}$$

This result can be understood qualitatively by noting from Eq. (8.2.2) that the requirement $N = 1$ can be maintained, in spite of power losses, if both $|\beta_2|$ and γ decrease exponentially at the same rate. The fundamental soliton then maintains its shape and width even in a lossy fiber.

Fibers with a nearly exponential GVD profile have been fabricated [53]. A practical technique for making such DDFs consists of reducing the core diameter along the fiber length in a controlled manner during the fiber-drawing process. Variations in the fiber diameter change the waveguide contribution to β_2 and reduce its magnitude. Typically, GVD can be varied by a factor of 10 over a length of 20 to 40 km. The accuracy realized by the use of this technique is estimated to be better than 0.1 ps^2/km [54]. The propagation of solitons in DDFs has been observed in several experiments [54]–[56]. In a 40-km DDF, solitons preserved their width and shape in spite of energy losses of more than 8 dB [55]. In a recirculating loop made using DDFs, a 6.5-ps soliton train at 10 Gb/s could be transmitted over 300 km [56].

In an alternative approach, the exponential GVD profile of a DDF is approximated with a staircase profile by splicing together several constant-dispersion fibers with different β_2 values. This approach was studied during the 1990s, and it was found that most of the benefits of DDFs can be realized using as few as four fiber segments [57]–[61]. How should one select the length and the GVD of each fiber used for emulating a DDF? The answer is not obvious, and several methods have been proposed. In one approach, power deviations are minimized in each section [57]. In another approach, fibers of different GVD values D_m and different lengths L_{map} are chosen such that the product $D_m L_{\text{map}}$ is the same for each section. In a third approach, D_m and L_{map} are selected to minimize the shading of dispersive waves [58]. Advantages offered by DDFs for soliton systems include a lower timing jitter [50] and a reduced noise level [62]. In spite of these benefits, DDFs are rarely used in practice.

8.3.2 Periodic Dispersion Maps

The main disadvantage of DDFs from the standpoint of system design is that the average dispersion along the link is relatively large for them. Dispersion maps consisting of alternating-GVD fibers are attractive because their use lowers the average dispersion of the entire link, while keeping the GVD of each section large enough that the FWM crosstalk remains negligible in WDM systems.

The use of dispersion management forces each soliton to propagate in the normal-dispersion regime of a fiber during each map period. At first sight, such a scheme should not even work because the normal-GVD fibers do not support solitons and lead to considerable broadening and chirping of the pulse. So, why should solitons survive in a dispersion-managed fiber link? An intense theoretical effort devoted to this issue has led to the discovery of dispersion-managed (DM) solitons [63]–[86]. Physically speaking, if the dispersion length associated with each fiber section used to form the map is a fraction of the nonlinear length, the pulse would evolve in a linear fashion over a single map period. On a longer length scale, solitons can still form if the SPM effects are balanced by the average dispersion. As a result, solitons can survive in an average sense, even though not only the peak power but also the width and shape of such solitons oscillate periodically.

Consider a simple dispersion map consisting of two fibers with opposite GVD characteristics. Soliton evolution is governed by Eq. (8.1.2) in which β_2 is a piecewise continuous function of z taking values β_{2a} and β_{2n} in the anomalous and normal GVD sections of lengths l_a and l_n, respectively. The map period $L_{\text{map}} = l_a + l_n$ can be different from the amplifier spacing L_A. As is evident, the properties of DM solitons will depend on several map parameters even when only two types of fibers are used in each map period. Numerical simulations show that a nearly periodic solution can often be found by adjusting input pulse parameters (width, chirp, and peak power) even though these parameters vary considerably in each map period. The shape of such DM solitons is closer to a Gaussian profile rather than the "sech" shape associated with standard solitons [64]–[66].

Numerical solutions, although essential, do not lead to much physical insight. Several techniques have been used to solve the NLS equation (8.1.2) approximately. A common approach makes use of the variational method [67]–[69]. Another approach expands $B(z,t)$ in terms of a complete set of the Hermite–Gauss functions that are solutions of the linear problem [70]. A third approach solves an integral equation, derived in the spectral domain using perturbation theory [72]–[74].

To simplify the following discussion, we focus on the variational equations (8.1.5) and (8.1.6) used earlier in Section 8.1.2. Because the shape of DM solitons is close to a Gaussian pulse, they can be applied for them. These two equations should be solved with the periodic boundary conditions given in Eq. (8.2.16) to ensure that the DM soliton recovers its initial state after each amplifier. The periodic boundary conditions fix the values of the initial width T_0 and the chirp C_0 at $z = 0$ for which a soliton can propagate in a periodic fashion for a given value of pulse energy E_0. A new feature of the DM solitons is that the input pulse width depends on the dispersion map and cannot be chosen arbitrarily. In fact, T_0 cannot fall below a critical value that is set by the map itself.

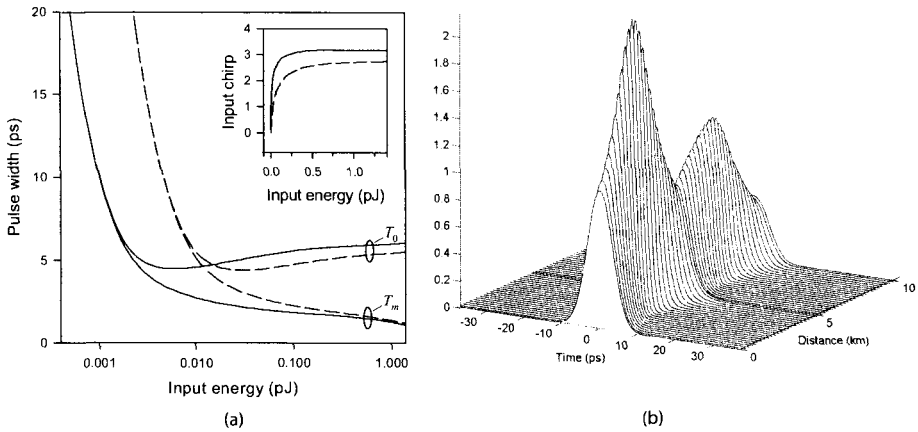

Figure 8.9: (a) Changes in T_0 (upper curve) and T_m (lower curve) with input pulse energy E_0 for $\alpha = 0$ (solid lines) and 0.25 dB/km (dashed lines). The inset shows the input chirp C_0 in the two cases. (b) Evolution of the DM soliton over one map period for $E_0 = 0.1$ pJ and $L_A = 80$ km.

Figure 8.9 shows how the pulse width T_0 and the chirp C_0 of allowed periodic solutions vary with input pulse energy for a specific dispersion map. The minimum value T_m of the pulse width occurring in the middle of the anomalous-GVD section of the map is also shown. The map is suitable for 40-Gb/s systems and consists of alternating fibers with GVD of -4 and 4 ps^2/km and lengths $l_a \approx l_n = 5$ km such that the average GVD is -0.01 ps^2/km. The solid lines show the case of ideal distributed amplification for which $p(z) = 1$ in Eq. (7.1.5). The lumped-amplification case is shown by the dashed lines in Figure 8.9, assuming 80-km amplifier spacing and 0.25 dB/km losses in each fiber section.

Several conclusions can be drawn from Figure 8.9. First, both T_0 and T_m decrease rapidly as pulse energy is increased. Second, T_0 attains its minimum value at a certain pulse energy E_c while T_m keeps decreasing slowly. Third, T_0 and T_m differ by a large factor for $E_0 \gg E_c$. This behavior indicates that pulse width changes considerably in each fiber section when this regime is approached. An example of pulse breathing is shown in Figure 8.9(b) for $E_0 = 0.1$ pJ in the case of lumped amplification. The input chirp C_0 is relatively large ($C_0 \approx 1.8$) in this case. The most important feature of Figure 8.9 is the existence of a minimum value of T_0 for a specific value of the pulse energy. The input chirp $C_0 = 1$ at that point. It is interesting to note that the minimum value of T_0 does not depend much on fiber losses and is about the same for the solid and dashed curves, although the value of E_c is much larger in the lumped amplification case because of fiber losses.

As seen from Figure 8.9, both the pulse width and the peak power of DM solitons vary considerably within each map period. Figure 8.10(a) shows the width and chirp variations over one map period for the DM soliton of Figure 8.9(b). The pulse width varies by more than a factor of 2 and becomes minimum nearly in the middle of each fiber section where frequency chirp vanishes. The shortest pulse occurs in the middle of the anomalous-GVD section in the case of ideal distributed amplification in which

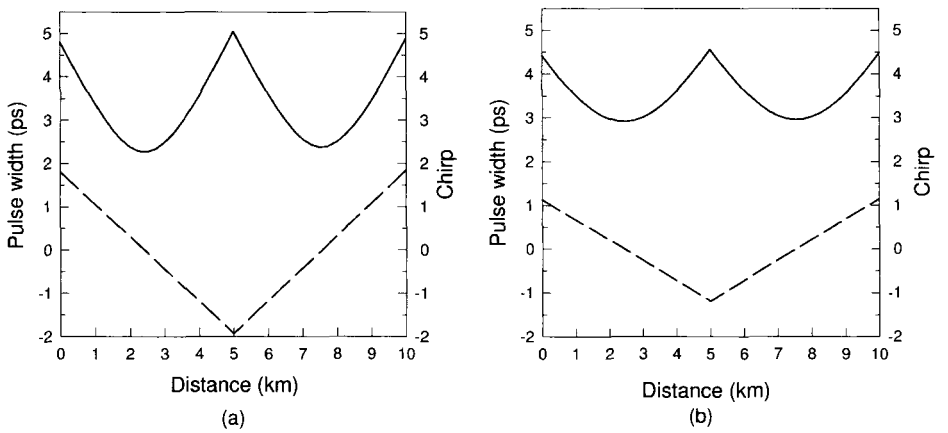

Figure 8.10: Variations of pulse width and chirp (dashed line) over one map period for DM solitons with the input energy (a) $E_0 = 0.1$ pJ and (b) E_0 close to E_c.

fiber losses are compensated fully at every point along the fiber link. For comparison, Figure 8.10(b) shows the width and chirp variations for a DM soliton whose input energy is close to E_c where the input pulse is shortest. Breathing of the pulse is reduced considerably together with the range of chirp variations. In both cases, the DM soliton is quite different from a standard fundamental soliton as it does not maintain its shape, width, or peak power. Nevertheless, its parameters repeat from period to period at any location within the map. For this reason, DM solitons can be used for optical communications in spite of oscillations in the pulse width. Moreover, such solitons perform better from a system standpoint.

8.3.3 Design Issues

Figures 8.9 and 8.10 show that Eqs. (8.1.5) and (8.1.6) permit periodic propagation of many different DM solitons in the same map by choosing different values of E_0, T_0, and C_0. How should one choose among these solutions when designing a soliton system? Pulse energies much smaller than E_c (corresponding to the minimum value of T_0) should be avoided because a low average power would then lead to rapid degradation of SNR as amplifier noise builds up with propagation. On the other hand, when $E_0 \gg E_c$, large variations in the pulse width in each fiber section would induce XPM-induced interaction between two neighboring solitons if their tails begin to overlap considerably. For this region, the region near $E_0 = E_c$ is most suited for designing DM soliton systems. Numerical solutions of the NLS equation (8.1.2) confirm this conclusion.

The 40-Gb/s system design used for Figures 8.9 and 8.10 was possible only because the map period L_{map} was chosen to be much smaller than the amplifier spacing of 80 km, a configuration referred to as the *dense* dispersion management. When L_{map} is increased to 80 km using $l_a \approx l_b = 40$ km, while keeping the same value of average dispersion, the minimum pulse width supported by the map increases by a factor of 3. The bit rate is then limited to below 20 Gb/s.

It is possible to find the values of T_0 and T_m by solving Eqs. (8.1.5) and (8.1.6) approximately. Equation (8.1.6) shows that $T^2(z) = T_0^2 + 2\int_0^z \beta_2(z)C(z)\,dz$ any point within the map. The chirp equation cannot be integrated analytically but the numerical solutions show that $C(z)$ varies almost linearly in each fiber section. As seen in Figure 8.10, $C(z)$ changes from C_0 to $-C_0$ in the first section and then back to C_0 in the second section. Noting that the ratio $(1+C^2)/T^2$ is related to the spectral width that changes little over one map period when the nonlinear length is much larger than the local dispersion length, we average it over one map period and obtain the following relation between T_0 and C_0:

$$T_0 = T_{\text{map}}\sqrt{\frac{1+C_0^2}{|C_0|}}, \qquad T_{\text{map}} = \left(\frac{|\beta_{2n}\beta_{2a}l_n l_a|}{\beta_{2n}l_n - \beta_{2a}l_a}\right)^{1/2}, \tag{8.3.4}$$

where T_{map} is a parameter with dimensions of time involving only the four map parameters [83]. It provides a time scale associated with an arbitrary dispersion map in the sense that the stable periodic solutions supported by it have input pulse widths that are close to T_{map} (within a factor of 2 or so). The minimum value of T_0 occurs for $|C_0| = 1$ and is given by $T_0^{\min} = \sqrt{2}T_{\text{map}}$.

Equation (8.3.4) can also be used to find the shortest pulse within the map. Recalling from Section 3.3 that the shortest pulse occurs at the point at which the pulse becomes unchirped, we obtain $T_m = T_0/(1+C_0^2)^{1/2} = T_{\text{map}}/\sqrt{|C_0|}$. When the input pulse corresponds to its minimum value ($C_0 = 1$), T_m is exactly equal to T_{map}. The optimum value of the pulse stretching factor is equal to $\sqrt{2}$ under such conditions. These conclusions are in agreement with the numerical results shown in Figure 8.10 for a specific map for which $T_{\text{map}} \approx 3.16$ ps. If dense dispersion management is not used for this map and L_{map} equals $L_A = 80$ km, this value of T_{map} increases to 9 ps. Since the FWHM of input pulses then exceeds 21 ps, such a map is unsuitable for 40-Gb/s soliton systems. In general, the required map period becomes shorter as the bit rate increases, as is evident from the definition of T_{map} in Eq. (8.3.4).

It is useful to look for other combinations of the four map parameters that may play an important role in designing a DM soliton system. Two parameters that are useful for this purpose are defined as [67]

$$\bar{\beta}_2 = \frac{\beta_{2n}l_n + \beta_{2a}l_a}{l_n + l_a}, \qquad S_{\text{map}} = \frac{\beta_{2n}l_n - \beta_{2a}l_a}{T_{\text{FWHM}}^2}, \tag{8.3.5}$$

where $T_{\text{FWHM}} \approx 1.665T_m$ is the FWHM at the location where pulse width is minimum in the anomalous-GVD section. Physically, $\bar{\beta}_2$ represents the average GVD of the entire link, while the map strength S_{map} is a measure of how much GVD changes abruptly between two fibers in each map period. The solutions of Eqs. (8.1.5) and (8.1.6) as a function of map strength S for different values of $\bar{\beta}_2$ reveal the surprising feature that DM solitons can exist even when the average GVD is normal, provided the map strength exceeds a critical value S_{cr} [75]–[79].

Figure 8.11 shows periodic DM-soliton solutions as contours of constant S_{map} by plotting peak power as a function of the dimensionless ratio $\bar{\beta}_2/\beta_{2a}/$ [67]. The map strength is zero for the straight line (the case of a constant-dispersion fiber). It increases

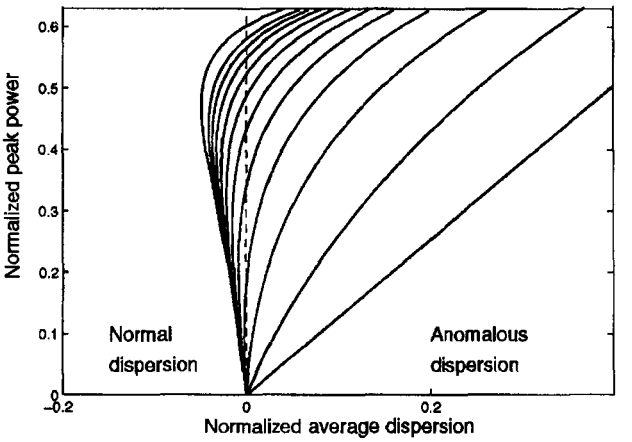

Figure 8.11: Peak power of DM solitons as a function of $\bar{\beta}_2/\beta_{2a}$. The map strength is zero for the straight line, increases in step of 2 until 20, and becomes 25 for the leftmost curve. (After Ref. [67]; ©1998 OSA.)

in steps of 2 for the next 10 curves and takes a value of 25 for the leftmost curve. Periodic solutions in the normal-GVD regime exist only when S_{map} exceeds a critical value of 4.8, indicating that pulse width for such solutions changes by a large factor in each fiber section. Moreover, when $S_{\text{map}} > S_{\text{cr}}$, a periodic solution can exist for two different values of the input pulse energy in a small range of positive values of $\bar{\beta}_2 > 0$. Numerical solutions of Eq. (8.3.2) confirm these predictions, except that the critical value of the map strength is found to be 3.9.

The existence of DM solitons in maps with normal average GVD is quite intriguing as one can envisage dispersion maps in which a soliton propagates in the normal-GVD regime most of the time. An example is provided by the dispersion map in which a short section of standard fiber ($\beta_{2a} \approx -20$ ps^2/km) is used with a long section of dispersion-shifted fiber ($\beta_{2n} \approx 1$ ps^2/km) such that $\bar{\beta}_2$ is close to zero but positive. The formation of DM solitons under such conditions can be understood by noting that when S_{map} exceeds 4, the input energy of a pulse becomes large enough that its spectral width is considerably larger in the anomalous-GVD section compared with the normal-GVD section. Noting that the phase shift imposed on each spectral component varies as $\beta_2\omega^2$ locally, one can define an effective value of the average GVD as [79]

$$\bar{\beta}_2^{\text{eff}} = \langle \beta_2 \Omega^2 \rangle / \langle \Omega^2 \rangle, \tag{8.3.6}$$

where Ω is the local value of the spectral width and the angle brackets indicate an average over the map period. If $\bar{\beta}_2^{\text{eff}}$ is negative, the DM soliton can exist even if $\bar{\beta}_2$ is positive.

For map strengths below a critical value (about 3.9 numerically), the average GVD is anomalous for DM solitons. In that case, one is tempted to compare them with standard solitons forming in a uniform-GVD fiber link with $\beta_2 = \bar{\beta}_2$. For relatively small values of S_{map}, variations in the pulse width and chirp are small enough that

one can ignore them. The main difference between the average-GVD and DM solitons then stems from the higher peak power required to sustain DM solitons. The energy enhancement factor for DM solitons is defined as [63]

$$f_{\mathrm{DM}} = E_0^{\mathrm{DM}}/E_0^{\mathrm{av}} \tag{8.3.7}$$

and can exceed 10 depending on the system design. The larger energy of DM solitons benefits a soliton system in several ways. Among other things, it improves the SNR and decreases the timing jitter.

Dispersion-management schemes were used for solitons as early as 1992 although they were referred to by names such as partial soliton communication and dispersion allocation [87]. In the simplest form of dispersion management, a relatively short segment of dispersion-compensating fiber (DCF) is added periodically to the transmission fiber, resulting in dispersion maps similar to those used for nonsoliton systems. It was found in a 1995 experiment that the use of DCFs reduced the timing jitter considerably [88]. In fact, in this 20-Gb/s experiment, the timing jitter became low enough when the average dispersion was reduced to a value near -0.025 ps^2/km that the 20-Gb/s signal could be transmitted over transoceanic distances.

Since 1996, a large number of experiments have shown the benefits of DM solitons for lightwave systems [89]–[97]. In one experiment, the use of a periodic dispersion map enabled the transmission of a 20-Gb/s soliton bit stream over 5,520 km of a fiber link containing amplifiers at 40-km intervals [89]. In another 20-Gb/s experiment [90], solitons could be transmitted over 9,000 km without using any in-line optical filters since the periodic use of DCFs reduced timing jitter by more than a factor of 3. A 1997 experiment focused on the transmission of DM solitons using dispersion maps such that solitons propagated most of the time in the normal-GVD regime [91]. This 10-Gb/s experiment transmitted signals over 28,000 km using a recirculating fiber loop consisting of 100 km of normal-GVD fiber and 8 km of anomalous-GVD fiber such that the average GVD was anomalous (about -0.1 ps^2/km). Periodic variations in the pulse width were also observed in such a fiber loop [92]. In a later experiment, the loop was modified to yield the average-GVD value of zero or a slightly positive value [93]. Stable transmission of 10-Gb/s solitons over 28,000 km was still observed. In all cases, experimental results were in excellent agreement with those of numerical simulations [94].

An important application of dispersion management consists of upgrading the existing terrestrial networks designed with standard fibers [95]–[97]. A 1997 experiment used fiber gratings for dispersion compensation and realized 10-Gb/s soliton transmission over 1,000 km. Longer transmission distances were realized using a recirculating fiber loop [96] consisting of 102 km of standard fiber with anomalous GVD ($\beta_2 \approx -21$ ps^2/km) and 17.3 km of DCF with normal GVD ($\beta_2 \approx 160$ ps^2/km). The map strength S was quite large in this experiment when 30-ps (FWHM) pulses were launched into the loop. By 1999, 10-Gb/s DM solitons could be transmitted over 16,000 km of standard fiber when soliton interactions were minimized by choosing the location of amplifiers appropriately [16].

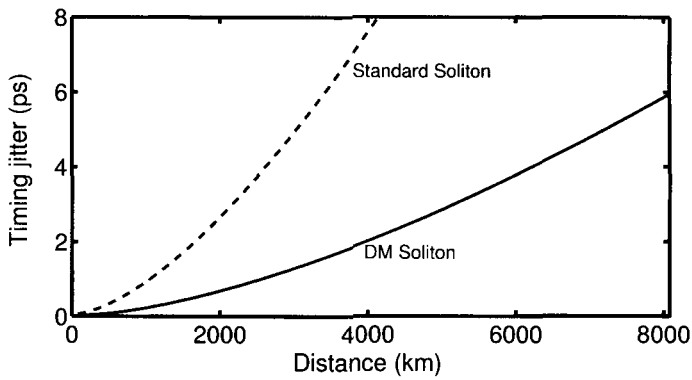

Figure 8.12: (a) ASE-induced timing jitter as a function of length for a 20-Gb/s system designed with DM (solid curve) and standard (dashed line) solitons.

8.3.4 Timing Jitter

As discussed in Section 6.5.5, noise added by optical amplifiers perturbs the position of each optical pulse in its time slot. Timing jitter induced by amplifier noise is especially severe for soliton-based systems and it limits the total transmission distance of any long-haul soliton link. This limitation was first pointed out in 1986 in the context of standard constant-width solitons. It persists even for DM soliton systems, although jitter is reduced for them [98]–[110]. In all cases, the dominant source of timing jitter is related to changes in the soliton carrier frequency, occurring because of phase fluctuations induced by amplifier noise.

One can follow the moment method of Section 6.5.2 to calculate the variance of fluctuations in the frequency and pulse position. Since pulse shape remains approximately Gaussian for DM solitons, the treatment of Sections 6.5.4 and 6.5.5 applies for them with minor changes. The final result can be written as [107]

$$\sigma_t^2 = \frac{S_{\rm ASE} T_m^2}{E_0}[N_A(1+C_0^2)+N_A(N_A-1)C_0 d+\tfrac{1}{6}N_A(N_A-1)(2N_A-1)d^2], \quad (8.3.8)$$

where N_A is the number of amplifiers along the link and the dimensionless parameter d is defined as in Eq. (8.1.9), except that the minimum width T_m should be used in place of T_0. The first term inside the square brackets results from direct position fluctuations of a soliton within each amplifier. The second term is related to the cross-correlation between frequency and position fluctuations. The third term is solely due to frequency fluctuations. For a soliton system designed with $L_{\rm map} = L_A$ and $N_A \gg 1$, jitter is dominated by the last term in Eq. (8.3.8) because of its N_A^3 dependence and is approximately given by

$$\frac{\sigma_t^2}{T_m^2} \approx \frac{S_{\rm ASE}}{3E_0} N_A^3 d^2 = \frac{S_{\rm ASE} L_T^3}{3E_0 L_D^2 L_A}, \quad (8.3.9)$$

where $L_D = T_m^2/|\bar{\beta}_2|$ and $N_A = L_T/L_A$ for a lightwave system with the total transmission distance L_T.

Because of the cubic dependence of σ_t^2 on the system length L_T, the timing jitter can become an appreciable fraction of the bit slot for long-haul systems, especially at bit rates exceeding 10 Gb/s for which the bit slot is shorter than 100 ps. Such jitter would lead to large power penalties if left uncontrolled. As discussed in Section 5.4.5, jitter should be less than 10% of the bit slot in practice. Figure 8.12 shows how timing jitter increases with L_T for a 20-Gb/s DM soliton system, designed using a dispersion map consisting of 10.5 km of anomalous-GVD fiber and 9.7 km of normal-GVD fiber [$D = \pm 4$ ps/(km-nm)]. Optical amplifiers with $n_{sp} = 1.3$ (or a noise figure of 4.1 dB) are placed every 80.8 km (4 map periods) along the fiber link for compensating 0.2-dB/km losses. Variational equations were used to find the input pulse parameters for which solitons recover periodically after each map period ($T_0 = 6.87$ ps, $C_0 = 0.56$, and $E_0 = 0.4$ pJ). The nonlinear parameter γ was 1.7 W^{-1}/km.

An important question is whether the use of dispersion management is helpful or harmful from the standpoint of timing jitter. The timing jitter for standard solitons can also be found in a closed form using the moment method and is given by [107]

$$\sigma_t^2 = \frac{S_{ASE} T_0^2}{3E_s}[N_A + \tfrac{1}{6}N_A(N_A - 1)(2N_A - 1)d^2], \tag{8.3.10}$$

where we have used E_s for the input soliton energy to emphasize that it is different from the DM soliton energy E_0 used in Eq. (8.3.8). For a fair comparison of the DM and standard solitons, we consider an identical soliton system except that the dispersion map is replaced by a single fiber whose GVD is constant and equal to the average value $\bar{\beta}_2$. The soliton energy E_s can be found by using $E_0 = 2P_0T_0$ with $P_0 = |\bar{\beta}_2|/(\gamma T_0^2)$ and is given by

$$E_s = 2f_{LM}|\bar{\beta}_2|/(\gamma T_0), \tag{8.3.11}$$

where the factor f_{LM} is the enhancement factor resulting from loss management ($f_{LM} \approx 3.8$ for a 16-dB gain). The dashed line in Figure 8.12 shows the timing jitter using Eqs. (8.3.10) and (8.3.11). A comparison of the two curves shows that the jitter is considerably smaller for DM solitons. The physical reason behind the jitter reduction is related to the enhanced energy of the DM solitons. In fact, the energy ratio E_0/E_s equals the energy enhancement factor f_{DM} introduced earlier in Eq. (8.3.7). From a practical standpoint, the reduced jitter of DM solitons permits much longer transmission distances as evident from Figure 8.12. Note that Eq. (8.3.10) also applies for DDFs because the GVD variations along the fiber can be included through the parameter d defined in Eq. (8.1.9).

For long-haul soliton systems, the number of amplifiers is large enough that the N_A^3 term dominates in Eq. (8.3.10), and the timing jitter for standard solitons is approximately given by [99]

$$\frac{\sigma_t^2}{T_0^2} = \frac{S_{ASE} L_T^3}{9E_s L_D^2 L_A}. \tag{8.3.12}$$

Comparing Eqs. (8.3.9) and (8.3.12), we find that timing jitter is reduced by a factor of $(f_{DM}/3)^{1/2}$ when DM solitons are used.

To find a simple design rule, we can use Eq. (8.3.12) with the condition $\sigma_t < b_j/B$, where b_j is the fraction of the bit slot by which a soliton can move without affecting

the system performance adversely. Using $B = (2q_0T_0)^{-1}$ and E_s from Eq. (8.3.11), the bit rate–distance product BL_T for standard solitons is found to be limited by

$$BL_T < \left(\frac{9b_j^2 f_{\rm LM} L_A}{S_{\rm ASE} q_0 \gamma \bar{\beta}_2} \right)^{1/3}. \tag{8.3.13}$$

For DM solitons the energy enhancement factor $f_{\rm LM}$ is replaced by $f_{\rm LM} f_{\rm DM}/3$. The tolerable value of b_j depends on the acceptable BER and on details of the receiver design; typically, $b_j < 0.1$. To see how amplifier noise limits the total transmission distance, consider a standard soliton system operating at 10 Gb/s with parameter values $T_0 = 10$ ps, $q_0 = 5$, $\alpha = 0.2$ dB/km, $\gamma = 2$ W^{-1}/km, $\bar{\beta}_2 = -1$ ps/(km-nm), $n_{\rm sp} = 1.5$, $L_A = 50$ km, and $b_j = 0.08$. Using $G = 10$ dB, we find $f_{\rm LM} = 2.56$ and $S_{\rm ASE} = 2.16 \times 10^{-6}$ pJ. With these values, BL_T must be below 70 (Tb/s)-km, and the transmission distance is limited to below 7,000 km at 10 Gb/s. This value can be increased to beyond 10,000 km for DM solitons.

8.3.5 Control of Timing Jitter

As the timing jitter ultimately limits the performance of soliton systems, it is essential to find a solution to the timing-jitter problem before the use of solitons can become practical. Several techniques were developed during the 1990s for controlling timing jitter [111]–[132]. This section is devoted to a brief discussion of them.

The use of optical filters for controlling the timing jitter of solitons was proposed as early as 1991 [111]–[113]. This approach makes use of the fact that the ASE occurs over the entire amplifier bandwidth but the soliton spectrum occupies only a small fraction of it. The bandwidth of optical filters is chosen such that the soliton bit stream passes through the filter but most of the ASE is blocked. If an optical filter is placed after each amplifier, it improves the SNR because of the reduced ASE and also reduces the timing jitter simultaneously. This was indeed found to be the case in a 1991 experiment [112] but the reduction in timing jitter was less than 50%.

The filter technique can be improved dramatically by allowing the center frequency of the successive optical filters to slide slowly along the link. Such *sliding-frequency* filters avoid the accumulation of ASE within the filter bandwidth and, at the same time, reduce the growth of timing jitter [114]. The physical mechanism behind the operation of such filters can be understood as follows. As the filter passband shifts, solitons shift their spectrum as well to minimize filter-induced losses. In contrast, the spectrum of ASE cannot change. The net result is that the ASE noise accumulated over a few amplifiers is filtered out later when the soliton spectrum has shifted by more than its own bandwidth.

The moment method can be extended to include the effects of optical filters by noting that each filter modifies the soliton field such that

$$U_f(z_f,t) = \frac{1}{2\pi} \int_{-\infty}^{\infty} H_f(\omega - \omega_f) \tilde{U}(z_f,\omega) e^{-i\omega t}\, d\omega, \tag{8.3.14}$$

where $\tilde{U}(z_f,\omega)$ is the pulse spectrum and H_f is the transfer function of the optical filter located at z_f. The filter passband is shifted by ω_f from the soliton carrier frequency.

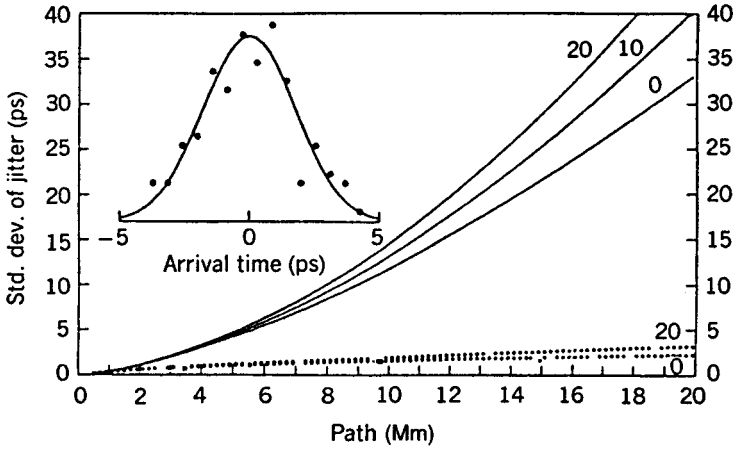

Figure 8.13: Timing jitter with (dotted curves) and without (solid curves) sliding-frequency filters at several bit rates as a function of distance. The inset shows a Gaussian fit to the numerically simulated jitter at 10,000 km for a 10-Gb/s system. (After Ref. [114]; ©1992 OSA; reprinted with permission.)

If we approximate the filter spectrum by a parabola over the soliton spectrum and use $H_f(\omega - \omega_f) = 1 - b(\omega - \omega_f)^2$, it is easy to see that the filter introduces an additional loss for the soliton that should be compensated by increasing the gain of optical amplifiers. The analysis of timing jitter shows that sliding-frequency filters reduce jitter considerably for both the standard and DM solitons [127].

Figure 8.13 shows the predicted reduction in the timing jitter for standard solitons. The bit-rate dependence of jitter is due to the contribution of acoustic waves; the $B = 0$ curves show the contribution of the Gordon–Haus jitter alone. Optical filters help in reducing both types of timing jitter and permit transmission of 10-Gb/s solitons over more than 20,000 km. In the absence of filters, timing jitter becomes so large that a 10-Gb/s soliton system cannot be operated beyond 8,000 km. The inset in Figure 8.13 shows a Gaussian fit to the timing jitter of 10-Gb/s solitons at a distance of 10,000 km calculated by solving the NLS equation numerically after including the effects of both the ASE and sliding-frequency filters [114]. The timing-jitter distribution is approximately Gaussian with a standard deviation of about 1.76 ps. In the absence of filters, the jitter exceeds 10 ps under the same conditions.

Optical filters benefit a soliton system in many other ways. Their use reduces interaction between neighboring solitons [115]. The physical mechanism behind the reduced interaction is related to the change in the soliton phase at each filter. A rapid variation of the relative phase between neighboring solitons, occurring as a result of filtering, averages out the impact of soliton interaction by alternating the nature of the interaction force from attractive to repulsive. Optical filters also help in reducing the accumulation of dispersive waves [116]. The reason is easy to understand. As the soliton spectrum shifts with the filters, dispersive waves produced at earlier stages are blocked by filters together with the ASE.

Solitons can also be controlled in the time domain using the technique of *synchronous* amplitude modulation, implemented in practice using a $LiNbO_3$ modulator [117]. The technique works by introducing additional losses for those solitons that have shifted from their original position (center of the bit slot). The modulator forces solitons to move toward its transmission peak where the loss is minimum. Mathematically, the action of the modulator is to change the soliton amplitude as

$$U(z_m,t) \to T_m(t-t_m)U(z_m,t), \tag{8.3.15}$$

where $T_m(\tau)$ is the transmission coefficient of the modulator located at $z = z_m$. The moment method or perturbation theory can be used to show that timing jitter is reduced considerably by modulators.

The synchronous modulation technique can also be implemented by using a phase modulator [118]. One can understand the effect of periodic phase modulation by recalling that a frequency shift is associated with all time-dependent phase variations. Since a change in soliton frequency is equivalent to a change in the group velocity, phase modulation induces a temporal displacement. Synchronous phase modulation is implemented in such a way that the soliton experiences a frequency shift only if it moves away from the center of the bit slot, which confines it to its original position despite the timing jitter induced by ASE and other sources. Intensity and phase modulations can be combined together to further improve system performance [119].

Synchronous modulation can be combined with optical filters to control solitons simultaneously in both the time and frequency domains. In fact, this combination permits arbitrarily long transmission distances [120]. The use of intensity modulators also permits a relatively large amplifier spacing by reducing the impact of dispersive waves. This property of modulators was exploited in 1995 to transmit a 20-Gb/s soliton train over 150,000 km with an amplifier spacing of 105 km [121]. Synchronous modulators also help in reducing the soliton interaction and in clamping the level of amplifier noise. The main drawback of modulators is that they require a clock signal that is synchronized with the original bit stream.

A relatively simple approach uses postcompensation of accumulated dispersion for reducing timing jitter [122]. The basic idea can be understood from Eq. (8.3.8) or Eq. (8.3.10) obtained for the timing jitter of DM and standard solitons, respectively. The cubic term that dominates the jitter at long distances depends on the accumulated dispersion through the parameter d. If a fiber is added at the end of the link such that it reduces the accumulated dispersion, it should help in reducing the jitter. It is easy to include the contribution of the postcompensation fiber to the timing jitter using the moment method. In the case of DM solitons, the jitter variance at the end of a postcompensation fiber of length L_c and GVD β_{2c} is given by [107]

$$\sigma_c^2 = \sigma_t^2 + (S_{\rm ASE}T_m^2/E_0)[2N_AC_0d_c + N_A(N_A-1)dd_c + N_Ad_c^2], \tag{8.3.16}$$

where σ_t^2 is given by Eq. (8.3.8) and $d_c = \beta_{2c}L_c/T_m^2$. If we define $y = -d_c/(N_Ad)$ as the fraction by which the accumulated dispersion N_Ad is compensated and retain only the dominant cubic terms in Eq. (8.3.16), this equation can be written as

$$\sigma_c^2 = N_A^3d^2T_m^2(S_{\rm ASE}/E_0)(y^2 - y + 1/3). \tag{8.3.17}$$

The minimum value occurs for $y = 0.5$ for which σ_c^2 is reduced by a factor of 4. Thus, the timing jitter of solitons can be reduced by a factor of 2 by postcompensating the accumulated dispersion by 50%. The same conclusion holds for standard solitons [122].

Several other techniques can be used for controlling timing jitter. One approach consists of inserting a fast saturable absorber periodically along the fiber link. Such a device absorbs low-intensity light, such as ASE and dispersive waves, but leaves the solitons intact by becoming transparent at high intensities. To be effective, it should respond at a time scale shorter than the soliton width. It is difficult to find an absorber that can respond at such short time scales. A nonlinear optical loop mirror (see Section 2.3.3 of LT1) can act as a fast saturable absorber and reduce the timing jitter of solitons, while also stabilizing their amplitude [123]. Re-timing of a soliton train can also be accomplished by taking advantage of cross-phase modulation [124]. The technique overlaps the soliton data stream and another pulse train composed of only 1 bits (an optical clock) inside a fiber where cross-phase modulation (XPM) induces a nonlinear phase shift on each soliton in the signal bit stream. Such a phase modulation translates into a net frequency shift only when the soliton does not lie in the middle of the bit slot. Similar to the case of synchronous phase modulation, the direction of the frequency shift is such that the soliton is confined to the center of the bit slot. Other nonlinear effects such as stimulated Raman scattering [125] and four-wave mixing (FWM) can also be exploited for controlling the soliton parameters [126]. The technique of distributed amplification also helps in reducing timing jitter. As an example, if solitons are amplified using distributed Raman amplification, timing jitter can be reduced by about a factor of 2 [110].

8.4 Pseudo-linear Lightwave Systems

Pseudo-linear lightwave systems operate in the regime in which the local dispersion length is much shorter than the nonlinear length in all fiber sections of a dispersion-managed link. This approach is most suitable for systems operating at bit rates of 40 Gb/s or more and employing relatively short optical pulses that spread over multiple bits quickly as they propagate along the link. This spreading reduces the peak power and lowers the impact of SPM on each pulse. There are several ways one can design such systems. In one case, pulses spread throughout the link and are compressed back at the receiver end using a dispersion-compensating device. In another, pulses are spread even before the optical signal is launched into the fiber link using a DCF (precompensation) and they compress slowly within the fiber link, without requiring any postcompensation.

It is not essential to compensate dispersion only once at the transmitter or the receiver end, and one can employ in-line compensation. In this case, the dispersion map is made such that the pulse broadens by a large factor in the first section and is compressed in the following section with opposite dispersion characteristics. An optical amplifier restores the signal power after the second section, and the whole process repeats itself. Often, a small amount of dispersion is left uncompensated in each map period. This residual dispersion per span can be used to control the impact of intrachannel nonlinear effects in combination with the amounts of pre- and postcompensation.

As optical pulses spread considerably outside their assigned bit slot in all pseudo-linear systems, they overlap considerably and interact with each other through the nonlinear term in the NLS equation. It turns out that the spreading of bits belonging to different WDM channels produces an averaging effect that reduces the *interchannel* nonlinear effects considerably [26]. However, at the same time, an enhanced nonlinear interaction among the 1 bits of the same channel produces new *intrachannel* nonlinear effects that limit the system performance, if left uncontrolled. Thus, pseudo-linear systems are far from being linear. The important question is whether pulse spreading helps to lower the overall impact of fiber nonlinearity and allows higher launched powers into the fiber link. The answer to this question turned out to be affirmative. In this section we focus on the intrachannel nonlinear effects and study how they affect a pseudo-linear lightwave system.

8.4.1 Intrachannel Nonlinear Effects

The main limitation of pseudo-linear systems stems from the nonlinear interaction among the neighboring overlapping pulses. Starting in 1999, such intrachannel nonlinear effects were studied extensively [133]–[145]. In a numerical approach, one solves the NLS equation (8.1.2) for a pseudo-random bit stream with the input

$$U(0,t) = \sum_{j=1}^{M} U_j(0, t - t_j), \tag{8.4.1}$$

where $t_j = jT_b$, T_b is the duration of the bit slot, M is the total number of bits included in numerical simulations, and $U_m = 0$ if the mth pulse represents a 0 bit. In the case of 1 bits, U_m governs the shape of input pulses.

Although numerical simulations are essential for a realistic system design, considerable physical insight can be gained with a semianalytic approach that focuses on three neighboring pulses. If we write the total field as $U = U_1 + U_2 + U_3$ in Eq. (8.1.2), it reduces to the following set of three coupled NLS equations [26]:

$$i\frac{\partial U_1}{\partial z} - \frac{\beta_2}{2}\frac{\partial^2 U_1}{\partial t^2} + \gamma P_0 p(z)[(|U_1|^2 + 2|U_2|^2 + 2|U_3|^2)U_1 + U_2^2 U_3^*] = 0, \tag{8.4.2}$$

$$i\frac{\partial U_2}{\partial z} - \frac{\beta_2}{2}\frac{\partial^2 U_2}{\partial t^2} + \gamma P_0 p(z)[(|U_2|^2 + 2|U_1|^2 + 2|U_3|^2)U_2 + 2U_1 U_2^* U_3] = 0, \tag{8.4.3}$$

$$i\frac{\partial U_3}{\partial z} - \frac{\beta_2}{2}\frac{\partial^2 U_3}{\partial t^2} + \gamma P_0 p(z)[(|U_3|^2 + 2|U_1|^2 + 2|U_2|^2)U_3 + U_2^2 U_1^*] = 0. \tag{8.4.4}$$

The first nonlinear term corresponds to SPM. The next two terms result from XPM induced by the other two pulses. Since these terms represent XPM interaction between pulses belonging to the same channel, this phenomenon is referred to as intrachannel XPM. The last term is FWM-like (see Section 4.3) and is responsible for intrachannel FWM. Although it may seem odd at first sight that FWM can occur among pulses of the same channel, one should remember that the spectrum of each pulse has modulation side bands located on both sides of the carrier frequency. If different sidebands of two or more overlapping pulses are present simultaneously in the same temporal window,

they can interact through FWM and transfer energy among the interacting pulses. This phenomenon can also create new pulses in the time domain. Such pulses are referred to as a *shadow* pulse [133] or a *ghost* pulse [134]. They impact the system performance considerably, especially those created in the 0-bit time slots [142].

We can extend the preceding method to the case of more than three pulses. Assuming that Eq. (8.4.1) can be used at any distance z, the NLS equation (8.1.2) can be written as

$$\sum_{j=1}^{M}\left(i\frac{\partial U_j}{\partial z}-\frac{\beta_2}{2}\frac{\partial^2 U_j}{\partial t^2}\right)=-\gamma P_0 p(z)\sum_{j=1}^{M}\sum_{k=1}^{M}\sum_{l=1}^{M}U_j U_k^* U_l. \tag{8.4.5}$$

The triple sum on the right side includes all the nonlinear effects. SPM occurs when $j=k=l$. The terms responsible for XPM correspond to $j=k\neq l$ and $j\neq k=l$. The remaining terms lead to intrachannel FWM. Each nonlinear term in the triple sum on the right side of Eq. (8.4.5) provides its contribution in a temporal region near $t_j+t_l-t_k$, a relation analogous to the phase-matching condition among waves of different frequencies [26]. This relation can be used to identify all nonlinear terms that can contribute to a specific pulse. It is important to note that, whereas the total energy of all pulses remains constant during propagation, the energy of any individual pulse can change because of intrachannel FWM.

In the case of a single pulse surrounded by several zero bits on both sides, we can set $U_1=U_3=0$ in Eqs. (8.4.2) through (8.4.4). The resulting equation for U_2 is identical to the original NLS equation (8.1.2). The SPM effects in this case have been studied in Section 8.1 through Eqs. (8.1.5) and (8.1.6) obtained with the help of the variational or the moment method. As was found there, the impact of SPM is reduced considerably for pseudo-linear systems because of the much lower peak power of the pulse. It is also reduced because of spectral breathing occurring as pulse spectrum broadens and narrows from one fiber section to the next. However, the effects of intrachannel XPM and FWM are not negligible. Even though intrachannel XPM affects only the phase of each pulse, this phase shift is time-dependent and affects the carrier frequency of the pulse. As discussed later, the resulting frequency chirp leads to timing jitter through fiber dispersion [136].

The impact of intrachannel XPM and FWM on the performance of a pseudo-linear system depends on the choice of the dispersion map, among other things [26]. We discuss these two nonlinear phenomena in the following sections. In general, the optimization of a dispersion-managed system requires the adjustment of many design parameters, such as launch power, amplifier spacing, and the location of DCFs [135]. In a 2000 experiment, a 40-Gb/s signal could be transmitted over transoceanic distances, in spite of its use of standard fibers, through a synchronous modulation technique [22]. In a 2002 experiment, distance could be increased to 10^6 km using synchronous modulation in combination with all-optical regeneration [146].

8.4.2 Intrachannel XPM

To understand how intrachannel XPM introduces timing jitter in a pseudo-linear system, consider two isolated 1 bits by setting $U_3=0$ in Eqs. (8.4.2) through (8.4.4). The

optical field associated with each pulse satisfies an equation of the form

$$i\frac{\partial U_n}{\partial z} - \frac{\beta_2}{2}\frac{\partial^2 U_n}{\partial t^2} + \gamma P_0 p(z)(|U_n|^2 + 2|U_{3-n}|^2)U_n = 0, \tag{8.4.6}$$

where $n = 1$ or 2. Clearly, the last term is due to XPM. If we ignore the effects of GVD for the moment, this term shows that, over a short distance Δz, the phase of each pulse is shifted nonlinearly by the other pulse by this amount:

$$\phi_n(z,t) = 2\gamma P_0 p(z)\Delta z|U_{3-n}(z,t)|^2. \tag{8.4.7}$$

As this phase shift depends on pulse shape, it varies across the pulse and produces a frequency chirp

$$\delta\omega_n \equiv -\frac{\partial \phi_n}{\partial t} = -2\gamma P_0 p(z)\Delta z\frac{\partial}{\partial t}|U_{3-n}(z,t)|^2. \tag{8.4.8}$$

This frequency shift is known as the XPM-induced chirp.

Similar to the case of ASE-induced frequency shift discussed in Chapter 6, an XPM-induced shift in the carrier frequency of the pulse translates into a shift in the pulse position through changes in the group velocity of the pulse. If all pulses were to shift in time by the same amount, this effect would be harmless. However, the time shift depends on the pattern of bits surrounding each pulse that varies from bit to bit depending on the data transmitted. As a result, pulses shift in their respective time slots by different amounts, a feature referred to as XPM-induced timing jitter. As will be seen later, XPM also introduces some amplitude fluctuations.

A more quantitative estimate of the XPM effects can be obtained by extending the variational or the moment method of Section 4.6 to the case of two interacting pulses. In this case, one must include the expected frequency and temporal shifts and assume that Eq. (8.4.6) has the following solution:

$$U_n(z,t) = a_n \exp[-\tfrac{1}{2}(1+iC_m)(t-t_n)^2/T_n^2 - i\Omega_n(t-t_n) + i\phi_n], \tag{8.4.9}$$

where t_n represents the position and Ω_n represents the frequency shift for the nth pulse. In the moment method of Section 4.6.1, these two quantities can be calculated using

$$t_n = \frac{1}{E_0}\int_{-\infty}^{\infty} t|U_n|^2 dt, \quad \Omega_n = \frac{i}{2E_0}\int_{-\infty}^{\infty} t\left(U_n^*\frac{\partial U_n}{\partial t} - U_n\frac{\partial U_n^*}{\partial t}\right)dt, \tag{8.4.10}$$

where E_0 is the input energy of each pulse.

Since each pulse is quantified through six parameters, this approach leads to 12 first-order differential equations. As before, the two phase equations can be ignored if one neglects interactions that are phase-dependent. The amplitude equations are not needed since $E_0 = \sqrt{\pi}a_n^2 T_n$ for each pulse. Furthermore, only the frequency difference $\Delta\Omega = \Omega_1 - \Omega_2$ and the pulse separation $\Delta t = t_1 - t_2$ are relevant for describing the intrachannel XPM effects. We are thus left with the following set of equations:

$$\frac{dT_n}{dz} = \frac{\beta_2(z)C_n}{T_n}, \tag{8.4.11}$$

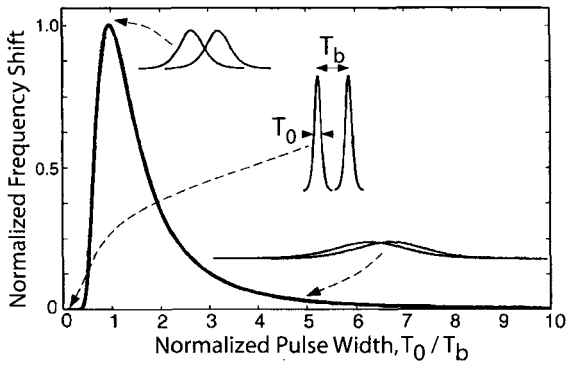

Figure 8.14: Normalized XPM-induced frequency shift as a function of pulse width T_0 for two Gaussian pulses separated by T_b. The insets show schematically the extent of overlap between two pulses in three cases. (After Ref. [134]; ©1999 OSA.)

$$\frac{dC_n}{dz} = (1+C_n^2)\frac{\beta_2(z)}{T_n^2} + \frac{\gamma(z)p(z)E_0}{\sqrt{2\pi}T_n}\left[1 - \frac{2T_n^3}{T_a^3}(1-\mu^2)e^{-\mu^2/2}\right], \quad (8.4.12)$$

$$\frac{d\Delta\Omega}{dz} = \gamma(z)p(z)E_0\frac{8\mu}{\pi T_a^2}e^{-\mu^2/2}, \quad (8.4.13)$$

$$\frac{d\Delta t}{dz} = \beta_2(z)\Delta\Omega, \quad (8.4.14)$$

where $n = 1$ or 2, $\mu = \Delta t/T_a$, and $T_a^2 = \frac{1}{2}(T_1^2 + T_2^2)$.

A comparison of Eqs. (8.4.11) and (8.4.12) with Eqs. (8.1.5) and (8.1.6) shows that, although the width equation remains unchanged, overlapping of two neighboring pulses modifies the chirp equation. However, any change in the chirp also affects the pulse width, as the two equations are coupled. Moreover, changes in pulse width would manifest through changes in pulse amplitude since $E_0 = \sqrt{\pi}a_n^2 T_n$ remains constant for each pulse. Thus, the amplitude of any 1 bit would depend whether it is surrounded by 0 or 1 bits. As this pattern varies randomly in an optical bit stream, pulse amplitude would vary from bit to bit. This is the origin of XPM-induced amplitude jitter.

As evident from Eqs. (8.4.13) and (8.4.14), XPM-induced timing jitter results from the frequency shift $\Delta\Omega$. If $\Delta\Omega$ were to vanish, the pulse separation would remain fixed at its initial value, and no jitter would occur. At a bit rate B two neighboring pulses are initially spaced by $\Delta t = T_b \equiv B^{-1}$. When both pulses have the same initial width T_0, clearly $T_a = T_0$. Equation (8.4.13) shows that the amount of frequency shift depends on the ratio $x = T_0/T_b$ as $F(x) = x^{-3}\exp[-1/(2x^2)]$. Figure 8.14 shows how this function varies with x [134]. It peaks near $x = 1$, indicating that frequency shift $\Delta\Omega$ is largest when pulse widths are comparable to their temporal spacing. For pulses much smaller than the bit slot, $x \ll 1$, and $\Delta\Omega$ nearly vanishes. This is expected on physical grounds because the tails of such narrow pulses do not overlap significantly, and pulses cannot interact through XPM. What is surprising is that $\Delta\Omega$ is also relatively small when pulses are much wider than their spacing so that $x \gg 1$. Intuitively, one would guess this to be the worse situation since pulses almost completely overlap under such conditions.

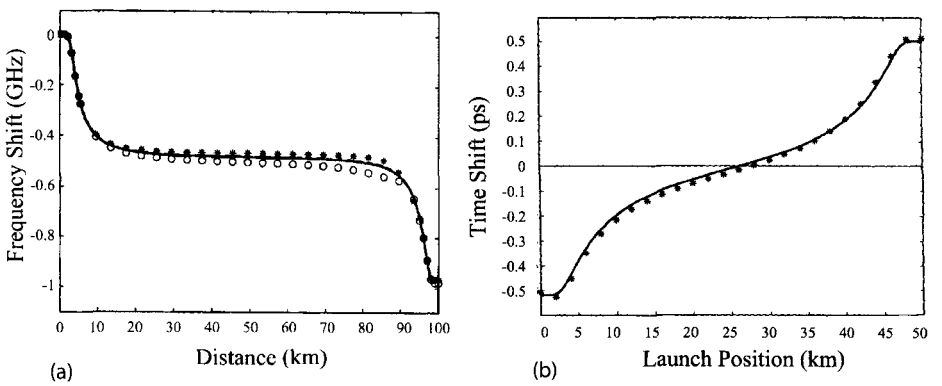

Figure 8.15: (a) XPM-induced frequency shift over one map period and (b) temporal shift in pulse spacing as a function of launch position within the anomalous-GVD fiber for two 5-ps Gaussian pulses separated by 25 ps. The two curves almost coincide. Symbols show the numerical results obtained from the NLS equation. (After Ref. [138]; ©2001 OSA.)

The reason is related to the fact that the XPM-induced frequency chirp in Eq. (8.4.8) depends on the slope of the pulse power. This slope is smaller for wider pulses and also changes sign, resulting in an averaging effect. The main conclusion is that XPM-induced timing jitter can be reduced by stretching optical pulses over multiple bit slots. This is precisely what is done in pseudo-linear lightwave systems.

To study how the frequency shift $\Delta\Omega$ and pulse spacing Δt change with z as two pulses propagate inside the fiber link, one should solve Eqs. (8.4.11) through (8.4.14) numerically for a given dispersion map [138]. Figure 8.15(a) shows $\Delta\Omega/2\pi$ along a 100-km link formed by using two 50-km fiber sections with $D = \pm 10$ ps/(km-nm). The nonlinear parameter $\gamma = 2\ \mathrm{W}^{-1}/\mathrm{km}$ for both fibers. Losses are assumed to be compensated through distributed amplification so that $p(z) = 1$. Two Gaussian pulses have 5-ps width (FWHM) at the input and are separated by 25 ps. The solid curve shows the case in which pulses are launched at the input end of the section with anomalous GVD. The almost coinciding dashed curve corresponds to the case in which the dispersion map is made symmetric by launching pulses at the midpoint of this section. Stars and circles show the results obtained in these two cases by solving the NLS equation directly. Most of the frequency shift occurs near the two ends of the map period where pulses are relatively short and overlap only partially.

Even though the frequency shift is nearly the same for the symmetric and asymmetric maps, the shift in pulse spacing Δt from its initial 25-ps value depends considerably on the exact location where input pulses are launched. This is evident from Figure 8.15(b) that shows this shift as a function of the launch position within the anomalous-GVD fiber. Timing shift can be positive or negative depending on whether the first fiber section exhibits anomalous or normal dispersion. The reason is related to the fact that two pulses attract each other in the case of anomalous GVD but they repel each other for normal GVD. As the frequency shift in Figure 8.15(a) grows monotonically, it is the second section that produces the most shift [138]. The most important feature

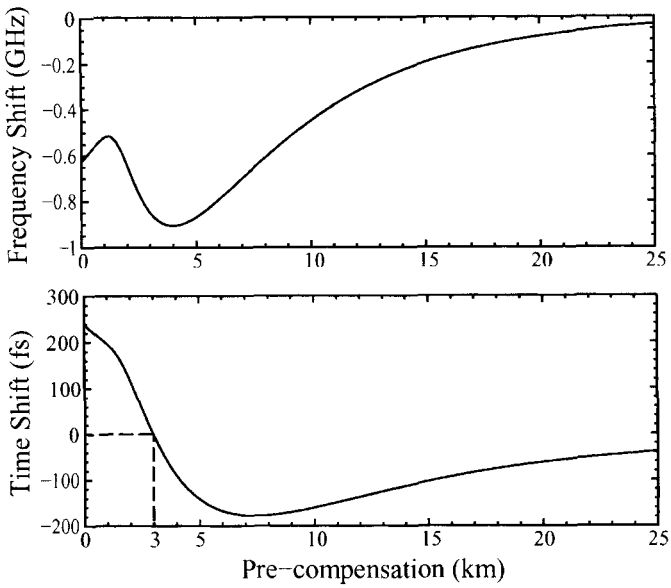

Figure 8.16: Frequency and time shifts after 100 km as a function of DCF length used for precompensation. (After Ref. [26]; ©2002 Elsevier.)

of this figure is that pulse position does not shift at all for a symmetric dispersion map. In this case, timing shifts produced in the two sections completely cancel each other. This cancellation can occur only when distributed amplification is used, and we can set $p(z) \approx 1$. In the case of lumped amplification, large power variations make the XPM effects much stronger in the first section of a periodic dispersion map.

Even when lumped amplification is used and the dispersion map is not symmetric, it is possible to cancel the XPM-induced time shift by suitably chirping input pulses before launching them into the fiber link. Experimentally, a fiber of suitable length is used to chirp the pulse. This technique is equivalent to the precompensation technique discussed in Section 7.2. Figure 8.16 shows the frequency and temporal shifts acquired after one map period as a function of fiber length used for precompensation. The 100-km-long map consists of a 75-km section with $\beta_2 = -5$ ps^2/km, followed with a 25-km DCF section with $\beta_2 = 20$ ps^2/km. The same DCF is used for precompensation. Even though there is always a net frequency shift after one map period, the temporal shift vanishes when the length of precompensation fiber is about 3 km.

XPM-induced timing jitter depends on details of the dispersion map and can become quite large if care is not taken to suppress it. As an example of the degradation caused by such jitter [26], Figure 8.17 shows the results of numerical simulations when a 128-bit-long pseudo-random bit stream (with a 25-ps bit slot) was propagated through 80 km of dispersion-shifted fiber with $D = 4$ ps/(km-nm). Launched power was taken to be 18 dBm to enhance the XPM effects. The 5-ps Gaussian input pulses were first chirped by propagating them through a precompensation fiber with $DL = -17$ ps/nm. The output bit stream exhibits both the amplitude and timing jitters that produce severe

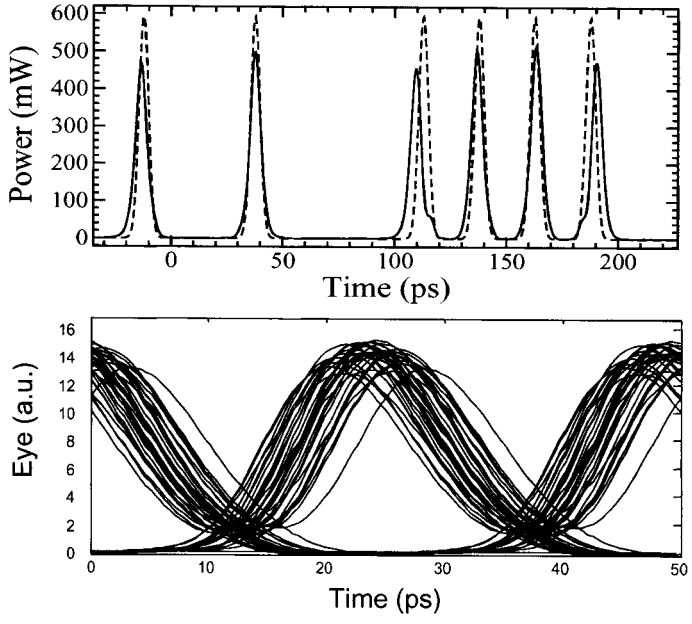

Figure 8.17: Bit stream and eye diagram at the end of a 80-km fiber with $D = 4$ ps/(km-nm). The dashed curve shows for comparison the input bit stream. (After Ref. [26]; ©2002 Elsevier.)

degradation of the "eye" at the receiver. Numerical simulations, such as those shown in Figure 8.17, are performed with a pseudo-random sequence of 0 and 1 bits. The length of this sequence is typically kept below 512 bits to keep the computation time under control. It turns out that the results for some transmission lines depend on the sequence length and may not provide an accurate estimate until the number of bits is increased to beyond 10,000 [147].

8.4.3 Intrachannel FWM

In contrast to the case of intrachannel XPM, intrachannel FWM transfers energy from one pulse to neighboring pulses. In particular, it can create new pulses in bit slots that represent 0's and contain no pulse initially. Such FWM-generated pulses (called ghost or shadow pulses) are undesirable for any lightwave system because they can lead to additional errors if their amplitude becomes substantial [133]. Ghost pulses were observed as early as 1992 when a pair of ultrashort pulses, each stretched to 90 ps, was propagated through an optical fiber [148]. However, this phenomenon attracted attention only after 1999 when it was found to impact the performance of lightwave systems employing strong dispersion management [133], [134].

As an example of the system degradation caused by intrachannel FWM [26], Figure 8.18 shows the results of numerical simulations for a 40-Gb/s system at the end of a 80-km-long standard fiber with $D = 17$ ps/(km-nm). The 5-ps Gaussian input pulses were first chirped by propagating them through a precompensation fiber with $DL = -527$

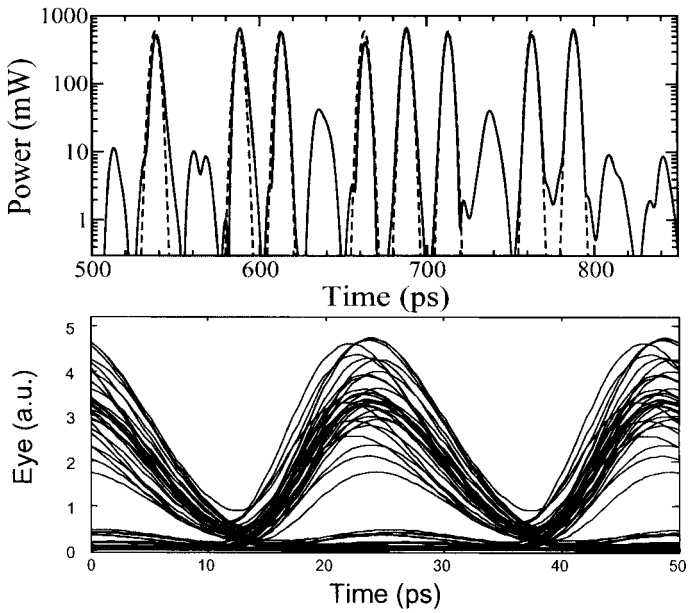

Figure 8.18: Bit stream and eye diagram at the end of a 80-km fiber with $D = 17$ ps/(km-nm). The dashed curve shows for comparison the input bit stream. (After Ref. [26]; ©2002 Elsevier.)

ps/nm. Other parameters are identical to those used for Figure 8.16. Because of the rapid broadening of input pulses, timing jitter is reduced considerably. However, ghost pulses appear in all 0 slots, and they degrade the eye diagram considerably. Amplitude fluctuations seen in this figure also result from intrachannel FWM.

An analytic treatment of intrachannel FWM is more complex compared with the case of XPM. A perturbative approach has been used with considerable success to describe the impact of intrachannel nonlinearities [136], even though its accuracy decreases rapidly for large timing jitter. Its main advantages are that one does not need to assume a specific pulse shape and that it can be extended easily even to the case of a pseudo-random bit stream [139]–[141].

The main idea is to assume that the solution of the NLS equation (8.1.2) can be written in the form

$$U(z,t) = \sum_{j=1}^{M} U_j(z, t - t_j) + \sum_{j=1}^{M} \sum_{k=1}^{M} \sum_{l=1}^{M} \Delta U_{jkl}(z,t), \tag{8.4.15}$$

where M the number of bits, U_j represents the amplitude of the jth bit located at $t = t_j$ initially, and ΔU_{jkl} is the perturbation created by the nonlinear term. The first term in Eq. (8.4.15) represents the zeroth-order solution obtained by neglecting the nonlinear term in the NLS equation ($\gamma = 0$). This solution can be obtained in an analytic form. The second term represents the contribution of all nonlinear effects. It can also be obtained in a closed form by employing first-order perturbation theory [136].

In the case of Gaussian input pulses of width T_0, the perturbation produced by the nonlinear term is given by [26]

$$\Delta U_{jkl}(L,t_j+t_l-t_k) = \gamma P_0 \exp\left(-\frac{t^2}{6T_0^2}\right) e^{i\Delta\phi} \int_0^L \frac{ip(z)\,dz}{\sqrt{1+2id+3d^2}}$$
$$\times \exp\left(-\frac{3[2t/3+(t_j-t_k)][2t/3+(t_l-t_k)]}{T_0^2(1+3id)} - \frac{(t_j-t_l)^2}{T_0^2(1+2id+3d^2)}\right), \quad (8.4.16)$$

where $\Delta\phi = \phi_k + \phi_l - \phi_j$ is related to the phases of individual pulses and the parameter $d(z)$ is defined as $d(z) = T_0^{-2}\int_0^z \beta_2(z)\,dz$. All intrachannel nonlinear effects produced by SPM, XPM, and FWM are included in this perturbative solution. The number of terms that must be included in the triple sum in Eq. (8.4.15) scales as M^3 for a bit stream with M bits.

The integral in Eq. (8.4.16) can be performed analytically in some limiting cases. For example, if we consider a constant-dispersion fiber, set $p(z) = 1$ assuming ideal distributed amplification, and consider a fiber length L much longer than the dispersion length $L_D = T_0^2/|\beta_2|$, we obtain [136]

$$\Delta U_{jkl}(L,t_j+t_l-t_k) = (i\gamma P_0 L_D/\sqrt{3})\exp(-t^2/6T_0^2)e^{i\Delta\phi}E_1(ir_{jkl}L_D/L), \quad (8.4.17)$$

where $r_{jkl} = (t_j-t_k)(t_l-t_k)/T_0^2$ and $E_1(x)$ represents the exponential integral function.

Considerable insight can be gained by considering the simplest case of two 1 bits located at $t_1 = T_b$ and $t_2 = 2T_b$. In this case, j, k, and l take values 1 or 2, and 8 terms are contained in the triple sum in Eq. (8.4.15). The SPM effects are governed by the combinations 111 and 222. The effects of intrachannel XPM are governed by the four combinations 112, 122, 211, and 221. The remaining two combinations, 121 and 212, produce intrachannel FWM and perturbations that are located not at the original position of the input pulses but at locations 0 and $3T_b$. If these two time slots contain pulses (and represent 1 bits), this perturbation beats with them and manifests as amplitude jitter. In contrast, if they represent 0 bits, a ghost pulse appears in these time slots.

The peak power of the ghost pulse located at $t = 0$ is found from Eq. (8.4.17), after setting $j = l = 1$ and $k = 2$, to be

$$P_g(L) = |\Delta U_{121}(L,0)|^2 = \frac{1}{3}(\gamma P_0 L_D)^2 \exp(-t^2/3T_0^2)\left|E_1\left(\frac{2iT_b^2}{|\beta_2|L}\right)\right|^2, \quad (8.4.18)$$

where we used $t_1 = T_b$ and $t_2 = 2T_b$ for the location of two pulses whose overlapping generated the ghost pulse through intrachaneel FWM. Figure 8.19 shows (a) how the peak power grows with the link length L for a 40-Gb/s signal ($T_b = 25$ ps) and (b) how it decreases at $L = 20$ km with the duration T_b of the bit slot, when a bit stream is launched with 10-mW average power into a link made of standard fibers [136]. The dotted curve is obtained when $E_1(x)$ is replaced with its asymptotic approximation in which $|E_1(x)| \sim \ln(|1/x|)$. Such a logarithmic growth of P_g with L holds only for links with constant dispersion. The power transferred to ghost pulses can be reduced by increasing T_b. Indeed, Eq. (8.4.18) predicts that P_g varies with T_b as T_b^{-4} when we use

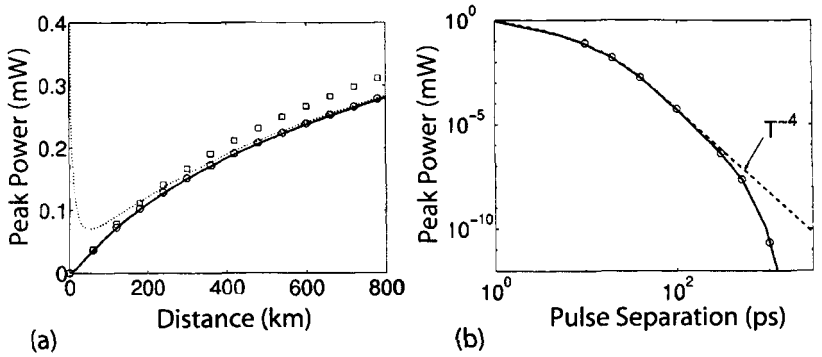

Figure 8.19: Peak power of a ghost pulse as a function of (a) link length L and (b) pulse separation T_b. The dotted curves indicate asymptotic approximations. Symbols show for comparison the results of numerical simulations. (After Ref. [136]; ©2000 IEEE.)

an asymptotic approximation in which $|E_1(x)| \sim 1/x$ for large value of x. As seen in Figure 8.19, the predictions of this equation are in good agreement with the numerical simulations based on the NLS equation.

The preceding results change considerably when a periodic dispersion map is employed [138]–[143]. Even though peak power or energy of each ghost pulse grows in a logarithmic fashion during a single map period [138], it can still build up rapidly along the link because of a resonance related to the periodic nature of loss and dispersion variations [141]. Physically speaking, the amplitudes of ghost pulse generated in each map period add up in phase because of this resonance. As a result, the total peak power at the end of a link length L grows as

$$P_t(L) = |\Delta U_{121}(L,0)|^2 \equiv P_g(L_{\text{map}})(L/L_{\text{map}})^2, \tag{8.4.19}$$

where L_{map} is the map period. Such quadratic growth of the ghost-pulse energy becomes of considerable concern for long-haul systems.

As mentioned earlier, intrachannel FWM also leads to amplitude fluctuations. Physically speaking, whenever the perturbation ΔU_{jkl} falls within the bit slots occupied by 1 bits, it beats with the amplitude of that bit. This beating modifies the amplitude of each 1 bit by an amount that depends not only on the pseudo-random bit pattern but also on the relative phases of neighboring pulses. In the case of a periodic dispersion map, energy fluctuations grow only linearly with length of the fiber link [141]. Moreover, they can be reduced considerably by adopting a distributed amplification scheme such that the average power does not vary much along the link.

8.5 Control of Intrachannel Nonlinear Effects

As seen in Section 8.4, intrachannel XPM as well as FWM can limit the performance of a pseudo-linear system. Both these effects occur even for systems making use of DM solitons because pulses overlap partially during each map period. It is thus important

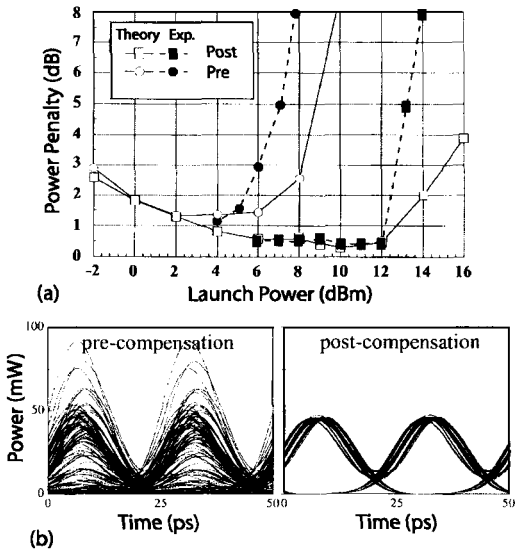

Figure 8.20: (a) Measured (dashed curves) and calculated (solid curves) power penalties as a function of launched power in the cases of pre- and postcompensation. (b) Simulated eye diagrams at a power level of 12 dBm in the two cases. (After Ref. [149]; ©1998 IEEE.)

to find ways to reduce their impact through a proper system design. In this section we focus on three such schemes.

8.5.1 Optimization of Dispersion Maps

The first step in designing any lightwave system is to choose an appropriate dispersion map. There are two main choices. In one, dispersion accumulates along most of the link length and is compensated using DCFs only at the transmitter and receiver ends (pre- and postcompensation). In the other, dispersion is compensated periodically along the link (in-line compensation), either completely or partially. In the later situation, DCFs may be used at the two ends for compensating the residual dispersion.

Both types of dispersion maps have been used for 40-Gb/s experiments. In a 1998 experiment, dispersion accumulated over a 150-km link with $D = 2.3$ ps/(km-nm) was fully compensated through pre- or postcompensation [149]. Figure 8.20 shows the measured and calculated power penalties as a function of launched power in the two cases. Eye diagrams simulated numerically are also shown at a power level of 12 dBm. Much higher powers could be launched, while keeping the penalty below 0.5 dB, in the case of postcompensation. A similar dispersion map was employed in a 2000 experiment in which a 40-Gb/s signal was transmitted over 800 km by amplifying it periodically every 80 km [150]. This experiment used standard fibers and compensated the entire accumulated dispersion ($d_a > 12$ ns/nm) at the receiver end. It also operated in the pseudo-linear regime as it employed 2.5-ps pulses to generate the 40-Gb/s bit stream. The amplifier spacing was increased to 120 km in a later experiment [151].

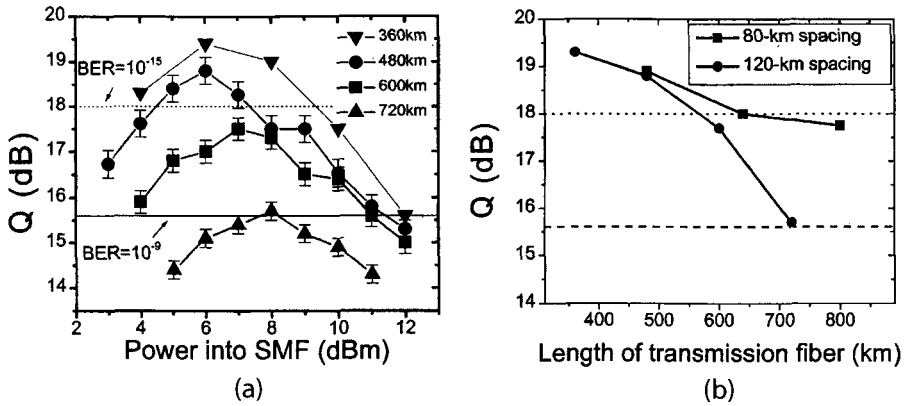

Figure 8.21: Measured Q factors (symbols) in a 40-Gb/s experiment (a) as a function of launched power after 3, 4, 5, and 6 amplifiers spaced 120 km apart and (b) as a function of distance for amplifier spacings of 80 and 120 km. The dashed and dotted lines show the value of Q needed to maintain a BER below 10^{-9} and 10^{-15}. (After Ref. [151]; ©2000 IEEE.)

Figure 8.21(a) shows the measured Q factor as a function of launched power after 3, 4, 5, and 6 amplifiers. At a distance of 600 km, Q^2 exceeded 15.6 dB (a value needed to keep the BER below 10^{-9}) over a large power range from 4 to 11 dBm. However, when link length was 720 km, this value of Q^2 was obtained only for an input power level close to 8 dBm. As seen in Figure 8.21(b), much longer distances could be realized by reducing the spacing between amplifiers to 80 km.

Periodic dispersion maps have been used in several 40-Gb/s experiments, typically performed in a recirculating-loop configuration [152]–[155]. In one experiment operating in the pseudo-linear regime [152], dispersion accumulated over 100 km of dispersion-shifted fiber was compensated using a higher-order-mode DCF (see Section 7.2). The span loss of 22 dB was compensated using a hybrid amplification scheme, with 15 dB of distributed Raman gain realized through backward pumping. In this experiment, 40-Gb/s data could be transmitted over 1,700 km while maintaining a BER below 10^{-9}. The same approach was used in another loop experiment in which loop length was 75 km, and the DCF did not fully compensate its dispersion [153]. The residual dispersion of -1.4 ps/nm per round trip was compensated outside the loop, just before the receiver. The DCF location was changed within the loop to simulate the pre- and postcompensation situations. Similar to the results shown in Figure 8.20, postcompensation provided better performance in the case of the RZ format. The FWM theory of Section 8.4.3 shows that the power transferred to ghost pulses is sensitive to the amount of precompensation, and it could explain the experimental data. In this experiment, the transmission distance was limited to about 700 km.

Several 40-Gb/s experiments designed the dispersion map such that the system operated in the DM-soliton regime. In one set of experiments, the average GVD of a 106-km-long recirculating loop was varied to optimize system performance [154]. It was found that the system could be operated over more than 1,500 km by adjusting the launched power as long as the average dispersion was anomalous in the range of

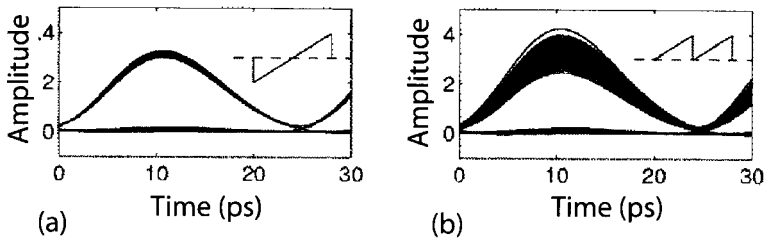

Figure 8.22: Numerically simulated eye diagrams at 1,600 km for (a) symmetric and (b) asymmetric dispersion maps. (After Ref. [157]; ©2001 IEEE.)

0 to 0.1 ps/(km-nm). Much better performance was realized in another experiment in which a 40-Gb/s signal in the form of DM solitons could be transmitted over 6,400 km [155]. In general, soliton systems are found to be limited by XPM-induced timing jitter, whereas pseudo-linear systems are limited by FWM-generated ghost pulses [156].

The optimization of a dispersion map is not a trivial task as it involves varying a large number of design parameters (lengths and dispersion of individual fibers used to make the map, the amount of pre- and postcompensation employed, pulse width, etc.) for a given set of system parameters (such as bit rate, link length, amplifier spacing). Extensive numerical simulations reveal several interesting features [26]. Both the pseudo-linear and DM-soliton regimes can be used to design 40-Gb/s systems, but the dispersion map for them is generally quite different. When fiber dispersion is relatively small along most of the link [$D < 4$ ps/(km-nm)], the soliton regime works best with an RZ duty cycle near 50% and requires some residual dispersion per map period. The system can also be designed in the pseudo-linear regime if the duty cycle is reduced to below 30% and the amount of pre- and postcompensation is suitably optimized. In contrast, when dispersion is large along most of the link (as is the case when standard single-mode fibers are employed), operation in the pseudo-linear regime may be more desirable for designing a 40-Gb/s system. Even though a single-channel soliton system may operate at 40 Gb/s over longer lengths under some conditions [145], the pseudo-linear regime is often preferred for WDM systems [26].

One can ask if the intrachannel nonlinear effects can be controlled by modifying a dispersion map suitably. As discussed earlier, XPM-induced timing jitter can be reduced considerably by making the dispersion map symmetric. In fact, as seen in Figure 8.22, both timing and amplitude jitters can be reduced by making the accumulated dispersion $d_a(z) = \int_0^z D(z)\,dz$ symmetric over the link such that $d_a(z) = d_a(L-z)$ [157]. In practice, this can be realized by compensating 50% of dispersion at the transmitter end and the remaining 50% at the receiver end. Such a map was used for numerical simulations shown in Figure 8.22 for which 2.5-ps Gaussian pulses with a 25-ps bit slot were propagated over 1,600 km of standard fiber with $D = 17$ ps/(km-nm). Equation (8.4.16) can be used to understand why jitter may be reduced for symmetric maps by noting that the limits of integration should be changed from $-L/2$ to $L/2$ for such maps [157]. As discussed earlier, timing jitter results from XPM-induced frequency shifts that cancel for a symmetric map. Indeed, timing jitter would vanish under such conditions if $p(z) = 1$ in Eq. (8.4.16). The residual jitter seen in Figure 8.22 is due

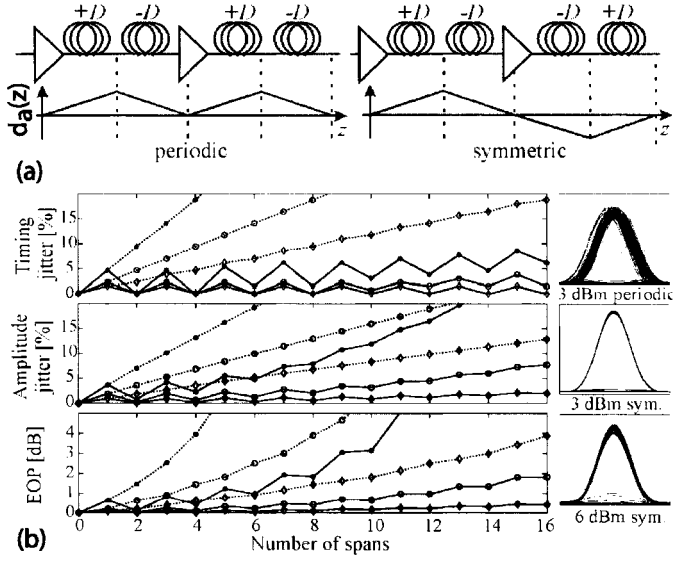

Figure 8.23: (a) Design of symmetric and asymmetric fiber links with corresponding changes in accumulated dispersion. (b) Timing jitter, amplitude jitter, and eye-opening penalty over 16 spans (each 80 km long) for symmetric (solid curves) and asymmetric (dashed) links. Launched power is 3, 6, and 9 dBm for diamonds, circles, and squares, respectively. Eye diagrams are also shown for all three cases. (After Ref. [158]; ©2004 IEEE.)

to variations in the average power of the signal along the link induced by a lumped amplification scheme. The amplitude jitter depends on the relative phase between the existing pulse in a bit slot and the nonlinear perturbation ΔU produced in that bit slot by other neighboring pulses. The in-phase part of the perturbation nearly vanishes for symmetric maps, resulting in reduced amplitude fluctuations.

If a periodic dispersion map is employed with two fiber sections of equal lengths but opposite dispersions, the jitter reduction can be realized by reversing the two fibers in every alternate map period. Figure 8.23 shows the reduction realized in the amplitude and timing jitters at three power levels [158] with such symmetrization of the dispersion map. The calculated eye-opening penalty (EOP) is also shown. Each span employs two 40-km fiber sections with $D = \pm 17$ ps/(km-nm), $\alpha = 0.2$ dB/km, and $\gamma = 1.1$ W^{-1}/km. In the case of a conventional periodic dispersion map, both the amplitude and timing jitters increase linearly with the link length and become so large that the EOP exceeds 4 dB after 700 km for a launched power of 6 dBm. In contrast, when the map is made symmetric, jitter accumulated over one span is cancelled to a large extent in the following span. As a result, the net timing jitter oscillates and increases much more slowly for symmetric maps. With a simple change that involves only flipping the fibers in alternate spans, the same system can operate over more than 1,200 km with negligible penalty.

The length of two fiber sections in the dispersion map does not need to be equal for

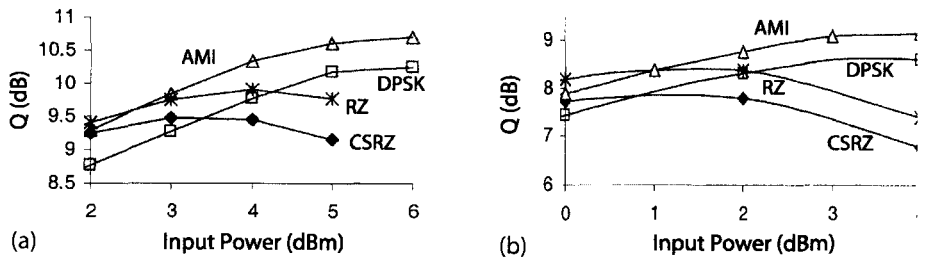

Figure 8.24: Power dependence of the Q factor found numerically for a 40-Gb/s channel at a distance of 1,000 km for four modulation formats and two dispersion maps (a) and (b). (After Ref. [165]; ©2003 IEEE.)

the cancellation of jitter to occur. The concept of scaled translation symmetry can be used to show that both the amplitude and timing jitters can be reduced for a wide variety of maps [159], even when variations in the average power are not symmetric around the midpoint. Another approach that can reduce the intrachannel nonlinear effects for any dispersion map consists of placing a single optical phase conjugator in the middle of the entire fiber link [160]. As discussed in Section 7.5, such a device is equivalent to reversing the sign of the dispersion parameters of all fiber sections in the second half of the link. System-level experiments have confirmed that phase conjugation can reduce the impact of intrachannel nonlinear effects considerably [161].

8.5.2 Phase-Alternation Techniques

As the nonlinear perturbation in Eq. (8.4.16) depends on the phase of pulses generating it, the input phase of optical pulses forming the bit stream can be used to control the intrachannel nonlinear effects [162]. The basic idea consists of introducing a relative phase shift between any two neighboring bits, resulting in a modulation format referred to as the alternate-phase RZ format. Several other formats, such as carrier-suppressed RZ (CSRZ), duobinary RZ, RZ-DPSK, and alternate-mark-inversion RZ (AMI-RZ), can also be employed. The last format was used in a 2003 experiment to transmit a 40-Gb/s signal over 2,000 km [163]. The improvement in the Q factor was typically less than 1 dB when compared with the standard RZ format.

The important question is which phase-alternation technique is the optimum choice for suppressing the intrachannel nonlinear effects. Since ghost pulses generated through intrachannel FWM are often the limiting factor for pseudo-linear systems, one can ask which technique reduces their amplitude most [164]–[166]. Four modulation formats were compared in a numerical study [165], whose results are shown in Figure 8.24. The Q factor is plotted for a 40-Gb/s system at a distance of 1000 km for two dispersion maps with a 100-km map period. The map (a) consists of three sections such that $D = 19$ ps/(km-nm) for the first and third sections (each 30 km long) but $D = -28$ ps/(km-nm) for the 40-km-long middle section. The map (b) employs 100 km of standard fiber with $D = 17$ ps/(km-nm) whose dispersion is compensated using DCFs. The duty cycle is typically 66% for the CSRZ format but only 33% for the standard RZ

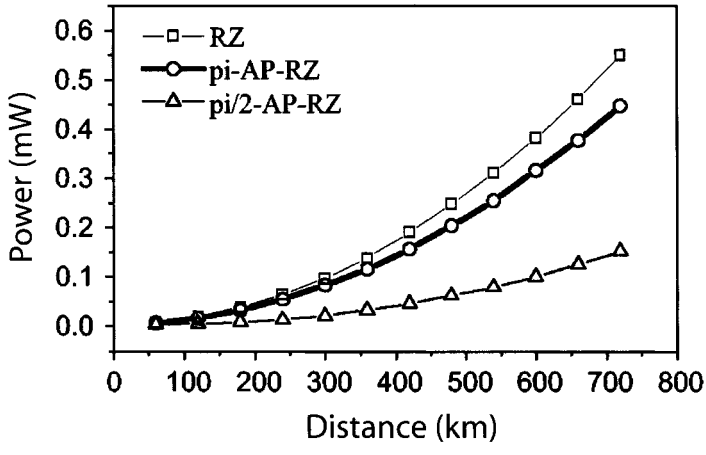

Figure 8.25: Growth of power in 0 bits as function of distance for a 40-Gb/s signal with 6.25-ps pulses and three RZ-type formats. (After Ref. [166]; ©2004 IEEE.)

format. As seen in Figure 8.24, both the DPSK and AMI formats provide better performance compared with RZ and CSRZ formats. This can be understood by noting that the amplitude of ghost pulses generated through various combinations of the subscripts j k, and l in Eq. (8.4.16) depends on the phase of neighboring bits, among other things. The amount of improvement realized with the use of DPSK and AMI-RZ formats depends on the launched power. In general, more power can be launched when phase-alternation techniques are employed.

The CSRZ format is an example of the AP-RZ format for which the phase difference $\delta\phi$ between two neighboring bits is fixed at a value of π. Clearly, one can choose $\delta\phi$ in the range of 0 to π, although the optical carrier may then not be suppressed completely. A numerical study shows that the optimum value of $\delta\phi$ is close to $\pi/2$, as this choice minimizes the buildup of ghost pulses generated through intrachannel FWM [166]. Figure 8.25 shows the standard deviation of power in 0 bits (calculated numerically) as the function of distance for a 40-Gb/s signal with 25% duty-cycle pulses. The dispersion map consists of 60 km of standard fiber, followed by 12 km of a DCF. As expected from the theory of Section 8.4.3, power in 0 bits increases rapidly in a quadratic fashion for a standard RZ signal ($\delta\phi = 0$). The growth is reduced slightly in the case of the CSRZ format ($\delta\phi = \pi$). However, it is suppressed by a large amount for $\delta\phi = \pi/2$. Experimental results support this conclusion.

8.5.3 Polarization Bit Interleaving

Another technique for controlling the intrachannel nonlinear effects alternates the polarization of neighboring bits in an RZ signal. It makes use of the fact that both the XPM and FWM processes depend on the state of polarization (SOP) of the interacting waves. The technique of polarization bit interleaving was first used in 1991 for reducing interaction between neighboring solitons [167]. In another approach, used

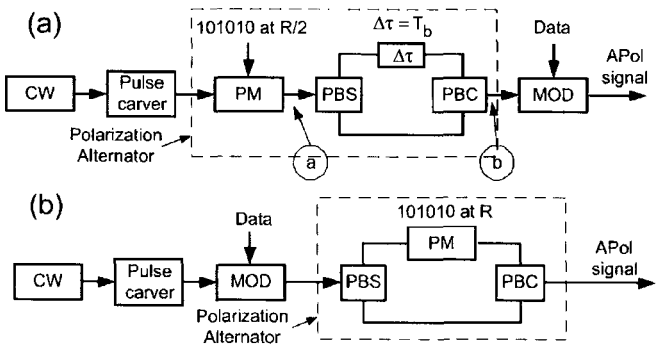

Figure 8.26: Schematic illustration of two schemes for alternating polarization such that neighboring bits are orthogonally polarized. Acronyms PM, PBS, PBC, MOD, and APol stand for phase modulator, polarization beam splitter, polarization beam combiner, data modulator, and alternate polarization, respectively. (After Ref. [173]; ©2004 IEEE.)

commonly for increasing the spectral efficiency of WDM systems, neighboring channels are orthogonally polarized [168]. However, this scheme is quite different from the one considered in this section in which neighboring bits of a single channel are orthogonally polarized through time-domain interleaving [169]–[173].

Figure 8.26 shows two schemes that can be used for polarization alternation on a

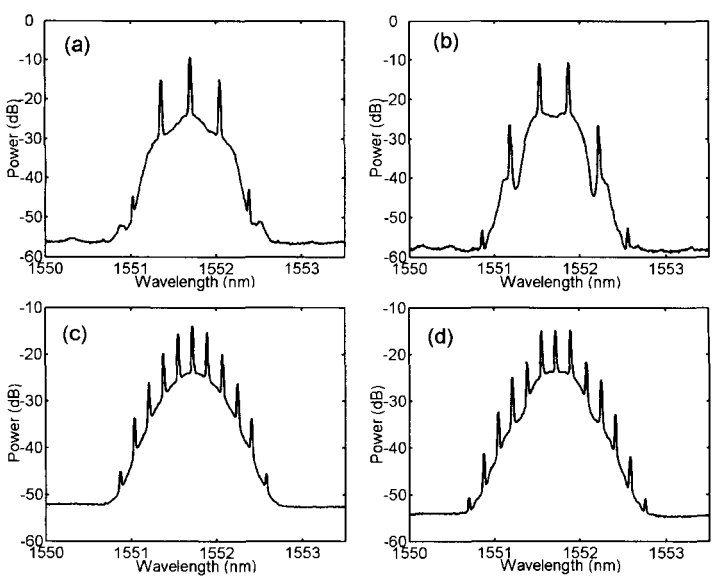

Figure 8.27: Spectra of standard (a) RZ and (b) CSRZ signals. Modified spectra of (c) RZ and (d) CSRZ signals when neighboring bits are orthogonally polarized. (After Ref. [173]; ©2004 IEEE.)

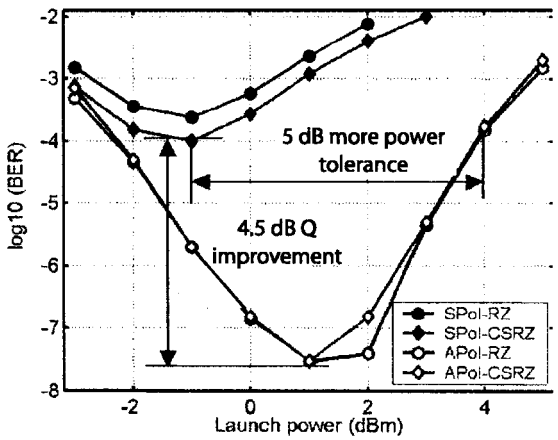

Figure 8.28: BER measured as a function of launch power at a distance of 2,000 km in the case of four modulation formats whose spectra are shown in Figure 8.27. SPol and APol stand for the same- and alternate-polarization bit patterns. (After Ref. [173]; ©2004 IEEE.)

bit by bit basis [173]. In both of them, a pulse carver is used to create an uncoded train of RZ pulses at the bit rate rate. In scheme (a), a phase modulator operating at half the bit rate first imposes a phase shift on this pulse train, which is split into its orthogonally polarized components that are combined back after one bit delay. A data modulator then codes the RZ signal. In scheme (b), in contrast, the pulse train is first coded with the data. It is then split into its orthogonally polarized components that are combined back after a phase modulator first imposes a phase shift on one of the components. The second scheme is much easier to implement in practice. The signal spectrum is affected considerably with polarization alternation. Figure 8.27 compares the spectra of RZ and CSRZ signals at 42.7 Gb/s when neighboring bits have the same or orthogonal SOPs. Two changes are apparent: The carrier is not suppressed even for the CSRZ format and the spectrum develops side bands at half the bit rate. Both these features can be understood by noting that the spectra of orthogonally polarized components have side bands spaced apart by the bit rate B, but they are shifted by $B/2$.

Considerable reduction in the power level of ghost pulses generated through intra-channel FWM was observed in a 40-Gb/s recirculating-loop experiment [173]. The loop included four spans of 82.3 km, each span formed with 70 km or so of standard fiber followed with a DCF that left a residual dispersion of 40 ps/nm per span. Backward Raman pumping was used for compensating span losses in a distributed fashion. Figure 8.28 shows the measured BER as a function of launch power after a distance of 2,000 km (six round trips in the loop). Four curves correspond to four modulation formats whose signal spectra are depicted Figure 8.27. The duty cycle of RZ and CSRZ bit streams was 33% and 66%, respectively.

Several features of Figure 8.28 are noteworthy. First, the minimum BER was $\geq 10^{-4}$ for both the RZ and CSRZ formats when all bits had the same SOP and it was realized at a relatively low value of launch power. When the polarization-alternation technique was implemented, the BER improved considerably and its minimum value

occurred at a higher power level (about 1 dBm). These results indicate that the Q^2 factor improves by 4.5 dB when neighboring bits are orthogonally polarized and can be understood as follows. With polarization alternation, intrachannel nonlinear impairments are reduced significantly and lead to a much lower BER for the RZ format, as evident from Figure 8.28. Since the duty cycle was 66% for the CSRZ signal, and each 1 bit had a wider pulse width, its performance was slightly lower than the RZ signal (with a 33% duty cycle) under the same operating conditions. The main conclusion is that the use of polarization alternation in the time domain helps considerably to reduce the intrachannel nonlinear effects in high-speed lightwave systems operating at bit rates of 40 Gb/s or more. A low-duty RZ format is often the optimum choice for such systems so that the system operates in the pseudo-linear regime.

8.6 High-Speed Lightwave Systems

So far we have focused on a single channel operating at most at a bit rate of 40 Gb/s. If intrachannel nonlinear effects can be controlled, it is possible to increase the bit rate beyond 40 Gb/s. Such optical signals cannot be generated electrically because of the limitations imposed by high-speed electronics. However, as mentioned in Section 1.4.1, the TDM technique can be employed in the optical domain to create bit streams at data rates higher than 100 Gb/s. Experimentally, optical TDM (OTDM) has been used to transmit data at a single carrier wavelength at bit rates as high as 1.128 Tb/s [174]–[186]. The use of OTDM requires new types of transmitters and receivers based on all-optical multiplexing and demultiplexing techniques. In this section we first discuss these techniques and then focus on the performance issues related to OTDM lightwave systems.

8.6.1 OTDM Transmitters and Receivers

In OTDM lightwave systems, several channels, each operating at a bit rate of $B \leq 40$ Gb/s, share the same carrier frequency and are multiplexed optically to form a composite bit stream at the bit rate NB, where N is the number of channels. Several multiplexing techniques can be used for this purpose [181]. Figure 8.29 shows the design of an OTDM transmitter based on the delay-line technique. It requires a laser capable of generating a periodic pulse train at the repetition rate equal to the single-channel bit rate B. Moreover, the laser should produce pulses of width T_p such that $T_p < T_b = (NB)^{-1}$ to ensure that each pulse will fit within its allocated time slot T_b. The laser output is split equally into N branches, after amplification if necessary. A modulator in each branch blocks the pulses representing 0 bits.

The multiplexing of N bit streams is achieved by a technique that can be implemented optically in a simple manner. In this scheme, the bit stream in the nth branch is delayed by an amount $(n-1)/(NB)$, where $n = 1, \ldots, N$. The output of all branches is then combined to form a composite signal. The multiplexed bit stream produced using such a scheme has a bit slot corresponding to the bit rate NB. Furthermore, N consecutive bits in each interval of duration B^{-1} belong to N different channels, as required by the TDM scheme (see Section 1.4.1). The optical delay lines can be implemented using

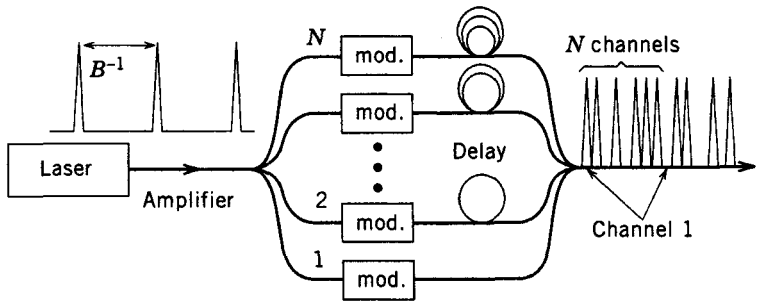

Figure 8.29: Design of an OTDM transmitter based on optical delay lines.

fiber segments of controlled lengths. The delay lines can be relatively long (10 cm or more) because only the length difference has to be matched precisely. As an example, a 1-mm length difference introduces a delay of about 5 ps.

An alternative approach makes use of planar lightwave circuits fabricated with the silica-on-silicon technology (see Section 4.3.3 of LT1). Such devices can be made polarization-insensitive while providing precise control of the delay lines. However, optical modulators cannot be integrated with this technology. A simple approach consists of inserting an InP chip containing an array of electroabsorption modulators in between the silica waveguides that are used for splitting, delaying, and combining the multiple channels (see Figure 8.29). The main problem with this approach is the spot-size mismatch as the optical signal passes from Si to InP waveguide (and vice versa). This problem can be solved by integrating spot-size converters with the modulators. Such an integrated OTDM multiplexer was used in a 160-Gb/s experiment in which 16 channels, each operating at 10 Gb/s were multiplexed [182].

The OTDM technique requires the use of a RZ format, but the duty cycle of RZ pulses for each channel should be relatively small, as it scales inversely with the number of channels. In other words, one needs an optical source that emits a train of short optical pulses at a repetition rate as high as 40 GHz. Several different techniques can be employed for this purpose [181]. In one approach, gain switching or mode locking of a semiconductor laser provides 10 to 20 ps pulses at a high repetition rate, which can be compressed using a variety of techniques [187]. In another approach, a fiber laser is harmonically mode-locked using an intracavity $LiNbO_3$ modulator [187]. Such lasers can provide pulse widths $\sim$1 ps at a repetition rate of up to 40 GHz. In a third approach, a DFB laser operating continuously is used in combination with two or more cascaded electroabsorption modulators to carve short RZ pulses [180].

OTDM receivers need to demultiplex individual channels from the OTDM signal. Such devices require ultrafast optical switches that can operate at a time scale of a few picoseconds or less [188] and have been discussed in Section 10.4.1 of LT1. In one approach, electroabsorption modulators are used as optical gates [180]. In another, several $LiNbO_3$ modulators are employed in series. Other techniques make use of XPM and FWM, the same two nonlinear effects that are often harmful to lightwave systems (see Section 10.1 of LT1). Figure 8.30 shows two such schemes schematically. They both require an optical clock—a periodic pulse train at the single-channel bit rate.

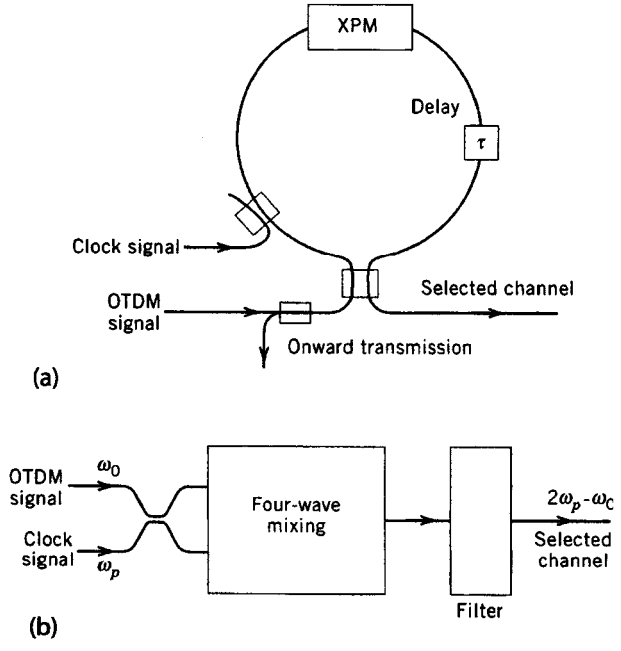

Figure 8.30: Demultiplexing schemes for OTDM signals based on (a) XPM within a nonlinear optical-loop mirror and (b) FWM inside a nonlinear medium.

The XPM-based technique makes use of a nonlinear optical loop mirror (NOLM) acting as an ultrafast optical switch [187]. Such a device is also referred to as the Sagnac interferometer. The NOLM is called a mirror because it reflects its input entirely when the counterpropagating waves experience the same phase shift over one round trip. However, if the symmetry is broken by introducing a relative phase shift of π between them through XPM, the signal is fully transmitted. The clock signal is injected into the loop such that it propagates only in the clockwise direction and introduces a phase shift of π through XPM for pulses belonging to a specific channel within the OTDM signal. As a result, only that channel is not reflected by the NOLM. Fiber nonlinearity is fast enough that such a device can respond at femtosecond time scales. In a 1998 experiment, an NOLM was used to demultiplex a 640-Gb/s OTDM signal [189].

The second scheme shown in Figure 8.30 makes use of FWM inside a nonlinear medium. The OTDM signal is launched together with the clock signal (at a different wavelength), which plays the role of the pump for the FWM process. In time slots in which a clock pulse overlaps with a "1" bit of the channel that needs to be demultiplexed, FWM produces a pulse at the new wavelength. As a result, pulse train at this new wavelength is an exact replica of the channel to be demultiplexed. An optical filter is used to separate the demultiplexed channel from the OTDM and clock signals. A polarization-maintaining fiber is often used as the nonlinear medium for FWM. As early as 1996, demultiplexing of 10-Gb/s channels from a 500-Gb/s OTDM signal was

demonstrated using clock pulses of about 1-ps duration [175]. This scheme can also amplify the demultiplexed channel (by up to 40 dB) through parametric amplification inside the same fiber.

The main limitation of a fiber-based demultiplexer stems from its relatively weak nonlinearity. Typically, fiber length should be 5 km or more for the device to function at practical power levels of the clock signal. This problem can be solved in two ways. In one approach, the required fiber length is reduced by up to a factor of 10 by using special fibers designed such that the nonlinear parameter γ is enhanced because of the reduced spot size of the fiber mode [190]. Alternatively, a semiconductor optical amplifier (SOA) can be used in place of the fiber. In the case of a NOLM, an SOA is inserted within the fiber loop but its location is carefully adjusted (see Section 10.3.1 of LT1). The XPM-induced phase shift by a 1-mm-long SOA is large enough that a value of π can be realized at moderate power levels. The silica-on-silicon technology has also been used to make a compact demultiplexer in the form of a a Mach–Zehnder interferometer. Such devices are capable of demultiplexing a 160-Gb/s signal [20].

8.6.2 Performance of OTDM System

The transmission distance of OTDM systems is limited in practice by fiber dispersion because of the use of short optical pulses ($\sim$1 ps or less) dictated by their relatively high bit rates. Clearly, an OTDM signal carrying N channels at the bit rate B is equivalent to transmitting a single channel at the composite bit rate of NB, and its performance is restricted by the dispersion limits found in Sections 3.3.4. As an example, it is evident from Figure 3.4 that a 200-Gb/s system is limited to below $<$50 km even when the system is designed to operate exactly at the zero-dispersion wavelength of the fiber. Thus, OTDM systems require simultaneous compensation of both the second- and third-order dispersions. Even then, PMD is likely to become a limiting factor for long fiber lengths, and its compensation is also necessary. The intrachannel nonlinear effects also limit the performance of OTDM systems, and the use of a pseudo-linear regime is often beneficial [26].

In spite of these difficulties, many laboratory experiments have realized transmission at a bit rate of 100 Gb/s or more with the OTDM technique [175]–[186]. As early as 1996, a 100-Gb/s OTDM signal consisting of 16 channels at 6.3 Gb/s was transmitted over 560 km by using optical amplifiers (80-km spacing) together with dispersion management [176]. The laser source in this experiment was a mode-locked fiber laser, producing 3.5-ps pulses at a repetition rate of 6.3 GHz. A multiplexing scheme similar to that shown in Figure 8.29 was used to generate the 100-Gb/s OTDM signal. The total capacity was extended within a few months to 1 Tb/s by multiplexing 10 such OTDM signals through WDM [177], demonstrating how the time- and spectral-domain multiplexing techniques can be combined in practice. Within a year, the same technique was used to combine seven WDM channels, each operating at 200 Gb/s through OTDM, but the transmission distance was limited to 50 km [178]. By 1999, a capacity of 3 Tb/s could be realized by combining 19 WDM channels such that each channel was operating at 160 Gb/s [179]. The channels were spaced 450 GHz apart (about 3.6 nm) to avoid overlap between neighboring WDM channels at the 160-Gb/s bit rate. The 70-nm WDM signal occupied both the C and L bands.

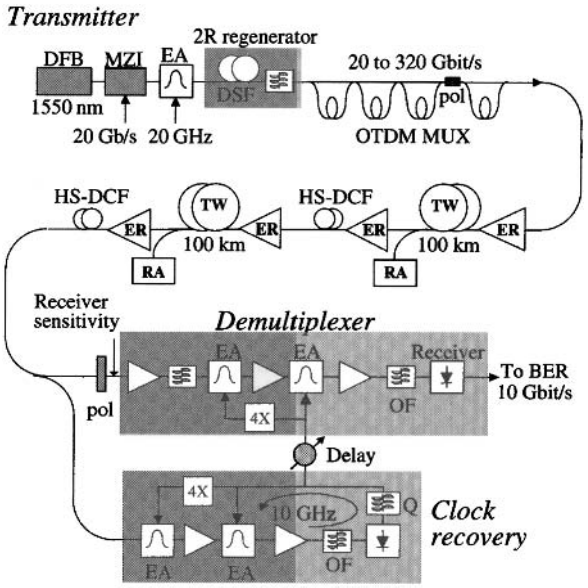

Figure 8.31: Schematic of a 320-Gb/s OTDM experiment used to transmit 16 20-Gb/s channels over 200 km. Except for the $LiNbO_3$ modulator, mostly semiconductor components are used within the transmitter and receiver. TW: TrueWave reduced-slope fiber, HS-DCF: high-slope dispersion-compensating fiber, EA: electroabsorption, RA: Raman pump, OF: optical filter. (After Ref. [170]; ©2000 IEEE.)

In another set of experiments the objective was to transmit a single channel at high bit rates, while employing a more practical design for OTDM transmitters and receivers. In a 1999 experiment, both these components were made using standard semiconductor devices, and a 100-Gb/s OTDM signal was transmitted over 100 km using the pseudo-linear scheme [180]. By 2000, the same design was used to demonstrate the transmission of a 320-Gb/s signal (formed by multiplexing 16 20-Gb/s channels through OTDM) over 200 km of dispersion-shifted fiber. Figure 8.31 shows the setup for this experiment schematically [170]. First, a CW signal from a DFB laser operating at 1,553 nm is NRZ-coded with a 20-Gb/s bit stream using a $LiNbO_3$ modulator. This 20-Gb/s NRZ signal is converted into 1.8-ps RZ pulses using an electroabsorption modulator, followed by an optical 2R regenerator that compresses pulses to the desired width. The resulting 20-Gb/s RZ signal is used to generate the 320-Gb/s bit stream using four stages of fiber-delay lines. The last stage of the multiplexer also switches the polarization of adjacent bits to reduce the impact of intrachannel nonlinear effects on system performance. At the receiver end, demultiplexing as well as clock-recovery operations are performed using multiple electroabsorption modulators.

Dispersive effects played a critical role for 1.8-ps pulses used in the 320-Gb/s experiment. It was necessary to compensate both the dispersion and its slope over the 200-km-long fiber. If third-order dispersion is not compensated, it would distort optical pulses severely and produce a long oscillatory tail. In a 2000 experiment, a 1.28-Tb/s

ODTM signal could be transmitted over 70 km, but it required compensation of even the fourth-order dispersion [183]. To avoid excessive dispersion problems, it is common to limit the bit rate of each channel to 160 Gb/s but to multiplex several of them through WDM and transmit the resulting signal over long distances. In a 2003 experiment, it was possible with a careful design to transmit six 160-Gb/s channels (actual bit rate was 170.6 Gb/s to accommodate FEC overhead) over 2,000 km [185].

Problems

8.1 Solve the NLS equation (8.1.2) numerically using the same dispersion map employed for Figure 8.1. Consider a 40-Gb/s system designed using RZ pulses of Gaussian shape with a 6.25-ps width (FWHM). Use a 128-bit pseudo-random bit pattern to construct curves similar to those shown in Figure 8.1(a), assuming that the maximum distance corresponds to a 1-dB penalty in the eye opening. Is this system design better than the 50% duty cycle used for Figure 8.1? Justify your answer in physical terms.

8.2 Derive Eqs. (8.1.5) and (8.1.6) using the moment method discussed in Section 4.6.

8.3 Repeat the derivation of Eqs. (8.1.5) and (8.1.6) using the variation method, also discussed in Section 4.6.

8.4 Write a computer program for solving Eqs. (8.1.5) and (8.1.6) using Fortran, Matlab, or another programming language. Use it to reproduce the results shown in Figures 8.3 and 8.4.

8.5 A 10-Gb/s soliton system is operating at 1.55 μm using fibers with a constant dispersion of $D = 2$ ps/(km-nm). The effective core area of the fiber is 50 μm^2. Calculate the peak power and the pulse energy required for fundamental solitons of 30-ps width (FWHM). Use $n_2 = 2.6 \times 10^{-20}$ m^2/W.

8.6 The soliton system of the preceding problem needs to be upgraded to 40 Gb/s. Calculate the pulse width, peak power, and energy of the solitons when soliton width (FWHM) is 20% of the bit slot. What is the average launched power for this system?

8.7 Verify by direct substitution that the soliton solution given in Eq. (8.2.9) satisfies the NLS equation.

8.8 Solve the NLS equation numerically (8.2.1) and plot the evolution of the fourth- and fifth-order solitons over one soliton period. Compare your results with those shown in Figure 8.5 and comment on the main differences.

8.9 Verify numerically by propagating a fundamental soliton over 100 dispersion lengths that the shape of the soliton does not change on propagation. Repeat the simulation using a Gaussian input pulse shape with the same peak power and explain the results.

8.10 A 10-Gb/s soliton lightwave system is designed with $T_0/T_b = 0.1$ to ensure well-separated solitons in the RZ bit stream. Calculate pulse width, peak power, pulse

energy, and the average power of the RZ signal, assuming $\beta_2 = -1$ ps^2/km and $\gamma = 2$ W^{-1}/km.

8.11 Prove that the energy of standard solitons should be increased by the factor $G \ln G/(G-1)$ when fiber loss α is compensated periodically using optical amplifiers. Here, $G = \exp(\alpha L_A)$ is the amplifier gain and L_A is the spacing between amplifiers.

8.12 A 10-Gb/s soliton communication system is designed with 50-km amplifier spacing. What should the peak power of the input pulse be to ensure that a fundamental soliton is maintained in an average sense in a fiber with 0.2 dB/km loss? Assume 100-ps pulse width (FWHM), $\beta_2 = -0.5$ ps^2/km, and $\gamma = 2$ W^{-1}/km. What is the average launched power for such a system?

8.13 Calculate the maximum bit rate for a soliton system designed with $q_0 = 5$, $\beta_2 = -1$ ps^2/km, and $L_A = 50$ km. Assume that the condition (8.2.15) is satisfied when $B^2 L_A$ is at the 20% level. What is the soliton width at the maximum bit rate?

8.14 Use the NLS equation (8.1.2) to prove that solitons remain unperturbed by fiber losses when fiber dispersion decreases exponentially as $\beta_2(z) = \beta_2(0)\exp(-\alpha z)$.

8.15 Solve Eqs. (8.1.5) and (8.1.6) numerically by imposing the periodicity condition given in Eq. (8.2.16). Plot T_0 and C_0 as a function of input pulse energies in the range of 0.1 to 10 ps for a dispersion map made using 70 km of the standard fiber with $D = 17$ ps/(km-nm) and 10 km of DCF with $D = -115$ ps/(km-nm). Use $\gamma = 2$ W^{-1}/km and $\alpha = 0.2$ dB/km for the standard fiber and $\gamma = 6$ W^{-1}/km and $\alpha = 0.5$ dB/km for the DCF.

8.16 Calculate the map strength S and the map parameter T_{map} for the map used in the preceding problem when 1-pJ input pulses are launched. Estimate the maximum bit rate that this map can support.

8.17 Explain in physical terms how intrachannel XPM among optical pulses representing 1 bits produces timing and amplitude jitter.

8.18 What is meant by a ghost pulse? Explain how such is pulse is generated through intrachannel FWM in a pseudo-linear system.

References

[1] G. P. Agrawal, *Nonlinear Fiber Optics*, 3rd ed., Academic Press, San Diego, CA, 2001.

[2] H. Taga, S. Yamamoto, N. Edagawa, Y. Yoshida, S. Akiba, and H. Wakabayashi, *J. Lightwave Technol.* **12**, 1616 (1994).

[3] S. Sekine, N. Kikuchi, S. Sasaki, and Y. Uchida, *Electron. Lett.* **31**, 1080 (1995).

[4] A. Naka and S. Saito, *J. Lightwave Technol.* **13**, 862 (1995).

[5] N. Kikuchi and S. Sasaki, *J. Lightwave Technol.* **13**, 868 (1995).

[6] N. Kikuchi, S. Sasaki, and K. Sekine *Electron. Lett.* **31**, 375 (1995); N. Kikuchi and S. Sasaki, *Electron. Lett.* **32**, 570 (1996).

[7] F. Matera and M. Settembre, *J. Lightwave Technol.* **14**, 1 (1996); *Opt. Fiber Technol.* **4**, 34 (1998).

[8] D. Breuer and K. Petermann, *IEEE Photon. Technol. Lett.* **9**, 398 (1997).

[9] F. Forghieri, P. R. Prucnal, R. W. Tkach, and A. R. Chraplyvy, *IEEE Photon. Technol. Lett.* **9**, 1035 (1997).

[10] A. Sahara, H. Kubota, and M. Nakazawa, *IEEE Photon. Technol. Lett.* **9**, 1179 (1997).

[11] T. Matsuda, A. Naka, and S. Saito, *J. Lightwave Technol.* **16**, 340 (1998).

[12] A. Sano, Y. Miyamoto, T. Kataoka, and K. Hagimoto, *J. Lightwave Technol.* **16**, 977 (1998).

[13] D. Breuer, K. Obermann, and K. Petermann, *IEEE Photon. Technol. Lett.* **10**, 1793 (1998).

[14] C. Caspar, H.-M. Foisel, A. Gladisch, N. Hanik, F. Kuppers, R. Ludwig, A. Mattheus, W. Pieper, B. Strebel, and H. G. Weber, *IEEE Photon. Technol. Lett.* **10**, 481 (1999).

[15] D. S. Govan, W. Forysiak, and N. J. Doran, *Opt. Lett.* **23**, 1523 (1998).

[16] I. S. Penketh, P. Harper, S. B. Alleston, A. M. Niculae, I. Bennion I, and N. J. Doran, *Opt. Lett.* **24**, 802 (1999).

[17] S. K. Turitsyn and E. G. Shapiro, *Opt. Fiber Technol.* **4**, 151 (1998).

[18] F. M. Madani and K.ikuchi, *J. Lightwave Technol.* **17**, 1326 (1999).

[19] C. M. Weinert, R. Ludwig, W. Pieper, H. G. Weber, D. Breuer, K. Petermann, and F. Küppers, *J. Lightwave Technol.* **17**, 2276 (1999).

[20] M. Nakazawa, H. Kubota, K. Suzuki, E. Yamada, and A. Sahara, *IEEE J. Sel. Topics Quantum Electron.* **6**, 363 (2000).

[21] M. Murakami, T. Matsuda, H. Maeda, and T. Imai, *J. Lightwave Technol.* **18**, 1197 (2000).

[22] A. Sahara, T. Inui, T. Komukai, H. Kubota, and M. Nakazawa, *J. Lightwave Technol.* **18**, 1364 (2000).

[23] T. Hoshida, O. Vassilieva, K. Yamada, S. Choudhary, R. Pecqueur, H. Kuwahara, *J. Lightwave Technol.* **20**, 1989 (2002).

[24] B. Konrad, K. Petermann, J. Berger, R. Ludwig, C. M. Weinert, H. G. Weber, and B. Schmauss, *J. Lightwave Technol.* **20**, 2129 (2002).

[25] M. Wu, and W. I. Way, *J. Lightwave Technol.* **22**, 1483 (2004).

[26] R.-J. Essiambre, G. Raybon, and B. Mikkelsen, in *Optical Fiber Telecommunications*, Vol. 4B, I. P. Kaminow and T. Li, Eds., Academic Press, San Diego, CA, 2002, Chap. 6.

[27] M. J. Ablowitz and P. A. Clarkson, *Solitons, Nonlinear Evolution Equations, and Inverse Scattering*, Cambridge University Press, New York, 1991.

[28] G. L. Lamb, Jr., *Elements of Soliton Theory*, Dover, New York, 1994.

[29] T. Miwa, *Mathematics of Solitons*, Cambridge University Press, New York, 1999.

[30] V. E. Zakharov and A. B. Shabat, *Sov. Phys. JETP* **34**, 62 (1972).

[31] A. Hasegawa and F. Tappert, *Appl. Phys. Lett.* **23**, 142 (1973).

[32] J. Satsuma and N. Yajima, *Prog. Theor. Phys.* **55**, 284 (1974).

[33] V. E. Zakharov and A. B. Shabat, *Sov. Phys. JETP* **37**, 823 (1973).

[34] A. Hasegawa and F. Tappert, *Appl. Phys. Lett.* **23**, 171 (1973).

[35] W. J. Tomlinson, R. J. Hawkins, A. M. Weiner, J. P. Heritage, and R. N. Thurston, *J. Opt. Soc. Am. B* **6**, 329 (1989).

[36] P. Emplit, M. Haelterman, and J. P. Hamaide, *Opt. Lett.* **18**, 1047 (1993).

[37] M. Nakazawa and K. Suzuki, *Electron. Lett.* **31**, 1084 (1995); *Electron. Lett.* **31**, 1076 (1995).

[38] R. Leners, P. Emplit, D. Foursa, M. Haelterman, and R. Kashyap, *J. Opt. Soc. Am. B* **14**, 2339 (1997).

[39] Y. S. Kivshar and B. Luther-Davies, *Phys. Rep.* **298**, 81 (1998).
[40] Y. Chen and J. Atai, *IEEE J. Quantum Electron.* **34**, 1301 (1998).
[41] M. Stratmann, M. Bohm, and F. Mitschke, *Electron. Lett.* **37**, 1182 (2001).
[42] Y. S. Kivshar and G. P. Agrawal, Eds., *Optical Solitons*, Academic Press, San Diego, CA, 2003, Chap. 4.
[43] Y. Kodama and A. Hasegawa, *Opt. Lett.* **7**, 339 (1982); **8**, 342 (1983).
[44] Z. M. Liao, C. J. McKinstrie, and G. P. Agrawal, *J. Opt. Soc. Am. B* **17**, 514 (2000).
[45] A. Hasegawa, *Opt. Lett.* **8**, 650 (1983); *Appl. Opt.* **23**, 3302 (1984).
[46] L. F. Mollenauer, R. H. Stolen, and M. N. Islam, *Opt. Lett.* **10**, 229 (1985).
[47] L. F. Mollenauer and K. Smith, *Opt. Lett.* **13**, 675 (1988).
[48] L. F. Mollenauer, B. M. Nyman, M. J. Neubelt, G. Raybon, and S. G. Evangelides, *Electron. Lett.* **27**, 178 (1991).
[49] A. Hasegawa and Y. Kodama, *Solitons in Optical Communications*, Clarendon Press, Oxford, 1995.
[50] R. J. Essiambre and G. P. Agrawal, in *Progress in Optics*, E. Wolf, Ed., Vol. 37, Elsevier, Amsterdam, 1997, Chap. 4.
[51] L. F. Mollenauer, J. P. Gordon, and P. V. Mamyshev, in *Optical Fiber Telecommunications*, vol. 3A, I. P. Kaminow and T. L. Koch, Eds., Academic Press, San Diego, CA, 1997, Chap. 12.
[52] K. Tajima, *Opt. Lett.* **12**, 54 (1987).
[53] V. A. Bogatyrjov, M. M. Bubnov, E. M. Dianov, and A. A. Sysoliatin, *Pure Appl. Opt.* **4**, 345 (1995).
[54] D. J. Richardson, R. P. Chamberlin, L. Dong, and D. N. Payne, *Electron. Lett.* **31**, 1681 (1995).
[55] A. J. Stentz, R. Boyd, and A. F. Evans, *Opt. Lett.* **20**, 1770 (1995).
[56] D. J. Richardson, L. Dong, R. P. Chamberlin, A. D. Ellis, T. Widdowson, and W. A. Pender, *Electron. Lett.* **32**, 373 (1996).
[57] W. Forysiak, F. M. Knox, and N. J. Doran, *Opt. Lett.* **19**, 174 (1994).
[58] T. Georges and B. Charbonnier, *Opt. Lett.* **21**, 1232 (1996); *IEEE Photon. Technol. Lett.* **9**, 127 (1997).
[59] S. Cardianal, E. Desurvire, J. P. Hamaide, and O. Audouin, *Electron. Lett.* **33**, 77 (1997).
[60] A. Hasegawa, Y. Kodama, and A. Murata, *Opt. Fiber Technol.* **3**, 197 (1997).
[61] S. Kumar, Y. Kodama, and A. Hasegawa, *Electron. Lett.* **33**, 459 (1997).
[62] S. Kumar, *IEEE Photon. Technol. Lett.* **16**, 810 (2004).
[63] N. J. Smith, F. M. Knox, N. J. Doran, K. J. Blow, and I. Bennion, *Electron. Lett.* **32**, 54 (1996).
[64] M. Nakazawa, H. Kubota, and K. Tamura, *IEEE Photon. Technol. Lett.* **8**, 452 (1996).
[65] M. Nakazawa, H. Kubota, A. Sahara, and K. Tamura, *IEEE Photon. Technol. Lett.* **8**, 1088 (1996).
[66] A. B. Grudinin and I. A. Goncharenko, *Electron. Lett.* **32**, 1602 (1996).
[67] A. Berntson, N. J. Doran, W. Forysiak, and J. H. B. Nijhof, *Opt. Lett.* **23**, 900 (1998).
[68] J. N. Kutz, P. Holmes, S. G. Evangelides, and J. P. Gordon, *J. Opt. Soc. Am. B* **15**, 87 (1998).
[69] S. K. Turitsyn, I. Gabitov, E. W. Laedke, V. K. Mezentsev, S. L. Musher, E. G. Shapiro, T. Schafer, and K. H. Spatschek, *Opt. Commun.* **151**, 117 (1998).
[70] T. I. Lakoba and D. J. Kaup, *Phys. Rev. E* **58**, 6728 (1998).
[71] S. K. Turitsyn and E. G. Shapiro, *J. Opt. Soc. Am. B* **16**, 1321 (1999).

[72] I. R. Gabitov, E. G. Shapiro, and S. K. Turitsyn, *Phys. Rev. E* **55**, 3624 (1997).
[73] M. J. Ablowitz and G. Bioindini, *Opt. Lett.* **23**, 1668 (1998).
[74] C. Paré and P. A. Bélanger, *Opt. Lett.* **25**, 881 (2000).
[75] J. H. B. Nijhof, N. J. Doran, W. Forysiak, and F. M. Knox, *Electron. Lett.* **33**, 1726 (1997).
[76] V. S. Grigoryan and C. R. Menyuk, *Opt. Lett.* **23**, 609 (1998).
[77] J. N. Kutz and S. G. Evangelides, *Opt. Lett.* **23**, 685 (1998).
[78] Y. Chen and H. A. Haus, *Opt. Lett.* **23**, 1013 (1998).
[79] J. H. B. Nijhof, W. Forysiak, and N. J. Doran, *Opt. Lett.* **23**, 1674 (1998).
[80] S. K. Turitsyn, J. H. B. Nijhof, V. K. Mezentsev, and N. J. Doran, *Opt. Lett.* **24**, 1871 (1999).
[81] S. K. Turitsyn, M. P. Fedoruk, and A. Gornakova, *Opt. Lett.* **24**, 969 (1999).
[82] L. J. Richardson, W. Forysiak, and N. J. Doran, *IEEE Photon. Technol. Lett.* **13**, 209 (2001).
[83] E. Poutrina and G. P. Agrawal, *Opt. Commun.* **206**, 193 (2002).
[84] S. Waiyapot, S. K. Turitsyn, and V. K. Mezentsev, *J. Lightwave Technol.* **20**, 2220 (2002).
[85] C. Xie, L. F. Mollenauer, and N. Mamysheva, *J. Lightwave Technol.* **21**, 769 (2003).
[86] E. Poutrina and G. P. Agrawal, *J. Lightwave Technol.* **21**, 990 (2003).
[87] H. Kubota and M. Nakazawa, *Opt. Commun.* **87**, 15 (1992); M. Nakazawa and H. Kubota, *Electron. Lett.* **31**, 216 (1995).
[88] M. Suzuki, I. Morita, N. Edagawa, S. Yamamoto, H. Taga, and S. Akiba, *Electron. Lett.* **31**, 2027 (1995).
[89] A. Naka, T. Matsuda, and S. Saito, *Electron. Lett.* **32**, 1694 (1996).
[90] I. Morita, M. Suzuki, N. Edagawa, S. Yamamoto, H. Taga, and S. Akiba, *IEEE Photon. Technol. Lett.* **8**, 1573 (1996).
[91] J. M. Jacob, E. A. Golovchenko, A. N. Pilipetskii, G. M. Carter, and C. R. Menyuk, *IEEE Photon. Technol. Lett.* **9**, 130 (1997).
[92] G. M. Carter and J. M. Jacob, *IEEE Photon. Technol. Lett.* **10**, 546 (1998).
[93] V. S. Grigoryan, R. M. Mu, G. M. Carter, and C. R. Menyuk, *IEEE Photon. Technol. Lett.* **10**, 45 (2000).
[94] R. M. Mu, C. R. Menyuk, G. M. Carter, and J. M. Jacob, *IEEE J. Sel. Topics Quantum Electron.* **6**, 248 (2000).
[95] A. B. Grudinin, M. Durkin, M. Isben, R. I. Laming, A. Schiffini, P. Franco, E. Grandi, and M. Romagnoli, *Electron. Lett.* **33**, 1572 (1997).
[96] F. Favre, D. Le Guen, and T. Georges, *J. Lightwave Technol.* **17**, 1032 (1999).
[97] M. Zitelli, F. Favre, D. Le Guen, and S. Del Burgo, *IEEE Photon. Technol. Lett.* **9**, 904 (1999).
[98] J. P. Gordon and H. A. Haus, *Opt. Lett.* **11**, 665 (1986).
[99] D. Marcuse, *J. Lightwave Technol.* **10**, 273 (1992).
[100] N. J. Smith, W. Foryisak, and N. J. Doran, *Electron. Lett.* **32**, 2085 (1996).
[101] G. M. Carter, J. M. Jacob, C. R. Menyuk, E. A. Golovchenko, A. N. Pilipetskii, *Opt. Lett.* **22**, 513 (1997).
[102] S. Kumar and F. Lederer, *Opt. Lett.* **22**, 1870 (1997).
[103] J. N. Kutz and P. K. A. Wai, *IEEE Photon. Technol. Lett.* **10**, 702 (1998).
[104] T. Okamawari, A. Maruta, and Y. Kodama, *Opt. Lett.* **23**, 694 (1998); *Opt. Commun.* **149**, 261 (1998).
[105] V. S. Grigoryan, C. R. Menyuk, and R. M. Mu, *J. Lightwave Technol.* **17**, 1347 (1999).

[106] M. F. S. Ferreira and S. C. V. Latas, *J. Lightwave Technol.* **19**, 332 (2001).
[107] J. Santhanam, C. J. McKinstrie, T. I. Lakoba, and G. P. Agrawal, *Opt. Lett.* **26**, 1131 (2001).
[108] C. J. McKinstrie, J. Santhanam, and G. P. Agrawal, *J. Opt. Soc. Am. B* **19**, 640 (2002).
[109] J. Santhanam and G. P. Agrawal, *IEEE J. Sel. Topics Quantum Electron.* **7**, 632 (2002).
[110] E. Poutrina and G. P. Agrawal, *IEEE Photon. Technol. Lett.* **14**, 39 (2002); *J. Lightwave Technol.* **20**, 762 (2002).
[111] A. Mecozzi, J. D. Moores, H. A. Haus, and Y. Lai, *Opt. Lett.* **16**, 1841 (1991).
[112] L. F. Mollenauer, M. J. Neubelt, M. Haner, E. Lichtman, S. G. Evangelides, and B. M. Nyman, *Electron. Lett.* **27**, 2055 (1991).
[113] Y. Kodama and A. Hasegawa, *Opt. Lett.* **17**, 31 (1992).
[114] L. F. Mollenauer, J. P. Gordon, and S. G. Evangelides, *Opt. Lett.* **17**, 1575 (1992).
[115] V. V. Afanasjev, *Opt. Lett.* **18**, 790 (1993).
[116] M. Romagnoli, S. Wabnitz, and M. Midrio, *Opt. Commun.* **104**, 293 (1994).
[117] M. Nakazawa, E. Yamada, H. Kubota, and K. Suzuki, *Electron. Lett.* **27**, 1270 (1991).
[118] N. J. Smith, W. J. Firth, K. J. Blow, and K. Smith, *Opt. Lett.* **19**, 16 (1994).
[119] S. Bigo, O. Audouin, and E. Desurvire, *Electron. Lett.* **31**, 2191 (1995).
[120] M. Nakazawa, K. Suzuki, E. Yamada, H. Kubota, Y. Kimura, and M. Takaya, *Electron. Lett.* **29**, 729 (1993).
[121] G. Aubin, E. Jeanny, T. Montalant, J. Moulu, F. Pirio, J.-B. Thomine, and F. Devaux, *Electron. Lett.* **31**, 1079 (1995).
[122] W. Forysiak, K. J. Blow. and N. J. Doran, *Electron. Lett.* **29**, 1225 (1993).
[123] M. Matsumoto, H. Ikeda, and A. Hasegawa, *Opt. Lett.* **19**, 183 (1994).
[124] T. Widdowson, D. J. Malyon, A. D. Ellis, K. Smith, and K. J. Blow, *Electron. Lett.* **30**, 990 (1994).
[125] S. Kumar and A. Hasegawa, *Opt. Lett.* **20**, 1856 (1995).
[126] V. S. Grigoryan, A. Hasegawa, and A. Maruta, *Opt. Lett.* **20**, 857 (1995).
[127] M. Matsumoto, *J. Opt. Soc. Am. B* **15**, 2831 (1998); *Opt. Lett.* **23**, 1901 (1998).
[128] S. K. Turitsyn and E. G. Shapiro, *J. Opt. Soc. Am. B* **16**, 1321 (1999).
[129] S. Waiyapot and M. Matsumoto, *IEEE Photon. Technol. Lett.* **11**, 1408 (1999).
[130] M. F. S. Ferreira and S. H. Sousa, *Electron. Lett.* **37**, 1184 (2001).
[131] M. Matsumoto, *Opt. Lett.* **23**, 1901 (2001).
[132] J. Santhanam and G. P. Agrawal, *J. Opt. Soc. Am. B* **20**, 284 (2003).
[133] R.-J. Essiambre, B. Mikkelsen, and G. Raybon, *Electron. Lett.* **35**, 1576 (1999).
[134] P. V. Mamyshev and N. A. Mamysheva, *Opt. Lett.* **24**, 1454 (1999).
[135] M. Zitelli, F. Matera, and M. Settembre, *J. Lightwave Technol.* **17**, 2498 (1999).
[136] A. Mecozzi, C. B. Clausen, and M. Shtaif, *IEEE Photon. Technol. Lett.* **12**, 392 (2000).
[137] R. I. Killey, H. J. Thiele, V. Mikhailov, and P. Bayvel, *IEEE Photon. Technol. Lett.* **12**, 1624 (2000).
[138] J. Mårtensson, A. Berntson, M. Westlund, A. Danielsson, P. Johannisson, D. Anderson, and M. Lisak, *Opt. Lett.* **26**, 55 (2001).
[139] A. Mecozzi, C. B. Clausen, and M. Shtaif, *IEEE Photon. Technol. Lett.* **12**, 1633 (2000).
[140] S. Kumar, *IEEE Photon. Technol. Lett.* **13**, 800 (2001); S. Kumar, J. C. Mauro, S. Raghavan, and D. Q. Chowdhury, *IEEE J. Sel. Topics Quantum Electron.* **18**, 626 (2002).
[141] M. J. Ablowitz and T. Hirooka, *Opt. Lett.* **25**, 1750 (2000); *IEEE J. Sel. Topics Quantum Electron.* **18**, 603 (2002).

[142] P. Johannisson, D. Anderson, A. Berntson, and J. Mårtensson, *Opt. Lett.* **26**, 1227 (2001).
[143] P. Bayvel and R. I. Killey, in *Optical Fiber Telecommunications*, Vol. 4B, I. P. Kaminow and T. Li, Eds., Academeic Press, San Diego, CA, 2002, Chap. 13.
[144] M. Daikoku, T. Otani, and M. Suzuki, *IEEE Photon. Technol. Lett.* **15**, 1165 (2003).
[145] D. Duce, R. I. Killey, and P. Bayvel, *J. Lightwave Technol.* **22**, 1263 (2004).
[146] G. Raybon, Y. Su, J. Leuthold, R.-J. Essiambre, T. Her, C. Joergensen, P. Steinvurzel, and K. D. K. Feder, Proc. Opt. Fiber Commun., Postdeadline Paper FD-10, March 2002.
[147] L. K. Wickham, R.-J. Essiambre, A. H. Gnauck, P. J. Winzer, and A. R. Chraplyvy, *IEEE Photon. Technol. Lett.* **16**, 1591 (2004).
[148] M. K. Jackson, G. R. Boyer, J. Paye, M. A. Franco, and A. Mysyrowicz, *Opt. Lett.* **17**, 1770 (1992).
[149] D. Breuer, H. J. Ehrke, F. Küppers, R. Ludwig, K. Petermann, H. G. Weber, and K. Weich, *IEEE Photon. Technol. Lett.* **10**, 822 (1998).
[150] A. H. Gnauck, S.-G. Park, J. M. Wiesenfeld, and L. D. Garrett, *Electron. Lett.* **35**, 2218 (1999).
[151] S.-G. Park, A. H. Gnauck, J. M. Wiesenfeld, and L. D. Garrett, *IEEE Photon. Technol. Lett.* **12**, 1085 (2000).
[152] S. Ramachandran, G. Raybon, B. Mikkelsen, M. Yan, and L. Cowsar, and R. J. Essiambre, Digest Europ. Conf. Opt. Commun., Amsterdam, 2001, p. 282.
[153] R. I. Killey, V. Mikhailov, S. Appathurai, and P. Bayvel, *J. Lightwave Technol.* **20**, 2282 (2002).
[154] Y. Takushima, T. Douke, X. Wang, and K. Kikuchi, *J. Lightwave Technol.* **20**, 360 (2002).
[155] R. Holzlöhner, H. N. Ereifej, V. S. Grigoryan, G. M. Carter, and C. R. Menyuk, *J. Lightwave Technol.* **20**, 1124 (2002).
[156] A. Pizzinat, A. Schiffini, F. Alberti, F. Matera, A. N. Pinto, and P. Almeida, *J. Lightwave Technol.* **20**, 1673 (2002).
[157] A. Mecozzi, C. B. Clausen, M. Shtaif, S.-G. Park, and A. H. Gnauck, *IEEE Photon. Technol. Lett.* **13**, 445 (2001).
[158] A. G. Striegler and B. Schmauss, *J. Lightwave Technol.* **22**, 1877 (2004).
[159] H. Wei and D. V. Plant, *Opt. Exp.* **12**, 4282 (2004).
[160] A. Chowdhury and R. J. Essiambre, *Opt. Lett.* **29**, 1105 (2004).
[161] A. Chowdhury, G. Raybon, R.-J. Essiambre, J. H. Sinsky, A. Adamiecki, J. Leuthold, C. R. Doerr, and S. Chandrasekhar, *J. Lightwave Technol.* **23**, 172 (2005).
[162] K. S. Cheng and J. Conradi, *IEEE Photon. Technol. Lett.* **14**, 98 (2002).
[163] P. J. Winzer, A. H. Gnauck, G. Raybon, S. Chandrasekhar, Y. Su, and J. Leuthold, *IEEE Photon. Technol. Lett.* **15**, 766 (2003).
[164] X. Liu, X.Wei, A. H. Gnauck, C. Xu, and L. K.Wickham, *Opt. Lett.* **13**, 1177 (2002).
[165] A. V. Kanaev, G. G. Luther, V. Kovanis, S. R. Bickham, and J. Conradi, *J. Lightwave Technol.* **21**, 1486 (2003).
[166] S. Appathurai, V. Mikhailov, R. I. Killey, and P. Bayvel, *J. Lightwave Technol.* **22**, 239 (2004).
[167] S. G. Evangelides, L. F. Mollenauer, J. P. Gordon, and N. S. Bergano, *J. Lightwave Technol.* **10**, 28 (1992).
[168] A. Agarwal, S. Banerjee, D. F. Grosz, A. P. Küng, D. N. Maywar, A. Gurevich, and T. H. Wood, *IEEE Photon. Technol. Lett.* **15**, 470 (2003).
[169] F. Matera, M. Settembre, M. Tamburrini, F. Favre, D. L. Guen, T. Georges, M. Henry, G. Michaud, P. Franco, A. Schiffini, M. Romagnoli, M. Guglielmucci, and S. Cascelli, *J. Lightwave Technol.* **17**, 2225 (1999).

[170] B. Mikkelsen, G. Raybon, R. J. Essiambre, A. J. Stentz, T. N. Nielsen, D. W. Peckham, L. Hsu, L. Gruner-Nielsen, K. Dreyer, and J. E. Johnson, *IEEE Photon. Technol. Lett.* **12**, 1400 (2000).

[171] A. Hodzic, B. Konrad, and K. Petermann, *IEEE Photon. Technol. Lett.* **15**, 153 (2003).

[172] X. Liu, C. Xu, and X. Wei, *IEEE Photon. Technol. Lett.* **16**, 30 (2004).

[173] C. Xie, I. Kang, A. H. Gnauck, L. Möller, L F. Mollenauer, and A. R. Grant, *J. Lightwave Technol.* **22**, 806 (2004).

[174] A. D. Ellis, D. M. Patrick, D. Flannery, R. J. Manning, D. A. O. Davies, and D. M. Spirit, *J. Lightwave Technol.* **13**, 761 (1995).

[175] T. Morioka, S. Kawanishi, H. Takara, O. Kamatani, M. Yamada, T. Kanamori, K. Uchiyama, and M. Saruwatari *Electron. Lett.* **32**, 468 (1996).

[176] S. Kawanishi, H. Takara, O. Kamatani, T. Morioka, and M. Saruwatari, *Electron. Lett.* **32**, 470 (1996).

[177] T. Morioka, H. Takara, S. Kawanishi, O. Kamatani, K. Takiguchi, K. Uchiyama, M. Saruwatari, H. Takahashi, M. Yamada, T. Kanamori, and H. Ono, *Electron. Lett.* **32**, 906 (1996).

[178] S. Kawanishi, H. Takara, K. Uchiyama, I. Shake, O. Kamatani, and M. Saruwatari, *Electron. Lett.* **33**, 1716 (1997).

[179] S. Kawanishi, H. Takara, K. Uchiyama, I. Shake, and K. Mori, *Electron. Lett.* **35**, 826 (1999).

[180] B. Mikkelsen, G. Raybon, R.-J. Essiambre, J. E. Johnson, K. Dreyer, and L. F. Nelson, *Electron. Lett.* **35**, 1866 (1999).

[181] M. Saruwatari, *IEEE J. Sel. Topics Quantum Electron.* **6**, 1363 (2000).

[182] T. G. Ulmer, M. C. Gross, K. M. Patel, , J.T. Simmons, P. W. Juodawlkis, B. R. Wasbburn, W. S. Astar, A. J. SpringThorpe, R. P. Kenan, C. M. Verber, and S. E. Ralph, *J. Lightwave Technol.* **18**, 1964 (2000).

[183] M. Nakazawa, T. Yamamoto, and K. R. Tamura, *Electron. Lett.* **36**, 2027 (2000).

[184] J. Inoue, H. Sotobayashi, W. Chujo, and H. Kawaguchi, *Electron. Lett.* **38**, 819 (2002).

[185] A. H. Gnauck, G. Raybon, P. G. Bernasconi, J. Leuthold, C. R. Doerr, and L. W. Stulz, *IEEE Photon. Technol. Lett.* **15**, 1618 (2003).

[186] T. Ohara, H. Takara, I. Shake, K. Mori, K. Sato, S. Kawanishi, S. Mino, T. Yamada, M. Ishii, I. Ogawa, T. Kitoh, K. Magari, M. Okamoto, R. V. Roussev, J. R. Kurz, K. R. Parameswaran, and M. M. Fejer, *IEEE Photon. Technol. Lett.* **16**, 650 (2004).

[187] G. P. Agrawal, *Applications of Nonlinear Fiber Optics*, Academic Press, San Diego, CA, 2001.

[188] E. Bødtker and J. E. Bowers, *J. Lightwave Technol.* **13**, 1809 (1995).

[189] T. Yamamoto, E. Yoshida, and M. Nakazawa, *Electron. Lett.* **34**, 1013 (1998).

[190] J. Hansryd and P. A. Andrekson, *IEEE Photon. Technol. Lett.* **13**, 732 (2001).

Chapter 9

WDM Systems

Chapter 8 focused on single-channel systems operating at 40 Gb/s or more through electrical and optical TDM. As discussed in Chapter 1, channels can also be multiplexed in the spectral domain through frequency-division multiplexing (FDM). Indeed, this technique is routinely used for radio waves and microwaves. Its extension to optical domain permits, in principle, the capacity of lightwave systems to exceed 10 Tb/s because of a large frequency associated with the optical carrier. Since the implementation of FDM in the optical domain requires multiple transmitters operating at different wavelengths, optical FDM is known as *wavelength-division multiplexing* (WDM). The WDM technique was first used in the 1980s when the capacity of existing fiber links operating at 1.3 μm was doubled by adding another channel operating near 1.55 μm. However, it was only after 1995 that WDM was used to transmit over the same fiber hundreds of optical channels in the 1.55-μm spectral region and to realize system capacities beyond 1 Tb/s. The design of such systems requires attention to many details related to the generation and propagation of multiple bit streams overlapping in the time domain. More specifically, interchannel nonlinear effects must be controlled to ensure that they do not limit system performance.

In this chapter the basic WDM scheme and related concepts are discussed first in Section 9.1. Section 9.2 is devoted to the linear mechanisms that can produce interchannel crosstalk. Sections 9.3 and 9.4 focus on several nonlinear mechanisms that cause crosstalk through interactions of bit streams in neighboring channels. Section 9.5 is devoted to various techniques that can be employed to reduce nonlinear crosstalk. The major design issues such as spectral efficiency are addressed in Section 9.6.

9.1 Basic WDM Scheme

The WDM technique corresponds to the scheme in which the capacity of a lightwave system is enhanced by employing multiple optical carriers at different wavelengths. Each carrier is modulated independently using different electrical bit streams (which may themselves use TDM and FDM techniques in the electrical domain) that are transmitted over the same fiber. Figure 9.1 shows schematically the layout of such

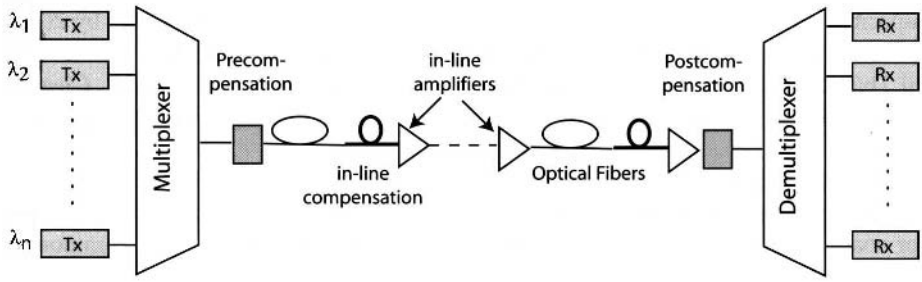

Figure 9.1: Schematic of a WDM fiber link. Each channel operates at a distinct wavelength through transmitters operating at different wavelengths. Pre-, post-, and in-line compensators are used to manage the dispersion of fiber link.

a dispersion-managed WDM link. The output of several transmitters is combined using an optical device known as a multiplexer. The multiplexed signal is launched into the fiber link for transmission to its destination, where a "demultiplexer" separates individual channels and sends each channel to its own receiver. The implementation of such a WDM scheme required the development of many new components such as multiplexers, demultiplexers, and optical filters (see Chapter 8 of LT1), all of which became available commercially during the 1990s.

9.1.1 System Capacity and Spectral Efficiency

It is evident from Figure 9.1 that the use of WDM can increase the system capacity because it transmits multiple bit streams over the same fiber simultaneously. When N channels at bit rates $B_1, B_2, \ldots$, and B_N are transmitted simultaneously over a fiber of length L, the total bit rate of the WDM link becomes

$$B_T = B_1 + B_2 + \cdots + B_N. \tag{9.1.1}$$

For equal bit rates, the system capacity is enhanced by a factor of N. The most relevant design parameters for a WDM system are the number N of channels, the bit rate B at which each channel operates, and the frequency spacing $\Delta\nu_{\text{ch}}$ between two neighboring channels. The product NB denotes the system capacity and the product $N\Delta\nu_{\text{ch}}$ represents the total bandwidth occupied by a WDM system.

Historically, the WDM technique has been pursued since commercial lightwave systems first became available in 1980 [1]–[5]. In its simplest form, WDM was used to transmit two channels in different transmission windows of an optical fiber. For example, an existing 1.3-μm lightwave system could be upgraded by adding another channel operating near 1.55 μm, resulting in a channel spacing of 250 nm. Considerable attention was directed during the 1980s toward reducing the channel spacing. An experiment in 1985 demonstrated the NBL product of 1.37 (Tb/s)-km by transmitting 10 channels at 2 Gb/s over 68.3 km of standard fiber with a channel spacing of 1.35 nm [3]. However, it was during the 1990s that WDM systems were developed most aggressively [6]–[10]. Commercial WDM systems first appeared around 1995. Initially, their

capacity was relatively small (around 40 Gb/s or so) but it exceeded 1.6 Tb/s by 2000. Since then, several laboratory experiments have demonstrated capacities of more than 10 Tb/s, although their transmission distance was limited to below 200 km. Clearly, the advent of WDM has led to a virtual revolution in designing high-capacity lightwave systems.

WDM systems are often classified as being coarse or dense, depending on their channel spacing. Although no precise definition exists, channel spacing exceeds 5 nm for coarse WDM but is typically <1 nm for dense WDM systems. It is common to introduce the concept of *spectral efficiency* for WDM systems as $\eta_s = B/\Delta\nu_{ch}$. Spectral efficiency is relatively low for coarse WDM systems [$\eta_s < 0.1$ (b/s)/Hz]. Such systems "waste the bandwidth" in a traditional sense, but are useful for metropolitan-area and local-area networks for which system cost must be kept relatively low. In contrast, long-haul links used for the backbone of an optical network attempt to make η_s as large as possible in order to utilize the bandwidth as efficiently as possible.

For a given system bandwidth, the capacity of a WDM link depends on how closely channels can be packed in the wavelength domain. Clearly, channel spacing $\Delta\nu_{ch}$ should exceed the bit rate B so that the channel spectrum can fit within the allocated bandwidth. The minimum channel spacing is limited by interchannel crosstalk, an issue covered later in this chapter. In practice, channel spacing $\Delta\nu_{ch}$ often exceeds the bit rate B by a factor of 2 or more. This requirement wastes considerable bandwidth as spectral efficiency is then <0.5 (b/s)/Hz. Many new modulation formats are being explored to bring spectral efficiencies closer to 1 (b/s)/Hz.

The channel frequencies (or wavelengths) of WDM systems have been standardized by the International Telecommunication Union (ITU) on a 100-GHz grid in the frequency range of 186 to 196 THz (covering the C and L bands in the wavelength range 1,530–1,612 nm). For this reason, channel spacing for most commercial WDM systems is 100 GHz (0.8 nm at 1,552 nm). This value leads to only 10% spectral efficiency at the bit rate of 10 Gb/s. More recently, ITU has specified WDM channels with a frequency spacing of 25 and 50 GHz. The use of 50-GHz channel spacing in combination with the bit rate of 40 Gb/s has the potential of increasing the spectral efficiency to 80%.

9.1.2 Bandwidth and Capacity of WDM Systems

WDM has the potential for exploiting the large bandwidth offered by optical fibers. Figure 9.2 shows the loss spectrum of a typical silica fiber and two low-loss transmission windows of optical fibers centered near 1.3 and 1.55 μm. Each of these spectral widows extends over more than 10 THz. If the so-called OH peak, resulting from residual water vapors trapped inside the core during manufacturing of silica fibers, can be eliminated using "dry" fibers, the entire spectral region extending from 1.25 to 1.65 μm can be exploited through WDM.

The ultimate capacity of WDM systems can be estimated by assuming that the 300-nm wavelength range extending from 1,300 to 1,600 nm is employed for transmission using dry fibers. The minimum channel spacing can be as small as 50 GHz (or 0.4 nm) for 40-Gb/s channels. Since 750 channels can be accommodated over the 300-nm bandwidth, the resulting capacity can be as large as 30 Tb/s. If we assume that such a

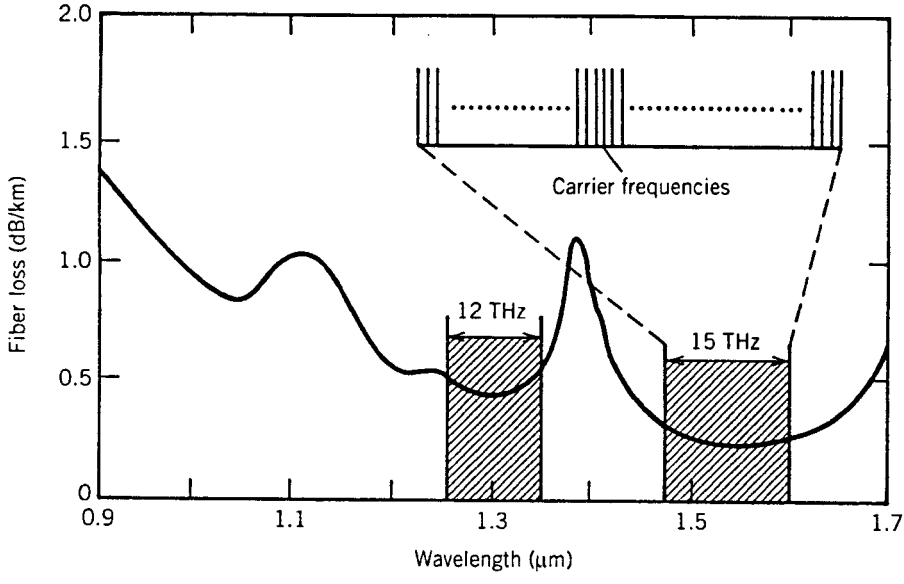

Figure 9.2: Typical loss spectrum of silica fibers and low-loss transmission windows (shaded regions) near 1.3 and 1.55 μm. The inset shows the basic idea behind WDM schematically.

WDM signal can be transmitted over 1,000 km using optical amplifiers with dispersion management, the *NBL* product can exceed 30,000 (Tb/s)-km with the use of WDM technology. This should be contrasted with the third-generation commercial lightwave systems, which transmitted a single channel over 80 km or so at a bit rate of up to 10 Gb/s, resulting in *NBL* values of at most 0.8 (Tb/s)-km.

In practice, many factors limit the use of the entire low-loss window. As seen in Chapter 6, most optical amplifiers have a finite bandwidth. The number of channels is often limited by the bandwidth over which amplifiers can provide nearly uniform gain. The bandwidth of erbium-doped fiber amplifiers is limited to 40 nm even with the use of gain-flattening techniques. The use of Raman amplification can solve the amplifier bandwidth problem to some extent. Among other factors that limit the number of channels are (1) wavelength stability and tunability of distributed feedback (DFB) lasers, (2) signal degradation during transmission because of various nonlinear effects, and (3) interchannel crosstalk during demultiplexing. High-capacity WDM fiber links require many high-performance components, such as transmitters integrating multiple DFB lasers, channel multiplexers and demultiplexers with add-drop capability, and large-bandwidth constant-gain amplifiers.

Experimental results on WDM systems can be divided into two groups based on whether the transmission distance is $\sim$100 km or exceeds 1,000 km. Since the 1985 experiment in which ten 2-Gb/s channels were transmitted over 68 km [3], both the number of channels and the bit rate of individual channels have increased considerably. A capacity of 340 Gb/s was demonstrated in 1995 by transmitting 17 channels, each operating at 20 Gb/s, over 150 km [11]. This was followed within a year by sev-

Table 9.1: High-capacity WDM transmission experiments

Channels N	Capacity NB (Tb/s)	Distance L (km)	NBL Product [(Pb/s)-km]	Conference and Year
256	10.24	100	1.02	OFC 2001
273	10.92	117	1.28	OFC 2001
128	5.12	1,280	6.66	ECOC 2002
40	1.6	5,200	8.32	ECOC 2002
159	6.4	2,100	14.44	ECOC 2002
80	3.2	5,200	16.64	ECOC 2002
160	6.4	3,200	20.48	OFC 2003
373	3.73	11,000	41.03	OFC 2003

eral experiments that realized a capacity of 1 Tb/s. By 2001, the capacity of WDM systems exceeded 10 Tb/s in several laboratory experiments. In one experiment, 273 channels, spaced 0.4 nm apart and each operating at 40 Gb/s, were transmitted over 117 km using three in-line amplifiers, resulting in a total capacity of 11 Tb/s and a NBL product of 1.28 (Pb/s)-km [12]. Table 9.1 lists several WDM experiments in which the NBL product exceeded 1 Pb/s. In this table, OFC and ECOC stand, respectively, for the Optical Fiber Communication Conference and European Conference on Optical Communication, the two conferences where most record-breaking results are often presented.

Another group of WDM experiments is concerned with transmission distances of more than 5,000 km for submarine applications. In a 1996 experiment, 100-Gb/s transmission (20 channels at 5 Gb/s) over 9,100 km was realized using the polarization-scrambling and forward-error-correction techniques [13]. The number of channels was later increased to 32, resulting in a 160-Gb/s transmission over 9,300 km [9]. In a 2003 experiment, a 3.73-Tb/s WDM signal (373 channels, each operating at 10 Gb/s) was transmitted over 11,000 km, resulting in a NBL product of almost 41 (Pb/s)-km (see Table 9.1). This should be compared with the first fiber-optic cable laid across the Atlantic Ocean (TAT-8); it operated at 0.27 Gb/s with $NBL \approx 1.5$ (Tb/s)-km. The use of WDM improved by 2003 the capacity of undersea systems by a factor of 27,000.

On the commercial side, WDM systems with a capacity of 40 Gb/s (16 channels at 2.5 Gb/s or 4 channels at 10 Gb/s) were available in 1996. The 16-channel system covered a wavelength range of about 12 nm in the 1.55-μm region with a channel spacing of 0.8 nm. WDM fiber links operating at 160 Gb/s (16 channels at 10 Gb/s) appeared in 1998. By 2001, WDM systems with a capacity of 1.6 Tb/s (realized by multiplexing 160 channels, each operating at 10 Gb/s) were available. This should be contrasted with the 10-Gb/s capacity of the third-generation systems available before the advent of the WDM technique. The use of WDM had improved by 2001 the capacity of commercial terrestrial systems by a factor of more than 6,000. Although systems with even higher capacities have been designed, they were not deployed commercially by 2004 because of the downturn in the telecommunication industry that began in 2001.

9.2 Linear Degradation Mechanisms

The most important issue in designing WDM lightwave systems is the extent of *interchannel crosstalk*. The system performance degrades whenever crosstalk leads to transfer of power from one channel to another. Such a transfer can occur because of the nonlinear effects in optical fibers, a phenomenon referred to as *nonlinear crosstalk* as it depends on the nonlinear nature of the communication channel. However, some crosstalk occurs even in a perfectly linear channel because of the imperfect nature of various WDM components such as optical filters, demultiplexers, and switches. In this section we focus on the linear crosstalk mechanisms; nonlinear crosstalk is considered in Sections 9.3. and 9.4.

Linear crosstalk can be classified into two categories depending on its origin [14]–[16]. Optical filters and demultiplexers often let a fraction of the signal power from neighboring channels leak, which interferes with the detection process. Such crosstalk is called *heterowavelength* or *out-of-band* crosstalk. It is less of a problem because of its incoherent nature than the *homowavelength* or *in-band* crosstalk that occurs during routing of the WDM signal through multiple nodes. The concatenation of optical filters can also lead to signal distortion through spectral clipping and dispersion caused by a nonlinear phase response. Although this distortion is not due to crosstalk, we include it in the section because its origin is related to channel selection.

9.2.1 Out-of-Band Linear Crosstalk

Consider the common situation in which a tunable optical filter is used to select a single channel among the N channels incident on it. The filter bandwidth is chosen large enough to let pass the entire spectrum of the selected channel. However, a small amount of power from the neighboring channels can leak whenever channels are not spaced far apart. This situation is shown schematically in Figure 9.3, where the transmissivity of a third-order Butterworth filter with the 40-GHz bandwidth (full width at 3-dB points) is shown together with the spectra of three 10-Gb/s NRZ-format channels, spaced 50 GHz apart. In spite of relatively sharp spectral edges associated with this filter, transmissivity is about -26 dB for the neighboring channels. The power leaked into the filter bandwidth acts as a noise source to the signal being detected and is a source of linear crosstalk.

It is relatively easy to estimate the power penalty induced by such out-of-band crosstalk. If the optical filter is set to pass the mth channel, the optical power reaching the photodetector can be written as $P = P_m + \sum_{n \neq m}^{N} T_{mn} P_n$, where P_m is the power in the mth channel and T_{mn} is the filter transmittivity for channel n when channel m is selected. Crosstalk occurs if $T_{mn} \neq 0$ for $n \neq m$. It is called out-of-band crosstalk because it belongs to the channels lying outside the spectral band occupied by the channel detected. Its incoherent nature is also apparent from the fact that it depends only on the power of the neighboring channels.

To evaluate the impact of such crosstalk on system performance, one should consider the power penalty, defined as the additional power required at the receiver to counteract the effect of crosstalk. The photocurrent generated in response to the inci-

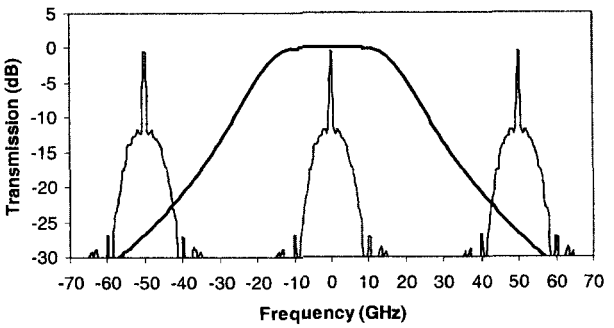

Figure 9.3: Transmissivity of an optical filter with a 40-GHz bandwidth shown superimposed on the spectra of three 10-Gb/s channels separated by 50 GHz. (After Ref. [16]; ©2003 IEEE.)

dent optical power is given by

$$I = R_m P_m + \sum_{n \neq m}^{N} R_n T_{mn} P_n \equiv I_{\text{ch}} + I_X, \tag{9.2.1}$$

where $R_m = \eta_m q / h\nu_m$ is the photodetector responsivity for channel m at the optical frequency ν_m and η_m is the quantum efficiency. The second term I_X in Eq. (9.2.1) denotes the crosstalk contribution to the receiver current I. Its value depends on the bit pattern and becomes maximum when all interfering channels carry 1 bits simultaneously (the worst case).

A simple approach to calculating the filter-induced power penalty is based on the eye closing occurring as a result of the crosstalk [17]. The eye closing is maximum in the worst case for which I_X is largest. In practice, I_{ch} is increased to maintain the system performance. If I_{ch} needs to be increased by a factor δ_X, the peak current corresponding to the top of the eye is $I_1 = \delta_X I_{\text{ch}} + I_X$. The decision threshold is set at $I_D = I_1/2$. The eye opening from I_D to the top level would be maintained at its original value $I_{\text{ch}}/2$ if

$$(\delta_X I_{\text{ch}} + I_X) - I_X - \tfrac{1}{2}(\delta_X I_{\text{ch}} + I_X) = \tfrac{1}{2} I_{\text{ch}}, \tag{9.2.2}$$

or when $\delta_X = 1 + I_X / I_{\text{ch}}$. The quantity δ_X is just the power penalty for the mth channel. By using I_X and I_{ch} from Eq. (9.2.1), δ_X can be written (in dB) as

$$\delta_X = 10 \log_{10} \left(1 + \frac{\sum_{n \neq m}^{N} R_n T_{mn} P_n}{R_m P_m} \right), \tag{9.2.3}$$

where the powers correspond to their on-state values. If the peak power is assumed to be the same for all channels, the crosstalk penalty becomes power-independent. Further, if the photodetector responsivity is nearly the same for all channels ($R_m \approx R_n$), δ_X is well approximated by

$$\delta_X \approx 10 \log_{10}(1 + X), \tag{9.2.4}$$

where $X = \sum_{n \neq m}^{N} T_{mn}$ is a measure of the out-of-band crosstalk; it represents the fraction of total power leaked into a specific channel from all other channels. The numerical

value of X depends on the transmission characteristics of the specific optical filter. However, it follows from Eq. (9.2.4) that values of X as large as 0.1 produce less than 0.5-dB penalty. For this reason, out-of-band crosstalk becomes of concern only when channels are so closely spaced that their spectra begin to overlap.

The preceding analysis of crosstalk penalty is based on the eye closure rather than the bit-error rate (BER). One can obtain an expression for the BER if I_X is treated as a random variable in Eq. (9.2.1) because its value depends on the bit patterns of the channels involved. Thus, this term acts as an additional source of noise during the detection of 1 and 0 bits. The distribution of I_X and the resulting power penalty have been calculated for a Fabry–Perot filter [18]. In general, power penalty depends on the finesse F of the filter and the number N of WDM channels. It can be kept below 0.5 dB to maintain a BER of 10^{-9} for values of N/F as large as 0.5. For this reason, spectral efficiency can approach 50% without much penalty when Fabry–Perot filters are employed.

9.2.2 In-Band Linear Crosstalk

In-band crosstalk, resulting from WDM components used for routing and switching along an optical network, has been of concern since the advent of WDM systems [19]–[33]. Its origin can be understood by considering a static routing device such as a waveguide grating router (see Section 9.2 of LT1). For a router with $N+1$ input and $N+1$ outport ports, there exist $(N+1)^2$ combinations through which a WDM signal with $N+1$ wavelengths can be split. Consider the output at one wavelength, say, λ_0. Among the $N(N+2)$ interfering components that can accompany the desired signal, N components have the same carrier wavelength λ_0, while the remaining $N(N+1)$ belong to different carrier wavelengths and produce out-of-band crosstalk. The N interfering signals at the same wavelength originate from incomplete filtering by the routing device and produce in-band crosstalk. The total electrical field reaching the receiver can be written as [21]

$$E_r(t) = \left[A_0(t) + \sum_{n=1}^{N} A_n(t)\right] \exp(-i\omega_0 t), \tag{9.2.5}$$

where A_0 is the desired signal at the frequency $\omega_0 = 2\pi c/\lambda_0$. The coherent nature of the in-band crosstalk is evident from Eq. (9.2.5).

To study the impact of in-band crosstalk on system performance, we consider the photocurrent generated at the receiver. Similar to the case of ASE discussed in Section 6.4.1, the receiver current $I(t) = R_d|E_r(t)|^2$, where R_d is the responsivity of the photodetector, contains interference or beat terms, in addition to the desired signal. One can identify two types of beat terms; signal–crosstalk beating resulting in terms like $A_0^* A_n$ and crosstalk–crosstalk beating with terms like $A_k^* A_n$, where $k \neq 0$ and $n \neq 0$. The latter terms are relatively small in practice. If we ignore them, the receiver current is given by

$$I(t) \approx R_d P_0(t) + 2R_d \sum_{n=1}^{N} \sqrt{P_0(t) P_n(t)} \cos[\phi_0(t) - \phi_n(t)], \tag{9.2.6}$$

where $P_n = |A_n|^2$ is the power and $\phi_n(t)$ is the phase. In practice, $P_n \ll P_0$ because a WGR is built to reduce this kind of crosstalk.

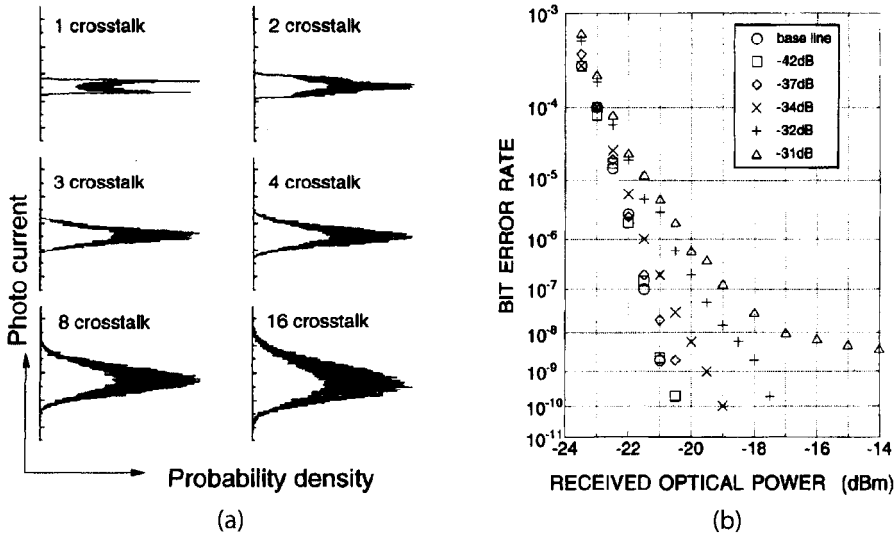

Figure 9.4: Measured (a) probability densities as a function of N and (b) BER curves for several values of X when $N = 16$. (After Ref. [21]; ©1996 IEEE.)

Since bit patterns in each channel change in an unknown fashion, and phases of all channels are likely to fluctuate randomly, each term in the sum in Eq. (9.2.6) acts as an independent random variable. We can thus write the photocurrent as $I(t) = R_d(P_0 + \Delta P)$ and treat the crosstalk as intensity noise. Even though each term in ΔP is not Gaussian, their sum follows a Gaussian distribution from the central limit theorem when N is relatively large. Indeed, the experimentally measured probability distributions shown in Figure 9.4(a) indicate that ΔP becomes a nearly Gaussian random variable for values N as small as 8 [21]. The BER curves in Figure 9.4(b) were measured in the case of $N = 16$ for several values of the crosstalk level, defined as $X = P_n/P_0$, with P_n being constant for all sources of in-band crosstalk. Considerable power penalty was observed for values of $X > -35$ dB.

We can use the approach of Section 5.4.2 for calculating the power penalty. In fact, the result is the same as in Eq. (5.4.11) and can be written as

$$\delta_X = -10 \log_{10}(1 - r_X^2 Q^2), \tag{9.2.7}$$

where

$$r_X^2 = \langle (\Delta P)^2 \rangle / P_0^2 = NX, \tag{9.2.8}$$

and X is assumed to be the same for all N sources of in-band crosstalk. An average over the phases in Eq. (9.2.6) was performed using $\langle \cos^2 \theta \rangle = \frac{1}{2}$. In addition, r_X^2 was multiplied by another factor of $\frac{1}{2}$ to account for the fact that P_n is zero on average half of the times (during 0 bits). The experimental data shown in Figure 9.4(b) agree well with this simple model when polarization effects are properly included [21].

The impact of in-band crosstalk can be estimated from Figure 9.5, where the crosstalk level X is plotted as a function of N to keep the power penalty less than a certain

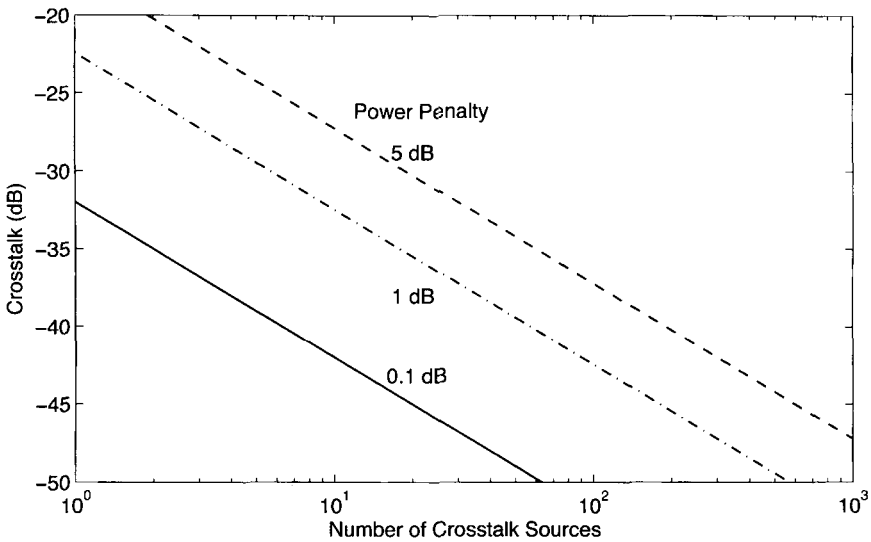

Figure 9.5: Crosstalk level X as a function of N for several values of power penalty induced by in-band crosstalk.

value, while maintaining a BER below 10^{-9} ($Q = 6$). To keep the penalty below 1 dB, $r_X < 0.1$ is required, a condition that limits XN to below -20 dB from Eq. (9.2.8). Thus, the crosstalk level X must be below -32 dB for $N = 16$ and below -40 dB for $N = 100$. Such requirements are relatively stringent for most routing devices. The situation is worse if the power penalty must be kept below 0.5 dB.

The expression (9.2.7) for the crosstalk-induced power penalty is based on the assumption that the power fluctuations ΔP induced by in-band crosstalk ΔP can be assumed to follow a Gaussian distributions. If the contribution of crosstalk–crosstalk beating terms in Eq. (9.2.5) is included, ΔP does not remain Gaussian. A more accurate calculation uses the moment-generating function for finding the BER under such conditions [33]. The results show that BER is degraded further when all beating terms are included and that the optimum value of decision threshold at the receiver is also affected.

The calculation of crosstalk penalty in the case of dynamic wavelength routing through optical cross-connects (see Section 9.4 of LT1) becomes quite complicated because of a large number of crosstalk elements that a signal can pass through in such WDM networks [22]. The worst-case analysis predicts a large power penalty (>3 dB) when the number of crosstalk elements becomes more than 25 even if the crosstalk level of each component is only -40 dB. The crosstalk also depends on the topology used for an optical cross-connect [28]. Clearly, the linear crosstalk has the potential of becoming a limiting factor in the design of WDM networks and should be controlled. A simple technique consists of scrambling the laser phase at the transmitter end at a frequency much larger than the laser linewidth [34]. Both theory and experiments show that the acceptable crosstalk level exceeds 1% (-20 dB) with this technique [30].

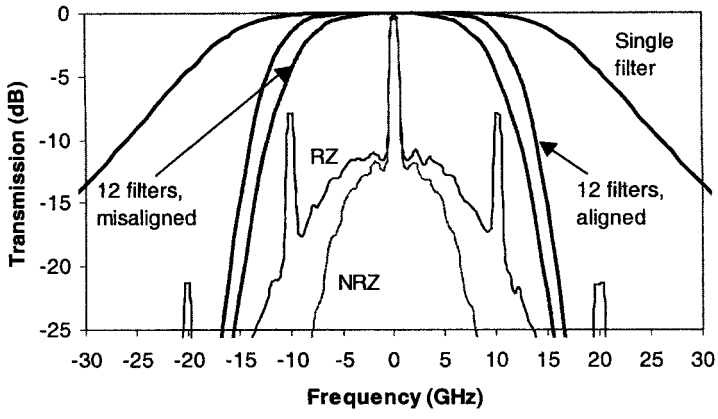

Figure 9.6: Transfer function of a single optical filter with 36-GHz bandwidth and changes produced by 12 cascaded filters aligned precisely or misaligned by ±5 GHz. The spectra of a 10-Gb/s signal are also shown for the RZ and NRZ formats. (After Ref. [16]; ©2003 IEEE.)

9.2.3 Filter-Induced Signal Distortion

So far we have considered linear crosstalk from a single device. In a realistic optical network, an optical signal may pass through many nodes before reaching its final destination, while suffering from crosstalk at each node. As a result, crosstalk can accumulate to a large level by the time signal reaches its destination. At the same time, signal may become distorted as it passes through many optical filters. In this section we address the filter-concatenation problem [35]–[37].

All filters in an optical network are designed to be wide enough to pass the signal spectrum without any distortion. However, if the signal passes through a large number of optical filters during its transmission, one must study the effects of filter concatenation. Consider a filter with the transfer function $H(\omega)$. Even when a signal passes through this filter twice, the effective filter bandwidth becomes narrower than the original value because $H^2(\omega)$ is a sharper function of frequency than $H(\omega)$. A cascade of many filters may narrow the effective bandwidth enough to produce clipping of the signal spectrum. This effect is shown schematically in Figure 9.6, where transmissivity of the signal is plotted after 12 third-order Butterworth filters of 36-GHz bandwidth. Since it may be difficult to align the passband of filters precisely at all locations, the response function is also shown when filters are misaligned within the range of ±5 GHz. Clearly, the effective transfer function after 12 filters is considerably narrower and its effective bandwidth is reduced further when individual filters are misaligned even by a relatively small amount.

To see how such bandwidth narrowing affects an optical signal, the spectrum of a 10-Gb/s signal is also shown in Figure 9.6 in the cases of the NRZ format and the RZ format with 50% duty cycle. Although the NRZ signal remains relatively unaffected, the RZ spectrum will be significantly clipped even after 12 filters, although the 36-GHz bandwidth of each filter exceeds the bit rate by a factor of 3.6. A second effect produced by optical filters is related to the phase of the transfer function. As discussed

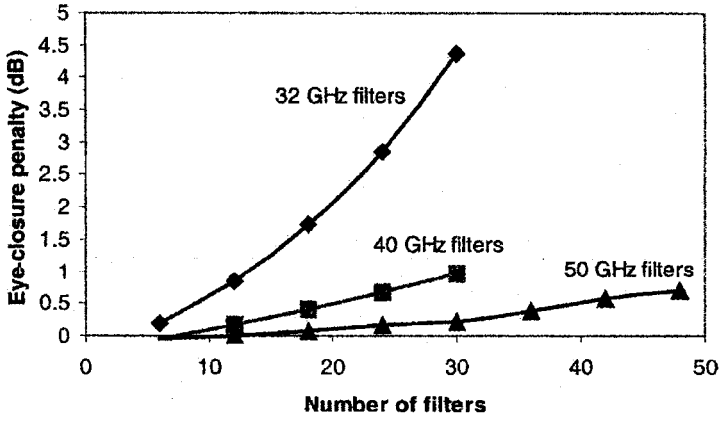

Figure 9.7: Eye-closure penalty as a function of the number of filters for a 10-Gb/s RZ signal with 50% duty cycle. The bandwidth of filters is varied in the range of 32 to 50 GHz. (After Ref. [16]; ©2003 IEEE.)

in Section 7.3, a frequency-dependent phase associated with the transfer function can produce a relatively large dispersion. The concatenation of many filters will enhance the total dispersion and may lead to considerable signal distortion [38].

The penalty induced by cascaded filters is quantified through the extent of eye closure at the receiver. Among other things, it depends on the shape and bandwidth of the filter passband. It also depends on whether the RZ or the NRZ format is employed for the signal and is generally larger for the RZ format. As an example, Figure 9.7 shows the increase in eye-closure penalty as the number of cascaded filters increases for a 10-Gb/s RZ signal with 50% duty cycle [16]. The transfer function of all filters corresponds to a third-order Butterworth filter. Although a negligible penalty occurs when the filter bandwidth is 50 GHz, it increases rapidly as the bandwidth is reduced below 40 GHz. The penalty exceeds 4 dB when the signal passes through 30 filters with 32-GHz bandwidth.

9.3 Nonlinear Crosstalk

Several nonlinear effects in optical fibers [39] lead to interchannel crosstalk and affect the performance of WDM systems considerably [40]–[44]. Among the nonlinear phenomena discussed in Chapter 4, the three most relevant for WDM systems are stimulated Raman scattering (SRS), four-wave mixing (FWM), and cross-phase modulation (XPM). This section focuses on SRS and FWM phenomena. The impact of XPM on WDM systems is discussed in the following section.

9.3.1 Raman Crosstalk

As discussed in Section 4.4, SRS is generally not of concern for single-channel systems because of its relatively high threshold (about 500 mW near 1.55 μm). The situation is

different for WDM systems because the transmission fiber can act as a Raman amplifier that is pumped by the multiwavelength signal launched into the fiber. Each channel is amplified by all shorter-wavelength channels as long as the wavelength difference is within the bandwidth of the Raman gain. The shortest-wavelength channel is most depleted as it can pump all other channels simultaneously. Variations in channel powers induced by Raman-induced interaction are one source of concern. However, this problem can be addressed in practice by adjusting the launch powers at the transmitter end or by employing a suitable optical filter at each amplifier.

Even of more concern is the fact that the power transfer between any two channels is time-dependent because it depends on the bit patterns of those channels. Clearly, amplification can occur only when 1 bits are present in both channels simultaneously and pulses inside them overlap, at least partially. As bit patterns are pseudo-random in nature, power transferred to each channel through SRS fluctuates and acts as a source of noise during the detection process. Such Raman-induced crosstalk can degrade the performance of a WDM system, if left uncontrolled, and its impact has been considered in several studies [45]–[57].

Raman crosstalk can be avoided if channel powers are made so small that SRS-induced amplification is negligible over the entire fiber length. It is thus important to estimate the limiting value of the channel power. A simple model considers the depletion of the highest-frequency channel in the worst case in which 1 bits of all channels overlap completely [40]. The amplification factor for the mth channel is $G_m = \exp(g_m L_{\text{eff}})$, where the Raman gain g_m and the effective interaction length L_{eff} are given by

$$g_m = g_R(\Omega_m)P_{\text{ch}}/A_{\text{eff}}, \qquad L_{\text{eff}} = [1-\exp(-\alpha L)]/\alpha, \tag{9.3.1}$$

with $\Omega_m = \omega_1 - \omega_m$. For $g_m L_{\text{eff}} \ll 1$, $G_m \approx 1 + g_m L_{\text{eff}}$, and the shortest-wavelength channel at ω_1 is depleted by a fraction $g_m L_{\text{eff}}$ owing to the amplification of the mth channel. The total depletion for an M-channel WDM system can be written as

$$D_R = \sum_{m=2}^{M} g_R(\Omega_m)P_{\text{ch}}L_{\text{eff}}/A_{\text{eff}}. \tag{9.3.2}$$

The summation in Eq. (9.3.2) can be carried out analytically if the Raman gain spectrum (see Figure 4.10) is approximated by a triangular profile such that g_R increases linearly for frequencies up to 15 THz with a slope $S_R = dg_R/d\nu$ and then drops to zero. Using $g_R(\Omega_m) = mS_R\Delta\nu_{\text{ch}}$, the fractional power loss for the shortest-wavelength channel becomes [40]

$$D_R = \tfrac{1}{2}M(M-1)C_R P_{\text{ch}}L_{\text{eff}}, \tag{9.3.3}$$

where $C_R = S_R\Delta\nu_{\text{ch}}/(2A_{\text{eff}})$. In deriving this equation, channels were assumed to have a constant spacing $\Delta\nu_{\text{ch}}$ and the Raman gain for each channel was reduced by a factor of 2 to account for the random polarization states of different channels.

A more accurate analysis should consider not only depletion of each channel because of power transfer to longer-wavelength channels but also its own amplification by shorter-wavelength channels. If all other nonlinear effects are neglected along with

GVD, the evolution of the power P_n associated with the nth channel is governed by the following equation (see Section 4.4.2):

$$\frac{dP_n}{dz} + \alpha P_n = C_R P_n \sum_{m=1}^{M} (n-m) P_m, \tag{9.3.4}$$

where α is assumed to be the same for all channels. This set of M coupled nonlinear equations can be solved analytically. For a fiber of length L, the result is given by [47]

$$P_n(L) = P_n(0) e^{-\alpha L} \frac{P_t \exp[(n-1) C_R P_t L_{\text{eff}}]}{\sum_{m=1}^{M} P_m(0) \exp[(m-1) C_R P_t L_{\text{eff}}]}, \tag{9.3.5}$$

where $P_t = \sum_{m=1}^{M} P_m(0)$ is the total input power in all channels. This equation shows that channel powers follow an exponential distribution because of Raman-induced coupling among all channels.

The depletion factor D_R for the shorter-wavelength channel ($n = 1$) is obtained using $D_R = (\bar{P}_1 - P_1)/\bar{P}_1$, where $\bar{P}_1 = P_1(0)\exp(-\alpha L)$ is the channel power expected in the absence of SRS. In the case of equal input powers in all channels, P_t equals MP_{ch} in Eq. (9.3.5), and D_R is given by

$$D_R = 1 - \exp\left[-\frac{1}{2} M(M-1) C_R P_{\text{ch}} L_{\text{eff}}\right] \frac{M \sinh(\frac{1}{2} M C_R P_{\text{ch}} L_{\text{eff}})}{\sinh(\frac{1}{2} M^2 C_R P_{\text{ch}} L_{\text{eff}})}. \tag{9.3.6}$$

In the limit $M^2 C_R P_{\text{ch}} L_{\text{eff}} \ll 1$, this complicated expression reduces to the simple result in Eq. (9.3.3). In general, Eq. (9.3.3) overestimates the Raman crosstalk.

The Raman-induced power penalty is obtained using $\delta_R = -10\log(1 - D_R)$ because the input channel power must be increased by a factor of $(1 - D_R)^{-1}$ to maintain the same system performance. Figure 9.8 shows how the power penalty increases with an increase in the channel power and the number of channels. The channel spacing is assumed to be 100 GHz. The slope of the Raman gain is estimated from the gain spectrum to be $S_R = 4.9 \times 10^{-18}$ m/(W-GHz) while $A_{\text{eff}} = 50\ \mu\text{m}^2$ and $L_{\text{eff}} \approx 1/\alpha = 21.74$ km. As seen from Figure 9.8, the power penalty becomes quite large for WDM systems with a large number of channels. If a value of at most 1 dB is considered acceptable, the limiting channel power P_{ch} exceeds 10 mW for 20 channels, but its value is reduced to below 1 mW when the number of WDM channels is larger than 70.

The foregoing analysis provides only a rough estimate of the Raman crosstalk as it neglects the fact that signals in each channel consist of a random sequence of 0 and 1 bits. It is intuitively clear that such pattern effects will reduce the level of Raman crosstalk. A statistical analysis shows that the Raman crosstalk is lower by about a factor of 2 when signal modulation is taken into account [46]. The GVD effects that were neglected in the above analysis also reduce the Raman crosstalk since pulses in different channels travel at different speeds because of the group-velocity mismatch [48]. Both the pattern and walk-off effects can be included if we replace Eq. (9.3.4) with

$$\frac{\partial P_n}{\partial z} + \frac{1}{v_{gn}} \frac{\partial P_n}{\partial t} + \alpha P_n = C_R P_n \sum_{m=1}^{M} (n-m) P_m, \tag{9.3.7}$$

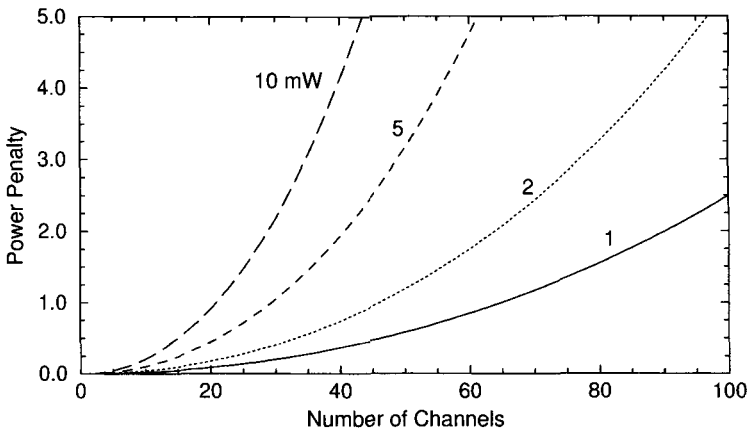

Figure 9.8: Raman-induced power penalty as a function of channel number for several values of P_{ch}. Channels are 100 GHz apart and are launched with equal powers.

where v_{gn} is the group velocity of the nth channel and $P_n(z,t)$ is the time-dependent channel power containing all pattern information.

The set of equations (9.3.7) is not easy to solve analytically. Consider, for simplicity, power transfer between two channels by setting $M = 2$. The resulting two equations can be written as

$$\frac{\partial P_1}{\partial z} + d_w \frac{\partial P_1}{\partial t} + \alpha P_1 = -C_R P_1 P_2, \tag{9.3.8}$$

$$\frac{\partial P_2}{\partial z} + \alpha P_2 = C_R P_1 P_2, \tag{9.3.9}$$

where $d_w = v_{g1}^{-1} - v_{g2}^{-1}$ is the walk-off parameter in a frame in which pulses for channel 2 are stationary [39]. If we neglect pump depletion, Eq. (9.3.8) has the solution $P_1(L,t) = P_1(0,t - d_w z)e^{-\alpha z}$. Using this solution in Eq. (9.3.9) and integrating over a fiber section of length L, we obtain $P_2(L,t) = P_2(0,t)\exp[x_2(t) - \alpha L]$, where

$$x_2(t) = C_R \int_0^L P_1(0,t - d_w z)e^{-\alpha z} dz \tag{9.3.10}$$

governs the extent of Raman-induced power transfer.

We can extend this approach for M interacting channels by adding contributions from all channels. Fluctuations in the power of the nth channel are then given by

$$x_n(t) = C_R \sum_{m=1}^{M} (n-m) \int_0^L P_m(0,t - d_{mn} z)e^{-\alpha z} dz, \tag{9.3.11}$$

where $d_{mn} = v_{gm}^{-1} - v_{gn}^{-1}$. Because of pseudo-random bit patterns in all channels, $x_n(t)$ fluctuates with time in a random fashion. When the number of channels is large, $x_n(t)$ represents a sum of many independent random variables and is expected to follow a

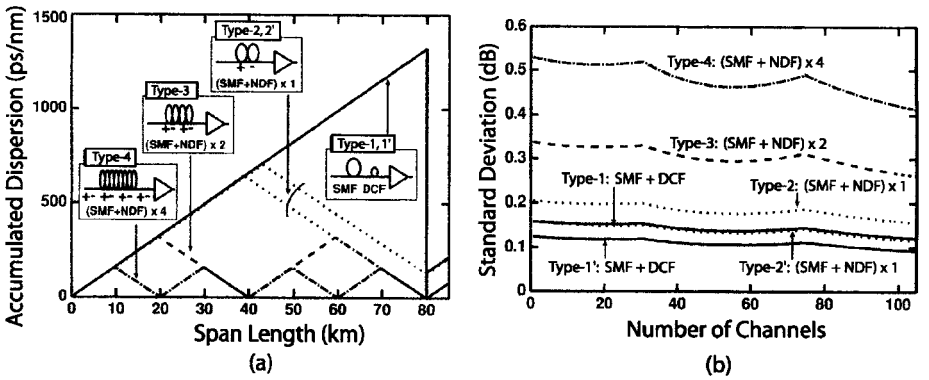

Figure 9.9: (a) Accumulated dispersion in one 80-km map period for four types of maps and (b) Raman crosstalk after 400 km for a WDM system whose 105 channels are separated by 200 GHz and launched with 6.3-mW power. (After Ref. [57]; ©2003 IEEE.)

Gaussian distribution from the central limit theorem. Since the channel power scales with $x_n(t)$ exponentially, it follows a log-normal distribution [51]. However, if powers are expressed in dBm units, channel power is related to x_n linearly, and its fluctuations obey a Gaussian distribution. From a practical standpoint, the first two moments of x_n are most relevant. The average value μ_x represents the Raman-induced change in the average power. If channel powers are equalized at each amplifier, the crosstalk is governed by the variance σ_x^2. The ratio σ_x/μ_x is often used as a measure of the Raman crosstalk. These quantities can be calculated in an analytic form in some cases [46].

The preceding discussion applies to a single fiber segment. For a realistic WDM system, one must consider dispersion management and add the contributions of multiple fiber segments separated by optical amplifiers [57]. In the case of distributed amplification, the WDM signal is amplified within the same fiber where the signal is degraded through SRS. The periodic power variations can be included by replacing the factor $e^{-\alpha z}$ in Eq. (9.3.11) with $p(z)$, introduced first in Section 3.2.2 and obtained by solving Eq. (3.2.6). The details of the dispersion map enter into Eq. (9.3.11) through the walk-off parameter d_m that takes on different values in each fiber segment used to form the dispersion map. In general, crosstalk depends on details of the dispersion map and is reduced considerably when the dispersion is not fully compensated in each map period.

Figure 9.9 shows calculated values of σ_x for a 105-channel (separated by 200 GHz) WDM system operating over a 400-km link with four types of dispersion maps. Each 40-Gb/s channel is launched with 6.3 mW of average power. Amplifiers are placed 80 km apart [57]. The type-1 map consists of a standard single-mode fiber (SMF) followed with a DCF. The maps of types 2 to 4 are designed using equal lengths of SMF and negative-dispersion fiber (NDF) but the map periods are 80, 40, and 20 km, respectively. For maps labeled type $1'$ and type $2'$, dispersion is not fully compensated (residual dispersion 130 ps/nm). The smallest crosstalk occurs for the type-1 map for which accumulated dispersion is high over most of the map period. It increases for the remaining three maps and becomes largest for the map with the shortest map

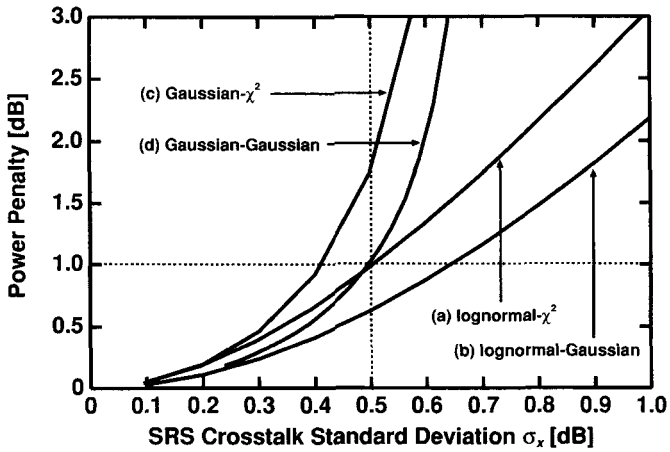

Figure 9.10: Power penalty as a function of Raman crosstalk in four cases in which ASE noise follows a χ^2 or Gaussian distribution and Raman-induced noise follows a log-normal or Gaussian distribution. (After Ref. [57]; ©2003 IEEE.)

period. Thus, dense dispersion management, although useful for several other reasons, makes the Raman crosstalk worse. This can be understood by noting that pulses in neighboring channels follow a zigzag path as they traverse from the SMF to the RDF section in a repetitive fashion. If the map period is small, two pulses that overlap initially never fully separate from each other. Clearly, Raman-induced power transfer is worst under such conditions. As seen in Figure 9.9, residual dispersion can be used to lower the level of Raman crosstalk.

Periodic amplification of the WDM signal can also magnify the impact of SRS-induced degradation. The reason is that in-line amplifiers add noise, which experiences less Raman loss than the signal itself, resulting in degradation of the SNR. Numerical simulations show that it can be reduced by inserting optical filters along the fiber link that block the low-frequency noise below the longest-wavelength channel [53]. Raman crosstalk can also be reduced using the technique of midspan spectral inversion [49].

How much Raman crosstalk can be tolerated in a WDM system? To answer this question, one must consider the BER at the receiver, assuming that the signal is corrupted both by amplified spontaneous emission (ASE) noise and Raman-induced noise. It should be kept in mind that the two noise sources may not follow the same statistics. The impact of ASE noise has been discussed in Section 6.4. If we assume that both noise sources are Gaussian in nature, one can simply add a third term $\sigma_{\rm SRS}^2$ to the definition of σ_1 in Eq. (6.4.3). A more precise treatment should follow the approach of Section 6.4.2 and employ the log-normal distribution associated with Raman crosstalk. In all cases, power penalty (increase in signal power required to maintain the same BER) can be calculated as a function of σ_x. Figure 9.10 shows this power penalty in four cases in which ASE noise follows a χ^2 or Gaussian distribution and Raman-induced noise follows a log-normal or Gaussian distribution [57]. The combination of log-normal with χ^2 distribution is the most accurate. It shows that the power penalty

can be kept below 1 dB for $\sigma_x < 0.5$ dB. One can use this condition to find the maximum distance over which a system can operate in the presence of Raman crosstalk. The answer depends on the dispersion map, the number of WDM channels, and the power launched into each channel. For type-1 and type-2 dispersion maps in Figure 9.9, the distance exceeds 5,000 km even for a 70-channel WDM system (40 Gb/s per channel) if the channel power is kept below 2 mW. Thus, the problem of Raman crosstalk can be solved to a large extent by designing the WDM system appropriately.

9.3.2 Four-Wave Mixing

FWM is considered the most dominant source of crosstalk in WDM systems, and its impact has been studied extensively [58]–[69]. As discussed in Section 4.3, FWM requires phase matching [39]. It becomes a major source of nonlinear crosstalk whenever the channel spacing and fiber dispersion are small enough to satisfy the phase-matching condition approximately [39]. This is the case when a dense WDM system operates close to the zero-dispersion wavelength of dispersion-shifted fibers with a channel spacing of 100 GHz or less.

The physical origin of FWM-induced crosstalk, and the resulting system degradation, can be understood by noting that FWM generates a new wave at the frequency $\omega_{ijk} = \omega_i + \omega_j - \omega_k$, whenever three waves at frequencies ω_i, ω_j, and ω_k copropagate inside the fiber. For an N-channel system, i, j, and k can vary from 1 to N, resulting in a large combination of new frequencies generated by FWM. In the case of equally spaced channels, the new frequencies coincide with the existing frequencies, leading to coherent in-band crosstalk. When channels are not equally spaced, most FWM components fall in between the channels and lead to incoherent out-of-band crosstalk. In both cases, system performance is degraded because power transferred to each channel through FWM acts as a noise source, but the coherent crosstalk degrades system performance much more severely.

A simple scheme for reducing the FWM-induced degradation consists of designing WDM systems with unequal channel spacings [41]. The main impact of FWM in this case is to reduce the channel power. This power depletion results in a power penalty that is relatively small compared with the case of equal channel spacings. Experimental measurements on WDM systems confirm the advantage of unequal channel spacings. In a 1999 experiment, this technique was used to transmit 22 channels, each operating at 10 Gb/s, over 320 km of dispersion-shifted fiber with 80-km amplifier spacing [64]. Channel spacings ranged from 125 to 275 GHz in the 1,532- to 1,562-nm wavelength region and were determined using a periodic allocation scheme [62]. The zero-dispersion wavelength of the fiber was close to 1,548 nm, resulting in near phase matching of many FWM components. Nonetheless, the system performed quite well with less than a 1.5-dB power penalty for all channels.

The use of a nonuniform channel spacing is not always practical because many WDM components, such as optical filters and waveguide grating routers, require equal channel spacings. A practical solution is offered by the periodic dispersion-management technique discussed in Section 7.1. In this scheme, fibers with normal and anomalous GVD are combined to form a dispersion map such that GVD is high locally all along the fiber link even though its average value is quite low. Efficiency of the FWM process

for a single type of fiber has been discussed in Section 4.3.1. The important question is how much this efficiency is reduced with the use of dispersion management.

The calculation of FWM-induced crosstalk is quite complicated in general because it requires adding coherently the amplitudes of all FWM components that fall within the bandwidth of a specific channel. The FWM process is also sensitive to the states of polarization of the four channels involved. In a simple model, all channels are assumed to remain copolarized. One can then use the analysis of Section 4.3.1 and extend it to the case of dispersion-managed fiber links [59]–[68]. For a periodic dispersion map consisting of two types of fibers and amplifiers placed at the end of all fiber sections, the field generated at a frequency $\omega_F = \omega_i + \omega_j - \omega_k$ through FWM is found by integrating Eq. (4.3.3) over all fiber sections. It depends on the channel powers and the map parameters as [61]

$$B_{jkl} = (d_f\gamma)^2 B_j B_k B_l^* \exp\left[-\tfrac{1}{2}(\alpha_1 L_1 + \alpha_2 L_2)\right] \times \left(\sum_{m=1}^{M} \exp(im\Delta\psi)\right) \left| \frac{1-e^{-\delta_1 L_1}}{\delta_1 L_1} + e^{-\delta_1 L_1} \frac{1-e^{-\delta_2 L_2}}{\delta_2 L_2} \right|^2, \qquad (9.3.12)$$

where $\delta_m = \alpha_m + i\Delta k_m$ ($m = 1,2$), the integers j, k, and l can vary from 1 to N for an N-channel WDM system. The degeneracy factor $d_f = 2$ for $j \neq k$ and 1 otherwise, $\Delta\psi = \Delta k_1 L_1 + \Delta k_2 L_2$ is the net phase shift after one map period, M is the number of map periods, and $\Delta k_m \equiv \beta_{2m}(2\pi\Delta\nu_{ch})^2$ ($m = 1,2$) represents the phase mismatch in the fiber section of length L_j with loss α_j and dispersion β_{2j}.

In general, one must sum B_{jkl} over all combinations of j, k, and l that contribute to a given channel. Consider the power in one such term. If we sum over m in Eq. (9.3.12), we find that $P_F \equiv |B_{jkl}|^2$ is proportional to $\sin^2(M\Delta\psi/2)/\sin^2(\Delta\psi/2)$ and is enhanced by a factor of M^2 whenever dispersion is fully compensated in each map period ($\Delta\psi = 0$). A simple solution to eliminate such a resonant enhancement of FWM is to leave some residual dispersion after each map period and use postcompensation at the end of the fiber link. Even in that case FWM can be enhanced, if the dispersion slope is not compensated, for those channels for which $\Delta\psi = 2\pi m$, where m is an integer. Such FWM resonances have been observed experimentally [63].

The crosstalk level for any channel is found by adding amplitudes B_{jkl} for all FWM components that fall within the channel bandwidth and comparing the resulting total power to the signal power in that channel. As an example, Figure 9.11 shows the FWM crosstalk calculated from Eq. (9.3.12) for a WDM system with 50-GHz channel spacing [68]. The dispersion map consists of seven spans of 70.5 km of dispersion-shifted fiber with $D = -2.4$ ps/(km-nm), followed with 70.5 km of standard fiber with $D = 16.8$ ps/(km-nm). The 1,128-km link consists of two such map periods. Multiple peaks seen in Figure 9.11 result from the FWM resonances. The peak heights are reduced significantly when the dispersion of each fiber section fluctuates around its average value with a standard deviation of 0.25 ps/(km-nm). Such fluctuations can occur for most practical fiber because of random variations in the core diameter of a fiber.

The preceding analysis is too simple to model an actual WDM system accurately. In practice, all channels carry optical pulses in the form of pseudo-random bit patterns.

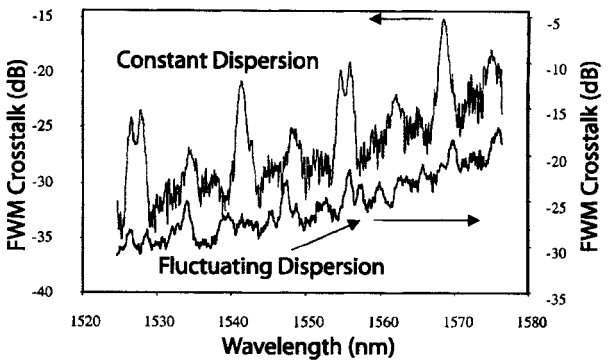

Figure 9.11: FWM crosstalk for a WDM system with 50-GHz channel spacing. FWM resonances are reduced considerably when the dispersion of each fiber section fluctuates around its average value. (After Ref. [68]; ©2002 IEEE.)

Moreover, pulses belonging to different channels travel at different speeds. FWM can occur only when all pulses participating in the FWM process overlap in time in a synchronous fashion. The net result is that the FWM contribution to any channel fluctuates in time and acts as a noise to that channel. In general, the noise level depends on details of dispersion management. Figure 9.12 shows the noisy bit patterns observed for the central channel of a 3-channel system (with a channel spacing of 1 nm) at the output of a 25-km-long fiber link with constant dispersion when each channel was launched with 3-mW average power. The noise level for 1 bits is quite large for low values of fiber dispersion but decreases significantly as $|D|$ increases to beyond 2 ps/(km-nm).

The random nature of the FWM crosstalk suggests that a statistical approach is more appropriate for estimating the impact of FWM on the performance of a WDM system. As early as 1994, it was suggested that this noise can be treated as being Gaussian in nature when the number of FWM terms contributing to a channel is large [59]. In a more realistic approach, the phase of each FWM term in Eq. (9.3.12) was assumed to be distributed uniformly in the 0 to 2π range, resulting in a bimodal distribution for the FWM noise [41]. In general, noise statistics depend on many factors [66]. The autocorrelation function of the FWM noise has also been calculated to show that different bit patterns in neighboring channels help to reduce the crosstalk level [69].

In summary, WDM systems designed with low-dispersion fibers suffer from FWM the most. The problem can be solved to a large extent with the use of dispersion management. Indeed, dispersion maps are used for all modern WDM systems for this reason. The FWM crosstalk is relatively small when the dispersion of each fiber section is large locally and FWM resonances are suppressed by matching the dispersion slope and avoiding full compensation over each map period. In fact, new kinds of fibers known as nonzero-dispersion-shifted fibers (NZDSFs) were designed and marketed after the advent of WDM systems. Typically, GVD is in the range of 4 to 8 ps/(km-nm) in such fibers to ensure that the FWM-induced crosstalk is minimized. FWM can still be a source of major concern in dense WDM systems in which each channel operates at 2.5 Gb/s, and the channel spacing is kept below 10 GHz [44].

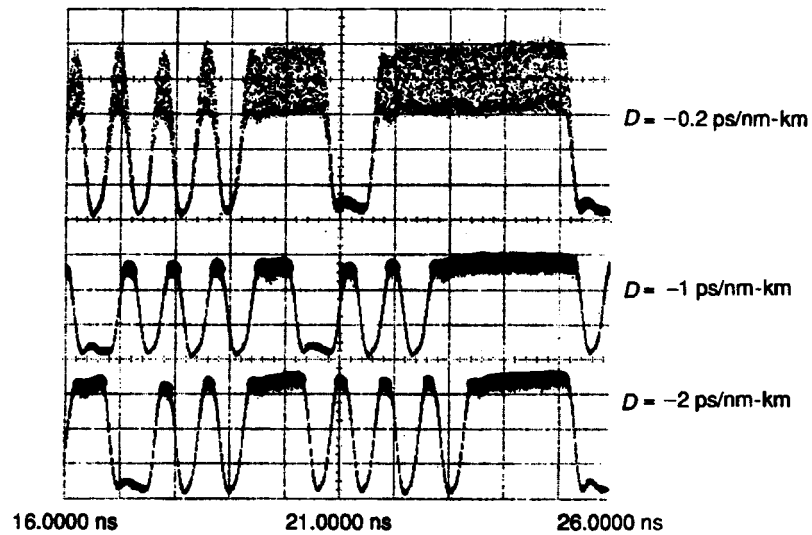

Figure 9.12: FWM-induced noise on the central channel at the output of a 25-km-long fiber when three 3-mW channels are launched with 1-nm spacing. (After Ref. [41]; ©1997 Elsevier.)

9.4 Cross-Phase Modulation

Both SPM and XPM affect the performance of WDM systems. The effects of SPM have been discussed in Sections 4.6 and 8.1 because, by definition, SPM represents an *intrachannel* nonlinear mechanism. In contrast, XPM is an important source of interchannel crosstalk in WDM lightwave systems, and its impact on the performance of WDM systems has been studied extensively [70]–[85]. Similar to the case of intrachannel XPM effects discussed in Section 8.4.2, XPM interaction among WDM channels leads to both amplitude fluctuations and timing jitter.

9.4.1 Amplitude Fluctuations

Consider the source of amplitude fluctuations first. As discussed in Section 4.2, XPM originates from the nonlinear nature of the refractive index, which produces a phase shift that depends on the bit patterns of neighboring channels. Strictly speaking, the XPM-induced phase shift should not affect system performance if the GVD effects were negligible. However, any dispersion in fiber converts pattern-dependent phase shifts to power fluctuations, reducing the SNR at the receiver. This conversion can be understood by noting that time-dependent phase changes lead to frequency chirping that affects dispersion-induced broadening of the signal. Such XPM-induced power fluctuations can become quite large for large values of dispersion parameter and channel powers. In a dispersion-managed system, they also depend on the dispersion map employed.

The pump-probe analysis developed in Sections 4.2.3 is often used to estimate the level of XPM-induced power fluctuations on a CW probe as it travels down the fiber

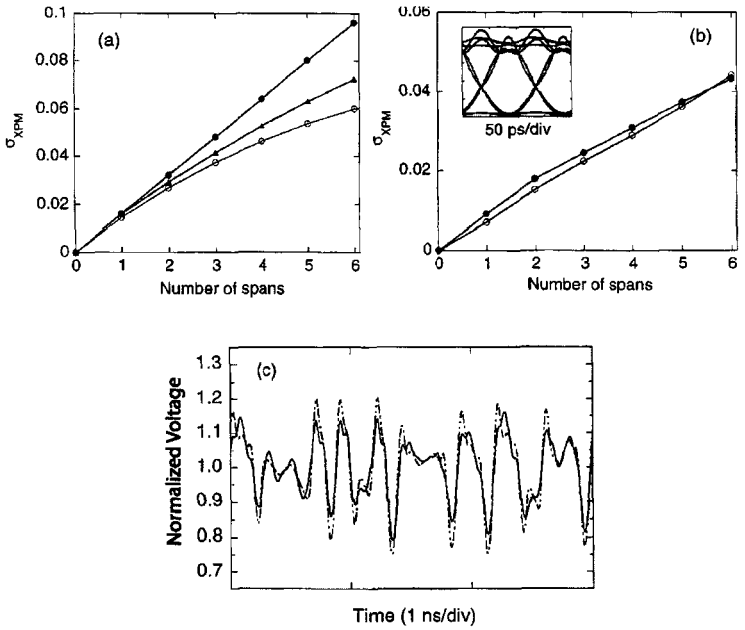

Figure 9.13: Standard deviation of XPM-induced probe fluctuations as a function of link length (each span is 60 km) when the DCF length in each span is (a) 12 km or (b) 10.8 km. (c) Probe fluctuations after 5 spans with an input level normalized to 1. (After Ref. [80]; ©2000 IEEE.)

link with a data channel acting as a pump at a different wavelength [70]–[73]. Figure 9.13(a) shows fluctuation level σ_{XPM} of a probe channel as a function of link length when it propagates with a 10-Gb/s channel separated by 50 GHz and launched with 10-mW power [80]. Each span consists of 60 km of standard fiber, followed with 12 km of DCF, resulting in zero dispersion on average. Symbols are used to compare the pump-probe approach (filled circles) with the numerical solutions obtained by solving the NLS equation (open circles). Clearly, the pump-probe approach provides an order-of-magnitude estimate as it ignores nonlinear distortion of the pump channel. The curve with triangles is obtained when pump distortions are taken into account. The level of pump distortion can be reduced if the DCF length is shortened to 10.8 km so that the average dispersion of the link is anomalous, and soliton effects become important. As seen in Figure 9.13(b), the pump-probe approach is then in better agreement with full numerical simulations. The inset shows the eye diagram for the pump channel after 6 spans. Temporal variations of the probe power (normalized to 1 at the input end) after five spans are displayed in part (c). Solid and dashed curves compare the solution of the NLS equation with the improved pump-probe approach. The important point is that the XPM generates power fluctuations that become larger than 20% after only 300 km. As a result, the SNR at the receiver end will be reduced considerably for all channels. Clearly, one must design a WDM system to minimize them.

The results of Figure 9.13 were obtained for a 50-GHz channel spacing. Because of the walk-off effects discussed in Section 4.2.3, XPM-induced power fluctuations

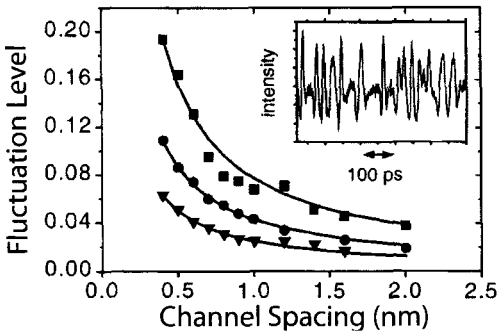

Figure 9.14: Measured standard deviation of probe fluctuations as a function of channel spacing with (circles) and without (squares) dispersion compensation. Triangles represent the data obtained under field conditions. Inset shows a temporal trace of probe fluctuations for $\Delta\lambda = 0.4$ nm. (After Ref. [78]; ©2000 IEEE.)

depend considerably on channel spacing and become less pronounced as it increases. The solid symbols in Figure 9.14 show the values of $\sigma_{\rm XPM}$ measured in an experiment in which channel spacing was varied from 0.4 to 2 nm [78]. The pump channel was launched with 20-mW power in all cases. Even though probe power was constant at the input end, it exhibited large variations (see the inset obtained for 0.4-nm channel spacing) after two spans, each consisting of 92 km of standard fiber and a DCF for dispersion compensation (circles). In the absence of DCF, probe fluctuations became larger (squares). The smallest values of $\sigma_{\rm XPM}$ were observed under actual field conditions. Numerical simulations provide only a qualitative agreement with the experimental data because of the influence of PMD on the XPM phenomenon and are consistent with a theory that incudes the PMD effects [84].

How much does the XPM-induced amplitude jitter affect system performance? In practice, a measure is provided either by the eye-closure penalty or by the power penalty induced by XPM effects for maintaining a specific BER. The impact of amplitude jitter can also be quantified through the degradation of the Q factor induced by the XPM. In a simple model, the Q factor, defined as $Q = (I_1 - I_0)/(\sigma_1 + \sigma_0)$, is calculated by replacing σ_1 with [80]

$$\sigma_1' = \sqrt{\sigma_1^2 + \sigma_{\rm XPM}^2}, \tag{9.4.1}$$

where $\sigma_{\rm XPM}$ is the value calculated with the pump-probe method [80]. The basic assumption is that XPM-induced amplitude fluctuations enhance the noise level of 1 bits (but leave the 0 bits relatively unaffected), and this noise can be added to other noise sources, assuming that it is governed by an independent Gaussian process. Such an approach works reasonably well when the WDM signal is in the the NRZ format. In the case of RZ format, one must include the impact of XPM-induced timing jitter, a topic we turn to next.

9.4.2 Timing Jitter

XPM interaction among neighboring channels can induce considerable timing jitter. The situation is somewhat different from the intrachannel case discussed in Section 8.4.2 where all pulses travel with the same speed and thus remain overlapped throughout the fiber. In contrast, pulses belonging to different channels travel at different speeds in a WDM system and walk through each other at a rate that depends on the wavelength difference of the two channels involved. Since XPM can occur only when pulses overlap in the time domain, one must include the walk-off effects in any study of interchannel XPM [86]–[96].

Physically, timing jitter is a consequence of the frequency shifts experienced by pulses in one channel as they overlap with pulses in other neighboring channels. Temporal overlapping of optical pulses in two neighboring channels is referred to as a collision. As a faster-moving pulse belonging to one channel collides with and passes through a pulse in another channel, the XPM-induced chirp shifts the pulse spectrum first toward the red side and then toward the blue side. In a lossless fiber, most collisions are perfectly symmetric, resulting in no net spectral shift, and hence no temporal shift, at the end of the collision.

In a loss-managed system with optical amplifiers placed periodically along the link, power variations make collisions between pulses of different channels asymmetric, resulting in a net frequency shift, and hence in a net temporal shift, that depends on the magnitude of channel spacing. Physically speaking, the speed of pulses belonging to a WDM channel depends on its carrier frequency, and any change in this frequency slows down or speeds up their speed, depending on the direction in which frequency changes. A constant temporal shift would be of little consequence if it were the same for all pulses. However, the XPM-induced shift in the pulse position is different for different pulses because it depends on the bit patterns and wavelengths of other channels, and thus manifests as a timing jitter at the receiver end. This timing jitter degrades the eye pattern, especially for closely spaced channels, and leads to an XPM-induced power penalty that depends on channel spacing and the type of fibers used for the WDM link. The power penalty increases for fibers with large GVD and for WDM systems designed with a small channel spacing and can become quite large when channel spacing is reduced to below 100 GHz. Such a restriction on channel spacing translates into a low spectral efficiency.

Mathematically, the effects of interchannel collisions on the performance of WDM systems can be best understood by considering the simplest case of two WDM channels separated by $\Omega_{\rm ch}$. Using the NLS equation (8.1.2) with

$$U = U_1 \exp(-i\Omega_{\rm ch} t/2) + U_2 \exp(+i\Omega_{\rm ch} t/2), \tag{9.4.2}$$

and neglecting the FWM terms, pulses in each channel are found to evolve according to the following two coupled equations:

$$i\frac{\partial U_1}{\partial z} - \frac{\delta}{2}\frac{\partial U_1}{\partial t} + \frac{\beta_2}{2}\frac{\partial^2 U_1}{\partial t^2} + \gamma P_0 p(z)(|U_1|^2 + 2|U_2|^2)U_1 = 0, \tag{9.4.3}$$

$$i\frac{\partial U_2}{\partial z} + \frac{\delta}{2}\frac{\partial U_2}{\partial t} + \frac{\beta_2}{2}\frac{\partial^2 U_2}{\partial t^2} + \gamma P_0 p(z)(|U_2|^2 + 2|U_1|^2)U_2 = 0, \tag{9.4.4}$$

where $\delta = |\beta_2|\Omega_{ch}$ is a measure of the mismatch between the group velocities of the two channels. In writing these equations, the common carrier frequency is chosen to be in the center of the two channels.

It is useful to define the *collision length* L_{coll} as the distance over which pulses in different channels remain overlapping during a collision before separating. It is difficult to determine precisely the instant at which a collision begins or ends. One convention uses $2T_s$ for the duration of the collision, where T_s is the full width at the half-maximum (FWHM) of each pulse, assuming that a collision begins and ends when two pulses overlap at their half-power points [86]. In another, the duration T_b of bit slot is used for this purpose. In the case of RZ format, the two conventions are related to each other because $T_s = T_b/2$ for a 50% duty cycle. Since δ is a measure of the relative speed of two pulses, the collision length can be written as

$$L_{coll} = \frac{T_b}{\delta} = \frac{T_b}{|\beta_2|\Omega_{ch}} = [B|\beta_2|(2\pi\Delta\nu_{ch})]^{-1}, \tag{9.4.5}$$

where B is the bit rate and $\Delta\nu_{ch}$ is the channel spacing. As an example, if we use $B = 10$ Gb/s and $|\beta_2| = 5$ ps^2/km, $L_{coll} \approx 32$ km for a channel spacing of 100 GHz and it reduces to below 8 km for a 40-Gb/s system. Even smaller values can occur if standard fibers are used with $|\beta_2| \approx 20$ ps^2/km. In contrast, L_{coll} can exceed 100 km when low-dispersion fibers are employed with a small channel spacing.

The last term in Eqs. (9.4.3) and (9.4.4) is due to XPM-induced coupling between two channels and is responsible for the temporal and frequency shifts during a collision. Similar to the analysis used in Section 8.4.2 for intrachannel XPM, we can employ the variational or the moment method to calculate these shifts [95]. In fact, details are similar to the intrachannel case, and the moment equations for the pulse parameters are almost identical to Eqs. (8.4.11) through (8.4.14). The only difference is that one needs to take into account the group-velocity mismatch between the two pulses. If we assume that pulses in two channel are identical in all respects, these equations take the form (after dropping the subscript on T and C)

$$\frac{dT}{dz} = \frac{\beta_2(z)C}{T}, \tag{9.4.6}$$

$$\frac{dC}{dz} = (1+C^2)\frac{\beta_2(z)}{T^2} + \frac{\gamma(z)p(z)E_0}{\sqrt{2\pi}T}\left[1-2(1-\mu^2)e^{-\mu^2/2}\right], \tag{9.4.7}$$

$$\frac{d\Delta\Omega}{dz} = \gamma(z)p(z)E_0\frac{8\mu}{\pi T^2}e^{-\mu^2/2}, \tag{9.4.8}$$

$$\frac{d\Delta t}{dz} = \beta_2(z)(\Omega_{ch}+\Delta\Omega), \tag{9.4.9}$$

where $\mu = \Delta t/T$. Notice that the temporal shift depends on the net frequency separation $\Omega_{ch} + \Delta\Omega$ between the two channels, where Ω_{ch} is the constant channel spacing and $\Delta\Omega$ is the XPM-induced frequency shift. Similarly, Δt represents net temporal spacing between two pulses and consists of two parts Δt_p and Δt_{XPM}. The first part represents the collision of two pulses because of a finite value of Ω_{ch}, while the second part is due to XPM-induced coupling between them.

The net XPM-induced frequency shift $\Delta\Omega$ can be calculated by integrating Eq. (9.4.8) over a distance longer than the collision length such that pulses are well separated before and after the collision. Using $z = z_c + \mu T/\delta$, where z_c is the location where pulses overlap completely (center of collision), the result can be written as

$$\Delta\Omega = \frac{8E_0}{\pi T \delta} \int_{-\infty}^{\infty} \gamma(z) p(z) \mu e^{-\mu^2/2} d\mu, \tag{9.4.10}$$

where we assumed that pulse width does not change significantly during a collision. The parameter $\mu \approx \Delta t_p/2T$ changes from negative to positive, becoming zero in the center of the collision where pulses overlap fully. Since the integrand is an odd function of μ when γ and p are z-independent, the integral in Eq. (9.4.10) vanishes in this case. This can happen if (1) a collision is complete entirely within one fiber section with constant γ and (2) distributed amplification is used such that $p \approx 1$. Under such conditions, two colliding pulses do not experience any temporal shift within their assigned bit slots.

Figure 9.15(a) shows how the frequency of the slow-moving pulse changes during the collision of two 50-ps solitons when channel spacing is 75 GHz. The frequency shifts up first as two pulses approach each other, reaches a peak value of about 0.6 GHz at the point of maximum overlap, and then decreases back to zero as two pulses separate. The maximum frequency shift depends on the channel spacing. It can be calculated by replacing the upper limit in Eq. (9.4.10) with 0. When $p = 1$ and γ is constant during a collision, it is given by

$$\Delta f_{\max} = \Delta\Omega_{\max}/(2\pi) = (\pi^{5/2}|\beta_2|\Delta\nu_{\text{ch}} L_{\text{NL}})^{-1}, \tag{9.4.11}$$

where $L_{\text{NL}} = (\gamma P_0)^{-1}$ is the nonlinear length and $\Delta\nu_{\text{ch}}$ is the channel spacing. One can follow the same procedure for the collision of two solitons with an amplitude of the form $\text{sech}(t/T_0)$ to find $\Delta f_{\max} = (3\pi^2 T_0^2 \Delta\nu_{\text{ch}})^{-1}$. For 40-Gb/s channels spaced 100 GHz apart, this maximum frequency shift can exceed 10 GHz.

Most interchannel collisions are rarely symmetric in WDM systems for a variety of reasons. When fiber losses are compensated periodically through lumped amplifiers, $p(z)$ is never an even function with respect to the center of collision. Physically, large peak-power variations occurring over a collision length destroy the symmetric nature of the collision. As a result, pulses suffer net frequency and temporal shifts after the collision is over. Equation (9.4.9) can be used to calculate the *residual* frequency shift for a given functional form of $p(z)$. Figure 9.15(b) shows the residual shift as a function of the ratio $L_{\text{coll}}/L_{\text{A}}$, where L_A is the amplifier spacing, in the case of solitons [86]. The residual frequency shift increases rapidly as L_{coll} approaches L_A and becomes $\sim$0.1 GHz. Such shifts are not acceptable in practice since they accumulate over multiple collisions and produce velocity changes large enough to move the pulse out of its assigned bit slot. When L_{coll} is so large that a collision lasts over several amplifier spacings, the effects of gain–loss variations begin to average out, and the residual frequency shift decreases. As seen in Figure 9.15(b), it virtually vanishes for $L_{\text{coll}} > 2L_A$ (safe region).

The preceding two-channel analysis focuses on a single collision of two pulses. Several other issues must be considered when calculating the timing jitter. First, neigh-

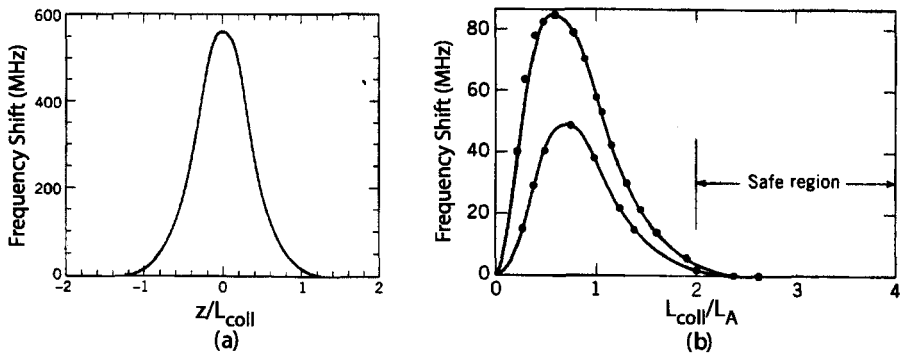

Figure 9.15: (a) Frequency shift during collision of two 50-ps solitons with 75-GHz channel spacing. (b) Residual frequency shift after a collision because of lumped amplifiers (L_A = 20 and 40 km for lower and upper curves, respectively). Numerical results are shown by solid dots. (After Ref. [86]; ©1991 IEEE.)

boring pulses in a given channel experience different number of collisons. This difference arises because adjacent pulses in a given channel interact with two different bit groups, shifted by one bit period. Since 1 and 0 bits occur in a random fashion, different pulses of the same channel are shifted by different amounts. Second, collisions involving more than two pulses can occur and should be considered. Third, a residual frequency shift always occurs when pulses in two different channels overlap at the input of the transmission link because their collisions are always incomplete (since the first half of the collision is absent). Such residual frequency shifts are generated only over the first few amplification stages but pertain over the whole transmission length and become an important source of timing jitter [87].

An entirely different situation is encountered in dispersion-managed systems where a collision may not be complete before the dispersion changes suddenly its nature at the end of a fiber section. As soon as the colliding pulses enter the fiber section with opposite dispersion characteristics, the pulse traveling faster begins to travel slower, and vice versa. Moreover, because of high values of local dispersion, the speed difference between two channels is relatively large. Also, the pulse width changes in each map period and can become quite large in some regions. The net result is that two colliding pulses move in a zigzag fashion and pass through each other many times before they separate from each other because of the much slower relative motion governed by the average value of GVD. Since the effective collision length becomes much larger than the map period (and the amplifier spacing), the condition $L_{\rm coll} > 2L_A$ is satisfied even when soliton wavelengths differ by 20 nm or more. This feature makes it possible to design WDM systems with a large number of channels.

The residual frequency shifts encountered in dispersion-managed systems depend on a large number of parameters, including map period, map strength, and amplifier spacing [90]–[96]. As before, residual frequency shifts occurring during complete collisions average out to zero. However, not all collisions are complete. For example, if pulses overlap initially, the incomplete nature of the collision will produce some resid-

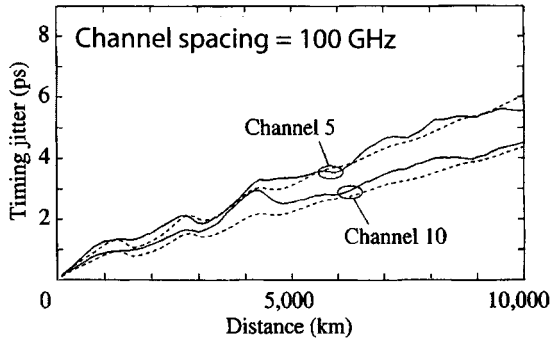

Figure 9.16: Growth of timing jitter in two channels as a function of distance for a 10-channel WDM system designed with a 100-km periodic dispersion map. Numerical (solid curves) and semianalytic (dashed curves) results are compared for 10-Gb/s channels spaced apart by 100 GHz. (After Ref. [96]; ©2000 IEEE.)

ual frequency shift. The zigzag motion of pulses can also produce frequency shifts if two pulses approach each other near the junction of opposite-dispersion fibers because they will reverse direction before crossing each other. Such partial collisions can result in large frequency shifts and thus produce a relatively large timing jitter. This situation can be avoided by optimizing the dispersion map used for a WDM system appropriately [95].

An accurate estimate of XPM-induced timing jitter for a WDM system requires numerical solutions of the NLS equation that become quite time-consuming as the number of channels increases. A semianalytic approach based on the moment method has been used with success [96]. It uses the optical field found numerically for a single pulse in each isolated channel (a relatively fast calculation) to calculate the timing jitter in all WDM channels by performing the average over random bit patterns in an analytic fashion. Figure 9.16 compares the results obtained using such an approach (dashed line) with those calculated using full numerical simulations (solid line) for a 10-channel dispersion-managed WDM system. All channels operate at 10 Gb/s and are spaced apart by 100 GHz. The dispersion map consists of a 95.6-km fiber with $D = 4$ ps/(km-nm) followed with 4.4 km of DCF with $D = -85$ ps/(km-nm). An amplifier is located in the middle of each fiber span. The peak power of each pulse representing 1 bit is taken to be 3.13 mW.

A noteworthy feature of Figure 9.16 is that timing jitter does not increase monotonically and exhibits periodic humps. The hump period is related to the distance over which pulses in two neighboring channels separate fully, after following a zigzag path, and is given by $L_h = T_b/(\bar{\beta}_2 \Delta\Omega_{\rm ch})$, where T_b is the duration of each bit slot and $\bar{\beta}_2$ is the avearage value of β_2. For the parameter values used for Figure 9.16, L_h is about 1,600 km. The other important feature of Figure 9.16 is that timing jitter is larger for the central channel compared with the first or last channel. This is easily understood by noting that pulses in the central channel collide with pulses in channels located on both sides and thus experience more jitter.

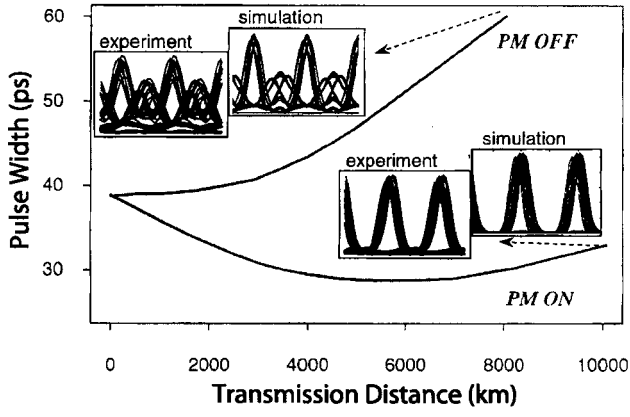

Figure 9.17: Evolution of pulse width along the link length in one channel of a 16-channel WDM system. Insets show the experimentally measured and numerically simulated eye diagrams at a distance marked by arrows. (After Ref. [99]; ©2000 IEEE.)

9.5 Control of Nonlinear Effects

Among the three nonlinear effects that create interchannel crosstalk and limit the performance of WDM systems, FWM and XPM constitute the dominant sources of power penalty. FWM can be reduced considerably with dispersion management. For this reason, modern WDM systems are often limited by the XPM effects, and one must design the system to minimize them as much as possible. In this section, we discuss several techniques that can be used for this purpose.

9.5.1 Optimization of Dispersion Maps

As discussed in Chapters 7 and 8, the performance of a single-channel lightwave system depends on details of the dispersion map (because of the nonlinear effects) and can be improved by optimizing the dispersion map. This is also the situation for WDM systems [97]–[106]. The parameters that can be adjusted are amount of precompensation, lengths and dispersions of each fiber section used to form the dispersion map, residual dispersion per map period, and the amount of postcompensation.

It has been observed in many system experiments that the use of precompensation helps to improve the performance of long-haul systems [99]–[101]. In fact, such a scheme is known as the CRZ format because precompensation using a piece of fiber is equivalent to chirping optical pulses representing 1 bits in a bit stream. As discussed in Section 7.6.1, a phase modulator can also be used to prechirp optical pulses. The reason behind the improved system performance with prechirping is partly related to the results of Section 3.3.1 where it was shown that a chirped Gaussian pulse undergoes a compression phase when it is chirped suitably.

Figure 9.17 shows how pulse width evolves with distance in one channel of a 16-chanel WDM system when a phase modulator is used to prechirp the pulses [99]. In this experiment, channels operated at 10 Gb/s with a channel spacing of 100 GHz and

a periodic dispersion map was employed with a small amount of residual anomalous dispersion per map period. As expected, the pulse width increases monotonically in the absence of phase modulation (PM) but is smaller than its input value even after 10,000 km when PM is employed to prechirp the pulse. The measured and simulated eye diagrams show clearly the improvement realized with the use of PM.

The amplitude and timing jitters induced by the XPM interaction among pulses of neighboring channels depend on the collision length L_{coll} introduced in Eq. (9.4.5). This length is below 10 km when standard fibers are used with $B = 10$ Gb/s and a 100-GHz channel spacing. The impact of XPM is reduced considerably for such systems because pulses pass over each other relatively rapidly. In contrast, when channel spacing is reduced to below 20 GHz, as is the case for ultradense WDM systems, and dispersion-shifted fibers with $|\beta_2|$ values < 10 ps^2/km are employed, L_{coll} exceeds 100 km, and XPM effects may be enhanced. The use of fibers with large dispersion helps to improve the performance of dense WDM systems [103].

An attractive scheme that is capable of cancelling the XPM-induced distortion for an arbitrary dispersion map makes use of midspan spectral inversion through optical phase conjugation [107]. The basic idea behind such a scheme has been discussed in Section 7.5 in the context of single-channel systems. The same scheme can also eliminate interchannel nonlinear effects. The reason can be understood by noting that the sign of dispersion parameters for all fiber sections is effectively inverted after the phase conjugator. When a phase conjugator is placed in the middle of the entire link, the dispersion map appears symmetric, and XPM effects nearly vanish. Another way to understand this process is to note that all XPM-induced frequency shifts introduced in the first half of the fiber link change sign and are cancelled in the second half. Figure 9.18 compares the numerically simulated eye patterns at a distance of 2,560 km for three channel spacings. Each NRZ-format channel of the 5-channel WDM system operates at 10 Gb/s and is launched with 1 mW of average power. Amplifiers are spaced 80 km apart. Each 80-km fiber section is made of standard fiber with $D = 16$ ps/(km-nm) and $\gamma = 1.2$ W^{-1}/km and its dispersion is fully compensated using DCFs. When a spectral inverter is placed after 16 spans at a distance of 1,280 km, the eye pattern is improved drastically because of the near cancellation of XPM-induced timing jitter. The predicted improvement in the Q factor exceeds 5 dB.

A simple approach to XPM suppression consists of introducing relative time delays among the WDM channels after each map period such that pulses in neighboring channels are unlikely to overlap most of the time [79]. The use of a RZ format is quite helpful in this context because pulses occupy only a fraction of the bit slot. In a 10-channel WDM experiment, time delays were introduced by using 10 fiber gratings spaced apart by varying distances chosen to enhance XPM suppression [81]. The BER floor observed after 500 km of transmission disappeared after the XPM suppressors (consisting of 10 Bragg gratings) were inserted every 100 km. The residual power penalty at a BER of 10^{-10} was below 2 dB for all channels.

Another design issue is related to whether the CRZ or the soliton format is employed. In both cases, optical pulses remain confined to their bit slots. The only difference is that the input launch conditions are adjusted in the soliton case such that all pulse parameters recover their input values after each map period in a periodic fashion, whereas no such condition is imposed in the CRZ case. Typically, pulses are shorter in

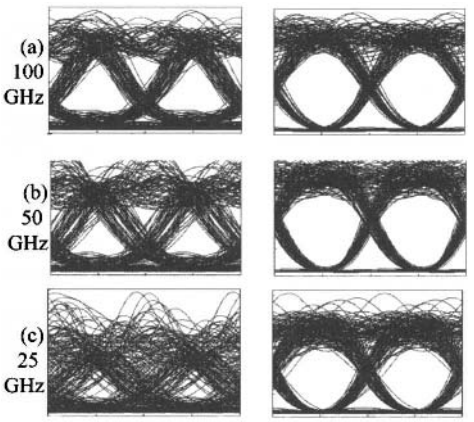

Figure 9.18: Numerically simulated eye patterns at a distance of 2,560 km for a channel spacing of (a) 100, (b) 50, and (c) 25 GHz obtained without (left column) and with (right column) a midspan spectral inverter. (After Ref. [107]; ©2004 IEEE.)

the soliton case and the map strength is relatively weak so that neighboring pulses in a given channel do not overlap significantly. However, collisions of pulses belonging to neighboring channels occur in both cases, and both types of WDM systems are affected by interchannel XPM. Indeed, it is sometimes argued that the soliton and CRZ formats have effectively merged as far as modern WDM systems are concerned [101].

Similar to the case of single-channel systems, sliding-frequency filters can reduce timing jitter in WDM soliton systems [108]. In practice, Fabry–Perot filters are used because their periodic transmission windows allow filtering of all channels simultaneously. For the best operation, mirror reflectivities are kept low (below 25%) to reduce the finesse. Such low-contrast filters remove less energy from pulses but are as effective as filters with higher contrast. The physical mechanism remains the same as for single-channel systems. More specifically, collision-induced frequency shifts are reduced because the filter forces the soliton frequency to move toward its transmission peak. Filtering can also relax the condition $L_{\text{coll}} > 2L_A$, allowing L_{coll} to approach L_A. The technique of synchronous modulation can also be applied to WDM systems for controlling the XPM-induced timing jitter.

As discussed in Section 8.3.3, the performance of a single-channel soliton system can be improved by using a dense dispersion map for which the map period L_{map} is a fraction of the amplifier spacing such that $L_A = mL_{\text{map}}$, where m is an integer. The same conclusion should hold for CRZ systems. Indeed, in a 2002 experiment in which 32 channels, each operating at 40 Gb/s, were transmitted over a distance of 3000 km, it was observed that system performance improved for $m = 2$ with $L_A = 50$ km [104]. Two fibers used to form the periodic map had dispersion of 20 and -63 ps/(km-nm). The launch power was optimized to maximize the Q factor at the receiver. Figure 9.19 shows the measured Q factors for all channels together with the eye patterns for 3 channels. Even the lowest value of 11.9 dB is large enough that this system can operate with a BER below 10^{-9} after forward error correction. Interestingly, it was

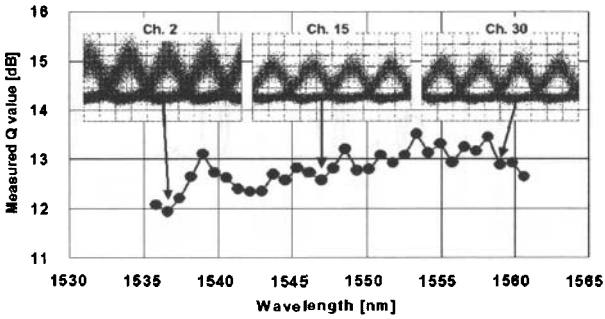

Figure 9.19: Measured Q factors after 3,000 km for 32 channels spaced 100 GHz apart. Insets show the eye patterns for three channels marked by arrows. (After Ref. [104]; ©2002 IEEE.)

observed in this experiment that the performance of the WDM system became worse for $m = 4$, even though this choice improved performance when only a single-channel was transmitted. We can thus conclude that the interchannel XPM effects are enhanced when the map period becomes too small. This behavior can be understood by noting that when the map period becomes smaller than the collision length, dispersion changes sign on such a short length scale, and the relative motion of two colliding pulses follows such a zigzag path, that the XPM-induced timing jitter is likely to be enhanced.

As discussed in Section 8.4, the pseudo-linear configuration, in which the map strength is made so large that optical pulses spread over multiple bits all along the link, is often useful at high bit rates for suppressing the intrachannel XPM effects. It turns out that this configuration also helps to suppress the interchannel XPM effects. The reason is that, as pulses in each channel spread over multiple bit slots, the total power P_t in all channels that produce XPM-induced phase shift on a specific channel becomes nearly constant. As a result, frequency shifts (related to the time derivative dP_t/dt) become negligible, and timing jitter is considerably reduced.

The pseudo-linear approach is most suitable for WDM systems in which the bit rate of each channel is relatively large (40 Gb/s or more) and RZ-format pulses shorter than 10 ps are employed. In one 1999 experiment, two 40-Gb/s channels were transmitted over 800 km of standard fiber using 2.5-ps pulses [109]. In this experiment, the entire dispersion accumulated over 800 km was compensated at the receiver end. However, the interchannel XPM effects played a relatively minor role since the channels were separated by 400 GHz, a relatively large channel spacing. In another 1999 experiment, four 40-Gb/s channels were transmitted with 250-GHz spacing using 4-ps pulses. Several other experiments have employed the pseudo-linear design for transmitting multiple 160-Gb/s channels. In a 3-Tb/s WDM experiment, 19 channels, each operating at 160 Gb/s, were transmitted over 40 km with 480-GHz spacing among channels [111]. In a 2001 experiment, several 160-Gb/s channels were transmitted over 400 km using a channel spacing of only 300 GHz [112]. More recently, four 160-Gb/s were transmitted over 225 km with 75-km amplifier spacing. The channel spacing was 400 GHz in this experiment, and the measured Q^2 values for all four channels were close to 15 dB.

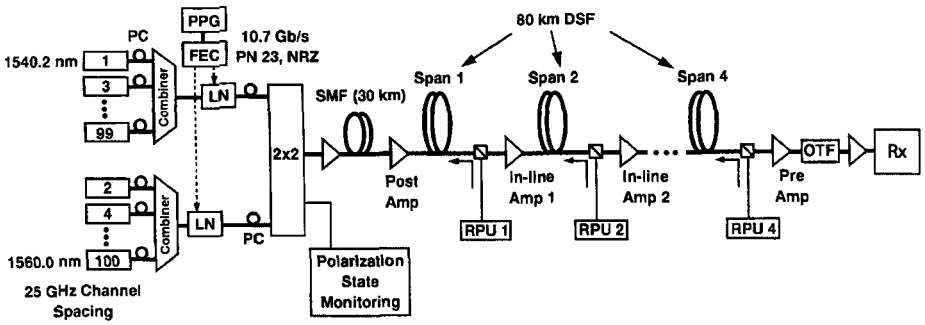

Figure 9.20: Schematic of experimental setup used to transmit 100 channels over 320 km with 25-GHz channel spacing. A Raman-pumping unit (RPU) compensates fiber losses every 80 km. FEC: forward error correction; LN: lithium niobate modulator, PC: polarization controller; OTF: optical tunable filter; Rx: optical receiver. (After Ref. [114]; ©2000 IEEE.)

9.5.2 Use of Raman Amplification

The nonlinear effects can also be controlled to some extent by using a distributed amplification scheme. This issue has been discussed in Section 6.6 in the context of single-channel systems. As was seen there, the use of Raman amplification allows one to obtain the same value of the Q factor at much lower values of the launch powers by lowering the level of accumulated noise. As one may expect, a lower launch power also helps in reducing the interchannel XPM effects in WDM systems. Indeed, the use of Raman amplification has become quite common for modern WDM systems [114]–[119].

There is a second reason why Raman amplification may help in reducing the XPM-induced timing jitter. Its use helps to make peak-power variations along the link much less drastic than those occurring when lumped amplifiers are used. As a result, the function $p(z)$ appearing in Eq. (9.4.10) becomes nearly constant and can be pulled out of the integral. If the collision of two pulses belonging to neighboring channels is complete in a fiber section with constant values of the dispersion and nonlinear parameter, the XPM-induced frequency shift vanishes, and no temporal shift is produced by such collisions.

Several experiments have shown that distributed Raman amplification can be used to transmit a large number of channels with a relatively small channel spacing. Such systems are referred to as superdense or ultradense WDM systems. In a 2000 experiment, 100 channels, each operating at 10 Gb/s and spaced by only 25 GHz from the neighboring channels, were transmitted over 320 km of dispersion-shifted fiber [114]. Figure 9.20 shows the experimental setup schematically. Link losses were compensated every 80 km through distributed Raman amplification using a backward pumping configuration. It was necessary to employ the technique of forward error correction (FEC) to ensure a BER of $<10^{-9}$. Because of a 25-GHz channel spacing, the entire WDM signal could fit in the wavelength range of 1,540 to 1,560 nm. The zero-dispersion wavelength of the dispersion-shifted fiber was near 1,550 nm, indicating that the dispersion was relatively low for all channels. Indeed, it was not necessary to

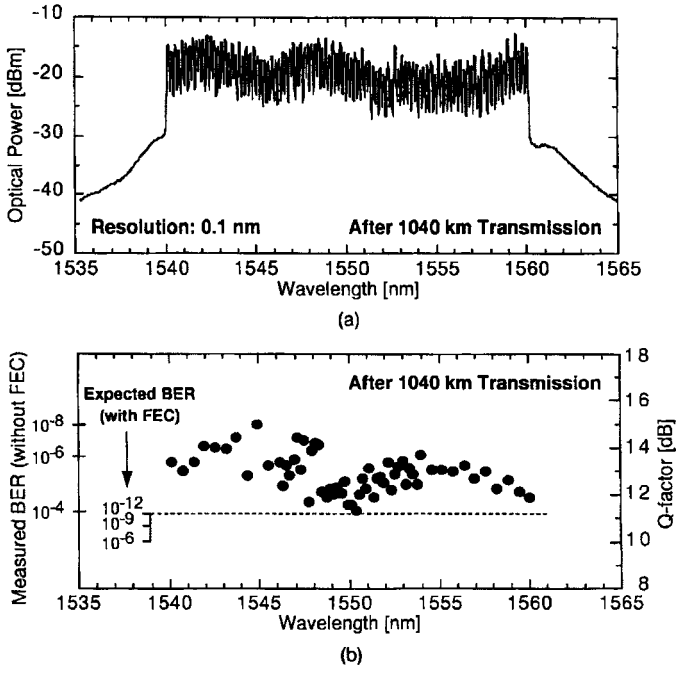

Figure 9.21: (a) Optical spectrum and (b) measured Q factors after 320 km for the 100-channel WDM system. The dotted line shows the Q value required to maintain a BER below 10^{-12} with FEC. (After Ref. [114]; ©2000 IEEE.)

compensate dispersion over the 320-km length.

The reason why the 100-channel system was not limited by interchannel crosstalk in spite of its 25-GHz channel spacing is related to a relatively low input power (only -16 dBm/channel) that was launched into the fiber link. The use of Raman amplification lowered the noise level enough that the system could be operated at such low input power levels without much penalty from the intrachannel as well as interchannel nonlinear effects. Indeed, the system performance after 320 km was limited by accumulated noise rather than the nonlinear effects. The transmission distance could be increased to beyond 1,000 km by employing the bidirectional pumping scheme that is known to lower the noise level even further. Figure 9.21 shows the optical spectrum recorded after 1,040 km together with the the BER and the Q factors (without FEC) measured as a function of channel wavelength [114]. The power launched into each channel was -18 dBm. In the absence of FEC, the BER varied in the range of 10^{-4} to 10^{-8}. However, the BER for all channels could be reduced to below 10^{-12} with the use of FEC. In a similar experiment, 100 channels with 25-GHz spacing were transmitted in the L band using a wavelength range of 1,570.9 to 1,591.6 nm [115]. A distinct advantage of the Raman amplification is that link losses can be compensated in the S, C, or L band by simply changing the pump wavelengths.

The performance of Raman-amplified WDM systems has improved considerably

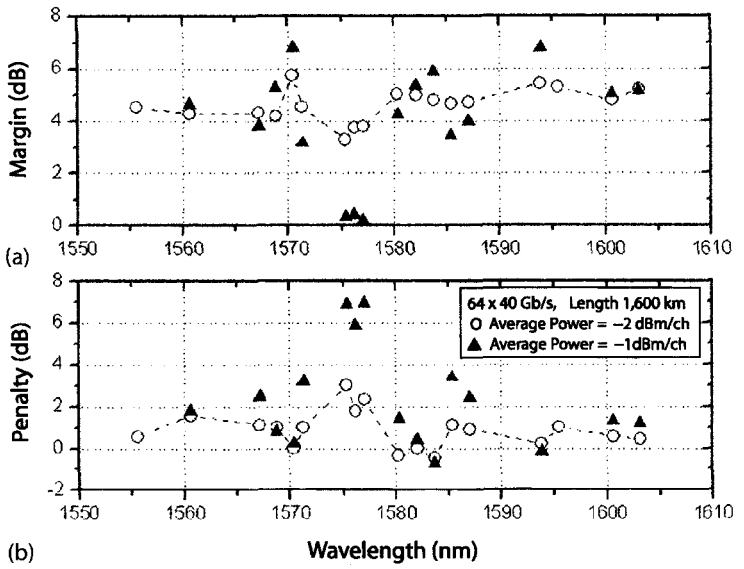

Figure 9.22: Measured (a) system margin and (b) power penalties after 1,600 km as a function of channel wavelengths for two values of launched power/channel for a 64-channel WDM system with 2.56-Tb/s capacity. (After Ref. [118]; ©2004 IEEE.)

in recent years [118]. In a 2001 experiment, 128 channels, each operating at 10 Gb/s, were transmitted over 4,000 km of reduced-slope dispersion-shifted fiber (RS-DSF) using a 100-km-long recirculating loop. An average power of −5 dBm was launched into each channel. The channel spacing was 50 GHz in this experiment. Even when standard fibers with a relatively large dispersion were employed, the WDM system could be operated over 3,200 km. Such performance is difficult to realize with lumped amplifiers. Several experiments have used Raman amplification for WDM systems in which each channel operates at 40 Gb/s. In one 64-channel experiment, the WDM signal with a capacity of 2.56 Tb/s could be transmitted over 1,600 km of RS-DSF. It was necessary to optimize the launch power as the system performance degraded considerably when power was increased from −2 to −1 dBm. Figure 9.22 shows the system margin and the penalty measured as a function of channel wavelength at these two power levels. The system margin is defined as the difference between the received and required optical SNR (both measured on a dB scale). The penalty is defined as the increase in required optical SNR compared with the value needed in the absence of fiber link (both measured on a dB scale). The penalty is below 3 dB for all channels at a power level of −2 dBm/channel but increases to beyond 6 dB for some channels when this power is increased by 1 dB.

9.5.3 Polarization Interleaving of Channels

As discussed in Section 8.5.3, the impact of intrachannel nonlinear effects can be reduced considerably by ensuring that the neighboring bits in a channel are orthogonally

polarized. The same idea can be extended to the case of interchannel nonlinearities by designing WDM systems such that the bit streams in two neighboring channels are orthogonally polarized [120]–[123]. Such a scheme is relatively easy to implement in practice. Figure 9.20 shows the experimental setup used typically for this purpose. The even and odd number channels are multiplexed together into two separate branches, whose states of polarization (SOPs) are adjusted using polarization controllers such that they are orthogonal. A polarization beam combiner or a device known as the channel polarization interleaver is then used to create a WDM signals whose neighboring channels are orthogonally polarized.

Why should polarization interleaving help in reducing the impact of interchannel nonlinear effects? The reason is that both XPM and FWM depend on the SOPs of the interacting channels. When two pulses in neighboring channels collide and interact through XPM, the phase, frequency, and temporal shifts induced by such a collision depend on the relative SOPs of the two channels. More precisely, the factor of 2 appearing in the last term in Eqs. (9.4.3) and (9.4.4) is replaced with 2/3, when the channels are orthogonally polarized [39]. As a result, interchannel collisions should produce smaller phase shifts and lead to much less amplitude and timing jitters.

Before reaching this conclusion, however, one should address the impact of polarization-mode dispersion (PMD) on channel polarizations [124]–[127]. As discussed in Section 3.4, PMD results from fluctuating residual birefringence inherent in all fibers used for designing lightwave systems. Its main effect is to change the SOP of each channel in a random fashion. If the two channels change their SOPs in a random fashion but remain nearly orthogonal, the technique of polarization interleaving can still be beneficial. In the language of Section 3.4, the Stokes vector of each channel would move in a random fashion on the Poincaré sphere but the Stokes vectors associated with two neighboring channels would remain antiparallel to each other.

The important question is over what lengths neighboring channels can maintain orthogonal SOPs in spite of birefringence fluctuations. As discussed in Section 3.4, the frequency dependence of the Stokes vector is governed by Eq. (3.4.27) and depends on the PMD vector. The length over which the relative SOP of neighboring channels can change significantly is known as the diffusion length L_{diff}. It depends on the PMD parameter of the fiber D_p and the channel spacing Ω_{ch} through the relation $L_{\text{diff}} = (D_p \Omega_{\text{ch}})^{-2}$. This length can vary over a wide range (<100 to >5,000 km) depending on the values of D_p and Ω_{ch}. For two channels spaced 50 GHz apart L_{diff} is about 1,000 km, if we use $D_p = 0.1$ ps/km$^{1/2}$ as a typical value for the PMD parameter. This estimate suggests that the polarization-interleaving technique is appropriate for suppressing interchannel nonlinear effects in WDM systems when fibers with relatively low values of D_p are employed and channel spacing is less than 100 GHz.

Figure 9.23 shows the results of numerical simulations for a 9,000-km dispersion-managed WDM system [122]. The 45-km-long dispersion map employs 28.5-km and 16.5-km sections with dispersions of 20 and −40 ps/(km-nm), respectively, and its residual dispersion is compensated every 500 km. Each 10-Gb/s channel carries an RZ bit stream with 33% duty cycle at an effective bit rate of 12.3 Gb/s because of FEC coding. Channel spacing is varied in the range of 25 to 50 GHz, and the PMD parameter of the fiber has a value of $D_p = 0.06$ ps/km$^{1/2}$. The Q factors were calculated numerically

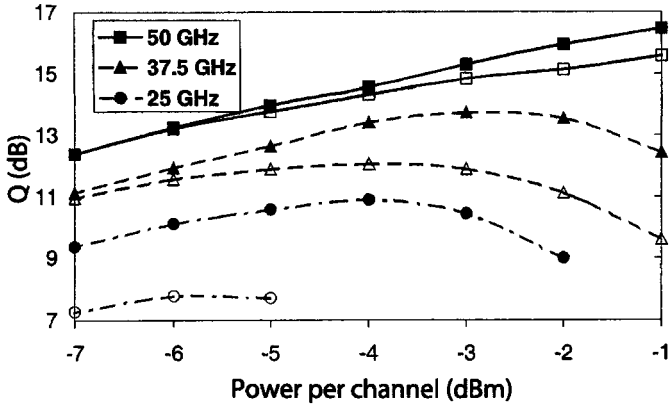

Figure 9.23: Q factors after 9,000 km as a function of launched power for three values of channel spacings when neighboring channels are copolarized (empty symbols) or orthogonally polarized (filled symbols) for a PMD parameter $D_p = 0.06$ ps/km$^{1/2}$. (After Ref. [122]; ©2002 IEEE.)

for several input power levels when neighboring channels were either copolarized or orthogonally polarized. A comparison of Q factors in the two cases, plotted as a function of launched power/channel for three channel spacings in Figure 9.23, shows that the use of polarization interleaving can improve the Q factor by more than 2 dB for a 25-GHz channel spacing but this advantage almost disappears when channel spacing is 50 GHz. The experiments performed over a distance of 6,500 km with 25-GHz channel spacing showed an improvement of more than 1 dB with the use of polarization interleaving [122].

It should be stressed that the use of polarization interleaving cannot eliminate the XPM-induced timing jitter completely. As an example, Figure 9.24 shows the frequency and temporal shifts calculated numerically for the middle channel, surrounded by four channels on each side, when channel spacing is 75 GHz [93]. Curve 1 shows that each pulse shifts by 100 ps (one bit slot) over 10,000 km because of XPM-induced frequency shift. The use of polarization interleaving (curve 2) improves the situation, but does not solve the problem. However, if sliding-frequency filters are employed, the temporal shift is reduced to below 15 ps for copolarized (curve 3) and to below 10 ps for orthogonally polarized channels (curve 4). In these numerical simulations, the map period and amplifier spacing were equal to 40 km. The dispersion map consisted of 36 km of anomalous-GVD fiber and 4 km of DCF such that the average value of dispersion was 0.1 ps/(km-nm), and the WDM system operated in the soliton regime.

9.5.4 Use of DPSK Format

Similar to the case of phase-alternation technique discussed in Section 8.5.2 for suppressing the intrachannel nonlinear effects, one may ask whether pulse phases can be adjusted to reduce the interchannel nonlinear effects. The answer turns out to be yes. The modulation format that has proved quite successful in this respect is the RZ-DPSK

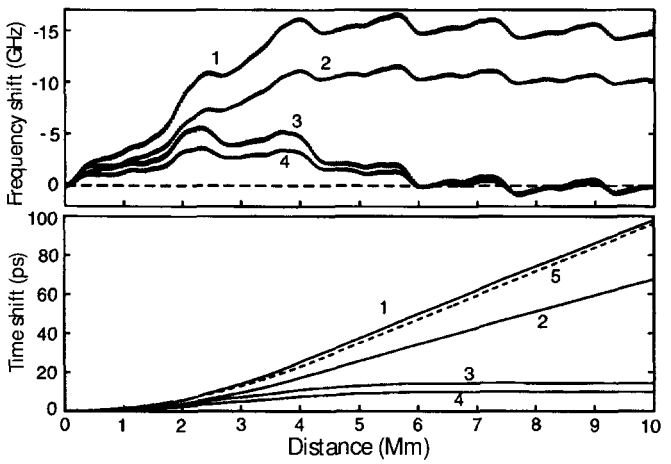

Figure 9.24: Collision-induced frequency and temporal shifts for a pulse in a channel surrounded by four channels with 75-GHz spacing on each side. Curves 1 and 2 represent the cases of copolarized and orthogonally polarized channels, respectively. Curves 3 and 4 show the improvement realized with sliding-frequency filters. The dashed line shows the prediction of an analytical model. (After Ref. [93]); ©1999 OSA.)

format (see Section 2.3.4) in which an optical pulse is present in all bit slots and the information is encoded in the phase of these pulses through DPSK [128]–[132]. Figure 9.25 shows schematically how the field amplitude and optical power vary with time for a DPSK-coded channel in which the phase of pulses is shifted by π whenever a bit transition occurs.

It is easy to understand qualitatively why XPM-induced penalties are reduced for systems designed with the RZ-DPSK format. The main reason why interchannel XPM leads to the amplitude and timing jitter is related to the randomness of bit patterns in two neighboring channels. It is easy to see that the XPM will be totally harmless if channel powers were constant in time because all XPM-induced phase shifts will be time-independent, producing no frequency and temporal shifts. However, this is not the case for the RZ-DPSK systems because, even though information is coded through phase shifts, an optical pulse is present in all bit slots. As seen in Figure 9.25, channel powers vary in a periodic fashion under such conditions. Nevertheless, the XPM effects are considerably reduced because all bits experience the same bit patterns in the neighboring channels and undergo nearly identical collision histories, especially if the average channel power does not vary too much along the link. Since all bits are shifted in time by nearly the same amount, little timing jitter is induced by interchannel collisions.

For a more quantitative analysis, we should include the walk-off effects through Eqs. (9.4.3) and (9.4.4) since pulses in two channels travel at different speeds. If we ignore pulse broadening induced by GVD in these equations, the XPM-induced phase

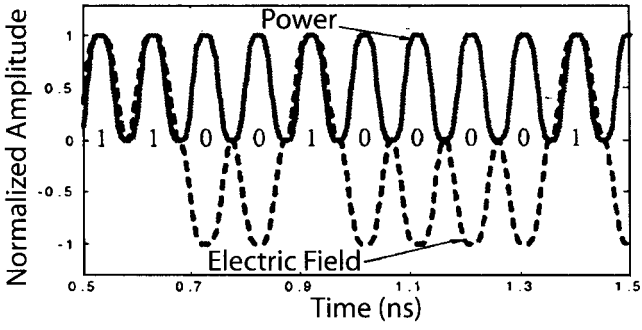

Figure 9.25: Temporal variations of the electric field and optical power for a 10-Gb/s channel coded using the RZ-DPSK format. (After Ref. [129]; ©2002 IEEE.)

shift on a pulse in channel 1 depends on power variations in channel 2 as

$$\phi_{\rm XPM}(t) = 2\gamma \int_0^L p(z) P_2(t + \delta z)\, dz, \tag{9.5.1}$$

where $P_2(t) = P_0 |U(0,t|^2$ governs power variations in channel 2 and $\delta = |\beta_2|\Omega_{\rm ch}$ depends on the channel spacing. If lumped amplifiers are used to compensate for fiber losses, $p(z) = \exp(-\alpha z)$ in each fiber section between two amplifiers. By taking the Fourier transform of Eq. (9.5.1), we obtain [129]

$$\tilde{\phi}_{\rm XPM}(\omega) = 2\gamma \tilde{P}_2(\omega) \int_0^L \exp[-(\alpha + i\omega\delta)z]\, dz \approx \frac{2N_A \gamma \tilde{P}_2(\omega)}{\alpha + i\omega\delta}, \tag{9.5.2}$$

where we used $L = N_A L_A$ and assumed that the link is made of N_A amplifiers spaced apart by L_A such that $\alpha L_A \gg 1$.

Equation (9.5.2) shows that the fiber link acts as a low-pass filter of bandwidth $f_b = \alpha/(2\pi|\beta_2|\Omega_{\rm ch})$ as far as the transfer of power variations into phase variations is concerned [129]. Using typical parameter values for a WDM system designed with standard fibers, $\alpha = 0.2$ dB/km, $D = 17$ ps/(km-nm), and 100-GHz channel spacing, this frequency is found to be around 540 MHz, a value much smaller than typical channel bit rates. Since the spectrum $\tilde{P}_2(\omega)$ of a periodic pulse train consists of discrete frequency components separated by the bit rate B, only the zero-frequency (dc) component is passed by the low-pass filter. As a result, the XPM-induced phase shift is nearly constant in time even for RZ pulses, and no frequency and temporal shifts occur during interchannel collisions.

Numerical simulations performed for an eight-channel WDM system confirm this simple analysis [129]. Figure 9.26 compares the calculated eye-opening penalty for the fourth channel in the case of standard RZ-ASK and RZ-DPSK formats, when channels operate at 10 Gb/s and are spaced 100 GHz apart. Each span between two amplifiers consists of 100 km of standard fiber, followed with a DCF of suitable length. Each channel carries chirp-free RZ pulses with 8-mW peak power. Residual dispersion of each channel is compensated at the receiver end to optimize the eye opening, measured

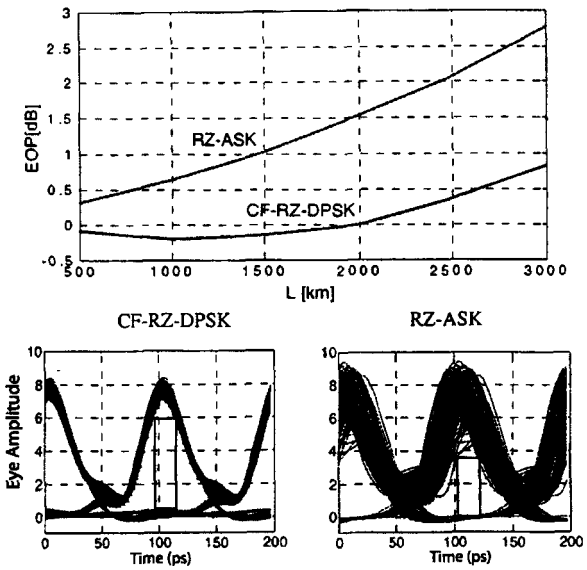

Figure 9.26: Eye-opening penalty (EOP) as a function of link length for one of eight channels in the case of RZ-ASK and RZ-DPSK formats. Eye diagrams at a distance of 3,000 km are also shown for the two formats. (After Ref. [129]; ©2002 IEEE.)

in a 20-ps time window. As seen in Figure 9.26, penalty increases rapidly for the standard RZ format but does not exceed even 1 dB at a distance of 3000 km when the DPSK format is employed.

It should be mentioned that the reduction of interchannel XPM effects through RZ-DPSK does not come without a penalty, as it is accompanied in practice with the enhanced intrachannel SPM effects [132]. The reason is related to the fact that SPM-induced phase shift depends on the channel power. As a result, any power fluctuations induced by the amplifier noise are converted through SPM into phase [133], which affect the detection of the phase difference between two neighboring bits of that channel. Moreover, interchannel XPM produces additional phase fluctuations [134]. As a result, the use of RZ-DPSK is rarely beneficial for a single-channel system or for WDM systems with a relatively large channel spacing. Nevertheless, this format provides better performance when spectral efficiency is enhanced by reducing the channel spacing. We discuss this issue in the following section.

9.6 Major Design Issues

The design of modern high-capacity WDM systems with a large number of channels transmitting data at 10 Gb/s or more is not a simple task and requires attention to many details. The accumulation of the dispersive and nonlinear effects along the link, addition of noise during optical amplification, and a desire to reduce channel spacing

make it necessary to employ a numerical approach for designing such systems. This section considers several major design issues that often limit system performance.

9.6.1 Spectral Efficiency

An important issue is related to the enhancement of spectral efficiency of dense WDM systems as much as possible. As discussed in Section 9.1.1, the spectral efficiency is defined as $\eta_s = B/\Delta\nu_{\text{ch}}$, where B is the single-channel bit rate and $\Delta\nu_{\text{ch}}$ is the channel spacing. Most commercial WDM systems in 2004 were operating with $\eta_s \leq 0.2(b/s)/Hz$, as they were designed to transmit 10-Gb/s channels with a spacing of 50 GHz or more. Many laboratory experiments have shown that WDM systems whose channels operate at 40 Gb/s with a spacing of 100 GHz can be designed to realize system capacities of more than 2 Tb/s with a spectral efficiency of 0.4 (b/s)/Hz. Such a 50-channel system occupies a bandwidth of 5 THz (around 40 nm near 1.55 μm) that covers the entire C band. Any increase in the capacity requires either the use of both the C and L bands or a reduction in channel spacing. For this reason, several experiments transmitted 40-Gb/s channels with a spacing of 50 GHz, resulting in a spectral efficiency of 0.8 (b/s)/Hz. Such WDM systems either employ modulation formats that are different than the standard RZ and NRZ formats or prefilter the optical signal at the transmitter end using an optical filter [135]–[142].

The idea behind prefiltering is simple. An optical bit stream generated by modulating an optical carrier has a symmetric spectrum with multiple peaks separated by a frequency equal to the bit rate. Since the left and right sidebands contain redundant information, one can borrow a technique from the microwave technology known as vestigial sideband (VSB) transmission, and launch only one of the sidebands into the fiber link. This technique has been used for NRZ-format WDM systems by filtering the signal spectrum with an optical filter that is detuned from the center by an optimum amount [141]. Figure 9.27(a) shows the location of filter passband (dashed curve) superimposed on the the spectrum of a 40-Gb/s NRZ bit stream. The penalty curve and the eye patterns for several detunings show that the optimum detuning is around 20 GHz for a 30-GHz bandwidth filter.

It turns out that the suppressed sideband can be reconstructed partially during transmission by the nonlinear effects occurring within the fiber link. An alternative scheme transmits the whole spectrum but employs an optical filter at the receiver end to select only one sideband. The spectral efficiency is enhanced in this scheme by using a channel allocation pattern as shown in Figure 9.27(b). Rather than using a constant channel spacing, it is alternated between 50 and 75 GHz for successive 40-Gb/s channels, resulting in a spectral efficiency of 0.64 (b/s)/Hz. At the receiver end, channels are selected with a 30-GHz filter that is detuned by 20 GHz or so toward the 75 GHz-spaced neighboring channel. With this arrangement, one always selects the sideband experiencing the smallest overlap with adjacent channels. This scheme was used as early as 2000 to transmit 128 channels at 40 Gb/s over 300 km, resulting in a system capacity of 5.12 Tb/s [141]. In later experiments, link length could be increased to around 1,500 km with the use of FEC, even though the effective bit rate of each channel increased to 42.7 Gb/s.

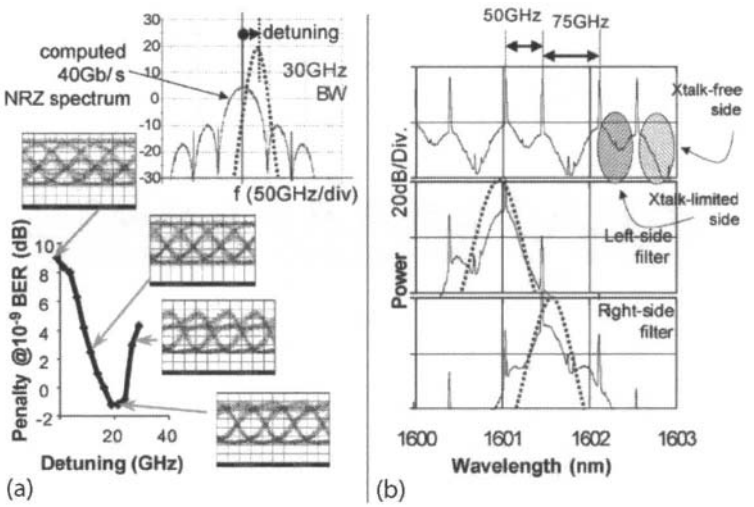

Figure 9.27: (a) Measured power penalty (thick solid curve) as a function of filter detuning (top inset) and eye diagrams at four values of detuning. (b) Measured spectra of filtered channels at the receiver end when channels are alternatively spaced by 50 and 75 GHz. (After Ref. [141]; ©2004 IEEE.)

In a 2001 experiment, the same scheme was used to realize a record capacity of 10.2 Tb/s by transmitting 256 channels at 40 Gb/s over 100 km [141]. This experiment employed the technique of PDM by transmitting two orthogonally polarized channels at each wavelength, and thus realized a spectral efficiency of 1.28 (b/s)/Hz. The PDM technique should be distinguished from polarization interleaving (see Section 9.5.3) in which neighboring channels are orthogonally polarized. In the case of PDM, the bit rate is effectively doubled as two orthogonally polarized bit streams are launched at each channel wavelength. Such a scheme suffers the most from the PMD problem. In a 2002 experiment, the distance could be increased to 300 km at 10.2 Tb/s by shifting the wavelengths slightly for the two orthogonally polarized bit streams.

In the case of RZ format, the channel bandwidth can be reduced to some extent by employing the CSRZ format (see Section 2.3.3) in which phases of the neighboring pulses in an optical bit stream differ by π. The carrier is suppressed for such a bit stream, and the two dominant spectral peaks are located at $\nu_0 \pm B/2$, rather than at $\nu_0 \pm B$, where ν_0 is the carrier frequency and B is the channel bit rate. This feature allows considerable filtering of the signal before it is launched into the optical filter, while still retaining both sidebands. Figure 9.28 shows in several situations the effects of filtering on the spectrum of a 40-Gb/s channel modulated with the CSRZ format [142]. The eye diagrams recorded under back-to-back conditions (no fiber) are also shown. When the filter passband was centered at the carrier frequency (symmetric filtering), even a 68-GHz filter produced an almost 3-dB penalty in the measured Q factor. In contrast, the penalty was below 1.5 dB even for a 35-GHz filter, detuned off-center by an optimum amount (asymmetric filtering). In a 2002 experiment, a spectral efficiency of 1 (b/s)/Hz was realized with asymmetric filtering by transmitting 25 channels at

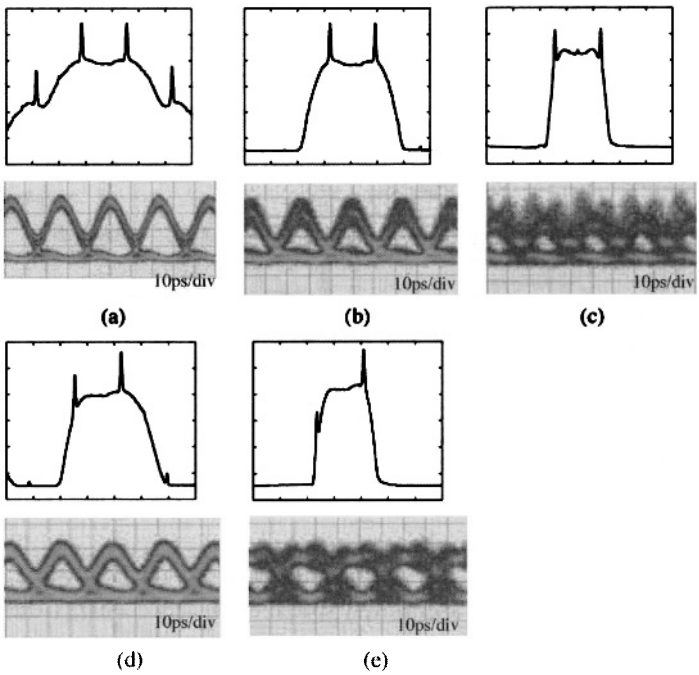

Figure 9.28: Effect of optical filtering on channel spectra and eye patterns: (a) unfiltered case; (b) symmetric 68-GHz filter; (c) symmetric 35-GHz filter; (d) asymmetric 68-GHz filter; (e) asymmetric 35-GHz filter. (After Ref. [142]; ©2004 IEEE.)

40 Gb/s, resulting in a capacity of 1 Tb/s. By 2003, a 5.12-Tb/s WDM signal (128 channels at 40 Gb/s per channel) was transmitted over 1,280 km by filtering each 42.7-Gb/s CSRZ bit stream (with 7% FEC overhead) with a 50-GHz optical filter [137]. Each channel was launched with −4 dBm of average power, and neighboring channels were orthogonally polarized to reduce interchannel crosstalk.

In the case of the CSRZ format, phases of neighboring pulses differ by π, but information is coded through ASK or on–off keying. In the case of the RZ-DPSK format, information is coded in the optical phase but a pulse is present in all bit slots. One can even employ the CSRZ format in which an additional phase shift of π is added to alternate pulses, in addition to the phase shift required for DPSK coding. This type of DPSK coding has proven to be quite useful for enhancing the performance of high-capacity WDM systems. In a 2003 experiment, 89 channels, each operating at 42.7 Gb/s (because of 7% FEC overhead), were transmitted over 4,000 km using the CSRZ-DPSK format, while employing Raman amplification with 100-km spacing between pump stations [131]. The channel spacing was 100 GHz in this experiment.

Several experiments have used the DPSK format for transmitting 40-Gb/s channels with 50-GHz channel spacing to realize a spectral efficiency of 0.8 (b/s)/Hz. In one experiment, 160 channels at 42.7 Gb/s (capacity 6.4 Tb/s) were transmitted over 3200 km of fiber [138]. Figure 9.29 shows the experimental setup schematically. Each 100-km

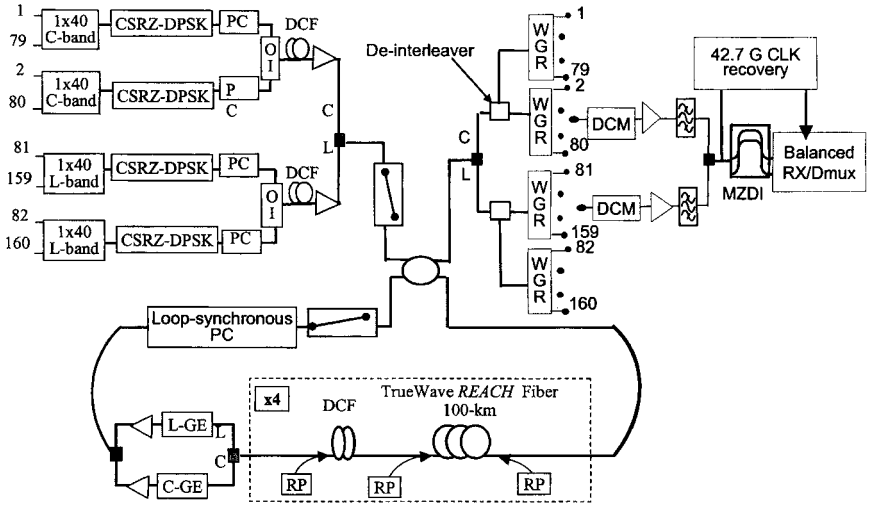

Figure 9.29: Experimental setup for the CSRZ-DPSK system with a 6.4-Tb/s capacity. PC: polarization controller; GE: gain-equalizing filter; RP: Raman pump; MZDI: Mach-Zehnder delay interferometer; WGR: waveguide grating router. (After Ref. [138]; ©2004 IEEE.)

section had a dispersion of 7.5 ps/(nm-km) and a dispersion slope of 0.039 ps/(nm^2-km). Its loss was compensated through Raman amplification, while its accumulated dispersion was compensated using a DCF such that residual dispersion after one round trip in a 400-km recirculating loop was below 0.03 ps/(nm-km) for all channels. Two dynamic gain equalizers were used to maintain nearly equal power for all channels after each round trip inside the loop. It was necessary to employ FEC coding to ensure a corrected BER of less than 10^{-12} after 3,200 km. The capacity–distance product exceeded 20 (Pb/s)-km for this experiment.

One may wonder whether it is possible to realize a spectral efficiency of >1 (b/s)/Hz, and if the answer is yes, how large it can be made. This question has attracted considerable attention in recent years as it is related to the ultimate capacity of a communication system operating over a finite channel bandwidth [143]–[148]. The issue of channel capacity was first studied by Shannon [149], who showed that for a finite-bandwidth signal, the maximum capacity C_{ch} of a linear channel of bandwidth Δf_{ch} in the presence of Gaussian noise is given by

$$C_{\text{ch}} = \Delta f_{\text{ch}} \log_2(1 + \text{SNR}), \tag{9.6.1}$$

where SNR is the signal-to-noise ratio at the receiver. If we assume that Δf_{ch} is nearly equal to the bit rate B and define the capacity per unit bandwidth as

$$\eta_c = C_{\text{ch}}/\Delta\nu_{\text{ch}} = \eta_s \log_2(1 + \text{SNR}), \tag{9.6.2}$$

we find that η_c for a linear channel can be increased beyond 1 (b/s)/Hz without an upper bound, as long as SNR is made large enough, even though $\eta_s \equiv B/\Delta\nu_{\text{ch}}$ remains

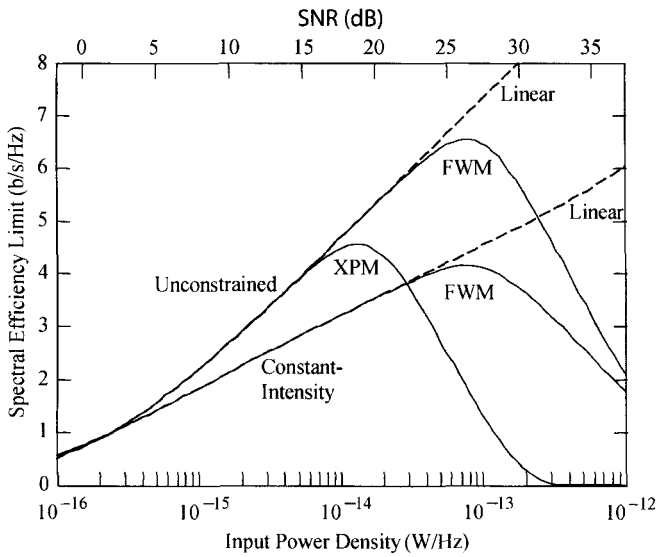

Figure 9.30: Spectral efficiency as a function of input power density. Solid lines show the limitation set by XPM or FWM; dashed lines are obtained in the absence of nonlinear effects. Information is coded in both the intensity and phase for the curves marked unconstrained. (After Ref. [148]; ©2004 IEEE.)

below 1 (b/s)/Hz. Sometimes, η_c is referred to as the spectral efficiency [148], and η_s is called the bandwidth utilization factor.

As we have seen, optical fibers do not constitute a linear channel, and the preceding equation cannot be applied to them. The degradation caused by the nonlinear effects eventually limits η_c to a maximum value. Figure 9.30 shows η_c as a function of input power density (defined as the average input power per unit bandwidth) when information is recovered using a coherent detection scheme. The intensity of the channel is kept constant for the lower curve but both the phase and intensity are modulated for the curve marked unconstrained. These results are obtained for a dense WDM system (101 channels at 40 Gb/s spaced 50 GHz apart), designed with fiber parameters $\alpha = 0.2$ dB/km, $D = 17$ ps/(km-nm), and $\gamma = 1.24$ W^{-1}/km. Fiber loss and dispersion are assumed to be compensated every 80 km. It is evident from Figure 9.30 that the nonlinear effects limit the maximum spectral efficiency to below 5 (b/s)/Hz even when information is coded in both the phase and amplitude of each channel.

In practice, a spectral efficiency of at most 1 (b/s)/Hz can be realized when a binary modulation scheme is employed. The use of polarization multiplexing can increase this value, but the enhancement is limited because of the difficulty in recovering a polarization-coded bit stream at the receiver end. Nevertheless, a value of 1.28 (b/s)/Hz has been realized with polarization multiplexing [141]. Larger values of η_c are possible if multilevel signaling is employed. A spectral efficiency of 1.6 (b/s)/Hz was realized in a 2003 experiment in which a format known as differential quadrature PSK (or DQPSK) was employed in combination with polarization multiplexing [150].

9.6.2 Dispersion Fluctuations

So far we have treated the dispersion of all fiber sections used to form a dispersion-managed fiber link as being uniform along the section length. We have also assumed that dispersion does not change with time. Both these assumptions are questionable for realistic fibers. The zero-dispersion wavelength λ_0 of a fiber depends on its core diameter, which can vary along the fiber length by a small amount (a few percent) in a random fashion during the fiber-pulling stage. Any variations in λ_0 manifest as changes in the value of the dispersion parameter $D(\lambda)$ at the channel wavelength. Although such dispersion variations are static in nature, they can affect system performance whenever nonlinear effects are not negligible along the link. For this reason, dispersion fluctuations have attracted the most attention in the context of solitons [151]–[153].

A second source of dispersion fluctuations is related to environmental changes. If the temperature of the fiber changes at a given location, the local dispersion would also change with it because D also depends on temperature [154]–[156]. Such dynamic fluctuations are of considerable concern for 40-Gb/s channels for which dispersion tolerance is relatively tight. In a simple model, D is assumed to vary with λ as

$$D(\lambda) = \frac{S_0}{4}\left(\lambda - \frac{\lambda_0^4}{\lambda^3}\right), \tag{9.6.3}$$

where S_0 is the dispersion slope at the zero-dispersion wavelength λ_0. Both S_0 and λ_0 vary along the fiber length and with temperature. Such variations affect system performance because the BER or the Q factor is sensitive to the distribution of dispersion along the link length. In the case of a linear system, their impact can be completely eliminated by employing a dynamic dispersion-compensation scheme (see Section 7.7.1). However, such a scheme does not work perfectly when nonlinear effects play a significant role.

To study the impact of dispersion fluctuations on the performance of a WDM channel operating at 40 Gb/s, the NLS equation is solved numerically, while including both the amplitude and phase fluctuations induced by the noise added by amplifiers. Dispersion fluctuations are included by writing the local dispersion parameter as

$$\beta_2(z) = \bar{\beta}_2(z) + \delta\beta_2(z), \tag{9.6.4}$$

where $\bar{\beta}_2$ is the average value of local dispersion and $\delta\beta_2$ is a random variable assumed to have a Gaussian distribution with zero mean and standard deviation σ_D. Every realization of the Gaussian process represents a different fiber link. Since time-dependent dispersion fluctuations related to temperature variations occur on a relatively long time scale, the Q factor can be calculated for each realization, but it changes in a random fashion for different realizations of dispersion distribution along the fiber link. Such changes in Q reflect the situation that the BER of a WDM channel can change during a day because of temperature-induced changes in fiber dispersion.

Figure 9.31 shows how Q changes with distance for 15 different realizations of the random variable $\delta\beta$ characterized by a standard deviation of $\sigma_D = 0.4$ ps^2/km [153]. In these simulations, the dispersion map consisted of two fiber sections of nearly equal lengths (5 km) with $\bar{\beta}_2 = \pm 8$ ps^2/km. The average dispersion of the link was set at

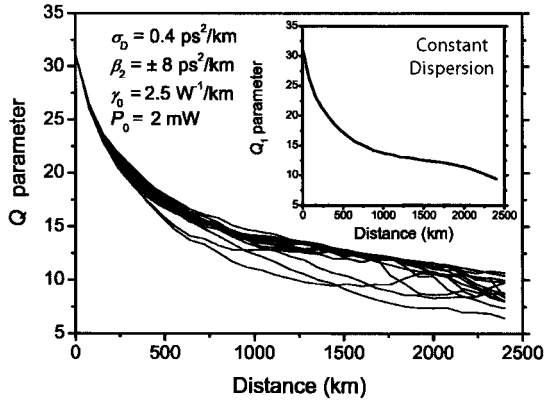

Figure 9.31: Q factor as a function of distance for 15 realizations of dispersion fluctuations for a 40-Gb/s channel. The inset shows Q values expected in the absence of dispersion fluctuations. The input peak power of 6-ps pulses was 2 mW. (After Ref. [153]; ©2003 IEEE.)

-0.01 ps^2/km. Link losses were compensated every 80 km through distributed Raman amplification. The RZ bit stream employed 6-ps Gaussian input pulses with a chirp parameter of 0.3 and a peak power of 2 mW, a value that was below the formation of dispersion-managed solitons. Figure 9.31 shows that Q can vary over a considerable range because of dispersion fluctuations. The worst case corresponds to the lowest value of Q.

Figure 9.32 shows for several different values of σ_D how the worst-case Q factor

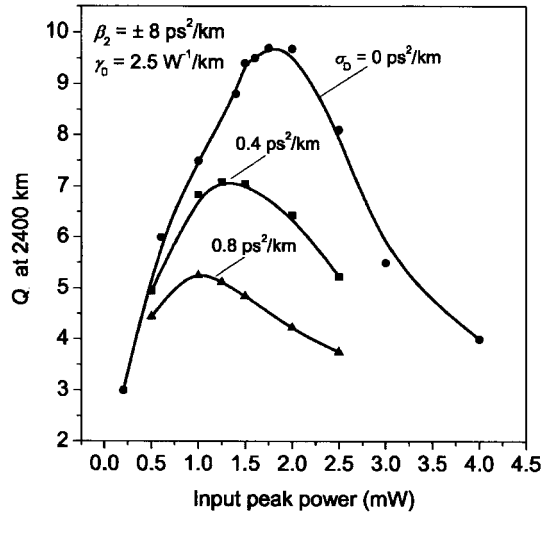

Figure 9.32: Worst-case Q factor for a 40-Gb/s channel at a distance of 2,400 km as a function of input peak power for three values of σ_D. (After Ref. [153]; ©2003 IEEE.)

changes with input peak power after 2,400 km. In the absence of dispersion fluctuations, the peak value of $Q \approx 9.5$ around 2 mW is large enough that the system can operate without FEC coding. However, the peak shifts toward lower values of peak powers, and its height is reduced considerably, in the presence of dispersion fluctuations. For $\sigma_D = 0.8$ ps^2/km, a value that corresponds to a fluctuation level of 10%, Q is around 5 at an input peak power of 1 mW. Such a system cannot operate reliably without FEC. These results illustrate that dispersion fluctuations, if left uncontrolled, can be detrimental to a lightwave system.

9.6.3 PMD and Polarization-Dependent Losses

As discussed in Section 3.4, fluctuations in the residual birefringence of optical fibers change the state of polarization (SOP) of all channels in a random fashion and also distort optical pulses because of random changes in the speeds of the orthogonally polarized components of the same pulse (PMD). In a realistic WDM system, one should also consider the effects of polarization-dependent loss (PDL) associated with various optical components (see Section 3.5). Moreover, when optical amplifiers are used periodically for loss compensation, the polarization-dependent gain (PDG) of such amplifiers can also degrade a WDM system. For this reason, considerable attention has been paid to understanding the impact of PMD, PDL, and PDG on the performance of WDM systems [157]–[163].

The main problem from the standpoint of system performance is that fiber birefringence can change with time in a random fashion owing to variations in temperature and stress along the fiber link. As a result, both PMD and PDL can lead to channel outage—a phenomenon in which the BER of a channel increases so much that it is effectively out of use. Such an outage can occur at random times for random durations. The only solution to this problem is to design the WDM system such that the outage probability remains below a certain value. Acceptable values of the outage probability are below 10^{-5}, a value that corresponds to an outage of less than 5 min/year.

As seen in Section 3.4, the impact of PMD depends on the differential group delay (DGD) that leads to distortion and broadening of optical pulses. The outage probability depends on the average value of DGD and can be reduced by controlling it below a certain value. The origin of PDL-induced outage is quite different and is related to how PDL affects the optical SNR as the signal traverses the fiber link. To understand why PDL changes the SNR, one should consider what happens to the signal and noise as they pass through an optical element with different losses along its principle axes. Since noise is unpolarized, on average half of the noise is polarized along the signal and the other half is orthogonal to it. Because of this feature, a part of the orthogonal noise component is transferred to the signal, and it affects the SNR by an amount that depends on the SOP of the signal before it enters the lossy element. Since signal SOP is random for different PDL elements, the SNR at the end of the fiber link fluctuates in a random fashion. When the number of PDL elements is relatively large, optical SNR as well as the Q factor follow a Gaussian distribution [162].

Because of PDL, the Q factor may increase or decrease, and channel outage occurs when the reduction in Q exceeds a certain value. One can introduce the concept of the PDL-induced penalty as the maximum change in the Q factor for a given amount

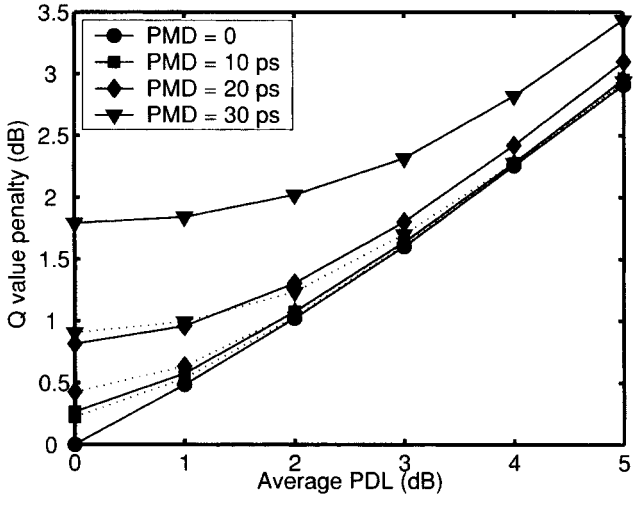

Figure 9.33: Q-factor penalty as a function of the average value of PDL along the fiber link for several values of DGD. Dotted lines show the improvement realized with PMD compensation. (After Ref. [162]; ©2003 IEEE.)

of PDL. However, since a Gaussian distribution has long tails, the penalty can be arbitrarily large albeit with a lower and lower probability. In one set of numerical simulations, the penalty was defined with 99% confidence, that is, the probability was at most 1% that the actual penalty may exceed the predicted value [162]. Figure 9.33 shows how the Q-factor penalty increases with the average value of accumulated PDL for several values of root-mean-square DGD. The simulations were performed for a 10-Gb/s channel carrying an RZ bit stream with 33% duty-cycle Gaussian pulses and operating over 4,000 km with 40 fiber spans. Each span had three PDL elements whose principle axes were oriented randomly. The dotted lines show the improvement that can be realized by employing a PMD compensation scheme. Such a scheme is beneficial but it does not affect the PDL-induced penalty. As seen in Figure 9.33, PDL can degrade the system even in the absence of PMD, and PMD compensation cannot reduce this penalty. Moreover, PDG can lead to additional penalties [158].

Many WDM systems employ a dynamic gain equalizer (DGE) at the location of amplifiers in an attempt to equalize channel powers. It has been noted that PDL-induced fluctuations of the SNR are reduced when such devices are employed [163]. The reason behind the SNR improvement can be understood by considering the noise components that are copolarized or orthogonally polarized with respect to the signal. DGEs reduce the effect of the copolarized noise component but leave the orthogonal part nearly unchanged. An analytic approach has been used to quantify the effects of PDL in the presence of DGEs. The results show that the magnitude of SNR improvement depends on the number of DGEs but as few as four DGEs placed along a long-haul fiber link can improve the SNR by more than 2 dB for accumulated PDL values in the range of 3 to 6 dB.

9.6.4 Wavelength Stability and Other Issues

The design of modern WDM systems requires a careful consideration of many transmitter and receiver characteristics. An important issue concerns the stability of the carrier frequency (or wavelength) associated with each channel. Most WDM systems employ for each channel a narrow-bandwidth semiconductor laser designed to operate in a single mode using either a DFB or distributed Bragg reflector (DBR) structure (see Section 5.2 of LT1). The output wavelength of such sources is set by a built-in grating through the relation $\lambda_c = 2\bar{n}\Lambda$, where $\bar{n}$ is the effective mode index and Λ is the period of the built-in grating.

The channel wavelength λ_c for DFB or DBR lasers can only change if the mode index $\bar{n}$ changes. The refractive index of any material depends on temperature. In the case of semiconductors, λ_c can change with temperature at a rate of about 0.1 nm/°C [164]. Similar changes can also occur with the aging of lasers [165]. Such wavelength changes are generally not of concern for single-channel systems or coarse WDM systems for which channel spacing exceeds 2 nm. However, they become critically important for dense WDM systems in which channel spacing can be below 25 GHz when the bit rate is 10 Gb/s, and the situation is worse for ultradense WDM systems in which each channel is designed to operate at 2.5 Gb/s. For such systems, it is important that the carrier frequencies of all channels remain stable to within 1 GHz or so. In fact, the maximum allowed wavelength drift throughout the laser lifetime is 10 pm for 10-Gb/s channels with a spacing of 25 GHz (ITU recommendation G.692).

Most DFB and DBR lasers stabilize chip temperature by integrating a thermoelectric cooler within the laser package. Such a device can stabilize the temperature to within 1°C or so and provides sufficient wavelength stability for WDM systems with a channel spacing of 100 GHz or more. However, a thermoelectric cooler is not sufficient when channel spacing is 50 GHz or less. A number of techniques have been developed for stabilizing the laser wavelength to meet the requirement of dense WDM systems [166]–[175]. One technique employs electrical feedback provided by a frequency discriminator based on molecular gases to lock the laser frequency to a specific resonance frequency. For example, one can use ammonia, krypton, or acetylene for semiconductor lasers operating in the 1.55-μm region, as all three have resonances near that wavelength. Frequency stability to within 1 MHz can be achieved by this technique. Another technique makes use of the optogalvanic effect to lock the laser frequency to an atomic or molecular resonance [167].

The use of a molecular gas is not always practical, and its resonance frequencies do not coincide with the standard channel frequencies on the ITU grid. What one really needs for WDM systems is a comb of uniformly spaced and well-stabilized frequencies [168]. In one approach, a Michelson interferometer, calibrated with a frequency-stabilized master DFB laser, was used to provide a set of equally spaced reference frequencies [169]. A filter, an arrayed waveguide grating, or any other filter with a comb-like periodic transmission spectrum can also be used for this purpose [170]. A fiber grating is useful for frequency stabilization but a separate grating is needed for each channel since its reflection spectrum is not periodic [171]. A frequency-dithering technique in combination with an arrayed waveguide grating and an amplitude modulator can stabilize channel frequencies to within 0.3 GHz [172].

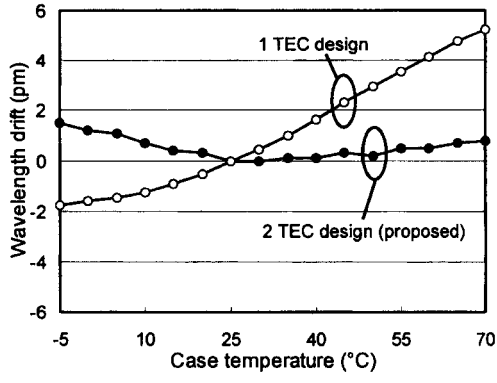

Figure 9.34: Measured wavelength drift as a function of module temperature at 20-mW output power for a laser module integrated with a wavelength monitor. (After Ref. [173]; ©2003 IEEE.)

In a more practical design, a wavelength monitor is integrated within the DFB-laser package, resulting in a laser module whose wavelength can be stabilized to within 5 pm or so [173]. Figure 2.15 in Section 2.4 shows schematically the design of a DFB laser packaged with a wavelength monitoring unit. In this device, light from the rear facet of the DFB laser is collimated by a lens and is split by a prism into two beams, one of which is used for monitoring the output power. The other beam is used for monitoring the laser wavelength and is passed through a Fabry–Perot étalon with periodic transmission peaks (separated by channel spacing) before it falls on a photodetector. To ensure that the comb of frequencies does not drift because of temperature variations, two separate thermoelectric coolers are used for the laser and the Fabry–Perot étalon. As shown in Figure 9.34, laser wavelength changes by less than 2 pm over a temperature range from -5 to 70°C when two thermoelectric coolers are employed. Such a scheme allows one to lock the laser wavelength precisely on the ITU grid.

An important issue for all-optical networks (see Chapter 10) is related to the loss of signal power occurring because of insertion losses associated with add–drop filters that may be used at multiple network modes. Optical amplifiers are used to compensate for such losses, but not all channels are amplified by the same factor, unless the gain spectrum is flat over the entire bandwidth of the WDM signal. Although gain-flattening filters are commonly employed, channel powers can still deviate by 10 dB or more depending on the route taken by a WDM signal. It may then become necessary to control the power of individual channels (through selective attenuation) at each node within a WDM network to make channel powers nearly uniform. The issue of power management in WDM networks is quite complex, and it requires attention to many details [176]–[180]. The buildup of amplifier noise can also become a limiting factor when the WDM signal passes through a large number of amplifiers. Another major issue concerns dispersion management [181]. In a reconfigurable network the exact path taken by a WDM channel can change in a dynamic fashion. Such networks will require compensation of residual dispersion at individual nodes. Network management is an active area of research and requires attention to many details [182].

Problems

9.1 Dry fibers have acceptable losses over a spectral region extending from 1.3 to 1.6 μm. Estimate the capacity of a WDM system covering this entire region using 40-Gb/s channels spaced apart by 50 GHz.

9.2 The C and L spectral bands cover a wavelength range from 1.53 to 1.61 μm. How many channels can be transmitted through WDM when the channel spacing is 25 GHz? What is the effective bit rate–distance product when a WDM signal covering the two bands using 10-Gb/s channels is transmitted over 2,000 km?

9.3 What is meant by the in-band linear crosstalk? Derive an expression for the power penalty induced by a waveguide-grating router through this phenomenon.

9.4 Explain why the cascading of identical optical filters can produce signal distortion even when filter bandwidth is wider than the signal bandwidth. Calculate the effective bandwidth of 20 cascaded filters with a Gaussian-shape transfer function of 50-GHz bandwidth.

9.5 Explain how stimulated Raman scattering can cause crosstalk in multichannel lightwave systems. Derive Eq. (9.3.3) after approximating the Raman gain spectrum by a triangular profile.

9.6 Derive Eq. (9.3.12) by extending the four-wave mixing theory of Section 4.3.1 to a fiber link with a two-section dispersion map.

9.7 Explain in physical terms the origin of FWM resonances in WDM systems. How do they affect such systems?

9.8 How does XPM lead to both amplitude fluctuations and timing jitter in WDM systems? How are such fluctuations affected by group-velocity mismatch? Use diagrams as necessary to support your arguments.

9.9 Explain what is meant by an interchannel collision. How is the collision length defined and how does it depend on the channel spacing?

9.10 Derive the set of Eqs. (9.4.6) through (9.4.9) by considering a collision of two Gaussian pulses in two channels spaced apart by Ω_{ch}.

9.11 Use Eqs. (9.4.6) through (9.4.9) with $p = 1$ and prove that the maximum frequency shift occurring during a collision is given by Eq. (9.4.11).

9.12 Describe how the technique of polarization interleaving is implemented for WDM systems. Why does it help in practice?

9.13 Explain why the use of the RZ-DPSK format is beneficial for WDM systems.

9.14 Start the OptSim software tool and load Example 9.A. Plot the channel spectra at the end of fiber link by changing the dispersion of fiber to $D = 0$, 2, and 4 ps/(km-nm) and interpret your results in terms of FWM.

9.15 Start the OptSim software tool and load Example 9.C. Run this example for link lengths of 250, 375, and 500 km and compare the eye diagrams for different channels.

References

[1] H. Ishio, J. Minowa, and K. Nosu, *J. Lightwave Technol.* **2**, 448 (1984).

[2] G. Winzer, *J. Lightwave Technol.* **2**, 369 (1984).

[3] N. A. Olsson, J. Hegarty, R. A. Logan, L. F. Johnson, K. L. Walker, L. G. Cohen, B. L. Kasper, and J. C. Campbell, *Electron. Lett.* **21**, 105 (1985).

[4] C. A. Brackett, *IEEE J. Sel. Areas Commun.* **8**, 948 (1990).

[5] P. E. Green, Jr., *Fiber-Optic Networks*, Prentice Hall, Upper Saddle River, NJ, 1993.

[6] I. P. Kaminow and T. L. Koch, Eds., *Optical Fiber Telecommunications*, Vols. 3A and 3B, Academic Press, San Diego, CA, 1997.

[7] G. E. Keiser, *Optical Fiber Communications*, 3rd ed., McGraw-Hill, New York, 2000.

[8] R. Ramaswami and K. Sivarajan, *Optical Networks: A Practical Perspective*, 2nd ed., Morgan Kaufmann Publishers, San Francisco, 2002.

[9] N. S. Bergano, in *Optical Fiber Telecommunications*, Vol. 4B, I. P. Kaminow and T. Li, Eds., Academic Press, San Diego, CA, 2002 Chap. 4.

[10] J. Zyskind and R. Berry, in *Optical Fiber Telecommunications*, Vol. 4B, I. P. Kaminow and T. Li, Eds., Academic Press, San Diego, CA, 2002, Chap. 5.

[11] A. R. Chraplyvy, A. H. Gnauck, R. W. Tkach, R. M. Derosier, C. R. Giles, B. M. Nyman, G. A. Ferguson, J. W. Sulhoff, and J. L. Zyskind, *IEEE Photon. Technol. Lett.* **7**, 98 (1995).

[12] K. Fukuchi, T. Kasamatsu, M. Morie, R. Ohhira, T. Ito, K. Sekiya, D. Ogasahara, and T. Ono, *Proc. Optical Fiber ommun. Conf.*, Optical Society of America, Washington, DC, 2001, Paper PD24.

[13] N. S. Bergano and C. R. Davidson, *J. Lightwave Technol.* **14**, 1287 (1996).

[14] E. L. Goldstein, L. Eskildsen, and A. F. Elrefaie, *IEEE Photon. Technol. Lett.* **6**, 657 (1994).

[15] I. T. Monroy and E. Tangdiongga, Eds., *Crosstalk in WDM Communication Networks*, Kluwer Academic, Norwell, MA, 2002.

[16] J. D. Downie and A. B. Ruffin *J. Lightwave Technol.* **21**, 1876 (2003).

[17] P. A. Rosher and A. R. Hunwicks, *IEEE J. Sel. Areas Commun.* **8**, 1108 (1990).

[18] P. A. Humblet and W. M. Hamdy, *IEEE J. Sel. Areas Commun.* **8**, 1095 (1990).

[19] E. L. Goldstein and L. Eskildsen, *IEEE Photon. Technol. Lett.* **7**, 93 (1995).

[20] Y. D. Jin, Q. Jiang, and M. Kavehrad, *IEEE Photon. Technol. Lett.* **7**, 1210 (1995).

[21] H. Takahashi, K. Oda, and H. Toba, *J. Lightwave Technol.* **14**, 1097 (1996).

[22] J. Zhou, R. Cadeddu, E. Casaccia, C. Cavazzoni, and M. J. O'Mahony, *J. Lightwave Technol.* **14**, 1423 (1996).

[23] G. Murtaza and J. M. Senior, *Opt. Fiber Technol.* **3**, 471 (1997).

[24] M. Gustavsson, L. Gillner, and C. P. Larsen, *J. Lightwave Technol.* **15**, 2006 (1997).

[25] C. X. Yu, W.-K. Wang, and S. D. Brorson, *J. Lightwave Technol.* **16**, 1380 (1998).

[26] L. Gillner, C. P. Larsen, and M. Gustavsson, *J. Lightwave Technol.* **17**, 58 (1999).

[27] Y. Shen, K. Lu, and W. Gu, *J. Lightwave Technol.* **17**, 759 (1999).

[28] T. Gyselings, G. Morthier, and R. Baets, *J. Lightwave Technol.* **17**, 1273 (1999).

[29] H. J. S. Dorren, H. de Waardt, and I. T. Monroy, *J. Lightwave Technol.* **17**, 2425 (1999).

[30] I. T. Monroy, E. Tangdiongga, R. Jonker, and H. de Waardt, *J. Lightwave Technol.* **18**, 637 (2000).

[31] K. Durrani and M. J. Holmes, *J. Lightwave Technol.* **18**, 1871 (2000).

[32] S. D. Dods and R. S. Tucker, *J. Lightwave Technol.* **19**, 1829 (2001).

[33] T. Kamalakis, T. Sphicopoulos, and M. Sagriotis, *J. Lightwave Technol.* **21**, 2172 (2003).

[34] P. R. Pepeljugoski and K. Y. Lau, *J. Lightwave Technol.* **10**, 257 (1992).

[35] N. N. Khrais, A. F. Elrefaie, R. E.Wagner, and S. Ahmed, *IEEE Photon. Technol. Lett.* **8**,1073 (1996).

[36] T. Otani, N. Antoniades, I. Roudas, and T. E. Stern, *IEEE Photon. Technol. Lett.* **11**, 1414 (1999).

[37] J. D. Downie, I. Tomkos, N. Antoniades, and A. Boskovic, *J. Lightwave Technol.* **20**, 218 (2002).

[38] K.-P. Ho, L.-K. Chen, and F. Tong, *IEEE J. Sel. Topics Quantum Electron.* **6**, 223 (2000).

[39] G. P. Agrawal, *Nonlinear Fiber Optics*, 3rd ed., Academic Press, San Diego, CA, 2001.

[40] A. R. Chraplyvy, *J. Lightwave Technol.* **8**, 1548 (1990).

[41] F. Forghieri, R. W. Tkach, and A. R. Chraplyvy, in *Optical Fiber Telecommunications*, Vol. 3A, I. P. Kaminow and T. L. Koch, Eds., Academic Press, San Diego, CA, 1997, Chap. 8.

[42] G. P. Agrawal, *Applications of Nonlinear Fiber Optics*, Academic Press, San Diego, CA, 2001.

[43] P. Bayvel and R. I. Killey, in *Optical Fiber Telecommunications*, Vol. 4B, I. P. Kaminow and T. Li, Eds., Academic Press, San Diego, CA, 2002, Chap. 13.

[44] M. Wu and W. I. Way, *J. Lightwave Technol.* **22**, 1483 (2004).

[45] X. Zhang, B. F. Jørgensen, F. Ebskamp, and R. J. Pedersen, *Opt. Commun.* **107**, 358 (1994).

[46] F. Forghieri, R. W. Tkach, and A. R. Chraplyvy, *IEEE Photon. Technol. Lett.* **7**, 101 (1995).

[47] D. N. Christodoulides and R. B. Jander, *IEEE Photon. Technol. Lett.* **8**, 1722 (1996).

[48] J. Wang, X. Sun, and M. Zhang, *IEEE Photon. Technol. Lett.* **10**, 540 (1998).

[49] M. E. Marhic, F. S. Yang, and L. G. Kazovsky, *J. Opt. Soc. Am. B* **15**, 957 (1998).

[50] A. G. Grandpierre, D. N. Christodoulides, and J. Toulouse, *IEEE Photon. Technol. Lett.* **11**, 1271 (1999).

[51] K.-P. Ho, *J. Lightwave Technol.* **18**, 915 (2000).

[52] S. Norimatsu and T. Yamamoto, *J. Lightwave Technol.* **19**, 159 (2001).

[53] C. M. McIntosh, A. G. Grandpierre, D. N. Christodoulides, J. Toulouse, and J. M. P. Delvaux, *IEEE Photon. Technol. Lett.* **13**, 302 (2001).

[54] A. G. Grandpierre, D. N. Christodoulides, W. E. Schiesser, C. M. McIntosh, and J. Toulouse, *Opt. Commun.* **194**, 319 (2001).

[55] W. Ding, Z. Chen, D. Wu, and A. Xu, *Electron. Lett.* **38**, 1265 (2002).

[56] X, Zhou, and M. Birk, *J. Lightwave Technol.* **21**, 2194 (2003).

[57] T. Yamamoto and S. Norimatsu, *J. Lightwave Technol.* **21**, 2229 (2003).

[58] N. Shibata, R. P. Braun, and R. G. Waarts, *IEEE J. Quantum Electron.* **23**, 1205 (1987).

[59] K. Inoue, K. Nakanishi, K. Oda, and H. Toba, *J. Lightwave Technol.* **12**, 423 (1994).

[60] F. Forghieri, R. W. Tkach, and A. R. Chraplyvy, *J. Lightwave Technol.* **15**, 889 (1995).

[61] W. Zeiler, F. Di Pasquale, P. Bayvel, and J. E. Midwinter, *J. Lightwave Technol.* **17**, 1933 (1996).

[62] J. S. Lee, D. H. Lee, and C. S. Park, *IEEE Photon. Technol. Lett.* **10**, 825 (1998).

[63] E. A. Golovchenko, N. S. Bergano, and C. R. Davidson, *IEEE Photon. Technol. Lett.* **10**, 1481 (1998).

[64] H. Suzuki, S. Ohteru, and N. Takachio, *IEEE Photon. Technol. Lett.* **11**, 1677 (1999).

[65] M. Nakajima, M. Ohashi, K. Shiraki, T. Horiguchi, K. Kurokawa, and Y. Miyajima, *J. Lightwave Technol.* **17**, 1814 (1999).

[66] M. Eiselt, *J. Lightwave Technol.* **17**, 2261 (1999).

[67] K.-D. Chang, G.-C. Yang, and W. C. Kwong, *J. Lightwave Technol.* **18**, 2113 (2000).

[68] M. Manna and E. A. Golovchenko, *IEEE Photon. Technol. Lett.* **13**, 929 (2002).

[69] S. Betti, M. Giaconi, and M. Nardini, *IEEE Photon. Technol. Lett.* **14**, 1079 (2003).

[70] T. Chiang, N. Kagi, M. E. Marhic, and L. G. Kazovsky, *J. Lightwave Technol.* **14**, 249 (1996).

[71] G. Bellotti, M. Varani, C. Francia, and A. Bononi, *IEEE Photon. Technol. Lett.* **10**, 1745 (1998).

[72] A. V. T. Cartaxo, *J. Lightwave Technol.* **17**, 178 (1999).

[73] R. Hui, K. R. Demarest, and C. T. Allen, *J. Lightwave Technol.* **17**, 1018 (1999).

[74] M. Eiselt, M. Shtaif, and L. D. Garettt, *IEEE Photon. Technol. Lett.* **11**, 748 (1999).

[75] L. E. Nelson, R. M. Jopson, A. H. Gnauck, and A. R. Chraplyvy, *IEEE Photon. Technol. Lett.* **11**, 907 (1999).

[76] M. Shtaif, M. Eiselt, and L. D. Garettt, *IEEE Photon. Technol. Lett.* **13**, 88 (2000).

[77] J. J. Yu and P. Jeppesen, *Opt. Commun.* **184**, 367 (2000).

[78] H. J. Thiele, R. I. Killey, and P. Bayvel, *IEEE Photon. Technol. Lett.* **12**, 669 (2000).

[79] G. Bellotti and S. Bigo, *IEEE Photon. Technol. Lett.* **12**, 726 (2000).

[80] R. I. Killey, H. J. Thiele, V. Mikhailov, and P. Bayvel, *IEEE Photon. Technol. Lett.* **12**, 804 (2000).

[81] G. Bellotti, S. Bigo, P. Y. Cortes, S. Gauchard, and S. LaRochelle, *IEEE Photon. Technol. Lett.* **12**, 1403 (2000).

[82] S. Betti and M. Giaconi, *IEEE Photon. Technol. Lett.* **13**, 43 (2001); *IEEE Photon. Technol. Lett.* **13**, 305 (2001).

[83] H. J. Thiele, R. I. Killey, and P. Bayvel, *Opt. Fiber Technol.* **8**, 71 (2002).

[84] Q. Lin and G. P. Agrawal, *J. Lightwave Technol.* **22**, 977 (2004).

[85] G. Goeger, M. Wrage, and W. Fischler, *IEEE Photon. Technol. Lett.* **16**, 1858 (2004).

[86] L. F. Mollenauer, S. G. Evangelides, and J. P. Gordon, *J. Lightwave Technol.* **9**, 362 (1991).

[87] T. Aakjer, J. H. Povlsen, and K. Rottwitt, *Opt. Lett.* **18**, 1908 (1993).

[88] J. F. L. Devaney, W. Forysiak, A. M. Niculae, and N. J. Doran, *Opt. Lett.* **22**, 1695 (1997).

[89] A. Mecozzi, *J. Opt. Soc. Am. B* **15**, 152 (1998).

[90] T. Hirooka and A. Hasegawa, *Opt. Lett.* **23**, 768 (1998).

[91] M. J. Ablowitz, G. Biondini, S. Chakvaraty, and R. L. Horne, *Opt. Commun.* **150**, 305 (1998).

[92] A. M. Niculae, W. Forysiak, A. J. Gloag, J. H. B. Nijhof, and N. J. Doran, *Opt. Lett.* **23**, 1354 (1998).

[93] P. V. Mamyshev and L. F. Mollenauer, *Opt. Lett.* **24**, 448 (1999).

[94] Y. Chen and H. A. Haus, *Opt. Lett.* **24**, 217 (1999).

[95] H. Sagahara, H. Kato, T. Inoue, A. Maruta, and Y. Kodama, *J. Lightwave Technol.* **17**, 1547 (1999).

[96] V. S. Grigoryan and A. Richter, *J. Lightwave Technol.* **18**, 1148 (2000).

[97] A. R. Chraplyvy and R. W. Tkach, *IEEE J. Quantum Electron.* **34**, 2103 (1998).

[98] J. Kani, M. Jinno, T. Sakamoto, S. Aisawa, M. Fukui, K. Hattori, and K. Oguchi, *J. Lightwave Technol.* **17**, 2249 (1999).

[99] E. A. Golovchenko, A. N. Pilipetskii, N. S. Bergano, C. R. Davidson, F. I. Khatri, R. M. Kimball, and V. J. Mazurczyk, *IEEE J. Sel. Topics Quantum Electron.* **6**, 337 (2000).

[100] M. Murakami, T. Matsuda, H. Maeda, and T. Imai, *J. Lightwave Technol.* **18**, 1197 (2000).

[101] R. M. Mu and C. R. menyuk, *J. Lightwave Technol.* **20**, 608 (2002).

[102] J.-X. Cai et al, *J. Lightwave Technol.* **20**, 2247 (2002).

[103] E. Ciaramella, *IEEE Photon. Technol. Lett.* **14**, 804 (2002).

[104] Y. Inada, H. Sugahara, K. Fukuchi, T. Ogata, and Y. Aoki, *IEEE Photon. Technol. Lett.* **14**, 1366 (2002).

[105] M. Suzuki and N. Edagawa, *J. Lightwave Technol.* **21**, 916 (2003).

[106] B. Bakhshi, M. Manna, G. Mohs, D. I. Kovsh, R. L. Lynch, M. Vaa, E. A. Golovchenko, W. W. Patterson, W. T. Anderson, P Corbett, S. Jiang, M. M. Sanders, H. Li, G. T. Harvey, A. Lucero, and S. M. Abbott, *J. Lightwave Technol.* **22**, 233 (2004).

[107] G. L. Woods, P. Papaparaskeva, M. Shtaif, Member, I. Brener, and D. A. Pitt, *IEEE Photon. Technol. Lett.* **16**, 677 (2004).

[108] L. F. Mollenauer, J. P. Gordon, and P. V. Mamychev, in *Optical Fiber Telecommunications*, vol. 3A, I. P. Kaminow and T. L. Koch, Eds., Academic Press, San Diego, CA, 1997, Chap. 12.

[109] A. H. Gnauck, S.-G. Park, J. M. Wiesenfeld, and L. D. Garrett, *Electron. Lett.* **35**, 2218 (1999).

[110] C. M. Weinert, R. Ludwig, W. Pieper, H. G. Weber, D. Breuer, K. Petermann, and F. Küuppers, *J. Lightwave Technol.* **17**, 2276 (1999).

[111] S. Kawanishi, H. Takara, K. Uchiyama, I. Shake, and K. Mori, *Electron. Lett.* **35**, 826 (1999).

[112] B. Mikkelsen, G. Raybon, B. Zhu, R. J. Essiambre, P. G. Bernasconi, K. Dreyer, L. W. Stulz, and S. N. Knudsen, Proc. Opt. Fiber Commun. Conf., Optical Society of America, Washington, DC, 2001, paper THF2.

[113] M. Daikoku, T. Otani, and M. Suzuki, *IEEE Photon. Technol. Lett.* **15**, 1165 (2003).

[114] H. Suzuki, J. Kani, H. Masuda, N. Takachio, K. Iwatsuki, Y. Tada, and M. Sumida, *IEEE Photon. Technol. Lett.* **12**, 903 (2000).

[115] A. K. Srivastava, S. Radic, C. Wolf, J. C. Centanni, J. W. Sulhoff, K. Kaantor, and Y. Sun, *IEEE Photon. Technol. Lett.* **12**, 1570 (2000).

[116] N. Takachio and H. Suzuki, *J. Lightwave Technol.* **19**, 60 (2001).

[117] H. Suzuki, N. Takachio, H. Masuda, and K. Iwatsuki, *J. Lightwave Technol.* **21**, 973 (2003).

[118] D. F. Grosz, A. Agarwal, S. Banerjee, D. N. Maywar, and A. P. Küng, *J. Lightwave Technol.* **22**, 233 (2004).

[119] D. F. Grosz, A. Agarwal, A. P. Küng, S. Banerjee, D. N. Maywar, and T. H. Wood, *IEEE Photon. Technol. Lett.* **16**, 1197 (2004).

[120] A. R. Chraplyvy, G. H. Gnauck, R. W. Tkach, J. L. Zyskind, J. W. Sulhoff, A. J. Lucero, Y. Sun, R. M. Jopson, F. Forghieri, R. M. Derosier, C. Wolf, and A. R. McCormick, *IEEE Photon. Technol. Lett.* **8**, 1264 (1996).

[121] T. Ono and Y. Yano, *IEEE J. Quantum Electron.* **34**, 2080 (1998).

[122] D. I. Kovsh, L. Liu, B. Bakhshi, A. N. Pilipetskii, E. A. Golovchenko, and N. S. Bergano, *IEEE J. Sel. Topics Quantum Electron.* **8**, 597 (2002).

[123] L. Leng, S. Stulz, B. Zhu, L. E. Nelson, B. Edvold, L. Gruner-Nielsen, S. Radic, J. Centanni, and A. Gnauck, *IEEE Photon. Technol. Lett.* **15**, 1153 (2003).

[124] L. E. Nelson and H. Kogelnik, *Opt. Exp.* **7**, 350 (2001).
[125] L. E. Nelson, T. N. Nielsen, and H. Kogelnik, *IEEE Photon. Technol. Lett.* **13**, 738 (2001).
[126] A. Hodžić, B. Konrad, and K. Petermann, *IEEE Photon. Technol. Lett.* **15**, 153 (2003).
[127] E. Ciaramella, *IEEE Photon. Technol. Lett.* **15**, 227 (2003).
[128] M. Rohde, C. Caspar, N. Heimes, M. Konitzer, E.-J. Bachus, and N. Hanik, *Electron. Lett.* **36**, 1483 (2000).
[129] J. Leibrich, C. Wree, and W. Rosenkranz, *IEEE Photon. Technol. Lett.* **14**, 155 (2002).
[130] A. H. Gnauck, G. Raybon, S. Chandrasekhar, J. Leuthold, C. Doerr, L. Stulz, and E. Burrows, *IEEE Photon. Technol. Lett.* **15**, 467 (2003).
[131] B. Zhu, C. R. Doerr, P. Gaarde, L. E. Nelson, S. Stulz, L. Stulz, and L. Gruner-Nielsen, *Electron. Lett.* **39**, 1528 (2003).
[132] T. Mizuochi, K. Ishida, T. Kobayashi, J. Abe, K. Kinjo, K. Motoshima, and K. Kasahara, *J. Lightwave Technol.* **21**, 1933 (2003).
[133] J. P. Gordon and L. F. Mollenauer, *Opt. Lett.* **15**, 1351 (1990).
[134] C. J. McKinstrie, C. Xie, and C. Xu, *Opt. Lett.* **28**, 604 (2003).
[135] T. Ito, K. Fukuchi, K. Sekiya, D. Ogasahara, R. Ohira, and T. Ono, Proc. Europ. Conf. Opt. Commun., Munich, Germany, 2000, postdeadline paper PD1.
[136] H. Bissessur, G. Charlet, W. Idler, C. Simonneau, S. Borne, L. Pierre, R. Dischler, C. De Barros, and P. Tran, *Electron. Lett.* **38**, 377 (2002).
[137] A. Agarwal, S. Banerjee, D. F. Grosz, A. P. Küng, D. N. Maywar, A. Gurevich, and T. H. Wood, *IEEE Photon. Technol. Lett.* **15**, 470 (2003).
[138] B. Zhu, L. E. Nelson, S. Stulz, A. H. Gnauck, C. Doerr, J. Leuthold, L. Grner-Nielsen, M. O. Pedersen, J. Kim, and R. L. Lingle, Jr., *J. Lightwave Technol.* **22**, 208 (2004).
[139] C. Xu, X. Liu, and X. Wei, *IEEE J. Sel. Topics Quantum Electron.* **10**, 281 (2004).
[140] G. Bosco, A. Carena, V. Curri, R. Gaudino, and P. Poggiolini, *IEEE J. Sel. Topics Quantum Electron.* **10**, 321 (2004).
[141] S. Bigo, *IEEE J. Sel. Topics Quantum Electron.* **10**, 329 (2004).
[142] T. Tsuritani, A. Agata, I. Morita, N. Edagawa, and S. Akiba, *IEEE J. Sel. Topics Quantum Electron.* **10**, 403 (2004).
[143] P. P. Mitra and J. B. Stark, *Nature* **411**, 1027 (2001).
[144] A. Mecozzi and M. Shtaif, *IEEE Photon. Technol. Lett.* **13**, 1029 (2001).
[145] J. Tang, *J. Lightwave Technol.* **19**, 1104 (2001); *J. Lightwave Technol.* **20**, 1095 (2002).
[146] E. E. Narimanov and P. Mitra, *J. Lightwave Technol.* **20**, 530 (2002).
[147] K. S. Turitsyn, S. A. Derevyanko, I. V. Yurkevich, and S. K. Turitsyn, *Phys. Rev. Lett.* **91**, 203901 (2003).
[148] J. M. Kahn and K.-P. Ho, *IEEE J. Sel. Topics Quantum Electron.* **10**, 259 (2004).
[149] C. E. Shannon, *Proc. IRE* **37**, 10 (1949).
[150] C. Wree, Student N. Hecker-Denschlag, E. Gottwald, P. Krummrich, J. Leibrich, E. Schmidt, B. Lankl, and W. Rosenkranz, *IEEE Photon. Technol. Lett.* **15**, 1303 (2003).
[151] F. K. Abdullaev and B. B. Baizakov, *Opt. Lett.* **25**, 93 (2000).
[152] C. Xie, L. F. Mollenauer, and N. Mamysheva, *J. Lightwave Technol.* **21**, 769 (2003).
[153] E. Poutrina and G. P. Agrawal, *J. Lightwave Technol.* **21**, 990 (2003).
[154] T. Kato, Y. Koyano, N. Nishimura, *Opt. Lett.* **25**, 1156 (2000).
[155] V. M. Schneider, *Electron. Lett.* **37**, xx, (2001).
[156] M. J. Hamp, J. Wrigtht, M. Hubbard, and R. Brimacombe, *IEEE Photon. Technol. Lett.* **14**, 1524 (2002).
[157] B. Huttner, C. Geiser, and N. Gisin, *IEEE J. Sel. Topics Quantum Electron.* **6**, 317 (2000).

[158] D. Wang and C. R. Menyuk, *J. Lightwave Technol.* **19**, 487 (2001).

[159] A. Mecozzi and M. Shtaif, *IEEE Photon. Technol. Lett.* **14**, 313 (2002); *IEEE Photon. Technol. Lett.* **16**, 671 (2004).

[160] M. Yu, C. Kan, M. Lewis, and A. Sizmann, *IEEE Photon. Technol. Lett.* **14**, 1418 (2002).

[161] A. Galtarossa and L. Palmieri, *IEEE Photon. Technol. Lett.* **15**, 57 (2003).

[162] C. Xie and L. F. Mollenauer, *J. Lightwave Technol.* **21**, 1953 (2003).

[163] A. Mecozzi and M. Shtaif, *J. Lightwave Technol.* **22**, 1856 (2004).

[164] G. P. Agrawal and N. K. Dutta, *Semiconductor Lasers*, 2nd ed., Kluwer Academic, Norwell, MA, 1993.

[165] H. Mawatari, M. Fukuda, F. Kano, Y. Tohmori, Y. Yoshikuni, and H. Toba, *J. Lightwave Technol.* **17**, 918 (1999).

[166] T. Ikegami, S. Sudo, and Y. Sakai, *Frequency Stabilization of Semiconductor Laser Diodes*, Artec House, Boston, 1995.

[167] U. H. P. Fischer and C. von Helmolt, *J. Lightwave Technol.* **14**, 139 (1996).

[168] M. Teshima, M.Koga, and K. Sato, *J. Lightwave Technol.* **14**, 2277 (1996).

[169] M. Guy, B. Villeneuve, C. Latrasse, and M. Têtu, *J. Lightwave Technol.* **14**, 1136 (1996).

[170] H. J. Lee, G. Y. Lyu, S. Y. Park, and J. H. Lee, *IEEE Photon. Technol. Lett.* **10**, 276 (1998).

[171] Y. Park, S. T. Lee, and C. J. Chae, *IEEE Photon. Technol. Lett.* **10**, 1446 (1998).

[172] Y. Horiuchi, S. Yamamoto, and M. Suzuki, *IEICE Trans. Comm.* **E84B**, 1145 (2001).

[173] H. Nasu, T. Mukaihara, T. Takagi, M. Oike, T. Nomura, and A. Kasukawa, *IEEE Photon. Technol. Lett.* **15**, 293 (2003).

[174] S.-Y. Kim, S.-W. Huh, Y.-S. Hurh, K.-H. Seo, and J.-S. Lee, *IEEE Photon. Technol. Lett.* **15**, 2891 (2003).

[175] M. Funabashi, H. Nasu, T. Mukaihara, T. Kimoto, T. Shinagawa, T. Kise, K. Takaki, T. Takagi, M. Oike, T. Nomura, and A. Kasukawa, *IEEE J. Sel. Topics Quantum Electron.* **10**, 312 (2004).

[176] J. Zhou and M. J. O'Mahony, *IEE Proc.* **143**, 178 (1996).

[177] Y. Hamazumi, T. Kawai, M. Koga, and K. Sato, *IEEE Photon. Technol. Lett.* **11**, 370 (1999).

[178] Y. S. Fei, X. P. Zheng, H. Y. Zhang, Y. L. Guo, and B. K. Zhou, *IEEE Photon. Technol. Lett.* **11**, 1189 (1999).

[179] K. J. Zhang, D. L. Hart, K. I. Kang, and B. C. Moore, *Opt. Eng.* **40**, 1199 (2001).

[180] M. Boroditsky, C. F. Lam, S. L. Woodward, N. J. Frigo, and M. D. Feuer, *IEE Proc.* **150**, 229 (2003).

[181] B. J. Wilson, N. G. Stoffel, J. L. Pastor, M. J. Post, K. H. Liu, T. Li, K. A. Walsh, J. Y. Wei, and Y. Tsai, *J. Lightwave Technol.* **18**, 2038 (2000).

[182] M. Vasilyev, I. Tomkos, M. Mehendale, J.-K. Rhee, A. Kobyakov, M. Ajgaonkar, S. Tsuda, and M. Sharma, *J. Lightwave Technol.* **21**, 2661 (2003).

Chapter 10

Optical Networks

The preceding chapter focused on long-haul WDM systems serving as point-to-point links. This chapter is devoted to optical networks that use such point-to-point links for interconnecting a large number of users. Two examples of such networks are provided by the Internet and the telephone network. Section 10.1 provides an overview of network architectures and topologies. Section 10.2 is devoted to network protocols and their evolution with the advent of modern WDM systems. Section 10.3 focuses on WDM networks in which optical cross-connects are employed for switching individual channels. Packet-switched networks are covered in Section 10.4, where we discuss how individual packets can be routed across the network through a technique known as optical label swapping. Section 10.5 focuses on optical burst switching and photonic slot routing. Section 10.6 is devoted to access networks, with an emphasis on broadcast-and-select and passive optical networks.

10.1 Network Architecture and Topologies

From an architectural standpoint, optical networks can be divided into several broad categories [1]–[12]. Since networks may cover a small geographical area or spread over an entire continent, it is useful to classify them into three groups named as local-area networks (LANs), metropolitan-area networks (MANs), and wide-area networks (WANs), depending on the area they cover. An alternative classification used by the telephone industry refers to LANs as access networks, MANs as metro networks, and WANs as transport networks. Another terminology employs the term core network for WANs, while MANs and LANs constitute edge networks.

10.1.1 Wide-Area Networks

Consider first a WAN covering a large area such as a country or a whole continent. Historically, telecommunication networks occupying a large geographical region have employed a hub topology in combination with the SONET/SDH proptocol [13]. Figure 10.1 shows an example of a WAN covering a large part of the United States. Such

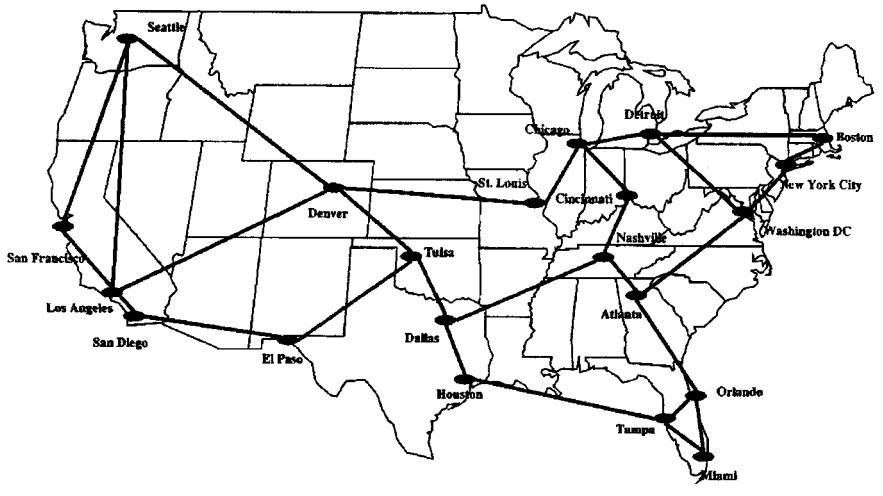

Figure 10.1: An example of a wide-area mesh network designed with hub topology. (After Ref. [14]; ©2000 IEEE.)

networks are also called mesh networks [14]. Hubs or nodes, located in large metropolitan areas and housing electronic switches, connect any two nodes by creating a "virtual circuit" between them. This scheme is referred to as *circuit switching*. An alternative scheme, used for the Internet, is known as *packet switching*. It routes packets through a protocol known as *Internet protocol* (IP). Another packet-based protocol, called the *asynchronous transfer mode* (ATM), is also used for providing diverse services (audio, video, and data) simultaneously over the network.

In the mesh-network architecture of Figure 10.1, only some nodes are connected directly through point-to-point links. For this reason, the creation of a virtual circuit between two arbitrary nodes requires switching at one or more intermediate nodes. Such networks are called multihop networks. With the advent of WDM during the 1990s, it became possible to transmit multiple WDM channels over each point-to-point link, but the switching of channels at each node was being done electronically even in 2004. Such transport networks are termed "opaque" because they require optical-to-electrical conversion at each node. As a result, neither the bit rate nor the modulation format can be altered without changing the optical hardware at each node.

The concept of all-optical WDM networks is quite important for core networks. In such a network, a WDM signal passes through intermediate nodes without being converted to the electrical domain. An optical add–drop multiplexer (see Section 8.3 of LT1) is used at the destination node to add or drop channels at specific wavelengths. Such a network is referred to as being "transparent." Transparent WDM networks are desirable as they do not require demultiplexing and optical-to-electrical conversion of all WDM channels. As a result, they are not limited by the electronic-speed bottleneck and may also help in reducing the cost of installing and maintaining a network. As discussed in Section 10.3, nodes in a transparent WDM network (see Figure 10.1) employ optical cross-connects (OXCs) for switching channels.

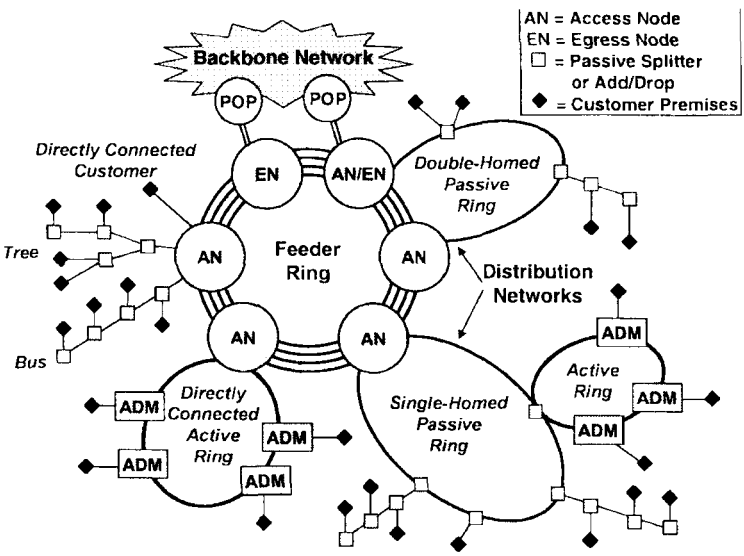

Figure 10.2: Schematic of a MAN with a ring topology. It is connected to a WAN at egress nodes (EN) and to multiple LANs at access nodes (AN). ADM stands for add–drop multiplexer. (After Ref. [15]; ©1999 IEEE.)

10.1.2 Metropolitan-Area Networks

Each node in a WAN, such as that shown in Figure 10.1, is often located in a metropolitan area and connects to a MAN. Figure 10.2 shows the architecture of a MAN schematically [15]. The topology of choice for MANs is a ring that connects to the WAN at one or two egress nodes [16]. This ring employs up to four fibers to provide protection against network failures. Two of the fibers are used to route the data in the clockwise and counterclockwise directions. The other two fibers are called protection fibers and are deployed when a point-to-point link fails. A network is called self-healing if the fiber is switched automatically. The central ring in Figure 10.2 is called a feeder ring as it provides access to multiple LANs at access nodes. Add–drop multiplexers are used at nodes to drop or add individual WDM channels.

Several MANs can be interconnected with a ring to form a regional network. This trend is clearly apparent in Figure 10.1. The advantage of a WAN in the form of regional rings is that such a configuration provides protection against failures. The use of protection fibers in each ring ensures that an alternate path between any two nodes can be found if a single point-to-point link fails. The main difference between the rings used for regional and metropolitan networks stems from the scaling and cost considerations. In a metro ring, traffic flows at a modest bit rate compared with a regional ring forming the backbone of a transport network. Typically, each channel operates at 2.5 Gb/s in MANs. To reduce the cost, a coarse WDM technique is employed in place of dense WDM common in transport networks. Moreover, often just two fibers are used inside a metro ring, one for carrying the data and the other for protecting against a failure.

Most metro networks were using electronic switching in 2004, although optical switching remains the ultimate goal. In a test-bed implementation of an optically switched metro network, called the *multiwavelength optical network* (MONET), several sites within the Washington, DC, area of the United States were connected using a set of eight standard wavelengths with a channel spacing of 200 GHz [17]. Switching ar each node was performed through add–drop multiplexers or wavelength-selective OXCs based on the $LiNbO_3$ technology. Each WDM channel operated at a bit rate of up to 10 Gb/s and transported data using several different protocols.

10.1.3 Local-Area Networks

Many applications require LANs in which a large number of users within a local area (e.g., a town or a university campus) are interconnected in such a way that any user can access the network randomly to transmit data to any other user [18]–[21]. Access networks used in a subscriber loop (often called a local loop) also fall into this category [20]. As transmission distances are relatively short ($<$10 km), fiber losses as well as the dispersive and nonlinear effects occurring inside fibers are not of much concern for LANs. The major motivation behind using optical fibers is a much larger bandwidth offered by them compared with a coaxial cable.

System architecture plays an important role for LANs. Three commonly used topologies are shown in Figure 10.3 and are known as the bus, ring, and star topologies. In the case of bus topology, all users communicate with each other by tapping into a cental optical fiber (the bus) that transports all data in one direction. An optical tap diverts a small fraction of optical power at each node on the bus. The bus topology is often employed for cable-television (CATV) networks.

In the case of ring topology, users are connected at nodes located on a ring. The network functions by passing a token (a predefined bit sequence) around the ring. Each node monitors this token and accepts the datum if it contains its own address. It can also transmit by appending data to an empty token. The use of ring topology for fiber-optic LANs was commercialized in the 1990s with the standardized interface known as the fiber-distributed data interface (FDDI). This protocol transmits data at 100 Mb/s over multimode fibers using 1.3-μm transmitters containing a light-emitting diode.

In the case of star topology, all nodes are connected to a star coupler (see Section 4.5.3 of LT1) at a central location. The star coupler receives the signal power transmitted by each node and distributes it equally to all nodes such that all nodes receive the entire traffic. The signal power reaching each node depends on the number of users and decreases as their number increases. This type of loss is known as *distribution loss* and is much smaller for the star topology compared with the bus topology. It can be virtually eliminated by integrating one or more amplifiers within the star coupler.

Some LANs distribute information to a group of subscribers, without requiring a two-way connection. A common example is provided by CATV networks in which multiple video channels are broadcast to a group of subscribers. Each subscriber selects one video channel from the entire broadcasted signal and can switch among channels as desired. Such networks fall into the category of broadcast-and-select networks, discussed later in Section 10.6.1. Although coaxial cables were originally used by the cable industry, the use of optical fibers permits the distribution of more video channels

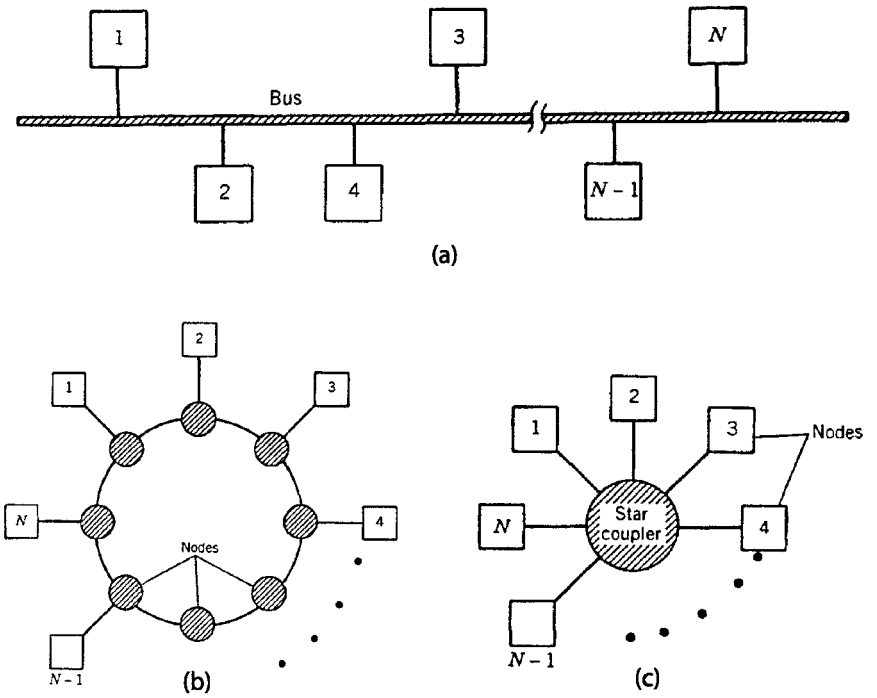

Figure 10.3: Schematic illustration of the (a) bus, (b) ring, and (c) star topologies employed for local-area networks.

because of the larger bandwidth associated with them. The advent of *high-definition* television (HDTV) also requires transmission over fibers because of the large bandwidth associated with this video format.

Most CATV networks employ the bus topology. A single optical fiber carries multiple video channels on the same optical wavelength through a technique known as *subcarrier multiplexing* (SCM). In the SCM technique, a separate microwave subcarrier is used for each video channel before the entire microwave signal is transferred to the optical domain using a suitable modulation format. Distribution occurs through optical taps that divert a small fraction of optical power to each node located on the central bus.

A problem with bus topology is that distribution losses increase exponentially with the number of taps and limit the number of subscribers that can be served by a single optical bus. Even when fiber losses are neglected, the power available at the Nth tap is given by

$$P_N = P_T C[(1-\delta)(1-C_f)]^{N-1}, \tag{10.1.1}$$

where P_T is the transmitted power, C_f is the fraction of power coupled out at each tap, and δ accounts for the insertion loss, assumed to be the same at each tap. If we use $\delta = 0.05$, $C_f = 0.05$, $P_T = 1$ mW, and $P_N = 0.1$ μW as illustrative values, N should

not exceed 60. Optical amplifiers can be used to boost the optical power along the bus periodically to solve the distribution-loss problem.

10.2 Network Protocols and Layers

The complexity of designing and maintaining a network is handled through specific protocols and a layered architecture in which network functions are divided among several layers [8]. Each layer performs a specific function and provides a specific service to the layer above it. This layered approach has proven to be quite successful. In this section we focus on several network protocols and discuss how their use in core networks has evolved with the advent of WDM technology.

10.2.1 Evolution of Protocols

The open-systems-interconnection (OSI) reference model divides any network into seven layers from the standpoint of functionality [22]. Such a scheme is known as the OSI seven-layer model. The interface between layers dictates how one layer interacts with other layers. The logical separation of layer functions makes it possible to design elaborate networks, while maintaining reliability. Each layer performs services for the layer on top of it and makes requests to the layer lying below it.

The lowest layer in the OSI reference model constitutes the *physical layer*. Its role is to provide an "optical pipe" with a certain amount of bandwidth to the *data link layer* located above it. This second layer is responsible for creating a bit stream through multiplexing and framing that is transmitted over the physical layer. The third layer is known as the *network layer*. Its function is to create a virtual circuit between any two nodes of the network and provide end-to-end routing between them. In the case of packet switching, this layer routes packets or *datagrams*. The fourth layer, known as the *transport layer*, is responsible for the error-free delivery of data between any two nodes across the entire network. The last three layers are known as the session, presentation, and application layers. They provide higher-order services and are not relevant in the context of this chapter.

In the case of circuit-switched SDH networks, the combination of bottom three layers implements the SONET protocol. For such networks, the physical layer consists of fibers, amplifiers, transmitters, receivers, and other network elements. The data link layer multiplexes various 64-kb/s audio channels into a bit stream at the desired bit rate through electrical TDM. The network layer provides switching at intermediate nodes to establish a connection between any two nodes of the network.

This simple mode of operation for SONET/SDH networks was modified when the transmission of both audio and computer data was required over the same physical layer [23]. A new packet-based protocol, known as the ATM protocol, was developed during the 1980s. It employs 53-byte packets (with a 5-byte header) that are transmitted over the network. As shown schematically in Figure 10.4(a), the ATM protocol was built on top of the SONET in the sense that the SONET infrastructure (bottom three layers that are shown shaded in the diagram) became the physical layer of the ATM network. With the advent of the Internet during the 1990s, the same idea was used to transmit Internet

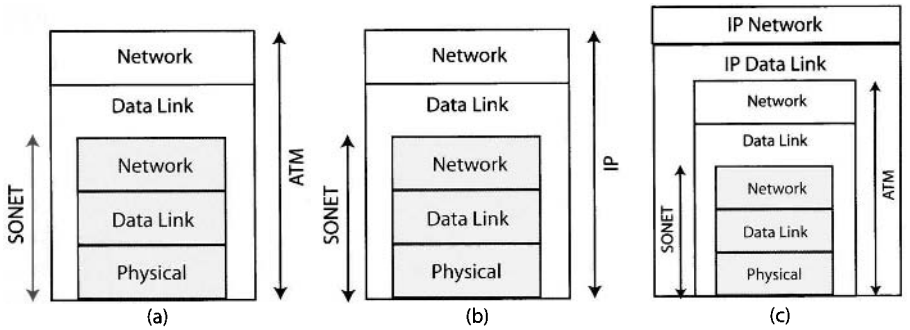

Figure 10.4: Layered architecture for SDH networks: (a) ATM over SONET, (b) IP over SONET, and (c) IP over ATM.

traffic over a SONET network [24]. As mentioned earlier, this traffic makes use of the IP protocol and consists of packets whose size can vary from hundreds to thousands of bits. A header contains information about the size, source, and destination of each packet. As seen in Figure 10.4(b), IP traffic can be carried directly over SONET using the layer model. It can also be transported over the ATM protocol. In the latter case, the network design becomes quite complicated, as shown schematically in Figure 10.4(c), because of the nesting of three separate protocols.

10.2.2 Evolution of WDM Networks

With the advent of WDM systems, ITU has introduced a new layer known as the *optical layer*. This layer sits at the bottom of the layer stack and may be thought of as a part of the physical layer. Its role is to provide lightpaths to the physical layer. The term *lightpath* refers to an end-to-end optical connection between two nodes of the network. A lightpath transmits data between these two nodes at the bit rate at which individual channels of a WDM system operate; it is also called a *clear channel*.

As shown schematically in Figure 10.5, the optical layer in fact consists of three sublayers or sections, known as the optical transmission section, optical multiplex section, and optical channel section. Not all sections need to be present at every component along the fiber-optic link. For example, only the transmission section is required at the location of each amplifier, where all WDM channels are amplified without any channel switching. In contrast, if an add–drop multiplexer is employed at a node, both the transmission and multiplex sections are needed. At more complex nodes with an optical cross-connect, all three sections of the optical layer are present.

Figure 10.6(a) shows the layered approach for WDM networks in which IP traffic is routed over ATM switches through the SONET protocol. The use of three different protocols makes it difficult to scale such networks to high volumes in a cost-effective manner. Several new schemes were developed during the 1990s to solve this problem. It is possible to eliminate the ATM layer through a switching scheme known as *multiprotocol label switching* (MPLS). As the name suggests, MPLS deals with multiple

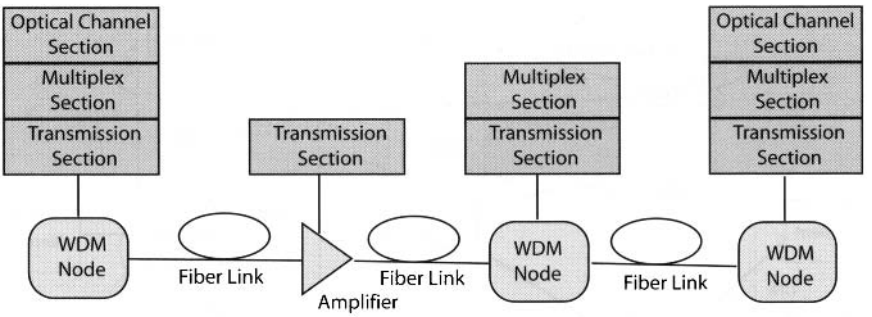

Figure 10.5: Optical layer associated with a fiber-optic WDM link. It may consist of up to three sections depending on the role of each network element.

protocols through a label attached to each packet and provides a unified scheme that can transport both the ATM and IP packets across a packet-switched network.

MPLS works by encapsulating each packet with an MPLS header containing one or more labels at the start of the packet [25]. Labels are used to specify a *forwarding equivalence class* in which all packets with the same label are treated in the same way. The labeled packets are forwarded along a label-switched path (also called an MPLS tunnel) that constitutes a virtual circuit. The entry point of the MPLS tunnel is at the ingress router and the exit point is at the egress router. Intermediate routers between these two routers are called transit or label-switching routers. At each transit router, the topmost label is examined. Based on the contents of this label, the label is either removed or swapped with a new label. The packet is then forwarded to the next transit router along the MPLS tunnel. Since the contents of the packet are not examined by transit routers, such a scheme is protocol-independent.

At the next stage of the evolution, IP traffic is planned to be routed directly over WDM networks. This scenario is referred to as IP over WDM or the *optical Internet* [10]. Such WDM networks are designed to transport packets across its nodes and require all-optical packet switching. To accommodate voice traffic with the SONET protocol, the MPLS scheme has been modified, resulting in a new scheme known as

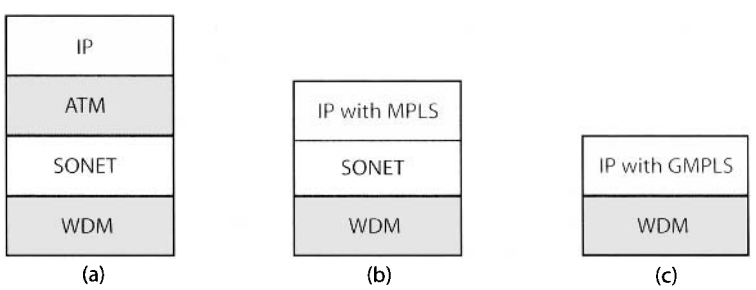

Figure 10.6: Evolution of modern WDM networks through MPLS and GMPLS schemes: (a) IP over ATM; (b) IP over SDH; (c) IP over WDM.

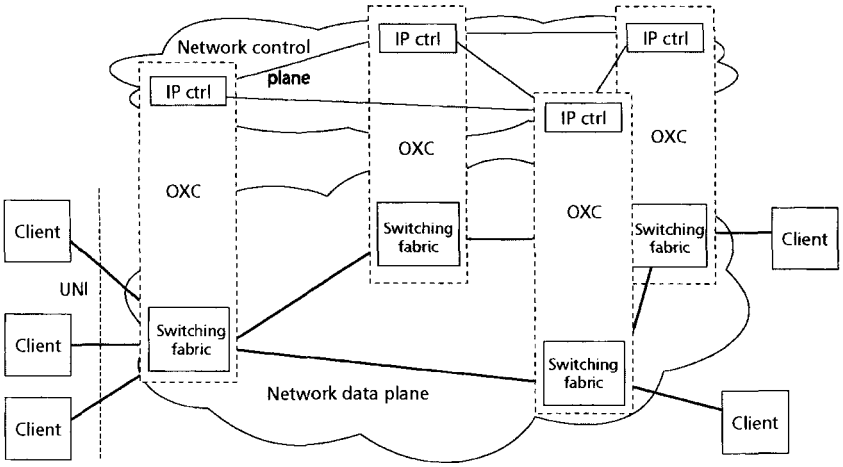

Figure 10.7: Optical transport and control planes associated with a WDM network. (After Ref. [29]; ©2002 IEEE.)

generalized MPLS, or GMPLS [26]–[28]. With GMPLS, a label can be encoded as a time slot or a specific wavelength and thus can be used to control a switch based on the TDM or WDM technique. Even spatial switching among different fibers can be employed if the GMPLS label is used to control data traffic among a set of fibers.

10.2.3 Network Planes

In the seven-layer OSI model discussed earlier, functions performed by a network were grouped into different layers. An alternative scheme divides the operation of a network into three separate planes called (1) transport plane, (2) control plane, and (3) management plane. The tasks performed by these planes are divided as follows.

As the name itself suggests, the transport plane focuses on the transport of data across a network; for this reason, it is also called the data plane. It should provide the bidirectional flow of information among various nodes, while maintaining signal quality. In the case of WDM networks, the transport plane not only provides transmission among nodes but it also performs all-optical routing, detects faults, and monitors signal quality. The routing function is performed by an OXC that can switch WDM channels at each node in a controlled fashion. In an automatic-switched optical network, all-optical switching is performed in the transport plane to set up lightpaths in a dynamic fashion.

The role of a control plane is to control electronically how optical switching is performed in the transport plane [29]–[31]. This plane supports the setup and removal of connections between any two nodes of the network. It also provides protection and restoration services in case of a failure. Figure 10.7 shows how the control plane interfaces and directs the traffic being transported over the transport plane of a WDM network. In the case of IP-over-WDM networks, one can make use of the GMPLS protocol at IP routers, as shown schematically in Figure 10.7. An alternative approach

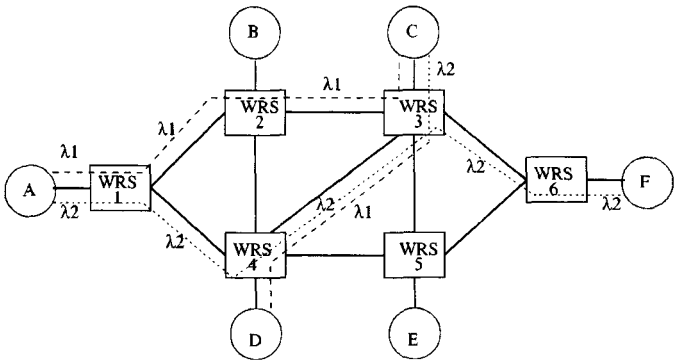

Figure 10.8: Schematic of a six-node network. Wavelength-routing switches (WRS) are used to establish lightpaths among various nodes using only two wavelengths. The dashed and dotted lines show the paths taken by the λ_1 and λ_2 channels, respectively. (After Ref. [33]; ©2002 IEEE.)

makes use of the private network-to-network interface in combination with the ATM protocol [31].

The management plane deals with the overall management of the whole network. Its role is to reconfigure WDM channels so that the bandwidth is utilized in an efficient fashion and to monitor network performance. The OSI management model, known as FCAPS and standing for fault, configuration, accounting, performance and security, is often used for telecommunication networks [32]. The ITU has also recommended a telecommunications management network reference model. It consists of four layers devoted to the management of business, service, network elements, and network performance.

10.3 Wavelength-Routing Networks

In an automatic-switched optical network, lightpaths in the transport plane connect any two nodes of the network. OXCs are used at the intermediate nodes to set up lightpaths in a fast and flexible manner [33]–[35]. Even though many WDM channels are transported simultaneously over each point-to-point link, each lightpath delivers one channel to the destination node (extracted through an add–drop multiplexer). Since individual channels in the core network operate at a bit rate of 10 Gb/s or more, it is important that traffic be aggregated appropriately to avoid wasting the bandwidth. In the case of the SONET protocol, this is accomplished through electrical TDM within access networks. In the case of the IP protocol, multiple IP packets can be combined into TDM frames, which are then aggregated into a single WDM channel transported over a lightpath. This process is referred to as traffic grooming [36]–[38].

10.3.1 Wavelength Switching and Its Limitations

Figure 10.8 illustrates a simple six-node WDM network in which two wavelengths λ_1 and λ_2 are used to establish multiple lightpaths among its six nodes through OXCs. The dashed and dotted lines show the paths taken by the channels at these two wavelengths. In the absence of wavelength converters, a lightpath must have the same wavelength on all fiber links that connect any two nodes. This requirement is referred to as the *wavelength-continuity constraint* [33]. A second obvious constraint is that two lightpaths transported over the same physical fiber link must have different wavelengths. These two constraints make the problem of wavelength assignments across the network quite complex. In fact, it may not even be possible to connect all nodes with a unique lightpath. Figure 10.8 shows two wavelength-continuous lightpaths. Nodes A and C are connected through λ_1, whereas a lightpath at λ_2 connects nodes A and F.

The design of a wavelength-routing network is simplified considerably if wavelength converters are employed within each OXC [8]. Such devices change the carrier wavelength of a channel without affecting the data carried by it (see Section 9.3 of LT1). For example, it is not possible to connect the nodes D and C directly in Figure 10.8 because WRS-3 receives data at the same wavelength λ_1 from WRS-2 and WRS-4. However, if a wavelength converter switches the wavelength to λ_2 for one of the channels, nodes D and C can be connected with a lightpath whose wavelength changes from λ_1 to λ_2 at the WRS-3.

It is easy to see from Figure 10.8 that, in general, any two nodes on the network may be connected with more than one potential lightpaths. For example, nodes A and B can be connected either through the path A-1-2-B or A-1-4-2-B, where the numbers represent different routers in Figure 10.8. Several other combinations are possible. Two schemes can be used for selecting an appropriate lightpath among various alternate routes [33]. In the case of *fixed-alternate routing*, each wavelength router in the network contains a routing table. This table assigns a priority number to various potential routes. The router tries the first route with the highest priority. If this lightpath is not possible, it selects alternate routes from the routing table until a valid lightpath is found. This kind of routing scheme is simple to implement in the control plane and it can be used to recover from a link failure.

In the second scheme, known as *adaptive routing*, the lightpath connecting two network nodes is chosen dynamically, depending on the state of the network at the time decision is being made. This approach requires an algorithm that computes the "cost" of each potential lightpath in terms of some specific design objectives. Such objectives may include, among other things, (1) efficient operation of an entire network, (2) optimum use of available bandwidth, (3) minimum number of hops at intermediate nodes, and (4) minimum use of wavelength conversion. The cost function should be designed to meet these objectives, and the algorithm chooses the lightpath with the minimum cost [33].

10.3.2 Architecture of Optical Cross-Connects

As seen in Figures 10.7 and 10.8, wavelength-routing networks employ OXCs at each node within the core network. The architecture of OXCs depends on several factors

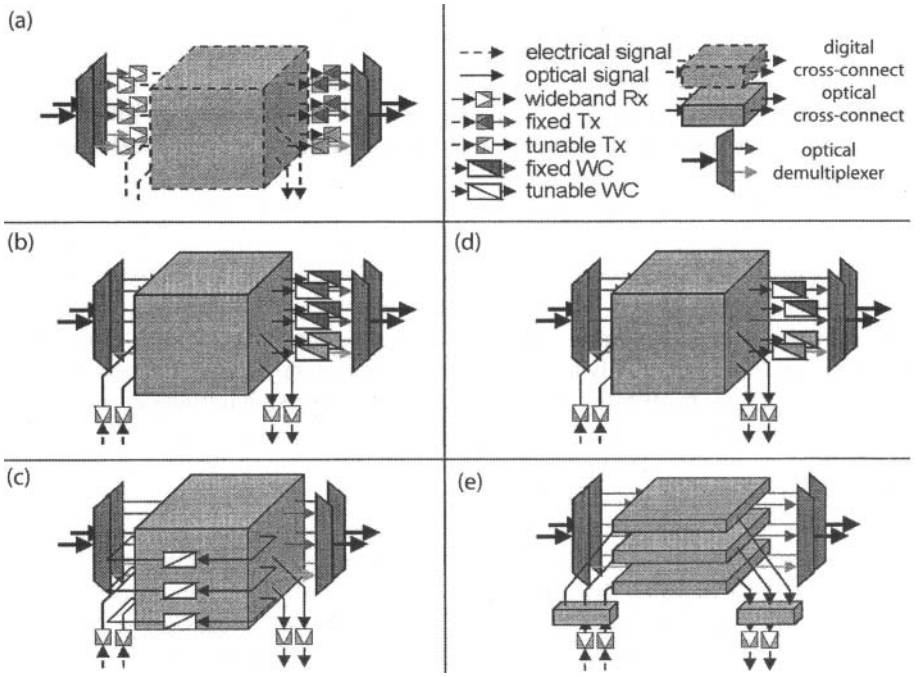

Figure 10.9: (a) An OXC with electronic switching; (b) an OXC with wavelength conversion at each node; (c) an OXC with shared conversion; (d) an OXC with partial conversion; (e) a wavelength-selective OXC with no conversion. (After Ref. [35]; ©2003 IEEE.)

and requires a tradeoff between the cost of optical hardware and the ease of network management. For example, one can utilize wavelength conversion at every network node to eliminate wavelength blocking completely, but the hardware cost then increases considerably. For this reason, OXC designs with limited wavelength conversion have also attracted attention [39]–[44].

Figure 10.9 shows five architectures for OXCs [35]. The design shown in part (a) is the traditional approach in which WDM signals reaching the node over different input fibers are first demultiplexed into individual channels (operating typically at a bit rate of 10 Gb/s) and then converted into the electric domain using a set of receivers. All electrical bit streams enter a digital cross-connect (dashed box) that routes them to different transmitters, as dictated by the control software. The output of transmitters is then multiplexed to form WDM signals that are transported over output fibers. Full wavelength conversion is possible if tunable transmitters are employed at each node. Such electronic switches were in use in commercial telecommunication systems in 2004. However, considerable effort was being directed toward developing OXCs that avoid conversion of optical signals to the electric domain at each node.

Figure 10.9(b) shows an OXC that provides the same functionality without requiring electronic conversion. In this device, demultiplexed optical channels are fed into a photonic cross-connect (solid box) consisting of a bank of directional switches that

direct each channel to a different port, as dictated by the control software. Because all signals remain in the optical domian, channel wavelength can only be changed by employing wavelength converters—devices that produce a copy of the signal at one wavelength to another wavelength. Such devices make use of nonlinear effects such as cross-phase modulation and four-wave mixing inside semiconductor optical amplifiers or silica fibers (see Section 9.3 of LT1).

The number of wavelength converters required in Figure 10.9(b) equals MN when the node is designed to handle traffic on M fibers, each carrying N wavelengths. To reduce the hardware cost, several solutions are possible. In one approach, wavelength converters are employed only at a few intermediate nodes [44]. In another, wavelength converters are shared in a loop-back configuration as shown in part (c). The option shown in part (d) employs only a small number of wavelength converters at each node (partial conversion). In all cases, limited wavelength conversion introduces some probability of wavelength blocking. This probability can be reduced considerably if wavelength converters are made tunable such that they accept input signals over the entire WDM-signal bandwidth and can also produce output in the entire range.

The final design shown in Figure 10.9(e) is the most economical as it eliminates all wavelength converters. Such a device is referred to as the wavelength-selective OXC (see Section 9.4.1 of LT1). It is designed to distribute all input signals at a specific wavelength to a separate switching unit. If each WDM signal consists of N distinct wavelengths, N switching units are employed. Each unit consists of a $M \times M$ switching fabric that can be configured to route the signals at a fixed wavelength in any desirable fashion. Extra input and output ports can be added to allow the dropping or adding of a local channel at that wavelength. As the number of ports required on a single switching unit is relatively small (it equals the number of incoming and outgoing fibers), such devices are relatively easy to fabricate, and their use helps to lower the OXC cost. Wavelength-selective OXCs can be made with silica-on-silicon technology. They can also be fabricated with the InP technology used commonly to make semiconductor lasers and detectors.

Wavelength-selective OXCs are transparent to both the format and bit rate of the WDM signal. They are also cheaper and help to reduce overall cost. However, these advantages are overshadowed by the wavelength-blocking nature of such a cross-connect. Their use in a realistic network requires sophisticated routing software and wavelength assignment algorithms. The constraint that every lightpath must use the same wavelength across all point-to-point links eventually limits the capacity of the network. How much capacity is lost depends on the network topology that determines the average number of hops required for connecting two nodes of the network. In general, short lightpaths with only a few hops experience little or no wavelength blocking.

The number of wavelength converters required to eliminate wavelength blocking depends on the algorithm used for assigning wavelengths and routing channels across the network. In the case of a static network (permanent lightpaths), even 5% wavelength conversion was found to eliminate wavelength blocking in a 24-node network [42]. In the case of dynamic networks (traffic-dependent lightpaths), the number of converters needed at a node changes with time in a random fashion. However, if the bandwidth utilization on average is kept in the range of 50 to 60%, it is relatively easy to establish lightpaths with a continuous wavelength with just a few wavelength con-

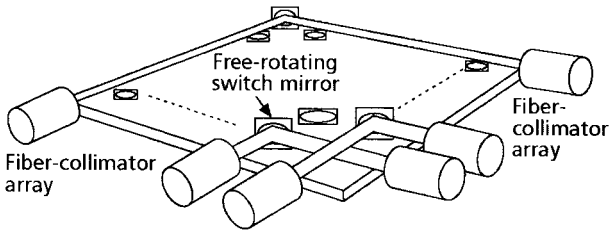

Figure 10.10: Schematic of a two-dimensional MEMS-based OXC. Microscopic mirrors are rotated to connect input and output fibers in an arbitrary fashion. (After Ref. [48]; ©2002 IEEE.)

verters. Several optimization methods have been developed for wavelength assignment in such networks [39]–[44].

10.3.3 Switching Technologies for Cross-Connects

All OXCs need a switching fabric capable of interconnecting a large number of input and output ports in an arbitrary fashion with suitable electronic control signals. As discussed in Section 9.1 of LT1, several technologies can be employed for this purpose. Examples include electro-optic switches based on $LiNbO_3$ waveguides, thermo-optic switches based on silica waveguides and fabricated with silica-on-silicon technology, microscopic mirrors built with micro-electro-mechanical system (MEMS) technology, bubble switches based on total internal reflection and fabricated with ink-jet technology, and liquid-crystal switches based on birefringence-induced polarization changes.

The MEMS technology has attracted the most attention for constructing OXCs as it can provide relatively compact devices [45]–[52]. It is used to fabricate microscopic mirrors that can be rotated by applying an electric signal. The MEMS switches are divided into two broad categories, referred to as two-dimensional (2-D) and three-dimensional (3-D) configurations, depending on the geometry used to interconnect the input and output fibers.

Figure 10.10 shows schematically the configuration of a two-dimensional OXC in which a two-dimensional array of free-rotating MEMS mirrors is used to switch light from any input fiber to any output fiber. The entire matrix of microscopic mirrors can be integrated monolithically on a silicon chip [45]. The input and output fibers are placed on two neighboring edges of the chip and are aligned with the location of the micromirrors precisely. An input signal from one of the fibers can be forced to couple to any output fiber by simply flipping the mirror lying at the intersection of these two fibers. The switching time typically exceeds 5 ms for MEMS mirrors. Insertion losses depend on the size of the chip but remain close to 3 dB for a 16×16 switch with a chip size of about 2×2 cm^2 (1-mm spacing between two neighboring mirrors). The chip size scales linearly with the number N of input and output ports but the number of mirrors increases as N^2. Because of this quadratic dependence on N, the two-dimensional geometry is rarely used when N exceeds 100.

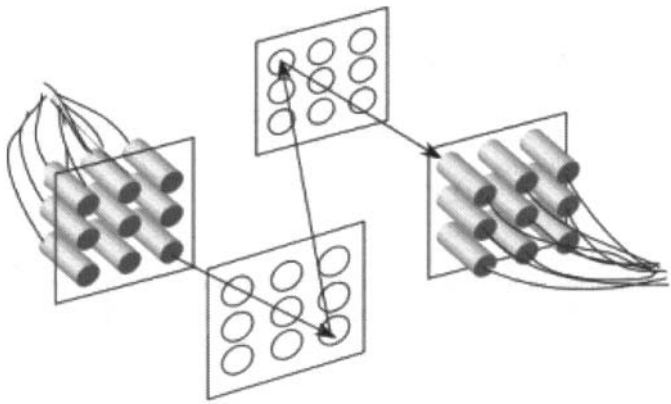

Figure 10.11: Schematic of a three-dimensional MEMS-based OXC. Two MEMS devices containing arrays of microscopic mirrors connect any input fiber to any output fibers by rotating mirrors in an analog fashion (After Ref. [52]; ©2004 IEEE.)

The three-dimensional configuration is preferred for MEMS-based OXCs when the number of input and output ports is relatively large. Figure 10.11 shows schematically how two MEMS devices, each with N mirrors, can be used to interconnect N input fibers with N output fibers. Since only $2N$ mirrors are required in the three-dimensional configuration, it can be scaled to thousands of ports. The main difference from the two-dimensional architecture is that each mirror should operate in an analog fashion and be able to tilt freely around two axes. Such devices have been fabricated with the MEMS technology, the so-called LambdaRouter being one example [46]. Since 2000, three-dimensional MEMS switches have been used for developing OXCs with a large number of ports. Indeed, by 2003, switching fabrics that could interconnect more than 1,000 input and output ports have been realized, while keeping insertion losses below 4 dB for any two ports [50]. The electronics and software required to control such OXCs have also been developed [51].

The successful operation of OXCs has been realized in several test-bed demonstrations. The use of GMPLS in telecommunication networks was demonstrated in a 2003 test-bed demonstration in which OXCs (built with electronic switching elements) from two different vendors were used to set up and tear down lightpaths among different nodes [53]. In a Japanese field trail, an arrayed-waveguide (AWG) router was employed to show wavelength switching in a LAN configured with star topology [54]. However, such OXCs were yet to be deployed within commercial systems by the end of 2004.

10.4 Packet-Switched Networks

As discussed earlier, Internet traffic consists of IP packets that are switched electronically by routers using destination information contained in the packet header. If the dream of an *all-optical Internet* (with IP over WDM) were to be realized, IP packets

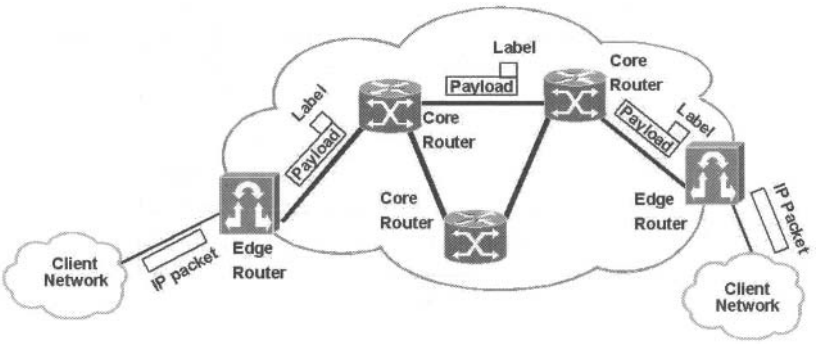

Figure 10.12: Schematic illustration of the optical label swapping technique for packet-switched networks. Edge routers assign and remove the label, while core routers swap it with new ones as they route the packet through the core network. (After Ref. [61]; ©2003 IEEE.)

must be switched optically at each node within the core network. Such packet-switched optical networks would make use of "optical routers" whose design has been under investigation since the advent of WDM technology [55]–[62]. This section focuses on a technique known as optical label swapping.

10.4.1 Optical Label Swapping

Optical routers in a packet-switched network make use of an optical label that is coded with the routing information such as the destination address. This label is added on top of the electronic header associated with all IP packets. It helps to transport packets across the core network in an all-optical fashion, that is, contents of an IP packet are never converted into the electric domain until the packet arrives at an edge router.

Two different techniques can be used to assemble packets in the form of an optical bit stream. In one scheme, known as slotted packet switching, the bit stream consists of fixed-duration time slots that are filled with packets in a synchronous fashion. In such a slotted network, all packets have the same size, and some time slots may remain empty depending on the level of traffic congestion. An optical label is attached to each time slot as switching is performed on a slot-by-slot basis. Some TDM techniques make use of short optical pulses (width <5 ps for a 100-Gb/s bit stream) and require ultrafast optical switching devices to process the label [63]. Another TDM technique transmits multiple packets at different wavelengths simultaneously using a concept known as the photonic slot. We discuss such slotted techniques in Section 10.5.

In the scheme shown schematically in Figure 10.12, IP packets reaching an edge router are assembled, as they arrive, to form a nearly continuous bit stream (statistical multiplexing). If two or more packets arrive simultaneously, a buffer is used to hold them temporarily. Each packet is assigned an optical label that contains all routing information and is sent toward a core router located on one of the intermediate nodes that the packet must pass through. The core router reads the label, swaps it with a new label, and forwards it toward the next node. It may also perform wavelength conversion on the packet, if necessary. Throughout this process, the contents of the

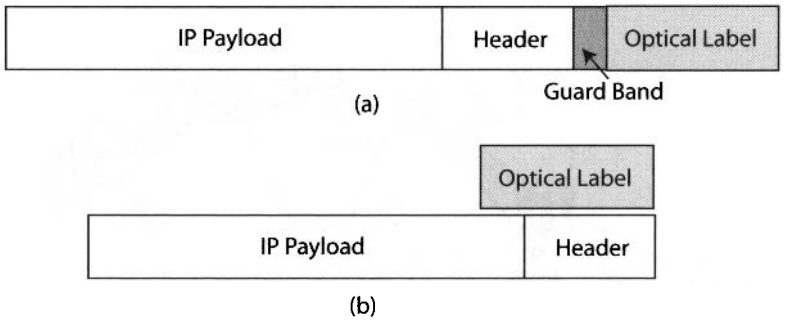

Figure 10.13: Schematic illustration of two label-coding schemes: (a) serial label next to the IP header with a guard band and (b) label transmitted in parallel with the packet through subcarrier multiplexing.

IP packet (both the header and payload) are not converted into an electronic form by any core router, that is, only the optical label is used for all routing decisions. Once the packet reaches an edge router, the optical label is removed, and the packet itself is processed electronically to recover the actual data transmitted. Such a scheme is referred to as *optical label swapping*. All routing functions at the internal nodes (such as label recovery, label swapping, packet regeneration, and wavelength conversion) are handled without converting the contents of a packet into the electric domain.

To perform the routing and forwarding functions, each optical router makes use of an internal routing table that converts the IP addresses of various nodes of the network into optical labels at assigned wavelengths. This table is generated and distributed across the network through a generalized version of the MPLS protocol. Core routers use the routing table to determine the new label and swap the current label with the new one before forwarding it to the next node. They may also change the wavelength of the packet, if required. As discussed later in Section 10.4.3, core routers also employ mechanisms for avoiding packet collisions that occur when two packets arrive at a node simultaneously and both of them need to be directed toward the same output port.

10.4.2 Techniques for Label Coding

An advantage of optical label swapping is that labels can be produced and processed at a bit rate lower than that used for packets so that high-speed electronic processing is not needed at optical routers. Even the modulation format may be different for the label attached to each packet. For example, labels may utilize the NRZ format at 2.5 Gb/s even though packets themselves are transmitted at 10 or 40 Gb/s using the RZ format or its variants. The separation of packet and label coding formats is useful in practice because it makes the implementation of label swapping transparent to the actual format and bit rate employed for transmitting data across the network.

Two techniques, shown schematically in Figure 10.13, are commonly used for attaching optical labels to IP packets. In one approach, the label is attached serially to the IP packet (called a bit-serial label) at the same wavelength [58]. It is separated

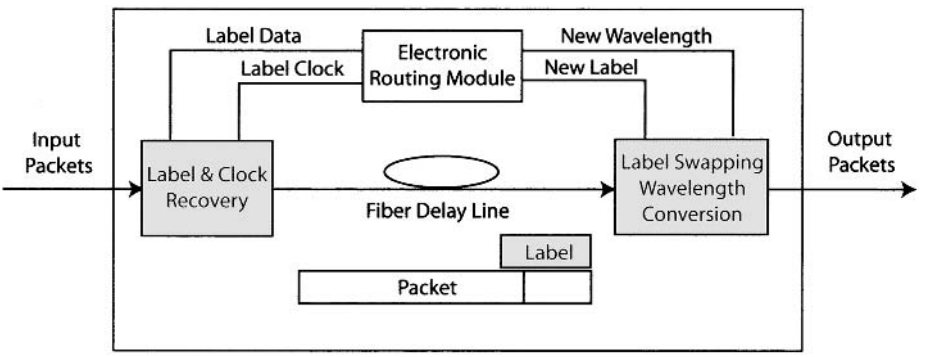

Figure 10.14: Schematic illustration of functions performed by a core router designed to process packets with SCM labels.

from the packet header by a "guard band" that is used to guard against temporal delays encountered during label processing. The router should be able to recognize the serially attached label and process it separately from the packet itself. The use of bit-serial labels requires synchronization between the packet and the label that is difficult to realize in practical networks. Another disadvantage of this approach is that the network throughput is reduced because no packets can be transmitted during the time slot occupied by the label and the guard band.

A simple alternative is to transmit the label in parallel with the IP packet such that the two overlap temporally but can still be separated in the spectral domain. The use of different carrier wavelengths for the packet and the label is possible but it wastes the fiber bandwidth. An alternative is provided by the SCM technique, discussed earlier in the case of cable-television networks. In the context of optical packet switching, a single microwave subcarrier at a frequency higher than the packet bit rate (>12 GHz for 10-Gb/s channels) is used to transport the label and the packet at the same optical wavelength [61]. No guard band is necessary as the label is transmitted in parallel with the packet. Moreover, the label can be as wide as the packet itself as the only requirement is that its duration should not exceed the time slot occupied by the packet. This feature allows the use of a much lower bit rate for the label compared with that of the packet. The modulation format of the packet is also independent of that used for the packet.

Figure 10.14 shows the design of a core router when SCM labels are used for packet switching [58]. The label-processing module (first gray box) uses a few percent of the signal power to decode the label and recover the clock. The rest of the signal is passed through an optical delay line (a fiber of suitable length) whose length is chosen to match the label-processing delay and to ensure that the packet reaches the label-swapping module (second gray box) just in time. The label-processing module first converts the optical signal into the electric domain and then passes it through a high-pass filter so that packet bits are removed from it [57]. The filtered signal is converted to baseband frequencies through homodyne detection using a local oscillator at the microwave subcarrier frequency, thus recovering the label. The label and the clock

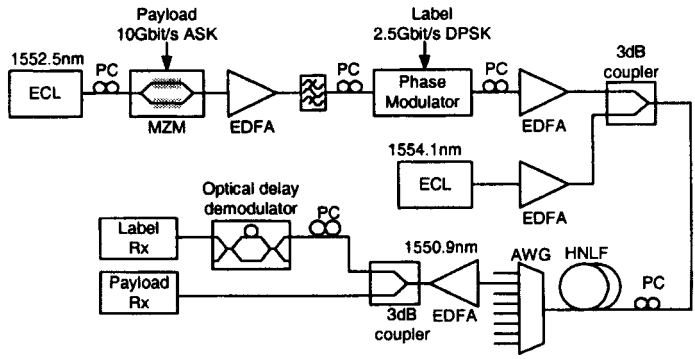

Figure 10.15: Experimental setup for superimposing the label on top of the packet through the DPSK format. ECL, MZM, and PC stand for external-cavity laser, Mach–Zehnder modulator, and polarization controller, respectively. (After Ref. [65]; ©2003 IEEE.)

are sent to the cental routing module, where electronic logic circuits and a routing table are used to find the node toward which the packet must be directed. This unit also determines the new SCM label and the wavelength assigned to the packet. This information is used by the label-swapping unit to produce the outbound packet with the new label.

A drawback of the SCM technique is that the interference between the label and packet contents is unavoidable, as the two occupy the same temporal window. SCM also requires the use of high-frequency microwave electronics because the frequency of microwave subcarrier must exceed the bit rate of the packet. Its use becomes questionable when the channel bit rate exceeds 10 Gb/s. Al alternative solution is to employ orthogonal modulation schemes for the packet and the label [64]–[66]. The basic idea is to use the same carrier wavelength for the packet and the label but employ a combination of amplitude- and phase-modulation techniques such that the two can be separated in spite of their overlapping nature in both the time and frequency domain.

In a 2003 experiment, the packet bits were modulated at 10 Gb/s using the ASK format, while the DPSK format was used at 2.5 Gb/s for the optical label [65]. Figure 10.15 shows the experimental setup schematically. At the transmitter end, two separate modulators are used to impose the ASK and DPSK formats on the same optical carrier. At the receiver end, the label is extracted using an optical delay-line demodulator capable of decoding a DPSK signal (see Section 2.3.4). It was necessary to lower the extinction ratio of the packet bits to detect the DPSK label successfully. In this experiment, the extinction ratio was reduced to 3 dB to ensure that the label was decoded with a receiver sensitivity that was 3 dB better than that of the payload. As shown in Figure 10.15, the FWM inside a highly nonlinear fiber (HNLF) can be used to convert the wavelength of the packet by launching a CW beam at an appropriate wavelength.

A large reduction in the extinction ratio may not be acceptable for core networks as it is likely to limit the maximum distance over which packets can be routed over. In a technique known as "optical carrier suppression and separation," a dual-arm $LiNbO_3$ modulator is used to create two sidebands while suppressing the optical carrier [67].

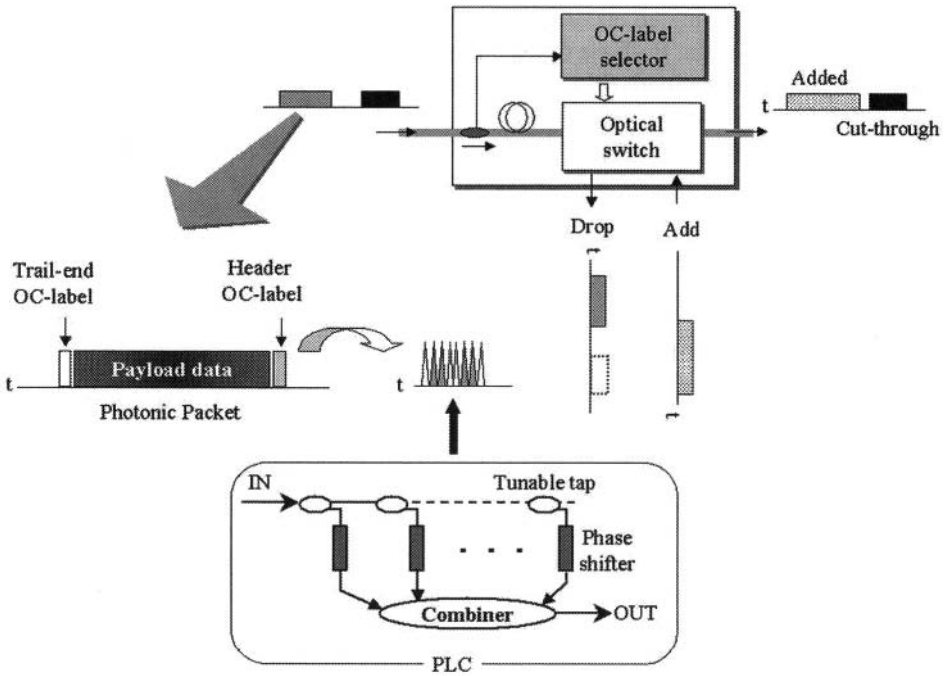

Figure 10.16: Design of an optical switch used to add or drop the packets depending on CDM-encoded labels. (After Ref. [71]; ©2004 IEEE.)

For example, if the carrier is modulated sinusoidally at 10 GHz, two sidebands separated by 20 GHz can be generated by this technique. The packet and the label are transmitted through the network on these two distinct sidebands. Experimental results show that 10-Gb/s packets with 2.5-Gb/s labels can be routed through a DWDM network designed with standard 50-GHz channel spacing on the ITU grid. Other advantages offered by this technique include high spectral efficiency, high-speed operation, and little crosstalk between the packet and the label.

All the preceding techniques process optical labels in the electric domain. A technique that permits the label-based routing of packets in the optical domain makes use of code-division multiplexing (CDM). As discussed in Section 1.4.3, CDM allows transmission of several data channels at the same carrier wavelength through orthogonal codes. If orthogonal codes are employed for packets intended for different nodes, it becomes possible to design an optical device that switches individual packets based on these codes [68]–[71]. Such a packet-selective switch is sometimes referred to as the photonic add–drop multiplexer. The basic idea consists of assigning to each node a unique CDM code. If labels are coded with one of these codes, each node can pass or divert them after reading the label.

Figure 10.16 shows the architecture employed for a CDM-based packet switch in a 2004 experiment [71]. Each packet reaching the switch contains serial labels at both the head and tail ends. The head-end label consists of multiple pulses whose relative

phases are shifted using an encoder (see bottom part) according to the code assigned to the destination node. Both the CDM encoders and decoders can be built in the form of a planar lightwave circuit (PLC) with silica-on-silicon technology. At the switch, a small portion of incoming signal is directed toward a label-processing unit containing the decoder, where an optical correlation technique is used to compare the label with the CDM code assigned to that node. The packet is dropped only if the code matches; otherwise, it is passed unchanged. The label at the tail end of the packet is used to reset the switch from the cross to bar state after the drop. New packets can also be added by such a switch.

10.4.3 Contention Resolution

Packet-switched optical networks may route each packet through several core nodes before it reaches its destination. Contention occurs when two packets arrive at a node simultaneously and both of them need to leave from the same output port of the router. In electronic routers, this problem is solved by storing one packet temporarily (until it can be forwarded) in a buffer consisting of a random-access memory (RAM) module. This conventional store-and-forward method of contention resolution is not a viable option for optical packet switching because optical buffers capable of storing packets while providing random access are not available. Optical buffers are made using fixed-length fibers that can only delay the packet by a fixed amount.

Contention resolution for optical packets makes use of three distinct processes in time, spectral, and space domains [72]–[75]. Fiber-optical delay lines acting as optical buffers are employed to delay one of the two conflicting packets by a fixed amount in the time domain. One can also employ wavelength conversion to resolve the conflict since optical routers are designed to handle two packets at different wavelengths simultaneously. Compared with the time-domain resolution, wavelength conversion induces no additional latency. A third approach deflects the packet to a different node with a suitably swapped label so that it can be routed toward its destination by that node (conflict resolution in the space domain). In essence, the entire network is used for storing one packet temporarily when two packets contend for the same destination. The combination of these three techniques can help to improve the network efficiency considerably.

The use of deflection routing for contention resolution leads to the possibility that some packets may end up hopping from node to node within the core network for a long time. To guard against this possibility, the optical label can be coded with the number of maximum allowed hops; the packet is discarded if that limit is reached. This approach is similar to the conventional time-to-live bits used in the electronic switching of IP packets. The design objective of any optical router then becomes to minimize the packet-loss rate while maximizing the network throughput. The router should also employ some technique for monitoring network performance.

Figure 10.17 shows the architecture of an optical router designed for edge-to-edge contention resolution in a packet-switched network [74]. It has multiple inputs and output ports through which WDM signals enter and exit. A demultiplexer is used after each input port to recover channels at individual wavelengths. The bit stream in each channel consists of packets with a SCM label attached to each of them. A grating-

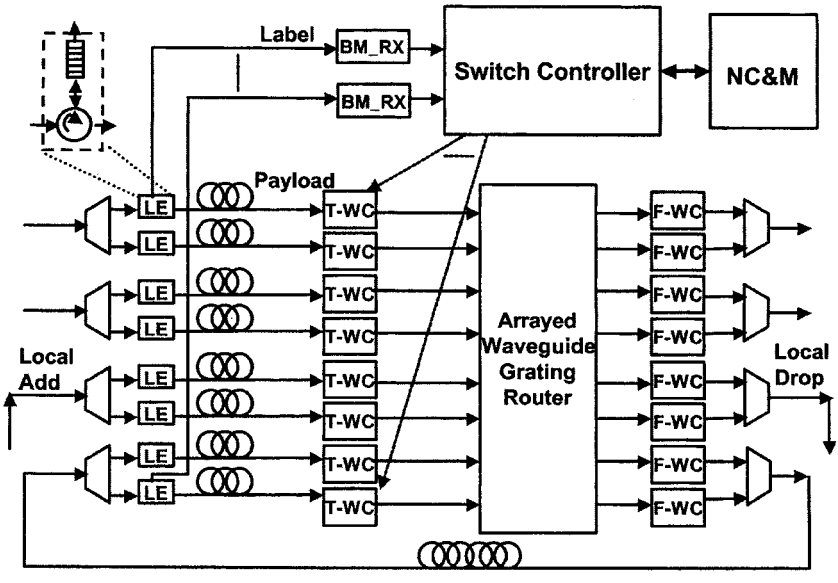

Figure 10.17: Architecture of an optical router designed for contention resolution in packet-switched networks. LE, WC, BM-RX, and NC&M stand for label extractor, wavelength converter (T: tunable; F: fixed), burst-mode receiver, and network control and management, respectively. (After Ref. [74]; ©2003 IEEE.)

circulator combination is used to extract the label. A burst-mode receiver converts the label into electric domain and sends it to the switch controller. The switch itself consists of a set of tunable wavelength converters, an AWG router, and another set of fixed-wavelength converters. Moreover, some input and output ports are interconnected through fiber delay lines. With this arrangement, packet collisions can be avoided using a combination of temporal delays, conversion of packet wavelengths, and rerouting of selected packets. Two sets of wavelength converters are employed so that packet wavelengths can be temporarily changed to specific wavelengths internal to the switch to enure that the AWG router functions properly. The second set of wavelength converters are used to change the wavelength back to the original one. Such a router performs in a strictly nonblocking fashion. It is also possible to drop and add packets for the traffic destined for the node where the optical router is located.

10.5 Other Routing Techniques

Packet-switched networks route individual packets that last for less than 1 μs at high bit rates (up to 40 Gb/s) prevalent in modern core networks. Optical routers used for packet switching not only must operate at relatively high speeds but they also suffer from packet-contention problems that become more and more severe as the network throughput increases. Several routing schemes have been proposed to solve this problem. We focus on a few of them in this section.

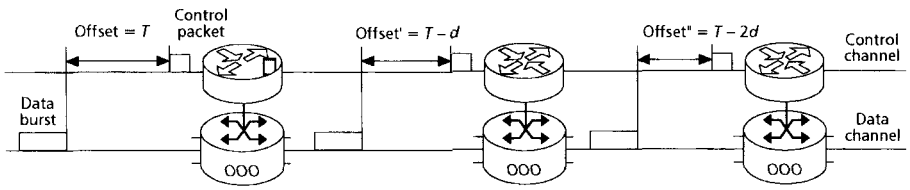

Figure 10.18: Schematic illustration of optical burst switching. A control packet is sent before the optical burst to set up a lightpath across the core network. (After Ref. [82]; ©2004 IEEE.)

10.5.1 Optical Burst Switching

In addition to circuit and packet switching, a new type of scheme known as *optical burst switching* has been proposed for optical networks [76]–[82]. Whereas a circuit establishes a connection between two network nodes that may last for minutes or hours, a 1,000-byte packet can be transmitted in less than a microsecond at a bit rate of 10 Gb/s, and this time drops further by a factor of 4 for 40-Gb/s channels. Optical burst switching is designed to operate between these two extremes. It transmits bursts of data (e.g., a group of packets with the same destination) through the core network by first setting up a connection and reserving resources. As a result, the lightpath established in the physical layer between the two egress nodes lasts for the entire duration of the burst that may range from a few milliseconds to minutes, depending on the burst size.

How is the lightpath set for optical burst switching? Clearly, resources must be allocated electronically in the control plane, even though each burst itself is switched in the optical domain. Figure 10.18 shows a scheme in which a control packet is first transmitted. This packet is processed electronically in the control plane with the help of the GMPLS protocol, using the same technique utilized for packet-switched networks, to set up a lightpath (or an MPLS tunnel) through the core network. The control packet is transmitted at a wavelength different from the burst itself, but it contains all the information, such as the duration and the destination of burst, that is needed to route the burst optically through the core network. As the packet passes through, all optical cross-connects are configured to set up a lightpath between the source and the destination nodes for the entire burst duration. The optical burst is then transmitted over this lightpath without requiring any other further switching or processing.

The temporal offset T between the control packet and the burst should be chosen properly (see Figure 10.18). It should be large enough for the packet to reach the destination node and to set a lightpath across the core network. At the same time, it should not be much larger than that to avoid wasting the network bandwidth. This creates a dilemma since the exact path taken by the packet may not be known in advance. Many protocols have been developed to address this issue and are known under names such as reserve-a-fixed-duration, tell-and-wait, tell-and-go, and just-enough-time [79]. The last protocol assumes that information about the potential path taken by the control packet is available to the source node via the control plane. It also assumes that the processing delay d encountered by the control packet at each intermediate node does not exceed d, as shown schematically in Figure 10.18. For a lightpath with n intermediate nodes, the total delay would then not exceed nd. The source node sends a control

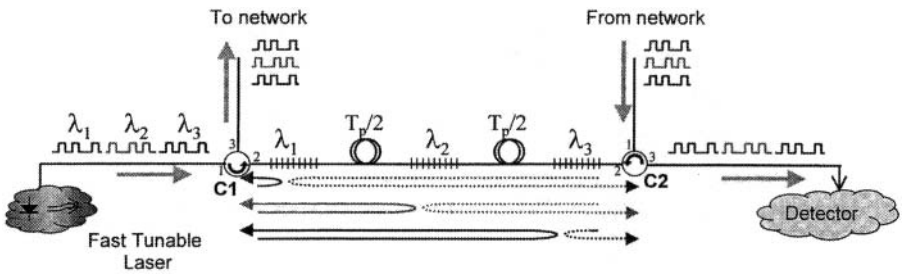

Figure 10.19: Scheme for stacking and unstacking packets of different wavelengths within a single photonic slot. C1 and C2 are optical circulators and T_p is the duration of a photonic slot. Solid and dotted paths show the reflection of packets by gratings. (After Ref. [86]; ©2003 IEEE.)

packet to reserve the bandwidth, and the data burst follows the packet after a temporal delay of $T = nd$.

Since optical burst arrives at intermediate nodes after some delay, the just-enough-time protocol also employs the delayed-reservation technique in which bandwidth allocation at each node is delayed until the instant the burst is expected to arrive. Moreover, the bandwidth is reserved just for the duration of the burst so that network resources are available immediately after the burst has passed through. This approach helps to increase the network throughput since intermediate nodes can process other data rather than waiting for the burst to arrive.

10.5.2 Photonic Slot Routing

A synchronous routing scheme known as *photonic slot routing* has been proposed for packet-switched optical networks [83]–[87]. Like any slotted network, it makes use of a temporal slot whose duration can vary from a few nanoseconds to a few seconds. The new feature of this routing scheme is that each slot may contain multiple packets of different wavelengths, all aligned precisely within the same temporal window. Such a multiwavelength slot is referred to as the *photonic slot*. Packets are assembled into photonic slots at an ingress node such that each photonic slot contains packets destined for the same egress nodes. As each photonic slot is routed through the network as a single unit, there is no need to demultiplex individual wavelengths at intermediate nodes. Since photonic slot routing makes use of WDM to only transport more packets, it eliminates the need of WDM components within the core network; this feature helps to reduce overall cost and also makes the network scalable.

An important question is how multiple packets at different wavelengths can be stacked within the same photonic slot to form a composite optical packet. Figure 10.19 shows a device that can stack as well as unstack photonic slots using fiber gratings and delay lines in combination with two optical circulators [86]. The gratings are designed to reflect lights at specific wavelengths at which packets are produced using a laser. They are separated from each other by an amount $T_p/2$, where T_p is the duration of the photonic slot. Such a device reflects multiple packets of different wavelengths

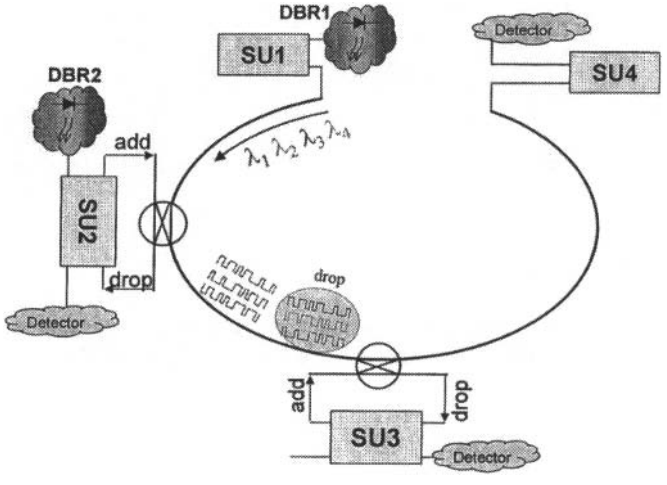

Figure 10.20: Four-node ring network used for photonic slot routing using four wavelengths with 100-GHz spacing. The stacker/unstacker unit (SU) at each node is combined with a $LiNbO_3$ switch for dropping and adding photonic slots. (After Ref. [86]; ©2003 IEEE.)

arriving in a serial fashion with just the right delay that they occupy the same temporal window after they exit from port 3 of the optical circulator. The same device can unstack composite packets and send them to a detector after performing the reverse operation in which the composite packet is split into individual packets separated in time.

The potential of photonic slot routing was demonstrated in a 2003 experiment [86] using a four-node ring network with 15-km circumference as shown schematically in Figure 10.20. It employed the stacking device of Figure 10.19 with four wavelengths spaced 100 GHz apart. Nodes 1 and 2 generate composite packets destined for other nodes using a tunable distributed Bragg reflector (DBR) laser, while nodes 3 and 4 are equipped with photodetectors. The output wavelength of this laser could be changed by 100 GHz in less than 5 ns. All nodes contained a stacker/unstacker unit in which adjacent fiber gratings were separated by 200 m (with a slot duration of 2 s). Nodes 2 and 3 were equipped with a $LiNbO_3$ switch (with a switching time of 20 ns), whose operation was independent of input wavelength or input polarization. In the example shown in Figure 10.20, the switch at node 2 either drops packets from a photonic slot from node 1 or passes them to node 3. It can also add a composite packet to an empty photonic slot. Node 3 provides the same functionality. It was found that 1-Gb/s packets could be routed through the ring network while maintaining good performance.

Although photonic slot routing was originally proposed for access networks [83], it can be adopted for core networks by attaching a label to each photonic slot [84] that is routed through the core network using the label-swapping technique discussed in Section 10.4. The slot label not only contains information about the destination but also indicates which wavelengths in the slot are occupied. At each intermediate node, individual packets are unstacked from the photonic slot, switched by a wavelength-

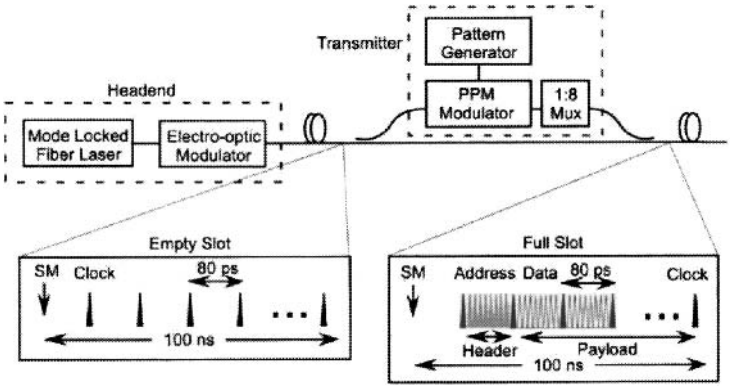

Figure 10.21: Transmitter configuration for a TDM network designed with the PPM format. Insets show an empty slot with 12.5-GHz clock pulses and the filled slot after header and payload bits have been inserted. (After Ref. [93]; ©2002 IEEE.)

insensitive core router, and then assembled back into different photonic slots depending on their destination. Such networks do not need any WDM components but they need to maintain synchronization of photonic slots at each node. For example, the boundaries of all incoming photonic slots from different input fibers are unlikely to coincide because of different link lengths. Clearly, adjustable delay lines are needed to ensure the synchronization of incoming photonic slots. Another issue is related to fiber dispersion. Different packets in each photonic slot do not take the same time to traverse a fiber link because of the wavelength dependence of group velocity in optical fibers. As a result, packets of different carrier wavelengths do not remain aligned within the photonic slot. This problem can be addressed by making the slot wider than the packet size, but this solution reduces the network throughput and efficiency. A better approach would be to employ dispersion management.

10.5.3 High-Speed TDM Networks

Another TDM-based routing scheme combines low-bit-rate packets serially in the same slot by compressing them temporally, resulting in a high-speed bit stream at a bit rate of 100 Gb/s or more. Similar to the case of a photonic slot, multiple packets are transported within one slot, but they all have the same wavelength. Such high-speed TDM networks have attracted considerable attention for applications related to LANs and MANs [88]–[94].

Figure 10.21 shows the transmitter configuration for a 100-GHz TDM network designed with a 100-ns-long time slot [93]. An actively mode-locked fiber laser operating near 1,550 nm generates 2-ps pulses at a 12.5-GHz repetition rate. These pulses serve as an optical clock for the whole system. A $LiNbO_3$ modulator is used to remove one of every 1,250 clock pulses; the absence of this clock pulse indicates the beginning of each TDM slot. The 80-ps spacing between two neighboring clock pulses is used to store 8 data bits (1 byte). The whole slot contains 1,250 bytes, a few of which can be

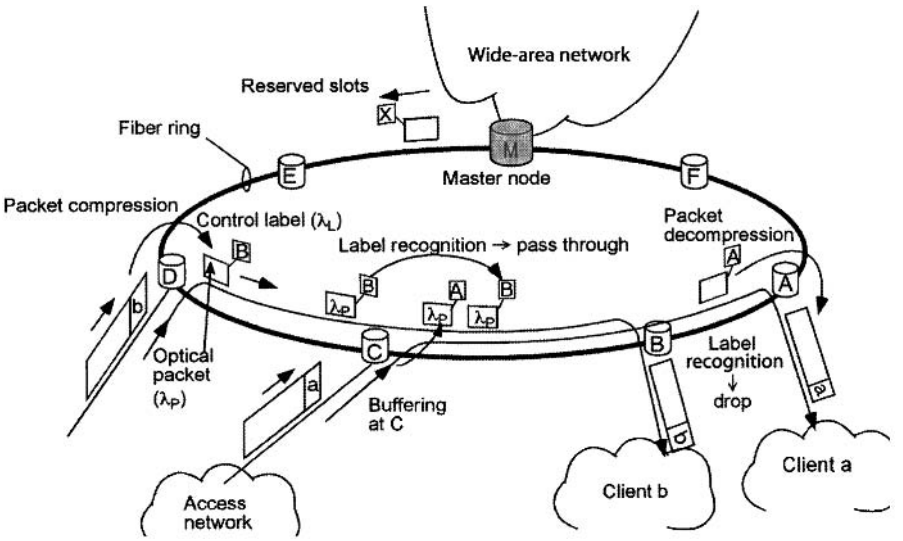

Figure 10.22: A high-speed slotted ring network in which optical labels at a wavelength different from that of packets are used for adding and dropping packets at various nodes. (After Ref. [94]; ©2002 IEEE.)

used to store the packet header. The header and data-payload bits are inserted into an empty TDM slot using pulse-position modulation in combination with delay lines that create 8 pulses from each clock pulse. The use of pulse-position modulation helps to mitigate pattern-dependent effects occurring in logic gates based on semiconductor optical amplifiers (see Chapter 10 of LT1). With the addition of 12.5-Gb/s clock pulses, the total bit rate is 112.5 Gb/s for this configuration. At the receiver end, the header of each packet is processed optically to route the packet using high-speed optical logic circuits built with an ultrafast nonlinear interferometer in the Mach–Zehnder or Sagnac configuration (see Section 10.3 of LT1).

Such a high-speed TDM network suffers from several problems related to packet synchronization and contention resolution. Most of these problems can be solved if optical labels are employed for routing. Figure 10.22 shows schematically a ring network based on this concept. Packets arriving from access networks at an ingress node are stored in an electronic buffer. When an empty time slot is detected, the stored packets are used to fill it with bits at the packet wavelength λ_p and the bit rate employed within the ring (typically >40 Gb/s). At the same time, an optical label with all the routing information is transmitted at a much lower bit rate (say, 2.5 Gb/s) using a different wavelength λ_l. As packets circulate, the label contents are examined at each node by converting the label to the electric domain. If the destination address matches with that of the node, the packet in that time slot is dropped at the egress node. Otherwise, it is passed to the next node on the ring. No label swapping is needed in the ring configuration. If the same scheme is used for a core network with mesh configuration, each node should swap the label for routing purposes. The use of a control label at a wavelength different than that used for filling time slots makes this scheme similar to optical burst

switching discussed earlier. The main difference is that TDM slots are of fixed duration and typically last <1 μs, in contrast with the bursts that have variable durations and employ statistical multiplexing. Each time slot can still carry multiple packets because of compression and decompression of packet bits at the ingress and egress nodes.

10.6 Distribution and Access Networks

The preceding three sections dealt mostly with WANs or core networks that transport WDM channels operating at relatively high bit rates (10 Gb/s or more) across a wide geographical region. In this section, we focus on LANs and MANs that operate in a limited geographical area, employ lower bit rates, and may also provide access to the core network. We begin with the broadcast-and-select networks and then consider passive optical networks useful for providing access to MANs and WANs.

10.6.1 Broadcast-and-Select Networks

An example of broadcast-and-select networks is provided by CATV networks. However, as discussed in Section 10.1.3, CATV networks employ the SCM technique for transmitting multiple video channels over a single optical wavelength. The use of WDM permits a novel approach for broadcast-and-select networks. The main idea is to employ the wavelength as a marker for routing each channel to its destination, resulting in an all-optical network. Since wavelength is used for multiple access, such an approach is referred to as *wavelength-division multiple access* (WDMA). A considerable amount of research and development work has been done on WDMA networks [19]. Broadly speaking, WDMA networks can be classified as single-hop or multihop networks [3]. Every node is directly connected to all other nodes in a single-hop network, resulting in a fully connected network. In contrast, multihop networks are only partially connected, and an optical signal sent by one node may require several hops through intermediate nodes before reaching its destination. In each category, transmitters and receivers may have either fixed or tunable operating frequencies.

Several architectures can be used for all-optical multihop networks [3]–[5]. Hypercube architecture provides one example: It has been used for interconnecting multiple processors in a supercomputer [95]. In general, the number of nodes N must be of the form 2^m, where m is the dimensionality of the hypercube. Each node is connected to m different nodes. The maximum number of hops is limited to m, while the average number of hops is about $m/2$ for large N. Each node requires m receivers. The number of receivers can be reduced by using a variant, known as the *deBruijn network*, but it requires more than $m/2$ hops on average. Another example of a multihop WDM network is provided by the shuffle network, or its bidirectional equivalent called the *Banyan network*.

Single-hop networks employ star topology for interconnecting all nodes (see Figure 10.3). Data transmitted by all nodes are multiplexed within the star coupler, and the entire traffic is directed toward each node (broadcasting operation) that selects the desired part (selecting operation). Figure 10.23 shows an example of a single-hop network designed to take advantage of the WDM technique. This network is known as

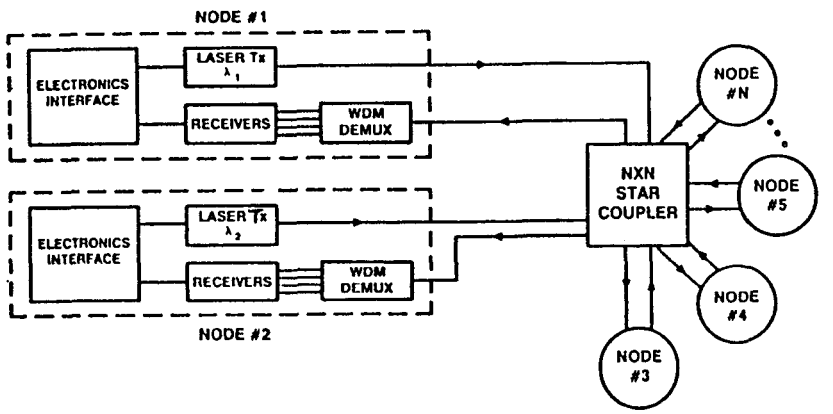

Figure 10.23: Schematic of the Lambdanet with N nodes. Each node consists of one transmitter and N receivers. (After Ref. [96]; ©1990 IEEE.)

the *Lambdanet*, and its architecture was developed in the late 1980s [96]. Each node in the Lambdanet is equipped with one transmitter emitting at a unique wavelength and N receivers operating at N distinct wavelengths, where N is the number of nodes. The output of all transmitters is combined in a passive star and distributed to all receivers equally. Each node receives the entire traffic and employs a bank of receivers. This feature creates a nonblocking network whose capacity and connectivity can be reconfigured electronically, depending on the application. The network is also transparent to the bit rate or the modulation format. Different users can transmit data at different bit rates with different modulation formats. This flexibility on the part of the Lambdanet makes it suitable for many applications. Its main drawback is that the number of users is limited by the number of available wavelengths. Moreover, each node requires many receivers (equal to the number of nodes), resulting in a considerable investment in hardware costs. The initial experiment employed 18 wavelengths spaced apart by 2 nm and carrying data at 1.5 Gb/s.

A tunable receiver can reduce the cost and complexity of the Lambdanet. This was the approach adopted in a 1993 experiment in which 100 nodes were interconnected using 100 wavelengths with 10-GHz spacing [97]. Such a small channel spacing was possible because of the use of a 622-Mb/s bit rate with coherent detection. A single receiver was employed at each node in combination with a Mach–Zehnder filter fabricated with silica-on-silicon technology (see Section 8.1.2 of LT1). Such a filter can be tuned thermally for selecting individual WDM channels.

Another network, called the Rainbow network, employed a similar channel-selection technique through a Fabry–Perot filter that was tuned electrically with the help of a piezoelectric transducer [98]. This network can support up to 32 nodes using 32 wavelengths spaced 1 nm apart. Each node can transmit 1-Gb/s signals over 10 to 20 km. The Rainbow network has been used for connecting multiple computers with a high-performance parallel interface. The main shortcoming of such networks is that the tuning of filters is a relatively slow process, making it difficult to employ packet

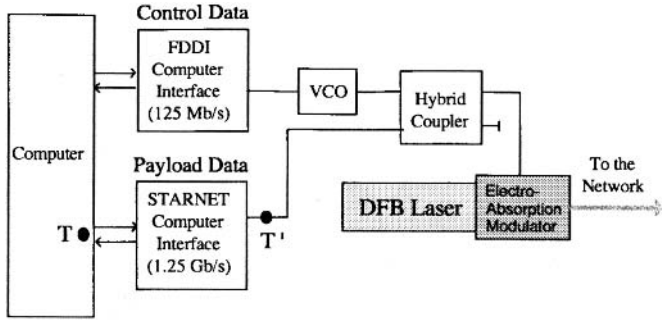

Figure 10.24: Schematic of transmitter design for the Starnet architecture; VCO stands for voltage control oscillator. (After Ref. [99]; ©1997 IEEE.)

switching.

An example of a WDM network designed with packet switching is provided by the Starnet architecture. It can transmit data at bit rates of up to 2.5 Gb/s per node over a 10-km diameter while maintaining a signal-to-noise ratio close to 24 dB [99]. Starnet differs from other implementations inasmuch as it employs a microwave subcarrier to create an FDDI-compatible control subnetwork. In a 1997 experiment, data packets assembled in a 1.25-Gb/s bit stream were transmitted together with the 125-Mb/s control signal multiplexed through SCM over a single optical carrier. Figure 10.24 shows the design of such a transmitter schematically. The SCM technique used for Starnet is identical to that discussed in Section 10.4.2 in the context of optical label swapping. The receiver separates the data packets and the control signal using an approach similar to that adopted for SCM labels in Section 10.4.2.

10.6.2 Passive Optical Networks

Access networks connect individual homes and businesses in a local area to a central office where different bit streams (or packets) are aggregated. The traffic is then moved to a MAN and then eventually transported over the core network. Although electronic techniques still dominate in access networks, there is considerable interest in bringing fiber to the home (or at least to the curb) to provide diverse services at higher bit rates (10 Mb/s or more) to individual users [100]–[104]. The basic idea is to employ a scheme that avoids any active switching elements between the central office and the user. Such access networks are referred to as *passive* optical networks (PONs). Figure 10.25 shows an example of a PON schematically [105]. It makes use of star couplers at multiple remote nodes.

As early as 1988, a *passive photonic loop* configuration was proposed that took advantage of multiple distinct wavelengths for routing signals from homes and offices to the central office [105]. Figure 10.26 shows a block diagram of such an access network. For a network supporting N users, the central office contains N transmitters emitting at wavelengths $\lambda_1, \lambda_2, \ldots, \lambda_N$ and N receivers operating at wavelengths $\lambda_{N+1}, \ldots, \lambda_{2N}$. Two distinct wavelengths, λ_k and λ_{N+k}, are assigned to the kth user, one for transmit-

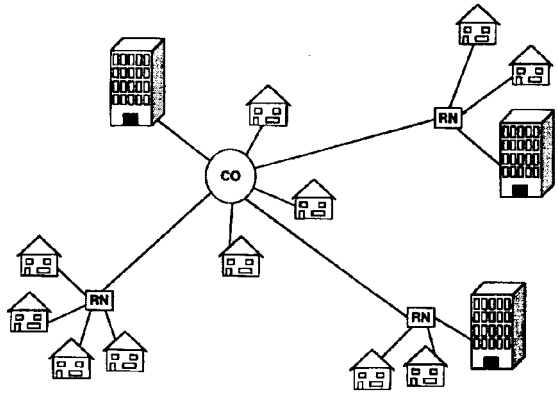

Figure 10.25: A passive optical network connecting homes and businesses to the central office (CO) using star couplers at remote nodes (RNs). (After Ref. [105]; ©1989 IEEE.)

ting and the other for receiving data. A remote node multiplexes data transmitted by several users and sends the combined signal to the central office. It also demultiplexes signals intended for those users. The remote node is passive and requires little maintenance if passive WDM components are used. A switch at the central office routes the WDM signal depending on their wavelengths. In the 1988 demonstration, 16 users were connected using 16 wavelengths in the 1,300-nm region for downstream traffic and another 16 wavelengths in the 1,550-nm region for upstream traffic.

The main advantage of the passive photonic-loop configuration is that the optical network unit (ONU) at each user's location is "colorless" as it does not contain any laser [103]. It does house a modulator that is used to transpose data on the optical

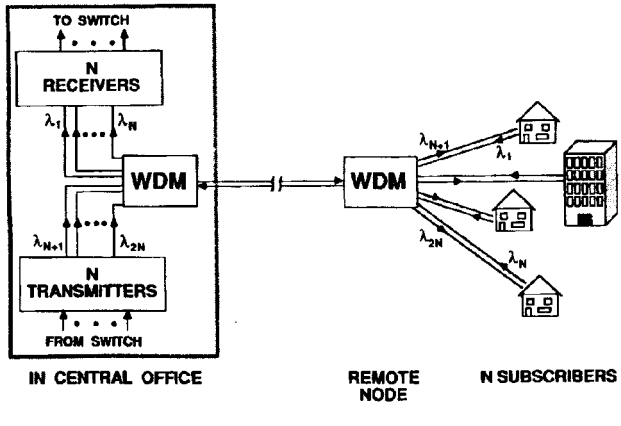

Figure 10.26: Schematic of a passive photonic loop. The central office houses all active elements. WDM couplers at remote nodes are used to deliver two wavelengths to each user for transmitting and receiving data. (After Ref. [105]; ©1989 IEEE.)

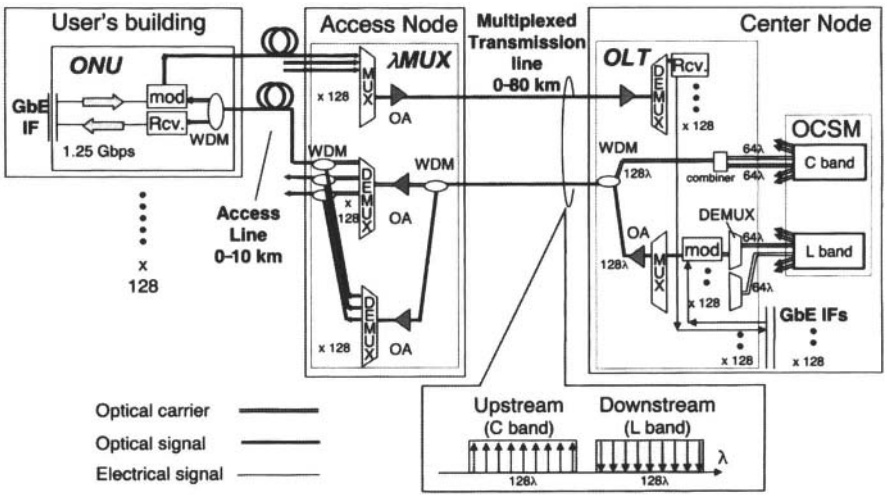

Figure 10.27: Setup for a 128-user access network utilizing 128 wavelengths in the C and L bands for upstream and downstream traffic; OA, OLT, and OCSM stand for optical amplifier, optical line terminal, and optical carrier supply module, respectively. (After Ref. [103]; ©2004 IEEE.)

carrier supplied by the central office at a predetermined wavelength. The colorless nature of ONUs makes it possible to reduce their cost through mass production. The number of wavelengths required for even a 150-user PON is relatively large. Even with 25-GHz channel spacing, it becomes necessary to employ both the C and L bands. Figure 10.27 shows the experimental setup employed for a 128-user access network. The optical carrier supply module at the central office provides 128 wavelengths with 25-GHz spacing in the C band for upstream traffic and another set of 128 wavelengths in the L band for downstream traffic. Although 256 individual lasers can be used for this purpose, the overall cost can be reduced substantially if a broadband source (such as a superluminescent diode) whose spectrum covers the entire C and L bands (1,530–1,610 nm) is employed. If such a single source is not available, two separate sources for the C and L bands can be employed. In both cases, an AWG is used to slice the broadband source spectrum into distinct carrier wavelengths.

The design of access networks for telecommunication applications was still evolving in 2004 [100]–[104]. PONs are often divided into several groups depending on the architecture and the protocol employed for them. In all cases, the eventual goal is to provide broadband access to each user and to deliver audio, video, and Internet traffic on demand, while keeping down the cost. B-PONs (B stands for broadband) are at the most advanced stage as their operating features have been standardized by the ITU through several recommendations [106]–[108]. They are designed to provide upstream transmission in the wavelength region near 1.3 μm. The data are transferred downstream at two distinct wavelengths. The telephone and Internet services occupy a band near 1.5 μm, whereas video is delivered in the wavelength region near 1.55 μm. B-PONs are capable of transferring downstream and upstream data at a bit rate of 622

and 155 Mb/s, respectively, through the ATM protocol. There is considerable interest in boosting the downstream bit rate above 1 Gb/s, at least in the form of bursts. G-PONs (G stands for Gb/s) are being proposed for this purpose [104].

Another category of access networks is referred to as Ethernet PONs, or E-PONs [109]–[111]. As the name suggests, such networks employ a protocol similar to that used for the Ethernet and thus can be designed with low-cost Ethernet equipment. With the advent of the Gigabit Ethernet, one can increase the underlying bit rate to 1 Gb/s. Such PONs are referred to as GE-PONs [104]. They are also called full-service access networks as they can provide a full array of services with different levels of quality of service. Both ITU and IEEE were working in 2004 on the standardization issues related to G-PONS and GE-PONs.

Problems

10.1 A distribution network uses an optical bus to distribute the signal to 10 users. Each optical tap couples 10% of the power to the user and has a 1-dB insertion loss. Assuming that 1 mW of power is launched into the optical bus, calculate the power received by the stations 8, 9, and 10.

10.2 A cable-television operator uses an optical bus to distribute video channels to its subscribers. Each receiver needs a minimum of 100 nW to operate satisfactorily. Optical taps couple 5% of the power to each subscriber. Assuming a 0.5-dB insertion loss for each tap and 1-mW transmitter power, estimate the number of subscribers that can be added to the optical bus.

10.3 Describe the three main protocols used in modern optical networks. Compare the three and discuss the advantages and disadvantages of each.

10.4 Describe the seven-layer OSI reference model and explain the function of the bottom four layers in detail.

10.5 What is the role of the optical layer in modern WDM systems? Describe the three sections associated with this layer.

10.6 What is meant by multiprotocol label switching (MPLS)? Explain how this concept is extended for WDM systems through generalized MPLS.

10.7 What is meant by the term lightpath? How are lightpaths established? Do they have a unique wavelength throughout the network?

10.8 What is the role of optical cross-connects (OXC) in a WDM network? Sketch the design of a wavelength-selective OXC. Describe why such a device can lead to wavelength blocking.

10.9 How do wavelength converters solve the wavelength-blocking problem in a WDM network? Describe an all-optical scheme for realizing a wavelength converter.

10.10 Sketch the two- and three-dimensional configurations for optical cross-connects designed with MEMS technology. Compare the two designs and discuss their relative merits.

10.11 What is meant by an optical label in the context of packet-switched networks? Describe the optical label swapping scheme and discuss its advantages.

10.12 What is subcarrier multiplexing (SCM)? How is this technique used for optical labels? Explain how an SCM-coded label is extracted from the packet to which it is attached.

10.13 Packet-switched networks suffer from packet collisions. Describe three techniques that can be used for contention resolution in such networks.

10.14 What is the main idea behind optical burst switching? Describe how it can be used to transport packets across a core network.

10.15 Explain the concept of photonic slot routing. Sketch a device design for stacking and unstacking packets in a photonic slot.

10.16 What is meant by a passive optical network? Describe a WDM scheme for connecting multiple users to the central office for bidirectional data transmission without requiring any optical sources at the user's location.

References

[1] S. E. Miller and I. P. Kaminow, Eds., *Optical Fiber Telecommunications*, Vol. 2, Academic Press, San Diego, CA, 1988, Chaps. 21–25.

[2] P. E. Green, Jr., *Fiber-Optic Networks*, Prentice Hall, Upper Saddle River, NJ, 1993.

[3] B. Mukherjee, *Optical Communication Networks*, McGraw-Hill, New York, 1997.

[4] I. P. Kaminow and T. L. Koch, Eds., *Optical Fiber T elecommunications*, Vol. 3A, Academic Press, San Diego, CA, 1997.

[5] K. M. Sivalingam and S. Subramaniam, Eds., *Optical WDM Networks: Principles and Practice*, Kluwer Academic, Norwell, MA, 2000.

[6] B. Ramamurthy, *Design of Optical WDM Networks: LAN, MAN and WAN Architectures*, Kluwer Academic, Norwell, MA, 2001.

[7] C. S. Murthy and G. Mohan, *WDM Optical Networks: Concepts, Design and Algorithms*, Prentice-Hall, Upper Saddle River, NJ, 2001.

[8] R. Ramaswami and K. Sivarajan, *Optical Networks: A Practical Perspective*, 2nd ed., Morgan Kaufmann Publishers, San Francisco, 2002.

[9] I. P. Kaminow and T. Li, Eds., *Optical Fiber Telecommunications*, Vol. 4A, Academic Press, San Diego, CA, 2002.

[10] S. Dixit, *IP over WDM: Building the Next Generation Optical Internet*, Wiley, Hoboken, NJ, 2003.

[11] J. Zheng and H. T. Mouftah, *Optical WDM Networks: Concepts and Design Principles*, Wiley, Hoboken, NJ, 2004.

[12] A. K. Dutta and N. K. Dutta, Eds., *WDM Technologies: Optical Networks*, Academic Press, San Diego, CA, 2004.

[13] J. Strand, in *Optical Fiber Telecommunications*, Vol. 4A, I. P. Kaminow and T. Li, Eds., Academic Press, San Diego, CA, 2002, Chap. 3.

[14] I. S. Binetti, A. Bragheri, E. Iannone, and F. Bentivoglio, *J. Lightwave Technol.* **18**, 1677 (2000).

[15] A. A. M. Saleh and J. M. Simmons, *J. Lightwave Technol.* **17**, 2431 (1999).

[16] N. Ghani, J.-Y. Pan, and X. Cheng, in *Optical Fiber Telecommunications*, Vol. 4B, I. P. Kaminow and T. Li, Eds., Academic Press, San Diego, CA, 2002, Chap. 8.

[17] W. T. Anderson, J. Jackel, G. K. Chang, H. Dai, X. Wei. M. Goodman, C. Allyn, M. Alvarez,O. Clarke, A. Gottlieb, F. Kleytman, J. Morreale, V. Nichols, A. Tzathas, R. Vora, L. Mercer, H. Dardy, E. Renaud, L. Williard, J. Perreault, R. McFarland, and T. Gibbons, *J. Lightwave Technol.* **18**, 1988 (2000).

[18] P. E. Green, Jr., *IEEE J. Sel. Areas Commun.* **14**, 764 (1996).

[19] A. Borella, G. Cancellieri, F. Chiaraluce, *Wavelength Division Multiple Access Optical Networks*, Artech House, Boston, 1998.

[20] E. Harstead and P. H. Van Heyningen, in *Optical Fiber Telecommunications*, Vol. 4B, I. P. Kaminow and T. Li, Eds., Academic Press, San Diego, CA, 2002, Chap. 9.

[21] G. Kramer and G. Pesavento, *IEEE Commun. Mag.* **40**(2), 66 (2002).

[22] H. Zimmermann, *IEEE Trans. Commun.*, **28**, 425 (1980).

[23] A. Hac and H. B. Mutlu, *Computer*, **22**(11), 26 (1989).

[24] G. J. Armitage and K. M Adams, *IEEE Network*, **9**(1), 18 (1995).

[25] A. Viswanathan, N. Feldman, Z. Wang, and R. Callon, *IEEE Commun. Mag.*, **26**(5), 165 (1998).

[26] A. Banerjee, J. Drake, J. P. Lang, B. Turner, K. Kompella, and Y. Rekhter, *IEEE Commun. Mag.* **39**(1), 144 (2001).

[27] K. Sato, N. Yamanaka, Y. Takigawa, M. Koga, S. Okamoto, K. Shiomoto, E. Oki, and W. Imajuku, *IEEE Commun. Mag.* **40**(3), 96 (2002).

[28] A. Elwalid, D. Mitra, I. Saniee, and I. Widjaja, *J. Lightwave Technol.* **21**, 2828 (2003).

[29] G. Li, J. Yates, D. Wang, and C. Kalmanek, *IEEE Commun. Mag.* **40**(2), 90 (2002).

[30] D. Saha, B. Rajagopalan, and G. Bernstein, *IEEE Commun. Mag.* **41**(8), S29 (2003).

[31] S. Sánchez-López, J. Solé-Pareta, J. Comellas, J. Soldatos, G. Kylafas, and M. Jaeger, *J. Lightwave Technol.* **21**, 2673 (2003).

[32] H. Hegering, S. Abeck, B. Neumair, *Integrated management of networked systems*, Morgan Kaufman Publishers, San Francisco, 1999.

[33] R. Ramamurthy and B. Mukherjee, *IEEE Trans. Networking.*, **10**, 352 (2002).

[34] P. Ho and H. T. Mouftah, *J. Lightwave Technol.* **20**, 1292 (2002).

[35] C. Nuzman, J. Leuthold, R. Ryf, S. Chandrasekhar, C. R. Giles, and D. T. Neilson, *J. Lightwave Technol.* **21**, 648 (2003).

[36] K. Zhu, H. Zhu, and B. Mukherjee, *IEEE Network*, **17**(2), 8 (2003).

[37] K. Zhu and B. Mukherjee, *IEEE J. Sel. Areas Commun.*, **21**, 1173 (2003).

[38] R. Parthiban, R. S. Tucker, and C. Leckie, *J. Lightwave Technol.* **21**, 2476 (2003).

[39] R. Ramaswami and G. Sasaki, *IEEE Trans. Networking* **6**, 744 (1998).

[40] G. Xiao and Y.-W. Leung, *IEEE Trans. Networking* **7**, 545 (1999).

[41] S. Subramaniam, M. Azizoglu, and A. Somani, *IEEE Trans. Networking* **7**, 754 (1999).

[42] M. Listanti and R. Sabella, *Photonic Network Commun.*, **2**, 333 (2000).

[43] V. Sharma and E. Varvarigos, *J. Lightwave Technol.* **18**, 1606 (2000).

[44] G. Shen, W. Grover, T. H. Cheng, and S. Bose, *J. Opt. Networking* **1**, 424 (2002).

[45] L. Y. Lin, E. L. Goldstein, and R. W. Tkach, *IEEE J. Sel. Topics Quantum Electron.* **5**, 4 (1999); *J. Lightwave Technol.* **18**, 482 (2000).

[46] D. J. Bishop, C. R. Giles, and G. P. Austin, *IEEE Commun. Mag.* **40**(3), 75 (2002).

[47] P. B. Chu, S.-S. Lee, and S. Park, *IEEE Commun. Mag.* **40**(3), 80 (2002).

[48] L. Y. Lin and E. L. Goldstein, *IEEE J. Sel. Topics Quantum Electron.* **8**, 163 (2002).

[49] V. A. Aksyuk, F. Pardo, D. Carr, D. Greywall, H. B. Chan, M. E. Simon, A. Gasparyan, H. Shea, V. Lifton, C. Bolle, S. Arney, R. Frahm, M. Paczowski, M. Haueis, R. Ryf, D. T. Neilson, J. Kim, C. R. Giles, J. Gates, and D. Bishop, *J. Lightwave Technol.* **21**, 634 (2003).

[50] J. Kim, C. J. Nuzman, B. Kumar, D. F. Lieuwen, J. S. Kraus, A. Weiss, C. P. Lichtenwalner, A. R. Papazian, R. E. Frahm, N. R. Basavanhally, D. A. Ramsey, V. A. Aksyuk, F. Pardo, M. E. Simon, V. Lifton, H. B. Chan, M. Haueis, A. Gasparyan, H. R. Shea, S. Arney, C. A. Bolle, P. R. Kolodner, R. Ryf, D. T. Neilson, and J. V. Gates, *IEEE Photon. Technol. Lett.* **15**, 1537 (2003).

[51] A. Olkhovets, P. Phanaphat, C. Nuzman, D. J. Shin, C. Lichtenwalner, M. Kozhevnikov, and J. Kim, *IEEE Photon. Technol. Lett.* **16**, 780 (2004).

[52] J. J. Bernstein, W. P. Taylor, J. D. Brazzle, C. J. Corcoran, G. Kirkos, J. E. Odhner, A. Pareek, M. Waelti, and M. Zai, *J. Microelctro. Sys.* **13**, 526 (2004).

[53] C. Cavazzoni, V. Barosco, A. D'Alessandro, A. Manzalini, S. Milani, G. Ricucci, R. Morro, R. Geerdsen, U. Hartmer, G. Lehr, U. Pauluhn, S. Wevering, D. Pendarakis, N. Wauters, Ra. Gigantino, J. P. Vasseur, K. Shimano, G. Monari, and A. Salvioni, *J. Lightwave Technol.* **21**, 2791 (2003).

[54] K. Noguchi, Y. Koike, H. Tanobe, K. Harada, and M. Matsuoka, *J. Lightwave Technol.* **22**, 329 (2004).

[55] A. Carena, M. D. Vaughn, R. Gaudino, M. Shell, and D. J. Blumenthal, *J. Lightwave Technol.* **16**, 2135 (1998).

[56] K. Kitayama, N. Wada, and H. Sotobayashi, *J. Lightwave Technol.* **18**, 1834 (2000).

[57] B. Meagher, G. K. Chang, G. Ellinas, Y. M. Lin, W. Xin, T. F. Chen, X. Yang, A. Chowdhury, J. Young, S. J. Yoo, C. Lee, M. Z. Iqbal, T. Robe, H. Dai, Y. J. Chen, and W. I. Way, *J. Lightwave Technol.* **18**, 1978 (2000).

[58] D. J. Blumenthal, B.-E. Olsson, G. Rossi, T. E. Dimmick, L. Rau, M. Mašanović, O. Lavrova, R. Doshi, O. Jerphagnon, J. E. Bowers, V. Kaman, L. A. Coldren, and J. Barton, *J. Lightwave Technol.* **18**, 2058 (2000).

[59] K.-H. Park and T. Mizumoto, *J. Lightwave Technol.* **19**, 1076 (2001).

[60] A. E. Wiliner, D. Gurkan, A. B. Sahin, J. E. Mcgeehan, and M. C. Hauer, *IEEE Commun. Mag.* **41**(5), S38 (2003).

[61] M. Y. Jeon, Z. Pan, J. Cao, Y. Bansal, J. Taylor, Z. Wang, V. Akella, K. Okamoto, S. Kamei, J. Pan, and S. J. B. Yoo, *J. Lightwave Technol.* **21**, 2273 (2003).

[62] D. Gurkan, S. Kumar, A. E. Willner, K. R. Parameswaran, M. M. Fejer, Member, *J. Lightwave Technol.* **21**, 2739 (2003).

[63] I. Glesk, B. C. Wang, L. Xu, V. Baby, and P. R. Prucnal, in *Progress in Optics*, Vol. 45, E. Wolf, Ed., Noth-Holland, Amsterdam, 2003, Chap. 2.

[64] M. Hickey, C. Barry, C. Noronha, and L. Kazovsky, *IEEE Photon. Technol. Lett.* **5**, 568 (1993).

[65] N. Chi, J. Zhang, P. V. Holm-Nielsen, C. Peucheret, and P. Jeppesen, *IEEE Photon. Technol. Lett.* **15**, 760 (2003).

[66] K. Vlachos, J. Zhang, J. Cheyns, Sulur, N. Chi, E. Van Breusegem, I. Tafur Monroy, J. G. L. Jennen, P. V. Holm-Nielsen, C. Peucheret, R. O'Dowd, P. Demeester, and A. M. J. Koonen, *J. Lightwave Technol.* **21**, 2617 (2003).

[67] J. Yu, G.-K. Chang, A. Chowdhury, and J. L. Long, *J. Lightwave Technol.* **22**, 2469 (2004).

[68] K. Kitayama, H. Sotobayashi, and N. Wada, *IEEE J. Sel. Areas Commun.* **16**, 1309 (1998).

[69] K. Kitayama and M. Murata, *J. Lightwave Technol.* **19**, 1401 (2001).

[70] G. Cincotti, *J. Lightwave Technol.* **22**, 337 (2004); *J. Lightwave Technol.* **22**, 1642 (2004).

[71] N. Kataoka, N. Wada, F. Kubota, and K. Kitayama, *J. Lightwave Technol.* **22**, 2377 (2004).

[72] S. Yao, B. Mukherjee, S. J. B. Yoo, and S. Dixit, *J. Lightwave Technol.* **21**, 672 (2003).

[73] Z. Pan, M. Y. Jeon, Y. Bansal, J. Cao, J. Taylor, V. Akella, S. Kamei, K. Okamoto, and S. J. B. Yoo, *J. Lightwave Technol.* **21**, 1312 (2003).

[74] F. Xue, Z. Pan, Y. Bansal, J. Cao, M. Y. Jeon, K. Okamoto, S. Kamei, V. Akella, and S. J. B. Yoo, *J. Lightwave Technol.* **21**, 2595 (2003).

[75] F. Xue, Z. Pan, H. Yang, J. Yang, J. Cao, K. Okamoto, S. Kamei, V. Akella, and S. J. Ben Yoo, *J. Lightwave Technol.* **22**, 2570 (2004).

[76] M. Yoo, C. Qiao, and S. Dixit, *IEEE J. Sel. Areas Commun.* **18**, 2062 (2000).

[77] J. Y. Wei and R. I. McFarland, Jr., *J. Lightwave Technol.* **18**, 2019 (2000).

[78] S. Verma, H. Chaskar, and R. Ravikanth, *IEEE Network*, **14**(6), 48 (2000).

[79] C. Qiao, *IEEE Commun. Mag.* **38**(9), 101 (2000).

[80] L. Xu, H. G. Perros, and G. Rouskas, *IEEE Commun. Mag.* **39**(1), 136 (2001).

[81] T. Battestilli and H. Perros, *IEEE Commun. Mag.* **41**(8), S10 (2003).

[82] Y. Chen, C. Qiao and X. Yu, *IEEE Network*, **18**(3), 16 (2004).

[83] I. Chlamtac, V. Elek, A. Fumagalli, and C. Szabo, *IEEE Trans. Networking*, **7**, 1 (1999).

[84] H. Zang, J. P. Jue, and B. Mukherjee, *J. Lightwave Technol.* **18**, 1728 (2000).

[85] V. Elek, A. Fumagalli, and G. Wedzinga, *IEEE Commun. Mag.* **39**, 164 (2001).

[86] M. Boroditsky, N. J. Frigo, C. F. Lam, K. F. Dreyer, D. A. Ackerman, J. E. Johnson, L. J. P. Ketelsen, A. Chen, and A. Smiljanic, *J. Lightwave Technol.* **21**, 1717 (2003).

[87] G. Wedzinga, *Photonic Slot Routing in Optical Transport Networks*, Kluwer, Boston, 2003.

[88] R. A. Barry, V. W. S. Chan, K. L. Hall, E. S. Kintzer, J. D. Moores, K. A. Rauschenbach, E. A. Swanson, L. E. Adams, C. R. Doerr, S. G. Finn, H. A. Haus, E. P. Ippen, W. S. Wong, and M. Haner, *IEEE J. Sel. Areas Commun.* **14**, 999 (1996).

[89] S.-W. Seo, K. Bergman, and P. R. Prucnal, *IEEE J. Sel. Areas Commun.* **14**, 1996 (1996).

[90] V. W. S. Chan, K. L. Hall, E. Modiano, and K. A. Rauschenbach, *J. Lightwave Technol.* **16**, 2146 (1998).

[91] P. Toliver, I. Glesk, R. J. Runser, K.-L. Deng, B. Y. Yu, and P. R. Prucnal, *J. Lightwave Technol.* **16**, 2169 (1998).

[92] K.-L. Deng, R. J. Runser, P. Toliver, I. Glesk, and P. R. Prucnal, *J. Lightwave Technol.* **18**, 1892 (2000).

[93] S. A. Hamilton, B. S. Robinson, T. E. Murphy, S. J. Savage, and E. P. Ippen, *J. Lightwave Technol.* **20**, 2086 (2002).

[94] A. Takada and J. H. Park, *J. Lightwave Technol.* **20**, 2306 (2002).

[95] P. W. Dowd, *IEEE Trans. Comput.* **41**, 1223 (1992).

[96] M. S. Goodman, H. Kobrinski, M. P. Vecchi, R. M. Bulley, and J. L. Gimlett, *IEEE J. Sel. Areas Commun.* **8**, 995 (1990).

[97] K. Nosu, H. Toba, K. Inoue, and K. Oda, *J. Lightwave Technol.* **11**, 764 (1993).

[98] E. Hall, J. Kravitz, R. Ramaswami, M. Halvorson, S. Tenbrink, and R. Thomsen, *IEEE J. Sel. Areas Commun.* **14**, 814 (1996).

[99] D. Sadot and L. G. Kazovsky, *J. Lightwave Technol.* **15**, 1629 (1997).

[100] F.-T. An, K. S. Kim, D. Gutierrez, S. Yam, E. Hu, K. Shrikhande, and L. G. Kazovsky, *J. Lightwave Technol.* **22**, 2557 (2004).

[101] S.-J. Park, C.-H. Lee, K.-T. Jeong, H.-J. Park, J.-G. Ahn, and K.-H. Song, *J. Lightwave Technol.* **22**, 2582 (2004).

[102] S. Wright, H. Fahmy, and A. J. Vernon, *J. Lightwave Technol.* **22**, 2606 (2004).

[103] K. Iwatsuki, J. Kani, H. Suzuki, and M. Fujiwara, *J. Lightwave Technol.* **22**, 2623 (2004).

[104] M. Nakamura, H. Ueda, S. Makino, T. Yokotani, and K. Oshima, *J. Lightwave Technol.* **22**, 2631 (2004).

[105] S. S. Wagner and H. L. Lemberg, *J. Lightwave Technol.* **7**, 1759 (1989).

[106] F. J. Effenberger, H. Ichibangase, and H. Yamashita, *IEEE Commun. Mag.* **39**(12), 118 (2001).

[107] Y. Maeda, K. Okada, and D. Faulkner, *IEEE Commun. Mag.* **39**(12), 126 (2001).

[108] H. Ueda, K. Okada, B. Ford, G. Mahony, S. Hornung, D. Faulkner, J. Abiven, S. Durel, R. Ballart, and J. Erickson, *IEEE Commun. Mag.* **39**(12), 134 (2001).

[109] G. Kramer and G. Pesavento, *IEEE Commun. Mag.* **40**(2), 66 (2002).

[110] C. M. Assi, Y. Ye, S. Dixit, and M. A. Ali, *IEEE J. Sel. Areas Commun.* **21**, 1467 (2003).

[111] M. P. McGarry, M. Maier, and M. Reisslein, *IEEE Commun. Mag.* **42**(2), S8 (2004).

Appendix A

System of Units

The international system of units (known as the SI, short for *Système International*) is used in this book. The three fundamental units in the SI are meter (m), second (s), and kilogram (kg). A prefix can be added to each of them to change its magnitude by a multiple of 10. Mass units are rarely required in this book. On the other hand, measures of distance required in this text range from nanometers (10^{-9} m) to kilometers (10^{3} m), depending on whether one is dealing with planar waveguides or silica fibers. Similarly, time measures range from picoseconds (10^{-12} s) to a few minutes. Other common units in this book are Watt (W) for optical power and W/m^2 for optical intensity. They can be related to the fundamental units through energy because optical power represents the rate of energy flow (1 W = 1 J/s). The energy can be expressed in several other ways using $E = h\nu = k_B T = mc^2$, where h is the Planck constant, k_B is the Boltzmann constant, and c is the speed of light. The frequency ν is expressed in hertz (1 Hz = 1 s^{-1}). Of course, because of the large frequencies associated with optical waves, most frequencies in this book are expressed in GHz or THz.

In designing lightwave systems, optical powers can vary over several orders of magnitude as the signal travels from the transmitter to the receiver. Such large variations are handled most conveniently using decibel units, abbreviated dB, commonly used by engineers in many different fields. Any ratio R can be converted into decibels by using the general definition

$$R\ (\text{in dB}) = 10 \log_{10} R. \tag{A.1}$$

The logarithmic nature of the decibel allows a large ratio to be expressed as a much smaller number. For example, 10^9 and 10^{-9} correspond to 90 dB and -90 dB, respectively. Since $R = 1$ corresponds to 0 dB, ratios smaller than 1 are negative in the decibel system. Furthermore, negative ratios cannot be written using decibel units.

The most common use of the decibel scale occurs for power ratios. For instance, the signal-to-noise ratio (SNR) of an optical or electrical signal is given by

$$\text{SNR} = 10 \log_{10}(P_S/P_N), \tag{A.2}$$

where P_S and P_N are the signal and noise powers, respectively. For example, the loss of an optical fiber is expressed in decibel units in Section 1.3 because it corresponds

to a decrease in the optical power during transmission through the fiber and thus can be expressed as a power ratio. For example, if a 1-mW signal reduces to 1 μW after transmission over 100 km of fiber, the 30-dB loss over the entire fiber span translates into a loss of 0.3 dB/km. The same technique can be used to define the insertion loss of any passive optical component. For instance, a 1-dB loss of a fiber connector implies that the optical power is reduced by 1 dB (by about 20%) when the signal passes through the connector. The bandwidth of an optical filter is defined at the 3-dB point, corresponding to a 50% reduction in the signal power. The modulation bandwidth of semiconductor lasers in Section 5.3 is also defined at the 3-dB point.

Since losses of all passive components in a lightwave system are expressed in dB units, it is useful to express the transmitted and received powers also by using a decibel scale. This is achieved by using a derived unit, denoted as dBm and defined as

$$\text{power (in dBm)} = 10 \log_{10}\left(\frac{\text{power}}{1 \text{ mW}}\right), \tag{A.3}$$

where the reference level of 1 mW is chosen simply because typical values of the transmitted power are in that range (the letter m in dBm is a reminder of the 1-mW reference level). In this decibel scale for the absolute power, 1 mW corresponds to 0 dBm, whereas powers below 1 mW are expressed as negative numbers. For example, a 10-μW power corresponds to -20 dBm. Because of the logarithmic nature of the decibel scale, powers ranging over a wide range from 1 pW to 1 GW are expressed in dBm units over a much smaller range from -90 to 120 dBm.

Appendix B

Software Package

The back cover of the book contains a software package on a compact disc (CD) provided by RSoft Design Group, Inc. (http://www.rsoftdesign.com). This state-of-the art software package should prove useful to readers of this book for solving problems provided at the end of each chapter. It also contains additional problems for each chapter that may help in understanding the difficult material. The CD contains a specially prepared version of the design software marketed commercially by RSoft under the trade name OptSim^{TM}. The latest version of this software available in March 2005 (OptSim 4.0) was used to prepare a large number of examples that can be simulated on a computer for a better understanding of the material presented in this book.

The CD should work on any personal computer (PC) and is intended for PCs running under Windows 2000 and Windows XP operating systems. The first step is to install the software package on the computer. The installation procedure should be straightforward for most users: Insert the CD in the CD-ROM drive and follow the instructions. If the installer does not start automatically for some reason, one may have to click on the "setup" program in the root directory of the CD. After the installation, the user can start the program from the Windows Start menu program group for the RSoft OptSim Demo. The documentation accompanying the software is also available in the same program group from the Start menu. Figure B.1 shows how the computer screen looks when one of the examples has been opened.

The basic approach used by the OptSim package consists of providing a library of modules for various components (such as lasers, modulators, fibers, filters, etc.) that are used to form a lightwave system. These modules are first used to construct a layout of the actual system whose performance needs to be simulated. Calculations are then performed by pressing the "Go" button. The final step consists of analyzing the numerical data through plots that are generated during simulations. The user should read the documentation files that are provided with the software to understand the purpose of various tools available in the two toolbars on the top and to the left of this window.

The examples that can be solved by the OptSim software are stored in a folder under the name `C:\RSoftDemo\examples\books\lightwave_technology_v2_agrawal`. Within this folder, subfolders are arranged with chapter numbers. Each subfolder contains several examples that are related to the material presented in that chapter of this

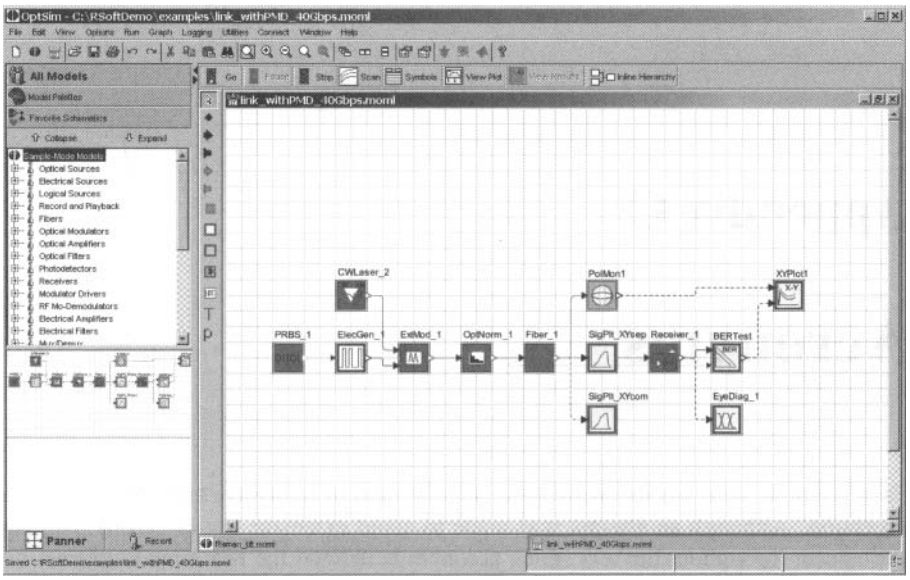

Figure B.1: Main window of OptSim simulation software showing various components interconnected to solve a specific problem. It contains two toolbars on the top and to the left of the window in addition to the standard menu bar at the top and a status line at the bottom.

book. For example, the subfolder marked "chapter4" contains four problems related to Chapter 4. These four examples illustrate the impact of different nonlinear effects on the performance of lightwave systems. All examples are documented in a file named "Examples.pdf" and accessible from the Start menu program group for the software. This file is also located in the directory `C:\RSoftDemo\examples\books\lightwave_technology_v2_agrawal`. It provides a detailed description of the problems that are solved by the OptSim software for each of the examples. Readers should read this document prior to running the examples included with the software for a better understanding of the problems.

Appendix C

Acronyms

Each scientific field has its own jargon, and the field of lightwave technology is not an exception. Although an attempt was made to avoid extensive use of acronyms, many still appear throughout the text. Each acronym is defined the first time it appears in a chapter so that the reader does not have to search the entire text to find its meaning. As a further help, we list all the acronyms here, in alphabetical order.

ADM	add–drop multiplexer
AM	amplitude modulation
AMI	alternate mark inversion
AN	access node
APD	avalanche photodiode
ASE	amplified spontaneous emission
ASK	amplitude-shift keying
ATM	asynchronous transfer mode
AWG	arrayed-waveguide grating
BER	bit-error rate
CATV	common-antenna (cable) television
CDM	code-division multiplexing
CNR	carrier-to-noise ratio
CRZ	chirped return-to-zero
CSRZ	carrier-suppressed return-to-zero
CW	continuous wave
DBR	distributed Bragg reflector
DCF	dispersion-compensating fiber
DDF	dispersion-decreasing fiber
DFB	distributed feedback
DGD	differential group delay
DM	dispersion-managed
DPSK	differential phase-shift keying
DQPSK	differential quadrature phase-shift keying
EDFA	erbium-doped fiber amplifier

EN	egress node
FDDI	fiber distributed data interface
FDM	frequency-division multiplexing
FEC	forward error correction
FM	frequency modulation
FSK	frequency-shift keying
FWHM	full-width at half-maximum
FWM	four-wave mixing
GMPLS	generalized multiprotocol label switching
GT	Gires–Tournois
GVD	group-velocity dispersion
IP	Internet protocol
ISDN	integrated services digital network
ITU	International Telecommunication Union
LAN	local-area network
LEAF	large effective-area fiber
LED	light-emitting diode
LT1	Lightwave Technology, Vol. 1
MAN	metropolitan-area network
MEMS	micro-electro-mechanical system
MMI	multimode interference
MONET	multiwavelength optical network
MPEG	motion-picture entertainment group
MPLS	multiprotocol label switching
MQW	multiquantum well
MTTF	mean time to failure
MZ	Mach–Zehnder
NEP	noise-equivalent power
NLS	nonlinear Schrödinger
NOLM	nonlinear optical-loop mirror
NRZ	nonreturn to zero
NSE	nonlinear Schrödinger equation
NZDSF	nonzero-dispersion-shifted fiber
OC	optical carrier
OEIC	optoelectronic integrated circuit
ONU	optical network unit
OOK	on–off keying
OPC	optical phase conjugation
OSI	open systems interconnection
OTDM	optical time-division multiplexing
OXC	optical cross-connect
PCD	polarization chromatic dispersion
PCM	pulse-code modulation
PDF	probability density function
PDL	polarization-dependent loss
PDM	polarization-division multiplexing

PM	phase modulation
PMD	polarization-mode dispersion
PON	passive optical network
PSK	phase-shift keying
PSP	principal state of polarization
QPSK	quadrature phase-shift keying
RDF	reverse-dispersion fiber
RF	radio frequency
RIN	relative intensity noise
RMS	root-mean-square
RPU	Raman pumping unit
RS	Reed–Solomon
RZ	return to zero
SBS	stimulated Brillouin scattering
SCM	subcarrier multiplexing
SDH	synchronous digital hierarchy
SI	Système International
SMF	single-mode fiber
SNR	signal-to-noise ratio
SOA	semiconductor optical amplifier
SONET	synchronized optical network
SOP	state of polarization
SPM	self-phase modulation
SRS	stimulated Raman scattering
STM	synchronous transport module
TDM	time-division multiplexing
TE	transverse electric
TM	transverse magnetic
TOD	third-order dispersion
VCSEL	vertical-cavity surface-emitting laser
VSB	vestigial sideband
WAN	wide-area network
WDM	wavelength-division multiplexing
WDMA	wavelength-division multiple access
WGR	waveguide-grating router
XPM	cross-phase modulation
YIG	yttrium iron garnet
ZDWL	zero-dispersion wavelength

Index